UNIVERSITÀ DEGLI STUDI DELL'INSUBRIA

DIPARTIMENTO DI SCIENZA E ALTA TECNOLOGIA

PhD Thesis in Chemical and Environmental Sciences – Chemical Sciences

FROM MOLECULES TO MATERIALS: UNDERSTANDING FUNCTIONAL NANOMATERIALS FROM FIRST-PRINCIPLES APPROACHES

Supervisor: Prof. Dr. Gloria Tabacchi

PhD Candidate: Cristiano Invernizzi

ID: 730317

ACADEMIC YEAR 2024/2025

A Giulia,

per esserci sempre stata

– Table of Contents –

Scientific Profile of the Candidate

Cristiano Invernizzi

PhD Candidate in Chemistry – Physical Chemistry Area, Computational Chemistry.

I conducted my PhD in Chemistry at the Insubria University of Como (Italy), within the Department of Science and High Technology (DiSAT), as a member of the Physical Chemistry Group led by Prof. Dr. Gloria Tabacchi. During that period, I employed first-principles computational methods to investigate how functional nanomaterials can be rationally understood by exploring molecular interactions. Despite addressing distinct phenomena, all parts of my research share a common methodological backbone: Density Functional Theory (DFT) calculations applied to molecules and periodic systems. This approach enabled me to systematically investigate how molecular-level interactions could explain material properties, supporting a rational understanding of functional materials across different length scales and application fields, including gas sensing, thin-film growth, and supramolecular recognition.

- Publications:

- Mattia Benedet, Davide Barreca, Ettore Fois, Roberta Seraglia, Gloria Tabacchi, Marco Roverso, Gioele Pagot, **Cristiano Invernizzi**, Alberto Gasparotto, Alexandra A. Heidecker, Alexander Pöthig, Emanuela Callone, Sandra Dirè, Sara Bogialli, Vito Di Noto and Chiara Maccato – "*Interplay between coordination sphere engineering and properties of nickel diketonate-diamine complexes as vapor phase precursors for the growth of NiO thin films*", Dalton Trans., **2023**, 52, 10677–10688. (Selected for the Outside Front Cover (Dalton Transactions, 2023, Vol. 52, Issue 31)).

- Mattia Benedet, Chiara Maccato, Gioele Pagot, **Cristiano Invernizzi**, Cinzia Sada, Vito Di Noto, Gian Andrea Rizzi, Ettore Fois, Gloria Tabacchi, and Davide Barreca – *"Growth of NiO Thin Films in the Presence of Water Vapor: Insights from Experiments and Theory"*, The Journal of Physical Chemistry C, **2023**, 127 (45), 22304-22314.

- **Cristiano Invernizzi**, Gloria Tabacchi, Roberta Seraglia, Mattia Benedet, Marco Roverso, Chiara Maccato, Sara Bogialli, Davide Barreca, and Ettore Fois – *"On the fragmentation of Ni(II) β-diketonate-diamine complexes as molecular precursors for NiO films: a theoretical and experimental investigation",* Molecules, **2024**, 29 (3), 642.

- Helena Roithmeyer, Jan Bühler, Olivier Blacque, Isik Tuncay, Thomas Moehl, **Cristiano Invernizzi**, Florian Keller, Marcella Iannuzzi, S. David Tilley – "*The Swiss Army Knife of Electrodes: Pillar[6]arene-Modified Electrodes for Molecular Electrocatalysis Over a Wide pH Range*"; Angew. Chem. Int. Ed., **2025**, 64, e202413144.

- Ettore Fois, Chiara Maccato, Davide Barreca, **Cristiano Invernizzi** and Gloria Tabacchi – "*Impact of -OH surface defects on the electronic and structural properties of nickel oxide thin films*"; Dalton Trans., **2025**, 54, 2765. (Selected for the Back Cover (Dalton Transactions, 2025, Vol. 54)).

- **Cristiano Invernizzi**, Laura M. Grimm, Frank Biedermann, Ettore Fois and Gloria Tabacchi – "*Mechanistic insights into water-stabilized dye-neurotransmitter intermolecular complexes in zeolite channels*"; Chem. Commun., **2025**, 61, 4160. (Selected for the Outside Front Cover (Chemical Communications, 2025, Vol. 61)).

- In preparation:

- **Cristiano Invernizzi**, Florian Keller, Marcella Iannuzzi – "*Unraveling the molecular stabilization of Pillar[6]arene macrocycles on In_2O_3 and ITO surfaces".*

- **Cristiano Invernizzi**, Luca Imbrighi, Emanuele Pasquini, Ettore Fois, Gloria Tabacchi – "*First-Principles Insights into Nitrogen Mustard CWAs and Their Simulant on Zinc Oxide Surfaces".*

- Conference Presentations:

- **C. Invernizzi**, L. Grimm, F. Biedermann, G. Tabacchi, E. Fois
  Electronic Properties of Neurotransmitters in a Hybrid System with Zeolite L,
  AIZ Day 2022 - International Workshop on Zeolites Science and Technology, Politecnico of Turin, Turin, Italy, 24th – 25th of November 2022,
  Participation with Poster Presentation.

- **C. Invernizzi**, L. Grimm, F. Biedermann, G. Tabacchi, E. Fois
  Electronic Properties of Neurotransmitters in a Hybrid System with Zeolite L,
  30 YEARS OF INSTM: PAST, PRESENT AND FUTURE OF THE CONSORTIUM, Casa della Gioventù, Bressanone, Italy, 22nd – 25th of January 2023,
  Participation with Poster Presentation.

- **C. Invernizzi**, L. Grimm, F. Biedermann, G. Tabacchi, E. Fois
  Electronic Properties of Neurotransmitters in a Zeolite L-Based Nanosensor,
  XLIX National Congress of the Physical Chemistry Division of the Società Chimica Italiana,
  University of Turin, Turin, Italy, 04th – 07th of September 2023,
  Oral Presentation.

- Scientific Contributions to Conference Presentations:

- M. Benedet, D. Barreca, E. Fois, R. Seraglia, G. Tabacchi, M. Roverso, G. Pagot, **C. Invernizzi**, A. Gasparotto, A. Heidecker, A. Pöthig, E. Callone, C. Sada, S. Dirè, S. Bogialli, V. Di Noto, C. Maccato
  Interplay between coordination sphere engineering and properties of nickel diketonate-diamine complexes as vapor phase precursors for the growth of NiO thin films,
  EUROCVD / Baltic ALD,
  Leuven, Belgium, 29th – 02nd May 2023
  Poster presentation (work based on article co-authored by the candidate).

- E. Fois, **C. Invernizzi**, G. Tabacchi, R. Seraglia, M. Benedet, M. Roverso, C. Maccato, S. Bogialli, D. Barreca
  On the fragmentation of Ni(II) β-diketonate-diamine complexes as molecular precursors for NiO films: a theoretical and experimental investigation,
  EUROCVD & ALD,
  Monastery of San Nicolò l'Arena, Catania, Italy, 02nd – 05th June 2025
  Oral presentation (original article co-authored by the candidate; presentation given by a research group member due to author's absence).

- E. Fois, **C. Invernizzi**, G. Tabacchi, L. Imbrighi
  Chemical Warfare Agents and Their Simulants from First Principles,
  Joint 50th Congress of the Physical Chemistry Division of the Società Chimica Italiana and 5th European Conference on Physical Chemistry,
  University of Pisa, Pisa, Italy, 29th June – 03rd July 2025
  Poster presentation (designed by the candidate and based on ongoing work).

- Period Abroad / Mobility:

Zurich – University of Zurich (UZH), Department of Chemistry (Winterthurerstrasse 190)

Prof. Dr. Jürg Hutter and Prof. Dr. Marcella Mauri Iannuzzi Group

From: 11.03.2024 - Till: 31.08.2024 (six months)

Research topic: Computational study of the adsorption of an organic molecule on a metal oxide surface. The project aimed to evaluate a promising system for the development of advanced nanomaterials with potential applications in energy conversion, sensing, electrocatalysis, and environmental remediation.

- Collaborations:

- Dr. Frank Biedermann Research Group, Karlsruhe Institute of Technology (KIT), Germany.

- Multi-Functional Nanomaterial Group, Prof. Dr. Chiara Maccato (Padova University, Italy) and Dr. Davide Barreca (ICMATE-CNR, Italy).

- Other Activities:

- Tutoring activity (Exercises) for the “Chimica Fisica 1” course given by Prof. Dr. Gloria Tabacchi, 26th October 2022 - 6th March 2025.

- Tutoring activity (Laboratory) for the “Chimica Fisica 2” course given by Prof. Dr. Ettore Silvestro Fois, 12th December 2022 - 17th January 2025.

- PhD Students' Representative, December 2022 - November 2024.

- Orientation activities for high school and bachelor's degree students, April 2022 – March 2024.

– Introduction –

Functional nanomaterials represent a rapidly expanding class of systems characterized by properties that emerge from their structural organization at the nanoscale. Their relevance spans a broad range of applications, including energy conversion, chemical sensing, and molecular recognition. Understanding and predicting the atomistic or molecular interactions that govern their formation and properties has become an essential step toward developing efficient and targeted design strategies. This Thesis addresses this challenge by adopting a fully computational perspective, based on first-principles approaches, to investigate how molecular-level interactions can be modulated and exploited to engineer functional nanomaterials with controlled physicochemical behavior. The central goal of this work is to demonstrate that the rational design of functional nanomaterials can be achieved by understanding molecular interactions along three distinct, yet conceptually related, molecule-to-material strategies: (i) fragmentation of molecular precursors, (ii) encapsulation in confined nanospaces, and (iii) surface adsorption. Taken together, these strategies enable the investigation of different aspects of nanomaterial formation, each corresponding to a specific condition, ranging from gas-phase reactivity to molecular confinement and surface interactions. In this context, rather than treating these studies as isolated case analyses, this Thesis proposes a unified framework in which fragmentation, confinement, and surface binding are regarded as different manifestations of the same principal outcome: control at the molecular scale determines the structure and function of the resulting nanomaterial. The work relies on a combination of first-principles computational approaches, with Density Functional Theory (DFT) as the methodological core. Time-Dependent DFT (TD-DFT) is employed to study electronic excitations in photoactive systems, while periodic DFT calculations are used to model extended solid-state structures and molecule-surface interfaces. This multi-method approach enables the characterization of complex systems under realistic conditions and provides access to detailed information on structure, energetics, charge distribution, and electronic behavior. In particular, the computational investigation provides insights into structure-function relationships that are often not directly accessible by experimental techniques, and thus plays a crucial complementary role in understanding the material behavior at the atomic scale. The Thesis is organized into four Chapters:

- Chapter 1 provides a theoretical background on the computational methods used throughout this work. It introduces the Hartree-Fock approach and its post-HF extensions, including second-order Møller-Plesset perturbation theory (MP2), and discusses the foundations of DFT and TD-DFT. In addition, a short Section is devoted to the treatment of periodic systems, introducing concepts such as plane-wave basis sets, k-point sampling, and pseudopotentials. This theoretical introduction is intended to offer the reader the necessary context for understanding the computational tools employed in the subsequent Chapters.
- Chapter 2 presents a computational study of Ni(II) β-diketonate-TMEDA molecular precursors used in chemical vapor deposition (CVD) processes for the fabrication of NiO nanostructures. The analysis combines several levels of investigation. First, the structural and electronic properties of the precursors are characterized in the gas phase and in the

presence of water molecules, providing insight into their thermal stability and reactivity under CVD-like conditions. Then, gas-phase fragmentation behavior is explored via DFT and compared with ESI-HRMS/MS data, enabling the identification of key fragments. Finally, periodic slab models of NiO(100) surfaces, both regular and with hydroxyl defects, are used to describe the structural and electronic features of the resulting oxide material. The study was conducted in collaboration with Dr. Davide Barreca and Prof. Dr. Chiara Maccato at the Department of Chemical Sciences and CNR-ICMATE, University of Padova (Italy), who provided the experimental data.

- Chapter 3 investigates a supramolecular nanosensor composed of a fluorescent dicationic dye encapsulated within the channel of a zeolite L framework. The confined system is first characterized in terms of structural organization and optical properties, using periodic DFT, TD-DFT, and ab initio molecular dynamics (AIMD). Subsequently, the interaction of this pre-organized nanosensor with serotonin, a molecular target of biological relevance, is explored to assess the emergence of a new band in the optical spectra, and evaluate the nanosensor's response. TD-DFT calculations and thermally averaged spectra reveal that this new band falls within the visible region and originates from a stable supramolecular arrangement. This work illustrates how confinement within nanoporous materials can be leveraged to modulate optoelectronic properties and enable selective molecular recognition. The computational study was developed in collaboration with Dr. Laura M. Grimm and Dr. Frank Biedermann at the Institute of Nanotechnology, Karlsruhe Institute of Technology (KIT, Germany), who provided the experimental support.

- Chapter 4 focuses on surface adsorption as a strategy to either construct functional hybrid nanomaterials or promote molecular recognition through interactions with metal oxide surfaces. Two systems are considered, corresponding to independent but complementary research lines. In Section 4.1, the covalent anchoring of a Pillar[6]arene macrocycle onto indium oxide (In_2O_3) and indium tin oxide (ITO) surfaces is modeled via two plausible pathways and analyzed through energy profiles, charge density difference (CDD) maps, and Bader charge calculations. This work was conducted during a research period abroad at the University of Zurich (UZH, Switzerland) in the group of Prof. Dr. Juerg Hutter and Prof. Dr. Marcella Iannuzzi, in collaboration with the experimental group of Prof. Dr. David Tilley. Section 4.2 presents preliminary results on the interaction of Chemical Warfare Agents (CWAs) and a structurally distinct simulant with ZnO$(10\bar{1}0)$ surfaces, both regular and oxygen-enriched. The objective is to assess whether the simulant can reproduce CWAs' behavior, despite structural differences, by comparing their properties in vacuum and upon adsorption. The study combines gas-phase modeling, surface calculations, charge analysis, and TD-DFT spectra, offering early insights into the electronic mechanisms underlying chemiresistive detection.

Across these Chapters, the Thesis aims to highlight how first-principles computational methods can provide a consistent and predictive framework for understanding and engineering functional nanomaterials. While each Chapter addresses a distinct molecular or periodic system, they are unified by a common methodological and conceptual core: the control of molecular interactions as a fundamental design parameter. This unified approach enables the

connection between molecular structure, electronic properties, and material function, offering insights that complement experimental observations and support the rational design of systems for real-life applications. Although applied to chemically and functionally different systems, the computational strategies employed throughout the Thesis remain coherent, underscoring its reliability and general applicability to the study of functional nanomaterials.

– Chapter 1 –

Theoretical Foundations of First Principles Approaches in Molecular and Periodic Systems

The accurate description of matter at the atomic and molecular scale requires a rigorous theoretical framework rooted in quantum mechanics. In the last few decades, first-principles electronic structure methods, firmly grounded in quantum mechanical principles, have become indispensable tools in computational chemistry and materials science, enabling not only the prediction, but also a deep rationalization of structural, electronic, and spectroscopic properties across a wide range of chemical systems [1-3]. In this context, this Chapter provides a theoretical overview of the main quantum chemical approaches employed in this Thesis, with a particular focus on methods applicable to both molecular and periodic systems. The discussion begins with the time-independent Schrödinger equation and the Born-Oppenheimer approximation, which together provide the conceptual foundation for all electronic structure calculations [4,5]. It then explores the Hartree-Fock method and its limitations, highlighting the motivation for the development of correlated methods such as Møller-Plesset perturbation theory (MP2) [4-7]. The Chapter then introduces Density Functional Theory (DFT), which has become the method of choice for studying large and complex systems due to its balance between accuracy and computational cost [8-11]. Particular attention is given to the conceptual background of DFT, its practical implementations, and the role of exchange-correlation functional within its approximations [8-11]. Extensions to excited states via Time-Dependent DFT (TD-DFT) are also discussed [12,13]. Finally, the Chapter concludes with a concise Section devoted to the theoretical foundations of periodic first principles simulations. Concepts such as periodic boundary conditions, plane-wave basis sets, and reciprocal space sampling are briefly introduced, providing essential background for the modeling of crystalline solids and extended surfaces, which are extensively treated in subsequent Chapters [14].

1.1 The Time-Independent Schrödinger Equation

The mathematical description of matter at the atomic and molecular scale is fundamentally governed by quantum mechanics. At the heart of this formalism lies the time-independent Schrödinger equation, formulated by Erwin Schrödinger, which provides access to both the total energy and the wavefunction of any chemical system. In its general form, the equation is written as an eigenvalue problem:

$$\hat{H}\varphi(r) = E\varphi(r) \qquad \textit{Eqn.1}$$

Here, in the case of one particle with spatial coordinates r = (x,y,z), $\hat{H}$ is the Hamiltonian operator, $\varphi(r)$ is the particle's wavefunction, and E is the associated energy eigenvalue [4,5].

For a general chemical system composed of N electrons and nuclei, the full molecular Hamiltonian in atomic units is given by:

$$\hat{H} = -\sum_{i=1}^{N}\frac{1}{2}\nabla_i^2 - \sum_{A=1}^{M}\frac{1}{2M_A}\nabla_A^2 - \sum_{i=1}^{N}\sum_{A=1}^{M}\frac{Z_A}{r_{iA}} + \sum_{i=1}^{N}\sum_{j>i}^{N}\frac{1}{r_{ij}} + \sum_{A=1}^{M}\sum_{B>A}^{M}\frac{Z_A Z_B}{R_{AB}}$$

In this expression:

- r_{iA} is the distance between electron *i* and nucleus *A*,
- r_{ij} is the distance between electrons i and j,
- R_{AB} is the distance between nuclei A and B,
- M_A is the nuclear-to-electron mass ratio for nucleus A and B
- Z_A are the atomic numbers of nuclei A and B, respectively.

The first two terms describe the kinetic energy of electrons and nuclei, respectively. The third term accounts for the attractive Coulomb interaction between electrons and nuclei, while the fourth and fifth terms represent electron-electron and nucleus-nucleus repulsions [4,5]. In practice, the exact solution of Eqn.1 is only achievable for systems with one electron, such as hydrogen-like atoms. For multi-electron systems, approximations are essential. In this context, the solution strategy typically involves assuming a trial wavefunction constructed as a linear combination of atomic orbitals [3]. To make the problem tractable, two foundational approximations are introduced: i) the Born-Oppenheimer approximation (discussed in Section 1.2), which separates nuclear and electronic motion, and the variational principle (see Section 1.3), which allows for the optimization of the trial wavefunction to minimize the total energy [3-5]. These fundamental principles form the theoretical basis for the development of quantum chemical methods, starting from the Hartree-Fock approximation and extending to electron correlation techniques.

1.2 Born-Oppenheimer Approximation

Given that nuclear motion is significantly slower than electronic motion, due to the much greater mass of nuclei compared to electrons, it is possible to treat the nuclei as stationary while allowing the electrons to move within electrostatic field generated by fixed nuclei. This approximation, known as the Born-Oppenheimer approximation [3-5], enables the total wavefunction of a molecular system to be factorized into two components: one describing the electronic motion in the field of fixed nuclei, and the other accounting for the nuclear dynamics. As a result, the full time-independent Schrödinger equation can be separated into two distinct equations, one for the electronic motion and another for the nuclear motion. The electronic Schrödinger equation is given by:

$$\hat{H}_{elec}\Psi_{elec} = E_{elec}\Psi_{elec} \qquad Eqn.2$$

Where the electronic Hamiltonian $\hat{H}_{elec}$ in atomic units is:

$$\widehat{H}_{elec} = \sum_{i=1}^{N}\left(-\frac{1}{2}\nabla_i^2 - \sum_{A=1}^{M}\frac{Z_A}{r_{iA}} + \sum_{j>i}\frac{1}{r_{ij}}\right)$$

In this expression, N is the number of electrons, M is the number of nuclei, Z_A is the atomic number of nucleus A, r_{iA} is the distance between electron i and nucleus A, and r_{ij} is the distance between electrons i and j. The first term corresponds to the electronic kinetic energy, the second term to the electron-nucleus Coulomb attraction interaction, and the third to the electron-electron repulsion. The electronic energy E_{elec} and the electronic wavefunction Ψ_{elec} depend parametrically on the fixed nuclear positions [3-5]. The total energy of the system for a given nuclear configuration also includes the repulsive Coulomb interaction between nuclei, which is constant for fixed nuclei:

$$E_{tot} = E_{elec} + \sum_{A=1}^{M}\sum_{B>A}^{M}\frac{Z_A Z_B}{R_{AB}} \qquad Eqn.3$$

Where R_{AB} is the distance between nuclei A and B. In practice, determining the most stable structure of a molecule implies computing the electronic wavefunction and energy over a range of nuclear arrangements, namely solving the electronic Schrödinger equation, thus generating a potential energy surface (PES). The minimum of this PES corresponds to the minimum energy structure of the system [3-5].

1.3 The Variational Principle

One of the fundamental tools in quantum chemistry for approximating the ground-state energy of a molecular system is the variational principle [3,4]. According to this principle, the expectation value of the Hamiltonian operator $\widehat{H}$, computed using any normalized trial wavefunction ψ_i, will always be greater than or equal to the exact ground-state energy E_0 of the system [3,4]. This is formally expressed as follows:

$$E[\psi_i] = \frac{\int \psi_i^*(r_1,\dots,r_N)\widehat{H}\psi_i(r_1,\dots,r_N)d\tau}{\int \psi_i^*(r_1,\dots,r_N)\psi_i(r_1,\dots,r_N)d\tau} \geq E_0 \qquad Eqn.4$$

Here, $E[\psi_i]$ is the energy expectation value for the chosen trial wavefunction ψ_i, while E_0 and ψ_0 represent the exact ground-state energy and wavefunction, respectively, quantities that are typically unknown for many-electron systems [3,4]. The power of the variational principle lies in its ability to transform the problem of solving the time-independent Schrödinger equation into a minimization problem. That is: by systematically varying the parameters of a suitably chosen trial wavefunction, one can obtain successively lower estimates of the energy, converging toward the true ground-state value [6]. In practical quantum chemical calculations, the trial wavefunction ψ_i is expressed as a linear combination of atomic basis functions φ_μ:

$$\psi_i = \sum_{\mu=1}^{N} c_{\mu i}\varphi_\mu \qquad Eqn.5$$

Where $c_{\mu i}$ are the variational parameters (typically expansion coefficients) to be optimized [6]. These coefficients are determined by applying the variational principle and solving the resulting secular equations, which lead to a generalized eigenvalue problem. Through this diagonalization process, one obtains the molecular orbital energies and the corresponding coefficients that define each orbital [3,4,6]. In essence, the variational theorem provides a rigorous foundation for methods such as Hartree-Fock theory (see Section 1.5), where a trial wavefunction is constructed as a Slater determinant (see Section 1.4) composed of single-particle spin orbitals. The optimal determinant is found by minimizing the total energy with respect to the molecular orbital coefficients, under orthonormality constraints. This principle also underpins more advanced post-Hartree-Fock methods (Section 1.6) and serves as a cornerstone of modern electronic structure theory [3,4,6].

1.4 Slater Determinants

In quantum chemistry, the antisymmetry requirement for electronic wavefunctions, derived from the Pauli exclusion principle, dictates that the total wavefunction for a system of indistinguishable electrons must change sign upon exchange of any two electrons. A powerful mathematical construct that naturally enforces this antisymmetry is the Slater determinant [2-6]. This is based on a fundamental property of determinants: if two rows (or columns) of a determinant are exchanged, the determinant changes sign; if two rows are identical, i.e., if two electrons occupy the same spin-orbital, the determinant is zero. Therefore, constructing the electronic wavefunction as a determinant ensures that two electrons cannot occupy the same quantum state, as required by the Pauli principle [2-6].

For an N-electron system, the Slater determinant is written as:

$$\psi(x_1, x_2, \ldots, x_N) = \frac{1}{\sqrt{N!}} \begin{vmatrix} \phi_1(x_1) & \phi_2(x_1) & \cdots & \phi_N(x_1) \\ \phi_1(x_2) & \phi_2(x_2) & \cdots & \phi_N(x_2) \\ \vdots & \vdots & \ddots & \vdots \\ \phi_1(x_N) & \phi_2(x_N) & \cdots & \phi_N(x_N) \end{vmatrix} \qquad Eqn.6$$

Where ϕ_i denotes the spin-orbital (a one-electron function including spatial and spin coordinates) occupied by the i-th electron, and x_j represents the space and spin coordinates of electron j. The pre-factor $(N!)^{1/2}$ ensures proper normalization.

These monodeterminantal wavefunctions form the cornerstone of Hartree-Fock theory, which approximates the total electronic wavefunction as a single Slater determinant composed of optimized spin-orbitals. While this approach captures the exchange interaction arising from antisymmetry, it neglects electron correlation, i.e., the instantaneous Coulomb interaction between electrons that move to avoid each other in real systems [3,4,6]. Despite this limitation, the use of Slater determinants remains a foundational concept in electronic structure theory, enabling the construction of more sophisticated methods that go beyond the Hartree-Fock approximation by including correlation effects, either through configuration interaction [4,5], Møller-Plesset perturbation theory (Section 1.6), or density functional theory (DFT, Section 1.7).

1.5 The Hartree-Fock Method

The Hartree-Fock (HF) method [3,4] is a fundamental first principles approach in quantum chemistry that approximates the many-electron wavefunction by a single Slater determinant constructed from orthonormal spin-orbitals. This ansatz ensures the antisymmetry of the total wavefunction, as required by the Pauli exclusion principle (see Section 1.4). In the Hartree-Fock framework, electrons are treated as independent particles moving in the average electrostatic field generated by all other electrons. The explicit electron-electron repulsion terms in the full Hamiltonian are replaced by mean-field operators, which include both Coulomb and exchange contributions. As a result, the problem of solving the many-body Schrödinger equation is recast into a set of effective one-electron equations known as the Hartree-Fock equations [3-6]:

$$\widehat{F}_i \phi_i = \varepsilon_i \phi_i \qquad \text{Eqn.7}$$

Here, $\widehat{F}_i$ is the Fock operator, which governs the motion of electron i in the mean field generated by the other electrons. It is defined as:

$$\widehat{F}_i = \widehat{h}_i + \sum_{j}^{N} \left(\widehat{J}_J - \widehat{K}_J \right)$$

Where $\widehat{h}_i$ is the one-electron core Hamiltonian (kinetic energy + nuclear attraction), $\widehat{J}_J$ is the Coulomb operator, and $\widehat{K}_J$ is the exchange operator, both of which depend on the occupied spin-orbitals ϕ_j. Due to this dependence, the Hartree-Fock equations must be solved iteratively in a procedure known as the Self-Consistent Field (SCF) method [3-6]. To render the problem tractable for molecular systems, each spin-orbital ϕ_i is expanded as a linear combination of a finite set of atomic basis functions ϕ_α [3-6]:

$$\phi_i = \sum_{\alpha=1}^{N} c_{\alpha i} \varphi_\alpha$$

Substituting this into the Hartree–Fock equation leads to the matrix form of the problem [4,5]:

$$\hat{F}_i \sum_{\alpha}^{N} c_{\alpha i}\varphi_\alpha = \varepsilon_i \sum_{\alpha}^{N} c_{\alpha i}\varphi_\alpha \qquad \text{Eqn. 8}$$

This equation can be rewritten compactly in matrix notation as: $FC = SC\varepsilon$, known as the Roothaan-Hall equations, where: F is the Fock matrix, S is the overlap matrix between basis functions, C is the matrix of molecular orbital coefficients $c_{\alpha i}$, ε is the diagonal matrix of orbital energies [3-6]. Solving the Roothaan-Hall equations involves diagonalizing the Fock matrix, but since F itself depends on the molecular orbitals (through the Coulomb and exchange integrals), the solution requires an iterative SCF loop, as summarized below [2,3,6]:

(1) Initial guess of the molecular orbitals ϕ_i or the coefficients $c_{\alpha i}$ (e.g., from a core Hamiltonian).

(2) Construction of the Fock matrix F using the current orbitals.

(3) Evaluation of the electron repulsion integrals, including Coulomb and exchange contributions.

(4) Diagonalization of the Fock matrix to obtain updated molecular orbital energies and coefficients.

(5) Update of the density matrix and recomputation of F.

(6) Convergence check: if the change in energy and orbitals is below a threshold, the procedure terminates. Otherwise, return to step 2.

1.6 Møller-Plesset (MP) Perturbation Theory

While the Hartree-Fock (HF) method (see Section 1.5) provides a valuable first approximation to the electronic structure of molecules, it inherently neglects electron correlation, namely the instantaneous interaction between electrons that is not captured by the mean-field approximation [4,5]. Post-Hartree-Fock methods [1-7] aim to recover this missing correlation energy by going beyond the single-determinant description. One of the most widely used approaches in this category is Møller–Plesset perturbation theory (MP) [4,5,7]. This method is based on Rayleigh-Schrödinger perturbation theory, in which the exact electronic Hamiltonian is written as the sum of a zeroth-order Hamiltonian and a perturbation term:

$$\hat{H} = \hat{H}_0 + \hat{V} \qquad \text{Eqn. 9}$$

where:

- $\hat{H}$ is the full electronic Hamiltonian,
- $\hat{H}_0$ is the unperturbed Hamiltonian,
- $\hat{V}$ is the perturbation operator that accounts for the remaining interactions.

In the Møller-Plesset (MP) approach, the zeroth-order Hamiltonian is taken to be closely related to the Fock operator derived from the Hartree-Fock method [5,7]. Specifically, the unperturbed Hamiltonian is defined as:

$$\widehat{H_0} \equiv \hat{F} + \langle \Phi_0 | (\hat{H} - \hat{F}) | \Phi_0 \rangle \qquad \text{Eqn. 10}$$

This choice ensures that the zeroth-order wavefunction Φ_0 is the Hartree-Fock determinant, and the zeroth-order energy is simply the sum of the Fock orbital energies [4,5,7]. The perturbation operator is then defined as the correlation potential:

$$\hat{V} \equiv \hat{H} - \widehat{H_0} = \hat{H} - (\hat{F} + \langle \Phi_0 | (\hat{H} - \widehat{F}) | \Phi_0 \rangle) \qquad \textit{Eqn.11}$$

In this formulation, the Fock operator $\hat{F}$ represents the motion of independent electrons in a mean field, and Φ_0 is its lowest energy eigenfunction:

$$\hat{F}\Phi_0 \equiv \sum_{k=1}^{N} \hat{f}(k)\, \Phi_0 = 2 \sum_{i=1}^{\frac{N}{2}} \varepsilon_i\, \Phi_0 \qquad \textit{Eqn.}\, 12$$

Here, $\hat{f}(k)$ is the one-electron Fock operator acting on electron k, ε_i is the orbital energy of the doubly occupied i-th spin-orbital, and N is the total number of electrons. The factor of 2 accounts for spin pairing in closed-shell systems [5,7]. In second-order Møller–Plesset theory (MP2), the first non-null correction to the energy appears at second order in perturbation theory. The MP2 total energy is given by $E = E_{HF} + E^2$, where E^2 is the second-order energy correction [5,7]. This term quantitatively estimates the contribution of electron correlation by accounting for virtual excitations from the Hartree-Fock reference determinant to doubly excited configurations. The MP2 energy correction can be computed analytically using the spin-orbital basis and is computationally efficient compared to more elaborate post-HF methods (e.g., CI or CCSD) [4-7]. However, it assumes that the HF reference is a good zeroth-order approximation, which is not always valid, particularly for systems with significant static correlation (e.g., near-degenerate states, transition metals) [4-7]. Despite these limitations, MP2 remains a widely adopted method due to its favorable balance between computational cost and accuracy, particularly for closed-shell, weakly correlated systems [7].

1.7 Density Functional Theory (DFT)

As shown in the previous Sections, first principles methods typically begin with the Hartree-Fock (HF) approximation, in which one-electron equations are solved to determine a set of spin-orbitals, antisymmetrized products of single-electron wavefunctions that satisfy the Pauli exclusion principle [5]. Within this framework, based on the Born-Oppenheimer

approximation, each electron experiences an average potential field generated by all other electrons in the system. This antisymmetrized product ensures an exact treatment of exchange interactions, enforcing the fundamental property that the total wavefunction changes sign upon particle exchange: $\Psi(1,2,...i,j,\ldots N) = -\Psi(1,2,...j,i,\ldots N)$, for the exchange of two i,j fermions [4,5]. While the HF method accounts for exchange, it neglects dynamic electron correlation. To address this limitation, post-Hartree-Fock methods have been developed, which retain the HF determinant as a reference and incorporate electron correlation effects by expanding the wavefunction beyond a single Slater determinant [4,5,7]. These methods have become standard in quantum chemistry, especially when high accuracy is required. However, they involve a significant computational cost, which increases considerably with system size, typically with a power law N^m, where $m \geq 5$ and N is the number of basis functions. In comparison, HF scales as N^4 [4-7]. The correlation energy is conventionally defined as the difference between the total energy obtained from a post-HF method and the HF energy. Although this contribution often represents only a small percentage of the total electronic energy, it can be crucial for the accurate description of bond dissociation, intermolecular interactions, and reaction energetics [5]. An alternative approach is offered by Density Functional Theory (DFT) [5,8-11]. Unlike HF-based methods, DFT does not rely on the electronic wavefunction as a central quantity, but rather on the electron density $\rho(r)$, a three-dimensional scalar field that integrates to the total number of electrons in the system. Modern DFT techniques provide approximate, but often reliable, descriptions of both exchange and correlation effects, while remaining computationally less demanding than post-HF methods [5,8-11]. DFT thus enables the treatment of medium to large molecular systems, including those containing hundreds of atoms, at a significantly reduced computational cost [1,2,6]. The conceptual origins of DFT can be traced back to the early years of quantum mechanics, specifically to the Thomas-Fermi model (1920-1930), which proposed an approximate relationship between the electron density and total energy [8-11]. However, it was not until the formulation of the Hohenberg-Kohn theorems that DFT acquired a rigorous theoretical foundation [10]. These theorems established that, for a given external potential (typically determined by the positions and charges of atomic nuclei), the ground-state energy E of an interacting electron system is a unique functional of the electron density $\rho(r)$ [10]. This result guarantees the existence and uniqueness of a universal density functional, although it does not provide an explicit expression for it. A major breakthrough came with the development of the Kohn-Sham formalism [11], which allows one to map the complex interacting system onto a fictitious system of non-interacting electrons that reproduces the same ground-state density. This leads to a set of self-consistent one-electron equations that are computationally accessible and form the basis of nearly all practical DFT implementations [8-11].

1.7.1 The Hohenberg-Kohn Theorems

Before introducing the foundational theorems of density functional theory (DFT), it is useful to clarify the concept of a functional, in contrast to that of a function. A function $y = f(x)$ returns a single value of y for a given value of x. In contrast, a functional $Y = F[X]$ takes an entire function X as its input and returns a single number as output. This is different from a regular

function *f(x)*, which takes a single number *x* as input. For example, $f(x) = e^{-x}$ is a function, while the expression:

$$Y = \int_0^\infty e^{-x} dx$$

is a functional, as it maps the entire function $x \mapsto e^{-x}$ onto a single numerical value. In the context of DFT, the total ground-state energy of a many-electron system is expressed as a functional of the electron density, namely $E_0[\rho(r)]$.

The Hohenberg-Kohn theorems [10], published in 1964, represent the theoretical cornerstone of DFT and provide a rigorous basis for replacing the many-electron wavefunction with the electron density as the central variable [5,8-10]. The first Hohenberg-Kohn theorem states that, for any system of interacting electrons in an external potential $v_{ext}(r)$, the ground-state electron density $\rho_0(r)$ uniquely determines the external potential, and thus the full Hamiltonian, the many-electron wavefunction, and all properties of the system. Formally: *"There exists a one-to-one correspondence between the ground-state electron density ρ(r) and the external potential $v_{ext}(r)$, up to a constant."* [10]. This implies that the ground-state energy E_0 is a unique functional of the electron density, namely $E_0 = E_0[\rho]$. Although the theorem ensures the existence and uniqueness of this functional, it does not provide an explicit form for it; this remains one of the central challenges of DFT [8-10].

The second Hohenberg-Kohn theorem [10] introduces a variational principle for the density. It states that the ground-state energy of the system is minimized by the true ground-state density $\rho_0(r)$. In other words: *"For any trial density $\tilde{\rho}(r)$ that is N-representable and integrates to the correct number of electrons, the corresponding energy functional satisfies the inequality: $E[\tilde{\rho}] \geq E[\rho_0]$, with equality if and only if $\tilde{\rho} = \rho_0$."* [10]. This result is analogous to the variational principle in wavefunction-based quantum mechanics (see Section 1.3) and legitimizes the search for the ground state by minimizing the energy functional over all reasonable densities [8-10].

Together, these two theorems provide the formal justification for DFT: all ground-state properties of an electronic system are functionals of the electron density, and the correct density minimizes the total energy functional [5,6,8,9]. However, to make DFT practical, an explicit construction of the energy functional is needed: this challenge is addressed in the Kohn-Sham formalism [11], discussed in the next Sub-section.

1.7.2 The Kohn-Sham Equations

While the Hohenberg-Kohn theorems [10] guarantee that the ground-state energy is a unique functional of the electron density, they do not provide any guideline on how to determine this density in practice. This problem was addressed by Kohn and Sham in 1965 [11], who proposed a formally exact method to map the original many-electron system onto a fictitious system of non-interacting electrons that reproduces the same ground-state density as the real interacting system [5,6,8-11]. In the Kohn-Sham formalism [11], the total ground-state energy of the system is written as a functional of the electron density $\rho(r)$:

$$E_0[\rho(r)] = T_s[\rho(r)] + V_{ne}[\rho(r)] + J[\rho(r)] + E_{XC}[\rho(r)] \qquad \textit{Eqn.13}$$

Where:

- $T_s[\rho(r)]$ is the kinetic energy of a fictitious non-interacting electron system with the same density ρ,
- $V_{ne}[\rho(r)]$ is the nuclear-electron attraction energy,
- $J[\rho(r)]$ is the classical Coulomb (electron-electron repulsion) energy,
- $E_{XC}[\rho(r)]$ is the exchange-correlation functional, which accounts for: (i) the difference between the true kinetic energy and T_s (i.e., the kinetic correlation); (ii) the non-classical contributions to electron-electron repulsion, including exchange and dynamic correlation effects [8-11].

This decomposition corresponds to the more detailed expression sometimes written as:

$$E_0[\rho(r)] = T_s[\rho(r)] + V_{ne}[\rho(r)] + J[\rho(r)] + \Delta T[\rho(r)] + \Delta V_{ee}[\rho(r)] \qquad Eqn.14$$

Where $E_{XC}[\rho(r)] = \Delta T[\rho(r)] + \Delta V_{ee}[\rho(r)]$ [5,6,8-11].

The electron density is reconstructed from the Kohn-Sham orbitals ψ_i, which are obtained by solving a set of self-consistent one-electron equations:

$$\rho(r) = \sum_{i=1}^{n} |\psi_i(r)|^2$$

$$\widehat{h_i}^{KS}\psi_i = \varepsilon_i^{KS}\psi_i \qquad Eqn.15$$

where $\widehat{h_i}^{KS}$ is the Kohn-Sham Hamiltonian (or operator), ε_i^{KS} are the Kohn-Sham energies. The Kohn-Sham operator includes four components:

$$\widehat{h_i}^{KS} = \hat{T} + \hat{V}_{ne} + \hat{J} + \hat{V}_{XC} \qquad Eqn.16$$

With: $\hat{T}$ as the kinetic energy operator; $\hat{V}_{ne}$ as the electron-nuclear attraction; $\hat{J}$ as the classical Coulomb repulsion; $\hat{V}_{XC}$ as the exchange-correlation potential, defined as the functional derivative of the exchange-correlation energy with respect to the density [8-11]:

$$V_{XC}(r) = \frac{\delta E_{XC}[\rho(r)]}{\delta \rho(r)} \qquad Eqn.17$$

It is important to note that the Kohn-Sham orbitals ψ_i do not have a direct physical meaning [8-11]. Unlike Hartree-Fock orbitals, which are variational solutions to a wavefunction-based theory [4,5], Kohn-Sham orbitals are simply auxiliary functions used to reproduce the correct density. Their eigenvalues ε_i^{KS} should not, in general, be interpreted as physical orbital

energies [5,11]. Because the exchange-correlation potential V_{XC} depends on the electron density, which in turn depends on the orbitals ψ_i, the Kohn-Sham equations must be solved iteratively, using a self-consistent field (SCF) approach analogous to that employed in the Hartree-Fock method [5,6,8–11]. The accuracy of DFT calculations ultimately depends on the choice of the exchange-correlation functional $E_{XC}[\rho]$, the exact form of which remains unknown [8-11]. Numerous approximations have been developed, giving rise to different classes of DFT functionals, which will be discussed in the following Section.

1.8 DFT Functionals

The accuracy of a density functional theory (DFT) calculation critically depends on the choice of the exchange-correlation functional $E_{XC}[\rho]$, which incorporates the quantum-mechanical effects of electron exchange and correlation [8,9]. Since the exact form of this functional is unknown, a wide variety of approximate functionals have been developed over the years, differing in the level of information used to construct them and in their theoretical foundations [8,9]. The earliest DFT functionals were based on the Local Density Approximation (LDA), in which the exchange-correlation energy at each point in space depends only on the value of the electron density $\rho(r)$ at that point. This approximation is inspired by the uniform electron gas model and performs reasonably well for systems with slowly varying densities [5,6,8,9]. However, LDA often fails to capture the rapid density variations near atomic nuclei or in bonding regions, leading to significant errors in molecular properties such as bond lengths, dissociation energies, and reaction barriers [5,6,8,9]. To improve upon LDA, the Generalized Gradient Approximation (GGA) was introduced [8,9]. In GGA functionals, $E_{XC}[\rho]$ depends not only on the density $\rho(r)$ itself, but also on its first derivative (i.e., the gradient $\nabla\rho$):

$$E_{XC}^{GGA} = \int f(\rho, \Delta\rho) dr \qquad Eqn.\,18$$

This allows for a better description of inhomogeneous electron distributions, particularly in molecular systems [8,9]. Further refinement is provided by meta-GGA functionals, which include additional terms such as the second derivative of the density or the kinetic energy density, improving the treatment of non-local effects and offering better accuracy for thermochemistry and hydrogen bonding [8,9]. LDA, GGA, and meta-GGA functionals are often referred to as pure DFT functionals, as they rely solely on the electron density and its derivatives [8,9]. An important advancement came with the development of hybrid functionals, which combine a portion of the exact exchange energy calculated from Hartree-Fock (HF) theory [4,5] (E_X^{HF}) with the DFT exchange-correlation energy ($E_X^{DFT} + E_C^{DFT}$) [5,8,9]. This approach takes advantage of the fact that HF provides an exact expression for the exchange energy of a system of fermions [3-5], whereas pure DFT functionals approximate both exchange and correlation contributions [8-9]. Hybrid functionals differ in the proportion of HF exchange

they incorporate and in how the remaining portion is described via semi-local DFT approximations:

$$E_{XC}^{hybrid} = a \cdot E_X^{HF} + (1 - a) \cdot E_X^{DFT} + E_C^{DFT} \qquad Eqn.19$$

The specific mixing ratios and empirical parameters (a) are often optimized to reproduce experimental observables or high-level theoretical results, and they represent a distinguishing feature among different hybrid approaches [5,6,8,9]. A brief description of some of the most widely used density functionals is presented below, classified according to the categories previously discussed:

1. *GGA Functionals*: Notable examples are BLYP [15] and revPBE [17]. The BLYP functional combines the exchange functional developed by Becke in 1988 [15] with the correlation functional introduced by Lee, Yang, and Parr in 1989 [16]. The revPBE functional, on the other hand, is a revised version of the exchange–correlation functional originally proposed by Perdew, Burke, and Ernzerhof [17], designed to improve accuracy for weakly bound systems. Another functional in this category is rPW86-PBE, which uses a revised form of the Perdew-Wang 1986 exchange functional [18], combined with the standard PBE correlation term [17].
2. *Hybrid GGA Functionals*: this class includes B3LYP [19], B3PW91 [15,20], and PBE0 [21]. B3LYP employs the same exchange and correlation expressions as BLYP, but introduces three empirical parameters that determine the proportion of exchange energy derived from Hartree-Fock theory and from DFT-based approximations [19]. B3PW91 follows a similar approach, differing in that the correlation functional used is the one developed by Perdew and Wang in 1991. The PBE0 functional [21] represents a hybrid variant of PBE, in which one-quarter of the exchange energy is calculated exactly via Hartree-Fock theory, while the remaining three-quarters rely on the original PBE exchange formulation.
3. *Range-Separated Functionals*: Representative examples are CAM-B3LYP [22] and ωB97X-D [23]. Range-separated functionals partition the exchange interaction into short- and long-range components, which are treated using different methods. CAM-B3LYP, developed by Yanai et al. [22], employs error functions (erf and erfc) to interpolate between short-range interactions, described by the B3LYP exchange, and long-range interactions, treated using exact Hartree-Fock exchange. This approach is known as the Coulomb-Attenuating Method (CAM). The ωB97X-D functional, proposed by Chai et al. [23], combines range separation with an empirical dispersion correction (DFT-D), thereby enhancing the accuracy for non-covalent and long-range interactions.

1.9 Time-Dependent Density Functional Theory (TD-DFT)

The conventional formulation of Density Functional Theory (DFT) is fundamentally restricted to ground-state systems, making it unsuitable in its original form for describing processes

involving electronic excitations, such as electronic transitions or photochemical phenomena [8-11]. To address such cases, alternative approaches or extensions of DFT must be employed. One of the most widely used extensions is Time-Dependent Density Functional Theory (TD-DFT) [12,13]. TD-DFT represents a formal extension of conventional ground-state DFT, designed to handle external time-dependent perturbations, such as electromagnetic fields. The presence of a time-dependent external potential can drive the system from its stationary ground state to higher-energy excited states, thereby requiring a proper theoretical framework capable of describing such transitions. A rigorous mathematical foundation for TD-DFT was established by Runge and Gross [12], who introduced two key theorems analogous to the Hohenberg-Kohn theorems of static DFT (see Sub-section 1.7.1). The first theorem asserts that the time-dependent electron density is a fundamental variable that uniquely determines all observables of the system. The second theorem provides a variational principle for time-dependent systems; however, unlike the ground-state case (see Section 1.3), it does not refer to the minimization of the total energy. Instead, it introduces a time-dependent functional, whose stationary point corresponds to the correct time evolution of the system under the applied perturbation [12]. A central ingredient in the computation of excitation energies is the functional derivative of the exchange-correlation (XC) potential with respect to time. The foundational insight lies in the Runge-Gross theorem [12], which asserts that the temporal evolution of the electron density encodes the same information as that obtainable from the full time-dependent wavefunction, under a given external perturbation. From a computational perspective, this is particularly advantageous, as the electronic density depends only on three spatial variables (x, y, z), whereas the many-body wavefunction depends on the coordinates of all electrons simultaneously [4,5,8,9]. Effectively, TD-DFT generalizes the static DFT formalism to time-dependent systems. For any interacting many-electron system under a time-dependent potential, all physical observables are uniquely determined by the time-dependent density and the initial state of the system at an arbitrarily chosen time t_0 [12]. In particular, if the time-dependent perturbation is introduced at t_0, and the system is initially in its ground state, then all observables can be regarded as unique functionals of the electronic density. In this case, the initial state of the system at t_0 is itself a unique functional of the ground-state density, as guaranteed by the Hohenberg-Kohn theorem (Sub-section 1.7.1) for the unperturbed system. This one-to-one correspondence forms the basis for a time-dependent Kohn-Sham scheme [12], in which the complex dynamics of the interacting many-body system are mapped onto an auxiliary non-interacting system evolving under an effective potential that depends on the time-dependent density. This mapping enables the study of electronic excitations through the numerical solution of a time-dependent single-particle problem. Further simplifications arise in the linear response regime [13], where excitation energies can be computed efficiently by analyzing the system's response to weak external fields. As in the case of static DFT, the main challenge in TD-DFT lies in the construction of accurate exchange-correlation potentials. For the reliable prediction of electronic excitations, range-separated hybrid functionals, such as CAM-B3LYP [23], have proven particularly effective.

1.10 Justification and Comparative Discussion of the DFT Functionals Employed in this Thesis

The selection of exchange-correlation functionals in Density Functional Theory (DFT) is a crucial aspect of first-principles approaches. Different classes of functionals exhibit different accuracy and limitations depending on the property of interest, from energetics and geometries to vibrational and excited-state spectra. In the present Thesis, different functionals were adopted in line with the specific demands posed by the investigated systems, e.g. molecular precursors, periodic oxide surfaces, and the simulation of electronic excitation spectra (UV-Vis). As already discussed in Section 1.8, exchange-correlation functionals in DFT can be classified into hierarchical categories (LDA, GGA, meta-GGA, hybrid and range-separated hybrid). In this perspective, this Section offers a brief discussion of the functional classes employed in this work, the reasons for their selection, and a comparative perspective that places these choices within established benchmarks.

ωB97XD, M06 and PBE

Across Chapters 2 and 4, the ωB97XD functional [23] was adopted for ground-state geometry optimizations and for harmonic vibrational analysis. This family (ωB97X variants) combines long-range corrected exchange with empirical dispersion corrections, addressing two common limitations of traditional GGAs: inadequate long-range exchange and missing van der Waals interactions [23]. Its use in non-periodic systems is justified by its reliable performance for geometries, relative energetics, and non-covalent interactions. Benchmark studies have shown ωB97XD to yield good agreement with high-level coupled-cluster reference data for medium-sized organic systems, especially where dispersion plays a non-negligible role [24]. In Chapter 2, the ωB97XD functional was employed to investigate the structure, vibrational features, and gas-phase fragmentation energetics of a Ni(II) β-diketonate-TMEDA precursor series (Par. 2.1). Furthermore, it allowed for an accurate treatment of the precursors' hydrogen bonding with explicit water molecules, which were essential to rationalize the experimentally observed enhancement in NiO thin film growth under humid CVD conditions (Par. 2.2). In Chapter 4, ωB97XD was employed to optimize the geometries of selected organic molecules in the gas phase before their adsorption on ZnO surfaces (Par. 4.2). This step was essential to define reliable starting configurations for subsequent adsorption modeling. Notably, the ωB97XD geometries were benchmarked against those obtained at the post-HF MP2 theory level, confirming the robustness of the adopted DFT approach for describing this class of molecular systems and their interaction with oxide surfaces.

In Chapter 2 (Par. 2.3), the M06 functional was adopted to investigate the gas-phase fragments of Ni(II) β-diketonate-TMEDA complexes. This choice was motivated by the need to accurately describe systems involving transition metals and spin-state multiplicity changes. M06, a meta hybrid functional, has been reported to offer improved performance for thermochemistry, non-covalent interactions, and particularly for transition-metal complexes exhibiting open-shell configurations [25,26]. Preliminary tests using ωB97XD had yielded inconsistencies in the relative energetics of low-spin and high-spin fragments, prompting the adoption of M06, which provided more chemically reasonable results in line with literature

expectations [27]. As such, M06 offered a reliable alternative to ωB97XD, complementing the computational strategy employed in this Thesis.

When treating periodic materials, such as the NiO surfaces in Paragraph 2.4, the Zeolite L channel in Chapter 3, and the metal oxide surfaces examined in Chapter 4, the Perdew-Burke-Ernzerhof (PBE) [17] functional, belonging to the GGA family, was selected due to its known reliability in reproducing structural properties of solid-state oxide systems. Empirical dispersion corrections were systematically included to address the intrinsic limitations of GGA functionals in describing long-range van der Waals interactions. In particular, Grimme's D2 and D3bJ schemes [28,29] were adopted in this Thesis. For instance, PBE+D3bJ was used in simulations of NiO and ZnO surfaces, while PBE+D2 was adopted in the modeling of zeolite-based systems. Additionally, for the In_2O_3 surface discussed in Paragraph 4.1, the rVV10 nonlocal correlation functional [30] was employed to achieve a more accurate description of dispersion interactions in periodic systems. In general, GGA functionals, like PBE, are widely used in surface science and materials modeling, as they provide a good compromise between accuracy and computational cost, particularly for the prediction of lattice parameters, defect energetics, and adsorption geometries [31,32]. The incorporation of dispersion corrections is essential in improving the reliability of PBE when applied to hybrid organic-inorganic systems, where noncovalent interactions play a crucial role in determining the interfacial structure and energetics [28].

CAM-B3LYP

Across the chapters of this Thesis (Chapters 2, 3, and 4), the simulation of UV-Vis absorption spectra was performed exclusively using the CAM-B3LYP [22] range-separated hybrid functional. This choice was motivated by the fact that this functional is particularly well-suited for systems in which frontier orbitals are spatially separated, such as supramolecular complexes or encapsulated chromophore pairs [22,30,33]. In this perspective, the choice of CAM-B3LYP for the simulation of UV-vis spectra of the MDAP+SERO complex in Chapter 3 finds solid justification in the CT character of the low-energy absorption bands, as supported by experimental and computational data [34]. Furthermore, benchmarking tests performed in this Thesis, comparing CAM-B3LYP to the higher-level method EOM-CCSD, confirmed its ability to provide reliable excitation wavelengths and oscillator strengths [35]. Notably, CAM-B3LYP outperformed the PBE0 functional, which is known to systematically underestimate CT excitation energies due to self-interaction errors and the incorrect asymptotic behavior of the exchange potential [36,37]. The choice of CAM-B3LYP as the exclusive functional for all the UV-Vis spectra simulations across this Thesis, including Ni(II) precursors (Chapter 2), supramolecular dye-neurotransmitter complexes (Chapter 3), and gas-phase Chemical Warfare Agents (CWAs) molecules (Chapter 4), was motivated by multiple considerations that extend beyond its well-documented performance for charge-transfer (CT) transitions [22,30,33,34]. First, CAM-B3LYP has demonstrated excellent versatility in simulating electronic excitations of various nature, not limited to CT states. Benchmark studies by Jacquemin et al. [38] and Peach et al. [39] have shown that this range-separated hybrid functional performs competitively also for local $\pi \rightarrow \pi^*$ transitions in neutral organic molecules, often outperforming other hybrid functionals, such as B3LYP or PBE0. This broader applicability makes CAM-B3LYP a reliable

choice for molecular excitation studies. CAM-B3LYP often proved to yield accurate excitation energies across a wide range of systems, including both neutral molecules and charged chromophore-analyte complexes, making it a practical and reliable choice. Although more accurate range-separated functionals, such as ωB97M-V [40], ωB2PLYP [41], or MN15 [42], have been developed, which may offer improved performance, their higher computational cost often limits their use in large systems. In this perspective, CAM-B3LYP represents a balanced and computationally efficient choice.

2.0 Periodic Systems in First Principles Simulations

First principles simulations of periodic systems play a fundamental role in modern computational materials science, as they allow for the accurate modeling of crystalline solids, surfaces, and extended frameworks [1]. Unlike isolated molecular systems, periodic materials require specific theoretical and computational treatments to account for their inherent translational symmetry. This is typically achieved by applying periodic boundary conditions (PBC), which assume that the system under investigation is replicated infinitely in space, thereby mimicking the bulk or extended nature of the material [1,2]. The adoption of PBC introduces a set of mathematical and computational simplifications. Most notably, it enables the use of plane-wave basis sets, which are particularly suited to represent delocalized electronic states in extended periodic systems [2,3]. A plane-wave basis set expands the Kohn-Sham orbitals as a linear combination of plane waves, characterized by well-defined kinetic energies. However, due to the infinite number of plane waves in principle required for a complete basis, a cutoff energy is introduced to limit the number of basis functions, balancing accuracy and computational cost [1,2]. In reciprocal space, the periodicity of the system leads to the definition of the Brillouin zone, the fundamental domain for wavevectors (k-points). Integrations over the Brillouin zone, necessary to compute properties such as total energy or electronic density, are performed using discrete sampling schemes, such as the Monkhorst-Pack grid, which selects a finite and representative set of k-points [1,14]. The choice of k-point density significantly affects the accuracy of the calculation and must be converged accordingly. Another key component in periodic DFT simulations is the use of pseudopotentials, which replace the all-electron potential of atomic cores with an effective potential that reproduces the scattering properties of valence electrons [2,3]. This approximation allows one to avoid explicitly treating tightly bound core states, thus reducing the computational cost while preserving the accuracy of valence properties. Common types include norm-conserving, ultrasoft, and projector-augmented wave (PAW) pseudopotentials [1,2,14]. As in molecular DFT, the electronic structure is determined via the self-consistent field (SCF) procedure (see Section 1.7), where the Kohn-Sham equations are iteratively solved until convergence of the electronic density is achieved. However, in periodic systems, the SCF loop includes additional complexity due to the reciprocal-space integration and the plane-wave expansion [1,2]. Altogether, first principles simulations of periodic systems provide essential insights into structural, electronic, and magnetic properties of materials, enabling predictive modeling and rational design of functional solids. When carefully parameterized and

adequately converged, these simulations represent a powerful and reliable tool in both fundamental research and materials engineering [1,2,14].

References

[1] N. Marzari, A. Ferretti, C. Wolverton, Electronic-structure methods for materials design, Nat. Mater., 2021, 20, 736-749

[2] R.M. Martin, Electronic Structure: Basic Theory and Practical Methods, Cambridge University Press, Cambridge, UK, 2004

[3] Andrew R. Leach, Molecular Modelling - Principles and Applications, second edition, Pearson Education Limited, 2001

[4] S. Attila, and Neil S. Ostlund, "Modern quantum chemistry: introduction to advanced electronic structure theory", Dover Publication, Inc., Mineola, New York, 1996

[5] P. W. Atkins, R. Friedman, "Molecular quantum mechanics" Fourth Edition, 2005

[6] James B. Foresman, E. Frisch, Exploring Chemistry with electronic structure methods, Second Edition, Gaussian, Inc., 1993

[7] C. Moller, M.S. Plesset, Note on an approximation treatment for many-electron systems, Phys. Rev., 1934, 46, 618-622

[8] M. Bursch, J.-M. Mewes, A. Hansen, S. Grimme, Best-Practice DFT Protocols for Basic Molecular Computational Chemistry, Angew. Chem. Int. Ed., 2022, 61

[9] J. P. Perdew and A. Ruzsinszky, Fourteen Easy Lessons in Density Functional Theory, Int. J. Quantum Chem, 2010, 110, 2801-2807

[10] P. Hohenberg, W. Kohn, Inhomogeneous Electron Gas, Phys. Rev., 1964, 136, B864-B871

[11] W. Kohn, L. J. Sham, Self-Consistent Equations Including Exchange and Correlation Effects, Phys. Rev., 1965, 140, A1133-A1138

[12] E. Runge, E.K.U. Gross, Density Functional Theory for Time-Dependent Systems, Phys. Rev. Lett., 1984, 52, 997-1000

[13] E. K. U. Gross and W. Kohn, Local density-functional theory of frequency-dependent linear response, Phys. Rev. Lett., 1985, 55, 2850-2852

[14] M. C. Payne, M. P. Teter, D. C. Allan, T. A. Arias, J. D. Joannopoulos, Iterative minimization techniques for ab initio total-energy calculations: molecular dynamics and conjugate gradients, Rev. Mod. Phys., 1992, 64, 1045-1097

[15] A. D. Becke, Density-functional exchange-energy approximation with correct asymptotic behavior, Physical review A. 1988, 38, 3098-3100

[16] C. Lee, W. Yang, R. G. Parr, Development of the Colle-Salvetti correlation-energy formula into a functional of electronic density, Physical review B. 1988, 37, 785-789

[17] J. P. Perdew, K. Burke, M. Ernzerhof, Generalized gradient approximation made simple, Phys. Rev. Lett., 1996, 77, 3865-3868

[18] J. P. Perdew, W. Yang, Accurate and simple density functional for the electronic exchange energy: generalized gradient approximation, Physical review B., 1986, 33, 8800-8802

[19] A. D. Becke, A new mix of Hartree-Fock and local density-functional theory, J. Chem. Phys., 1993, 98, 5648-5652

[20] J. P. Perdew, J. A. Chevary, S. H. Vosko, K. A. Jackson, M. R. Pederson, D. J. Singh, and C. Fiolhais, Atoms, molecules, solid and surface: applications of generalized gradient approximation for exchange and correlation, Phys. Rev. B., 1992, 46, 6671-6687

[21] M. Ernzerhof, G. E. Scuseria, Assessment of the Perdew-Burke-Ernzerhof exchange-correlation functional, J. Chem. Phys., 1999, 110, 5029-5036

[22] T. Yanai, D. P. Tew, N. C. Handy, A new hybrid exchange-correlation functional using the Coulomb-attenuating method (CAM-B3LYP), Chem. Phys. Lett. 2004, 393, 51-57

[23] J. Chai, M. Head-Gordon, Long-range corrected hybrid density functionals with damped atom-atom dispersion corrections, Phys. Chem. Chem. Phys., 2008, 10, 6615-6620

[24] L. Goerigk, S. Grimme, A thorough benchmark of density functional methods for general main group thermochemistry, kinetics, and noncovalent interactions, Phys. Chem. Chem. Phys., 2011, 13, 6670-6688

[25] Y. Minenkov, Å. Singstad, G. Occhipintia, V. R. Jensen, The accuracy of DFT-optimized geometries of functional transition metal compounds: a validation study of catalysts for olefin metathesis and other reactions in the homogeneous phase, Dalton Trans., 2012,41, 5526-5541

[26] H. Jacobsen, L. Cavallo, Directions for Use of Density Functional Theory: A Short Instruction Manual for Chemists Handbook of Computational Chemistry, 2017, 225-267

[27] Y. Zhao, D.G. Truhlar, The M06 suite of density functionals for main group thermochemistry, thermochemical kinetics, noncovalent interactions, excited states, and transition elements: two new functionals and systematic testing of four M06-class functionals and 12 other functionals, Theor Chem Account., 2008, 120, 215-241

[28] S. Grimme, J. Antony, S. Ehrlich, H. Krieg, A consistent and accurate ab initio parametrization of density functional dispersion correction (DFT-D) for the 94 elements H-Pu J. Chem. Phys., 2010, 132, 154104

[29] R. Sabatini, T. Gorni, S. De Gironcoli, Nonlocal van der Waals density functional made simple and efficient, Phys. Rev. B, 2013, 87, 041108

[30] M.J.G. Peach, P. Benfield, T. Helgaker, D.J. Tozer, Excitation energies in Density Functional Theory: An evaluation and a diagnostic test, J. Chem. Phys., 2008, 128, 044118

[31] P. Haas, F. Tran, P. Blaha, Calculation of the lattice constant of solids with semilocal functionals, Phys. Rev. B, 2009, 79, 085104

[32] D.S. Sholl, J.A. Steckel, Density Functional Theory: A Practical Introduction, Wiley, 2009

[33] C. Adamo, D. Jacquemin, The calculations of excited-state properties with Time-Dependent Density Functional Theory, Chem. Soc. Rev. 2013, 42, 845-856

[34] L. M. Grimm, **C. Invernizzi**, F. Biedermann, G. Tabacchi, E. Fois, Mechanistic insights into water-stabilized dye-neurotransmitter intermolecular complexes in zeolite channels, Chem. Commun., 2025, 61, 4160

[35] D. Jacquemin, E. A. Perpète, I. Ciofini, C. Adamo, Accurate simulation of optical properties in dyes, Acc. Chem. Res. 2009, 42, 326-334

[36] Y. Tawada, T. Tsuneda, S. Yanagisawa, T. Yanai, K. Hirao, A long-range-corrected time-dependent density functional theory, J. Chem. Phys. 2004, 120, 8425-8433

[37] D. Jacquemin, I. Duchemin, X. Blase, 0-0 energies using hybrid schemes: Benchmarks and insights, J. Chem. Theory Comput. 2015, 11, 5340-5359

[38] D. Jacquemin, T. Wathelet, E. A. Perpète, C. Adamo, Extensive TD-DFT benchmark: singlet-excited states of organic molecules, J. Chem. Theory Comput. 2009, 5, 2420-2435

[39] M. J. G. Peach, M. Williamson, D. J. Tozer, Influence of triplet instabilities in TDDFT, J. Chem. Theory Comput. 2011, 7, 3578-3585

[40] N. Mardirossian, M. Head-Gordon, ωB97M-V: A combinatorially optimized, range-separated hybrid, meta-GGA density functional with VV10 nonlocal correlation, J. Chem. Phys. 2016, 144, 214110

[41] L. Goerigk, S. Grimme, Double-hybrid density functionals, WIREs Comput. Mol. Sci. 2014, 4, 576-600

[42] H.S. Yu, X. He, S.L. Li, D.G. Truhlar, MN15: A Kohn-Sham global-hybrid exchange–correlation density functional with broad accuracy for multi-reference and single-reference systems and noncovalent interactions, Chem. Sci. 2016, 7, 5032-5051

– Chapter 2 –

NiO by design: From Molecular Fragmentation to the Nanomaterial

As mentioned in the Introduction, Chapter 2 focuses on the first steps of formation of a nanomaterial, specifically nickel(II) oxide, which is initiated through fragmentation reactions of molecular precursors occurring at high temperature conditions on a heated surface. In particular, the study centers on a series of Ni(II) β-diketonate-TMEDA complexes, used experimentally for the growth of NiO nanostructures. The central idea is that the fragmentation pathways of these compounds, triggered by thermal or photochemical activation, provide a bottom-up route to construct the target nanomaterial under conditions relevant to Chemical Vapor Deposition (CVD). By adopting a fully computational approach, this Chapter aims to investigate the relationship between the molecular architecture of the precursors and their reactivity/fragmentation path.

Nickel (II) oxide (NiO) is a transparent *p*-type semiconductor with high chemical stability and a wide band gap (E_G = 3.2-4.0 eV) [1-5]. It is characterized by a rock-salt structure featuring an antiferromagnetic ordering (AF), with collinear spins parallel to (111) planes. [6,7] Owing to this unique combination of properties, NiO-based nanomaterials and thin films have attracted increasing interest for a broad spectrum of high-impact technologies, including resistive random access memories [8-10], sensors [3,11], hole-extraction layers in solar cells [2,5,12,13], displays and light-emitting diodes (LEDs) [14], heterogeneous (photo)catalysis [15,16], and electrocatalysis for the oxygen evolution reaction [17-20], the bottleneck step in water splitting to generate clean H_2 fuel. The functional performance of these devices strongly depends on the preparation strategy, as high-quality interfaces and precise control over NiO nanostructure, morphology, and composition are essential [17]. Among the available routes to obtain NiO thin films and nanostructures [16,21-30], CVD [12,17,18,31-36] is particularly appealing, as it allows one to control material features under non-equilibrium conditions through a suitable choice of experimental parameters and of the starting precursors. [37-41] These precursors must possess specific physicochemical properties, such as adequate volatility, clean decomposition pathways, and tunable reactivity. β-diketonate complexes are among the most widely used precursors for the CVD of metal oxide films and nanomaterials [18,42], as their physicochemical properties can be tailored by modifying the steric hindrance and fluorination degree of the ligands backbone [18]. Nevertheless, as regards the CVD of NiO, conventional [$Ni(acac)_2$] [27,43] and [$Ni(thd)_2$] [8,9] (Hacac = 2,4-pentanedione; Hthd = 2,2,6,6-tetramethyl-3,5-heptanedionate) suffer from high melting points and limited gas-phase stability [27,28,32,44], which hinder precise process control and limit their large-scale applicability. [37,40,45-49] This Chapter presents a theoretical investigation of β-diketonate-diamine compounds of the general formula NiL_2TMEDA [HL = 1,1,1,-trifluoro-2,4-pentanedionate (tfa), 2,2-dimethyl-6,6,7,7,8,8,8-heptafluoro-3,5-octanedionate (fod), ; TMEDA = N,N,N',N'-tetramethylethylenediamine (thd)], used as precursors for the fabrication of NiO thin films through CVD, under both dry and water-assisted conditions. Moreover, in this Chapter, the fragments of these complexes are

examined in detail, providing hints for the driving force governing the fragmentation pathways.

Concerning the final materials, NiO surfaces, both pristine and functionalized with -OH defects, are simulated to illustrate how defect engineering can modulate the phisico-chemical properties of these nanomaterials.

Specifically, the following issues will be discussed:

i) Theoretical characterization of the three target Ni complexes, focusing on the interplay between the diketonate hindrance/fluorination degree, as well as the molecular-level factors that influence the thickness of the thin films formed by preliminary CVD experiments under conventional dry O_2 atmosphere (Paragraph 2.1, Ref. [50]);

ii) Computational investigation aimed at exploring the role of water molecules in the decomposition of Ni precursors, under conditions relevant to humid O_2 CVD conditions. The analysis seeks to understand how gaseous H_2O molecules promote precursor reactivity, providing a molecular-level rationale for the experimentally observed enhancement in NiO thin film growth and quality in the presence of water vapor (Paragraph 2.2, Ref. [51]);

iii) Based on High Resolution Mass spectrometry data, modelling and analysis of the fragmentation patterns of the target Ni(II) β-diketonate-diamine complexes in order to elucidate the molecular and electronic structures of their fragmentation products, providing for the first time insights into their gas-phase reactivity (Paragraph 2.3, Ref. [52]);

iv) Computational investigation of NiO (100) surfaces featuring -OH defects, aimed at providing atomistic-level insights into the structural and electronic properties of NiO-based thin films, that could be relevant for their use in various technological applications, including catalysis, sensing, and electronic devices (Paragraph 2.4, Ref. [53]).

2.1 Characterization of β-Diketonate Ni (II) Complexes

From an experimental standpoint, the complexes [Ni(tfa)$_2$TMEDA] (**1**), [Ni(fod)$_2$TMEDA] (**2**), and [Ni(thd)$_2$TMEDA] (**3**) were thoroughly characterized. Where applicable, their crystal structures were resolved, and both IR and UV-Vis spectra were recorded (Figures A.4-A.6 in Appendix 2 and Figure 2, respectively). Preliminary chemical vapor deposition (CVD) experiments conducted under dry O_2 atmospheres confirmed that all three complexes serve as effective precursors for the formation of NiO thin films. However, among them, only compound **3** (the non-fluorinated derivative one) exhibited significantly higher decomposition efficiency, resulting in the deposition of a notably thicker film (further details in Table 3, Section 2.1.5). This unexpected outcome prompted a computational investigation aimed at identifying the molecular-level factors responsible for such behavior. The results and analyses presented in this Paragraph (and subsequent ones) are organized to guide the reader through the key steps of the study.

2.1.1 Ni(II) Target Complexes: Modelling and Analysis

The crystal structures of **1** and **3** were obtained experimentally, and both exhibited positional disorder. On the other hand, all efforts to obtain crystals of **2** suitable for X-ray analysis turned out to be unsuccessful. Based on this, the geometry optimization of the three nickel complexes was carried out with the dual objective of locating the minimum energy structures of compounds **1** and **3** - providing a molecular-level interpretation of the observed positional disorder - and of proposing a reliable structure for compound **2**, which had not been previously reported in the literature. Figure 1 displays the solid-state structures of **1** and **3**, along with the minimum energy structures of **1**, **2** and **3** obtained by theoretical modelling. Computational Details are provided in Appendix 2, Section A.2.1.1. Experimental and computed structural data are presented in Table 1.

Figure 1 reveals that, in all the reported structures, the Ni(II) center, surrounded by two β-diketonates and a TMEDA moiety, is six-fold coordinated and exhibits a slightly distorted octahedral coordination environment. Despite DFT structural parameters refer to isolated complexes, data in Table 1 indicate that computed bond lengths and angles are in good agreement with experimental ones. This finding supports the reliability of the calculated structure of compound **2**, whose geometry was derived exclusively through modelling, thereby establishing a solid basis for a comparative analysis of the three target Ni(II) complexes. The DFT-computed minimum energy structures (Figure 1C, D, E) were obtained after evaluating alternative structural arrangements (see Section A.2.1.2 in Appendix 2), with the aim of also providing a possible explanation for the positional disorder experimentally observed in compounds **1** and **2**.

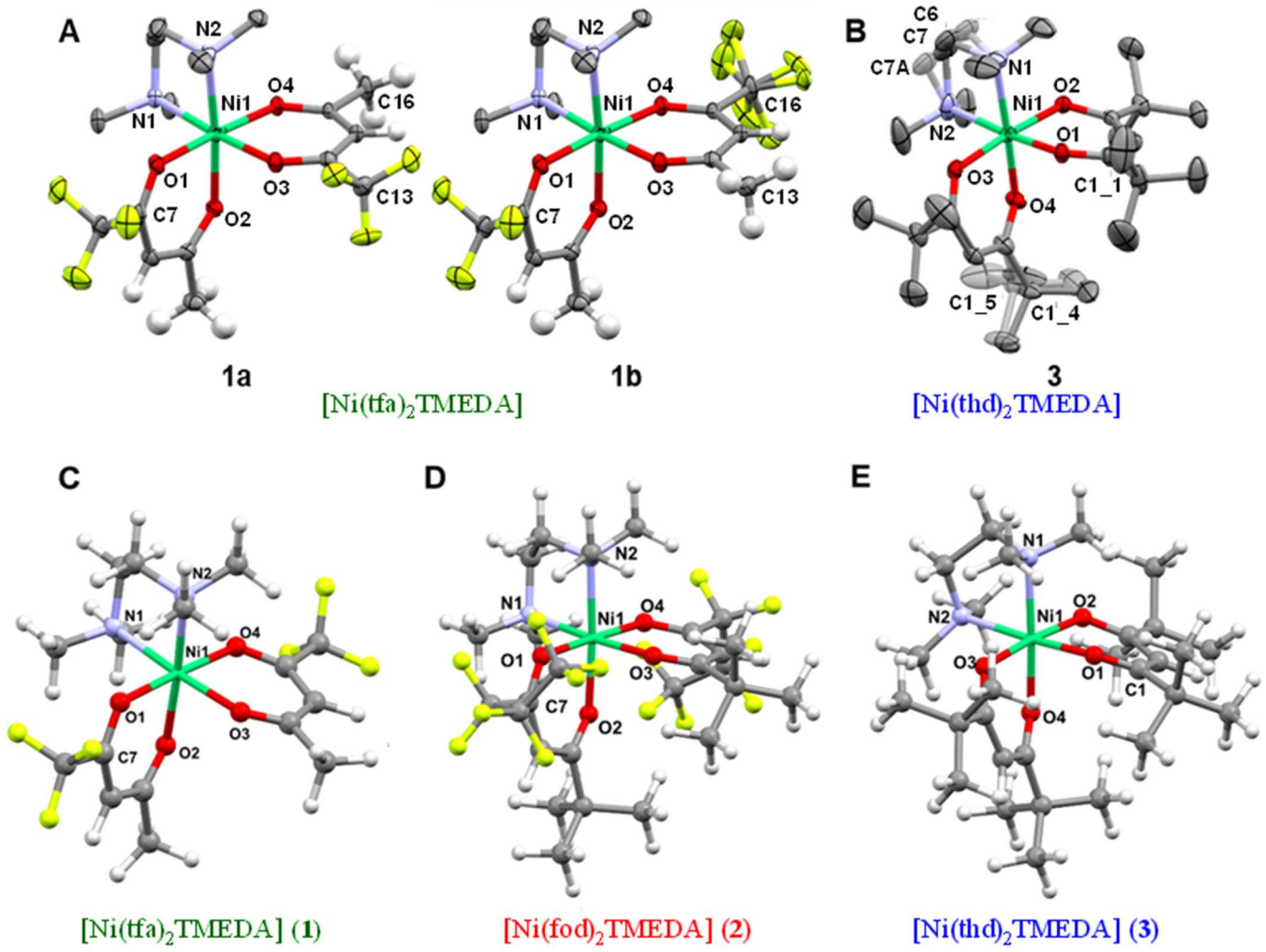

Figure 1: (A and B) Solid-state molecular structures of compounds **1** and **3**, respectively. A) Compound **1** showing two determined disordered isomers depending on the orientation of the -CF_3 group of one tfa ligand, **1a** and **1b**. The ratio **1a**:**1b** with the observed disorders is 13.7:86.3. For the **1b** isomer, an additional rotational disorder was detected and represented. B) Molecular structure of compound **3** with modelled positional disorder in the TMEDA backbone (C6,C7:C6A,C7A = 69.7:30.3) and one of the *tert*-butyl groups (C1_4:C1_5 = 63.5:36.5) of the thd ligand. C, D, E) Graphical representation of the DFT-computed minimum energy structures for **1, 2, 3**, respectively.

Table 1: Selected bond lengths and angles for compounds **1**, **2**, and **3**.

		1		**2**	**3**	
		Experimental	*Calculated*	*Calculated*	*Experimental*	*Calculated*
Bond length (Å)	Ni(1)-O(1)	2.0200(12)	2.028	2.039	1.9912(13)	2.016
	Ni(1)-O(2)	2.0484(12)	2.045	2.028	2.0217(13)	2.026
	Ni(1)-O(3)	2.0498(12)	2.045	2.028	2.0216(14)	2.026
	Ni(1)-O(4)	2.0361(11)	2.028	2.039	2.0039(14)	2.016
	Ni(1)-N(1)	2.1450(14)	2.169	2.171	2.1683(19)	2.182
	Ni(1)-N(2)	2.1617(14)	2.169	2.171	2.1522(18)	2.182
Bond angle (°)	O(1)-Ni(1)-O(4)	176.79(5)	177.9	178.1	93.45(5)	93.3
	O(1)-Ni(1)-O(2)	89.43(5)	89.2	88.9	89.66(5)	88.9
	O(2)-Ni(1)-O(3)	91.68(5)	90.5	90.0	175.05(6)	174.8
	O(3)-Ni(1)-O(4)	89.18(5)	89.2	88.9	89.17(6)	88.9
	N(1)-Ni(1)-N(2)	84.68(6)	84.8	84.6	84.16(9)	84.0
	O(1)-Ni(1)-O(3)	88.09(5)	89.2	89.8	87.84(6)	91.4
	O(1)-Ni(1)-N(1)	94.38(5)	92.6	92.4	90.50(7)	88.9
	O(1)-Ni(1)-N(2)	87.63(5)	88.9	89.1	174.66(7)	174.7
	Ni(1)-O(1)-C(7/1)	124.58(11)	124.2	124.1	126.29(12)	123.7

2.1.2 Insight through IR Spectral Analysis

In order to gain a more detailed understanding of bond length trends and to assess structural similarities/differences among the three investigated complexes, theoretical vibrational frequencies were computed on the minimum energy structures of **1**, **2**, and **3**. The experimental and simulated IR spectra of [Ni(tfa)$_2$TMEDA], [Ni(fod)$_2$TMEDA], and [Ni(thd)$_2$TMEDA] are displayed in Figures A.4-A.6 in Appendix 2, respectively. For all the compounds, which are characterized by all positive frequencies, the agreement between experimental and theoretical spectra is satisfactory, allowing thus a detailed band assignment based on the normal modes. The latter is reported in Tables A.1-A.3 in Appendix 2, Section A.2.1.3. This aspect may also be particularly relevant for understanding the decomposition efficiency of the precursors in the formation of NiO thin films.

Taken together, the computed stretching frequency values provide strong and consistent support for the trends observed in the bond lengths within the coordination sphere of Ni across all three complexes. More specifically, **1** and **3** exhibit shorter Ni-O bonds than Ni-N bonds, in accordance with other transition metal β-diketonates and ketoiminates. [37,38,40,54,55] Furthermore, while in the case of **1**, the two Ni-O bonds in *trans* to TMEDA are slightly elongated, in structure **3** the same bonds were found to be shortened. As observed for compounds **1** and **3**, even for **2** all Ni-O bonds are shorter than Ni-N ones. Notably, Ni-O distances in *trans* to TMEDA are slightly shorter than the other ones, measuring 2.028 Å and 2.039 Å, respectively (see Table 1). In this context, a clear trend emerges across the series: Ni-O bonds decrease progressively upon going from complex **1** to **3**, with the non-fluorinated **3** displaying the shortest Ni-O distances.

As previously discussed, both the IR spectra (Figures A.4-A.6) and the vibrational analysis (Tables A.1-A.3) provide a strong support for all these findings. Indeed, Ni-O stretching frequencies were found to be 578, 618, and 638 cm^{-1} for complexes **1**, **2**, and **3**, respectively. This outcome reflects a progressive strengthening of the Ni-O bonds, being strongest in complex **3**, suggesting that, in a hypothetical fragmentation process, the loss of a β-diketonate ligand may be less favorable for complex **3**, which bears non-fluorinated ligands. An interesting trend emerges in the Ni-N bond distances, which increase with the number of electron-donor *tert*-butyl groups on β-diketonate ligands. This bond elongation effect, most pronounced in compound **3**, can be reasonably ascribed to the steric hindrance of the two bulky *tert*-butyl groups on each thd ligand. Consistently, compound **3** exhibits the lowest Ni-N stretching frequency (461 cm^{-1}). In compound **2**, the competing effects of (electron-withdrawing) fluorine atoms' increment, and the steric hindrance of *tert*-butyl groups (electron-donor) appear to counterbalance, resulting in Ni-N stretching frequencies nearly identical to those observed for compound **1** (472 and 471 cm^{-1} for **2** and **1**, respectively). Overall, these results suggest that the *tert*-butyl-rich complex **3**, bearing non-fluorinated ligands, may be more prone to TMEDA release with respect to **1** and **2**. A key feature shared by all three complexes is that Ni-N stretching frequencies are lower than Ni-O ones, pointing to a weaker interaction between the Ni center and TMEDA nitrogen atoms. This analysis could suggest that, upon thermal activation, TMEDA detachment might be easier than β-diketonate loss. Another noteworthy trend emerges by comparing the C=O stretching frequencies across

the three complexes: the associated wavenumbers are significantly higher for the fluorinated compounds (**1** and **2**) than for the non-fluorinated complex **3**. This observation is in line with the opposite trend found for Ni-O stretching frequencies, which are the highest for **3**, characterized by the strongest Ni-O bonds (see above).

2.1.3 Energetic Considerations for a Hypothetical Fragmentation Event

Prompted by the trends discussed in Section 2.1.2, indicating a progressive strengthening of Ni-O bonds and a concomitant weakening of Ni-N interactions, particularly in the non-fluorinated complex **3**, in passing from **1** to **3**, a comparative energetic analysis was undertaken to assess the relative favorability of the TMEDA vs β-diketonate ligand loss. This investigation is especially relevant within the broader scope of Chapter 2, which focuses on nanomaterial formation via the fragmentation of molecular precursors. Evaluating which ligand is more prone to dissociation upon thermal activation may provide valuable insight into the early steps of the CVD process and into the reactivity of these Ni(II) complexes.

In this context, for compounds **1-3** the energetics correlated to the loss of TMEDA (ΔE_1, Equation 1) and of a β-diketonate ligand L (ΔE_2, Equation 2) were calculated according to the following pathways:

$$[NiL_2TMEDA] \rightarrow [NiL_2] + TMEDA \quad (1)$$

$$[NiL_2TMEDA] \rightarrow [NiL(TMEDA)]^+ + L^- \quad (2)$$

The calculated fragmentation energies, summarized in Table 2, clearly show that TMEDA detachment requires significantly less energy than β-diketonate loss for all three complexes. Notably, the energy required for TMEDA removal is substantially lower in compound **3** than in the fluorinated compounds, in line with the trends discussed previously. Overall, these findings suggest that TMEDA detachment should be the first fragmentation step for all three complexes, and that such event is thermodynamically most favorable in compound **3**.

For further details on the theoretical analysis of the fragmentation patterns of the three target complexes, the reader is encouraged to refer to Paragraph 2.3.

Table 2: DFT-computed energetics for TMEDA loss (ΔE_1), diketonate ligand loss (ΔE_2), and relative energy difference $\Delta(\Delta E) = \Delta E_2 - \Delta E_1$, for compounds **1**, **2**, and **3**.

Energies (kcal/mol)	**1**	**2**	**3**
ΔE_1	61.2	65.1	54.9
ΔE_2	142.9	143.9	146.6
$\Delta(\Delta E)$	81.7	78.8	91.7

2.1.4 Optical Spectra Analysis: Photophysical Insights into NiL$_2$[TMEDA] Complexes

Assessing the optical spectra of the compounds under investigation may offer further insight with regard to their potential applicability as precursors in UV photo-assisted CVD processes. [40] In this context, photo-induced dissociation of the complexes in the gas phase may give rise to highly reactive radical species, thereby enabling film growth at lower temperatures, particularly advantageous for deposition on thermally sensitive substrates. The optical spectra of **1-3**, shown in Figure 2, exhibited a strong absorption band in the near-UV region around 300 nm, further supporting their suitability for application in UV-assisted deposition strategies.

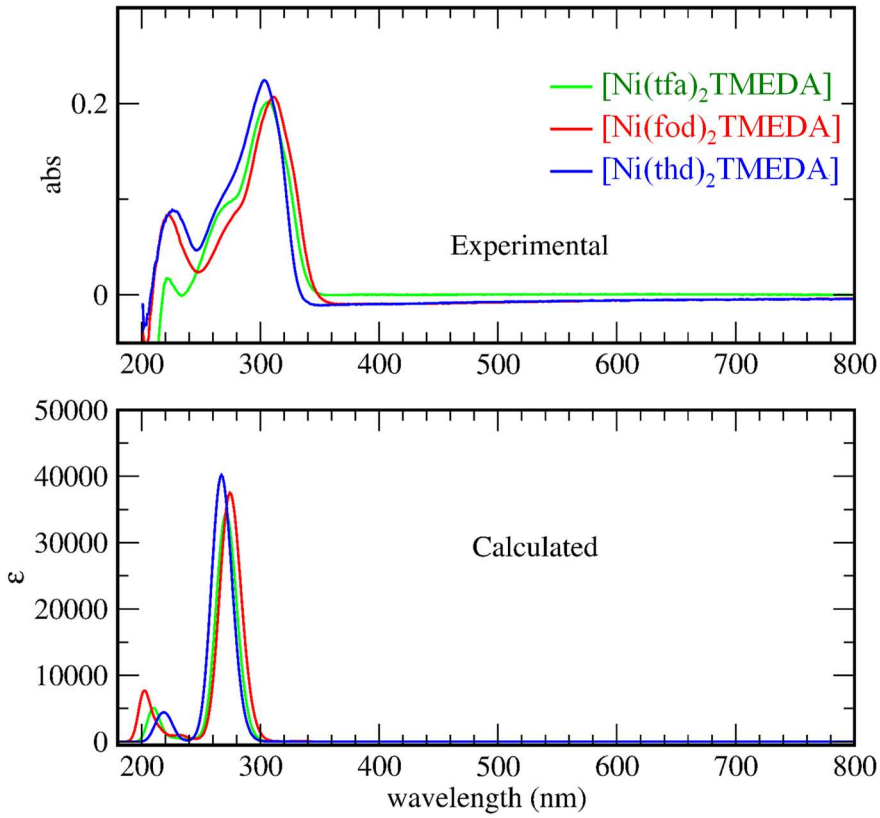

Figure 2: Experimental and computed optical absorption spectra of compounds **1**, **2**, **3**.

In the experimental spectra, the main absorption peaks are located at 303, 307, and 312 nm for compounds **3**, **1**, and **2**, respectively. TD-DFT calculations (see Appendix 2, Section A.2.1.1 for details) reproduced the same trend, yielding values of 271, 277, and 290 nm for **3**, **1**, and **2**, respectively. This result indicates that the absorption band progressively shifts to higher wavelengths with increasing fluorine content in the diketonate ligand, i.e., the lowest wavelength value is observed for the non-fluorinated complex **3**. For all compounds, electronic structure analysis provided molecular-level insight, not experimentally accessible, into the optical properties of the investigated Ni complexes. The molecular spin orbitals primarily involved in the electronic excitation components of the most intense absorption band in the spectra of **1-3** are illustrated in Figure A.7. In all cases, the character of the main absorption

band can be confidently assigned as ligand-ligand π-π* transition, consistent with previous findings for related metal systems. [37,45]

2.1.5 Tuning CVD Growth: Insights into NiL₂TMEDA Behavior under Dry O₂ Conditions

Experimental analyses of the chemico-physical properties of the three Ni(II) compounds show that their volatility directly depends on both the fluorination degree and the steric hindrance of the employed diketonate ligands. More specifically, complex **3** was found to be the least volatile, whereas the lighter tfa complex **1** exhibited the highest volatility. These findings are consistent with the fact that the presence of fluorinated groups in the ligands not only reduces intermolecular interactions, but also decreases the basicity of the β-diketonate oxygen donor sites through their electron-withdrawing effect, thereby enhancing the overall volatility of the compounds [40,56,57] (see Ref. [50] for further details). Based on the aforementioned properties, the suitability of the target Ni compounds for NiO CVD was evaluated through preliminary experiments conducted on Si(100) substrates at 400 °C under dry O_2 atmospheres. Key characteristics of the resulting thin films are collected in Table 3.

Table 3: Key features for NiO nanodeposits obtained on Si(100) at 400°C under dry O_2 atmospheres.

Precursor	Thickness (nm)	Growth rate ($nm \times min^{-1}$)
[Ni(tfa)₂TMEDA] (1)	(10±1)	0.08
[Ni(fod)₂TMEDA] (2)	(10±2)	0.08
[Ni(thd)₂TMEDA] (3)	(37±2)	0.31

Table 3 highlights how fluorination degree affects both the thickness and the growth rate of the resulting thin films. Notably, compound **3** exhibited a higher decomposition efficiency compared to compounds **1** and **2**, an unexpected outcome considering thermal analyses data, which had identified **3** as the least volatile member of the series. Such a result highlights that the sole volatility is not sufficient by itself to ensure an appreciable precursor decomposition efficiency on the growth surface. A possible explanation may be provided by theoretical considerations: the higher sublimation temperature of **3** (120°C) compared to compounds **1** (75°C) and **2** (80°C) indicates that **3** is introduced in the CVD reactor chamber more vibrationally excited than **1** and **2**, and thus potentially more reactive. [48] In fact, since deformation modes of the Ni coordination environment, strongly involving metal-ligand bond distances, are located around 250 cm^{-1} (see Tables A.1-A.3), thd is likely to be excited at 120°C ($kT \approx 273\ cm^{-1}$). Moreover, the non-fluorinated complex **3** should be the one characterized by the weakest Ni-N bonds, as suggested by the Ni-N stretching frequencies trend (see Section 2.1.2 and Section A.2.1.3 in Appendix 2). A further key indication is the energetic cost of TMEDA detachment computed for the three complexes (Table 2), which is lowest for

compound **3**, providing a plausible explanation for the more efficient film growth obtained in this case.

Based on the results discussed thus far, it appears that the fluorinated derivatives within this family of precursors, despite their higher volatility, lead to the formation of very thin films under the adopted CVD conditions. This observation suggests that compounds **1** and **2** exhibit high stability in the vapor phase, and that the main limiting factor of the process lies in their reactivity at the growth surface. Nonetheless, the findings presented here clearly demonstrate that all three NiL_2TMEDA complexes are promising Ni precursors for CVD applications, with their fragmentation reactions leading to the formation of the multi-functional nanomaterial NiO. The next step is to address a key question: how can the decomposition efficiency, and consequently the growth rate, of the target Ni precursors be enhanced? Previous studies on Fe and Co tfa-TMEDA adducts [38,40] have shown that introducing water vapor into the reaction atmosphere significantly promotes precursor decomposition, ultimately enabling the formation of thicker films by increasing their growth rate.

2.2 From Dry to Wet: why Water Promotes Precursors Fragmentation and Film Growth

The previous Paragraph addressed, at the computational level, the chemico-physical characterization of three β-diketonate-diamine Ni(II) adducts, namely, Ni(tfa)$_2$TMEDA (**1**), Ni(fod)$_2$TMEDA (**2**), and Ni(thd)$_2$TMEDA (**3**) (see Figure 1), which exhibit promising features as molecular precursors for the vapor-phase deposition of NiO thin films. As previously discussed, preliminary CVD validation experiments conducted under conventional dry O_2 atmospheres resulted in the formation of very thin deposits, suggesting limited decomposition efficiency for the used precursors in those conditions. This behavior was especially pronounced for the fluorinated derivatives (**1** and **2**), despite their superior transport properties compared to the non-fluorinated Ni(thd)$_2$TMEDA. These observations prompted a deeper investigation into the effects of modified growth conditions, with the aim of enhancing precursor conversion and better understanding the correlation between precursor structure and film-forming behavior. Previous studies of the research group on the CVD fabrication of Fe_2O_3 [38,58] and Co_3O_4 [39,40] nanosystems have demonstrated that the introduction of water vapor into the reaction atmosphere can significantly promote the overall growth process, positively impacting both the thickness and morphology of the resulting materials. Building upon this evidence, a water vapor-assisted CVD experiment was carried out for NiO film deposition from the target precursors. The process was performed on Si(100) substrates at 400 °C under humid O_2 conditions (see Ref. [51] for further details). The main features of the deposited thin films are summarized in Table 4.

Table 4: Key features for NiO nanodeposits obtained by H_2O-assisted CVD on Si(100) at 400°C under O_2 atmospheres.

Precursor	Thickness (nm)	Growth rate (nm×min^{-1})
[Ni(tfa)$_2$TMEDA] (1)	(180±6)	1.46
[Ni(fod)$_2$TMEDA] (2)	(90±4)	0.80
[Ni(thd)$_2$TMEDA] (3)	(170±6)	1.42

The obtained results evidenced that, under the same operating conditions, the presence of water vapor in the reaction atmosphere had a beneficial effect on all three precursors, promoting increased film thickness, as anticipated (see Table 3, Section 2.1.5 for comparison). Nevertheless, while experiments from Ni(tfa)$_2$TMEDA and Ni(thd)$_2$TMEDA yielded deposits of comparable thickness, Ni(fod)$_2$TMEDA led to significantly thinner films.

In this context, theoretical calculations aim not only to elucidate why compound **2** yields thinner films compared to the other two members of the series, but also to provide broader insight into the role of water vapor in the decomposition mechanisms of the precursors. These findings – which, to the best of our knowledge, have never been previously reported for comparable systems – are of fundamental importance for understanding, at the molecular level,

the growth process of oxide nanomaterials and the influence of water on the fragmentation pathways leading to their formation.

2.2.1 Modeling the Interaction of Ni(II) Complexes with Water Molecules

To investigate the influence of water vapor in the CVD reaction environment, the interaction of water molecules with $Ni(tfa)_2TMEDA$, $Ni(fod)_2TMEDA$, and $Ni(thd)_2TMEDA$ (Figure 1), was modeled using the DFT approach described in Appendix 2, Section A.2.2.1. The geometries of the three complexes were optimized including from one to three H_2O molecules in the second Ni coordination shell. This strategy enabled the evaluation of structural variations in compounds **1-3** as a function of a variable number *n* of water molecules (*n* = 1, 2, 3), offering insights into how hydration influences the geometry of the precursors. In particular, two different arrangements of water molecules were considered for both the di-hydrated and tri-hydrated complexes. In the di-hydrated species, water molecules were either symmetrically positioned in two different regions of the complex ($Ni(L)_2TMEDA•2H_2O$) or coordinated as a hydrogen-bonded dimer ($Ni(L)_2TMEDA•2H_2O_{dimer}$). For the tri-hydrated systems, the starting geometries included either a dimer and an isolated H_2O molecule on opposite sides of the complex ($Ni(L)_2TMEDA•3H_2O$), or a hydrogen-bonded trimer near the precursor ($Ni(L)_2TMEDA•3H_2O_{trimer}$). Furthermore, all the hydrated structures (Figures A.8-A.11) were generated by placing water molecules near the least hindered regions of the Ni coordination environment, starting from the optimized geometries of the dry $Ni(L)_2TMEDA$ complexes (L = tfa, fod, thd) reported in Figure 1 (Paragraph 2.1). In order to enhance the clarity of the presented data and to support a more effective interpretation of the observed trends, Figure 3 displays only the $Ni(L)_2TMEDA•2H_2O$ complexes, while Table 5 reports average Ni-O and Ni-N bond distances per ligand as a function of both the number and spatial arrangement of water molecules in complexes **1-3**. Full structural details are provided in Section A.2.2.2 of Appendix 2.

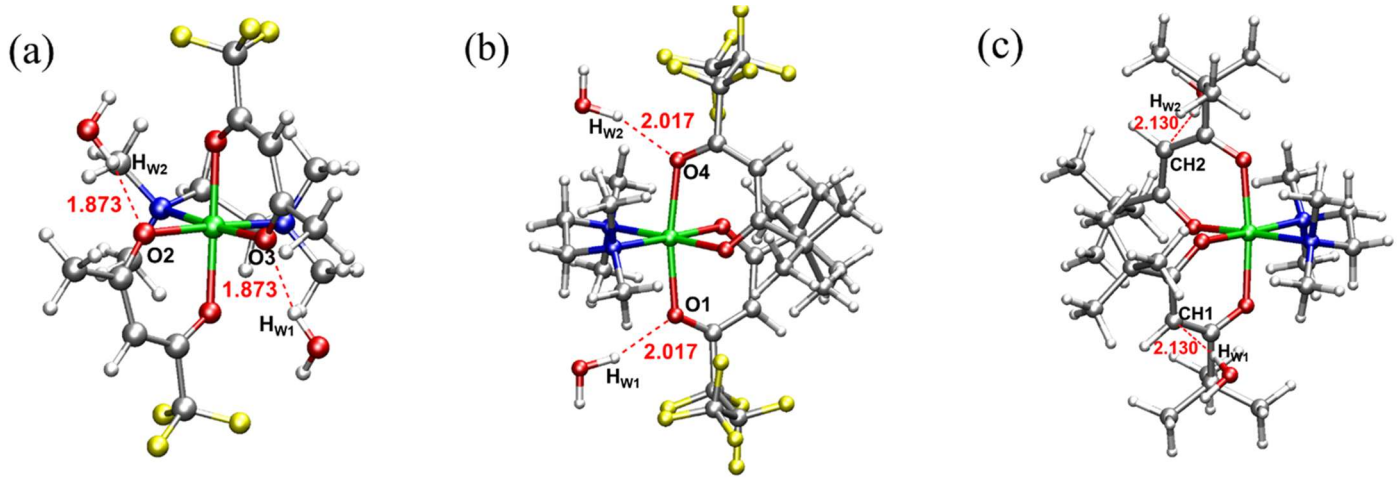

Figure 3: Graphical representation of the DFT-computed minimum energy structures of: (a) $Ni(tfa)_2TMEDA•2H_2O$; (b) $Ni(fod)_2TMEDA•2H_2O$; (c) $Ni(thd)_2TMEDA•2H_2O$. Atom colors code: Ni = green; F = yellow; O = red; N = blue, C = grey, H = white, dashed red lines = hydrogen bonds (bond lengths are in Å).

It should be noted that the adopted hydration levels (n = 1, 2, 3) were not meant to reproduce the full solvation environment of the complexes, but rather to provide a simplified computational model aimed at elucidating the effect of water vapor on the structure and stability of the precursors. In this context, the comparison between hydrated and dry species enabled the evaluation of water binding energies, key bond distances, and vibrational modes, which in turn offered molecular-level insights into the experimentally observed increase in NiO thin film thickness under humid conditions (see the following Sections). The choice to limit the models to a maximum of three water molecules was driven by the conditions adopted in the actual CVD experiment (low-pressure CVD reactor, T≥ 353 K, water vapor is a minor component of the transport gas) [50], which do not favor full solvation of the precursor molecules.

2.2.2 Theoretical IR Analysis: Hydrated versus Dry Ni(II) Precursors

Following the methodology adopted for the non-hydrated precursors (see Section 2.1.2), a study of the vibrational properties of the hydrated precursors via harmonic frequency analysis was performed. This investigation was not intended merely to explore the geometrical changes induced by water molecules, but rather to provide a deeper understanding of how the presence of water vapor may enhance the decomposition efficiency of the target precursors, thereby promoting the formation of thicker NiO thin films. The computed IR spectra (harmonic frequencies) for the hydrated precursors **1-3** are displayed in Figures A.12-A.14, Section A.2.2.3 of Appendix 2, respectively.

The main features of the IR spectra computed for the three hydrated complexes are consistent with those observed in the experimental IR spectra of the corresponding dry precursors (see Appendix 2, Figures A.4-A.6). As previously noted for the latter, the peaks associated to the C=O stretching modes appear at higher wavenumbers for the fluorinated complexes, namely $Ni(tfa)_2TMEDA$ and $Ni(fod)_2TMEDA$, compared to $Ni(thd)_2TMEDA$. In all cases, the stretching modes related to metal-ligand bonds in the Ni coordination environment fall within the 300-650 cm^{-1} range. Specifically, and in line with observations for the non-hydrated forms, Ni-O stretching modes generally occur at higher wavenumbers than those corresponding to Ni-N vibrations. In this context, particular attention was devoted to the di-hydrated complexes in which water molecules are symmetrically positioned close to the diketonate ligands, namely $Ni(L)_2TMEDA•2H_2O$ (L = tfa, fod, thd) depicted in Figure 3. For these systems, a detailed analysis was performed to evaluate the hydration effect on the vibrational modes primarily localized on the Ni-O bonds. This choice allows for a more direct comparison between the vibrational frequencies associated to metal-ligand bonds of the di-hydrated and dry complexes, both of which exhibit a slightly distorted C_2 symmetry (see Section A.2.2.2). As previously discussed, this comparison provides valuable insight into the molecular-level reasons on why the presence of water vapor in the reaction atmosphere enhances the formation of thicker NiO films compared to the growth under dry O_2 conditions. To ensure a thorough and cohesive interpretation of the results derived from structural and vibrational investigations, these findings will be jointly discussed in the subsequent section. The computed wavenumbers of

the normal modes mainly localized on Ni-O bonds for both dry and symmetrically di-hydrated precursors are summarized in Tables A.7-A.9.

2.2.3 Unveiling the Role of Water in Modulating Fragmentation and Film Growth of Ni(II) Precursors

As previously discussed in earlier Sections, to support a clearer interpretation of the observed data and trends, the average Ni-O and Ni-N bond distances *per* ligand are collected in Table 5 as a function of both the number and spatial arrangement of water molecules interacting with each of the three precursors. These values are reported alongside the corresponding binding energies *per* water molecule. For a more detailed overview of the relevant bond distances and angles, the reader is referred to Tables A.4-A.6 in Appendix 2.

Table 5: Average Ni-O and Ni-N bond lengths (in Å) along with computed binding energy *per* water molecule (W_{BE}, kcal mol^{-1}) for the optimized geometries of both dry and hydrated complexes illustrated in Figures A.8, A.10, A.11.

	No water	**+ 1 H_2O**	**+ 2 H_2O**	**+ dimer**	**+ 3 H_2O**	**+ trimer**
			Ni(tfa)$_2$TMEDA (1)			
Ni-O ligand 1 (Å)	2.037	2.040	2.040	2.046	2.045	2.051
Ni-O ligand 2 (Å)	2.037	2.036	2.040	2.035	2.039	2.040
Ni-N TMEDA (Å)	2.169	2.167	2.164	2.171	2.167	2.164
W_{BE} (kcal/mol)	-	9.77	9.14	9.95	9.64	10.14
			Ni(fod)$_2$TMEDA (2)			
Ni-O ligand 1 (Å)	2.034	2.076	2.087	2.043	2.085	2.040
Ni-O ligand 2 (Å)	2.034	2.044	2.087	2.086	2.095	2.077
Ni-N TMEDA (Å)	2.171	2.156	2.140	2.148	2.135	2.152
W_{BE} (kcal/mol)		6.97	6.85	7.40	7.13	8.08
			Ni(thd)$_2$TMEDA (3)			
Ni-O ligand 1 (Å)	2.021	2.021	2.024	2.019	2.024	2.019
Ni-O ligand 2 (Å)	2.021	2.025	2.024	2.025	2.024	2.036
Ni-N TMEDA (Å)	2.182	2.176	2.170	2.180	2.174	2.173
W_{BE} (kcal/mol)	-	7.67	7.37	7.51	7.38	7.44

As shown in Table 5, the binding energies *per* water molecule are notably higher than the thermal energy available under the adopted CVD conditions (approximately 1.3 kcal/mol at 400 °C) in all investigated cases. This suggests that the hydrated precursor species are likely to persist in the reaction environment during NiO film growth. These findings offer a plausible

molecular-level rationale for the remarkable increase in growth rate observed when water vapor is introduced into the CVD atmosphere, as compared to depositions carried out under dry O_2 conditions (see Section 2.1.5). Overall, the water binding energy trend suggests that the effect exerted by water vapor presence should be more pronounced for $Ni(tfa)_2TMEDA$ than for $Ni(fod)_2TMEDA$ and $Ni(thd)_2TMEDA$. Specifically, when $Ni(tfa)_2TMEDA$ is employed, film growth rate rises by ≈18 times under O_2+H_2O reaction atmospheres compared to dry O_2 conditions, whereas more moderate increases are observed for $Ni(fod)_2TMEDA$ (≈10 times) and $Ni(thd)_2TMEDA$ (≈5 times). These data highlight that the highest growth rate increase occurs for the precursor capable of forming stronger hydrogen bonds with gas-phase water, namely $Ni(tfa)_2TMEDA$. In fact, due to the absence of bulky tert-butyl groups, $Ni(tfa)_2TMEDA$ provides the most sterically favorable environment for strong hydrogen bonding interactions between water molecules and the diketonate oxygen atoms. As reported in Appendix 2, sub-Section A.2.2.2.3, in $Ni(fod)_2TMEDA$, bearing two tert-butyl groups, the formation of hydrogen bonds is still possible, although weaker and achievable only at the expense of a significant distortion of Ni coordination sphere. Indeed, complex **2** exhibits the largest water-induced distortion in both Ni-O and Ni-N distances (Tables A.5 and 5). As concerns $Ni(thd)_2TMEDA$, while water molecules cooperate to perturb the Ni coordination environment, thus indirectly influencing Ni-ligand bonding (Tables A.6 and 5), their influence is primarily exerted on the π-structure of the diketonate ligand (see sub-Section A.2.2.2.4). In general, the introduction of H_2O in the Ni second coordination shell induced an elongation of the Ni-O bonds for at least one diketonate ligand, while the Ni-N bonds are consistently shortened. This observation suggests that the presence of water may facilitate the detachment of a β-diketonate ligand, thereby reversing the trend proposed in Section 2.1.3, where energy-based analysis on the dry precursors indicated that the initial step in the fragmentation process involved the TMEDA loss. These findings thus offer new molecular-level insights into the fragmentation behavior of the three target complexes. Despite water-induced distortions, the Ni octahedral coordination environment is maintained in all hydrated complexes. In contrast, a significant alteration of such an environment is observed in the case of dissociated water (Figure A.9). However, the water binding energy obtained for this pentacoordinated structure (close to -50 kcal/mol) indicates that its formation in vapor-phase is highly unlikely or negligible.

Building on these water-induced structural changes and the pertaining binding energies, the vibrational study presented in Section 2.2.2 not only reinforced the impact of hydration on the investigated systems, but also provided further insights into how water vapor may affect the decomposition behavior of the target complexes. Indeed, a careful data inspection reveals that, as anticipated, the most pronounced variations are observed for $Ni(tfa)_2TMEDA•2H_2O$ (Table A.7). Specifically, although an overall frequency increase of the collective Ni-O stretching modes is noted, a significant decrease (15 cm^{-1}) in the stretching frequency of modes involving apical Ni-O bonds (*i.e.*, those not in *trans* to TMEDA) was computed, accompanied by a notable lengthening of such bonds (Table A.4). This result indicates that water plays a key role in weakening two Ni-O bonds, substantially perturbing the coordination of tfa ligands to the metal center and likely contributing to activate the precursor decomposition. In the case of $Ni(fod)_2TMEDA$, the interaction with water leads to a general decrease in the stretching

frequencies of modes localized on Ni-O bonds (Table A.8); however, the maximum frequency decrease observed (10 cm^{-1}) is less pronounced than that computed for complex **1**. Conversely, for Ni(thd)$_2$TMEDA, Ni-O stretching frequencies remain virtually unchanged upon hydration (Table A.9). This finding is consistent with the fact that, in this complex, water protons primarily interact with the π-system of the diketonate ligands, rendering them less effective in weakening Ni interaction with diketonate oxygen atoms. Therefore, although the computed H_2O binding energies suggest that the presence of water vapor should generally enhance the decomposition of all three complexes, both the binding energy trend and the observed decrease in Ni-O stretching frequencies indicate that the effect should be more pronounced in the case of Ni(tfa)$_2$TMEDA. These findings provide a molecular-level rationale for the experimentally observed highest growth rate associated with films deposited from precursor **1**, while also explaining the comparatively weaker influence of water vapor on the growth rate when using the non-fluorinated Ni(thd)$_2$TMEDA compound. However, even for the latter, a 5% increase of growth rate is observed upon introducing H_2O vapor into the CVD chamber. This behavior can be better understood through the analysis of low-energy vibrational modes in the hydrated precursors. Indeed, the computed IR (harmonic) spectra of the hydrated precursors, compared to those of their non-hydrated counterparts (Figures A.12-A.14), clearly show that, for all three systems, the presence of H_2O molecules in the Ni second coordination shell gives rise to relatively intense signals below ≈ 400 cm^{-1}, which are absent in the dry analogues. Such signals are primarily due to water libration modes, which are coupled with strong deformation modes of the Ni coordination shell. This coupling may play a key role in activating precursor fragmentation processes.[48] Notably, such modes are thermally accessible at the substrate temperatures adopted in the CVD deposition process (kT at 400 °C ≈ 435 cm^{-1}). Hence, these water-induced deformations of the Ni local coordination environment, observed for all three Ni(L)$_2$TMEDA precursors, might be at the origin of the general water-induced increase in rate growth. This effect is modulated by the nature of the ligands, which determines the extent of water-induced weakening of the Ni-O bonds in the three precursors.

2.2.4 Final Remarks

In conclusion**,** the results obtained provided a coherent and robust interpretation of the experimental observations. The theoretical approach adopted not only produced results in line with the experimental findings, but also provided molecular-level insights inaccessible to direct experimental investigation. More specifically, this Paragraph elucidates the positive role of water vapor in enhancing film growth rates, as revealed by modeling outcomes. The latter indicated that, under the CVD conditions, water molecules may form stable adducts with the precursors, perturbing their coordination environment and weakening the interaction between Ni and the coordinated β-diketonate ligands. The magnitude of this effect was shown to depend strongly on the chemical nature of the ligands involved. These findings also contributed to advancing the current understanding of the fragmentation pathways of these precursors to yield NiO nanomaterials, complementing and refining the hypotheses proposed in Paragraph 2.1. Particularly remarkable is the central role of water, which acts as a key molecular player in modulating the reactivity and structural behavior of the target complexes.

2.3 Where Bonds Break: Computational Insights into the Fragmentation of Ni(II) β-Diketonate-Diamine Complexes

In the previous two Paragraphs, three Ni(II) β-diketonate-TMEDA precursors were presented, with a focus on their computational characterization supported by experimental data. Moreover, benefiting from preliminary CVD validation experiments conducted under both dry O_2 and H_2O-enriched conditions, it was possible to theoretically elucidate the beneficial role of water in promoting the growth of NiO thin films for all three precursors. In this context, structural insights into the gas-phase fragments of the three precursors are presented in the current Paragraph, which serves as a conceptual bridge between the starting molecular systems (see Paragraphs 2.1 and 2.2) and the resulting nanomaterial (see Paragraph 2.4). This approach not only reflects the chronological order in which the studies were carried out during the PhD work, but also emphasizes the central theme of the present chapter: fragmentation as a driving force of nanomaterial formation.

Despite electron ionization mass spectrometry (EI-MS) being generally considered more appropriate for investigating the gas-phase reactivity of CVD precursors, especially in plasma-assisted processes [50], it is known that hard ionization conditions lead to the destruction of specific ions, which is diagnostic of compound fragmentation [40]. In contrast, similar insights can be effectively obtained using soft ionization methods like electrospray ionization mass spectrometry (ESI-MS) [37,46,47], which enable a deeper understanding of precursor decomposition behavior. For this reason, the fragmentation behavior of the three compounds $Ni(tfa)_2TMEDA$ (**1**), $Ni(fod)_2TMEDA$ (**2**), and $Ni(thd)_2TMEDA$ (**3**) was studied by theoretical investigations, based on electrospray ionization high resolution mass spectrometry (ESI-HRMS) and ESI-MS^n experiments.

2.3.1 Experimental Section

The positive ion mode ESI-HRMS mass spectra for the three complexes are presented in Figure 4, while the identification of the main fragments, their corresponding m/z ratios, and relative abundances are provided in Table 6. In all cases, the base peak (m/z = 327.0830, 469.1229, and 357.2041 for complexes **1**, **2**, and **3**, respectively) was related to $[M\text{-}L]^+$ species (where M denotes compound **1**, **2**, or **3**) resulting from the loss of one β-diketonate ligand (L). Ions due to the protonated diamine $[TMEDA+H]^+$ were detected at m/z = 117.1390, with relative abundance exceeding 45% for all three complexes. Only for **2**, the molecular ion was detected as a sodium adduct at m/z = 787.1690 ($[M+Na]^+$), along with a species resulting from TMEDA loss $[M\text{-}TMEDA+Na]^+$ (m/z = 671.0379). The presence of $[M+Na]^+$ for **2** can be ascribed to a good efficiency of Na adduct formation under ESI-MS conditions, promoted by the partial negative charge of $CF_2CF_2CF_3$ groups due to fluorine atoms [59]. For compound **3**, the signal at m/z = 425.2190 was attributed to TMEDA loss from the protonated molecular ion, which itself was not detected.

Table 6: Main fragments, *m/z* ratios, and relative abundances (%) obtained in ESI-HRMS analyses of compounds **1**, **2**, and **3**. Fragment signals corresponding to compounds 1, 2, and 3 are highlighted in green, red, and blue, respectively.

	1	2	3
Ionic Species	***m/z* (%)**	***m/z* (%)**	***m/z* (%)**
$[M+Na]^+$	---	787.1690 (25)	---
$[M-TMEDA+Na]^+$	---	671.0379 (12)	---
$[M-TMEDA+H]^+$	---	---	425.2190 (15)
$[M-L]^+$	327.0830 (100)	469.1229 (100)	357.2041 (100)
$[HL+H]^+$	---	---	185.1535 818)
$[TMEDA+H]^+$	117.1391 (70)	117.1389 (50)	117.1388 (55)

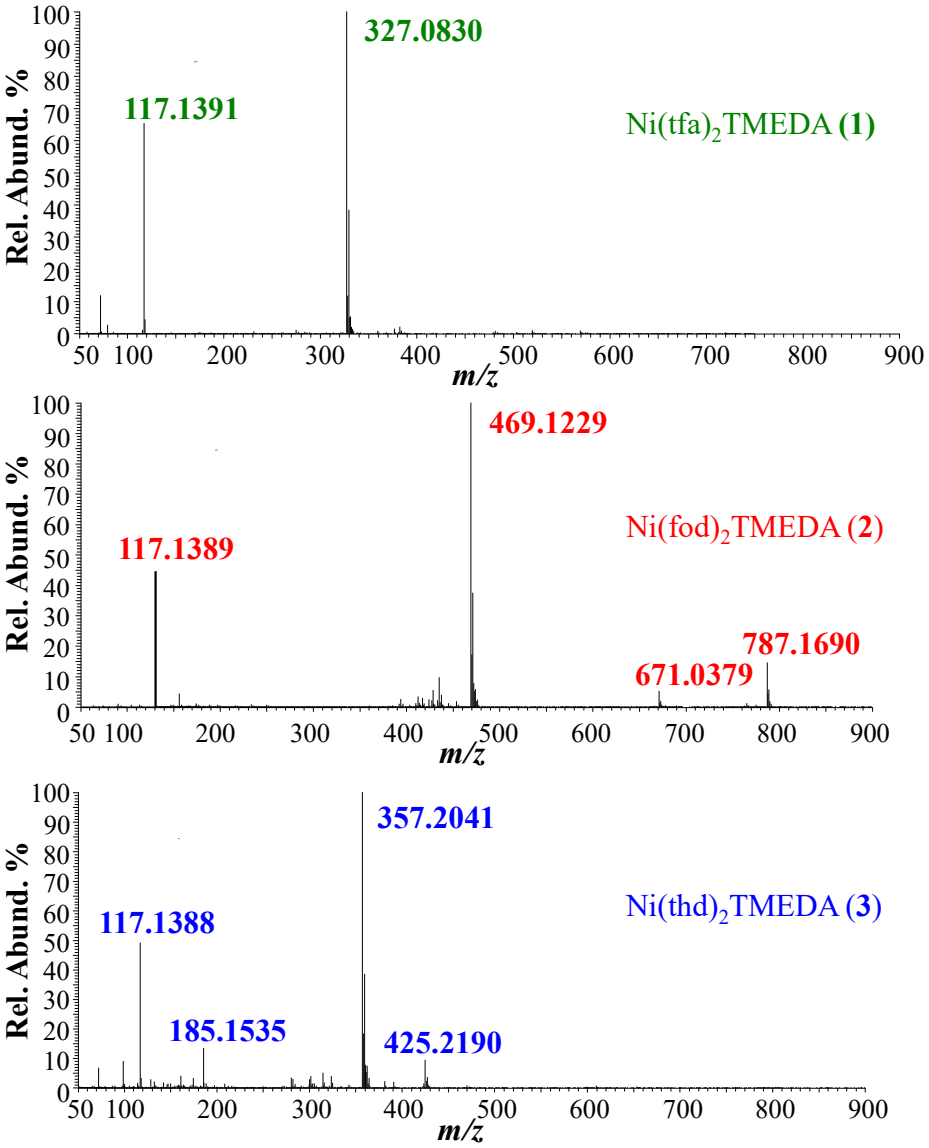

Figure 4: Positive ESI-HRMS spectra of compounds **1-3** recorded in methanolic solution. Fragment signals corresponding to compounds 1, 2, and 3 are highlighted in green, red, and blue, respectively.

MS/MS experiments (see Figure 5) on $[M-L]^+$ ions revealed further decomposition due to TMEDA-related rearrangements. In particular, the loss of a $NH(CH_3)_2$ species from the TMEDA moiety emerged as the most favored fragmentation process, resulting in the formation of ions at m/z = 282, 424, and 312 for **1**, **2**, and **3**, respectively. Additionally, for fluorinated compounds **1** and **2**, the loss of $-CH_3CH_2N(CH_3)_2$ from $[M-L]^+$ led to ionic species at m/z = 254 and 396, respectively. Notably, only for ion $[M-L]^+$ of compound **2**, an additional rearrangement of the fod ligand was observed, which led to species at m/z = 413, due to $C(CH_3)_2=CH_2$ loss.

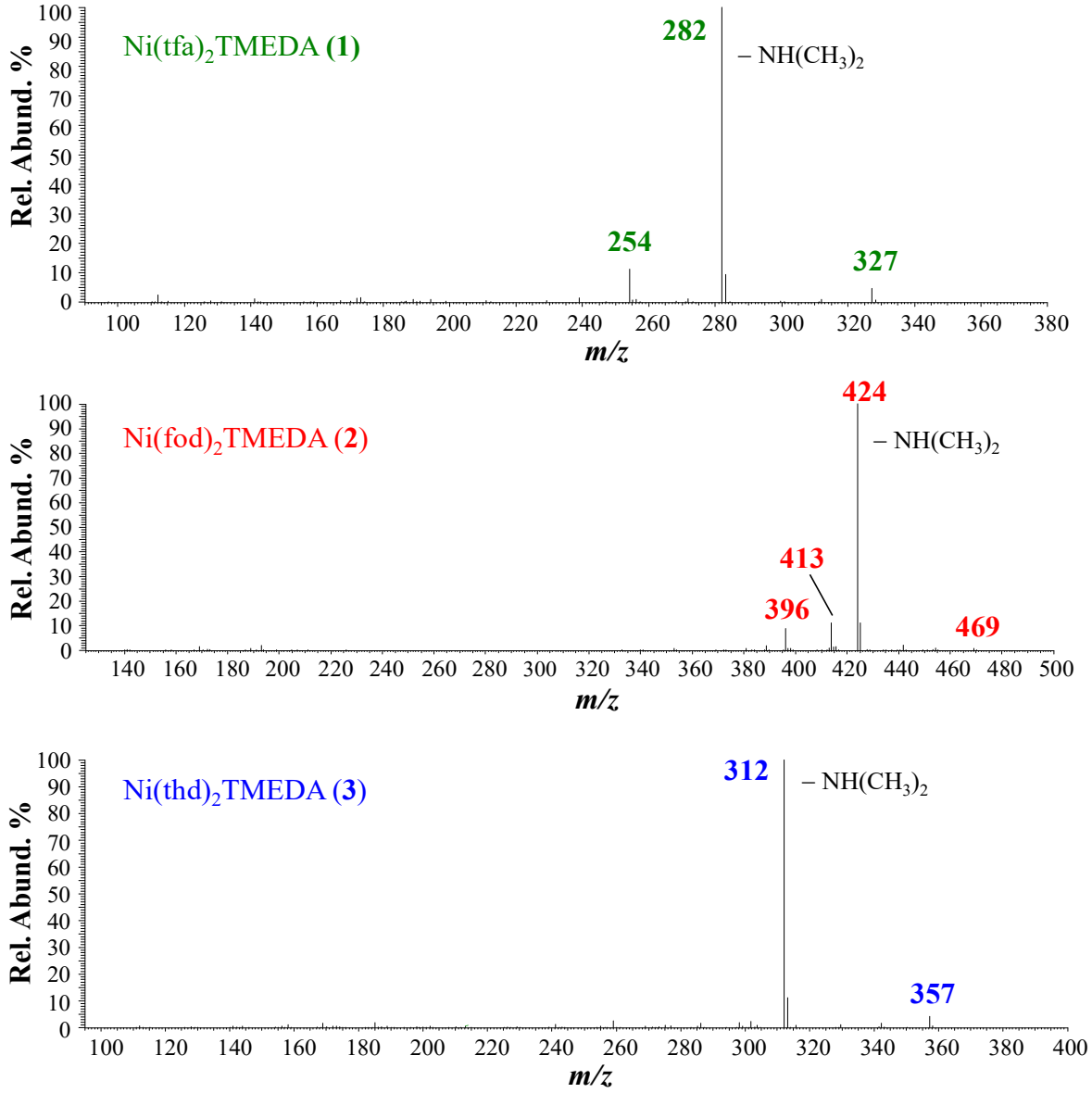

Figure 5: ESI-MS^2 spectra of $[M-L]^+$ ions for compounds **1**, **2**, and **3**. Fragment signals corresponding to compounds 1, 2, and 3 are highlighted in green, red, and blue, respectively.

2.3.2 $[M-L]^+$ Fragments: Structural and Electronic Insights

To gain a deeper understanding of the molecular structures of the fragment ions observed in MS experiments, DFT calculations were carried out (see Appendix 2, Section A.2.3.1), starting with the computation of the three neutral complexes $[Ni(L)_2TMEDA]$ minimum energy structures (Figure 6a, c, and e). In particular, the theoretical analysis provides valuable insights

into how the nature of the ligand influences the fragmentation behavior, thereby setting the basis for a molecular-level interpretation of the precursor chemical reactivity. In line with the experimental ESI-HRMS results, where the base peak in all spectra corresponds to the loss of one β-diketonate ligand L, minimum energy structures of the resulting $[M\text{-}L]^+$ fragments were also investigated. These were obtained by removing a β-diketonate ligand from the corresponding neutral complexes and subsequently optimizing the geometry of the resulting $[Ni(L)TMEDA]^+$ species. The optimized structures of these cationic fragments are shown in Figure 6b, d, and f.

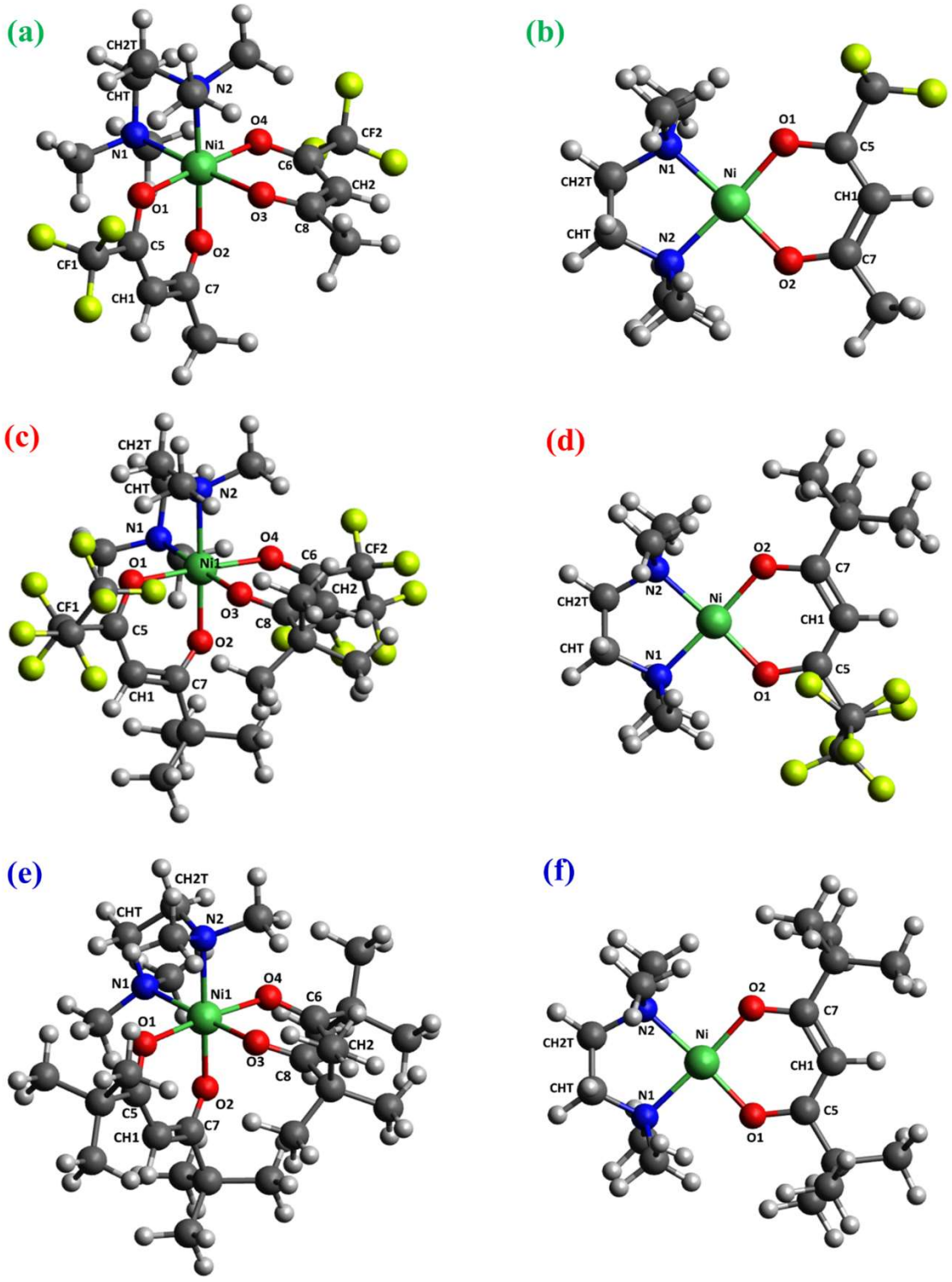

Figure 6: Graphical representation of the DFT-computed minimum energy structures for the pristine complexes $[Ni(L)_2TMEDA]$ with L = tfa (**a**), fod (**c**), thd (**e**), and for the corresponding $[Ni(L)TMEDA]^+$ fragments with L = tfa (**b**), fod (**d**), and thd (**f**). Color codes: green = Ni; yellow = F; blue = N; red = O; grey = C; white = H.

The molecular geometries of the three neutral complexes appear largely comparable. Despite the change in the density functional approximation compared to the analysis presented in Paragraph 2.1 (see Appendix 2, Section A.2.1.1), the computed structural parameters remain close to those previously obtained. In all cases, Ni exhibits a slightly distorted octahedral coordination environment, with Ni-O bond lengths shorter than the Ni-N ones (Table 7). This structural feature suggests stronger interactions between nickel and the oxygen atoms of the β-diketonate ligands compared to those with the nitrogen atoms of TMEDA. This hypothesis is further supported by the computed bond order (BO) values, which systematically indicate higher Ni-O than Ni-N BOs across all complexes (Table 7). Interestingly, while BO values for Ni-O bonds are quite similar, the Ni-N bond order for the non-fluorinated compound **3**, featuring two bulky tert-butyl groups per diketonate ligand, is slightly lower than for the fluorinated complexes **1** and **2**. This trend suggests that fluorinated substituents tend to enhance Ni-N interaction strength, whereas the steric hindrance introduced by tert-butyl groups exerts a weakening effect. Despite these slight differences, both molecular geometry and electronic structure underlying the metal-ligand bonding scheme appear strongly conserved across the three complexes (see Figure 6 and Table 7). This structural and electronic similarity may account for their comparable fragmentation behavior, particularly the consistent appearance of $[M-L]^+$ as the base peak in all ESI-HRMS spectra (Figure 4).

Table 7: Selected bond lengths (BL) (in Å) and corresponding bond orders (BO) values for the optimized structures of neutral complexes M and related fragments $[M-L]^+$ for compounds **1**, **2**, and **3**. Different colors in the BO columns refer to different ligands (brown and violet = first and second diketonate ligand, respectively; gray = TMEDA). Atom labels as in Figure 6.

	1				**2**				**3**			
	M		**[M-tfa]$^+$**		**M**		**[M-fod]$^+$**		**M**		**[M-thd]$^+$**	
	BL	BO	BL	BO	BL	BO	BL	BO	BL	BO	BL	BO
Ni-O1	2.024	0.284	1.831	0.471	2.035	0.242	1.833	0.454	2.018	0.241	1.828	0.476
Ni-O4	2.024	0.284			2.035	0.242			2.018	0.241		
Ni-O2	2.041	0.294	1.848	0.469	2.023	0.258	1.842	0.452	2.009	0.256	1.828	0.476
Ni-O3	2.041	0.294			2.023	0.258			2.010	0.256		
Ni-N1	2.147	0.230	1.946	0.405	2.153	0.201	1.946	0.393	2.165	0.178	1.957	0.368
Ni-N2	2.147	0.230	1.946	0.399	2.153	0.201	1.947	0.387	2.165	0.178	1.957	0.368
O1-C5	1.260	1.362	1.276	1.285	1.260	1.363	1.276	1.279	1.267	1.352	1.284	1.267
O2-C7	1.257	1.427	1.274	1.318	1.258	1.418	1.276	1.316	1.263	1.376	1.284	1.267
O4-C6	1.260	1.362			1.260	1.363			1.267	1.352		
O3-C8	1.257	1.427			1.258	1.418			1.263	1.376		
C5-CH1	1.392	1.423	1.380	1.450	1.393	1.421	1.381	1.451	1.411	1.348	1.400	1.367
C7-CH1	1.424	1.264	1.413	1.300	1.425	1.260	1.413	1.288	1.414	1.325	1.400	1.367
C6-CH2	1.392	1.423			1.393	1.421			1.411	1.348		
C8-CH2	1.424	1.264			1.425	1.260			1.414	1.325		
CHT-CH2T	1.520	1.021	1.508	1.027	1.518	1.021	1.507	1.027	1.520	1.020	1.508	1.026

Comparable features are observed in the minimum energy structures of $[M-L]^+$ fragments, which exhibit very similar geometric arrangements and metal-ligand bonding schemes. In all three cases, the ions adopt a square-planar geometry (Figure 6b, d, and f), typical of tetra-coordinated Ni(II) complexes in the singlet spin state. Furthermore, both the geometrical parameters and the computed BO values reveal only very slight differences across complexes

1, **2**, and **3** (see Table 7). This observation is further supported by natural bond orbital (NBO) analysis performed on the electronic structures of the three $[M\text{-}L]^+$ fragments. Particularly, the strong similarity between the NBOs localized on metal-ligand bonds is evident from data collected in Table A.10 in Appendix 2. As shown in Table A.10, all NBOs display σ-character, regardless of the nature of the diketonate ligand. The bonding orbitals [BD(σ)] are predominantly localized on the ligand's N and O atoms, with occupancies ≈ 90%, whereas the corresponding antibonding orbitals [BD(σ*)] are mostly localized on the Ni center. Taken together, NBO data suggest a net electron density transfer from the ligands to Ni. This interpretation is further supported by the graphical representation of the bonding NBOs (Figures A.15-A.17 in Appendix 2), which highlight their σ-character and the direct involvement of nickel in the bonding scheme.

Following this line of reasoning, NBO analysis offers the possibility of partitioning electron density between specific portions of a given molecule, thereby enabling an estimation of the total charge on each. In the present case, it is particularly insightful to examine the total NBO charges localized on the Ni center, the diketonate ligand (L), and TMEDA (Table 8).

Table 8: NBO charges on Ni, diketonate ligand L, and on TMEDA computed for the optimized structures of neutral complexes M and corresponding fragments $[M\text{-}L]^+$ of compounds **1**, **2**, and **3**. Different colors refer to different ligands (brown = diketonates, purple = TMEDA).

	1		**2**		**3**	
	M	**$[M\text{-}tfa]^+$**	**M**	**$[M\text{-}fod]^+$**	**M**	**$[M\text{-}thd]^+$**
Ni	1.00	0.73	1.08	0.75	1.12	0.75
L	−0.65	−0.35	−0.68	−0.36	−0.69	−0.32
TMEDA	0.30	0.62	0.28	0.61	0.26	0.57

Interestingly, the data reveal that the positive charge on Ni decreases by approximately 25-30% when moving from neutral complexes to $[M\text{-}L]^+$ cations. Although this trend might seem counterintuitive, given the overall fragments' positive charge, it can be rationalized by considering the enhanced electronic charge donation from both the diketonate ligand and TMEDA to Ni center upon loss of one L unit. In fact, the total negative charge on L decreases by 50%, while the total (positive) charge on TMEDA is more than doubled (Table 8). These findings therefore suggest that all $[M\text{-}L]^+$ species are stabilized by a strong electronic density donation from ligands towards Ni. This effect is slightly more pronounced in the fragment derived from compound **3**, due to the higher electron-donor character of the two *tert*-butyl groups on the diketonate moiety with respect to F-containing groups, present in compounds **1** and **2**. All these close similarities in the electronic structure suggest that all three ions possess comparable stability and may all easily form in ESI-HRMS conditions. From a purely geometrical perspective, it is also noteworthy that, for all three complexes, Ni-O and Ni-N bond lengths undergo a significant shortening when transitioning from the neutral compounds to the related $[M\text{-}L]^+$ fragments. This variation is accompanied by a substantial increase in the corresponding bond orders, which are nearly doubled in the fragment ions. As a result, the loss of one diketonate ligand leads to significant strengthening of both the Ni-TMEDA interactions

and the Ni-O bonds within the remaining diketonate moiety. In addition to the main peak common to the three complexes, ESI-HRMS spectra discussed in Section 2.3.1 also revealed the formation of additional cationic species (see Figure 4 and Table 6). A thorough computational search for their minimum energy structures was performed; however, since these results are not essential for the purposes of this Paragraph, they are presented in Appendix 2, Section A.2.3.3.

2.3.3 Fragmentation of [M-L]$^+$ Ions: Structures and Electronic Features of MS^2-Derived Species

With regard to the MS^2 spectra (see Section 2.3.1, Figure 5), attention was focused on the subsequent fragmentation of [M-L]$^+$ cations. Also in this case, the spectra of the three cations displayed common features, most notably, the formation of [M-L]$^+$-NH(CH$_3$)$_2$ species. The theoretical search for minimum energy structures for these moieties led to the results depicted in Figure 7a, c, and f. Consistently with findings in Section 2.3.2, these cations exhibit very similar geometries and Ni-ligand bonding patterns, as summarized in Table 9.

Table 9: Selected bond lengths (BL) (in Å) and corresponding bond orders (BO) values for the optimized structures of fragments detected in ESI-MS^2 spectra of [M-L]$^+$ ions for compounds **1**, **2**, and **3**. Different colors in the BO columns refer to different ligands (brown = diketonate, gray = TMEDA). Atom labels as in Figure 7.

	1				**2**						**3**	
	[M-tfa]$^+$-NH(CH$_3$)$_2$		**[M-tfa]$^+$-CH$_3$CH$_2$N(CH$_3$)$_2$**		**[M-fod]$^+$-NH(CH$_3$)$_2$**		**[M-fod]$^+$-CH$_3$CH$_2$N(CH$_3$)$_2$**		**[M-fod]$^+$-(CH$_3$)$_2$C=CH$_2$**		**[M-thd]$^+$-NH(CH$_3$)$_2$**	
	BL	BO	BL	BO	BL	BO	BL	BO	BL	BO	BL	BO
Ni-O1	1.811	0.523	1.799	0.557	1.814	0.506	1.794	0.554	1.837	0.450	1.808	0.535
Ni-O2	1.830	0.511	1.819	0.541	1.816	0.518	1.815	0.543	1.842	0.453	1.803	0.546
Ni-N1	-		-		1.929	0.391	1.946	0.402	1.938	0.415	1.941	0.368
Ni-N2	1.932	0.393	1.943	0.408					1.937	0.414		
Ni-CHT	1.972	0.248	1.987	0.264	1.976	0.239	1.986	0.264			1.974	0.243
Ni-CH2T	2.096	0.394	2.128	0.368	2.098	0.393	2.128	0.363			2.108	0.375
O1-C5	1.277	1.288	1.281	1.267	1.280	1.258	1.281	1.263	1.265	1.342	1.288	1.264
O2-C7	1.281	1.297	1.279	1.308	1.279	1.314	1.280	1.299	1.270	1.318	1.287	1.264
C5-CH1	1.384	1.444	1.381	1.463	1.380	1.468	1.381	1.458	1.400	1.345	1.399	1.381
C7-CH1	1.409	1.315	1.412	1.300	1.417	1.281	1.413	1.292	1.389	1.404	1.403	1.361
CHT-CH2T	1.379	1.566	1.373	1.588	1.380	1.567	1.373	1.590	1.508	1.027	1.378	1.579

While the β-diketonate ligand remains coordinated to the metal center through both its O atoms, only one N atom (the one that survived the fragmentation) is linked to the Ni center. Nevertheless, the latter preserves its nearly square-planar coordination geometry thanks to the interaction with a new C=C double bond formed upon -NH(CH$_3$)$_2$ release. In these fragments, the Ni-CHT and Ni-CH2T distances become ≈ 2 Å (see Table 9 and Figure 7 for atom labels). Moreover, a comparison of structural parameters reveals a net shortening of the CHT-CH2T bond length with respect to the corresponding distance in the [M-L]$^+$ species (cf. Tables 7 and 9; see also Figure 7). This structural change is accompanied by a significant increase in the

associated bond order, rising from ≈ 1 to values exceeding 1.5 (see Tables 7 and 9). Correspondingly, Ni-CHT and Ni-CH2T BO values become comparable to those of Ni-O and Ni-N bonds, indicating appreciable Ni-C interactions. The latter are greater for the terminal C atom (CH2T), which lies closer to the Ni center.

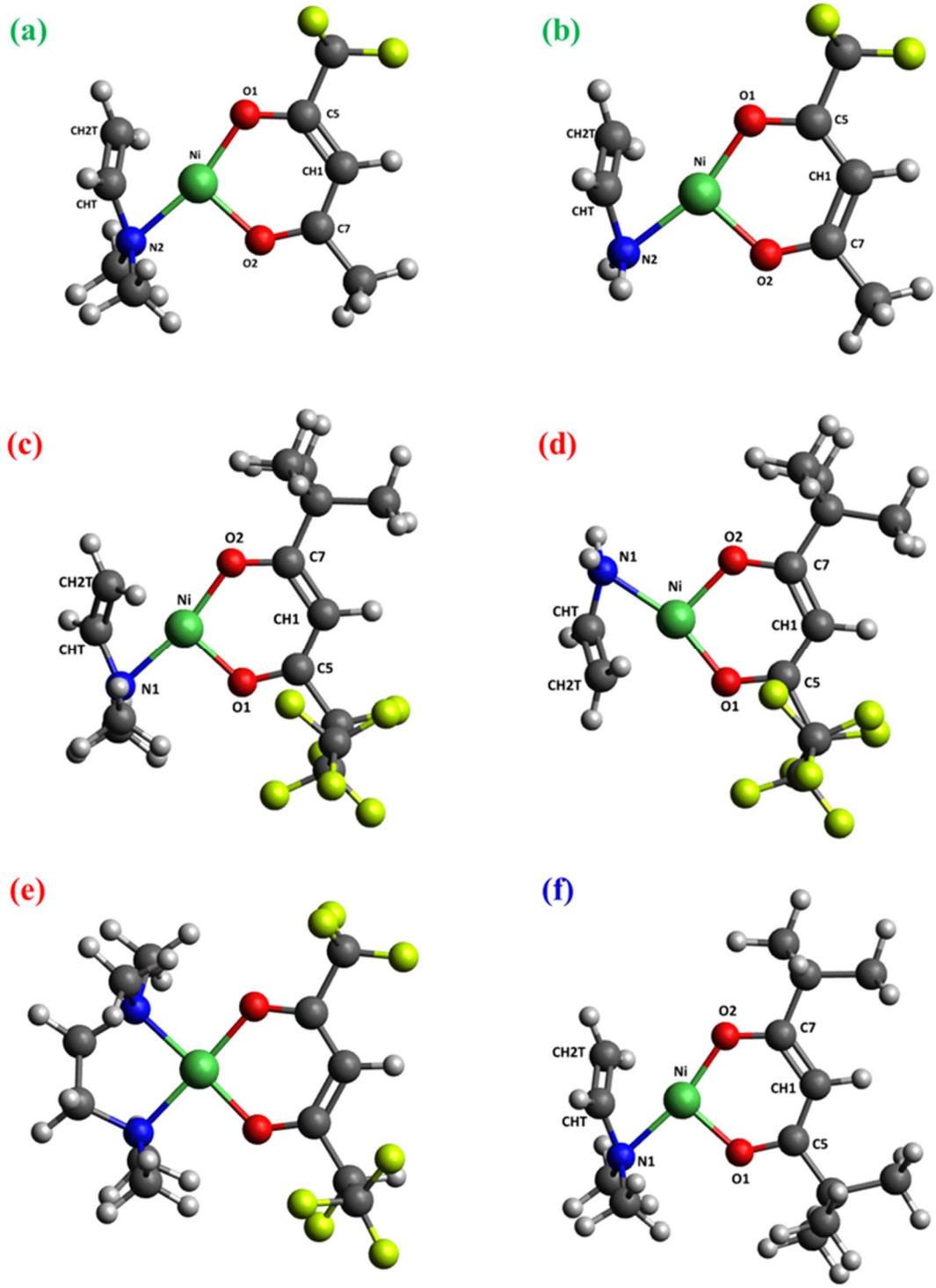

Figure 7: DFT-optimized structures of: (**a**) $[Ni(tfa)TMEDA]^+$-$NH(CH_3)_2$; (**b**) $[Ni(tfa)TMEDA]^+$-$CH_3CH_2N(CH_3)_2$; (**c**) $[Ni(fod)TMEDA]^+$-$NH(CH_3)_2$; (**d**) $[Ni(fod)TMEDA]^+$-$CH_3CH_2N(CH_3)_2$; (**e**) $[Ni(fod)TMEDA]^+$-$(CH_3)_2C{=}CH_2$, resulting from an additional fod ligand rearrangement; (**f**) $[Ni(thd)TMEDA]^+$-$NH(CH_3)_2$. Atom color codes: green = Ni; yellow = F; blue = N; red = O; grey = C; white = H.

To gain further insight into the chemical nature of this new interaction, a detailed natural bond orbital analysis was carried out (see Appendix 2, Section A.2.3.4). In this regard, Figures A.21-

A.23 display the relevant orbitals involved in the interaction, whereas Table A.13 reports the quantitative NBO data. As observed in the orbital representations, a cation-π intramolecular interaction occurs between the Ni center and the carbon atoms of the CHT=CH2T double bond. All these features are consistently observed across all three cations, further confirming once again the similarity of metal-ligand bonding schemes among the fragments derived from compounds **1**, **2**, and **3**.

The loss of a -$CH_3CH_2N(CH_3)_2$ group was also observed, but exclusively for fluorinated $[M-L]^+$ species derived from compounds **1** and **2**. In these cations (Figure 7b and 7d), the bonding pattern around Ni is virtually identical to that of the $[M-L]^+$-$NH(CH_3)_2$ fragments previously discussed. The square planar tetra-coordinated Ni geometry features two Ni-O bonds, one Ni-N bond, and a Ni···CHT=CH2T (cation-π) intramolecular interaction, with the π structure predominantly localized on the CHT=CH2T double bond (see Figures A.24 and A.25, and Table A.14 for orbital representations and NBO analysis, respectively).

Finally, in the case of compound **2**, fragments corresponding to the loss of a $CH_3C=CH_2$ group from $[Ni(fod)TMEDA]^+$, namely $[Ni(fod)TMEDA]^+$-$(CH_3)_2C=CH_2$), were detected in the ESI-MS spectra. The observed stoichiometry suggests a rearrangement of the fod ligand (see Paragraph 2.3.1). To elucidate the structure of these cations, geometry optimizations were performed on different hypothetical isomers consistent with the experimental composition (see Appendix 2, Section A.2.3.4). Figure 8 presents the most stable structure, which features a distribution of fluorine atoms on both sides of the diketonate ligand.

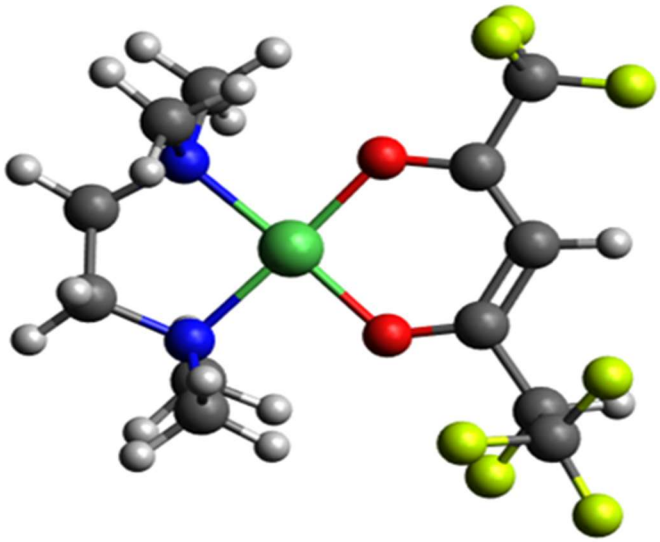

Figure 8: Graphical representation of the minimum energy structure of the fragment ion $[Ni(fod)TMEDA]^+$-$(CH_3)_2C=CH_2$, resulting from an additional rearrangement of fod ligand and detected in MS^2 spectra of precursor **2**. Atom color codes: green = Ni; yellow = F; blue = N; red = O; grey = C; white = H.

2.3.4 Bader Charge Analysis and Concluding Remarks on the Fragmentation of Ni(II) Complexes

To complement the insights gained from Natural Bond Orbital (NBO) calculations, Bader charge analysis, rooted in the Quantum Theory of Atoms in Molecules (QTAIM) [60,61] was

also performed. In the present work, this method was employed to further elucidate the redistribution of electron density occurring during the gas-phase fragmentation of Ni(II) β-diketonate-TMEDA complexes (see Appendix 2, Section A.2.3.5 for further details). The evolution of Bader charges from the neutral complexes to the corresponding positively charged fragments further evidences common features observed in the fragmentation pathways of all three species (see Tables A.15-A.18). In particular, the computed values reveal a net electron displacement from ligands toward the nickel center during the fragmentation process. This results in a significant reduction of the Ni atomic charge, despite the overall positive character of the fragments. These findings align well with the outcomes of the NBO analysis, further supporting the hypothesis of strong ligand-to-metal electron donation stabilizing the cationic species formed during the fragmentation processes.

In conclusion, the extensive DFT investigation presented in this Paragraph was aimed not only at gaining deeper insight into the gas-phase fragments of the three $Ni(L)_2TMEDA$ complexes (L = tfa, fod, thd), thus allowing to elucidate their molecular and electronic structures. The results clarify how metal-ligand bonding patterns evolve upon passing from the pristine precursors to the species detected in MS analyses. Overall, the computational data highlight a common decomposition route for all three complexes:

(i) in the first fragmentation event, each precursor loses a negatively charged β-diketonate ligand, yielding structurally analogous $[M\text{-}L]^+$ cations. In these fragments, Ni-O and Ni-N interactions become significantly stronger, and the Ni center undergoes a marked reduction in positive charge compared to the parent neutral complexes;

(ii) in the subsequent fragmentation step, the tendency of ligand electronic charge to migrate towards Ni further increases, likely due to enhanced ligand-to-metal electron donation. This process leads to the formation of a tetracoordinated Ni environment, in which the coordination sphere includes carbon atoms from a C=C double bond generated through partial TMEDA decomposition. NBO analysis, supported by bond order trends, confirms that this unsaturated moiety participates in a noteworthy intramolecular cation-π interaction with the Ni center.

From a broader perspective, the present findings provide for the first time a detailed molecular-level description of the fragmentation of such Ni(II) precursors as a function of ligand nature. The data also offer valuable insight into the geometric and electronic structures of the resulting fragments, laying the groundwork for a deeper understanding of their chemical behavior under CVD conditions and shedding light on their possible role in molecule-to-material conversion processes. Against this broader background, fragmentation should be understood as a fundamental chemical transformation initiating the pathway from molecular precursor to the resulting nanostructured material. In the specific case of Ni(II) β-diketonate-TMEDA complexes, the gas-phase dissociation steps examined here may dictate the early evolution of the system under activation conditions. Specifically, the obtained results have provided insight on how the metal coordination sphere is reorganized, how ligand frameworks are destabilized and reshaped, and how new metal-ligand interactions (such as the observed cation-π interactions) are established.

It should be noted that the present study does not aim to reconstruct the full fragmentation mechanism through the identification of transition states (TS). Instead, as already mentioned, it focuses on the structural and electronic characterization of the main fragments obtained upon gas-phase dissociation of the Ni(II) β-diketonate-diamine precursors. Such a mechanistic investigation would have required a multiconfigurational approach, since the initial complexes are in high-spin states while their fragments adopt mostly low-spin configurations. Considering all relevant spin states and possible spin state changes along the gas-phase fragmentation paths would have significantly increased the computational complexity and fall beyond the scope of the present work. Nevertheless, the insights provided here are expected to offer a solid basis for future mechanistic studies. Specifically, the studies of surface-induced fragmentations and adsorbed fragments – molecular oxygen interactions should be a future step towards a deeper understanding of the molecule-to-material conversion. Moreover, the difficulties in such studies are further enhanced by the key roles of both high-temperature regimes and spin state changes at the molecule-substrate interfaces.

2.4 Computational Investigation of NiO: From Bulk to Regular and Defective Surfaces

The present Paragraph shifts the focus from the molecular domain to the resulting material, nickel(II) oxide (NiO), via the CVD processes.

As introduced at the beginning of Chapter 2, NiO is a wide-gap *p*-type semiconductor of notable interest for a variety of technological applications, including gas sensors, solar energy conversion, electrochromic systems, and heterogeneous catalysis [18,34,65-71]. In its bulk form, NiO adopts a rock-salt crystal structure and exhibits antiferromagnetic ordering (AF) with collinear spins aligned along (111) planes, classifying it as an Antiferromagnetic Insulator (AFI) with an energy gap (E_{gap}) typically ranging from 4.0 to 4.3 eV [6,7,72]. Usually, in NiO materials the valence band (VB) mainly originates from O 2p-states, while the conduction band (CB) is dominated by Ni 3d-states [6]. Nonetheless, experimental E_{gap} values for NiO vary widely (3.2-4.3 eV) [3,4,6,72], largely depending on morphological differences (e.g., bulk, thin films, nanoparticles, etc.) [73] and on the presence of structural defects [1,2]. In particular, nanostructured NiO and thin films tend to show lower band gaps, closer to the visible (Vis) range, enhancing their potential in applications like photocatalysis and solar light harvesting [2,5,7,72,74-77]. While the electronic structure of bulk NiO has been well-studied [6,7,72,74,76,78-80], especially regarding its semiconducting behavior (involving both d-d transitions and charge transfer mechanisms), further research is needed to better understand the structure-property relationships in defective or nanostructured films. Factors such as growth temperature, film thickness, and annealing conditions can significantly impact the band gap [4,28,81]. Moreover, although *p*-type conductivity is typical, *n*-type or *p*-type behavior can be tuned by altering the oxygen partial pressure during synthesis [1], while defects can also crucially influence the resulting electronic properties [2,4,5,75].

In this context, NiO films presented and discussed in Paragraph 2.2, i.e. obtained from the CVD of $Ni(L)_2$TMEDA complexes in presence of water vapor, exhibited a strong (100) preferential orientation and a band gap of ≈ 3.40 eV [82]. This behavior is consistent with the presence of surface -OH moieties, as also frequently reported for films fabricated via various deposition routes [18,20,83,84]. Despite their widespread occurrence, the structural and electronic consequences of these hydroxylated species on NiO surface properties remain poorly understood, primarily due to the inherent experimental challenges in resolving their nature at the atomistic level [45,48,85]. Given the technological relevance of NiO(100) surfaces, characterized by low polarity and balanced number of spin-up and spin-down Ni atoms [75], theoretical studies have investigated only water adsorption on NiO(100) surfaces [86] and hydroxylation processes occurring on NiO(111) facets [87]. Nevertheless, to the best of our knowledge, to date no systematic computational investigation has been conducted on hydroxylated NiO(100) surfaces. Based on this gap, a theoretical exploration of -OH defects on NiO(100) can offer valuable insight into the atomistic origins of the experimentally observed optoelectronic properties.

Therefore, this Paragraph presents a computational study based on Density Functional Theory (DFT) with the Hubbard Hamiltonian method (DFT+U), aimed at modeling both bulk NiO

and a series of regular (stoichiometric) and -OH-functionalized NiO(100) surfaces. Computational Details are provided in Appendix 2, Section A.2.4.1. This approach balances accuracy and computational cost, enabling a reliable description of NiO electronic structure [74,86] and the simulation of extended models with various -OH defects. Specifically, different types of -OH defects are considered, including surface-bound hydroxyls on Ni and O atoms, dissociatively adsorbed water species, and surfaces with varying degrees of hydroxylation. This modeling strategy enables a realistic atomistic-level characterization of the structural and electronic effects associated with surface -OH groups, shedding light on their role in modulating properties such as band gap, spin distribution, and surface reactivity.

2.4.1 Regular NiO(100) Surfaces: Reference Models for Defect Analysis

In this Section, the defect-free systems are examined, namely bulk NiO and the regular NiO(100) slab models, from which all -OH-defective surfaces were derived. Since bulk NiO has been extensively investigated through theoretical studies, providing a solid foundation for understanding its structural, electronic, and magnetic properties [6,7,72,74,76,78-80,88], and given that the main goal of this Paragraph is to assess the impact of -OH defects on NiO(100) surfaces, the properties computed for the bulk models (specifically, optical band gap, magnetic moments, and total/partial density of states) are reported in Appendix 2, Section A.2.4.2, as benchmark data for comparison with those obtained for slab models using the same computational setup. By contrast, the analysis of the regular (stoichiometric) NiO(100) slabs offers essential insight into the intrinsic characteristics of the surface prior to functionalization. These systems not only help to quantify the perturbations induced by -OH groups, but also allow for assessing the role of defect nature and concentration to the overall electronic behavior of the material.

Two regular (defect-free) NiO(100) slab models were built: RegSurf 1 ($Ni_{32}O_{32}$, derived from Bulk 1, surface area: 69.65 $Å^2$) and RegSurf 2 ($Ni_{64}O_{64}$, derived from Bulk 2, surface area: 139.31 $Å^2$), as illustrated in Figure 9. Structural optimizations were carried out on both models. RegSurf 1 and RegSurf 2 exhibit several common features, with surface relaxation primarily affecting the two outermost layers (see Table 10). Indeed, the top layer shows slight distortions in Ni-O distances and interlayer separations, consistent with previously reported STM observations on NiO surfaces [89]. The antiferromagnetic (AF) ordering is preserved, with a slight increase in the magnetic moment (μ_{Ni}) per Ni atom compared to the bulk ($\approx$ 1.80, Table A.19). The computed band gap is significantly reduced with respect to bulk NiO ($\approx$ 3.00, Table A.19), in agreement with literature trends [7,72,74,75], and is likely related to the surface distortions described above.

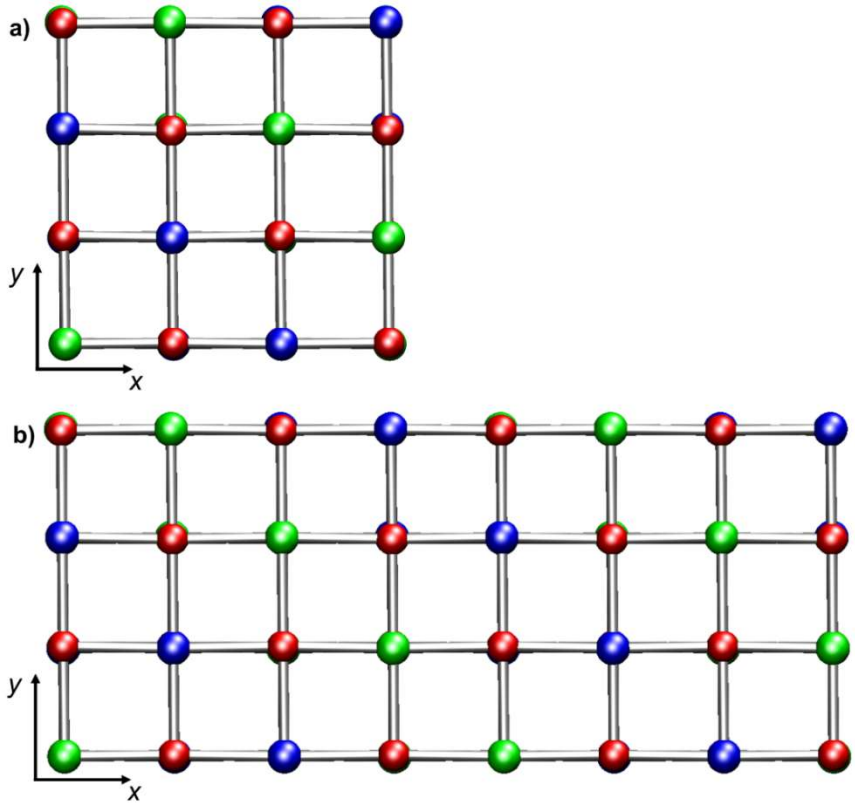

Figure 9: Ball-and-stick representation of the regular NiO(100) slab models simulation cell: **a)** RegSurf 1 ($Ni_{32}O_{32}$) projected on the *xy* plane; **b)** RegSurf 2 ($Ni_{64}O_{64}$) projected on the *xy* plane. Atoms color codes red = O; blue = Ni (spin-up); green = Ni (spin-down).

Table 10: Properties of NiO (100) slab models. E_{gap}: band gap energy; E_{VB}: VB top energy; E_{CB}: CB bottom energy; μ_{tot}: total magnetization; μ_{Ni}: absolute magnetization per Ni atom; d(Ni-O): Ni-O distances; d(Ni-Ni): Ni-Ni distances. For slab models, distances refer to top-layer atoms. Energies are given in eV, μ_{tot} and μ_N in Bohr Magnetons (μ_B), and distances in Å. E_{VB} and E_{CB} are relative to the Fermi Level, conventionally set to 0.

System	***E_{gap}***	***E_{VB}***	***E_{CB}***	***Type***	***μ_{tot}***	***μ_{Ni}***	***d(Ni-O)***	***d(Ni-Ni)***
RegSurf 1 ($Ni_{32}O_{32}$)	2.165	-0.656	+1.509	*p*	0	1.82	2.073 2.101	2.951
RegSurf 2 ($Ni_{64}O_{64}$)	2.165	-1.054	+1.121	*p*	0	1.82	2.080 2.092	2.951

Both slabs have *p*-type character, and the pDOS calculated for RegSurf 1 and RegSurf 2 are compared in Figure 10. As observed for the corresponding bulk systems (see Figure A.29), the two slab models display very similar pDOS profiles. In both cases, the pDOS reveals a dominant contribution from O 2*p*-states at the top of the VB, accompanied by a minor contribution from Ni *d*-states, while the bottom of the CB is mainly composed of unoccupied Ni *d*-states. The similarities between the pDOS of the regular slab and bulk models suggest that the key electronic structure features of bulk NiO are preserved in regular NiO(100) films.

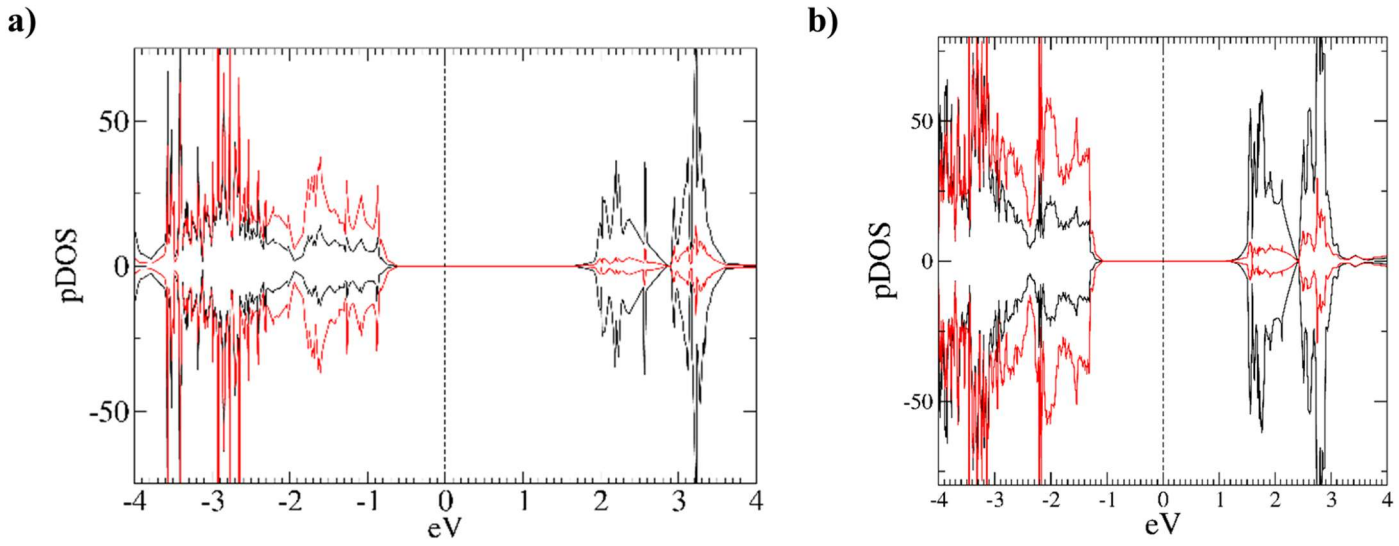

Figure 10: Computed pDOS for stoichiometric NiO(100) slab model systems: a) $Ni_{32}O_{32}$; b) $Ni_{64}O_{64}$. The black vertical dashed line represents the Fermi level position (0 eV). Positive and negative values correspond to spin-up and spin-down components, respectively. Red lines indicate O 2*p* states, while black lines represent Ni *d* states.

The comparison between bulk and regular slab models has highlighted the intrinsic structural and electronic features of stoichiometric NiO. However, real materials rarely exist in such idealized forms. Surface defects, in particular hydroxylation, play a crucial role in shaping surface reactivity and modulating the electronic behavior of the material. Taken together, the results obtained for bulk and regular NiO(100) models define a robust reference framework for interpreting defect-induced modifications. In this context, following Sections will focus on hydroxylated NiO(100) surfaces, aiming to assess how the introduction of -OH groups perturbs the surface and modulates its structural and electronic properties.

2.4.2 Monohydroxylated NiO(100) Surfaces: Structural and Electronic Impact of a Single Defect

Each layer of the regular NiO(100) surfaces features parallel rows of spin-up and spin-down Ni cations aligned along the (111) planes (Figure 9). As a result, each top-layer oxygen atom is coordinated by two spin-up and two spin-down Ni cations on opposite sides (see Figure 11). Additionally, these oxygen atoms are positioned above either spin-up or spin-down Ni cations of the layer below. Consequently, the formation of a surface -OH group, either through the addition of a hydrogen atom (H) to a surface oxygen site (Figure 11a) or through the coordination of an -OH moiety to a Ni center (Figure 11b), breaks the pristine magnetic symmetry, thereby affecting the antiferromagnetic (AF) ordering of the system. Nevertheless, it is of particular interest to investigate how the presence of a single hydroxyl group might influence the structural and electronic properties of regular NiO(100) slabs.

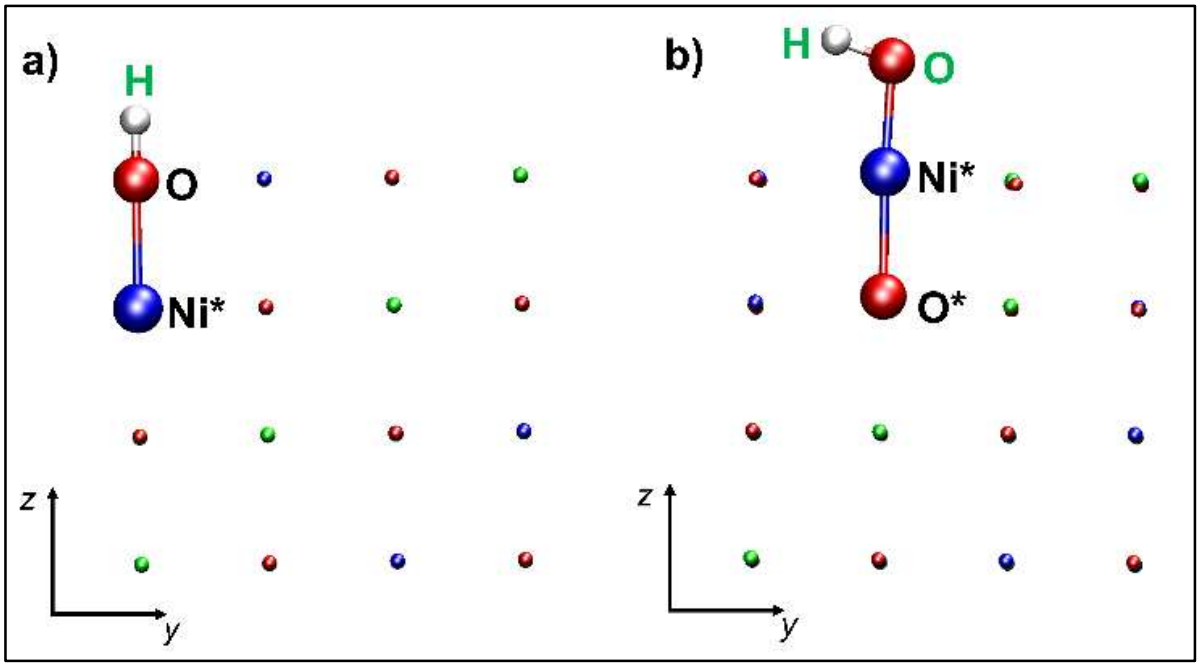

Figure 11: Ball-and-stick schematic representations of an -OH defect formed by adding: **a)** an H atom to a top-layer oxygen; **b)** a hydroxyl group to a top-layer Ni atom. Atoms directly involved in the defect are highlighted as spheres. Atoms color code: red = O; blue = Ni (spin-up); green = Ni (spin-down). The a) H and b) OH atoms adsorbed on the NiO(100) surface are labeled in green, Ni*: top- or lower-layer Ni atom bearing the -OH group; O*: lower-layer O atom bonded to Ni*.

In this context, three monohydroxylated NiO(100) slab models were considered, characterized by different simulation cell size: $Ni_{32}O_{32}(OH)$ (derived from Bulk 1, surface area: 69.65Å^2), $Ni_{16}O_{16}(OH)$ (derived from Bulk 3, surface area: 34.83 Å^2), and $Ni_{24}O_{24}(OH)$ (derived from Bulk 3, surface area: 34.832 Å^2), shown in Figure 12a, b, c, respectively.

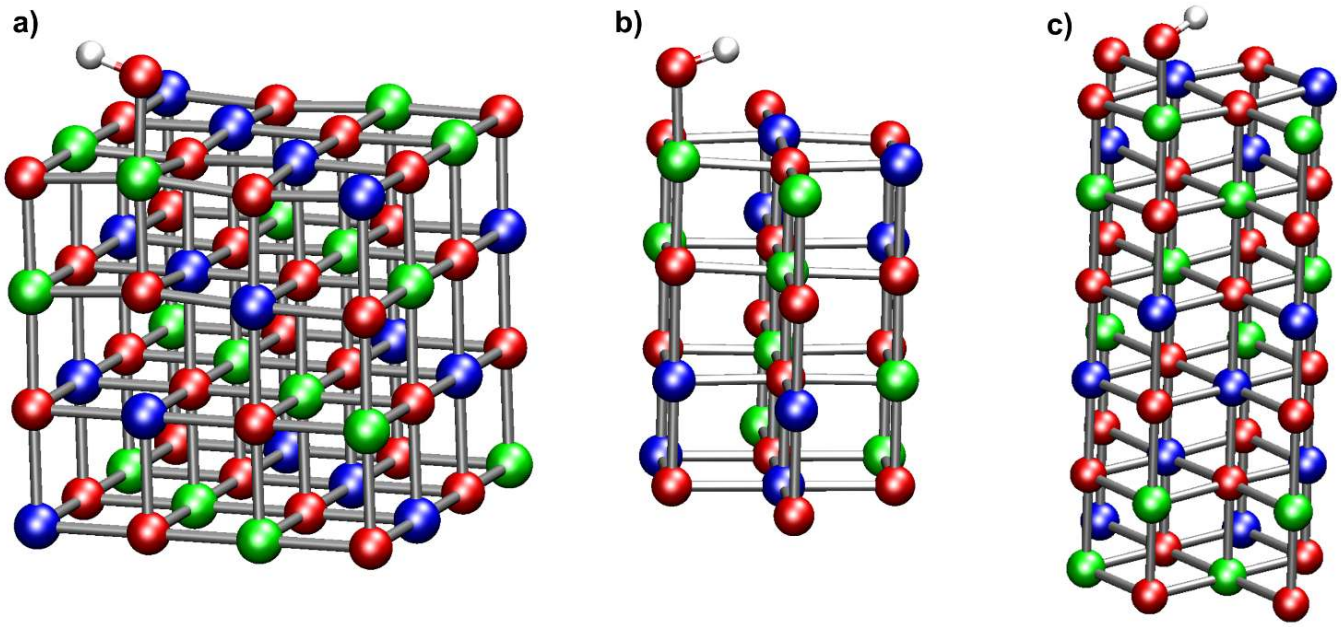

Figure 12: Ball-and-stick representation of the simulation cell of the mono-hydroxylated NiO(100) slab models: **a)** $Ni_{32}O_{32}(OH)$; **b)** $Ni_{16}O_{16}(OH)$; **c)** $Ni_{24}O_{24}(OH)$, Atoms color code: red = O; blue = Ni (spin-up); green = Ni (spin-down).

The relevant properties of the three minimum energy structures of the mono-hydroxylated NiO(100) slab models are reported in Table 11 (atom labels as in Figure 11). The structural analysis focused primarily on the local defect environment, namely O*-Ni*-OH atoms (Figure 11). For further details, see Appendix 2, Section A.2.4.4. Structural comparison of the three mono-hydroxylated NiO(100) slab models revealed highly similar coordination environments around the -OH group, with consistent O-H bond lengths and Ni*-$\widehat{O}$-H bond angles. While slab thickness had a negligible effect on the structure of the hydroxylated slabs, the surface area plays a crucial role in deviations of average Ni-O distances from the bulk value (2.086 Å), with more pronounced deviations observed in the smaller-surface models ($Ni_{16}O_{16}$(OH) and $Ni_{24}O_{24}$(OH)).

Table 11: Properties of mono-hydroxylated NiO(100) slab models. E_{gap}: band gap energy; μ_{tot}: total magnetization; μ_{Ni}: absolute magnetization per Ni atom. Energies are given in eV, μ_{tot} and μ_N in Bohr Magnetons (μ_B), Ni*-OH, O-H, Ni-O and Ni*-O*distances in Å, Ni*-$\widehat{O}$-H angles in degrees. ⟨Ni-O⟩ denotes the average Ni-O distance for the top-layer.

System	E_{gap}	Type	μ_{tot}	μ_{Ni}	Ni*-OH	O-H	⟨Ni-O⟩	Ni*-O*	Ni*-$\widehat{O}$-H
$Ni_{32}O_{32}$(OH)[a]	0	*Half-metal*	-0.91	1.81	1.817	0.980	2.081	2.118	107.2
$Ni_{16}O_{16}$(OH)[a]	0	*Half-metal*	-1.00	1.81	1.808	0.980	2.100	2.148	107.7
$Ni_{24}O_{24}$(OH)[a]	0	*Half-metal*	-1.00	1.77	1.808	0.980	2.100	2.152	107.2

As previously discussed, the addition of a single -OH group to a surface Ni atom unevenly perturbs the two magnetic sublattices, breaking the pristine spin symmetry. This disruption affects both the magnetic and electronic properties of the systems. Indeed, all mono-hydroxylated models exhibit non-zero total magnetization μ_{tot}, as reported in Table 11, with such an effect slightly more pronounced in the models with smaller surface area. More notably, the electronic structure undergoes a significant modification, with the appearance of a half-metallic character (Table 11), as further confirmed by the DOS shown in Figure 13. This behavior is consistent with previous literature findings. [90]

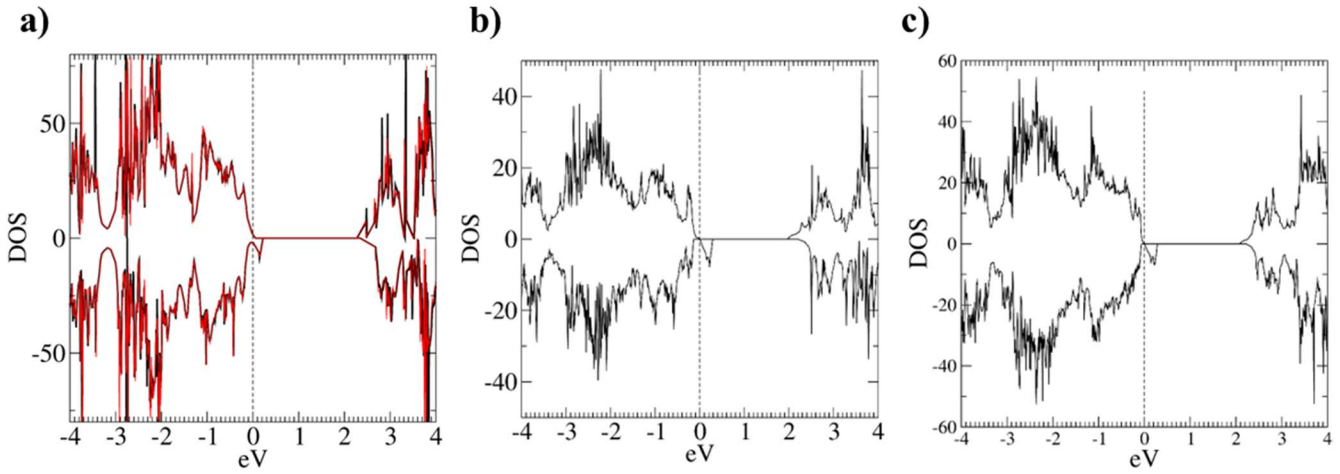

Figure 13: Computed DOS for mono-hydroxylated slab model systems: **a)** $Ni_{32}O_{32}$(OH); **b)** $Ni_{16}O_{16}$(OH); **c)** $Ni_{24}O_{24}$(OH). The black vertical dashed line represents the Fermi level position (0 eV). Positive and negative curves correspond to spin-up and spin-down components, respectively. In **a)**, the black and red curves were obtained using simulation cells with vacuum gaps of 14 Å and 17 Å, respectively.

For all those reasons, in all subsequent models, -H and -OH moieties were introduced in pairs, with their relative positioning arranged to preserve the magnetic symmetry between spin-up and spin-down sub-lattices. The effect of increasing the surface concentration of hydroxyl defects was investigated by constructing models containing either two or four -OH groups per slab, as detailed in the following Sections. For each configuration, slabs with surface areas of 139.31 $Å^2$ and 34.83 $Å^2$ were adopted to represent low and high surface densities of defects, respectively.

2.4.3 Effects of Di-Hydroxylation on NiO(100) Surfaces: Low vs. High -OH Concentration

As previously mentioned, the effect of introducing two -OH moieties on the NiO(100) surface was investigated using slab models with different surface areas, in order to evaluate the impact of increasing defect concentration. Accordingly, this section is divided into two subsections: *2.4.3.1 Low -OH concentration* and *2.4.3.2 High -OH concentration*, respectively. Each subsection first describes the geometry of the investigated models and then presents the corresponding structural, magnetic, and electronic results.

2.4.3.1 Low -OH concentration

To simulate a low concentration of -OH defects, four slab models were constructed using the largest regular slab, namely RegSurf 2 ($Ni_{64}O_{64}$, surface area: 69.65 $Å^2$; see Figure 9), as illustrated in Figure 14. Hydroxyl groups on top of Ni(100) can be obtained in two distinct ways: by adding either an -H atom to an O site, or an -OH group to a Ni site of the Ni(100) top-layer. Furthermore, the -H (or -OH) ad-atoms may be present also in their charged form (+1 for -H, -1 for -OH). Indeed, the presence of such charged defects on NiO(100) surfaces has been experimentally reported in the literature. [91] While modeling charged ad-atoms requires particular care, specifically the inclusion of a suitable charge background and the use of a sufficiently large supercell, this scenario was nonetheless considered (see Section A.2.4.5 in Appendix 2 for further details). In this context, the first two models, $[Ni_{64}O_{64}]2H$ and $[Ni_{64}O_{64}]2H^+$ (Figure 14a,b), and the latter two, $[Ni_{64}O_{64}]2(OH)$ and $[Ni_{64}O_{64}]2(OH^-)$ (Figure 14c,d), have the same simulation cell stoichiometry but differ in their total charge. The principal structural and electronic properties of the minimum energy structures depicted in Figure 14 are summarized in Table 12.

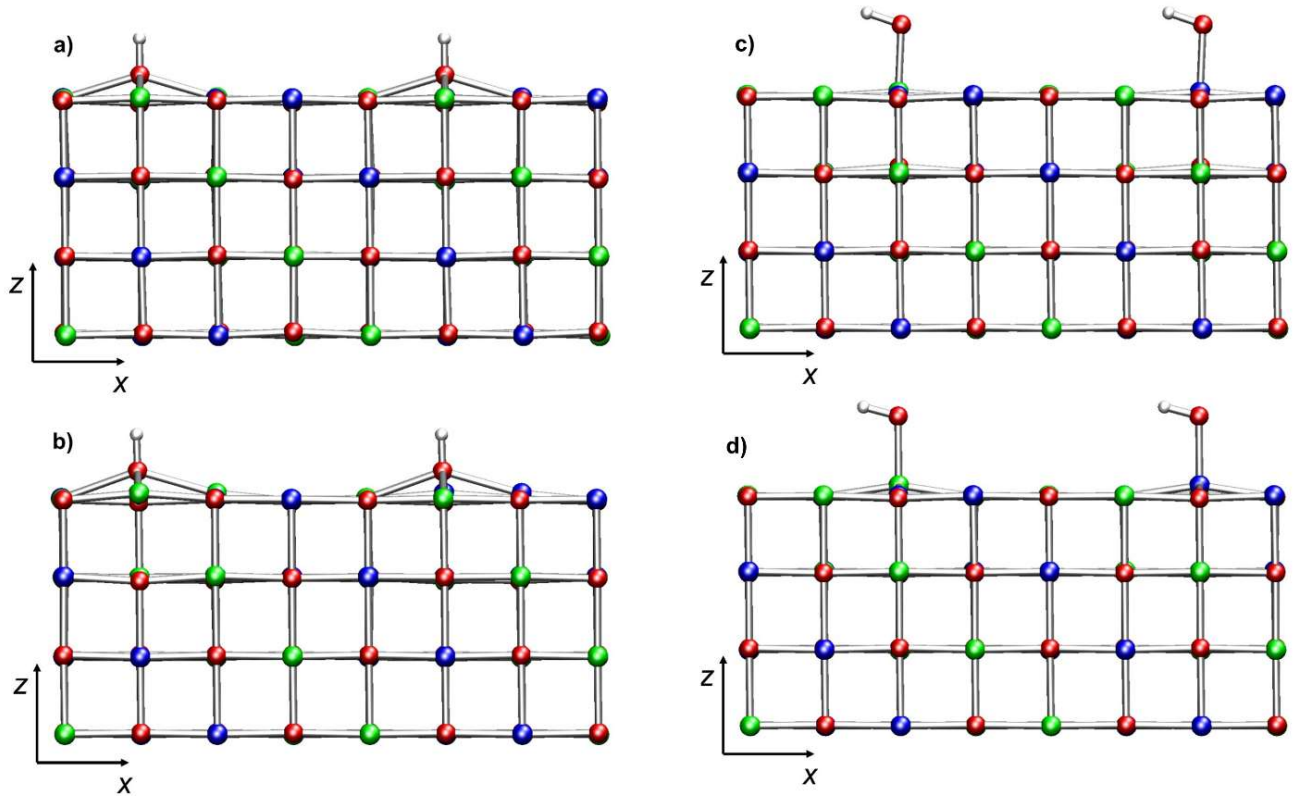

Figure 14: Ball-and-stick representation (projected on the *xz* plane) of the DFT-optimized structures of di-hydroxylated NiO(100) 4-layer slab models built from RegSurf 2, simulating a low concentration of surface hydroxyl groups: a) $(Ni_{64}O_{64})2H+$, containing two H^+, each bonded to a top-layer O atom; b) $(Ni_{64}O_{64})2H$, with two neutral H, each bonded to a top-layer O atom; c) $(Ni_{64}O_{64})2(OH)$, containing two neutral –OH defects; d) $(Ni_{64}O_{64})2(OH-)$, containing two negatively charged -OH^- defects. In c) and d), the two -OH groups are bonded to Ni atoms with opposite spin. Atoms color code: red = O; blue = Ni (spin-up); green = Ni (spin-down); white = H.

Table 12: Electronic and magnetic properties of the low -OH density di-hydroxylated slabs. E_{gap}: band gap energy; E_{VB}: VB top energy; E_{CB}: CB bottom energy; $E_{intra\text{-}gap}$: energy of intra-gap states; μ_{tot}: total magnetization; μ_{Ni}: absolute magnetization per Ni atom; d(OH-OH): distance between surface -OH groups. Energies are given in eV, μ_{tot} and μ_N in Bohr Magnetons (μ_B), and distances in Å, referring to top-layer atoms. All energy values are referenced to the Fermi level, conventionally set to 0.

System	E_{gap}	E_{VB}	E_{CB}	$E_{intra\text{-}gap}$	Type	μ_{tot}	μ_{Ni}	d(OH-OH)
$[Ni_{64}O_{64}]2H$	0.682 (1.86)	-1.637	+0.222	-1.36; -1.17; -0.46	*n*	0	1.78	9.168
$[Ni_{64}O_{64}]2(OH)$	0.250 (2.11)	-0.229	+1.881	+0.021	*p*	0	1.80	9.157
$(Ni_{64}O_{64})2(H^+)$	1.790	-1.270	0.520	-	*p*	0	1.82	9.168
$(Ni_{64}O_{64})2(OH^-)$	1.149 (1.29)	-0.165	1.129	-0.02	*p*	0	1.82	9.157

$[Ni_{64}O_{64}]2H$

The optimized structure of this model (Figure 14b) shows increased surface corrugation compared to the regular slab, as reported in Appendix 2, Section A.2.4.5. The AF structure is preserved even in this model, as evidenced by μ_{tot} = 0.00 μ_B, whereas μ_{Ni} is 1.78 μ_B. The introduction of two H atoms severely modifies the electronic structure with respect to regular NiO(100) surfaces (Table 12 and Figure 15a). In particular, the main changes detected in the

electronic properties are a drastic E_{gap} decrease (0.682 eV), the appearance of donor states in the gap, and the change from *p*-type to *n*-type character. This inversion is indicated by the relative positioning of the Fermi Level in the $[Ni_{64}O_{64}]2H$ pDOS (Figure 15a). As already mentioned, changes from *p*- to *n*-type have been reported for NiO thin films by varying the oxidative conditions in the film preparation.[1] Notably, the pDOS reveal a substantial Ni participation to the donor states in the gap (Figure 15a). To further explore the behavior of electrically charged OH defects, additional calculations were carried out by introducing diluted H^+ species on top of the $[Ni_{64}O_{64}]$ regular slab, as discussed in the following.

$[Ni_{64}O_{64}]2(OH)$

The optimized OH-type model (Figure 14c) displays surface corrugation, but milder than in the H-type one, as explained in Appendix 2, Section A.2.4.5. Nonetheless, the two slabs have very similar magnetization values (Table 12). The presence of empty states within the band gap is evident (Table 12), resulting in a drastic E_{gap} reduction, from 2.11 eV (energy difference between the bottom CB and the top VB, E_{CB}-E_{VB}) to 0.250 eV (energy difference between the lowest unoccupied and the highest occupied state). The system has a *p*-type character (Figure 15b), and both Ni* and hydroxyl O atoms directly contribute to the empty state in the gap, located very close to the Fermi Level (+0.021 eV). Additionally, there is a higher density of O 2*p*-states at the VB top. In contrast, the density of Ni *d*-states and O 2*p*-states at the bottom CB are similar, while Ni-*d*-states become predominant at higher energies (Figure 15b). For completeness, the influence of two diluted charged OH- defects on the $[Ni_{64}O_{64}]$ slab was also evaluated (see below).

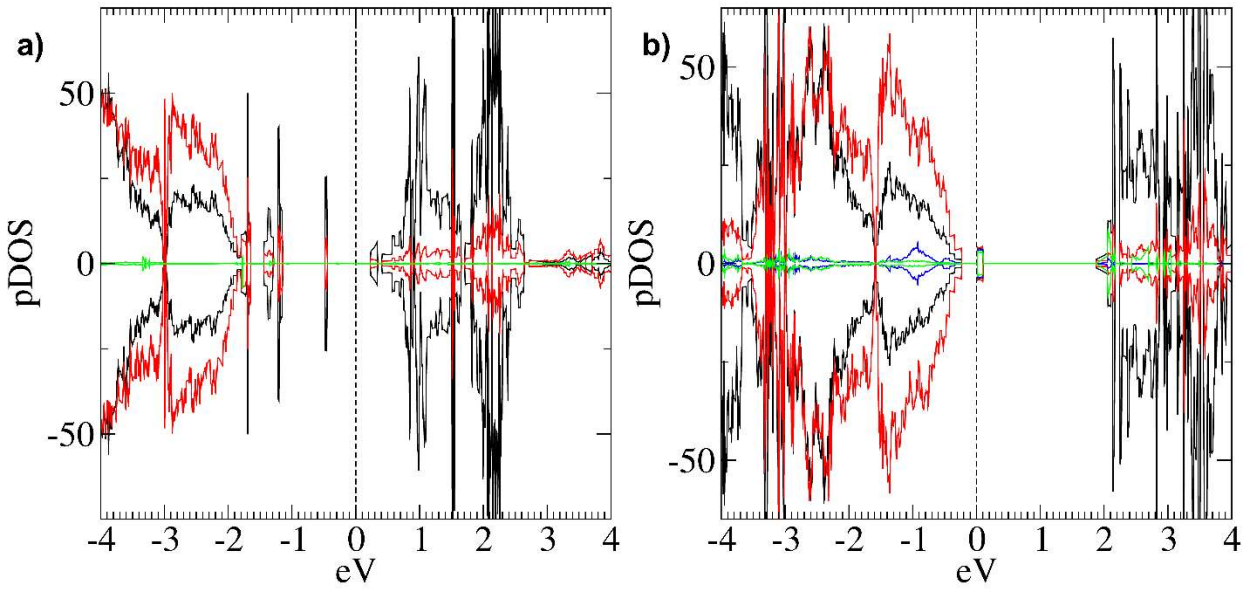

Figure 15: Computed pDOS for di-hydroxylated slab models: a) $[Ni_{64}O_{64}]2H$ and b) $[Ni_{64}O_{64}]2(OH)$. The vertical dashed line at 0 eV represents the Fermi level position. Positive and negative curves correspond to spin-up and spin-down components, respectively. In panel a): black lines represent Ni *d*-states, red lines O *2p*-states, and green lines hydroxyl O *2p*-states. In panel b): black lines represent Ni *d*-states, red lines O *2p*-states, green lines Ni* *d*-states, and blue lines hydroxyl O *2p*-states.

$[Ni_{64}O_{64}]2H+$

The minimum energy structure of this model (Figure 14a) shows structural features similar to the neutral counterpart, with local distortions around the protonated sites; full details are

provided in Appendix 2, Section A.2.4.5. The band gap for this *p*-type system is further reduced (1.790 eV) compared to both bulk and regular slabs, but no intra-gap states are detected (see Table 12). The pDOS for this model slab (Figure 16a) indicates an electronic structure analogous to both the bulk and stoichiometric surfaces. Notably, the Fermi level computed for the $[Ni_{64}O_{64}]2H+$ system is very close to the top of the VB. The AF ordering is preserved and μ_{Ni} is 1.82 μ_B, matching that of the regular slab (Table 12). The key distinction with respect to the neutral $[Ni_{64}O_{64}]2H$ system lies in the electronic structure: while the neutral slab exhibits intra-gap states and an *n*-type character, the charged $[Ni_{64}O_{64}]2H^+$ displays no intra-gap states and retains a *p*-type character (Table 12).

[Ni$_{64}$O$_{64}$]2(OH-)

The optimized $[Ni_{64}O_{64}]2(OH-)$ model (Figure 14d) shows structural features similar to the neutral counterpart, including comparable surface corrugation; see Appendix 2, Section A.2.4.5 for full details. The Antiferromagnetic ordering is maintained, and μ_{Ni} is 1.82 μ_B. The pDOS (Figure 16b) highlights the *p*-type character of this system and reveals the appearance of an occupied intra-gap state. The main contribution to this state results from the 2*p*-states of the adsorbed O atoms. Moreover, this state is located below the Fermi level, suggesting that it is filled by electrons belonging to the two negatively charged -OH^- groups. As in the neutral $[Ni_{64}O_{64}]2(OH)$ model, there is a higher density of O states at the VB top. On the other hand, the density of Ni *d*-states and O states at the bottom of the CB are comparable, whereas, at higher energies, the Ni-*d*-states become predominant. In summary, the main difference between the neutral $[Ni_{64}O_{64}]2(OH)$ and the negatively charged $[Ni_{64}O_{64}]2(OH-)$ model lies in the intra-gap states' occupancy. In the former, such states are empty and located just above the Fermi level; conversely, in the latter the excess electrons occupy these intra-gap states, thus increasing the computed E_{gap} (Figure 16b and Table 12).

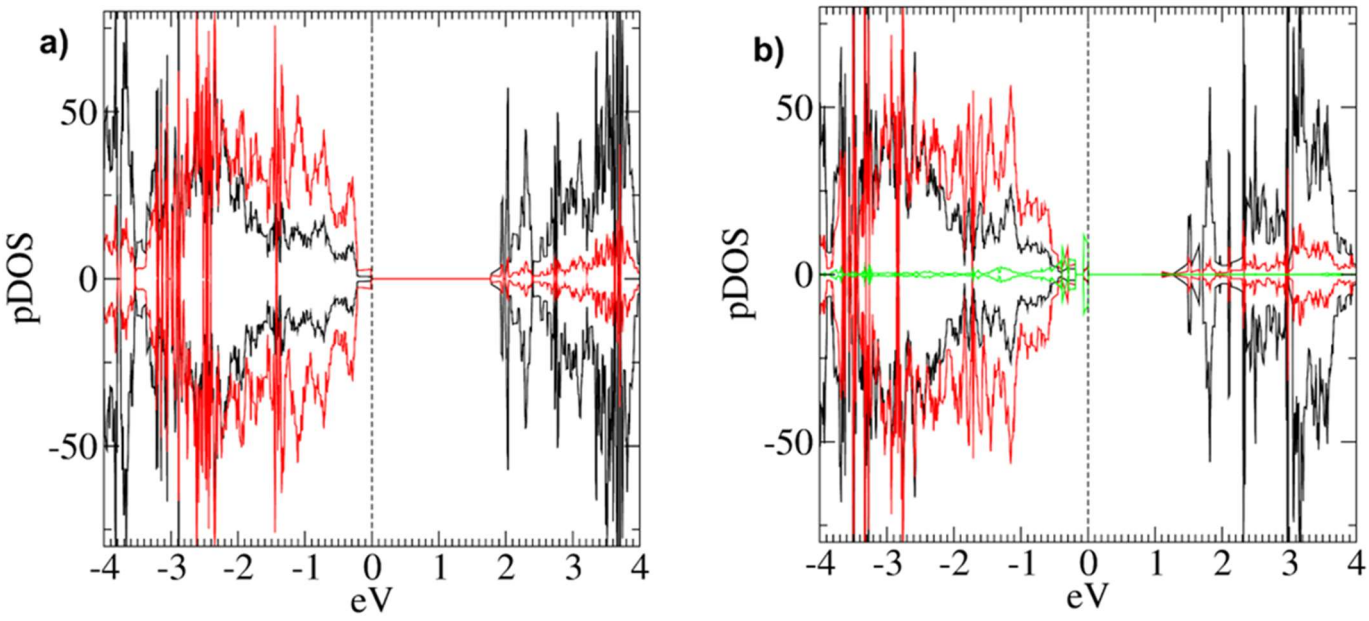

Figure 16: Computed pDOS for the charged defective slab models: a) $[Ni_{64}O_{64}]2H+$; b) $[Ni_{64}O_{64}]2(OH-)$. The vertical dashed line at 0 eV represents the Fermi level position. Positive and negative curves correspond to spin-up and spin-down components, respectively. Red lines indicate the contribution of O *2p*-states; black lines refer to Ni *3d*-states.

2.4.3.2 High -OH concentration

To explore the effects of high -OH surface coverage, three neutral slab models were constructed using the NiO(100) surface with the smallest area (34.83 $Å^2$). The first model, $(Ni_{24}O_{24})2H$ (Figures 17a and b), features two H atoms added to two top-layer O sites. The other two models, both with stoichiometry $(Ni_{24}O_{24})2(OH)$, include two -OH groups added on two Ni-sites of opposite spin at different distances. Indeed, the -OH groups were placed either on two near Ni-sites (Figure 17c and d, $(Ni_{24}O_{24})2(OHa)$) or on two more distant Ni-sites (Figure 17e and f, $(Ni_{24}O_{24})2(OHb)$). Further details are provided in Appendix 2, sub-Section A.2.4.5.2. Table 13 summarizes the key structural and electronic parameters of the minimum energy structures reported in Figure 17.

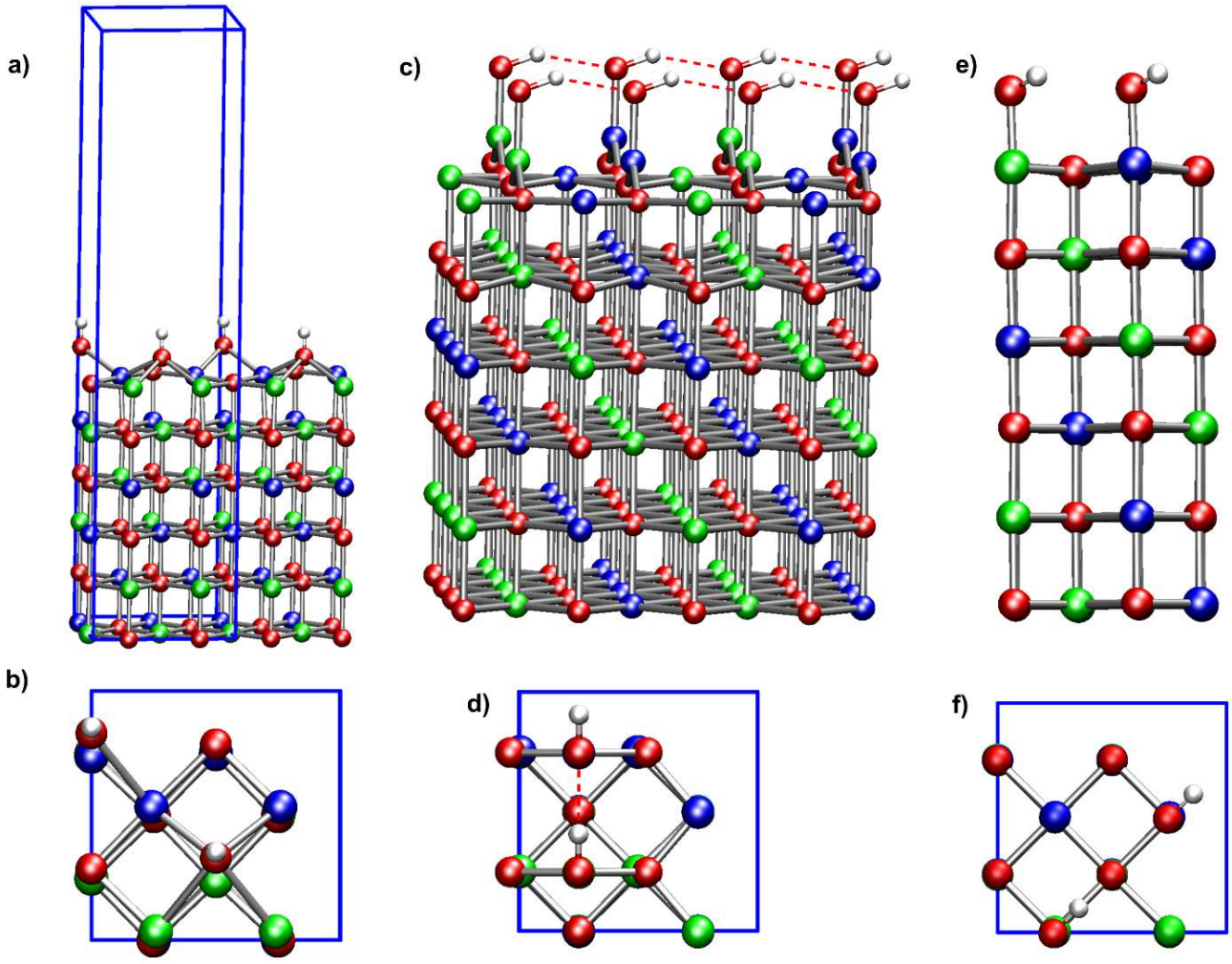

Figure 17: Graphical representations of the DFT-optimized structures of di-hydroxylated NiO(100) slab models (6-layer) built using the 2×2 tetragonal cell, representing a higher concentration of surface hydroxyl groups. a) side view and b) top view of $(Ni_{24}O_{24})2H$, containing two H, each bonded to a top-layer O atom; c) side view and d) top view of $(Ni_{24}O_{24})2(OHa)$, with two adsorbed -OH separated by 2.951 Å; e) side view and f) top view of $(Ni_{24}O_{24})2(OHb)$, with two adsorbed -OH groups separated by 4.171 Å. The two -OH groups are bonded to Ni atoms with opposite spin. Atoms color code: red = O; blue = Ni (spin-up); green = Ni (spin-down); white = H. Red dashed lines indicate hydrogen bonds; blue solid lines mark the simulation cell size.

Table 13: Electronic and magnetic properties of the high -OH density di-hydroxylated slabs. E_{gap}: band gap energy; E_{VB}: VB top energy; E_{CB}: CB bottom energy; $E_{intra\text{-}gap}$: energy of intra-gap states; μ_{tot}: total magnetization; μ_{Ni}: absolute magnetization per Ni atom; d(OH-OH): distance between surface –OH groups. Energies are given in eV, μ_{tot} and μ_N in Bohr Magnetons (μ_B), and distances in Å, referring to top-layer atoms. All energy values are referenced to the Fermi level, conventionally set to 0.

System	E_{gap}	E_{VB}	E_{CB}	$E_{intra\text{-}gap}$	Type	μ_{tot}	μ_{Ni}	d(OH-OH)
$[Ni_{24}O_{24}]2H$	1.100 (1.59)	-1.238	+0.352	+0.748	*n*	0	1.79	4.173
$[Ni_{24}O_{24}]2(OH^a)$	0				*metal*	0	1.82	2.951
$[Ni_{24}O_{24}]2(OH^b)$	0				*metal*	0	1.70	4.171

[Ni₂₄O₂₄]2H

The minimum energy structure (Figures 17a and b) of $[Ni_{24}O_{24}]2H$ is characterized by parallel rows of -OH moieties, resulting from the high surface density of defects. In this configuration, the separation between -OH defects is nearly halved compared to the low-concentration model $[Ni_{64}O_{64}]2H$ (Table 12). The distinctive arrangement of hydroxyl groups on the system top layer is further illustrated in Figure A.30 in Appendix 2. A comparison between the $[Ni_{24}O_{24}]2H$ and $[Ni_{64}O_{64}]2H$ models reveals a clear trend: structural distortions in comparison to regular NiO(100) become more pronounced as the surface hydroxyl defect concentration increases. Conversely, the magnetic and the main electronic properties of the two models are very similar (cfr. Tables 12 and 13). In particular, both models exhibit *n*-type character and feature occupied intra-gap states. The $[Ni_{24}O_{24}]2H$ pDOS (Figure 18) evidence a predominant contribution of Ni *d*-states to the occupied state in the gap. Notably, the hydroxyl oxygen atoms contribute both to these intra-gap states and to the bottom of the conduction band (CB), while the top of the valence band (VB) is primarily composed of O *2p*-states.

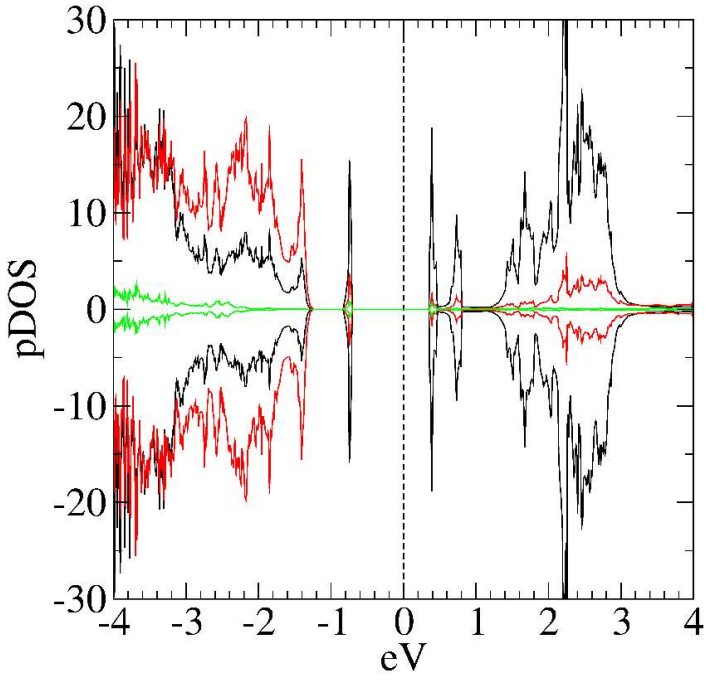

Figure 18: Computed pDOS for slab model $[Ni_{24}O_{24}]2H$. The vertical dashed line represents the Fermi level position (0 eV). Positive and negative curves correspond to spin-up and spin-down components, respectively. Red lines indicate the contribution of O *2p*-states; black lines refer to Ni *3d*-states.; green lines represent hydroxyl O 2*p*-states.

[$Ni_{24}O_{24}$]2(OH)

The optimized geometries of the two models with this stoichiometry, denoted as [$Ni_{24}O_{24}$]2(OHa) and [$Ni_{24}O_{24}$]2(OHb), are shown in Figures 17c-d and 17e-f, respectively. In these models, the hydroxyl groups differ in the distance and relative orientation. In the [$Ni_{24}O_{24}$]2(OHa) model, the close proximity of the two -OH groups led to a significant local rearrangement, with the formation of hydrogen-bonded chains and a tricoordinate environment around the Ni* centers. In contrast, the [$Ni_{24}O_{24}$]2(OHb) model, characterized by a larger -OH separation, did not undergo significant structural rearrangement and showed no evidence of hydrogen bonding. Full structural details are provided in Appendix 2, Sub-section A.2.4.5.2. Although both systems exhibit zero total magnetization (μ_{tot}), their μ_{Ni} values are different (Table 13), likely due to the very different geometric structures. The substantial difference in the top-layer structures results in significantly different pDOS profiles, particularly above the Fermi level (Figure 19). Nevertheless, both models, characterized by a high density of surface -OH groups, exhibit zero E_{gap}, thus indicating metallic behaviour (Table 13). Such a metallic behaviour is not predicted for the [$Ni_{64}O_{64}$]2(OH) system, which has the same number of -OH groups, but it is characterized by a lower surface coverage (0.125 *vs* 0.5) and a larger defect separation. The pDOS for [$Ni_{24}O_{24}$]2(OHa) and [$Ni_{24}O_{24}$]2(OHb) are shown in Figures 19a and 19b, respectively.

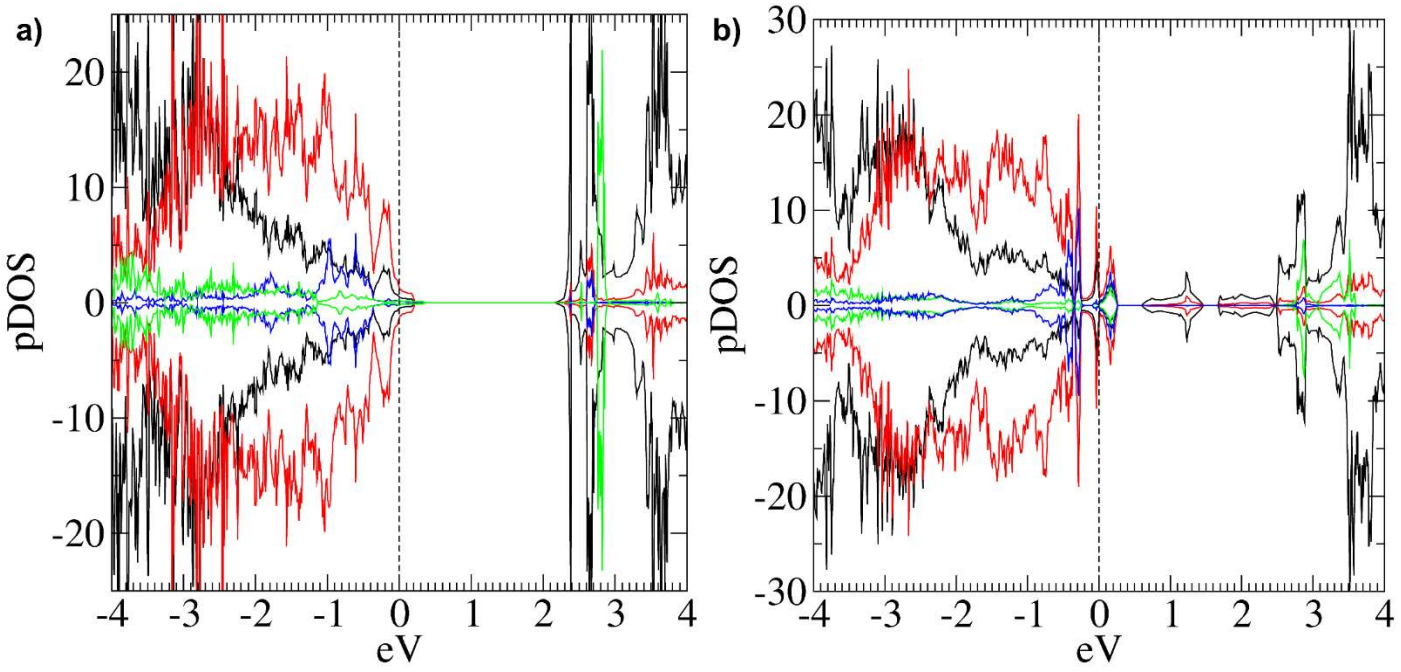

Figure 19: Computed pDOS for: a) [$Ni_{24}O_{24}$]2(OHa) and b) [$Ni_{24}O_{24}$]2(OHb). The vertical dashed line at 0 eV represents the Fermi level position. Positive and negative curves correspond to spin-up and spin-down components, respectively. Black lines refer to nickel *d*-states; red lines represent oxygen states; green lines indicate *d*-states of the Ni atoms bearing the -OH groups (Ni*); blue lines refer to *2p*-states of the hydroxyl oxygen atoms.

In the [$Ni_{24}O_{24}$]2(OHa) case (Figures 17c-d), the Fermi Level lies in a region predominantly composed of O-*2p* states, with a minor contribution from Ni-*d* states. Notably, the atoms directly linked to the defect (green and blue lines in Figure 19a) contribute appreciably in this

region. Between the top of the metallic band, located at +0.383 eV from the Fermi Energy, and the bottom of the unoccupied band there is a 1.91 eV wide region with no electronic states. This pDOS pattern closely resembles that found for the $[Ni_{64}O_{64}]2(OH)$ model (see Figure 15b), which, characterized by a lower surface density of hydroxyl groups, exhibited a very narrow electronic gap (0.250 eV) between the VB top and an empty state located just above the Fermi Level (+0.021 eV, see Table 12), with significant contributions from Ni* and hydroxyl O atoms (Table 12). Based on this comparison, it can be reasonably argued that the increase of -OH surface density on passing from $[Ni_{64}O_{64}]2(OH)$ (surface area: 139.31 $Å^2$) to $[Ni_{24}O_{24}]2(OHa)$ (surface area: 34.83 $Å^2$) has drastically altered the electronic structure of the slab, inducing a transformation from a small-gap *p*-type semiconductor to a metallic system. This effect is further supported by the significant reduction in the distance between neighboring -OH defects (from 9.157 Å to 2.951 Å, see Sub-section A.2.4.5.2), also associated with the transition from $[Ni_{64}O_{64}]2(OH)$ to $[Ni_{24}O_{24}]2(OHa)$.

Conversely, the pDOS of the $[Ni_{24}O_{24}]2(OHb)$ model (Figure 47b) reveals the Fermi Level positioned in a region characterized by a high density of both O-*2p* states and Ni-*d* states. The contribution of Ni* d-states and hydroxyl oxygen states at the Fermi Level is lower than that obtained for the $[Ni_{24}O_{24}]2(OHa)$ model (Figure 47a). However, a high density of defect states emerges immediately above the Fermi Level. In addition, several unoccupied states (with negligible contribution of Ni* and hydroxyl O atoms) are found in the region between the top of the metallic band and the bottom of the next empty band. Such differences, compared to the $[Ni_{24}O_{24}]2(OHa)$ case may be ascribed to the diverse structural features of the top-layer, in particular the larger separation between -OH groups (4.173 Å).

To better contextualize the data presented above, a concise summary is outlined below. The analysis demonstrates that the introduction of -OH defects to the regular NiO(100) surface leads to deep alterations in the electronic structure of the nanomaterial. Notably, the addition of a single hydroxyl group perturbs the magnetic sublattices, breaking the spin symmetry and resulting in a transition from *p*-type semiconductor to half-metallic character. This effect is particularly pronounced in models with reduced surface area, a parameter directly related to the defect density, that proves to be crucial in modulating the electronic properties of regular NiO(100) surfaces. In this context, the $[Ni_{64}O_{64}]2H$ model (low -OH concentration, surface area of 139.31 $Å^2$) shows that the presence of two hydroxyl moieties induces the appearance of intra-gap states and promotes a shift from *p*-type to *n*-type character. In contrast, the charged $[Ni_{64}O_{64}]2H+$ model retains both the *p*-type character and the absence of intra-gap states, closely resembling the electronic behavior of the regular surface. The increase in defect density in this system, as simulated by the $[Ni_{24}O_{24}]2H$ model (high -OH concentration, surface area of 34.83 $Å^2$), does not significantly alter its electronic nature: both models display *n*-type character and feature occupied intra-gap states. As concerns the neutral $[Ni_{64}O_{64}]2(OH)$ system (low -OH concentration), the presence of two hydroxyl groups induces a more moderate effect: intra-gap states appear just above the Fermi level (+0.021 eV), while the system retains its *p*-type character. These states become occupied in the charged $[Ni_{64}O_{64}]2(OH-)$ model, although the overall electronic structure remains largely unchanged. A more drastic effect is observed upon increasing the defect concentration in this system, i.e. in passing from $[Ni_{64}O_{64}]2(OH)$ to $[Ni_{24}O_{24}]2(OH)$: in this case, the electronic structure is

drastically altered, and a shift from small-gap *p*-type semiconductor to a metallic system takes place. Taken together, these findings demonstrate that the functionalization of NiO(100) surfaces with -OH groups can radically reshape the material's electronic structure, enabling transitions between different conduction regimes ($p \rightarrow n$ or $p \rightarrow$ metallic system). Such tunability suggests a potential application of NiO as material with tunable electronic properties, in which surface reactivity could be modulated in a controlled manner, for instance, in sensing technologies.

2.4.4 Structural and Electronic Features of Tetra-Hydroxylation on NiO(100) Surfaces: From Dissociated Water to Hydroxyl Networks

In order to explore the effects of increased hydroxylation, a series of NiO(100) slab models with varying surface areas and defect concentrations was considered. A low-defect-density model, $[Ni_{64}O_{64}]$2H-2(OH), was built using RegSurf 2 (Figure 9b, surface area 139.31 Å^2), by placing two H atoms on two top-layer O atoms and two -OH groups on two top-layer Ni of opposite spin, thus simulating two dissociated H_2O molecules (Figure 20a) at low coverage. To simulate higher -OH defect concentration, three additional models were built using the smallest surface (34.83 Å^2): $[Ni_{24}O_{24}]$4H, with four H atoms on four top-layer O sites (Figure 20b); $[Ni_{24}O_{24}]$4(OH), with four -OH groups on four top-layer Ni sites (Figure 20c); and $[Ni_{24}O_{24}]$2H-2(OH), mimicking two dissociated H_2O molecules at high concentration (Figure 20d). Further structural details are reported in Appendix 2, Section A.2.4.6.

It should be noted that Figures 20b and 20d illustrate the starting, unrelaxed configurations of the corresponding models. The optimized structures resulting from geometry optimization will be presented and discussed later. A summary of the key structural and electronic parameters of all the slab models shown in Figure 20, following geometry optimization, is provided in Table 14.

Table 14: Electronic and magnetic properties of the tetra-hydroxylated slabs. E_{gap}: band gap energy; E_{VB}: VB top energy; E_{CB}: CB bottom energy; $E_{intra\text{-}gap}$: energy of intra-gap states; μ_{tot}: total magnetization; μ_{Ni}: absolute magnetization per Ni atom; d(OH-OH): distance between surface –OH groups. Energies are given in eV, μ_{tot} and μ_N in Bohr Magnetons (μ_B), and distances in Å, referring to top-layer atoms. All energy values are referenced to the Fermi level, conventionally set to 0.

System	E_{gap}	E_{VB}	E_{CB}	$E_{intra\text{-}gap}$	Type	μ_{tot}	μ_{Ni}	d(OH-OH)
$[Ni_{64}O_{64}]$2H-2(OH)	1.225 (2.01)	-0.929	+1.085	-0.43; -0.30; -0.14	*p*	0	1.80	4.974/9.195
$[Ni_{24}O_{24}]$4H	1.330	-0.715	+0.615	–	*p*	0	1.70	2.879/4.176
$[Ni_{24}O_{24}]$4(OH)	0				*metal*	0	1.74	2.911/4.281
$[Ni_{24}O_{24}]$2H-2(OH)	2.100	-0.448	+1.652	–	*p*	0	1.81	4.127

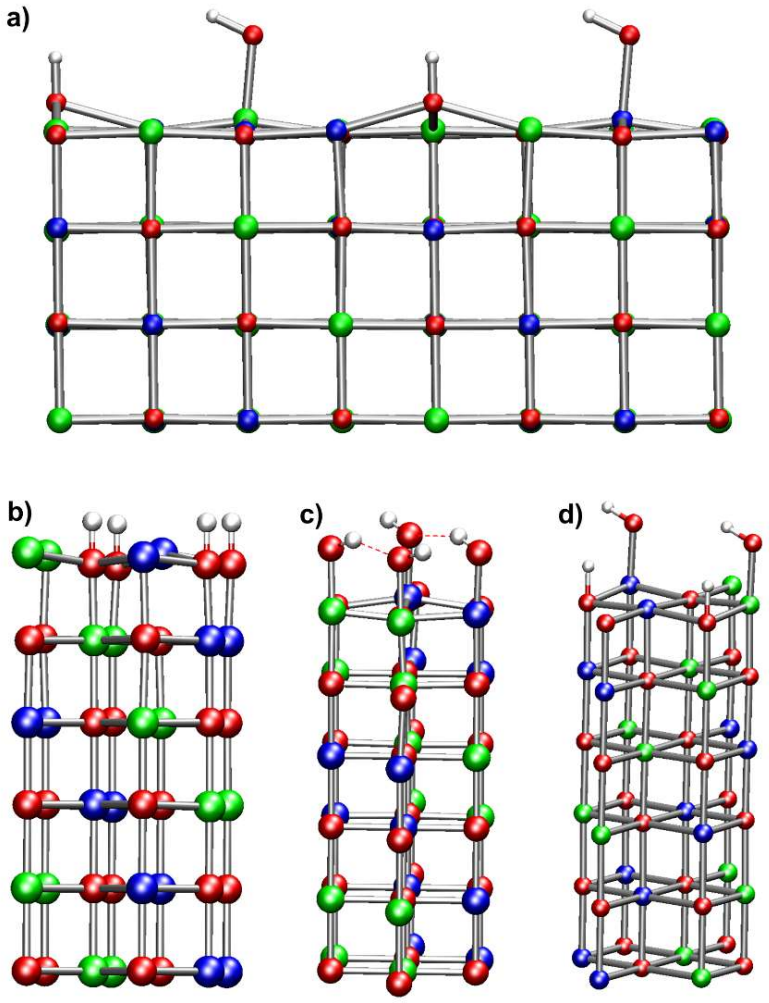

Figure 20: Graphical representations (side view) of tetra-hydroxylated NiO(100) slab models: a) $[Ni_{64}O_{64}]2H\text{-}2(OH)$ (optimized structure); b) $[Ni_{24}O_{24}]4H$ (starting configuration); c) $[Ni_{24}O_{24}]4(OH)$ (optimized structure); d) $[Ni_{24}O_{24}]2H\text{-}2(OH)$ (starting configuration). Atoms color code: red = O; blue = Ni (spin-up); green = Ni (spin-down); white = H. Red dashed lines indicate hydrogen bonds.

$[Ni_{64}O_{64}]2H\text{-}2(OH)$

In the optimized structure of the $[Ni_{64}O_{64}]2H\text{-}2(OH)$ system (Figure 20a), the typical surface corrugation observed in all previous models is preserved, and the geometric parameters are consistent with those found for the $[Ni_{64}O_{64}]2H$ and $[Ni_{64}O_{64}]2(OH)$ systems. Full structural data are provided in Appendix 2, Section A.2.4.6. The antiferromagnetic ordering is preserved (see Table 14). Concerning the electronic structure, this system exhibits a *p*-type character, as evidenced by the pDOS reported in Figure 21. The computed band gap (E_{gap}) is 1.225 eV, while the energy difference E_{CB}-E_{VB} amounts to 2.01 eV (Table 14). This discrepancy arises from the presence of occupied intra-gap states located between the top of the VB and the bottom of the CB, as clearly visible in the pDOS (Figure 21). These states, positioned below the Fermi level, originate predominantly from the *2p* states of hydroxyl oxygen atoms. The contribution of states belonging to oxygen atoms is predominant at the VB edge. In a different way, at the CB bottom edge, Ni *d*-states and O 2*p*-states show a very similar contribution. Only at higher energy, the density of Ni *d*-states becomes much larger.

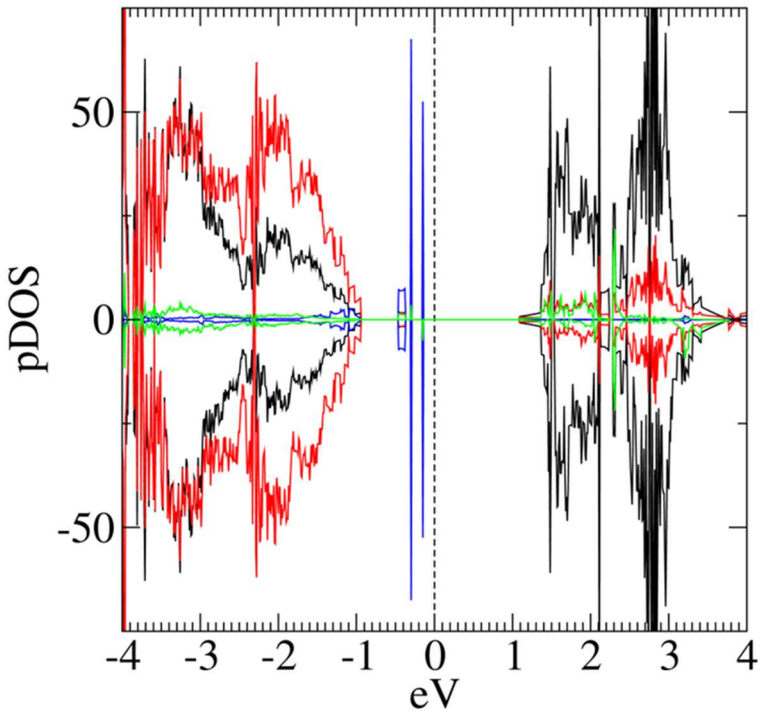

Figure 21: Computed pDOS for [$Ni_{64}O_{64}$]2H-2(OH) model. The vertical dashed line at 0 eV represents the Fermi level position. Positive and negative curves correspond to spin-up and spin-down components, respectively. Black lines refer to nickel *d*-states; red lines represent oxygen states; green lines indicate *d*-states of the Ni atoms bearing the -OH groups (Ni*); blue lines refer to *2p*-states of the hydroxyl oxygen atoms.

[$Ni_{24}O_{24}$]4H

In the optimized structure of this model (Figure 22b), geometry optimization led to a massive surface reconstruction, resulting in significant deviations from the starting configuration (Figure 20b and 22a). The top layer was displaced relative to the second layer along the [-110] direction (see arrow in Figure 50c), giving rise to both three- and tetra-coordinated Ni* sites and to a pronounced distortion of the Ni-O-Ni angles. These features suggest that high hydroxyl coverage strongly perturbs the NiO structural organization at the surface. Further geometric details are reported in Appendix 2, Section A.2.4.6.

Despite the significant structural relaxation observed with respect to regular NiO(100), this system maintains zero total magnetization. However, μ_{Ni} is lower than that of the bulk (see Tables A.29 and 13). Interestingly, the calculated electronic properties (Table 14 and Figure 23) evidence a *p*-type character with no intra-gap states. Upon increasing the density of this kind of defect, a shift from *n*-type (in [$Ni_{64}O_{64}$]2H and [$Ni_{24}O_{24}$]2H) to *p*-type behavior (in [$Ni_{24}O_{24}$]4H) is observed, along with the increase of defects states at the top of the valence band (see Figures 15a, 18, and 23). These findings suggest that the electronic behavior evolves with increasing hydroxyl defect concentration along the series $Ni_{64}O_{64}$ → [$Ni_{64}O_{64}$]2H → [$Ni_{24}O_{24}$]2H → [$Ni_{24}O_{24}$]4H, leading to a re-establishment of the original *p*-type character: *p* → *n* → *p*.

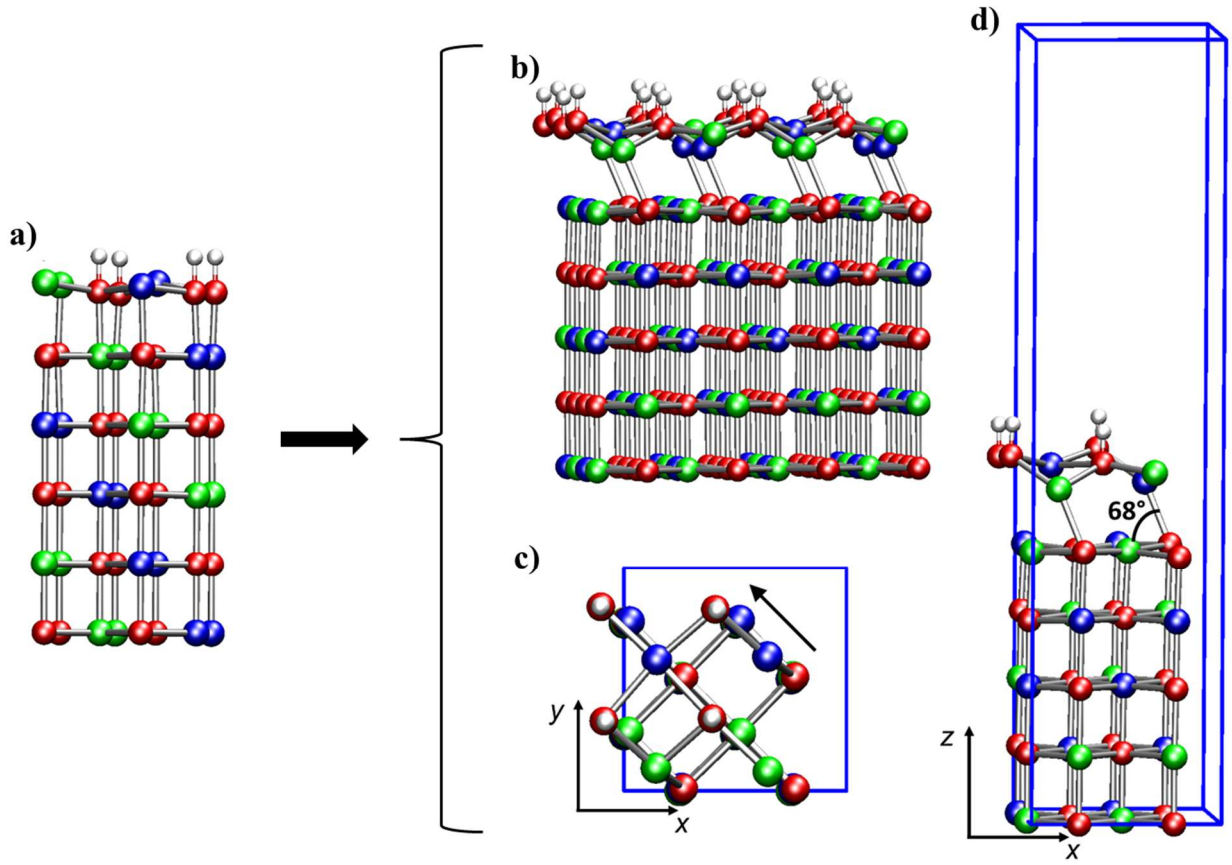

Figure 22: Graphical representation of a) starting configuration (side view) and DFT-computed minimum energy structure of the $[Ni_{24}O_{24}]4H$ system: b) side view; c) simulation cell top view; d) simulation cell side view. Atoms color code: red = O; blue = spin-up Ni; green = spin-down Ni; white = H. Blue lines outline the simulation cell.

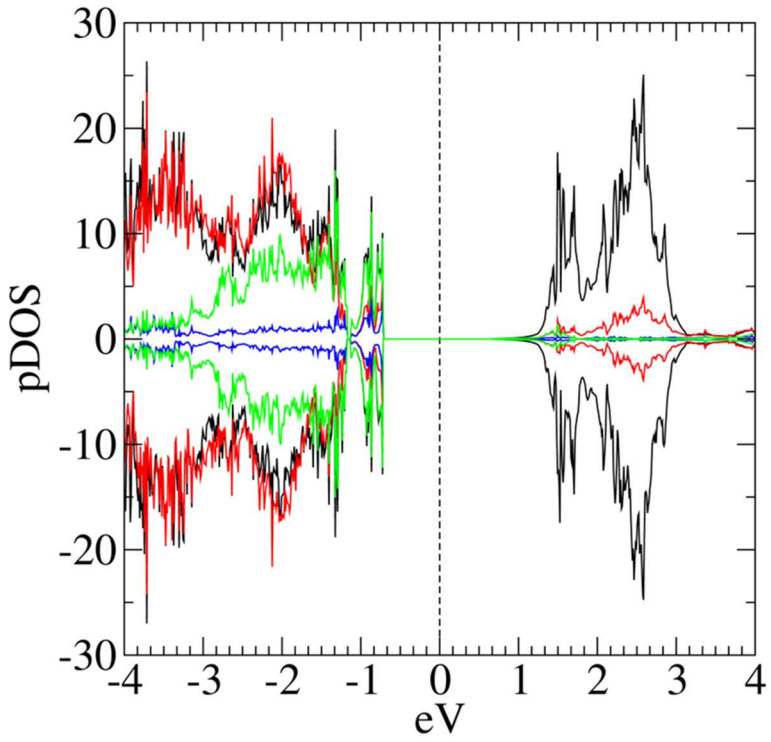

Figure 23: Computed pDOS for $[Ni_{24}O_{24}]4H$ model. The vertical dashed line at 0 eV represents the Fermi level position. Positive and negative curves correspond to spin-up and spin-down components, respectively. Black lines refer to nickel *d*-states; red lines represent oxygen states; green lines indicate *d*-states of the Ni atoms bearing the -OH groups (Ni*); blue lines refer to *2p*-states of the hydroxyl oxygen atoms.

[$Ni_{24}O_{24}$]4(OH)

This model (Figure 20c), that exhibits a surface -OH density twice as large as [$Ni_{24}O_{24}$]2(OH) and eight times greater than [$Ni_{64}O_{64}$]2(OH), did not undergo significant structural rearrangements upon optimization. The four -OH groups, bonded to top-layer Ni atoms, form ordered chains of moderately strong hydrogen bonds (Figure A.31). Further structural data are provided in Appendix 2, Section A.2.4.6.

The data reported in Table 14 indicate that the AF character is preserved in this model, which also exhibits metallic behavior. Notably, the pDOS (Figure 24) reveals a pronounced contribution of defect states at the Fermi level, significantly higher than that observed for the di-hydroxylated models (see Section 2.4.3), a feature that can be attributed to the increased density of surface hydroxyl groups.

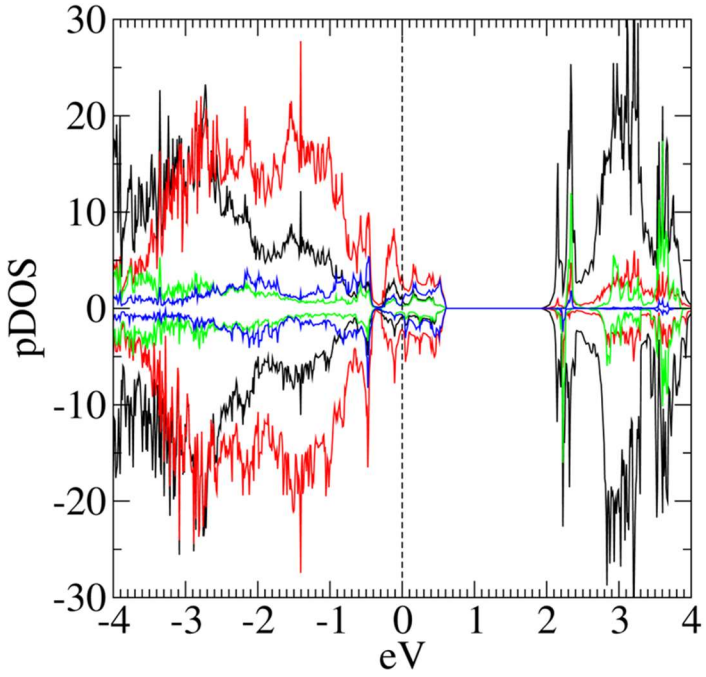

Figure 24: Computed pDOS for [$Ni_{24}O_{24}$]2(OH) model. The vertical dashed line at 0 eV represents the Fermi level position. Positive and negative curves correspond to spin-up and spin-down components, respectively. Black lines refer to nickel *d*-states; red lines represent oxygen states; green lines indicate *d*-states of the Ni atoms bearing the -OH groups (Ni*); blue lines refer to *2p*-states of the hydroxyl oxygen atoms.

[$Ni_{24}O_{24}$]2H-2(OH)

This final model (Figure 20d and 25a), initially built to mimic the adsorption of two dissociated water molecules at much higher concentration than in the [$Ni_{64}O_{64}$]2H-2(OH) model, evolved upon geometry optimization into a structure featuring two physisorbed H_2O molecules coordinated to two top-layer Ni atoms. The resulting configuration closely resembles that reported for hydrated NiO(100) at 0.5 monolayer coverage [92]. Further structural details are collected in Appendix 2, Section A.2.4.6.

The system exhibits zero total magnetization and a μ_{Ni} value of 1.81 μ_B. A *p*-type character is found, with an E_{gap} 2.10 eV (Table 14 and Figure 26). These findings suggest that the electronic

properties of NiO(100) are only moderately influenced by the physisorption of water molecules, even at high surface coverage, and that the *p*-type nature of the system is preserved.

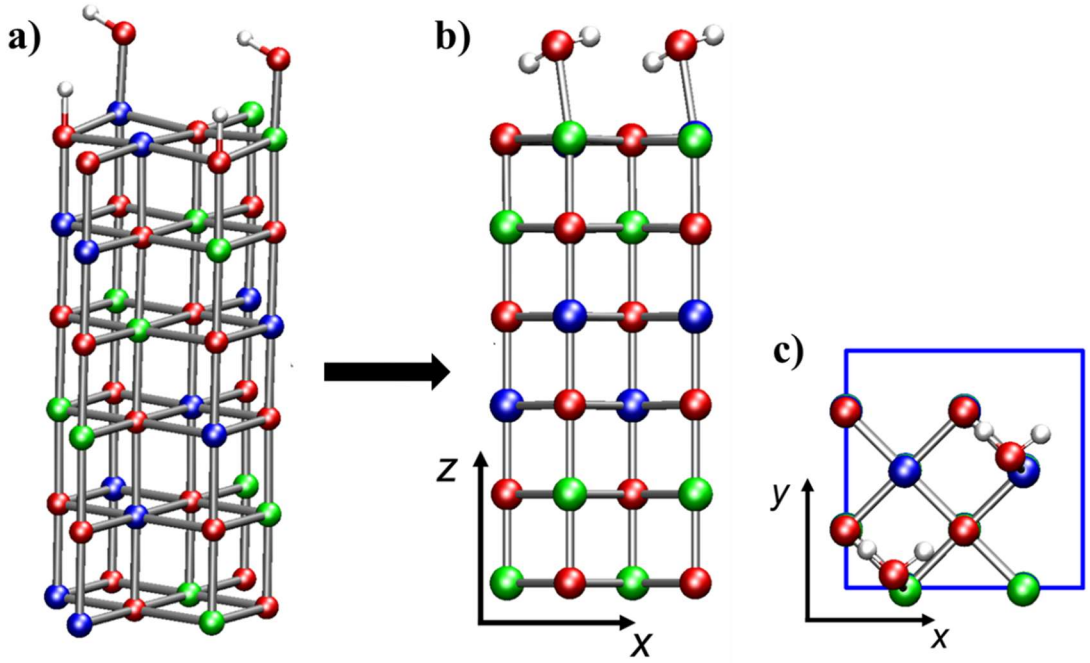

Figure 25: Graphical representation of the $[Ni_{24}O_{24}]2H\text{-}2(OH)$ model, which mimics two dissociated H_2O molecules: a) starting configuration (side view); b) DFT-optimized structure (side view); c) DFT-optimized structure (top view). Atoms color code: red = O; blue = spin-up Ni; green = spin-down Ni; white = H. Blue lines outline the simulation cell.

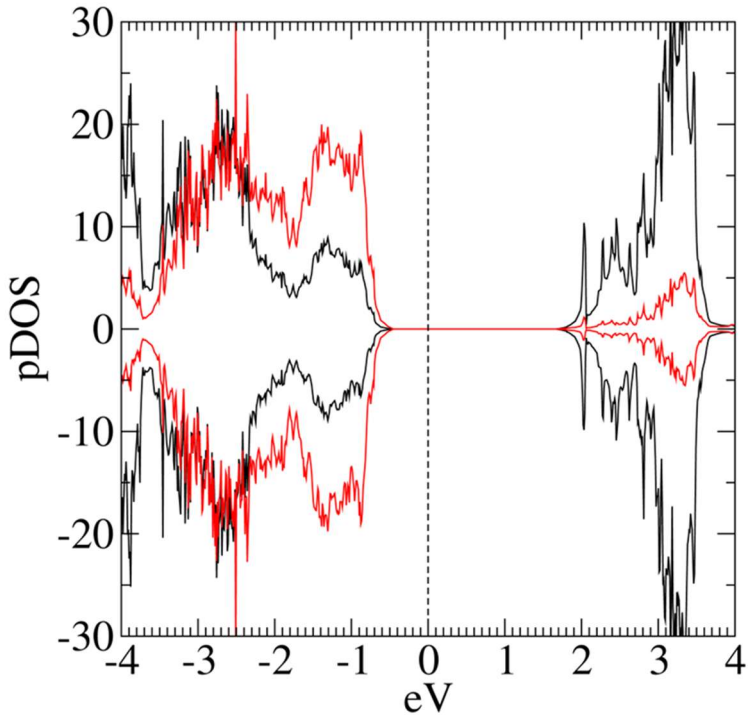

Figure 26: Computed pDOS for $[Ni_{24}O_{24}]2H\text{-}2(OH)$ model. The vertical dashed line at 0 eV represents the Fermi level position. Positive and negative curves correspond to spin-up and spin-down components, respectively. Black lines refer to nickel *d*-states; red lines represent oxygen states.

2.4.5 Final Remarks and Conclusion

The final set of results confirms and further expands the intermediate considerations outlined at the end of Section 2.4.3, providing an overview of the structural and electronic effects induced by surface hydroxylation. Overall, the analysis reveals that the introduction of -OH defects on regular NiO(100) surfaces leads to substantial alterations in the electronic structure of the material. In the slab models investigated, hydroxylation was simulated either by placing H atoms on top-layer oxygen atoms and/or by OH groups on top-layer Ni atoms (see Section 2.4.2, Figure 11). Notably, the introduction of a single hydroxyl group perturbs the magnetic sublattices, disrupting the AF ordering and leading to a change from *p*-type to half-metallic character. This effect is particularly pronounced in slab models with reduced surface area, which emerges as a critical factor in modulating the electronic properties of NiO(100) surfaces. In this context, the adoption of slab models with different surface areas enabled a systematic exploration of distinct defect coverage regimes.

When defects are introduced in pairs, in order to evenly affect the two spin sub-lattices, the surfaces are characterized by antiferromagnetic (AF) ordering, typical of the bulk phase. Computed band gap values systematically decrease when moving from bulk to slab models, in agreement with experimental findings reporting a reduced E_{gap} in NiO thin films compared to the bulk material. [7,72,74,75] Furthermore, the present calculations indicate that the introduction of surface -OH groups further reduces the band gap compared to the regular (100) surfaces. The electronic properties of defective slabs depend on how the -OH groups are bonded to the surface. Indeed, a different behavior as a function of coverage is found when the -OH groups are formed by linking H atoms to top-layer oxygen atoms (Figure 11a) or by linking -OH groups to surface Ni sites (Figure 11b). In the former case, passing from the regular NiO(100) slab to the $[Ni_{64}O_{64}]2H$ model (low -OH concentration), the introduction of two hydroxyl moieties leads to the appearance of intra-gap states and a transition from *p*-type to *n*-type character. Interestingly, further increasing the defect density, as in the $[Ni_{24}O_{24}]4H$ model, results in a decrease in the number of intra-gap states, a reversion from *n*-type back to *p*-type behavior, and an increment of the E_{gap} (cfr Tables 12, 13 and 14). Conversely, in the latter case, the transition from stoichiometric NiO(100) to $[Ni_{64}O_{64}]2(OH)$ (low -OH concentration), induces only moderate changes: intra-gap states appear just above the Fermi level (+0.021 eV), while the *p*-type character is preserved. However, upon increasing the -OH defect concentration in this system, a markedly different trend is observed. The defect concentration increase in passing from $[Ni_{64}O_{64}]2(OH)$ to $[Ni_{24}O_{24}]2(OH)$ is accompanied by a strong alteration of the electronic structure, resulting in a shift from a small-gap *p*-type semiconductor to a metallic system. A further increase in hydroxyl coverage, as in $[Ni_{24}O_{24}]4(OH)$, maintains the metallic character.

The effect of introducing charged defects at low surface coverage was also investigated. The addition of H^+, compared to the adsorption of neutral H atoms, induces a substantial modification of the system electronic structure, resulting in the disappearance of intra-gap states and a significant increase in the band gap. Notably, the charged $[Ni_{64}O_{64}]2H+$ model retains both the p-type character and the absence of intra-gap states, thus closely resembling the electronic behavior of the regular surface. A similar effect on the electronic structure is

observed upon the adsorption of negatively charged OH^- groups, which also leads to a marked increase in E_{gap} compared to neutral -OH species. The main difference between the neutral $[Ni_{64}O_{64}]$2(OH) and the negatively charged $[Ni_{64}O_{64}]$2(OH-) model lies in the occupancy of intra-gap states: in the former, these states are unoccupied and located just above the Fermi level, while in the latter they are filled by the excess electrons introduced with the OH^- groups, thus increasing the computed E_{gap}.

From a structural standpoint, two distinct surface reconstructions of NiO(100) were observed at high hydroxyl defect densities, namely in the $[Ni_{24}O_{24}]$2(OHa) and $[Ni_{24}O_{24}]$4H models. In both cases, the formation of three-coordinated Ni centers was detected. Notably, in the $[Ni_{24}O_{24}]$4H system, the surface reconstruction also gives rise to tetra-coordinated Ni atoms, along with the disappearance of intra-gap states and a shift from *n*-type to *p*-type behavior.

As a further insight, the simultaneous addition of -H and -OH groups to top-layer O and Ni sites, respectively, was explored under both low- and high-coverage regimes. In the low-coverage case ($[Ni_{64}O_{64}]$2H-2(OH)), the electronic behavior appears to reflect a combination of features observed in the charged $[Ni_{64}O_{64}]2H^+$ and $[Ni_{64}O_{64}]$2(OH-) models. Specifically, the calculated E_{gap} of 1.225 eV lies between those of the aforementioned charged systems, and the slab retains a *p*-type character with occupied donor states located just below the Fermi level. These states are mostly localized on the oxygen atoms of surface hydroxyl groups (Figure 21). Among the considered -OH-bearing NiO(100) slab, this system might be the model which approximates more closely NiO thin films fabricated *via* CVD under humid conditions, presented in Paragraph 2.2 of this Chapter. At higher coverages ($[Ni_{24}O_{24}]$2H-2(OH)), this type of defect is no longer stable, and the system evolves toward the formation of physisorbed water molecules. Notably, this structural rearrangement does not significantly affect the electronic structure, and the *p*-type character of the surface is preserved.

In conclusion, this Paragraph has presented an extensive DFT investigation on NiO(100) surfaces functionalized with hydroxyl (-OH) groups. The structural and electronic features emerging from this analysis provide a microscopic picture of the defective nanomaterial that may result from molecular precursor decomposition under humid conditions, such as those employed in CVD processes (see Paragraphs 2.1 and 2.2). The analysis has revealed that the presence of such defects leads to profound modifications in both the structural and electronic properties of the material. As expected, the computed band gap values decrease upon moving from the bulk phase to the (100) slabs, and this effect is further amplified by the introduction of -OH defects. Interestingly, the impact on the electronic structure strongly depends not only on the nature of the defects, obtained either by linking H atoms to surface O atoms or by attaching OH groups to surface Ni atoms, but also on their concentration and spatial distribution. In particular, low-density defects can induce transitions from *p*-type to *n*-type behavior, while higher coverages may restore the *p*-type character or even drive the system toward metallicity. This behavior underscores the central role of surface defect engineering in tuning the electronic structure of NiO. At higher coverages, surface reconstructions become prominent, as evidenced by two newly simulated NiO(100) terminations featuring either three- or four-coordinated Ni species. These reconstructions, together with the general upward

displacement of Ni atoms in the topmost layers caused by hydroxylation, may have important implications for the surface chemistry and reactivity of NiO, particularly in catalytic applications. Taken together, all these findings demonstrate that the functionalization of NiO(100) surfaces with -OH groups can radically reshape the material's electronic structure, enabling transitions between different conduction regimes (*p*-type → *n*-type or *p*-type → metallic system). Such tunability suggests a potential application of NiO as a material with tunable electronic properties, in which surface reactivity could be modulated in a controlled manner. Among the various systems explored, the $[Ni_{64}O_{64}]2H\text{-}2(OH)$ model emerges as particularly relevant, as it most closely resembles the hydroxylated NiO films experimentally observed under humid CVD conditions (see Paragraph 2.2). Its electronic and structural features suggest it may represent a realistic model for technologically relevant thin films. Lastly, the instability of highly hydroxylated systems containing both -H and -OH moieties leads to the formation of molecularly adsorbed water, with minimal effect on the electronic structure. This observation suggests that only specific configurations and coverages of surface defects result in meaningful changes to the material's properties.

2.5 Chapter 2 - Conclusions

Chapter 2 has presented an extensive and multifaceted computational investigation from Ni(II) β-diketonate-TMEDA precursors to functional nickel(II) oxide (NiO) nanomaterials.In Paragraph 2.1, the structural and electronic features of three Ni(II) β-diketonate-TMEDA complexes were analyzed in detail, revealing how the steric hindrance and fluorination degree of the β-diketonate ligands modulate the precursor's volatility, bonding scheme, and ultimately its reactivity. These insights were used to interpret experimental CVD results obtained under dry conditions, highlighting how ligand design directly influences the thickness and quality of the resulting NiO thin films [50].

Paragraph 2.2 extended this investigation to water-assisted CVD conditions, unveiling the crucial role played by water vapor in enhancing the growth of NiO films. DFT modeling showed that water promotes and facilitates the activation of the Ni precursor, thereby providing a microscopic rationale for the experimentally observed increase in film thickness and deposition efficiency under humid conditions [51].

In Paragraph 2.3, a systematic gas-phase study of the fragmentation behavior of the same complexes was conducted. Through combined analysis of ESI-HRMS, MS/MS, and DFT data, the properties of the fragmentation products were elucidated, with a particular emphasis on the role of Ni-ligand interactions and transient cation-π stabilization motifs. [52].

Paragraph 2.4 presents an in-depth DFT exploration of the structural and electronic properties of NiO(100) surfaces functionalized with hydroxyl (-OH) groups. These systems model the final defective nanomaterials that may arise from precursor decomposition under humid CVD conditions. A variety of configurations were studied, including neutral and charged hydroxyl defects, low and high coverage regimes, and mixed -H/-OH chemical nature of defects, showing how surface hydroxylation profoundly affects both the geometry and the electronic properties of NiO surfaces. The emergence of intra-gap states, and the changes in electronic

structure type (i.e., *p*-type, *n*-type, metallic) underscores the importance of defect engineering in tuning NiO properties for applications such as catalysis and sensing. Notably, among the systems investigated, one emerges as a particularly relevant structural model for CVD-grown hydroxylated NiO films, as discussed in Paragraph 2.2 [53].

– Appendix Chapter 2 –

Supplementary Information Paragraph 2.1

A.2.1.1 Computational details

The geometry optimizations of the three heteroleptic adducts, [Ni(tfa)$_2$TMEDA] (**1**), [Ni(fod)$_2$TMEDA] (**2**), and [Ni(thd)$_2$TMEDA] (**3**) – see Figure 1C, D, E in the main text –, were performed in the framework of hybrid density functional theory (DFT) with Gaussian basis set and spin multiplicity = 3. In particular, the optimized structures were calculated with the Gaussian 09 [93] code using the ωb97XD DFT approximation [94] for exchange and correlation functionals. Ni was described via Stuttgart-Dresden ECP pseudopotential and related basis set. [95] For all the other atoms (H, C, N, O, F), the chosen basis set was D95V(d). [96] This combination has already enabled to properly reproduce physico-chemical properties of other β-diketonate-TMEDA compounds. [41,45] Where available, the starting coordinates for the geometry optimization procedure were taken from crystallographic data. The computed optimized geometries of **1**-**3**, considered as isolated molecules, had all positive (harmonic) frequencies. All the reported energy differences include the Zero-Point-Energy correction. The compound optical absorption spectra were computed by time dependent (TD)-DFT at the CAM-B3LYP/D95++(2d,p) theory level. [97] TD-DFT excitations (40 in all cases) were calculated using a polarizable continuum model for the ethanol solvent, [98] and plotted using a Gaussian broadening (2 nm) to obtain the simulated spectra.

A.2.1.2 Ni(II) Target Complexes: Modelling and Analysis

In the case of [Ni(tfa)$_2$TMEDA] complex, three alternative structural models, characterized by the different relative positioning of -CF_3 group, were considered (Figure A.1). The first one (Figure A.1A) corresponds to the main component detected experimentally for **1** (isomer **1b**, 86.3%) and exhibits both -CH_3 groups in *trans* position with respect to the TMEDA. According to DFT results, the geometry shown in Figure A.1A represents the minimum energy structure of **1** (Figure 1C, main text).

Crystallographic data for isomer **1b** indicated an additional disorder, originating from -CF_3 group rotation, with a modelled occupancy ratio of 55.4% vs 44.6% between the main and minor split components. For this reason, the geometry of the two crystallographic structures of isomer **1b**, characterized by different orientations of the -CF_3 groups, were optimized. The corresponding geometry optimizations coalesced to a single energy minimum characterized by the -CF_3 orientation depicted in Figure A.1A, in line with that exhibited by the main modelled split-layer component. This result suggested that the -CF_3 rotational static disorder detected experimentally may be due to intermolecular interactions. The DFT-computed optimized geometry in Figure A.1B, obtained starting from the crystallographic coordinates of isomer **1a**, is characterized by a -CH_3 group and a -CF_3 group in the *trans* position with respect to TMEDA. This structure was 0.78 kcal/mol less stable than the minimum energy structure

(Figure A.1A). Such a small energy difference may justify the co-presence of both isomers **1b** and **1a** in the crystal structure of **1**.

Finally, the optimized geometry shown in Figure A.1C presents both -CF_3 groups in *trans* with respect to TMEDA and was found to be 2.36 kcal/mol less stable than the minimum energy structure (Figure A.1A). This appreciable energy difference, well above kT, may explain why such a conformation was not detected experimentally for [Ni(tfa)$_2$TMEDA].

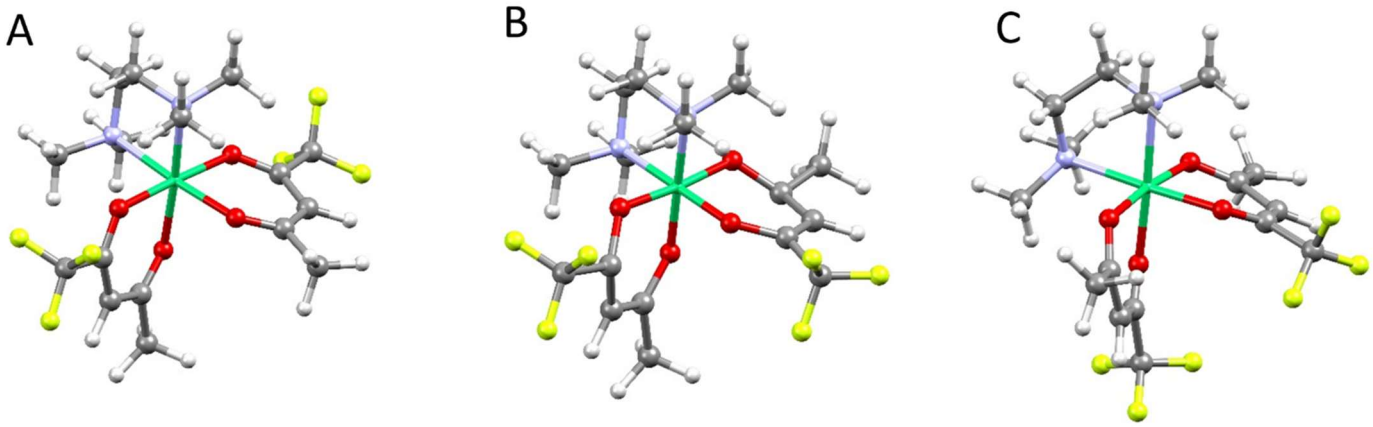

Figure A.1: DFT-computed optimized structures of the three structural isomers of compound 1.

XRD analysis of [Ni(thd)$_2$TMEDA] revealed the presence of two isomers characterized by two different TMEDA ethylene bridge arrangements. Specifically, the latter crystallizes in two conformationally disordered positions with 69.7 % of the main layer (C6, C7) *vs*. 30.3 % (C6A, C7A) for the minor one (Figure 1, dimmed, main text). The ratio of the disorder due to rotating tert-butyl was found to be 63.5 % vs. 36.5 % between the main (C1_4) and minor (C1_5) split layers. Geometry optimizations, performed starting from the XRD-coordinates of the two isomers, led to the structures reported in Figure A.2. In the most stable one (Figure A.2A), the ethylene bridge orientation is in line with the one found in the main crystallographic structure component. Conversely, the less stable structure (Figure A.2B), higher in energy only by 0.25 kcal/mol, reproduces the TMEDA ethylene bridge arrangement featured in the minor component. This small energy difference value supports the co-presence of both ethylene bridge arrangements in compound **3** crystals. In both structures (A and B), the tert-butyl group adopts the same orientation as that of the main split-layer component. These findings, in accordance with experimental data, confirm the reliability of the theory level used for the description of the compound structural features (see Section A.2.1.1).

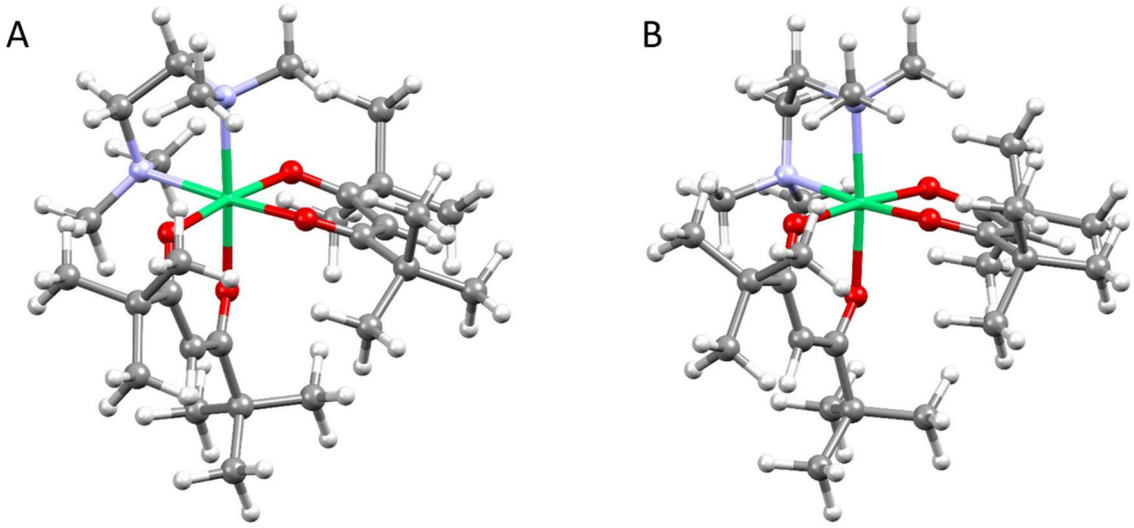

Figure A.2: DFT-computed optimized structures of the two structural isomers of compound 3.

At variance from [Ni(tfa)$_2$TMEDA] and [Ni(thd)$_2$TMEDA], for which single crystal X-ray diffraction data were available, the molecular structure of [Ni(fod)$_2$TMEDA] was characterised exclusively through computational methods. As a result, special attention was devoted to the exploration of the potential energy surface of this system in the search of the minimum energy structure. In this context, a thorough conformer search was performed involving different orientations of the -CF_2-CF_2-CF_3 chains. Despite the presence of several energy minima spanning an interval of ≈1.5 kcal/mol, the results evidenced that the most favourable arrangements of the fluorinated chains are the so-called "ortho" and "staggered" conformations, in line with previous studies on fluorinated hydrocarbons. [99] On this basis, three guess structures for compound **2** were generated by taking the optimized geometries of the three isomers of **1** (see Figure A.1) and substituting the -CF_3 groups with -CF_2-CF_2-CF_3 chains, and the -CH_3 groups with *tert*-butyl groups. Subsequent geometry optimization yielded the three structures reported in Figure A.3, characterized by different positioning of -CF_2-CF_2-CF_3 chains with respect to the TMEDA ligand. As for **1** and **3**, the three optimized geometries of **2** are characterized by a distorted octahedral coordination environment. The minimum energy structure (see Figure A.3A and Figure 1D in the main text) displays both *tert*-butyl groups in *trans* to TMEDA, while the -CF_2-CF_2-CF_3 chains occupy the apical positions of the Ni coordination sphere. As observed for compound **1**, the positioning of fluorinated groups in *trans* towards the diamine ligand appears to be slightly energetically unfavourable even in **2**. Indeed, the optimized geometry in Figure A.3B presents only one -CF_2-CF_2-CF_3 chain in *trans* to TMEDA and is 0.91 kcal/mol higher in energy than the minimum energy structure (Figure A.3A). The slight energy difference between these structures may suggest that, as for compound **1**, both isomers might coexist in solution at room temperature. This finding, along with the presence of multiple conformers of **2** characterized by different arrangements of the -CF_2-CF_2-CF_3 chains and very similar energy, might also be one of the reasons of the difficulties encountered in trying to solve the crystal structure of [Ni(fod)$_2$TMEDA] by X-ray diffraction. Conversely, the structure illustrated in Figure A.3C, exhibiting both the -CF_2-CF_2-CF_3 chains in *trans* towards TMEDA, is less stable by 2.41 kcal/mol with respect to the minimum energy structure (Figure A.3A). This higher ΔE value suggests that the co-presence of this isomer

might be less likely. This hypothesis is also supported by the fact that, in the case of **1**, no isomer presenting both fluorinated groups in *trans* to TMEDA (see Figure A.1C) was detected by X-ray analyses.

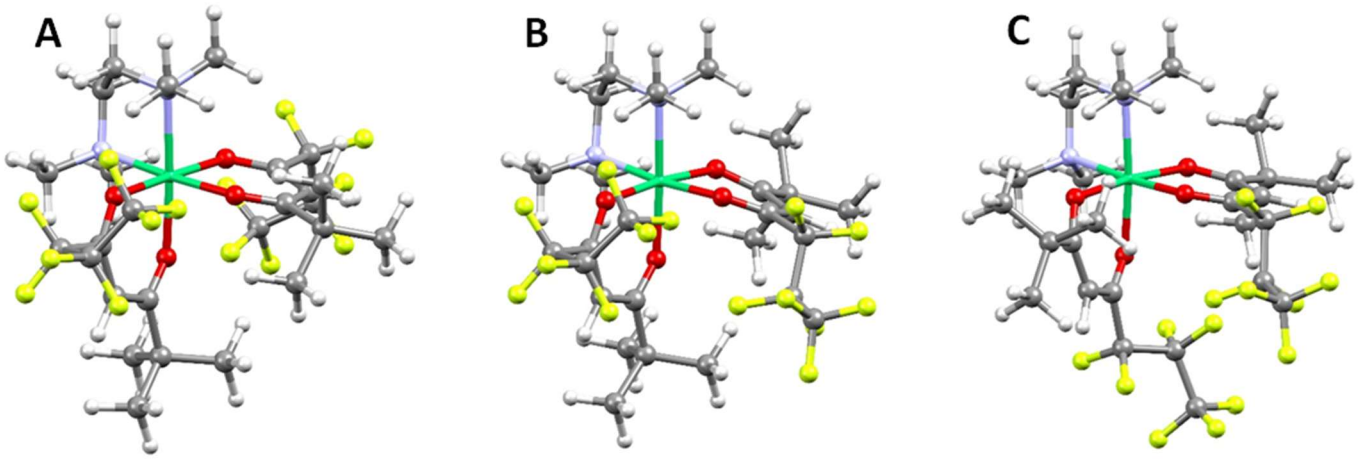

Figure A.3: DFT-computed optimized structures of the three structural isomers of compound 2.

A.2.1.3 IR Spectral Analysis

The experimental and simulated IR spectra of [Ni(tfa)$_2$TMEDA], [Ni(fod)$_2$TMEDA], and [Ni(thd)$_2$TMEDA] are displayed in Figures A.4, A.5 and A.6, respectively. The calculated spectra were broadened with a 2 cm^{-1} gaussian. For all the compounds, a detailed band assignment based on the normal modes has been done, as reported in Tables A.1-A.3 (wavenumbers refer to computed values; intensities are denoted as vs = very strong; s = strong; m = medium; w = weak; vw = very weak). A scaling factor of 0.952 was applied to the computed vibrational frequencies [100,101] for all the complexes. This correction factor essentially compensates for two intrinsic limitations of electronic structure calculations: (i) the electronic structure of the system is inherently affected by several approximations; (ii) normal modes are computed within the harmonic potential approximation, which fails to accurately reproduce the curvature near the energy minimum.

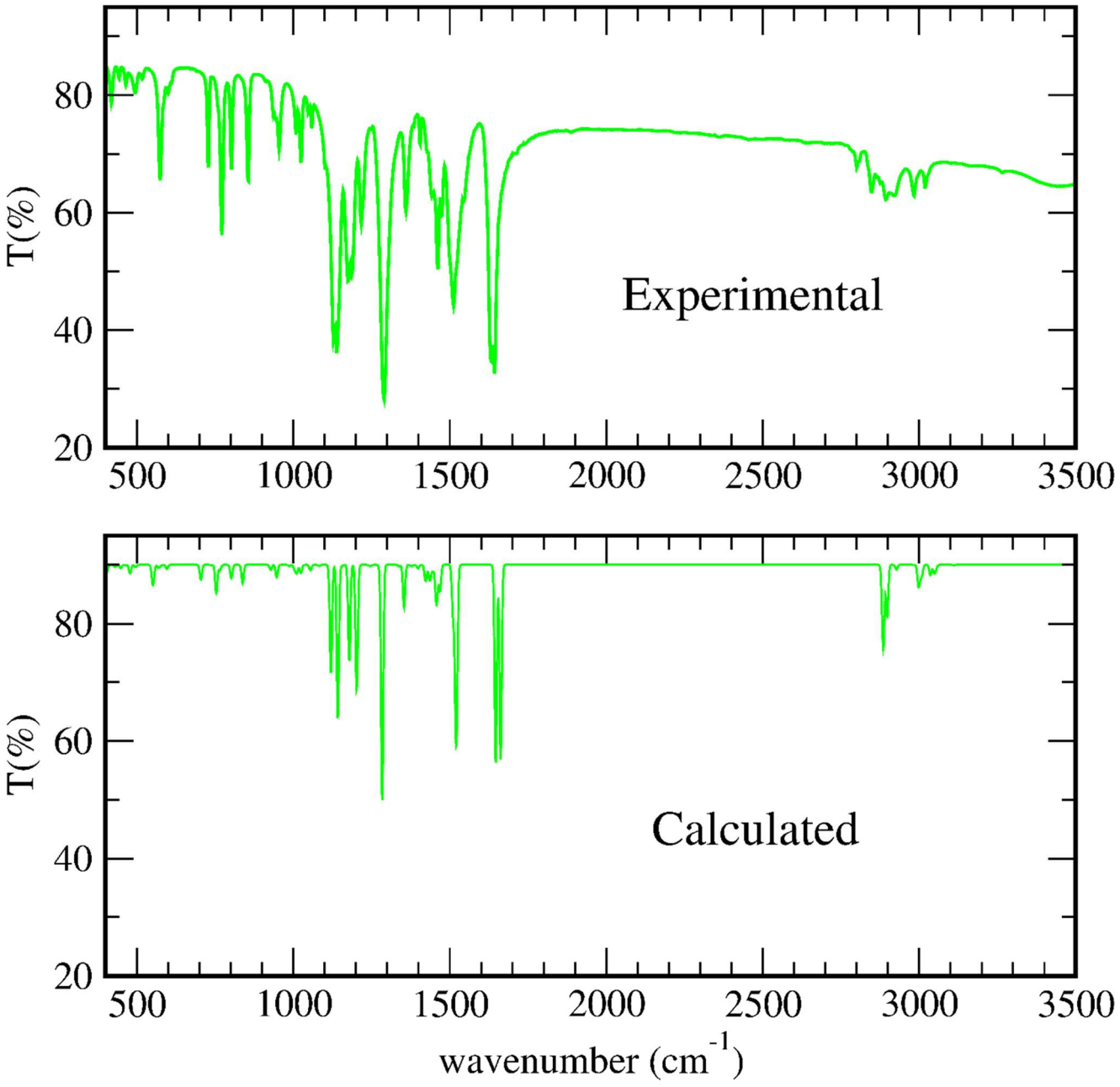

Figure A.4: Experimental and DFT-computed IR spectra of [Ni(tfa)$_2$TMEDA] (**1**).

Table A.1: Calculated wavenumbers $\tilde{\upsilon}$ and band assignment for [Ni(tfa)$_2$TMEDA] IR spectra shown in Figure A.4.

$\tilde{\upsilon}$ (cm^{-1})	Assignment
3268 (vw)	Stretching of tfa central C-H
3207-3027 (m,w)	TMEDA –CH_3/–CH_2 stretching
3188-3075 (m,w)	tfa –CH_3/–CH_2 stretching
1746 (vs)	Symmetric Stretching C=O in-phase
1730 (vs)	Symmetric Stretching C=O out-of-phase
1599-1586 (vs)	Asymmetric Stretching C=O (involving C=C–C stretching tfa)
1543-1500 (m,w)	Rocking and scissoring of all –CH_3/–CH_2
1494-1339 (w)	Wagging, rocking, twisting, scissoring of all –CH_3/–CH_2
1422 (m)	–CH_3 tfa scissoring + –CH and C=C–C bending
1349-1347 (vs,s)	TMEDA rocking and scissoring of –CH_3/–CH_2 +Stretching C–CF_3/C=C
1313-1307 (vw)	TMEDA stretching of N-C-C-N
1264-1199 (s)	Stretching C–F + bending –CH tfa + TMEDA –CH_3 wagging
1238-1213 (w)	N-Ni-N rocking and scissoring
1178-1176 (s)	In-plane bending –CH + stretching C-F, C-C=C, C–CF_3 tfa
1173-1137 (w)	Twisting –CH_3/–CH_2 TMEDA + asymmetric in-plane bending N-Ni-N
1108 (w)	TMEDA stretching C-C in-phase
1083-1075 (m)	TMEDA collective out-of-plane bending
1055-1037 (w)	In-plane and out-of-plane bending modes tfa (CH-C(=O)-C)
994-974 (w)	Collective bending N-C-C-N TMEDA
880 (m)	Bending O2-Ni-O3
842-804 (m)	Stretching Ni-N-C-C-N-Ni
791 (m)	Out-of-plane bending O-C-C, C-C-H, -CH_3 tfa
578 (m)	Symmetric and asymmetric stretching Ni-O2, Ni-O3
597 (w)	Symmetric out-of-plane bending O2-Ni-O3 (wagging)
503 (m,w)	Symmetric and asymmetric stretching Ni-O1, Ni-O4
471 (m,w)	Symmetric and asymmetric stretching Ni-N1, Ni-N2
424-197 (m,w)	Bending Ni-O, Ni-N bonds (all)
334-276 (w)	Symmetric stretching Ni-O2, Ni-O3
249-216 (w)	Vibration of Ni in out of the O2-O3-N1-N2 plane
228 (w)	Vibration of Ni in the O2-O3-N1-N2 plane
178-16 (w)	Collective stretching/bending modes of the Ni octahedron

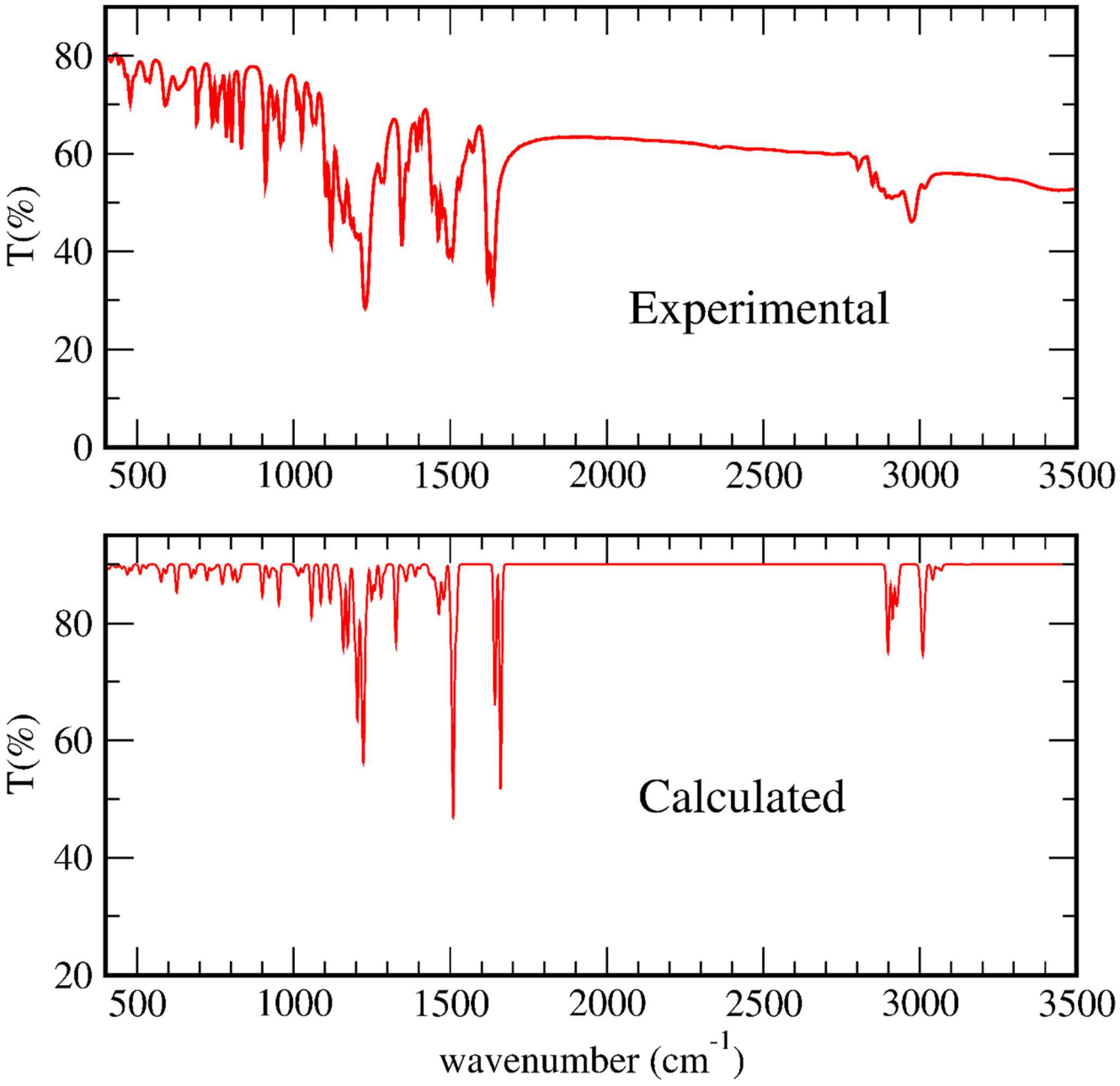

Figure A.5: Experimental and DFT-computed IR spectra of [Ni(fod)$_2$TMEDA] (**2**).

Table A.2: Calculated wavenumbers $\tilde{\upsilon}$ and band assignment for [Ni(fod)$_2$TMEDA] IR spectra shown in Figure A.5.

$\tilde{\boldsymbol{\upsilon}}$ (cm^{-1})	Assignment
3298 (wv)	Stretching of fod central C-H
3215-3197 (w)	TMEDA -CH_3 asymmetric stretching
3179-3057 (m)	fod -CH_3 asymmetric stretching
3156 (m)	TMEDA -CH_3 symmetric stretching
3147-3145 (m)	fod and TMEDA -CH_3 asymmetric stretching
3044-3027 (m,s)	TMEDA -CH_3/-CH_2 stretching
3145-3057 (m)	fod -CH_3 symmetric stretching
3045 (s)	TMEDA -CH_2 stretching
1739 (vs)	Symmetric stretching C=O in-phase
1721 (vs)	Symmetric stretching C=O out-of-phase
1590-1572 (vs)	Asymmetric stretching C=O (involving stretching C=C-C fod)
1552 (m)	fod -CH_3 scissoring
1546-1530 (m,s)	TMEDA -CH_3/-CH_2 wagging, rocking, twisting and scissoring
1523-1466 (m)	TMEDA -CH_3/-CH_2 in-plane bending
1452-1415 (m)	fod -CH_3 in-plane bending
1407 (m)	Rocking TMEDA
1389-1387 (s)	Stretching C=C-C and -CF_2-CF_3 fod
1349 (m)	TMEDA N-C-C-N wagging and -CH_3/-CH_2 twisting
1339-1340 (m)	Twisting TMEDA
1337-1306 (m)	Stretching C=C-C-CF_2 + fod -CH_3 twisting
1315 (m)	Wagging TMEDA
1286-1210 (s)	Collective bending fod
1273 (vs)	Symmetric in-plane bending fod
1271 (m)	TMEDA and fod out-of-plane bending
1266 (s)	Bending C-H fod
1259 (vs)	Bending C-H + Scissoring of -CF_2-CF_2-CF_3 fod
1251-1251(w)	fod -CH_3/-CH/-CF_3 bending
1228,-1210 (s)	Bending C-H + asymmetric stretching –CF_2 fod
1200 (m)	fod -CH_3/-CH/-CF_2/-CF_3 in-plane bending
1171-1169 (s)	Stretching C=C-C and -CH_3/-CF_3 fod wagging
1106 (s)	Breathing fod
1079-1062 (m,w)	Stretching C-N, C-C + bending N-C-C-N TMEDA
999 (s)	Bending modes of fod and TMEDA
996 (m)	Bending C-C=C fod
960 (m)	*tert*-butyl-C stretching + O=C-CF_2 stretching
865-806 (m)	fod deformation modes
843 (m)	TMEDA deformation mode
809, 788 (m)	Out-of-plane bending C-H fod
772-719 (w)	fod breathing modes
618-615 (w)	Ni-O2, Ni-O3 Symmetric and Asymmetric stretching, respectively
593-554 (w)	Stretching O1-Ni, O4-Ni, + CF_2 deformation modes
503-494 (w)	stretching of Ni-ligand bonds (Ni-N1, Ni-N2, Ni-O3, Ni-O2)
490-483 (m,w)	*tert*-butyl bending
472 (w)	Ni-N1, Ni-N2 asymmetric stretching
460, 459 (w)	Stretching Ni-O1, Ni-O4, + deformation –CF_2-CF_2-CF_3
451 (vw)	Ni-N symmetric stretching + deformation modes TMEDA
429 (w)	Ni-O symmetric stretching + deformation modes fod
426 (vw)	Ni-O asymmetric stretching
409 (vw)	N1-Ni-N2 stretching + TMEDA twisting
384-285 (w)	TMEDA and fod deformation modes
275 – 13 (vw)	Collective stretching/bending modes of the Ni octahedron

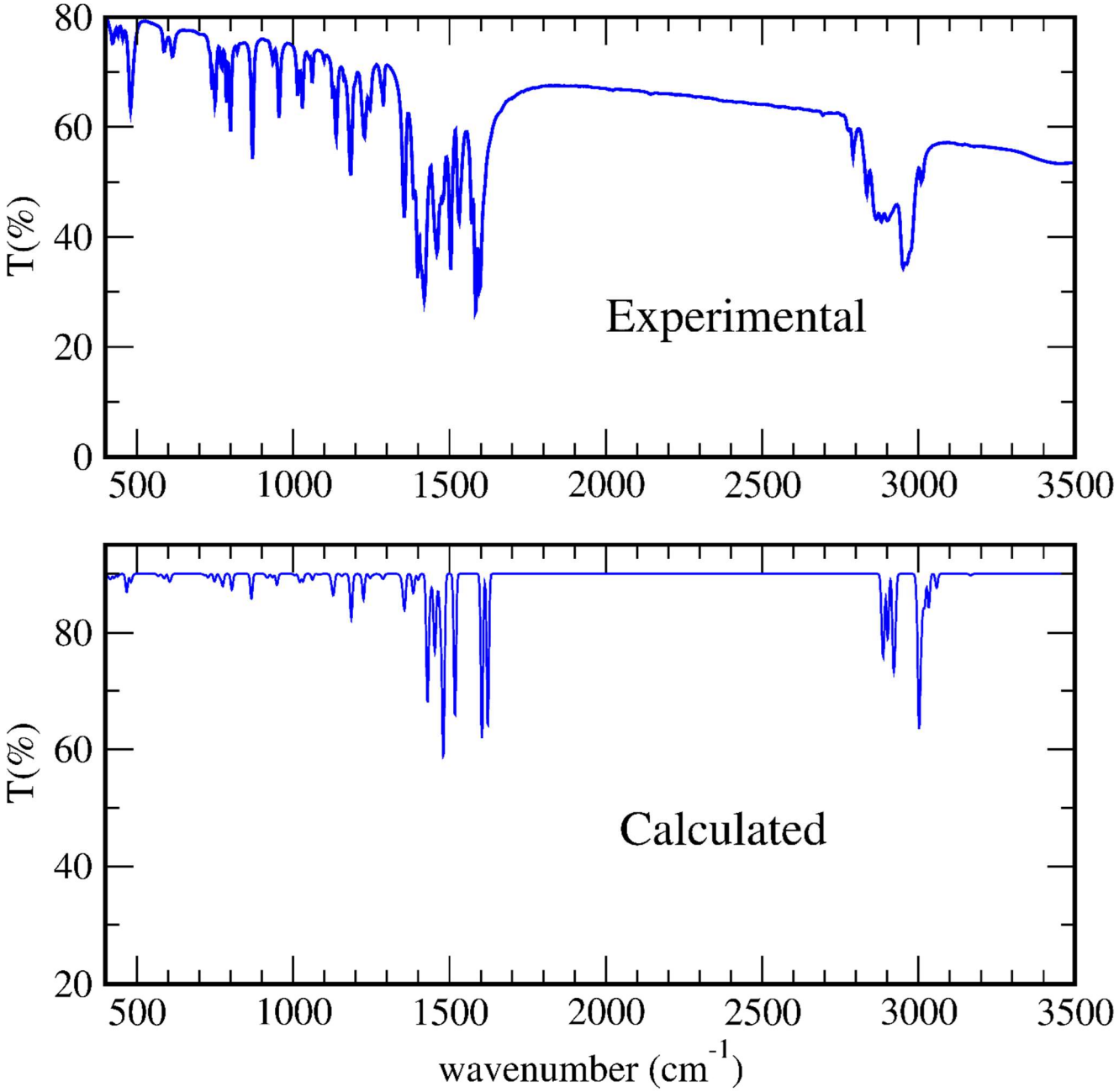

Figure A.6: Experimental and DFT-computed IR spectra of [Ni(thd)$_2$TMEDA] (**3**).

Table A.3: Calculated wavenumbers $\tilde{\upsilon}$ and band assignment for [Ni(thd)$_2$TMEDA] IR spectra shown in Figure A.6.

$\tilde{\upsilon}$ (cm^{-1})	Assignment
3310 (vw)	Symmetric stretching of thd central CH
3201-3198(m,w)	TMEDA –CH_3 stretching
3166-3055(m,w)	Symmetric and asymmetric thd –CH_3 stretching
3148-3015(m,w)	thd and TMEDA –CH_3 stretching
3146-3015 (m,s)	TMEDA –CH_3/-CH_2 stretching
3141-3135 (m)	All –CH_3 thd stretching
1700 (vs)	Symmetric stretching C=O in-phase
1680 (vs)	Symmetric stretching C=O out-of-phase
1593 (s)	Asymmetric stretching C=O (involving stretching C=C-C thd)
1553 (vs)	Stretching C=C-C thd + collective bending of –CH_3 groups
1549 (vs)	Collective rocking and scissoring of –CH_3 groups
1547 (w)	All -CH/CH_2/-CH_3 in-plane-bending + TMEDA -CH_3 scissoring
1546-1498 (m)	TMEDA rocking and scissoring of –CH_3/–CH_2 groups
1533-1500(m,w)	Collective rocking and scissoring of –CH_3/–CH_2 groups
1508-1495 (m)	Collective rocking /scissoring of –CH_3/–CH_2 groups + C=C-C thd stretching
1494-1487 (m)	Wagging, rocking, twisting, scissoring of TMEDA –CH_3/–CH_2
1466-1461 (w)	TMEDA –CH_2 wagging + N-CH_3 stretching
1450 (w)	thd -C-CH_3 collective stretching
1420-1413(m,w)	thd wagging, rocking, twisting, scissoring of C–CH_3 *tert*-butyl
1406 (vw)	TMEDA N-C-C-N symmetric out-of-plane-bending
1350 (m,w)	TMEDA N-C-C-N asymmetric out-of-plane-bending
1344 (vw)	thd *tert*-butyl-C-CH_2-C-tert-Butyl symmetric stretching
1310 (vw)	TMEDA stretching N-C-C-N out-of-phase
1282 (m)	thd *tert*-butyl C-CH_3 symmetric stretching
1280 (m)	thd *tert*-butyl C-CH_3 asymmetric stretching
1246-1244 (s)	O=C-CH-C=O bending
1210 (w)	Collective TMEDA bending
1184 (m)	thd C-CH-C symmetric stretching
1179 (m)	thd C-CH-C asymmetric stretching
1111 (m)	TMEDA stretching C-C in-phase
1080 (m)	TMEDA collective symmetric out-of-plane bending (wagging)
1065 (m)	TMEDA N-Ni-N wagging
995 (m)	Collective bending N-C-C-N TMEDA
906 (m)	Collective bending thd
840 (m)	Symmetric stretching Ni-N-C-C-N-Ni bond
810 (m,w)	Out-of-plane bending O-C-C
804 (w)	N-Ni-N asymmetric stretching
779 (m,w)	thd central CH bending
638-493 (m,w)	Symmetric stretching Ni-O
633-505 (m)	Asymmetric stretching Ni-O
599-490 (m,w)	Symmetric out-of-plane bending N-Ni-N (wagging)
461 (w)	Asymmetric stretching Ni-N1
447(w)	Symmetric in-plane bending N1-Ni-N2
433-335 (w)	Scissoring and bending O1-Ni-O4
284-256 (m,w)	Bending Ni bonds (all), thd, and TMEDA -CH_3
253-22 (vw)	Collective stretching/bending modes of the Ni octahedron

A.2.1.4 Optical Spectra Analysis

The optical spectra of compounds **1-3** were simulated through TD-DFT calculations (see Section A.2.1.1), showing good agreement with the experimental data (see Section 2.1.4 of the main text for further details). The molecular spin orbitals primarily involved in the electronic transitions responsible for the most intense absorption band in the spectra of **1-3** are illustrated in Figure A.7. In all cases, the initial and final states of the transition are predominantly localized on combinations of β-diketonate π- and π-* states, respectively, with only minimal contributions from Ni d-states. The initial states of the transition also include a very weak component ascribable to TMEDA states, which is greater in the case of **3** (Figure A.7C). Nevertheless, owing to the overwhelming predominance of β-diketonate contributions in the involved spin-orbitals, the character of the main absorption band can be confidently assigned as ligand-ligand π-π* for all the three complexes, in line with previous findings for related metal systems. [37,45]

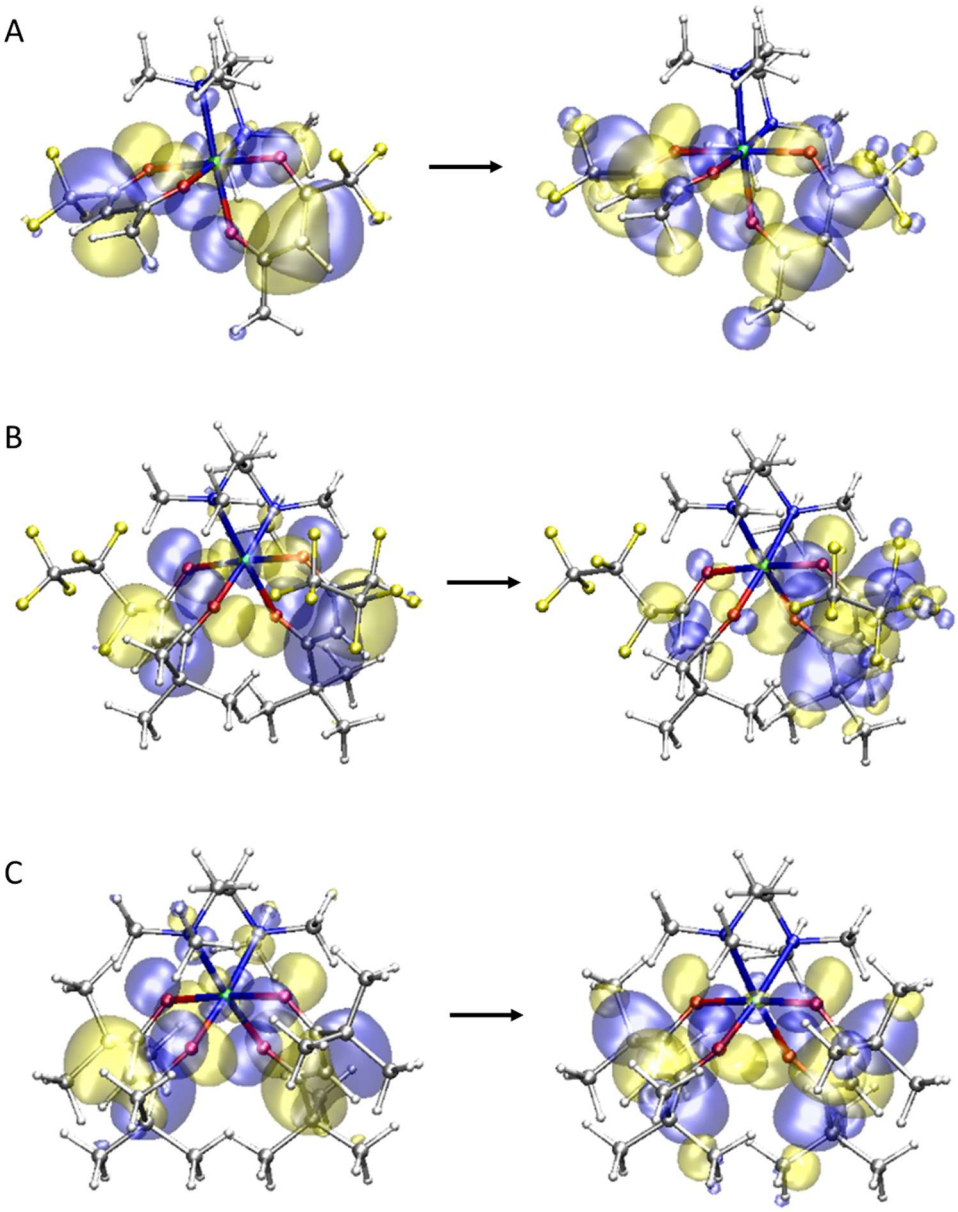

Figure A.7: Graphical representation of the spin orbitals primarily involved in the electronic transitions associated with the main absorption band in the UV-Vis spectra of the investigated Ni complexes. A: compound **1** (λ = 277 nm); B: compound **2** (λ = 290 nm); C: compound **3** (λ = 271 nm). Yellow and blue colors indicate positive (+0.02 e) and negative (-0.02 e) isosurface values of the spin orbitals, respectively.

Supplementary Information Paragraph 2.2

A.2.2.1 Theoretical Method

To investigate the influence of water vapor in the CVD reaction environment, the interaction of water molecules with Ni(tfa)$_2$TMEDA, Ni(fod)$_2$TMEDA, and Ni(thd)$_2$TMEDA (Figures A.8-A.11) was modeled using a DFT approach. The computational protocol adopted was the same as that employed for the characterization of the three precursors under dry conditions (see Section A.2.1.1). More specifically, the hydrated target compounds **1**-**3** were theoretically studied using the ωb97XD functional [94], used without modifications as coded in the Gaussian09 program package, which was employed to perform all calculations. [93] The Stuttgart-Dresden ECP pseudopotential and basis set were employed for Ni, [95] which accounts for 18 valence electrons. For all the other atoms the D95V(d) basis set was adopted. [96] Water binding energies (W_{BE}), expressed *per* water molecule, for the formation of hydrated precursors were calculated according to the following expression:

$$W_{BE} = -\frac{E(Ni(L)_2TMEDA \cdot n(H_2O)) - E(Ni(L)_2TMEDA) - n \cdot E(H_2O)}{n} \quad (1)$$

with L = tfa, fod, thd respectively, and n = number of water molecules. The zero-point-energy (ZPE) correction was considered in calculating water binding energies.

The calculated optimized structures of all hydrated Ni(L)$_2$TMEDA (triplet spin state, *i.e.* spin multiplicity = 3) did not feature any imaginary frequency.

A.2.2.2 Modeling Water-Precursor Interactions: Structural Impact of Hydration on Ni(II) Complexes

As mentioned in the main text (Section 2.2.1), the interaction of Ni(tfa)$_2$TMEDA, Ni(fod)$_2$TMEDA, and Ni(thd)$_2$TMEDA with water vapor was theoretically investigated by optimizing the geometries of the three complexes including from one to three H_2O molecules in the second Ni coordination shell. This approach enabled the evaluation of structural variations in compounds **1**-**3** as a function of a variable number *n* of water molecules (*n* = 1, 2, 3), offering insights into how hydration influences the geometry of the precursors. More specifically, two distinct arrangements of water molecules were examined for both the di-hydrated and tri-hydrated complexes. For the di-hydrated species, the two water molecules were either symmetrically positioned in two different regions of the complex or were coordinated as a hydrogen-bonded dimer interacting with it. In the case of three water molecules, two starting configurations were considered: one in which a dimer and an isolated water molecule were placed on opposite sides of the complex, and another featuring a hydrogen-bonded water trimer positioned in proximity to the precursor. These structural arrangements are illustrated in Figures A.8, A.10 and A.11. From a purely modeling standpoint, the guess geometries of Ni(L)$_2$TMEDA•H_2O (with L = tfa, fod, and thd,

respectively) were built starting from the minimum energy structures of isolated complexes (Figure 1, Paragraph 2.1 in the main text) and placing the water molecule in the less sterically hindered region of Ni coordination environment. A similar approach was performed for the starting geometries of $Ni(L)_2TMEDA•2H_2O$, in which the two water molecules were symmetrically placed in the less sterically hindered regions of the Ni coordination sphere. The guess structures of $Ni(L)_2TMEDA•3H_2O$ was achieved by adding one additional H_2O molecule to the previously optimized $Ni(L)_2TMEDA•2H_2O$ structures, positioning it in proximity to one of the already coordinated water molecules. Similarly, the starting geometries of $Ni(L)_2TMEDA•2H_2O_{dimer}$ and $Ni(L)_2TMEDA•3H_2O_{trimer}$ were built starting from previously optimized structures.

It is worth noting that all the minimum energy structures of dry precursors exhibit a slightly distorted octahedral coordination environment at the Ni center (C_1 symmetry). However, these structures present very tiny distortions from the C_2 and could be approximately considered as having an effective C_2 symmetry. These considerations might suggest that asymmetric placement of water molecules in the Ni second coordination shell could induce significant deviations from the C_2 symmetry in the hydrated complexes' structure.

The computed optimized structures of all hydrated $Ni(L)_2TMEDA$ in their triplet spin state exhibited no imaginary frequency. Bond lengths and angles achieved for the optimized geometries of $Ni(L)_2TMEDA•H_2O$, $Ni(L)_2TMEDA•2H_2O$, $Ni(L)_2TMEDA•2H_2O_{dimer}$, $Ni(L)_2TMEDA•3H_2O$, and $Ni(L)_2TMEDA•3H_2O_{trimer}$ are summarized in Tables A.4-A.6, alongside the corresponding values obtained for non-hydrated complexes (see Paragraph 2.1, Section 2.1.2, Table 1 in the main text). Meanwhile, average Ni-O and Ni-N bond distances per ligand as a function of both the number and spatial arrangement of water molecules in complexes **1-3** were collected in Table 5 (main text). This choice was intended to enhance the clarity of the presented data and to support a more effective interpretation of the observed trends. It is worth noting that in all the considered structures, water molecules were undissociated; however, in the case of $Ni(tfa)_2TMEDA$, a model with one dissociated H_2O molecule was considered as well (Figure A.9).

The following subsections present the structural properties of the hydrated compounds discussed above, along with graphical representations and tables reporting the calculated bond lengths and angles. These data are systematically organized based on both the number of water molecules included in the Ni second coordination shell and the specific Ni(II) precursor involved in the interaction.

A.2.2.2.1 $Ni(tfa)_2TMEDA•nH_2O$

Figure A.8 shows the optimized geometries of complex **1** before water interaction (i.e., the structure previously shown in Figure 1, main text) and after the addition of n = 1, 2, and 3 water molecules. This comparative visualization allows for a direct assessment of the structural modifications induced by hydration. The corresponding geometric parameters are summarized in Table A.4.

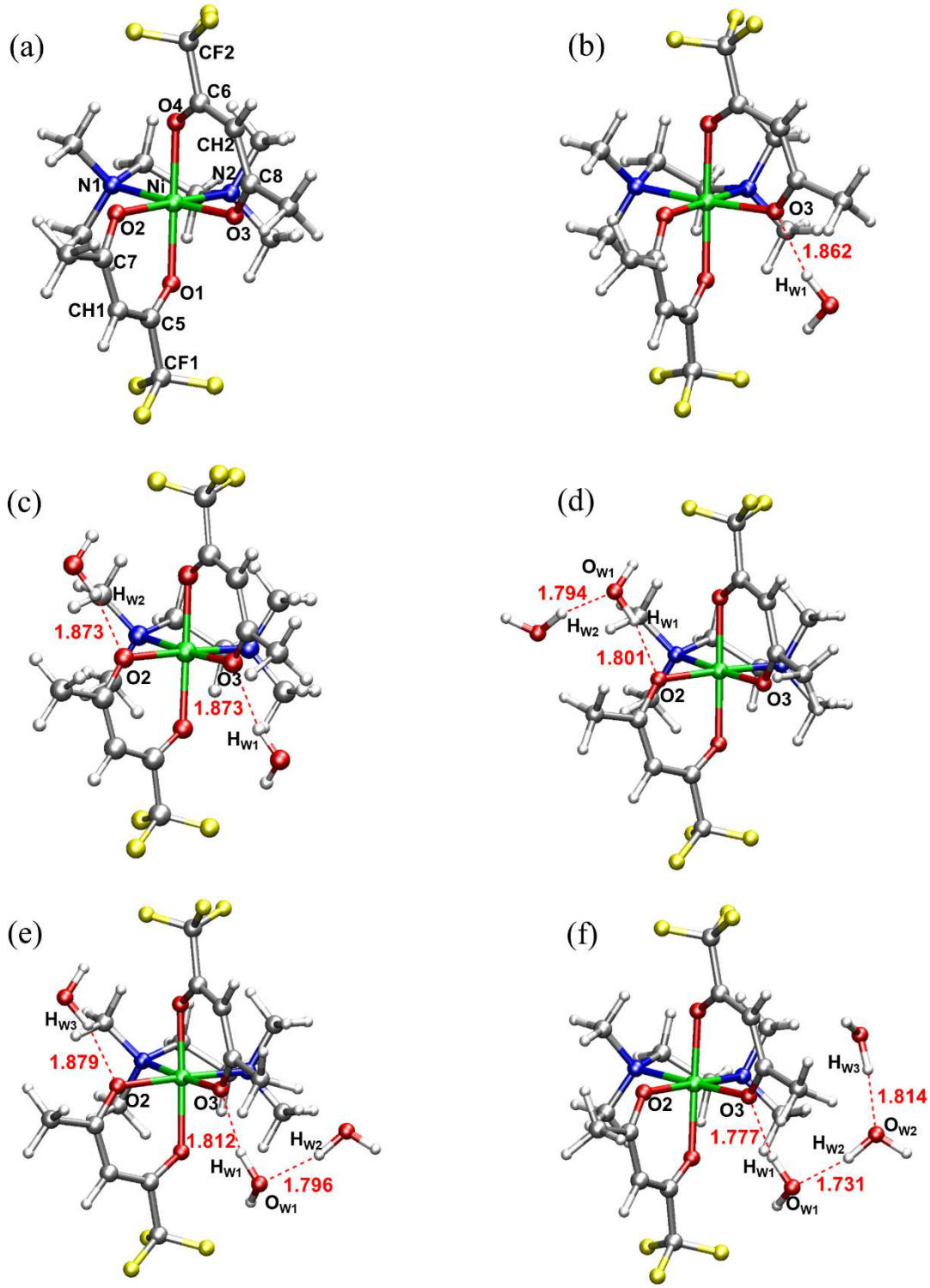

Figure A.8: Graphical representation of the DFT-computed minimum energy structures of: (a) $Ni(tfa)_2TMEDA$; (b) $Ni(tfa)_2TMEDA{\bullet}H_2O$; (c) $Ni(tfa)_2TMEDA{\bullet}2H_2O$; (d) $Ni(tfa)_2TMEDA{\bullet}2H_2O_{dimer}$; (e) $Ni(tfa)_2TMEDA{\bullet}3H_2O$; (f) $Ni(tfa)_2TMEDA{\bullet}3H_2O_{trimer.}$ Atom colors: Ni = green; F = yellow; O = red; N = blue, C = grey, H = white, dashed red lines = hydrogen bonds (bond lengths are in Å).

As previously noted, Figure A.8 clearly illustrates that H_2O molecules are positioned in the less sterically hindered regions within the coordination environment of the complex. In addition, water molecules are observed to engage in relatively strong hydrogen-bonding interactions with the oxygen atoms of the β-diketonate ligands.

Table A.4: Selected geometrical parameters of $Ni(tfa)_2TMEDA$ and its hydrated analogues $Ni(tfa)_2TMEDA•nH_2O$ (n = 1, 2, 3). Atom labels correspond to those reported in Figure A.8.

Ni(tfa)$_2$TMEDA						
Bond length (Å)	**No water**	**+ 1 H_2O**	**+ 2 H_2O**	**+ dimer**	**+ 3 H_2O**	**+ trimer**
Ni-O1	2.028	2.033	2.039	2.027	2.045	2.043
Ni-O4	2.028	2.033	2.039	2.039	2.033	2.027
Ni-O2	2.045	2.047	2.040	2.042	2.044	2.059
Ni-O3	2.045	2.039	2.040	2.052	2.044	2.052
Ni-N1	2.169	2.163	2.164	2.173	2.165	2.171
Ni-N2	2.169	2.170	2.164	2.168	2.169	2.156
O1-C5	1.260	1.264	1.261	1.258	1.262	1.265
O2-C7	1.255	1.253	1.261	1.265	1.260	1.252
O4-C6	1.260	1.258	1.261	1.265	1.262	1.255
O3-C8	1.255	1.263	1.261	1.251	1.264	1.265
C5-CF1	1.543	1.543	1.544	1.544	1.544	1.543
C5-CH1	1.391	1.387	1.391	1.392	1.389	1.386
C7-CH1	1.426	1.430	1.422	1.420	1.424	1.432
C6-CF2	1.543	1.544	1.544	1.543	1.544	1.545
C6-CH2	1.391	1.393	1.391	1.385	1.389	1.396
C8-CH2	1.426	1.420	1.422	1.432	1.423	1.417
H-Bond (Å)						
O3-H_{w1}		1.862	1.873	-	1.812	1.777
O2-H_{w2}		-	1.873	-	-	-
O2-H_{w1}		-	-	1.801	-	-
O2-H_{w3}		-	-	-	1.879	-
O_{w1}-H_{w2}		-	-	1.794	1.796	1.731
O_{w1}-H_{w3}		-	-	-	-	1.814
Bond angles (°)						
O1-Ni-O4	177.9	177.2	176.4	177.2	176.3	176.0
O1-Ni-O2	89.2	89.3	88.3	89.9	89.1	89.0
N1-Ni-N2	84.8	84.9	85.1	84.9	85.1	84.8
O2-Ni-O3	90.5	89.8	89.5	89.7	89.2	87.9
O2-Ni-N1	92.4	92.6	92.8	92.3	92.5	91.3
O1-Ni-N1	92.6	93.6	93.7	93.5	93.6	93.2

A.2.2.2.2 $Ni(tfa)_2TMEDA•nH_2O$ dissociated form

For compound **1**, a monohydrated $Ni(tfa)_2TMEDA•H_2O$ structure featuring a dissociated water molecule was also investigated. The guess geometry for this system was built by placing the ionized OH^- and H^+ water-fragments in the proximity of the Ni center and close to one of the nitrogen atoms of the TMEDA ligand, respectively. Upon geometry optimization (Figure A.9), one of the TMEDA nitrogen atoms was found to be protonated and no longer coordinated to the Ni center, displaying a distance of 4.092 Å from the latter. Furthermore, one β-diketonate ligand was converted into a ketocarboxilic acid, with the carboxylic group

positioned near the CF_3 group. The resulting optimized geometry (Figure A.9) therefore exhibited a pentacoordinated Ni environment, and the computed water binding energy for this structure was -49.32 kcal/mol. This species could potentially display higher reactivity, *i.e.* a greater propensity to undergo fragmentation if compared to the original hexacoordinated precursor, making it a potential interesting candidate for alternative fragmentation pathways toward NiO nanomaterial formation. Nevertheless, the significantly negative water binding energy value suggests that the direct dissociation of a water molecule in this family of complexes is energetically unfavored. Based on this result, no further structures with dissociated water molecules were considered in this work.

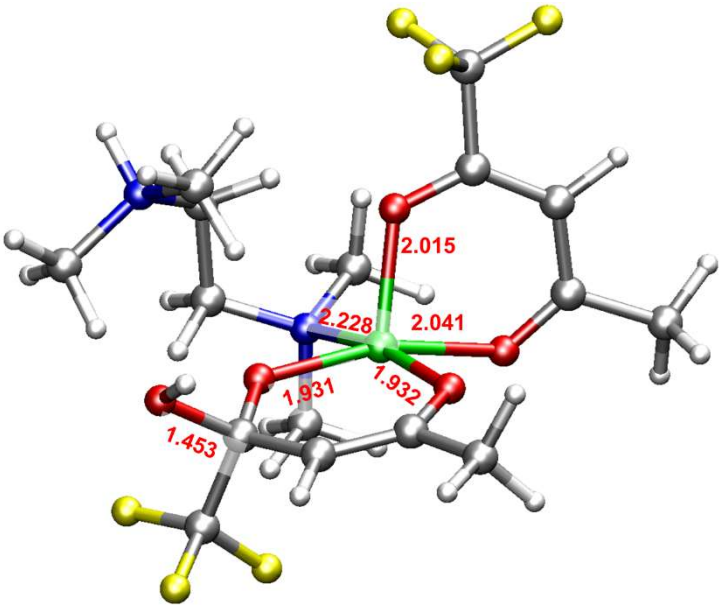

Figure A.9: Graphical representation of the DFT-computed minimum energy structure of $Ni(tfa)_2TMEDA{\bullet}H_2O_{dissociated}$, featuring a dissociated water molecule. Atom colors: Ni = green; F = yellow; O = red; N = blue, C = grey, H = white. Relevant Ni-O, Ni-N and C-OH distances are reported in Å.

A.2.2.2.3 $Ni(fod)_2TMEDA{\bullet}nH_2O$

As for complex **1**, the optimized geometries of complex **2** before hydration and after the addition of n = 1, 2, and 3 water molecules are shown in Figure A.10. As illustrated, H_2O molecules are positioned in the less sterically hindered regions within the coordination environment of the complex, thereby minimizing unfavorable spatial interactions.

Nevertheless, in contrast to the $Ni(tfa)_2TMEDA$ case, water molecules in $Ni(fod)_2TMEDA$ form weaker hydrogen bonds, which occur only at the expense of a pronounced distortion of the Ni coordination sphere. This behavior might be attributed to the presence of two bulky tert-butyl groups in the complex moiety, whose steric hindrance hampers effective interaction between water molecules and the second coordination shell of the Ni center. The relevant geometrical parameters are collected in Table A.5.

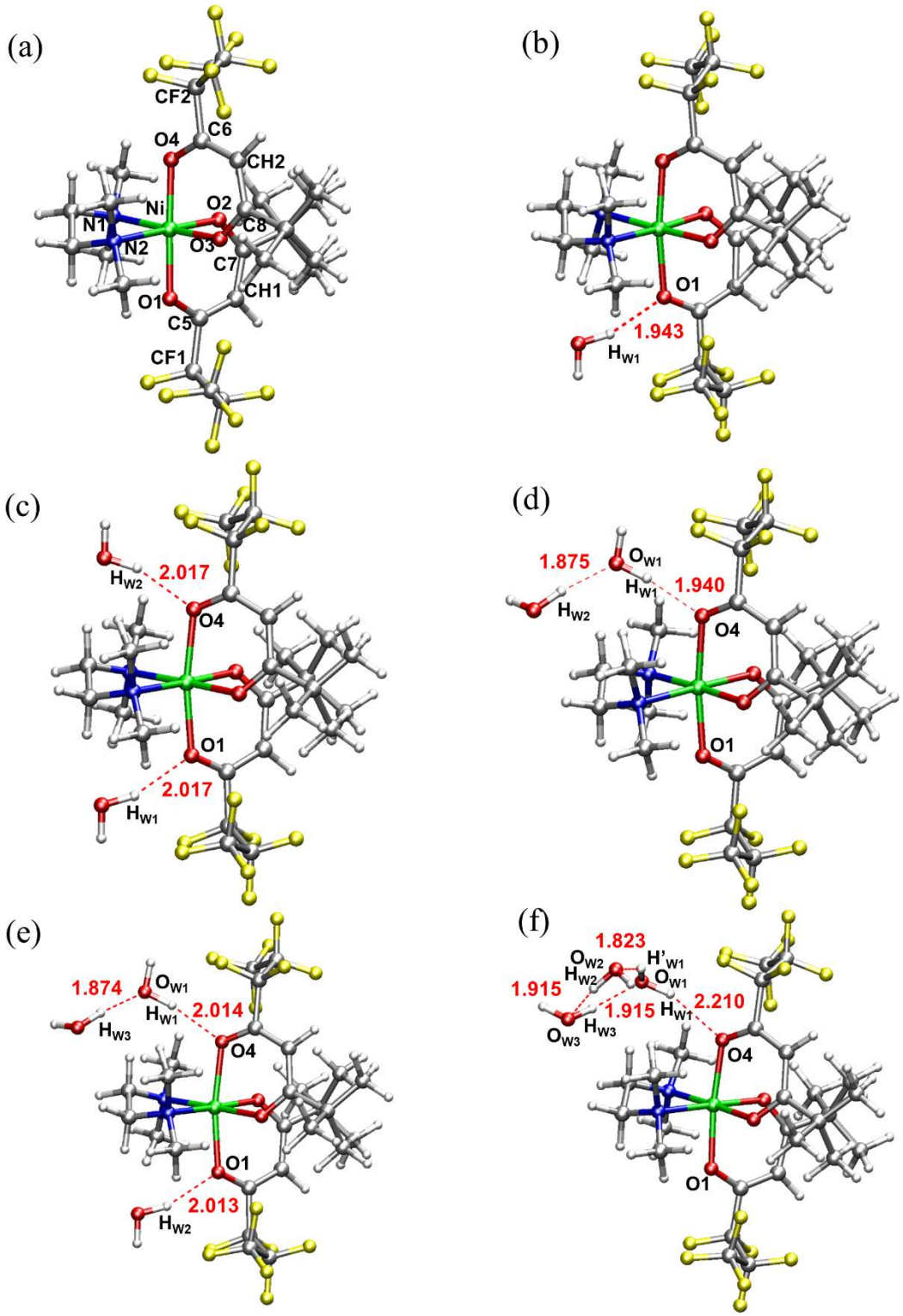

Figure A.10: Graphical representation of the DFT-computed minimum energy structures of: (a) $Ni(fod)_2TMEDA$; (b) $Ni(fod)_2TMEDA{\bullet}H_2O$; (c) $Ni(fod)_2TMEDA{\bullet}2H_2O$; (d) $Ni(fod)_2TMEDA{\bullet}2H_2O_{dimer}$; (e) $Ni(fod)_2TMEDA{\bullet}3H_2O$; (f) $Ni(fod)_2TMEDA{\bullet}3H_2O_{trimer}$. Atom colors: Ni = green; F = yellow; O = red; N = blue, C = grey, H = white, dashed red lines = hydrogen bonds (bond lengths are in Å).

Table A.5: Selected geometrical parameters of Ni(fod)$_2$TMEDA and its hydrated analogues Ni(fod)$_2$TMEDA•nH$_2$O (n = 1, 2, 3). Atom labels correspond to those reported in Figure A.10.

Ni(fod)$_2$TMEDA						
Bond length (Å)	**No water**	**+ 1 H$_2$O**	**+ 2 H$_2$O**	**+ dimer**	**+ 3 H$_2$O**	**+ trimer**
Ni-O1	2.039	2.120	2.143	2.055	2.136	2.052
Ni-O4	2.039	2.058	2.143	2.142	2.162	2.119
Ni-O2	2.028	2.032	2.031	2.031	2.033	2.028
Ni-O3	2.028	2.029	2.031	2.030	2.028	2.026
Ni-N1	2.171	2.152	2.140	2.151	2.136	2.153
Ni-N2	2.171	2.160	2.140	2.144	2.133	2.150
O1-C5	1.260	1.269	1.267	1.258	1.266	1.259
O2-C7	1.256	1.253	1.254	1.258	1.255	1.257
O4-C6	1.260	1.258	1.267	1.271	1.268	1.268
O3-C8	1.256	1.257	1.254	1.252	1.253	1.254
C5-CF1	1.551	1.553	1.555	1.551	1.554	1.551
C5-CH1	1.390	1.386	1.387	1.392	1.387	1.391
C7-CH1	1.425	1.427	1.425	1.423	1.425	1.424
C6-CF2	1.551	1.551	1.555	1.554	1.555	1.553
C6-CH2	1.390	1.391	1.387	1.385	1.386	1.388
C8-CH2	1.425	1.424	1.425	1.428	1.426	1.426
H-Bond (Å)						
O1-H$_{w1}$		1.943	2.017	-	-	-
O4-H$_{w1}$		-	-	1.940	2.014	2.210
O4-H$_{w2}$		-	2.017	-	-	-
O1-H$_{w2}$		-	-	-	2.013	-
F- H$_{w1}$		-	-	-	-	2.247
O$_{w1}$-H$_{w2}$		-	-	1.875	-	-
O$_{w1}$-H$_{w3}$		-	-	-	1.874	1.915
O$_{w2}$-H'$_{w1}$		-	-	-	-	1.823
H$_{w2}$-O$_{w3}$		-	-	-	-	1.915
Bond angles (°)						
O1-Ni-O4	178.1	172.5	170.4	172.8	170.8	173.9
O1-Ni-O2	88.9	87.1	87.4	88.6	87.5	88.8
N1-Ni-N2	84.6	84.9	85.2	85.3	85.7	85.2
O2-Ni-O3	90.0	88.4	88.2	88.4	87.9	88.8
O2-Ni-N1	92.7	93.5	93.3	93.1	93.3	93.1
O1-Ni-N1	92.4	95.0	93.2	91.6	93.3	91.5

A.2.2.2.4 Ni(thd)$_2$TMEDA•nH$_2$O

The optimized geometries of complex **3** in dry conditions and after the interaction with *n* = 1, 2, and 3 water molecules are shown in Figure A.11, while the corresponding geometric parameters are summarized in Table A.6. Unlike the previous cases, involving F-containing complexes **1** and **2**, no hydrogen bonds are formed between water molecules and ligands' atoms in Ni(thd)$_2$TMEDA. This outcome could be attributed to the presence of four bulky tert-butyl groups on the β-diketonate ligands bonded to the Ni centre, which sterically hinder the

access of H_2O molecules in the proximity of diketonate oxygen atoms. Nonetheless, water molecules are still present in Ni second coordination shell and interact *via* a proton with the thd diketonate π-structure. These weaker interactions may still play a role in modulating the precursor's overall geometry and reactivity.

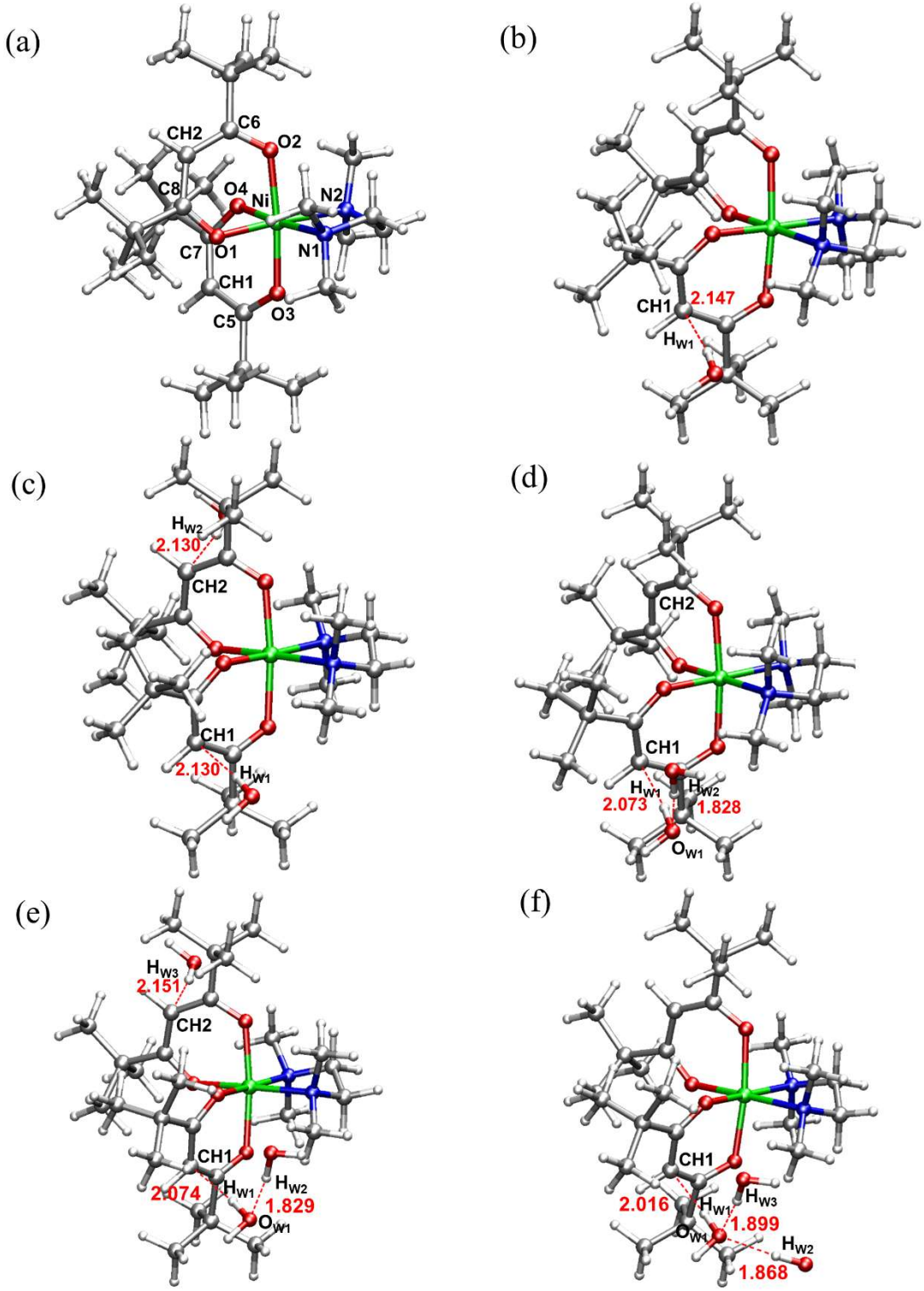

Figure A.11: Graphical representation of the DFT-computed minimum energy structures of: (a) $Ni(thd)_2TMEDA$; (b) $Ni(thd)_2TMEDA{\bullet}H_2O$; (c) $Ni(thd)_2TMEDA{\bullet}2H_2O$; (d) $Ni(thd)_2TMEDA{\bullet}2H_2O_{dimer}$; (e) $Ni(thd)_2TMEDA{\bullet}3H_2O$; (f) $Ni(thd)_2TMEDA{\bullet}3H_2O_{trimer}$. Atom colors: Ni = green; F = yellow; O = red; N = blue, C = grey, H = white, dashed red lines = hydrogen bonds (bond lengths are in Å).

Table A.6: Selected geometrical parameters of Ni(thd)$_2$TMEDA and its hydrated analogues Ni(thd)$_2$TMEDA•nH$_2$O (n = 1, 2, 3). Atom labels correspond to those reported in Figure A.11.

Ni(thd)$_2$TMEDA						
Bond length (Å)	**No water**	**+ 1 H$_2$O**	**+ 2 H$_2$O**	**+ dimer**	**+ 3 H$_2$O**	**+ trimer**
Ni-O3	2.026	2.029	2.027	2.030	2.026	2.048
Ni-O2	2.026	2.025	2.027	2.022	2.028	2.022
Ni-O4	2.016	2.020	2.020	2.020	2.021	2.023
Ni-O1	2.016	2.017	2.020	2.015	2.020	2.016
Ni-N1	2.182	2.175	2.170	2.184	2.169	2.180
Ni-N2	2.182	2.177	2.170	2.175	2.178	2.166
O3-C5	1.286	1.263	1.263	1.265	1.263	1.265
O4-C7	1.263	1.259	1.259	1.254	1.259	1.252
O2-C6	1.268	1.268	1.263	1.267	1.265	1.267
O1-C8	1.263	1.264	1.259	1.263	1.254	1.264
C5-CH1	1.409	1.415	1.415	1.412	1.416	1.413
C7-CH1	1.413	1.418	1.418	1.427	1.418	1.429
C6-CH2	1.409	1.409	1.415	1.410	1.412	1.411
C8-CH2	1.413	1.413	1.418	1.413	1.427	1.412
H-Bond (Å)						
CH1-H_{w1}		2.147	2.130	2.073	2.074	2.016
CH2-H_{w2}		-	2.130	-	-	-
CH2-H_{w3}		-	-	-	2.151	-
O_{w1}-H_{w2}		-	-	1.828	1.829	1.868
O_{w1}-H_{w3}		-	-	-	-	1.899
Bond Angles (°)						
O3-Ni-O2	174.8	174.4	174.0	174.0	173.7	173.0
O3-Ni-O4	88.9	88.9	89.0	88.9	88.9	88.3
N1-Ni-N2	84.4	84.3	84.5	84.1	84.4	84.2
O4-Ni-O1	93.3	92.6	91.8	93.8	92.9	93.8
O4-Ni-N2	91.4	91.6	91.9	90.6	91.7	90.2
O3-Ni-N1	90.2	93.5	90.7	93.6	93.5	94.2

A.2.2.3 Theoretical IR Analysis

As for the non-hydrated precursors (see Section A.2.1.3), all IR spectra were convoluted using a Gaussian function with a full width at half maximum of 2 cm^{-1}. A scaling factor of 0.952 was applied to the calculated vibrational frequencies, consistent with previous literature [100,101] and in accordance with the procedure adopted in Section A.2.1.3. The computed IR spectra (harmonic frequencies) of the hydrated precursors **1-3** are shown in Figures A.12-A.14, while the wavenumbers of the normal modes mainly localized on Ni-O bonds, calculated for both the dry and symmetrically di-hydrated complexes, are summarized in Tables A.7-A.9.

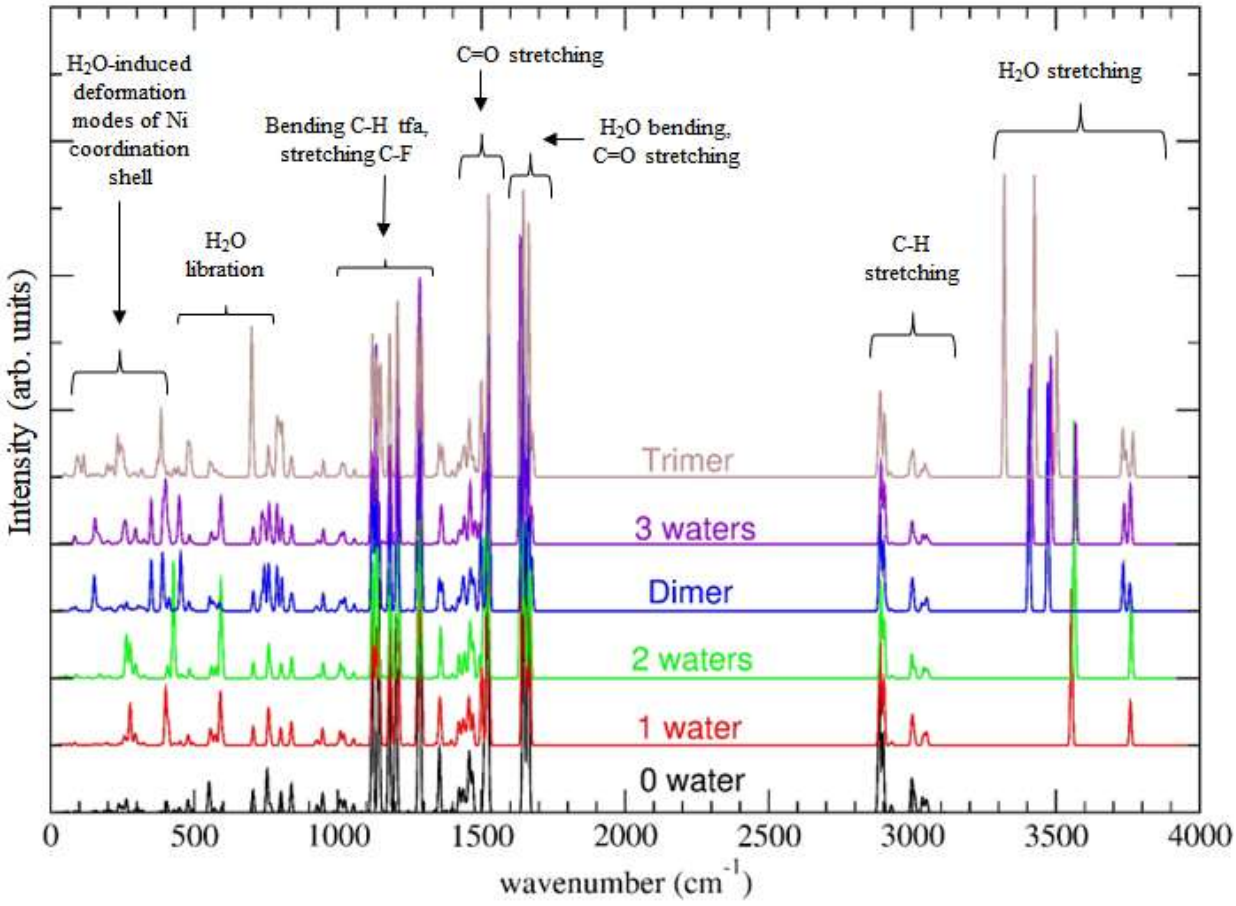

Figure A.12: DFT-computed IR spectra of: $Ni(tfa)_2TMEDA$; $Ni(tfa)_2TMEDA{\bullet}H_2O$; $Ni(tfa)_2TMEDA{\bullet}2H_2O$; $Ni(tfa)_2TMEDA{\bullet}2H_2O_{dimer}$; $Ni(tfa)_2TMEDA{\bullet}3H_2O$; $Ni(tfa)_2TMEDA{\bullet}3H_2O_{trimer}$.

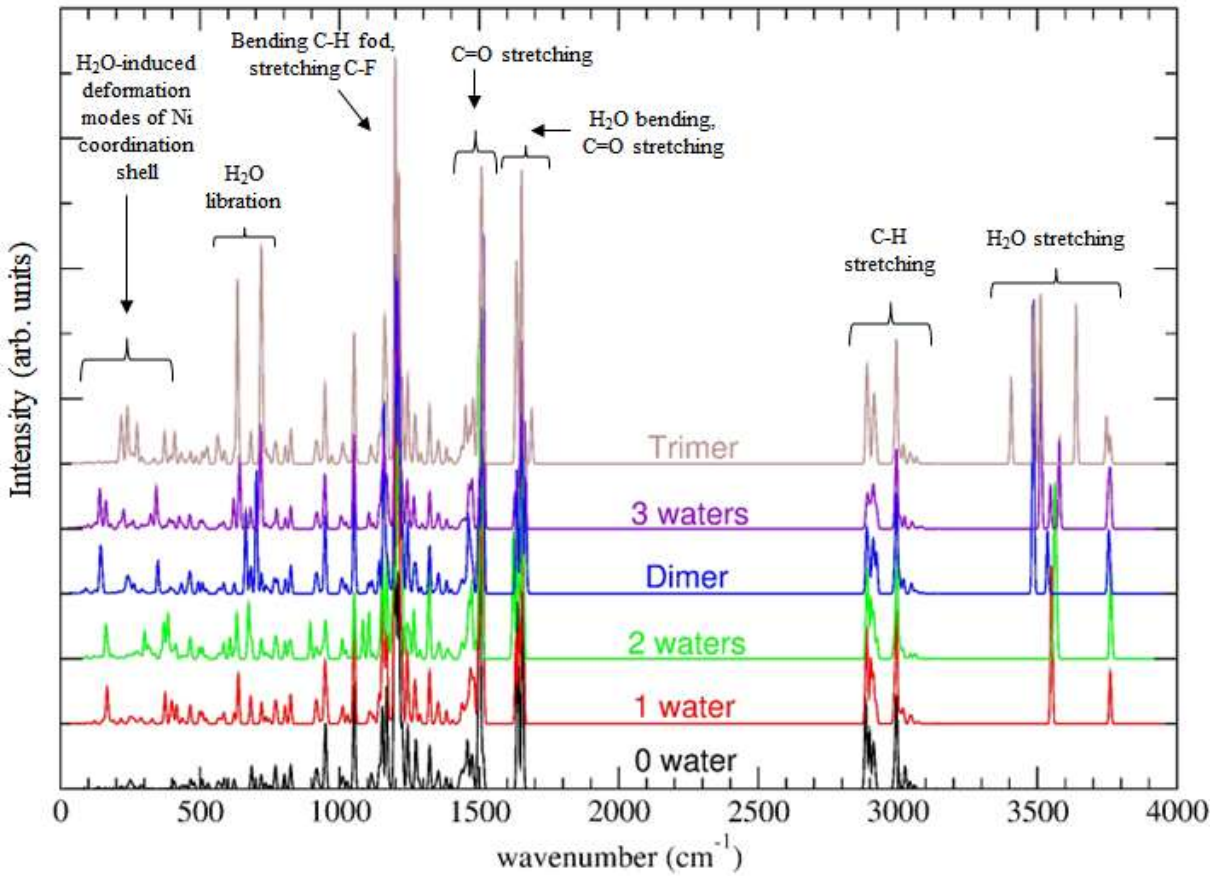

Figure A.13: DFT-computed IR spectra of: $Ni(fod)_2TMEDA$; $Ni(fod)_2TMEDA•H_2O$; $Ni(fod)_2TMEDA•2H_2O$; $Ni(fod)_2TMEDA•2H_2O_{dimer}$; $Ni(fod)_2TMEDA•3H_2O$; $Ni(fod)_2TMEDA•3H_2O_{trimer}$.

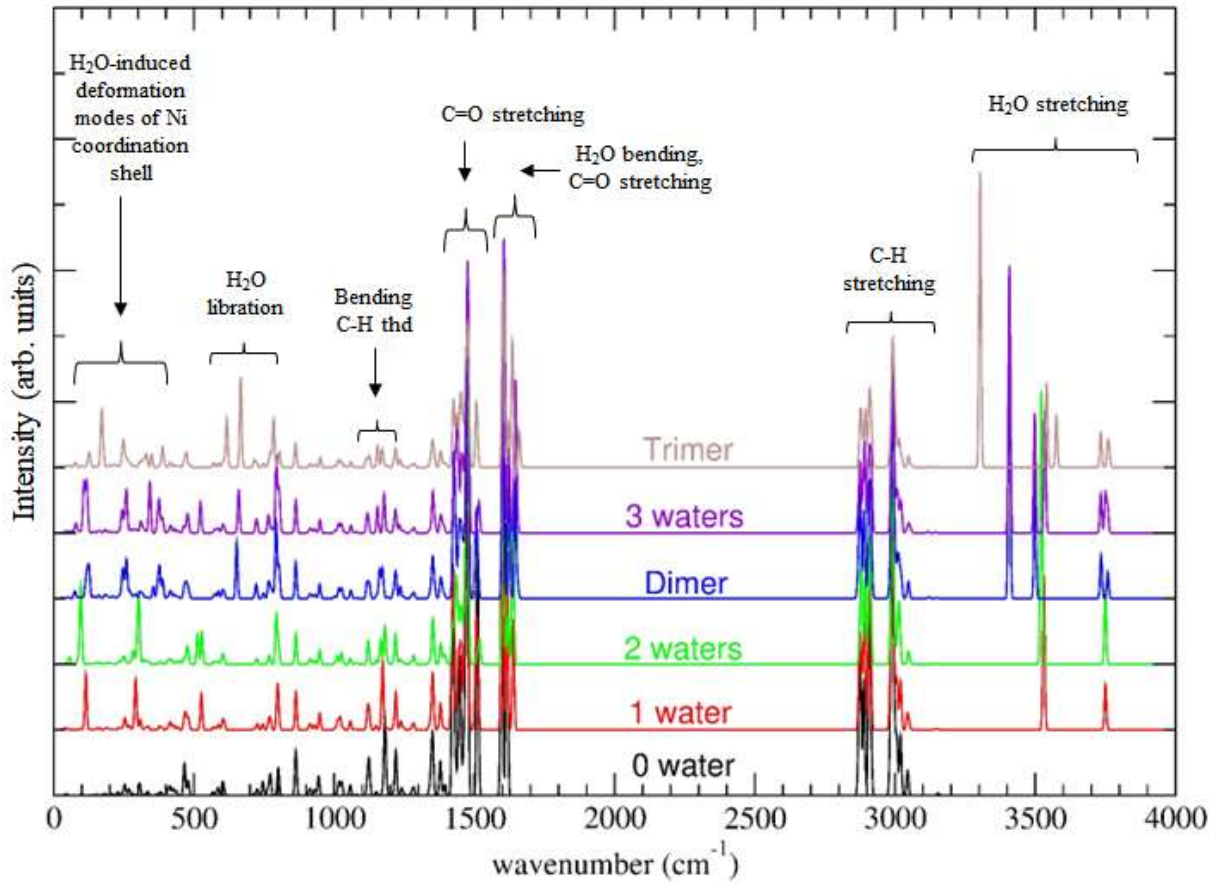

Figure A.14: DFT-computed IR spectra of: $Ni(thd)_2TMEDA$; $Ni(thd)_2TMEDA•H_2O$; $Ni(thd)_2TMEDA•2H_2O$; $Ni(thd)_2TMEDA•2H_2O_{dimer}$; $Ni(thd)_2TMEDA•3H_2O$; $Ni(thd)_2TMEDA•3H_2O_{trimer}$.

Table A.7: Calculated wavenumbers $\tilde{\upsilon}$ (cm^{-1}) for stretching modes mainly localized on Ni-O bonds in $Ni(tfa)_2TMEDA$ and $Ni(tfa)_2TMEDA \cdot 2H_2O$. Atom labels as in Figure A.12.

$Ni(tfa)_2TMEDA$	**mode**	**$Ni(tfa)_2TMEDA \bullet 2H_2O$**
581	Collective symmetric stretching (all Ni-O bonds)	587
578	Collective asymmetric stretching (all Ni-O bonds)	588
503	Asymmetric stretching of the apical Ni-O1 and Ni-O4 bonds	488
488	Symmetric stretching of the apical Ni-O1 and Ni-O4 bonds	481
337	Asymmetric stretching of the equatorial Ni-O2, Ni-O3 bonds	343
334	Symmetric stretching of the equatorial Ni-O2, Ni-O3 bonds	342

Table A.8: Calculated wavenumbers $\tilde{\upsilon}$ (cm^{-1}) for stretching modes mainly localized on Ni-O bonds in $Ni(fod)_2TMEDA$ and $Ni(fod)_2TMEDA \cdot 2H_2O$. Atom labels as in Figure A.13.

$Ni(fod)_2TMEDA$	**mode**	**$Ni(fod)_2TMEDA \bullet 2H_2O$**
618	symmetric stretching of the equatorial Ni-O2, Ni-O3 bonds	616
615	asymmetric stretching of the equatorial Ni-O2, Ni-O3 bonds	613
556	asymmetric stretching of the apical Ni-O1 and Ni-O4 bonds	544
554	symmetric stretching of the apical Ni-O1 and Ni-O4 bonds	544

Table A.9: Calculated wavenumbers $\tilde{\upsilon}$ (cm^{-1}) for stretching modes mainly localized on Ni-O bonds in $Ni(thd)_2TMEDA$ and $Ni(thd)_2TMEDA \cdot 2H_2O$. Atom labels as in Figure A.14.

$Ni(thd)_2TMEDA$	**mode**	**$Ni(thd)_2TMEDA \cdot 2H_2O$**
637	Collective symmetric stretching (localized on all Ni-O bonds)	637
632	Collective asymmetric stretching (localized on all Ni-O bonds)	632
615	Collective asymmetric stretching (localized on all Ni-O bonds)	617
607	Collective asymmetric stretching (localized on all Ni-O bonds)	609
508	Collective symmetric stretching (localized on all Ni-O bonds)	508
503	Collective asymmetric stretching (localized on all Ni-O bonds)	501
435	Collective asymmetric stretching Ni-O bonds (mainly localized on the apical Ni-O2, Ni-O3 bonds)	435
433	Collective symmetric stretching (mainly localized on the equatorial Ni-O1, Ni-O4 bonds)	433
429	Collective asymmetric stretching (mainly localized on the equatorial Ni-O1, Ni-O4 bonds)	428
423	symmetric stretching of the apical Ni-O2, Ni-O3 bonds	424

Although the frequency variations observed in Ni-O stretching modes upon hydration may appear modest when considered alone, they should not be interpreted as evidence of a negligible water effect. Indeed, when considered with the computed W_{BE} values (see Table 5), the structural distortions in the metal coordination sphere, and the low-frequency vibrational modes, these findings might support an interesting role of H_2O in modulating the stability and decomposition behavior of the investigated complexes, in agreement with the experimentally observed increase in NiO thin film thickness under humid conditions [51].

Supplementary Information Paragraph 2.3

A.2.3.1 Computational Details

Density functional theory (DFT) calculations were performed on [Ni(L)$_2$TMEDA] (with L = tfa, fod, thd) and related fragments. Specifically, the M06 hybrid meta-functional by Zhao and Truhlar was selected [102], using the Gaussian 09 code [93]. This functional was chosen for its capability to provide a good description of both the molecular and electronic structures of several [M(L)$_2$TMEDA] family complexes (M = Fe, Co, Cu, Zn) [41], including the detailed fragmentation behavior of [Cu(hfa)$_2$TMEDA] in ESI-MS experiments [49]. For nickel, an "energy-adjusted" ab initio pseudopotential was employed in conjunction with the (8s7p6d2f1g)/[6s5p3d2f1g] basis set [96]. All the other atoms were treated adopting the D95(d) basis set, except for Na, for which the 6-31G(d) set was employed [96]. All the computed optimized structures were characterized by no imaginary frequencies. Reported energy differences were calculated by including the zero-point-energy (ZPE) correction. Additionally, all fragments discussed in Section 2.3.1 of the main text were subjected to structural optimization.

In electrospray ionization/mass spectrometry, ions are ejected from charged solvent droplets through successive desolvation steps in the ion source region, such that only gas-phase ions reach the analyzer [103,104]. For this reason, all the ions observed and described in Paragraph 2.3 should be considered non-solvated. Consequently, solvation effects were not included in the DFT calculations. Bonding properties were theoretically investigated through Natural Bond Orbitals (NBOs) analysis [105]. Specifically, the NBO charges on Ni, β-diketonate ligand L, and TMEDA reported in Table 8 of the main text, bond order values (Tables 7 and 9), quantitative NBO data (Tables A.10, A.13, A.14), and graphical representations of natural bond orbitals (Figures A.15-A.17, A.21-A.23, A.24, A.25), were all obtained using the same DFT functional and basis sets employed for the geometry optimizations. The NBO analysis was performed by employing the NBO code (Version 3.1) available in Gaussian 09. Bond order values were calculated according to the Wiberg scheme [106]. Atomic charges reported in Tables A.15-A.18 were computed using the Bader approach [92,93]. As with the NBO analysis, Bader charges were also calculated using the same level of theory as adopted in the structural optimizations.

A.2.3.2 Structural and Electronic Features of [M-L]$^+$ Fragments

This Section presents a table reporting the results of the Natural Bond Orbital (NBO) analysis for the [Ni(L)TMEDA]$^+$ fragments, along with a graphical representation of their bonding NBOs.

Table A.10: NBO analysis for [Ni(L)TMEDA]$^+$ species, where L = tfa, fod, thd. The table reports the NBO type, the atoms on which NBOs are localized, the NBO occupancy, and the localization (%) of NBOs on the involved atoms. BD = bonding character; BD* = anti-bonding character; X = O or N. Atoms labels as in Figure 6 in the main text.

Fragment	NBO type	Bond	Occupancy	% Ni	% X
Ni(tfa)TMEDA$^+$					
	BD (σ)	*Ni-O2*	1.909	11	89
	BD (σ)	*Ni-O1*	1.904	11	89
	BD (σ)	*Ni-N1*	1.866	12	88
	BD (σ)	*Ni-N2*	1.868	12	88
	BD* (σ)	*Ni-O2*	0.100	89	11
	BD* (σ)	*Ni-O1*	0.102	89	11
	BD* (σ)	*Ni-N1*	0.128	88	12
	BD* (σ)	*Ni-N2*	0.128	88	12
Ni(fod)TMEDA$^+$					
	BD (σ)	*Ni-O2*	1.903	11	89
	BD (σ)	*Ni-O1*	1.897	11	89
	BD (σ)	*Ni-N1*	1.861	11	89
	BD (σ)	*Ni-N2*	1.863	11	89
	BD* (σ)	*Ni-O2*	0.111	89	11
	BD* (σ)	*Ni-O1*	0.112	89	11
	BD* (σ)	*Ni-N1*	0.132	89	11
	BD* (σ)	*Ni-N2*	0.133	89	11
Ni(thd)TMEDA$^+$					
	BD (σ)	*Ni-O2*	1.896	11	89
	BD (σ)	*Ni-O1*	1.896	11	89
	BD (σ)	*Ni-N1*	1.866	10	90
	BD (σ)	*Ni-N2*	1.866	10	90
	BD* (σ)	*Ni-O2*	0.110	89	11
	BD* (σ)	*Ni-O1*	0.110	89	11
	BD* (σ)	*Ni-N1*	0.137	90	10
	BD* (σ)	*Ni-N2*	0.137	90	10

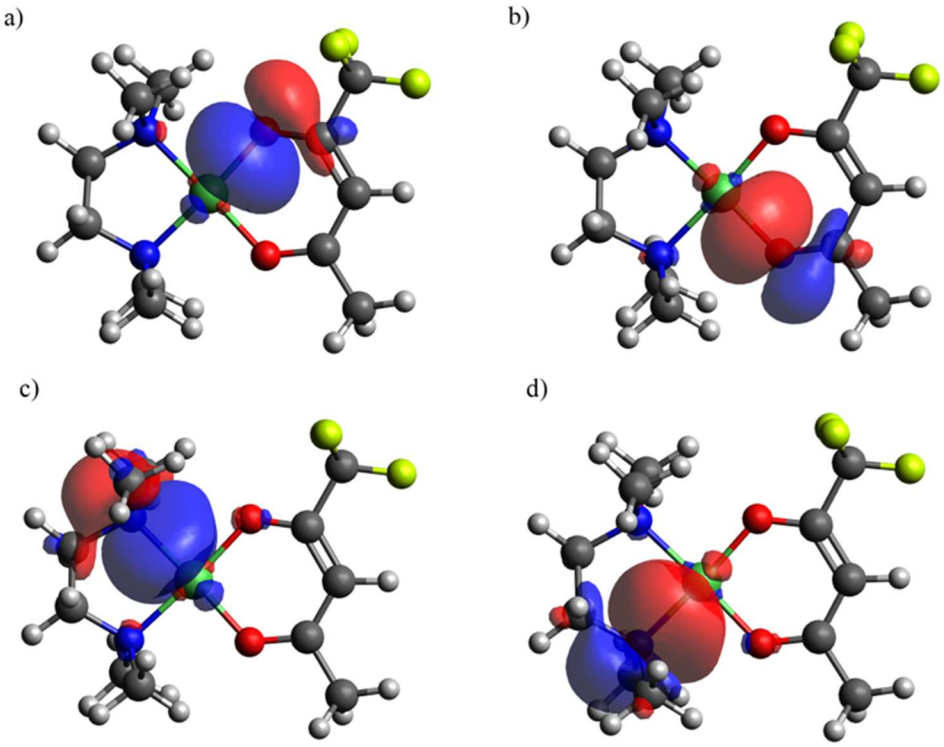

Figure A.15: Graphical representation of natural bond orbitals of $[Ni(tfa)TMEDA]^+$ localized on the following bonds: a) Ni-O1 (BD); b) Ni-O2 (BD); c) Ni-N1 (BD); d) Ni-N2 (BD) (see also Table A.10). Atom color codes: green = Ni; yellow = F; blue = N; red = O; grey = C; white = H.

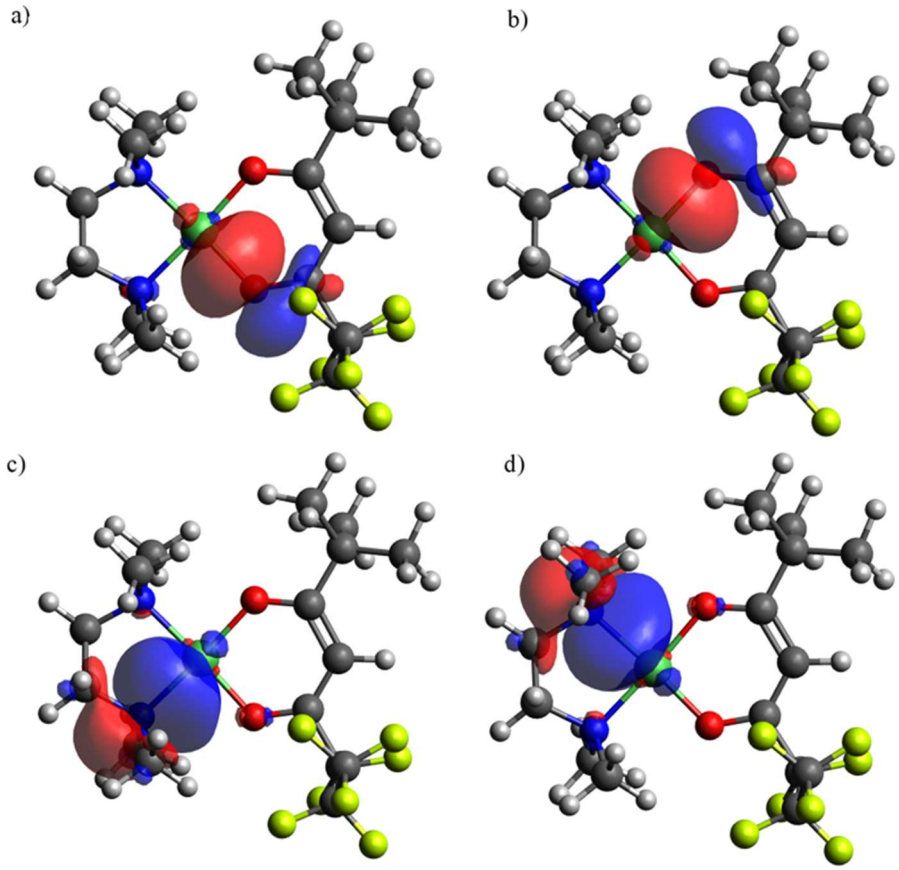

Figure A.16: Graphical representation of natural bond orbitals of $[Ni(fod)TMEDA]^+$ localized on the following bonds: a) Ni-O1 (BD); b) Ni-O2 (BD); c) Ni-N1 (BD); d) Ni-N2 (BD) (see also Table A.10). Atom color codes: green = Ni; blue = N; red = O; grey = C; white = H.

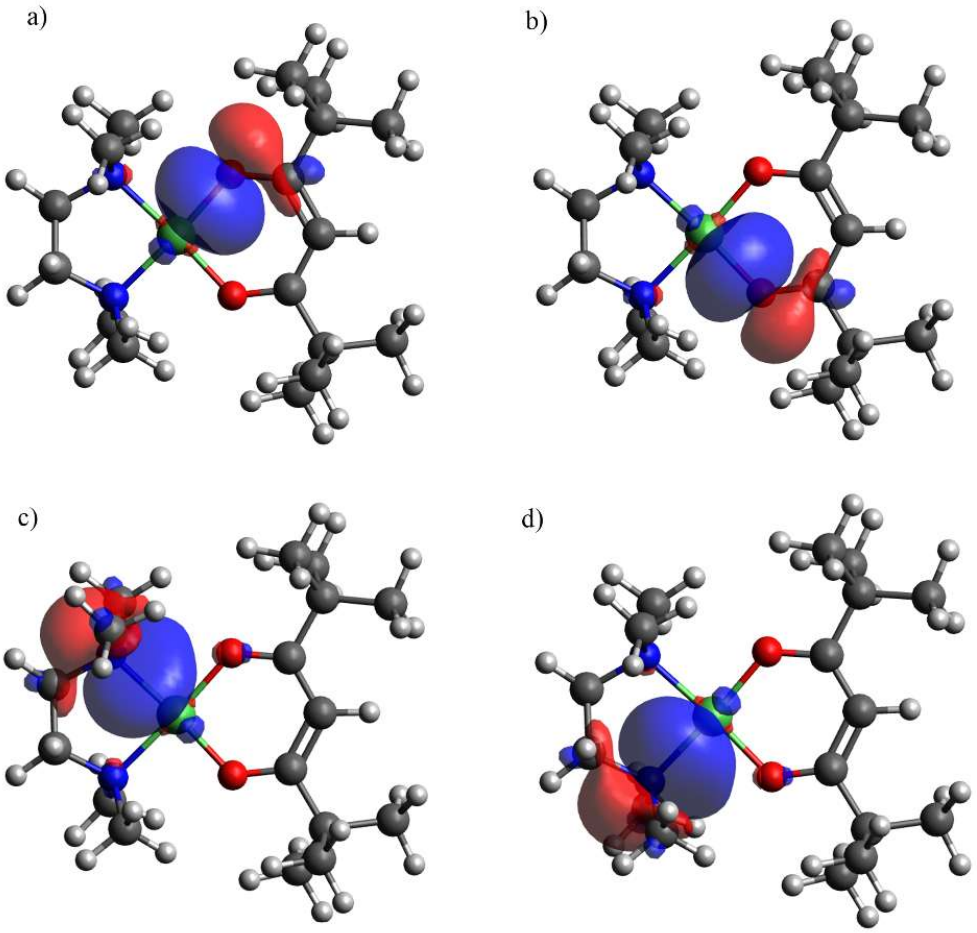

Figure A.17: Graphical representation of natural bond orbitals of $[Ni(thd)TMEDA]^+$ localized on the following bonds: a) Ni-O1 (BD); b) Ni-O2 (BD); c) Ni-N1 (BD); d) Ni-N2 (BD) (see also Table A.10). Atom color codes: green = Ni; blue = N; red = O; grey = C; white = H.

A.2.3.3 Modeling of Low-Abundance Cationic Species in ESI-HRMS spectra: Sodium Adducts and Protonated Species

In addition to the main peak common to the three complexes, ESI-HRMS spectra presented in Section 2.3.1 (main text) also revealed the formation of additional cationic species (see Figure 4 and Table 6), for which a thorough computational search of minimum energy structures was also conducted. Once again, it is worth highlighting that the computational analysis performed in this study plays a key role in predicting the molecular structures of these species, including those of lower abundance, thus providing valuable insights into the fragmentation reaction of these NiO precursors. Graphical representations of the optimized geometries of sodium adducts, namely $[M+Na]^+$ and $[M\text{-}TMEDA+Na]^+$, are shown in Figure A.18, whereas selected geometrical parameters are summarized in Table A.11.

It is worth noting that Na^+ is present exclusively in the ESI-HRMS spectra of compound **2**, which features the highest fluorine content among the series. In $[M+Na]^+$, the Ni center retains its octahedral coordination environment despite the incorporation of Na^+ into the second coordination shell (Figure A.18a). Notably, three oxygen atoms are located at coordination distances from Na^+ (average Na-O distance = 2.416 Å), which also interacts with a fluorine atom (Na-F distance = 2.441 Å). This results in a distortion of the Ni octahedral environment,

as evidenced by the elongation of both Ni-O and Ni-N bonds compared to the neutral $Ni(fod)_2TMEDA$. The effect is particularly relevant for the bonds involving the three oxygen atoms also coordinated with Na^+ (Table A.11). A similar trend is observed for the $[M\text{-}TMEDA+Na]^+$ ion, which features a distorted square-planar Ni coordination and exhibits significant $O\text{-}Na^+$ and $F\text{-}Na^+$ interactions (Table A.11, Figure A.18b). Although experimental evidence has linked the formation of sodium adducts to the presence of fluorine atoms [59], in this case located in the $CF_2CF_2CF_3$ moieties of the β-diketonates, the DFT-computed $O\text{-}Na^+$ and $F\text{-}Na^+$ distances for the two aforementioned species suggest that, in these systems, oxygen atoms play a more crucial role in adduct formation than fluorine. In both cases, $O\text{-}Na^+$ distances are shorter than $F\text{-}Na^+$ ones, indicating stronger interactions with oxygen.

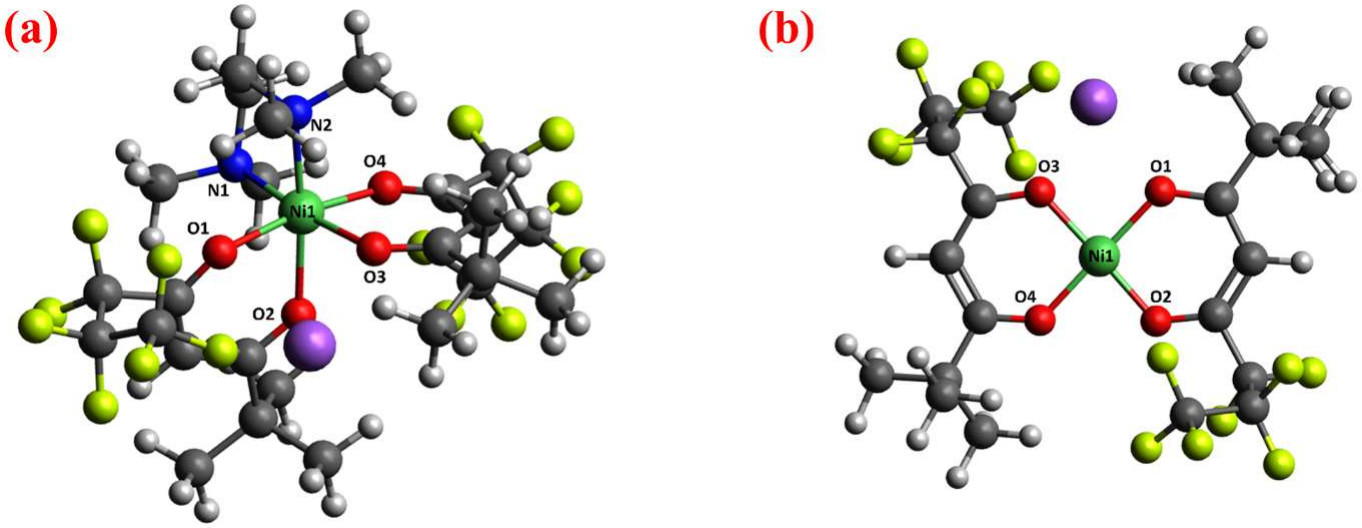

Figure A.18: DFT-computed minimum energy structures of: (a) $[M+Na]^+ = [Ni(fod)_2TMEDA+Na]^+$, (triplet state) and (b) $[M\text{-}TMEDA+Na]^+ = [Ni(fod)_2+Na]^+$, obtained by loss of TMEDA and addition of Na^+ from complex **2**. Atom color codes: purple = Na; green = Ni; yellow = F; blue = N; red = O; grey = C; white = H.

Table A.11: Ni-O and Ni-N bond distances for the species shown in Figure 23, namely: (a) $[M+Na]^+ = [Ni(fod)_2TMEDA+Na]^+$, (triplet state) and (b) $[M\text{-}TMEDA+Na]^+ = [Ni(fod)_2+Na]^+$, derived from complex **2** by TMEDA loss and Na^+ addition.

Bond Lenghts (Å)	$[M+Na]^+$	$[M\text{-}TMEDA+Na]^+$
Ni-O1	2.080	1.876
Ni-O2	2.112	1.822
Ni-O3	2.098	1.847
Ni-O4	1.989	1.837
Ni-N1	2.152	-
Ni-N2	2.126	-
Na-O1	2.502	2.389
Na-O2	2.532	-
Na-O3	2.215	2.240
Na-F	2.441	2.542; 2.470

In contrast, $[M\text{-}TMEDA+H]^+$ species was experimentally detected exclusively for compound **3**. This ion, identified as $[Ni(thd)_2+H]^+$, is protonated at the CH1 carbon of the diketonate backbone, suggesting a preferential site for protonation likely stabilized by the adjacent carbonyl groups. For this species, two nearly isoenergetic structures were identified ($\Delta E = 0.32$ kcal/mol), as shown in Figure A.19a and A.19b. The most stable conformer exhibits a distorted tetrahedral arrangement around the Ni center and a triplet spin multiplicity. On the other hand, the less stable structure displays a square-planar Ni coordination geometry and a singlet spin multiplicity. Key geometrical parameters for both structures are reported in Table A.12. Given the small energy difference between the two forms, it is plausible that both structures may coexist and be formed during the ESI process.

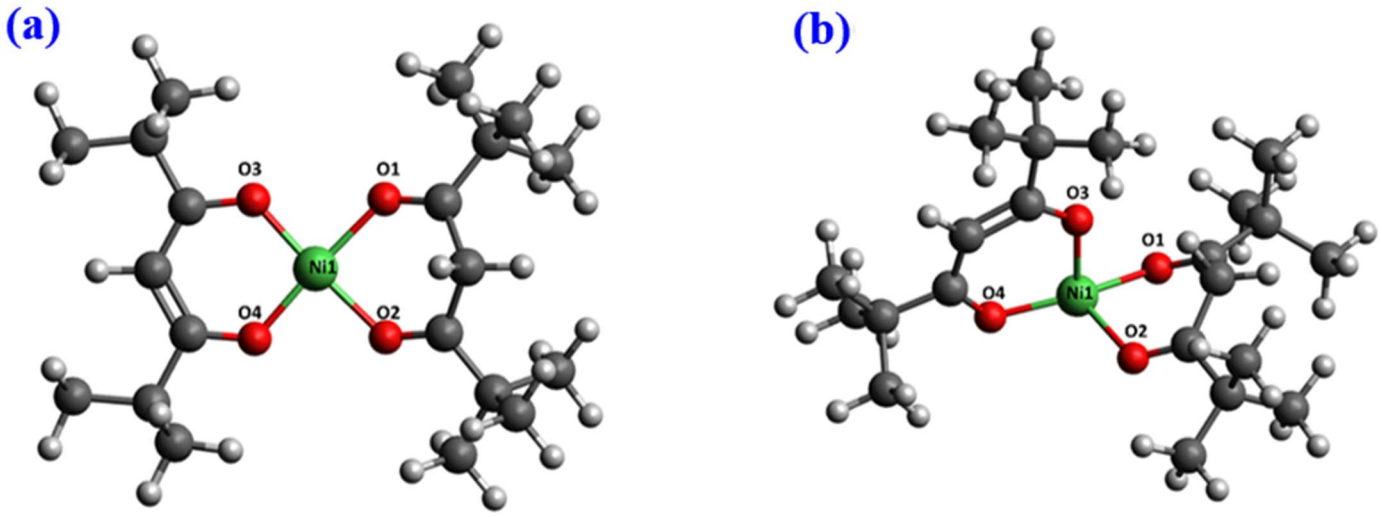

Figure A.19: DFT-computed minimum energy structures of $[M\text{-}TMEDA+H]^+ = [Ni(thd)_2+H]^+$: a) pseudo-planar geometry (singlet state) and b) distorted tetrahedral geometry (triplet state). The second one is 0.32 kcal×mol^{-1} lower in energy with respect to (a). Atom color codes: green = Ni; red = O; grey = C; white = H.

Table A.12: Ni-O and Ni-N bond distances for the species shown in Figure A.19, namely: $[M\text{-}TMEDA+H]^+ = [Ni(thd)_2+H]^+$ a) pseudo-planar geometry (singlet state) and b) distorted tetrahedral geometry (triplet state), derived from complex **3** by TMEDA loss and H^+ addition.

Bond Lenghts (Å)	$[M\text{-}TMEDA+H]^+$	$[M\text{-}TMEDA+H]^+$
Ni-O1	1.897	1.986
Ni-O2	1.897	1.981
Ni-O3	1.793	1.901
Ni-O4	1.793	1.842
Ni-N1	-	-
Ni-N2	-	-

The protonated diketonate species $[HL+H]^+$ was detected exclusively in the case of the more electron-donor thd ligand. Its optimized structure reveals protonation on both carbonyl groups (Figure A.20a). In contrast, the protonated ligand $[TMEDA+H]^+$ was observed in the fragmentation of all complexes; in this case, the proton is located on one of the N atoms of the TMEDA moiety (Figure A.20b).

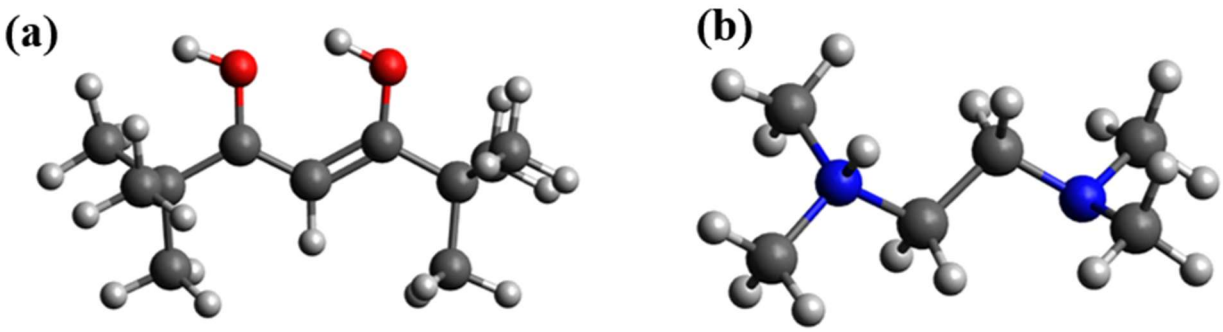

Figure A.20: DFT-computed minimum energy structures of a) $[HL+H]^+$ = $[thd+H]^+$ obtained by addition of H^+ to thd ligand; b) $[TMEDA+H]^+$ obtained by addition of H^+ to neutral TMEDA. Color codes blue = N; red = O; grey = C; white = H.

A.2.3.4 Electronic Features of MS²-Derived Species

This Section presents the NBO analysis results and related orbital graphical representations for the species formed upon subsequent fragmentation of the $[Ni(L)TMEDA]^+$ cations.

Table A.13: Natural bond orbital (NBO) analysis for $[Ni(L)TMEDA]^+$-$NH(CH_3)_2$ species, where L = tfa, fod, thd. The table reports the NBO type, the atoms on which NBOs are localized, the NBO occupancy, and the localization (%) of NBOs on the involved atoms. BD = bonding character; BD* = anti-bonding character; LP = lone-pair; Y = Ni or CHT; X = N1 or CH2T. Atoms labels as in Figure 7 of the main text.

Fragment	NBO type	Bond	Occupancy	% Y	% X
Ni(tfa)TMEDA⁺ -NH(CH₃)₂					
	BD (π)	*CHT-CH2T*	1.985	52	48
	BD (π)	*CHT-CH2T*	1.663	49	51
	BD (σ)	*Ni-N1*	1.878	26	74
	BD* (π)	*CHT-CH2T*	0.011	48	52
	BD* (π)	*CHT-CH2T*	0.187	51	49
	BD* (σ)	*Ni-N1*	0.527	74	26
Ni(fod)TMEDA⁺ -NH(CH₃)₂					
	BD (π)	*CHT-CH2T*	1.981	52	48
	LP (π)	*CH2T*	0.959	-	-
	BD (σ)	*CHT-N1*	1.749	22	78
	BD* (π)	*CHT-CH2T*	0.010	48	52
	BD* (σ)	*CHT-N1*	0.676	78	22
Ni(thd)TMEDA⁺ -NH(CH₃)₂					
	BD (π)	*CHT-CH2T*	1.985	52	48
	BD (π)	*CHT-CH2T*	1.691	49	51
	BD (σ)	*Ni-N1*	1.871	24	76
	BD* (π)	*CHT-CH2T*	0.011	48	52
	BD* (π)	*CHT-CH2T*	0.198	51	49
	BD* (σ)	*Ni-N1*	0.548	76	24

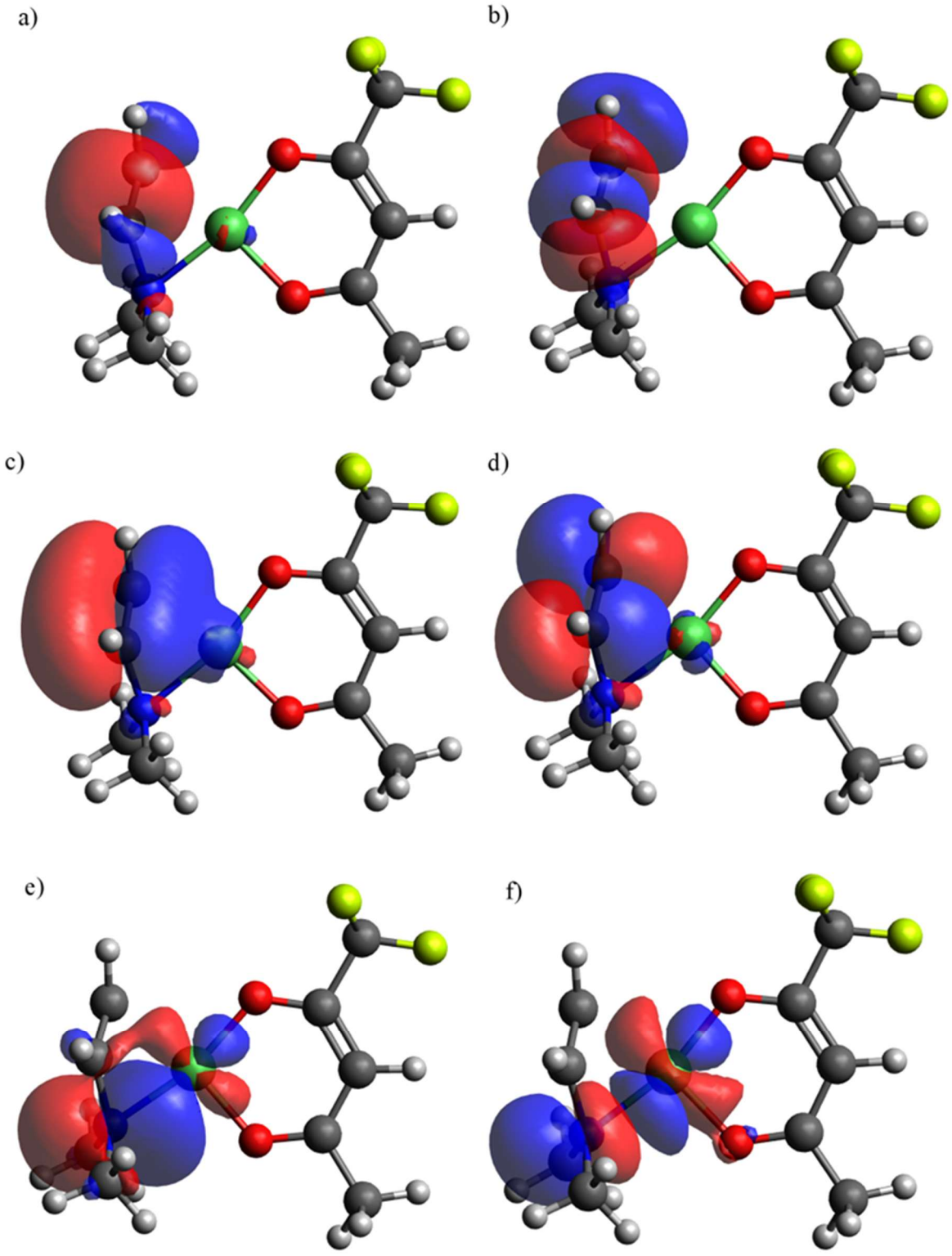

Figure A.21: Graphical representation of natural bond orbitals of $[Ni(tfa)TMEDA]^{+}$-$NH(CH_3)_2$ localized on the following bonds: a) CHT-CH2T (BD); b) CHT-CH2T (BD*); c) CHT-CH2T (BD); d) CHT-CH2T (BD*); e) Ni-N1 (BD); f) Ni-N1 (BD*) (see also Table A.13). Atom color codes: green = Ni; yellow = F; blue = N; red = O; grey = C; white = H.

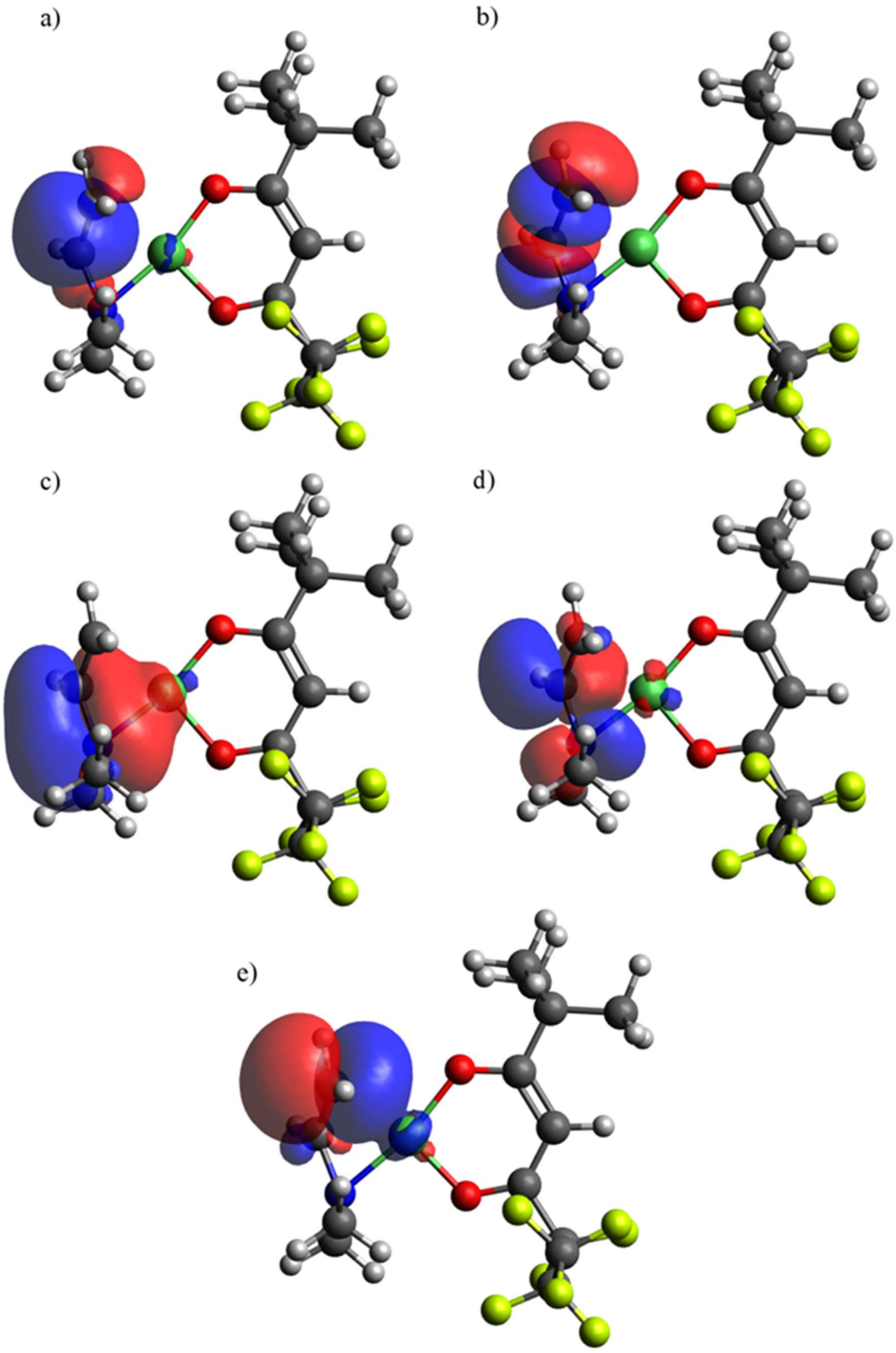

Figure A.22: Graphical representation of natural bond orbitals of $[Ni(fod)TMEDA]^{+}$-$NH(CH_3)_2$ localized on the following bonds: a) CHT-CH2T (BD); b) CHT-CH2T (BD*); c) Ni-N1 (BD); d) Ni-N1 (BD*); e) CH2T (LP) (see also Table A.13). Atom color codes: green = Ni; yellow = F; blue = N; red = O; grey = C; white = H.

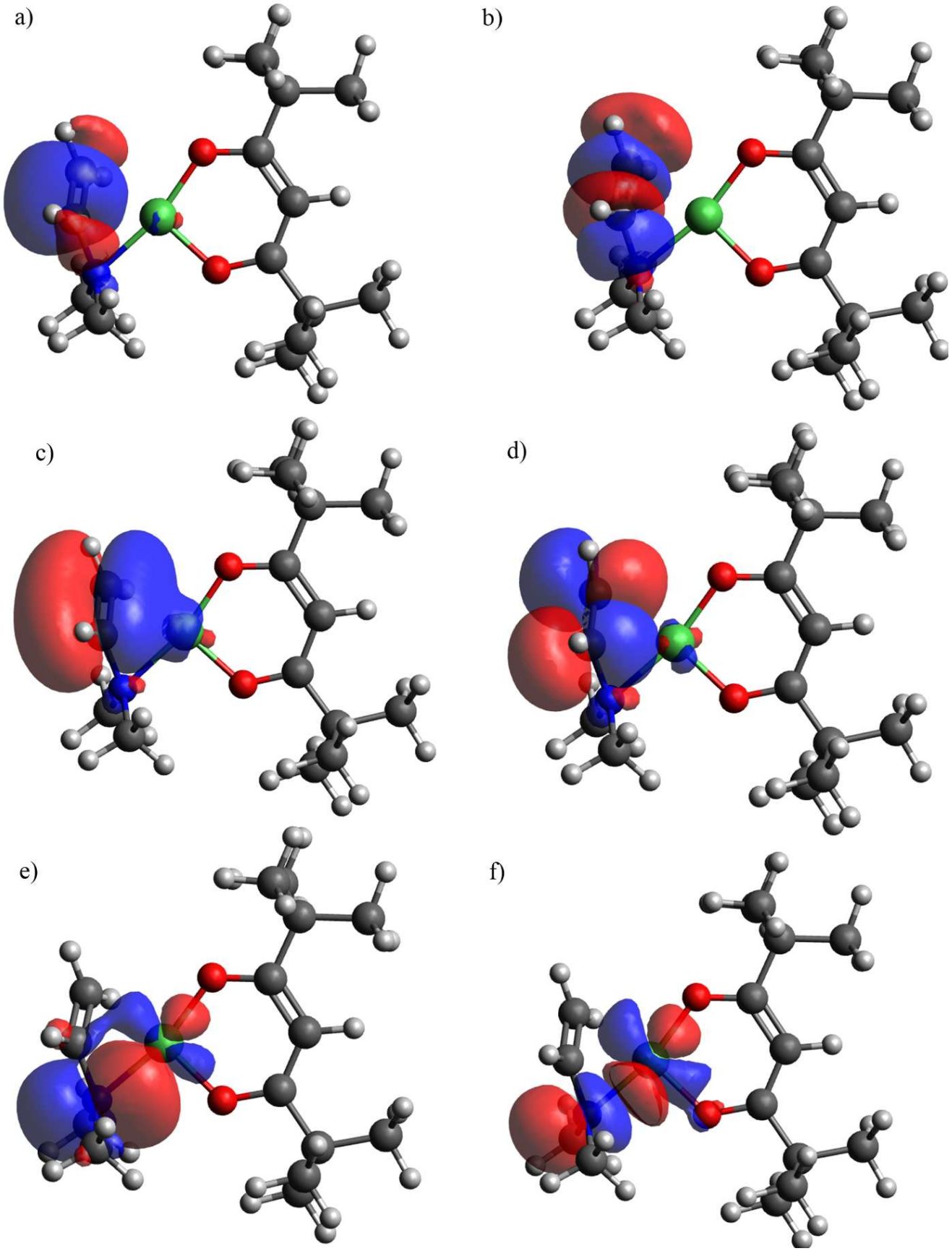

Figure A.23: Graphical representation of natural bond orbitals of $[Ni(thd)TMEDA]^{+}$-$NH(CH_3)_2$ localized on the following bonds: a) CHT-CH2T (BD); b) CHT-CH2T (BD*); c) CHT-CH2T (BD); d) CHT-CH2T (BD*); e) Ni-N1 (BD); f) Ni-N1 (BD*) (see also Table A.13). Atom color codes: green = Ni; blue = N; red = O; grey = C; white = H.

Table A.14: Natural bond orbital (NBO) analysis for $[Ni(L)TMEDA]^{+}$-$CH_3CH_2N(CH_3)_2$, where L = tfa and fod. The table reports the NBO type, the atoms on which NBOs are localized, the NBO occupancy, and the localization (%) of NBOs on the involved atoms. BD = bonding; BD* = anti-bonding; LP = lone-pair; Y = Ni or CHT; X = N1 or CH2T. Atoms labels as in Figure 7 of the main text.

Fragment	NBO type	Bond	Occupancy	% Y	% X
Ni(tfa)TMEDA^{+} -$CH_3CH_2N(CH_3)_2$					
	BD (π)	*CHT-CH2T*	1.987	52	48
	LP (π)	*CHT*	0.916	-	-
	LP (π)	*CH2T*	0.914	-	-
	BD (σ)	*Ni-N1*	1.836	14	86
	BD* (π)	*CHT-CH2T*	0.010	48	52
	BD* (σ)	*Ni-N1*	0.197	86	14
Ni(fod)TMEDA^{+} - $CH_3CH_2N(CH_3)_2$					
	BD (π)	*CHT-CH2T*	1.987	52	48
	LP (π)	*CHT*	0.920	-	-
	LP (π)	*CH2T*	0.914	-	-
	BD (σ)	*Ni-N1*	1.838	14	86
	BD* (π)	*CHT-CH2T*	0.010	48	52
	BD* (σ)	*Ni-N1*	0.197	86	14

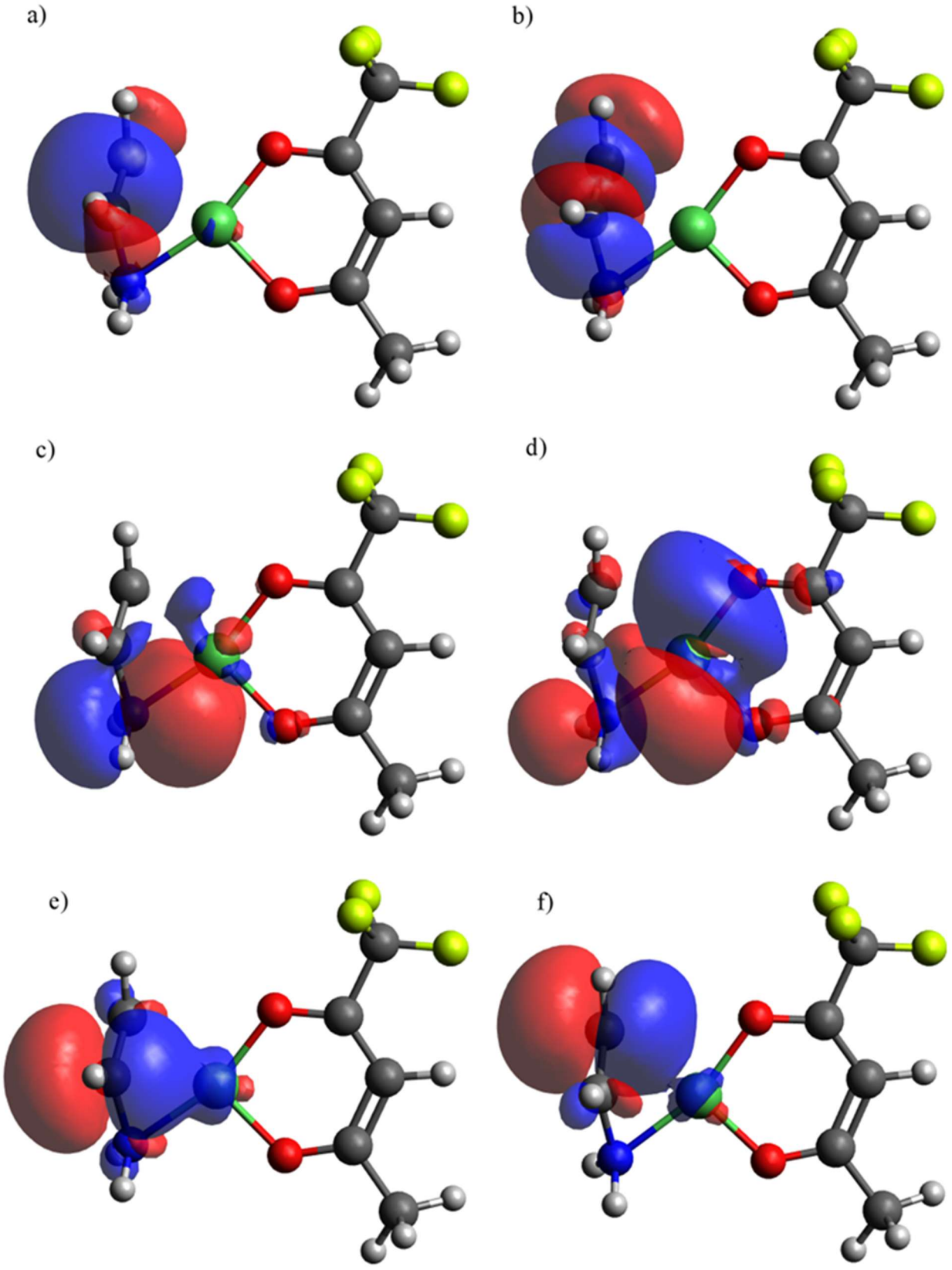

Figure A.24: Graphical representation of natural bond orbitals of $[Ni(tfa)TMEDA]^{+}$-$CH_3CH_2N(CH_3)_2$ localized on the following bonds: a) CHT-CH2T (BD); b) CHT-CH2T (BD*); c) Ni-N1 (BD); d) Ni-N1 (BD*); e) CHT (LP); f) CH2T (LP) (see also Table A.14). Atom color codes: green = Ni; yellow = F; blue = N; red = O; grey = C; white = H.

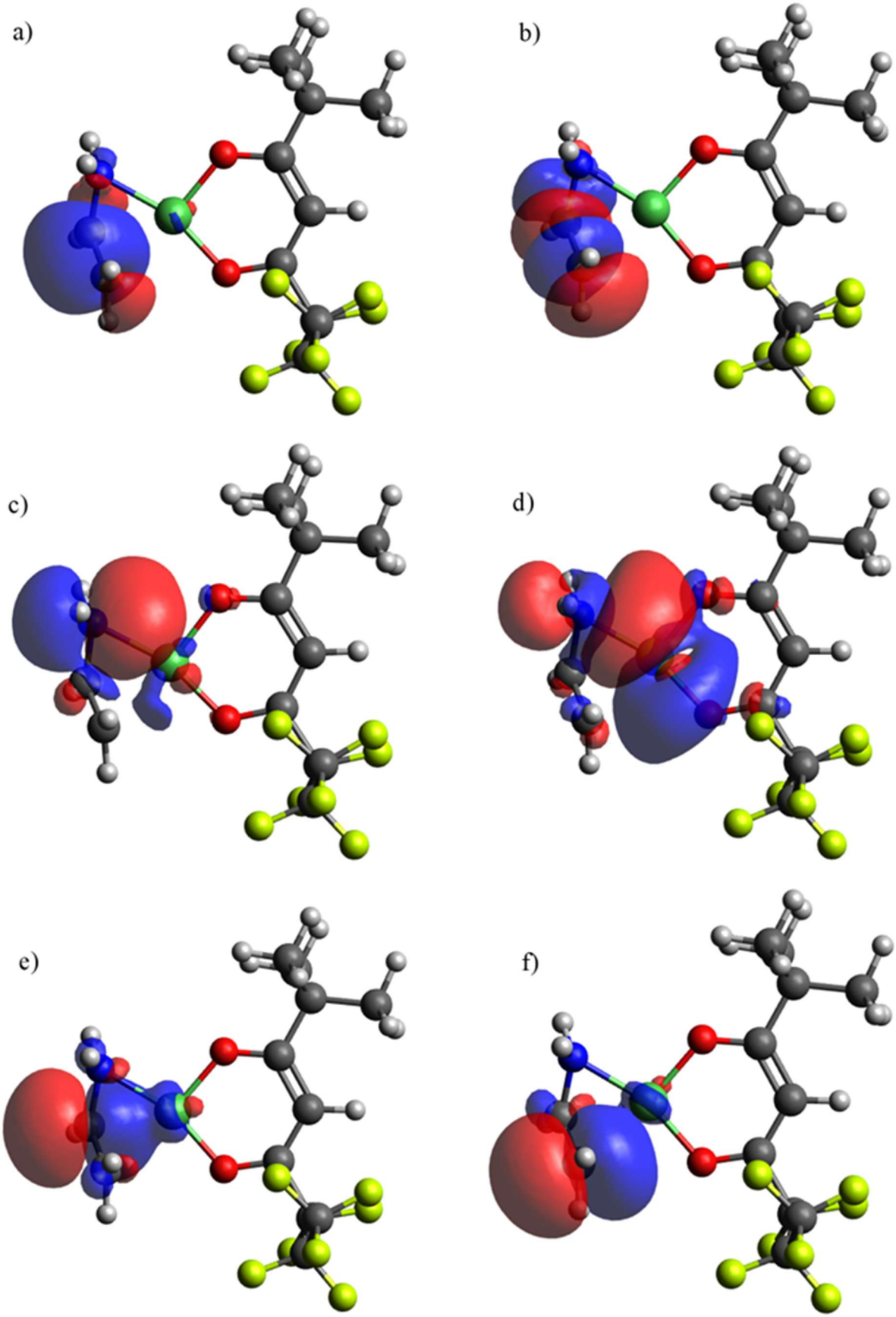

Figure A.25: Graphical representation of natural bond orbitals of $[Ni(fod)TMEDA]^{+}$-$CH_3CH_2N(CH_3)_2$ localized on the following bonds: a) CHT-CH2T (BD); b) CHT-CH2T (BD*); c) Ni-N1 (BD); d) Ni-N1 (BD*); e) CHT (LP); f) CH2T (LP) (see also Table A.14). Atom color codes: green = Ni; yellow = F; blue = N; red = O; grey = C; white = H.

In addition to the electronic structure analysis, geometry optimizations were carried out for selected isomers of the [Ni(fod)TMEDA]$^+$-$(CH_3)_2C{=}CH_2$) fragment (see Paragraph 2.3.3 of the main text). Figure A.26 shows the six most stable structures, along with their relative stability, including zero-point energy corrections. The lowest-energy isomer (Figure A.26a) features a distribution of fluorine atoms on both sides of the diketonate ligand, a characteristic also shared by other low-energy isomers, which differ only slightly in energy from the most stable one.

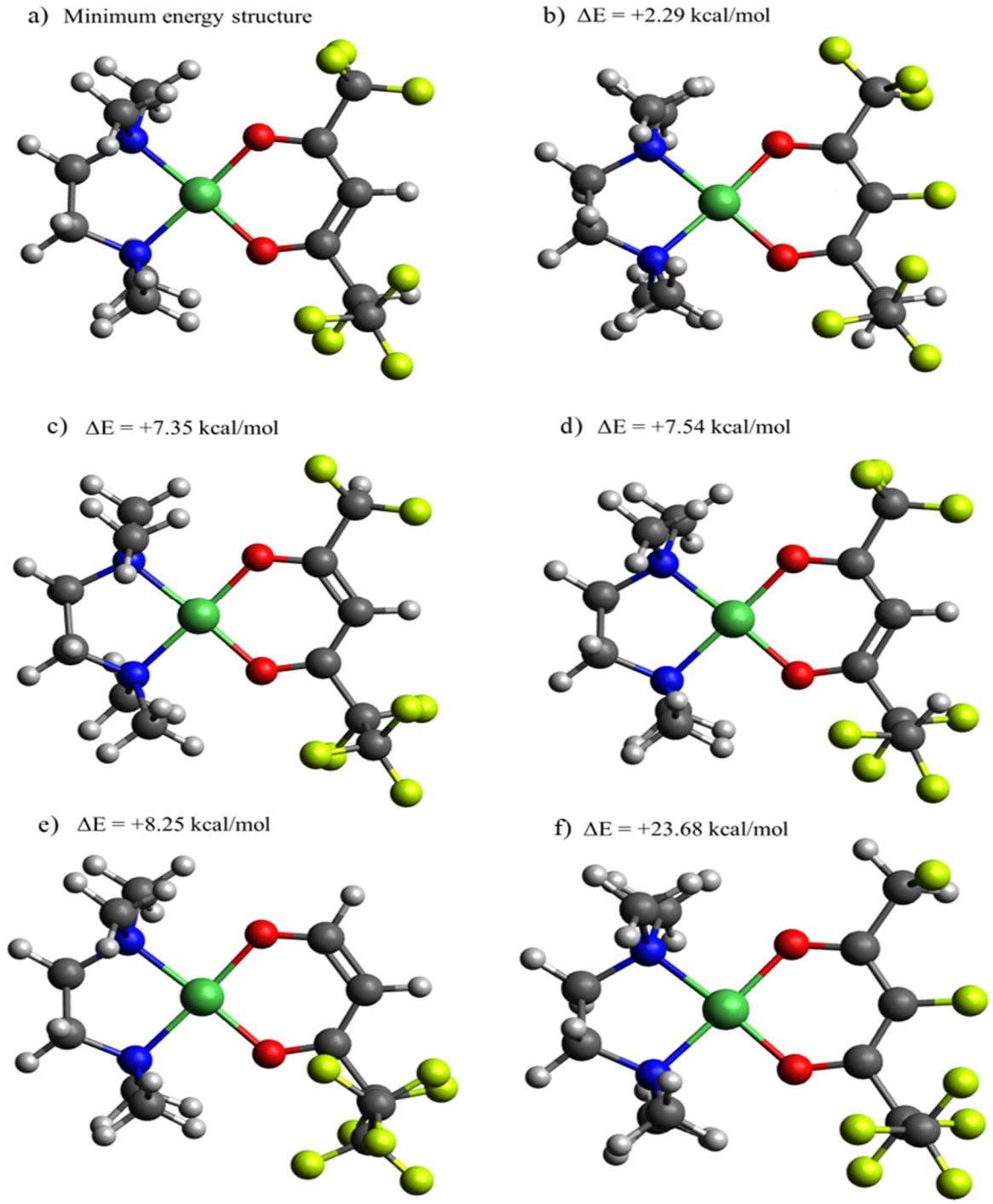

Figure A.26: Graphical representation of six possible structures of the fragment ion [Ni(fod)TMEDA]$^+$-$(CH_3)_2C{=}CH_2$, resulting from an additional rearrangement of fod ligand and detected in MS^2 spectra of precursor **2**. Relative energies (with respect to the minimum-energy structure, **a**) are reported above each model geometry. Atom color codes: green = Ni; yellow = F; blue = N; red = O; grey = C; white = H.

A.2.3.5 Bader Charge Analysis

Bader charge analysis offers a robust method for partitioning the electron density of a molecule into atomic contributions based on rigorous quantum mechanical principles [60,61]. Unlike Mulliken [107] or Löwdin [108] population analyses, which depend heavily on the basis set and orbital representation, the Bader approach relies exclusively on the topology of the electron density, providing a more physically meaningful and transferable definition of atomic regions [60,61]. In this model, each atom is defined by a zero-flux surface, i.e., a surface across which the gradient of the electron density vector field does not cross, ensuring that electron density is uniquely assigned to each atom [61]. This makes Bader analysis particularly well-suited for studying systems undergoing fragmentation, where a clear and basis-independent picture of electron redistribution is essential. In fact, previous studies have demonstrated that Bader charges are particularly informative in describing subtle shifts in electronic structure during processes such as ligand dissociation or ion formation [109,110]. For this reason, Bader analysis has been applied in the present work to further clarify how the electronic density is redistributed during the gas-phase fragmentation of Ni(II) β-diketonate-TMEDA complexes. Bader charges of all three species are reported in Tables A.15-A.18.

Table A.15: Computed Bader charges for [Ni(L)$_2$TMEDA], with L = tfa, fod, and thd. Atom labels as in Figure 6.

Atom	**Ni(tfa)$_2$TMEDA**	**Ni(fod)$_2$TMEDA**	**Ni(thd)$_2$TMEDA**
Ni	+1.33	+1.33	+1.33
O1	-1.19	-1.18	-1.21
O2	-1.20	-1.19	-1.21
O3	-1.20	-1.20	-1.19
O4	-1.19	-1.18	-1.21
N1	-1.03	-1.03	-1.04
N2	-1.05	-1.05	-1.04
C5	+0.81	+0.81	+0.78
C6	+0.82	+0.77	+0.77
C7	+0.86	+0.84	+0.78
C8	+0.86	+0.85	+0.78
CH1	-0.01	-0.03	-0.07
CH2	-0.03	0.00	-0.05
CHT	+0.27	+0.25	+0.28
CH2T	+0.31	+0.28	+0.28

Table A.16: Computed Bader charges for [Ni(L)TMEDA]$^+$, with L = tfa, fod, and thd. Atom labels as in Figure 6.

Atom	[Ni(tfa)TMEDA]$^+$	[Ni(fod)TMEDA]$^+$	[Ni(thd)TMEDA]$^+$
Ni	+0.99	+1.00	+1.00
O1	-1.14	-1.16	-1.16
O2	-1.14	-1.17	-1.17
N1	-1.03	-1.01	-1.01
N2	-1.01	-1.03	-1.03
C5	+0.71	+0.67	+0.67
C7	+0.72	+0.65	+0.65
CH1	+0.10	+0.08	+0.08
CHT	+0.28	+0.27	+0.27
CH2T	+0.28	+0.27	+0.27

Table A.17: Computed Bader charges for [Ni(L)TMEDA]$^+$ -$NH(CH_3)_2$, where L = tfa, fod, thd. Atom labels as in Figure 7. N denotes the nitrogen atom coordinated to the Ni center.

Atom	[Ni(tfa)TMEDA]$^+$ -$NH(CH_3)_2$	[Ni(fod)TMEDA]$^+$ -$NH(CH_3)_2$	[Ni(thd)TMEDA]$^+$ -$NH(CH_3)_2$
Ni	+0.95	+0.95	+0.95
O1	-1.12	-1.13	-1.13
O2	-1.17	-1.12	-1.12
N	-1.09	-1.10	-1.10
C5	+0.70	+0.67	+0.67
C7	+0.72	+0.71	+0.71
CH1	+0.09	+0.09	+0.09
CHT	+0.22	+0.21	+0.21
CH2T	-0.05	-0.08	-0.08

Table A.18: Computed Bader charges for [Ni(L)TMEDA]$^+$ - $CH_3CH_2N(CH_3)_2$, where L = tfa, fod, and for [Ni(fod)TMEDA]$^+$-$(CH_3)_2C{=}CH_2$. Atom labels as in Figure 7. In each case, N denotes the nitrogen atom(s) coordinated to the Ni center (for [Ni(fod)TMEDA]$^+$-$(CH_3)_2C{=}CH_2$, both N atoms are bound to Ni and bear identical Bader charges).

Atom	[Ni(tfa)TMEDA]$^+$ -$CH_3CH_2N(CH_3)_2$	[Ni(fod)TMEDA]$^+$ -$CH_3CH_2N(CH_3)_2$	[Ni(fod)TMEDA]$^+$ -$(CH_3)_2C{=}CH_2$
Ni	+0.97	+0.97	+1.00
O1	-1.11	-1.09	-1.12
O2	-1.12	-1.13	-1.14
N	-1.15	-1.14	-1.01
C5	+0.68	+0.68	+0.76
C7	+0.72	+0.69	+0.77
CH1	+0.09	+0.08	+0.07
CHT	+0.21	+0.19	+0.27
CH2T	-0.06	-0.05	+0.24

Supplementary Information Paragraph 2.4

A.2.4.1 Computational Details and Structural Models

With the aim of providing a clear and comprehensive overview of the computational methodology, this Section outlines the NiO models constructed and investigated in the present Paragraph. A very concise description of the employed structural models is presented here, while a detailed analysis of their structural and electronic features will be provided in the following Sections. Readers are therefore referred to those Sections whenever specific models introduced here are subsequently discussed in greater depth.

All calculations on bulk NiO, as well as on regular (stoichiometric) and -OH-defective NiO(100) surfaces, were performed using the Quantum ESPRESSO code. [111] Structural optimizations were carried out employing the spin polarized PBE approximation to DFT [112] in conjunction with D3-bj [113] empirical correction to dispersion interactions, a setup known to yield a reliable description of metal oxide structural properties. [37,45,113] In contrast, the electronic structure calculations for obtaining electronic band gap values were performed, on the optimized structures, using the Hubbard Hamiltonian approach. The latter offers effective strategies to correct the well-known tendency of Gradient Corrected DFT approximations (GGA) to severely underestimate band gaps in transition metal oxides. Specifically, the DFT + U method was adopted, in which the DFT total energy is augmented by a local Hubbard correction, defined by the on-site Coulomb interaction U. In this work, the simplest version of this approach was adopted, involving the addition of a U term to the Hamiltonian [114]. The selected value of the U term of 6.4 eV is in line with literature data [86]. The interactions between valence electrons and cores were treated using the Vanderbilt type ultra-soft pseudopotentials [115,116] for Ni, O and H atoms. In the case of Ni, a semicore pseudopotential was adopted, i.e. only the 1s and 2s-2p shells were included in the core, while the 3s, 3p, 3d, and 4s electrons were pseudized. Concerning the number of valence electrons, the core charge of Ni was 18, hence the 3s, 3p, 3d, and 4s electrons of Ni are explicitly accounted for in the calculations (18 valence electrons for each Ni, $3s^2 3p^6 3d^8 4s^2$). The core charge of O was 6, thus the 2s and 2p O electrons are explicitly represented (pseudized) in the calculations (6 valence electrons for each O, $2s^2 2p^4$). Concerning H, its core charge was 1, thus the electron in the 1s state was pseudized (1 valence electron for each H, $1s^1$). In all calculations, the electronic states were expanded in planewaves with a cutoff of 60 Ry for the wavefunction (320 Ry for the electron density). In the optimization procedure, the initial spin polarizations of the two kinds of Ni were given opposite sign. Both total and absolute magnetization values were computed self-consistently, as is appropriate for magnetic oxide systems. [117-119] The electronic structure character of each system (i.e., *p*-type, *n*-type, metal, semimetal) was determined from the pertaining Density of States (DOS) by comparing the energies of the VB and CB band edges with the Fermi Level, which was conventionally set to zero [120,121].

A.2.4.2 Bulk NiO Models

As previously mentioned, bulk NiO has a cubic rock-salt structure (a = 4.173 Å) [6] (Figure A.27). The cubic crystallographic unit cell contains four Ni and four O atoms (crystallographic

unit cell stoichiometry: Ni_4O_4, 8 atoms). Due to the antiferromagnetic (AF) ordering of NiO, the magnetic unit cell parameter is twice as large as *a*, resulting in a 2×2×2 crystallographic unit cell, with magnetic unit cell stoichiometry of $Ni_{32}O_{32}$ (64 atoms, Figure A.27a). Furthermore, a tetragonal 2×2 magnetic unit cell characterized by AF ordering as well can be constructed, with magnetic unit cell stoichiometry of $Ni_{16}O_{16}$ (32 atoms, FigureA.273c-d). In this study, Density Functional Theory (DFT) calculations on bulk NiO were performed on three different models, denoted Bulk 1, Bulk 2, and Bulk 3, illustrated in Figure 33 and defined as follows:

1) Bulk 1, containing 64 atoms ($Ni_{32}O_{32}$), and characterized by a cubic simulation cell, corresponding to the cubic 2×2×2 magnetic unit cell (Figure A.27a);
2) Bulk 2, containing 128 atoms ($Ni_{64}O_{64}$), and characterized by an orthorhombic simulation cell, obtained by doubling the cubic magnetic simulation cell along the *x* direction (Figure A.27b);
3) Bulk 3, containing 32 atoms ($Ni_{16}O_{16}$), and characterized by a tetragonal simulation cell, corresponding to the tetragonal 2×2 magnetic unit cell (Figure A.27c-d).

For all bulk models, full geometry optimizations (0 K) were performed, allowing both atomic positions and cell volumes to relax at a pressure of 0 kbar. All atoms were allowed to move during the optimization.

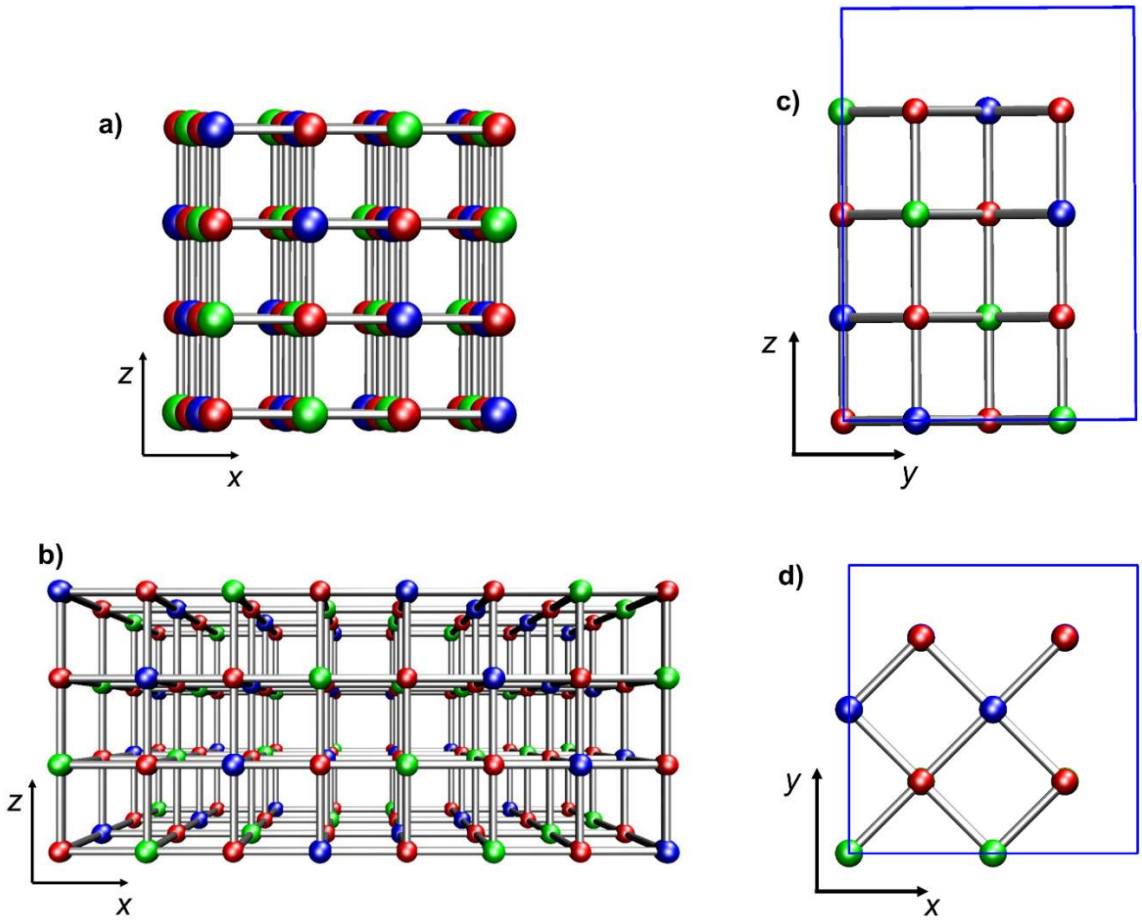

Figure A.27: Ball-and-stick representation of the bulk NiO models simulation cell: **a)** Bulk 1 ($Ni_{32}O_{32}$, cubic 2×2×2 cell) projected on the *xz* plane; **b)** Bulk 2 ($Ni_{64}O_{64}$, orthorhombic 4×2×2 cell) projected on the *xz* plane; **c)** and **d)** Bulk 3 ($Ni_{16}O_{16}$, tetragonal 2×2 cell) projected on the *yz* and *xy* planes, respectively. Atoms color codes red = O; blue = Ni (spin-up); green = Ni (spin-down). Blue lines in c)-d) indicate the simulation cell size.

The structural optimization of the three bulk models (Bulk 1-3) provided identical computed cell parameter (a = 4.175Å) and interatomic Ni-O and Ni-Ni nearest-neighbor distances, in excellent agreement with experimental values [6]. All models exhibited the same structural features and very similar electronic and magnetic properties (see Table A.19).

Table A.19: Properties of bulk models. E_{gap}: band gap energy; E_{VB}: VB top energy; E_{CB}: CB bottom energy; μ_{tot}: total magnetization; μ_{Ni}: absolute magnetization per Ni atom; d(Ni-O): Ni-O distances; d(Ni-Ni): Ni-Ni distances. Energies are given in eV, μ_{tot} and μ_N in Bohr Magnetons (μ_B), and distances in Å. E_{VB} and E_{CB} are relative to the Fermi Level, conventionally set to 0.

System	E_{gap}	E_{VB}	E_{CB}	*Type*	μ_{tot}	μ_{Ni}	*d(Ni-O)*	*d(Ni-Ni)*
Bulk 1 ($Ni_{32}O_{32}$)	3.030	-1.531	+1.679	*p*	0	1.77	2.086	2.951
Bulk 2 ($Ni_{64}O_{64}$)	3.030	-1.334	+1.696	*p*	0	1.77	2.086	2.951
Bulk 3 ($Ni_{16}O_{16}$)	2.980	-1.303	+1.677	*p*	0	1.80	2.086	2.951

Each Ni atom is surrounded by six O atoms at 2.086 Å distance. The total magnetization of the system (μ_{tot}) equals 0.00 Bohr Magnetons (μ_B), consistent with the antiferromagnetic (AF) ordering observed at the experimental level. The absolute magnetization per Ni atom (μ_{Ni}) is comparable with the reported experimental values (1.64-1.77 μ_B). [6,76] The computed E_{gap} (Table 29) is smaller than the quoted values reported in literature for bulk NiO systems (4.0-4.3 eV) [6,76,79,80,122], reflecting the well-known tendency of DFT, and even DFT+U approaches, to underestimate band gaps, [74,86,88,114] especially in NiO-based systems.[72] Nonetheless, the E_{gap}, magnetization and lattice parameters are in good agreement with the results obtained in other DFT+U studies on bulk NiO.[74] The investigated bulk systems reproduce the experimentally detected *p*-type behavior, as evidenced by the total electronic density of states (DOS) shown in Figure A.28a-c. The DOS profiles of the three bulk models are nearly identical, in agreement with their corresponding E_{gap} values (Table A.19).

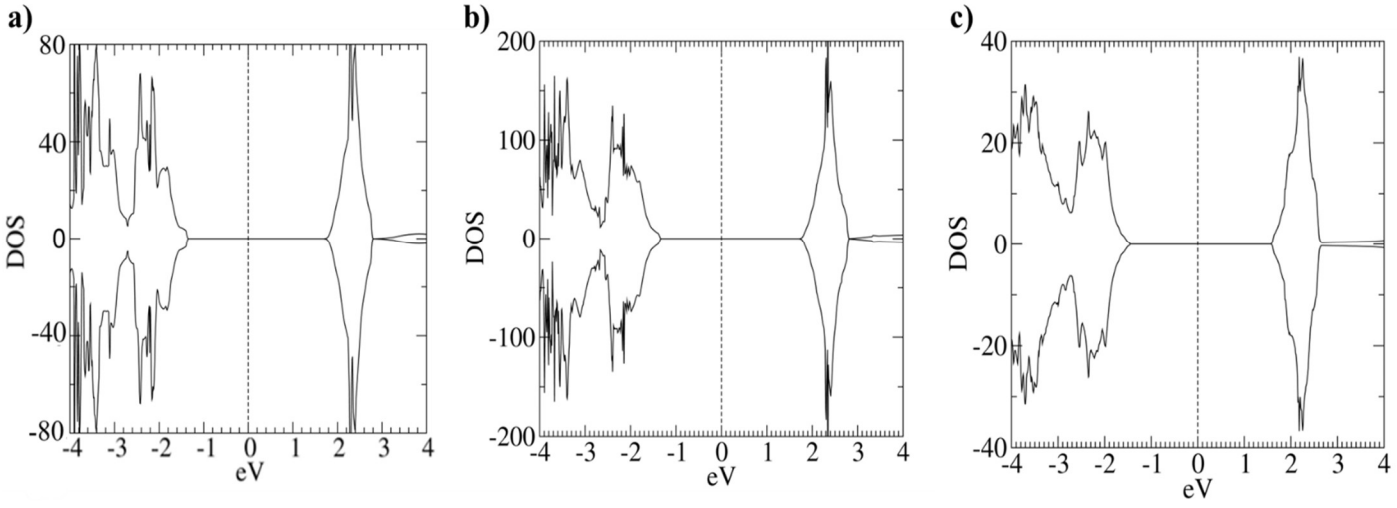

Figure A.28: Computed DOS for bulk NiO model systems: a) Bulk 1, $Ni_{32}O_{32}$; b) Bulk 2, $Ni_{64}O_{64}$; c) Bulk 3, $Ni_{16}O_{16}$. The black vertical dashed line represents the Fermi level position (0 eV). Positive and negative curves represent spin-up and spin-down components, respectively.

Given this close similarity in both total DOS and electronic properties, the partial DOS analysis was restricted to Bulk 1 and Bulk 2. A comparison of the partial density of states (pDOS) for Bulk 1 and Bulk 2 is presented in Figure A.29, confirming their close similarity. In both cases, the pDOS reveals a dominant contribution of O 2*p*-states at the top of the valence band (VB), whereas at the bottom of the conduction band (CB) there is a higher density of empty Ni *d*-states. This finding is in line with literature data on NiO materials. [6,76,79,80] Furthermore, the presence of a non-negligible contribution from occupied *d*-states at the top of the VB suggests that even *d*-*d* transitions may also play a key role in shaping the electronic properties of bulk NiO. [80]

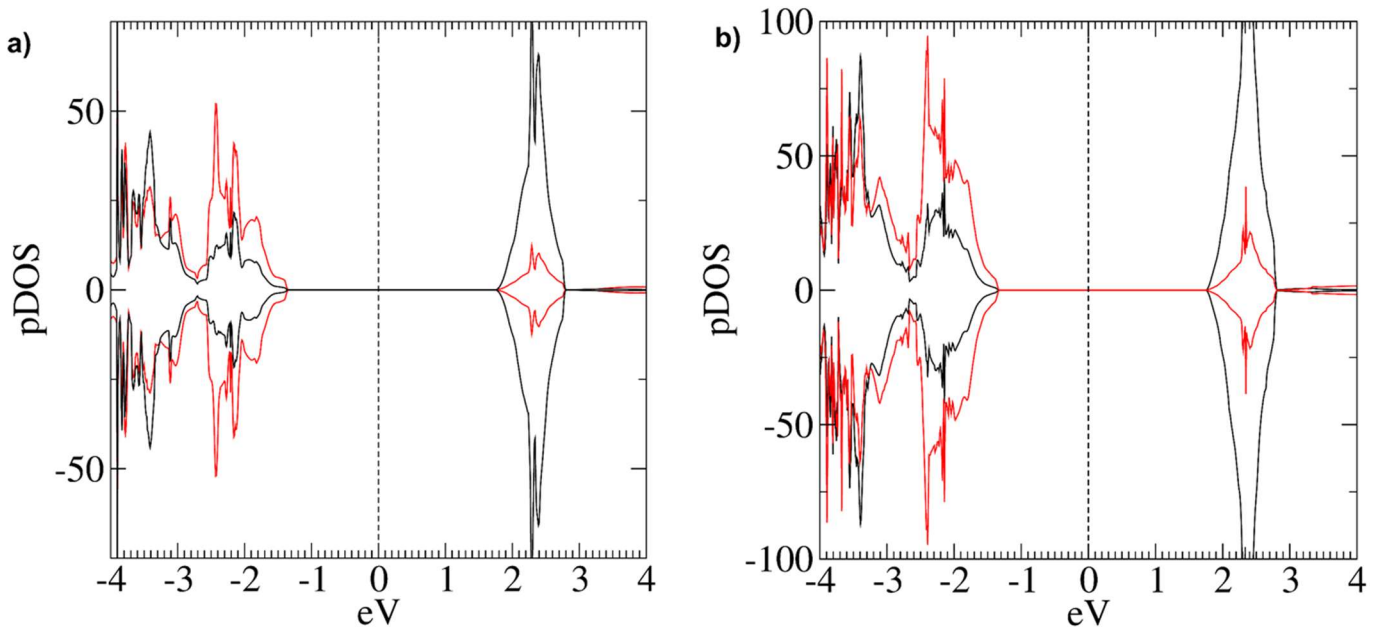

Figure A.29: Computed pDOS for bulk NiO model systems: a) $Ni_{32}O_{32}$; b) $Ni_{64}O_{64}$. The black vertical dashed line represents the Fermi level position (0 eV). Positive and negative curves correspond to spin-up and spin-down components, respectively. Red lines indicate O 2*p* states, while black lines represent Ni *d* states.

A.2.4.3 NiO(100) Regular Slab – Further Details

Regular NiO(100) surfaces were modeled including a vacuum region of 14 Å vacuum in the *z* direction with the aim of minimizing inter-slabs interactions. Two stoichiometric slabs were built (see Figure 9 main text):

1) RegSurf 1, with stoichiometry $Ni_{32}O_{32}$ (64 atoms), derived from Bulk 1. This model consists of four NiO layers and 8 top-layer Ni atoms (4 spin-up, 4 spin-down), with a surface area: 69.65 $Å^2$;

2) RegSurf 2, with stoichiometry $Ni_{64}O_{64}$ (128 atoms), derived from Bulk 2. This model also comprises four NiO layers but presents 16 top-layer Ni atoms (8 spin-up, 8 spin-down), with a surface area: 139.31 $Å^2$.

BZ sampling employed: 2×2×1 and 1×2×1 meshes for RegSurf 1 and RegSurf 2, respectively. Structural optimizations of NiO(100) slab models were carried out by relaxing the atomic coordinates, while keeping the *a* cell parameter fixed to the value obtained for the

corresponding bulk models. The Ni and O atoms in the bottom layer were constrained to their bulk positions during optimization. In both slab models, the surface relaxation primarily affects the two outermost layers (see Table 10 in the main text). The top layer displays a slight corrugation: O atoms are slightly displaced inwards (2.030 Å from the nearest Ni in the second layer), whereas Ni ones are slightly displaced outwards (2.090 Å from the nearest O in the second layer). For comparison, the Ni-O bond lengths in the bulk system are 2.086 Å (Table A.19). Moreover, Ni-O distances and interlayer separations between the (100) planes in the top layer differ, giving rise to chains of alternating short (2.073 Å) and long (2.101 Å) bonds (Table 10). In the second layer, this alternation is less pronounced, with Ni-O bond lengths of 2.082 Å and 2.091 Å, respectively, in the case of $Ni_{32}O_{32}$. Additionally, atoms in the second layer are all closer to the third one, with an average interlayer separation of 2.070 Å. This behavior of the Ni-O distances in NiO (100) topmost layers, which affects evenly the two magnetic sub-lattices, is in good agreement with the results of scanning tunnelling microscopy (STM) experiments on NiO surfaces. [89] The antiferromagnetic (AF) ordering is preserved in the stoichiometric NiO(100) slabs, although the magnetic moment per Ni atom (μ_{Ni}) increases slightly compared to the corresponding bulk value (Table A.19). The E_{gap} values computed for regular NiO(100) surfaces are collected in Table 10, showing a substantial decrease in comparison to the bulk structure (Table A.19), in line with the trend previously observed in the literature. [7,72,74,75] This behavior may be attributed to the surface deformations discussed above.

A.2.4.4 Monohydroxylated NiO(100) Slab – Further Details

Monohydroxylated NiO(100) surfaces were modeled with special care due to AF ordering [75,88]. A single -OH group breaks magnetic symmetry, perturbing the spin sub-lattices unevenly. Moreover, the same vacuum region of Regular NiO(100) was adopted (see Section A.2.4.3). This case was explored with three models of increasing size and thickness (see Figure 12 in the main text):

1) $Ni_{32}O_{32}(OH)$ (66 atoms), derived from Bulk 1 (cubic 2×2×2 simulation cell), containing four NiO layers and 8 top-layer Ni atoms (4 spin-up, 4 spin-down), surface area: 69.65Å^2;
2) $Ni_{16}O_{16}(OH)$ (34 atoms), derived from Bulk 3 (tetragonal 2×2 simulation cell), containing four NiO layers and 4 top-layer Ni atoms (2 spin-up, 2 spin-down), surface area: 34.83Å^2;
3) $Ni_{24}O_{24}(OH)$ (50 atoms), derived from Bulk 3 (tetragonal 2×2 simulation cell), containing six NiO layers and 4 top-layer Ni atoms (2 spin-up, 2 spin-down), surface area: 34.83 Å^2.

BZ meshes of 6×6×1 were used for $Ni_{32}O_{32}(OH)$ and $Ni_{16}O_{16}(OH)$ models, while 2×2×1 for $Ni_{24}O_{24}(OH)$. These mono-hydroxylated NiO(100) slab models were subjected to atomic position optimization. In the four-layer systems, Ni and O atoms in the bottom layer were fixed at their bulk positions, while in the six-layer model, atoms of the two bottom layers were fixed at their bulk coordinates. This setup was consistently applied across all hydroxylated slab models discussed in the Paragraph 2.4. A vacuum gap of 14 Å along *z* has been included in the simulation cell of the three models. To assess the convergence of structural, electronic, and

magnetic properties with respect to vacuum gap size, additional calculations were performed on the largest model $Ni_{32}O_{32}(OH)$ using a 17 Å vacuum region (see Table A.20).

Table A.20: Properties of $Ni_{32}O_{32}(OH)$ slab models. E_{gap}: band gap energy; μ_{tot}: total magnetization; μ_{Ni}: absolute magnetization per Ni atom. Energies are given in eV, μ_{tot} and μ_N in Bohr Magnetons (μ_B), Ni*-OH, O-H, Ni-O and Ni*-O*distances in Å, Ni*-$\widehat{O}$-H angles in degrees. ⟨Ni-O⟩ denotes the average Ni-O distance for the top-layer. [a] Computed with a vacuum gap of 14 Å. [b] Computed with a vacuum gap of 17 Å.

System	E_{gap}	*Type*	μ_{tot}	μ_{Ni}	*Ni*-OH*	*O-H*	*⟨Ni-O⟩*	*Ni*-O**	*Ni*-$\widehat{O}$-H*
$Ni_{32}O_{32}(OH)$[a]	0	*Half-metal*	-0.91	1.81	1.817	0.980	2.081	2.118	107.2
$Ni_{32}O_{32}(OH)$[b]	0	*Half-metal*	-0.91	1.81	1.817	0.980	2.081	2.118	107.2

The relevant properties of the three minimum energy structures of the mono-hydroxylated NiO(100) slab models are reported in Table 11 (main text). The structural analysis focused primarily on the local defect environment, namely O*-Ni*-OH atoms (Figure 11). As shown in Table 11, the three slab models exhibit very similar structural features. In all cases, the O-H bond lengths are identical and the -OH moiety forms a strong bond with a top-layer Ni atom (Ni*). The formation of the Ni*-OH bond brings to a significant elongation of the Ni*-O* distance with respect to the bulk value (2.086 Å, see Table A.19), suggesting a weakening of the Ni*-O* bond. This effect is more pronounced in the $Ni_{16}O_{16}(OH)$ and $Ni_{24}O_{24}(OH)$ models, which are characterized by smaller surface areas. In addition, the Ni*-$\widehat{O}$-H bond angle is also consistent across all the considered models (Table 11), further supporting the structural similarity of the local hydroxyl environment. Beyond the defect environment, the three slabs display very similar average Ni-O distances ⟨Ni-O⟩ between top-layer Ni and O atoms (Table 11). Overall, this analysis indicates that slab thickness has a negligible impact on the structure of the hydroxylated slabs. In contrast, surface area appears to play a more significant role: deviations of Ni-O distances from the bulk value (2.086 Å) are more pronounced in the smaller-surface $Ni_{16}O_{16}(OH)$ and $Ni_{24}O_{24}(OH)$ models, characterized by only four top-layer Ni atoms. The data reported in Table 11, along with the DOS profiles shown in Figure 13 (main text), clearly indicate that a vacuum gap of 14 Å is sufficient to achieve convergence.

A.2.4.5 Di-Hydroxylated NiO(100) Surfaces – Further Details

To preserve magnetic symmetry, paired hydroxyl groups were introduced on opposite magnetic sub-lattices. [75] -OH groups were modeled by placing either an -H atom to an O site or an -OH group to a Ni site, maximizing separation between defects. Models with different surface areas were evaluated to explore the increasing defect concentration. 2 × -OH groups models were generated from:

- RegSurf 2 (16 Ni sites): 4 models to simulate low -OH coverage (see Figures 14)
- Tetragonal 2×2 slabs (4 Ni sites): 3 models to mimic higher coverage (see Figures 17, A.30)

BZ meshes of 1×2×1 (RegSurf 2) and 6×6×1 (Tetragonal 2×2 slabs) were adopted.

The first two models (Figure 14a,b) have the same simulation cell stoichiometry $[Ni_{64}O_{64}]2H$ but differ in their total charge. The first one, $[Ni_{64}O_{64}]2H+$, characterized by total charge +2*e*, was obtained by adding two protons to two top-layer oxygen atoms (Figure 14a). A uniform

compensating background charge of -2*e* was applied to ensure the system's electrical neutrality during the calculations. The second one, electrically neutral, was obtained by adding two H atoms to two top-layer oxygen atoms (Figure 14b). The third and fourth models (Figure 14c,d) have simulation cell stoichiometry $[Ni_{64}O_{64}]2(OH)$. The third model, denoted as $[Ni_{64}O_{64}]2(OH)$, is electrically neutral and simulates the adsorption of two OH radicals on the surface (Figure 14c). In the fourth model, the hydroxyl groups were introduced in their anionic form (OH^-), resulting in a total negative charge of -2*e*. The latter was compensated by a +2*e* uniform charge background, and the model is denoted as $[Ni_{64}O_{64}]2(OH\text{-})$ (Figure 14d).

A.2.4.5.1 Low -OH concentration

To simulate a low concentration of -OH defects, four slab models were constructed: $[Ni_{64}O_{64}]2H$, $[Ni_{64}O_{64}]2H+$, $[Ni_{64}O_{64}]2(OH)$, and $[Ni_{64}O_{64}]2(OH\text{-})$ (see Figure 14, main text). In the "H-type models" (see Figure 14a,b, main text) the two H (or H^+) were positioned on top of the same top-layer oxygens, separated by 9.168 Å, the maximum distance compatible with the periodic boundary conditions. In the "OH-type models" (see Figure 14c,d), the two -OH groups were instead placed on two top-layer Ni atoms belonging to different magnetic sub-lattices, separated by 9.157 Å, again the maximum separation compatible with the periodic boundary conditions. In all these models, the *a* cell parameter was optimized as well, due to the presence of charged species in some of them. The resulting optimized *a* values were 4.100 Å for $[Ni_{64}O_{64}]2H$, 4.084 Å for $[Ni_{64}O_{64}]2H+$, 4.092 Å for $[Ni_{64}O_{64}]2(OH)$, and 3.980 Å for $[Ni_{64}O_{64}]2(OH\text{-})$.

$[Ni_{64}O_{64}]2H$

In the optimized structure of this model (Figure 14b), surface corrugation is more pronounced compared to the regular slab (see Table 10 and Figure 9, main text), with Ni top-layer atoms always upward with respect to oxygen ones (except for the O atoms bonded to H, which lie slightly higher due to the presence of the adsorbed protons). The two OH groups are oriented nearly perpendicular to the (100) surface and are separated by 9.168 Å (Table 12). The distance between each OH-bearing oxygen and the underlying Ni* atom is 2.905 Å, indicating that these O atoms are located approximately 0.7 Å above the top-layer plane.

$[Ni_{64}O_{64}]2(OH)$

The minimum energy structure of this model, illustrated in Figure 14c, exhibits an OH-OH separation of 9.157 Å. Within the Ni*-O-H groups (see Figure 11), the OH bond length is 0.979 Å, the Ni*-O one is 1.825 Å and the Ni*-O-H bond angle is 106.7°. The Ni* atoms bearing -OH groups are at 2.032 Å from the nearest oxygen atoms of the layer below (O*, Figure 11), which are slightly shifted upward compared to the other atoms in the same layer (Figure 14c). The bond distances between atoms in the top and second layers range from 2.008 Å to 2.117 Å. Even in this case, the top layer is corrugated, with Ni atoms positioned slightly upward (≈0.1 Å) with respect to oxygen atoms. However, the surface deformation induced by the binding of two hydroxyls to Ni* is less pronounced than that caused by the addition of two H atoms to two surface O sites (cfr. Figure 14c and 14b).

[$Ni_{64}O_{64}$]2H+

The minimum energy structure for this model is illustrated in Figure 14a. The optimized cell parameter (4.084 Å) is slightly shorter than the corresponding bulk value (4.175 Å). Overall, the structural feature of this charged slab closely resemble those of the neutral [$Ni_{64}O_{64}$]2H model**.** The top layers exhibit a slightly corrugated morphology, as already observed in non-defective slabs, with Ni atoms positioned about 0.05 Å above the neighboring O atoms along the *z*-direction. In contrast, the two oxygen atoms bearing the two protons are significantly displaced outward with respect to the surrounding Ni atoms. Both Ni*-O-H groups (Figure 11, main text) are characterized by a Ni*-O bond distance of 2.806 Å, an O-H bond length of 0.982 Å and a nearly linear Ni*-O-H angle of 179.5°. The two protons are separated by 9.130 Å. Notably, the Ni*-O distance in Ni*-OH groups is significantly larger than the average Ni-O separation between top- and second-layer atoms (2.077 Å), which itself is smaller than the Ni-O distance between second- and third-layer atoms (2.107 Å). Even in this model, an alternation of short and long Ni-O bonds is observed between atoms in the top layer. Nevertheless, the presence of the two OH groups in the top layer break this bond pattern, rendering it less regular (see Figure 14a).

[$Ni_{64}O_{64}$]2(OH-)

The minimum energy structure of this model is shown in Figure 14d. The introduction of two negatively charged OH defects leads to a decrease of the cell parameter to 3.980 Å. Despite this variation, the overall geometry of [$Ni_{64}O_{64}$]2(OH-) closely resembles the ones exhibited by the related neutral [$Ni_{64}O_{64}$]2(OH) model (Figure 14c). In particular, the O-H bond distances are both equal to 0.977Å, while each hydroxyl O atom is coordinated to a top-layer Ni* through a Ni*-OH bond of 1.895 Å. This Ni* is separated by 2.385 Å from the nearest second-layer oxygen O* (see Figure 11). The Ni*-O-H bond angle is 105.3°, indicating a slightly bent geometry. As a result, the Ni* atoms bearing the hydroxyl groups are shifted upward with respect to the other atoms in the layer. As found in all the previously discussed slabs, the top-layer is corrugated, exhibiting the Ni atoms located approximately 0.1 Å above the oxygen atoms along the *z*-axis. The extent of this surface distortion in [$Ni_{64}O_{64}$]2(OH-) is nearly identical to that found in the neutral counterpart [$Ni_{64}O_{64}$]2(OH) (cfr. Figures. 14c and 14d in the main text).

A.2.4.5.2 High -OH concentration

To simulate a high concentration of -OH defects, three new slab models were built using the tetragonal 2×2 cell (the one with the smallest surface area: 34.83 Å²), which includes six NiO layers and features only four Ni centers (Figure 17). In this case, only neutral -H and -OH ad-atoms were introduced, as the reduced surface area of the 2×2 cell precludes reliable modeling of charged species. Consequently, no optimization of the cell parameter was required. The first model of this series, denoted ($Ni_{24}O_{24}$)2H, was built by adding two -H atoms to two top-layer O sites, separated by 4.173 Å (Figures 17a and b). Two additional models with stoichiometry ($Ni_{24}O_{24}$)2(OH) were generated by adding two -OH groups on two Ni-sites of opposite spin, in different locations. In the former case (Figure 17c and d, ($Ni_{24}O_{24}$)2(OHa)), the two Ni centers were separated by 2.951 Å, while in the latter (Figure 17e and f, ($Ni_{24}O_{24}$)2(OHb)) the

separation among the Ni sites was 4.170 Å. As in all previous cases, a vacuum gap of 14 Å along the *z*-axis has been included in the simulation cell.

[$Ni_{24}O_{24}$]2H

The [$Ni_{24}O_{24}$]2H model (Figures 17a and b) is characterized by parallel rows of -OH moieties, arranged on the system top layer as illustrated in Figure A.30.

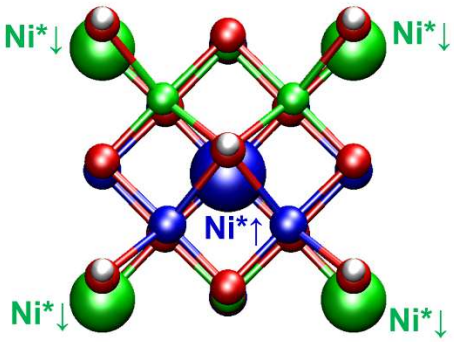

Figure A.30: Graphical representation of the surface hydroxyl defect arrangement in [$Ni_{24}O_{24}$]2H with respect to the two magnetic spin sublattices. Each -OH group is adsorbed on top of a Ni* cation and is surrounded by four -OH defects located on opposite spin Ni* centers.

Each hydroxyl group is surrounded by four -OH defects adsorbed on Ni* sites with opposite spin and bridges two top-layer Ni* centers of different spin, with Ni*-O distances of 2.175 Å and 2.454 Å, respectively, while the separation of the hydroxyl oxygen from Ni* is 3.037 Å. The -O-H bond lengths amount to 0.980 Å. The corresponding distances in [$Ni_{64}O_{64}$]2H were 2.174 Å, 2.208 Å, 2.905 and 0.980 Å, respectively (see Table 12, main text). This comparison highlights a notable trend: structural distortions with respect to regular NiO(100) become more pronounced as the concentration of surface hydroxyl defects rises. Conversely, the magnetic and the main electronic properties of the two models are very similar (cfr. Tables 12 and 13, main text).

[$Ni_{24}O_{24}$]2(OH)

The optimized geometries of the two models with this stoichiometry, denoted as [$Ni_{24}O_{24}$]2(OHa) and [$Ni_{24}O_{24}$]2(OHb), are shown in Figures 17c-d and 17e-f, respectively. In these models, the -OH groups are separated by 2.951 Å and 4.171 Å, respectively. In [$Ni_{24}O_{24}$]2(OHa), geometry optimization led to a notable rearrangement: each Ni*-OH group moved on top of two top-layer oxygen atoms, leaving an under-coordinated O atom in the layer below (Figures 17c and d). Each Ni* atom forms two strong bonds (1.888 Å) with the two neighboring top-layer oxygens, defining an O-Ni*-O angle of 127.6°. The Ni*-OH distances are 1.784 Å, the O-H bond lengths 0.990 Å, and the Ni*-O-H angles 110.8°, revealing a tricoordinate environment around the Ni* center. Notably, the -OH groups are aligned along the *y*-axis (Figures 17c and d), forming hydrogen-bonded chains characterized by an O···HO separation of 2.050 Å, indicating the occurrence of moderately strong hydrogen bonds. In contrast, the [$Ni_{24}O_{24}$]2(OHb) system exhibits very different structural features (Figures 17e and f). Indeed, there is no massive reconstruction like in the [$Ni_{24}O_{24}$]2(OHa)

model: the -OH groups are adsorbed on two top-layer Ni* atoms, which are moderately upward shifted (Figure 17e). In this case, the Ni*-O* distances (2.081 Å) exceed the average Ni-O distance between top- and second- layer atoms (1.998 Å), while Ni*-OH and O-H bond lengths are 1.801 Å and 0.981 Å, respectively, with a Ni*-O-H bond angle of 107.9°. Due to the large separation between -OH groups (4.171 Å), no hydrogen bond is observed.

A.2.4.6 Tetra-Hydroxylated NiO(100) Surfaces – Further Details

Following the same approach adopted for NiO(100) surface models bearing two -OH groups (see Section 2.4.3), slabs with different surface areas were employed to assess the impact of further increasing the defect concentration. The first model, simulating a relatively low -OH defect density, was built by placing two H atoms on two top-layer O atoms and two -OH groups on two top-layer Ni of opposite spin, using RegSurf 2 (the regular slab with the largest surface area). This model (optimized *a* cell parameter: 4.112 Å) mimics a NiO(100) slab with two dissociated water molecules at low concentration and is referred to as $[Ni_{64}O_{64}]2H\text{-}2(OH)$ (Figure 20a). To simulate a higher -OH defect density, three additional models were built using the tetragonal 2×2 cell (characterized by a smaller surface area). In the first of this series, $[Ni_{24}O_{24}]4H$, four H atoms were added to the four top-layer O sites (Figure 20b). The second model, $[Ni_{24}O_{24}]4(OH)$, was built by placing four -OH groups on the four top-layer Ni sites (Figure 20c). The third model, $[Ni_{24}O_{24}]2H\text{-}2(OH)$, was constructed by positioning two -OH groups on two Ni sites of opposite spins (Ni-Ni distance = 4.171 Å) and two H atoms on the respective neighboring oxygen atoms. This model represents a NiO(100) slab with two dissociated water molecules at high concentration (Figure 20d).

All tetra-hydroxylated Ni(100) models were sampled using a 6×6×1 mesh, except for the one generated from RegSurf 2 (denoted as $Ni_{64}O_{64}2H2(OH)$, for which a 1×2×1 mesh was adopted, as for RegSurf 2 (see Figure 20a). In summary, four models bearing four surface hydroxyl moieties were considered:

1. $[Ni_{64}O_{64}]2H\text{-}2(OH)$ (134 atoms): consists of four NiO layers and 16 top-layer Ni atoms (8 spin-up, 8 spin-down), built by adding two H atoms to two surface O atoms and two -OH groups to two surface Ni atoms of RegSurf 2.
2. $[Ni_{24}O_{24}]4H$ (52 atoms): contains six NiO layers and 4 top-layer Ni atoms (2 spin-up, 2 spin-down), built by adding four -H atoms to the four top-layer O sites of the 2×2 cell.
3. $[Ni_{24}O_{24}]4(OH)$ (56 atoms): contains six NiO layers and 4 top-layer Ni atoms (2 spin-up, 2 spin-down), constructed by adding four -OH groups to the four Ni sites of the 2×2 cell top layer.
4. $[Ni_{24}O_{24}]2H\text{-}2(OH)$ (54 atoms): contains six NiO layers and 4 top-layer Ni atoms (2 spin-up, 2 spin-down), built by adding two -H atoms to two surface O atoms and two -OH groups to two Ni sites of opposite spin within the 2×2 cell top layer.

All models were subjected to optimization of the atomic coordinates. A vacuum gap of 14 Å along the z-direction was applied in all simulation cells. It should be noted that Figures 20b

and 20d illustrate the starting, unrelaxed configurations of the corresponding models. The optimized structures resulting from geometry optimization will be presented and discussed in the main text.

[$Ni_{64}O_{64}$]2H-2(OH)

In this model, shown in Figure 20a (main text), the two H atoms are positioned at 0.981 Å from the top-layer oxygen atoms to which they are linked. These oxygen atoms, in turn, are located at 2.781 Å from the nearest second-layer Ni atom (Ni*, see Section 2.4.2 and Figure 11a). The Ni*-O-H angles are 178.4°, and the O-H bonds are nearly perpendicular to the top layer, as found for the [$Ni_{64}O_{64}$]2H and [$Ni_{64}O_{64}$]2H+ models (see Section 2.4.2). As regards the two -OH groups bonded to top-layer Ni atoms (Ni*-OH distances = 1.871 Å), the O-H bond lengths are both 0.977 Å. The Ni atoms bearing these hydroxyl groups (Ni*, see Section 2.4.2, Figure 11b) are separated by 2.309 Å from the nearest second-layer oxygen atoms. The two Ni*-bound -OH groups are separated by 9.195 Å, which is also the distance between the two H atoms bonded to the top-layer oxygen atoms. The shortest distance between different types of OH moieties is notably smaller (4.974 Å). As in all previous models, the top layers exhibit corrugation, with Ni atoms typically shifted upward with respect to O ones (except for the H-bearing oxygens). The average separation between top layer and second layer is 2.070 Å, while the separation between second and third layer is 2.094 Å.

[$Ni_{24}O_{24}$]4H

The optimized structure of this model (Figure 22b, main text) is very different from the starting configuration (Figures 20b and 22a) due to a substantial top layer reconstruction. Only two of the four Ni* remain at bonding distances (2.110 Å) from second-layer oxygen atoms (Figure 22b). Each of these two Ni* cations (of opposite spin) are also bonded to two hydroxyl oxygens, resulting in three-fold coordination. In contrast, the other two Ni* atoms are tetra-coordinated by the O atoms of the four -OH groups (Figure 22c). These tetra-coordinated Ni* are separated by 2.535 Å from the plane of the second layer, and by 2.730 Å from the closest second-layer oxygen. This massive reconstruction, featuring both three- and tetra-coordinated Ni, is due to the displacement of the entire top layer with respect to the second layer by approximately 0.898 Å along the [-110] direction (see arrow in Figure 22c). This distortion is also reflected in the Ni-O-Ni angle between top and second layer, which is 68° (Figure 22d), a substantial deviation from the 90° angle observed in the regular NiO(100) surface. As observed for the [$Ni_{64}O_{64}$]2H and [$Ni_{24}O_{24}$]2H models, the O-H bonds are nearly parallel to the *z*-direction. The O-H bond lengths occur in pairs (0.983 Å and 0.980 Å). For the tetra-coordinated Ni* atoms, the Ni*-O distances are 2.088 Å, 2.049 Å, 2.183 Å, and 2.140 Å, highlighting an asymmetric coordination environment defined by two shorter and two longer Ni*-O bonds. The four O-Ni-O angles are: 94.8°, 91.4°, 83.5°, and 86.5°.

$Ni_{24}O_{24}$]4(OH)

This system exhibits a surface -OH density twice as large as [$Ni_{24}O_{24}$]2(OH) and eight times greater than [$Ni_{64}O_{64}$]2(OH). In this case, the DFT-optimized slab structure (Figure 20c) does not show significant deviations from the geometry of the regular NiO(100) surface. The four -OH groups are bonded to the four top-layer Ni atoms. Within each spin sub-lattice, Ni*-OH

bond lengths alternate between shorter (1.826 Å) and longer (1.808 Å) values. All O-H bond lengths are 0.989 Å. The hydroxyl groups coordinated to spin-up and spin-down Ni* cations are oriented along the *-x* and *+x* direction, respectively, forming chains of moderately strong hydrogen bonds with alternating O···H distances of 2.015 Å and 2.089 Å (see Figure A.31). Likewise, Ni*-O-H bond angles occur in pairs within each hydrogen-bonded chain, amounting to 107.9° and 107.0°, respectively.

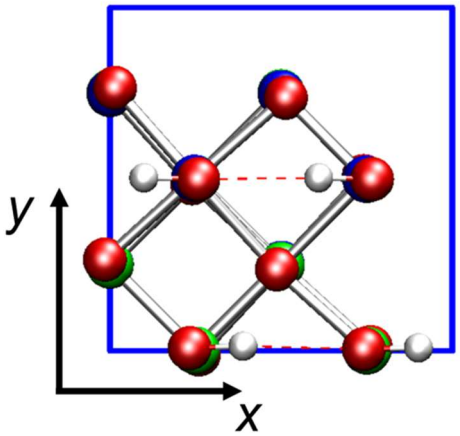

Figure A.31: Top-view graphical representation of the DFT-computed minimum energy structure of $[Ni_{24}O_{24}]4(OH)$, as depicted in Figure 48. Atom color codes are consistent with those used in Figure 48. Red dashed lines indicate hydrogen bonds, while blue lines delineate the simulation cell boundaries.

$[Ni_{24}O_{24}]2H$-2(OH)

The $[Ni_{24}O_{24}]2H$-2(OH) model results from the optimization of a system initially built by placing two -H and two -OH moieties on two top-layer O and Ni centers, respectively (Figures 20d and 25a), thereby mimicking the adsorption of two dissociated water molecules at a much higher concentration (eight times greater) than in the $[Ni_{64}O_{64}]2H$-2(OH) model. After geometry optimization, the system evolved toward the formation of two physisorbed water molecules coordinated to two Ni atoms with opposite spin (Figures 25b and c). The arrangement of the water molecules in the final structure closely resembles that reported for hydrated NiO(100) at 0.5 monolayer coverage.[92] The separation between the oxygen atoms of the two H_2O molecules is 4.127 Å, and water protons do not form hydrogen bonds with surface oxygen atoms. The geometry of the adsorbed water molecules is consistent with previous findings:[92] the O-H bond lengths are 0.980 Å and 1.000 Å, and the H-O-H bond angle is 104.2°. Regarding the local environment of H_2O molecules, the Ni*-O_{water} separation is 2.216 Å, the distance between Ni and the nearest second-layer oxygen (O*) is 2.110 Å, and the O*-Ni*-O_{water} angle is 167.1°

References

[1] M. I. Pintor-Monroy, B. L. Murillo-Borjas , M. Catalano, M. A. Quevedo-Lopez, Controlling Carrier Type and Concentration in NiO Films to Enable in situ PN Homojunctions, ACS Appl. Mater. Interfaces 2019, 11, 27048-27056

[2] W. Chen et al, F.-Z. Liu, X. Feng, A. B. Djurišić, W. K. Chan, Z.-B. He, Cesium Doped NiO_x as an Efficient Hole Extraction Layer for Inverted Planar Perovskite Solar Cells, Adv. Energy Mater. 2017, 7, 1700722

[3] C. Park, J. Kim, K. Lee, S. K. Oh, H. J. Kang, N. S. Park, Electronic, Optical and Electrical Properties of Nickel Oxide Thin Films Grown by RF Magnetron Sputtering, Appl. Sci. Convergence Technol. 2015, 24(3), 72-76

[4] Y. R. Denny, K. Lee, C. Park, S. K. Oh, H. J. Kang, D.-S. Yang, S. Seo, Electronic, Electrical and Optical Properties of Undoped and Na-Doped NiO Thin Films. Thin Solid Films 2015, 591, 255-260

[5] W. Chen et al, Understanding the Doping Effect on NiO: Toward High-Performance Inverted Perovskite Solar Cells. Adv. Energy Mater. 2018, 8, 1703519

[6] G. A. Sawatzky and J. W. Allen, Magnitude and Origin of the Band Gap in NiO**,** Phys. Rev. Lett., 1984, 53, 2339-2342

[7] J. Zaanen, G. A. Sawatzky and J. W. Allen, Band gaps and electronic structure of transition-metal compounds, Phys. Rev. Lett. 1985, 55, 418-421

[8] E. Lindahl, M. Ottosson, J. O. Carlsson, Atomic Layer Deposition of NiO by the $Ni(thd)_2/H_2O$ Precursor Combination, Chem. Vap. Deposition 2009, 15, 186-191

[9] E. Lindahl, M. Ottosson, J. O. Carlsson, Epitaxial NiO (100) and NiO (111) Films Grown by Atomic Layer Deposition, J. Cryst. Growth 2009, 311, 4082-4088

[10] K. C. Min et al, NiO Thin Films by MOCVD of $Ni(dmamb)_2$ and their Resistance Switching Phenomena, Surf. Coat. Technol. 2007, 201, 9252-9255

[11] J. Tian, H. Jiang, X. Zhao, G. Shi, Y. Dai, X. Deng, H. Xie, W. Zhang, Hydrogen Sensor with ppb-Level Detection Limit Prepared by Pd-Modified and Bi-Doped Oxidized Ni Foam, Sens. Actuators, B 2022, 366, 131981

[12] R. L. Wilson et al, Chemical Vapour Deposition (CVD) of Nickel Oxide using the Novel Nickel Dialkylaminoalkoxide Precursor $[Ni(dmamp')_2]$ (dmamp′ = 2-dimethylamino-2-methyl-1-propanolate), RSC Adv. 2021, 11, 22199-22205

[13] M. Imran, H. Coskun, N. A. Khan, J. Ouyang, Role of Annealing Temperature of Nickel Oxide (NiO_x) as Hole Transport Layer in Work Function Alignment with Perovskite, Appl. Phys. A 2021, 127, 117

[14] T. M. Roffi, S. Nozaki, K. Uchida, Growth Mechanism of Single-Crystalline NiO Thin Films Grown by Metal Organic Chemical Vapor Deposition. J. Cryst. Growth 2016, 451, 57-64

[15] S. W. Han, I. H. Kim, D. H. Kim, K. J. Park, E. J. Park, M.-G. Jeong, Y. D. Kim, Temperature Regulated-Chemical Vapor Deposition for Incorporating NiO Nanoparticles into Mesoporous Media. Appl. Surf. Sci. 2016, 385, 597-604

[16] N. Kitchamsetti, Mrunmay S. Ramteke, S. R. Rondiya, S. R. Mulani, M. S. Patil, R. W. Cross, N. Y. Dzade, R. S. Devan, DFT and Experimental Investigations on the Photocatalytic Activities of NiO Nanobelts for Removal of Organic Pollutants, J. Alloys Compd. 2021, 855, 157337

[17] W. J. An, E. Thimsen, P. Biswas, Aerosol-Chemical Vapor Deposition Method For Synthesis of Nanostructured Metal Oxide Thin Films With Controlled Morphology, J. Phys. Chem. Lett. 2010, 1, 249-253

[18] N. Weidler, J. Schuch, F. Knaus, P. Stenner, S. Hoch, A. Maljusch, R. Schäfer, B. Kaiser, W. Jaegermann, X-ray Photoelectron Spectroscopic Investigation of Plasma-Enhanced Chemical Vapor Deposited NiO_x, $NiO_x(OH)_y$, and $CoNiO_x(OH)_y$: Influence of the Chemical Composition on the Catalytic Activity for the Oxygen Evolution Reaction, J. Phys. Chem. C 2017, 121, 6455-6463

[19] N. Hussain, W. Yang, J. Dou, Y. Chen, Y. Qiana and L. Xu, Ultrathin Mesoporous F-Doped α-$Ni(OH)_2$ Nanosheets as an Efficient Electrode Material for Water Splitting and Supercapacitors, J. Mater. Chem. A 2019, 7, 9656-9664

[20] K. Hemmati et al, A. Kumar, A. Jadhav, O. Moradlou, A. Z. Moshfegh, H. Lee, Nanorod Array-Based Hierarchical NiO Microspheres as a Bifunctional Electrocatalyst for a Selective and Corrosion-Resistance Seawater Photo/Electrolysis System, ACS Catal. 2023, 13(8), 5516-5528

[21] P. Salunkhe, M. A. A V, D. Kekuda, Investigation on tailoring physical properties of Nickel Oxide thin films grown by dc magnetron sputtering**,** Mater. Res. Express, 2020, 7, 016427

[22] D. S. Kim and H. C. Lee, Nickel vacancy behavior in the electrical conductance of

nonstoichiometric nickel oxide film**,** J. Appl. Phys., 2012, 112, 034504

[23] D. Alders, F. C. Voogt, T. Hibma and G. A. Sawatzky, Nonlocal screening effects in 2*p* x-ray photoemission spectroscopy of NiO (100), Phys. Rev. B, 1996, 54, 7716-7719

[24] F. Hajakbari, Characterization of nanocrystalline nickel oxide thin films prepared at different thermal oxidation temperatures**,** J. Nanostruct. Chem., 2020, 10, 97-103

[25] R. S. Kate, S. C. Bulakhe and R. J. Deokate, Co doping effect on structural and optical properties of nickel oxide (NiO) thin films via spray pyrolysis, Opt. Quantum Electron., 2019, 51, 319

[26] S. Kerli and U. Alver, Effect of F-doping on structural, electrical, and optical properties of NiO thin films**,** Crystallogr. Rep., 2014, 59, 1103-1106

[27] M. Utriainen, M. Kröger-Laukkanen, L.-S. Johansson and L. Niinistö, Studies of metallic thin film growth in an atomic layer epitaxy reactor using $M(acac)_2$ (M=Ni, Cu, Pt) precursors**,** Appl. Surf. Sci., 2000, 157, 151-158

[28] M. Utriainen, M. Kröger-Laukkanen and L. Niinistö, Studies of NiO thin film formation by atomic layer epitaxy, Mater. Sci. Eng. B, 1998, 54, 98-103

[29] T. S. Yang et al, W. Cho, M. Kim, K.-S. An, T.-M. Chung, C. G. Kim, Y. Kim, Atomic layer deposition of nickel oxide films using $Ni(dmamp)_2$ and water, J. Vac. Sci. Technol., A, 2005, 23, 1238-1243

[30] Y. Zhang, L. Du, X. Liu and Y. Ding, High growth per cycle thermal atomic layer deposition of Ni films using an electron-rich precursor**,** Nanoscale, 2019, 11, 3484-3488

[31] A. Johnson, S. Richards, T. D. Manning, M. Hill, K. Molloy, Precursors for p-type nickel oxide: atmospheric-pressure metal-organic chemical-vapour deposition (MOCVD) of nickel oxide thin films with high work functions, Eur. J. Inorg. Chem., 2017, 1868-1876

[32] M. Chandrakala, S. Raj Bharath, T. Maiyalagan and S. Arockiasamy, Synthesis, crystal structure and vapour pressure studies of novel nickel complex as precursor for NiO coating by metalorganic chemical vapour deposition technique, Mater. Chem. Phys., 2017, 201, 344-353

[33] M. Z. Sialvi et al, R. J. Mortimer, G. D. Wilcox, M. A. M. Teridi, T. Varley, K. G. U. Wijayantha, C. Kirk, Electrochromic and colorimetric properties of nickel(II) oxide thin films prepared by aerosol-assisted chemical vapor deposition, ACS Appl. Mater. Interfaces, 2013, 5, 5675-5682

[34] D. Zywitzki, D. H. Taffa, L. Lamkowski, M. Winter, D. Rogalla, M. Wark, A. Devi,

Tuning coordination geometry of nickel ketoiminates and its influence on thermal characteristics for chemical vapor deposition of nanostructured NiO electrocatalysts**,** Inorg. Chem., 2020, 59, 10059-10070

[35] M. Basato, E. Faggin, C. Tubaro and A. C. Veronese, Volatile square planar β-imino carbonyl enolato complexes of Pd(II) and Ni(II) as potential MOCVD precursors**,** Polyhedron, 2009, 28, 1229-1234

[36] S. Battiato, M. M. Giangregorio, M. R. Catalano, R. Lo Nigro, M. Losurdo and G. Malandrino, Morphology-controlled synthesis of NiO films: the role of the precursor and the effect of the substrate nature on the films' structural/optical properties, RSC Adv., 2016, 6, 30813-30823

[37] C. Maccato et al, Molecular Engineering of Mn^{II} Diamine Diketonate Precursors for the Vapor Deposition of Manganese Oxide Nanostructures, Chem. Eur. J. 2017, 23, 17954-17963

[38] D. Barreca et al, A Versatile Fe(II) Diketonate Diamine Adduct: Preparation, Characterization and Validation in the Chemical Vapor Deposition of Iron Oxide Nanomaterials, Mater. Chem. Phys. 2022, 277, 125534

[39] D. Barreca, A. Gasparotto, O. I. Lebedev, C. Maccato, A. Pozza, E. Tondello, S. Turnerc, G. V. Tendeloo, Controlled Vapor-Phase Synthesis of Cobalt Oxide Nanomaterials with Tuned Composition and Spatial Organization, CrystEngComm 2010, 12, 2185-2197

[40] M. Klotzsche et al, Facile Preparation of a Cobalt Diamine Diketonate Adduct as a Potential Vapor Phase Precursor for Co_3O_4 Films. Dalton Trans. 2021, 50, 10374-10385

[41] G. Tabacchi, E. Fois, D. Barreca, A. Gasparotto, CVD Precursors for Transition Metal Oxide Nanostructures: Molecular Properties, Surface Behavior and Temperature Effects, Phys. Status Solidi A 2014, 211, 251-259

[42] C. Stienen, J. Grahl, C. Wölper, S. Schulz, G. Bendt, Fluorinated β-diketonate complexes $M(tfac)_2(TMEDA)$ (M = Fe, Ni, Cu, Zn) as precursors for the MOCVD growth of metal and metal oxide thin films, RSC Adv. 2022, 12, 22974-22983

[43] I. Utke, P. Swiderek, K. Höflich, K. Madajska, J. Jurczyk, P. Martinović, I.B. Szymańska, Coordination and organometallic precursors of group 10 and 11: Focused electron beam induced deposition of metals and insight gained from chemical vapour deposition, atomic layer deposition, and fundamental surface and gas phase studies, Coord. Chem. Rev., 2022, 458, 213851

[44] F. Emmenegger, C. W. Schlaepfer, H. Stoeckli-Evans, M. Piccand, H. Piekarski, Chelate effect in the gas phase. The complexes of Ni(2,2,6,6-tetramethyl-3,5-heptanedionate)$_2$ with bidentate ligands, Inorg. Chem. 2001, 40, 3884-3888

[45] D. Barreca et al, E. Fois, A. Gasparotto, C. Maccato, M. Oriani, G. Tabacchi, The early steps of molecule-to-material conversion in chemical vapor deposition (CVD): A case study, Molecules 2021, 26, 1988

[46] D. Barreca et al, β-Fe_2O_3 nanomaterials from an iron(II) diketonate-diamine complex: A study from molecular precursor to growth process, Dalton Trans. 2012, 41, 149-155

[47] G. Bandoli, D. Barreca, A. Gasparotto, C. Maccato, R. Seraglia, E. Tondello, A. Devi, R. A. Fischer, M. Winter, A cobalt(II) hexafluoroacetylacetonate ethylenediamine complex as a CVD molecular source of cobalt oxide nanostructures, Inorg. Chem. 2009, 48, 82-89

[48] E. Fois, G. Tabacchi, D. Barreca, A. Gasparotto, E. Tondello, "Hot" surface activation of molecular complexes: Insight from modeling studies, Angew. Chem. Int. Ed. 2010, 49, 1944-1948

[49] D. Barreca, E. Fois, A. Gasparotto, R. Seraglia, E. Tondello, G. Tabacchi, How does Cu^{II} convert into Cu^{I}? An unexpected ring-mediated single-electron reduction, Chem. Eur. J. 2011, 17, 10864-10870

[50] M. Benedet, D. Barreca, E. Fois, R. Seraglia, G. Tabacchi, M. Roverso, G. Pagot, **C. Invernizzi**, A. Gasparotto, A. A. Heidecker, A. Pöthig, E. Callone, S. Dirè, S. Bogialli, Interplay between coordination sphere engineering and properties of nickel diketonate diamine complexes as vapor phase precursors for the growth of NiO thin films, Dalton Trans., 2023, 52, 10677-10688

[51] M. Benedet, C. Maccato, G. Pagot, **C. Invernizzi**, C. Sada, V. Di Noto, G. A. Rizzi, E. Fois, G. Tabacchi and D. Barreca, Growth of NiO Thin Films in the Presence of Water Vapor: Insights from Experiments and Theory, J. Phys. Chem. C, 2023, 127 (45), 22304-22314

[52] **C. Invernizzi** et al, On the fragmentation of Ni(II) β-diketonate-diamine complexes as molecular precursors for NiO films: a theoretical and experimental investigation, Molecules, 2024, 29 (3), 642

[53] E. Fois, C. Maccato, D. Barreca, **C. Invernizzi** and G. Tabacchi, "Impact of -OH surface defects on the electronic and structural properties of nickel oxide thin films"; Dalton Trans., 2025, 54, 2765

[54] R. O' Donoghue et al, D. Peeters, D. Rogalla, H.-W. Becker, J. Rechmann, S. Henke, M. Winter, A. Devi, Systematic molecular engineering of Zn-ketoiminates for application as precursors in atomic layer depositions of zinc oxide, Dalton Trans., 2016, 45, 19012-19023

[55] K. J. Puring, D. Zywitzki, D. H. Taffa, D. Rogalla, M. Winter, M. Wark, A. Devi, Rational development of cobalt β-ketoiminate complexes: alternative precursors for vapor-phase deposition of spinel cobalt oxide photoelectrodes, Inorg. Chem., 2018, 57, 5133-5144

[56] S. Mishra and S. Daniele, Metal-Organic Derivatives with Fluorinated Ligands as Precursors for Inorganic Nanomaterials, Chem. Rev., 2015, 115, 8379-8448

[57] G. I. Zharkova, S.I. Dorovskikh, S.V. Sysoev, I.P. Asanov, A.V. Panin, N.B. Morozova, I.K. Igumenov, O,N-coordinated Ni(II) beta-diketonate derivatives: Synthesis, thermal properties, MOCVD applications, Surf. Coat. Technol., 2013, 230, 290-296

[58] J. Fragoso et al, Enhanced Photocatalytic Removal of NO_x Gases by β-Fe_2O_3/CuO and β-Fe_2O_3/WO_3 Nanoheterostructures, Chem. Eng. J. 2022, 430, 132757

[59] A. Kruve, K. Kaupmees, J. Liigand, M. Oss, I. Leito, Sodium adduct formation efficiency in ESI source, J. Mass Spectrom. 2013, 48, 695-702

[60] R. F. W. Bader, A quantum theory of molecular structure and its applications, Chem. Rev. 1991, 91, 893-928

[61] W. Tang, E. Sanville, G. Henkelman, A grid-based Bader analysis algorithm without lattice bias, J. Phys. Condens. Matter 2009, 21, 084204

[62] R. L. Puurunen, Surface Chemistry of Atomic Layer Deposition: A Case Study for the Trimethylaluminum/Water Process., J. Appl. Phys. 2005, 97, 121301

[63] V. Miikkulainen, M. Leskelä, M. Ritala, R. L. Puurunen, Crystallinity of Inorganic Films Grown by Atomic Layer Deposition: Overview and General Trends., J. Appl. Phys., 2013, 113, 021301

[64] S. M. George, Atomic Layer Deposition: An Overview, Chem. Rev., 2010, 110, 111-131

[65] X. Su, Z. Tu, L. Ji, H. Wu, H. Xu and C. Liu, Electrochromic properties of NiO films prepared by atomic layer deposition, J. Vac. Sci. Technol. A, 2023, 41, 062407

[66] T. Moriyama, K. Oda, T. Ohkochi, M. Kimata and T. Ono, Spin torque control of antiferromagnetic moments in NiO, Sci. Rep., 2018, 8, 14167

[67] R. L. Wilson et al, Chemical vapour deposition (CVD) of nickel oxide using the novel nickel dialkylaminoalkoxide precursor [Ni(dmamp′)$_2$] (dmamp′ = 2-dimethylamino-2-methyl-1-propanolate) RSC Adv., 2021, 11, 22199-22205

[68] Q.-S. Jiang, Y. Wu, Z. Xie, M. Wei, Y. Zhao, X. Yang, W. Xun, S. Cao, C. Wang, Syntheses of efficient nickel oxide film by low-temperature fabrication technique for high-performance perovskite solar cells, Mater. Today Commun., 2023, 35, 106401

[69] K. Rajesh, N. Pothukanuri and M. V. R. Reddy, Studies on pure and Zn doped NiO nanostructured thin films for enhanced ammonia gas sensing applications, Chem. Phys. Impact, 2024, 8, 100397

[70] S. Srivastava, C. Dwivedi, A. Yadav, A. Kumar, G. Gupta and P. Singh, Enhanced H_2S gas sensing of Pd functionalized NiO thin films deposited by magnetron sputtering process, Mater. Lett., 2023, 351, 135040

[71] K. Munawar, M. A. Mansoor, R. Naeem, M. Rizwan, M. S. Ahmad, T. Zaharinie, M. N. M. Zubir, Z. Aspanu, Effect of deposition temperature on topography and electrochemical water oxidation of NiO thin films, Thin Solid Films, 2023, 782, 140031

[72] C.-Y. Kuo, T. Haupricht, J. Weinen, H. Wu, K.-D. Tsuei, M. W. Haverkort, A. Tanaka, L. H. Tjeng, Challenges from experiment: electronic structure of NiO, Eur. Phys. J. Spec. Top., 2017, 226, 2445-2456

[73] P. Alastuey, D. Pais Ospina, D. Comedi, M. Tirado and O. Marin-Ramirez, On the properties of NiO powders obtained by different wet chemical methods and calcination, J. Am. Ceram. Soc., 2024, 107, 92-106

[74] A. Rohrbach, J. Hafner and G. Kresse, Molecular adsorption on the surface of strongly correlated transition-metal oxides: A case study for CO/NiO(100), Phys. Rev. B, 2004, 69, 075413

[75] K. O. Egbo, C. P. Liu, C. E. Ekuma and K. M. Yu, Vacancy defects induced changes in the electronic and optical properties of NiO studied by spectroscopic ellipsometry and first-principles calculations, J. Appl. Phys., 2020, 128, 135705

[76] B. E. F. Fender, A. J. Jacobson and F. A. Wedgwood, Covalency Parameters in MnO, α-MnS, and NiO, J. Chem. Phys., 1968, 48, 990-994

[77] K. P. Makhado, M. M. Mphahlele-Makgwane, N. Kumar, P. G. L. Baker and P. R. Makgwane, Current updates on p-type nickel oxide (NiO) based photocatalysts towards decontamination of organic pollutants from wastewater, Mater. Today Sustain., 2024, 25, 100664

[78] J. A. Dawson, Y. Guo and J. Robertson, Energetics of intrinsic defects in NiO and the consequences for its resistive random access memory performance, Appl. Phys. Lett., 2015, 107, 122110

[79] A. K. Cheetham and D. A. O. Hope, Magnetic ordering and exchange effects in the antiferromagnetic solid solutions $Mn_xNi_{1-x}O$, Phys. Rev. B, 1983, 27, 6964-6967

[80] A. Fujimori and F. Minami, Valence-band photoemission and optical absorption in nickel compounds, Phys. Rev. B, 1984, 30, 957-971

[81] S. Elmassi et al, A. Narjis, L. Nkhaili, A. Elkissani, L. Amiri, S. Drissi, A. Abali, M. Bousseta, A. Outzourhit, Effect of annealing on structural, optical and electrical properties of nickel oxide thin films synthesized by the reactive radio frequency sputtering, Physica B, 2022, 639, 413980

[82] G. Pagot, M. Benedet, C. Maccato, D. Barreca and V. Di Noto, XPS study of NiO thin films obtained by chemical vapor deposition, Surf. Sci. Spectra, 2023, 30, 024028

[83] D. Barreca et al, Manganese(II) Molecular Sources for Plasma-Assisted CVD of Mn Oxides and Fluorides: From Precursors to Growth Process, J. Phys. Chem. C, 2018, 122, 1367-1375

[84] B. P. Payne, M. C. Biesinger and N. S. McIntyre, The study of polycrystalline nickel metal oxidation by water vapour, J. Electron Spectrosc., 2009, 175, 55-65

[85] G. Tabacchi, E. Fois, D. Barreca and A. Gasparotto, Opening the Pandora's jar of molecule-to-material conversion in chemical vapor deposition: Insights from theory, Int. J. Quantum Chem., 2014, 114, 1-7

[86] M. Nolan, R. Long, N. J. English and D. A. Mooney, Hybrid density functional theory description of N- and C-doping of NiO, J. Chem. Phys., 2011, 134, 224703

[87] L. Li and Y. Kanai, Antiferromagnetic structures and electronic energy levels at reconstructed NiO(111) surfaces: A DFT+*U* study, Phys. Rev. B, 2015, 91, 235304

[88] A. M. Ferrari, C. Pisani, F. Cinquini, L. Giordano and G. Pacchioni, Cationic and anionic vacancies on the NiO(100) surface: DFT + U and hybrid functional density functional theory calculations, J. Chem. Phys., 2007, 127, 174711

[89] M. R. Castell, S. L. Dudarev, G. A. D. Briggs and A. P. Sutton, Unexpected differences in the surface electronic structure of NiO and CoO observed by STM and explained by first-principles theory, Phys. Rev. B, 1999, 59, 7342-7345

[90] D. Ködderitzsch, W. Hergert, Z. Szotek and W. M. Temmerman, Vacancy-induced half-metallicity in MnO and NiO, Phys. Rev. B, 2003, 68, 125114

[91] J. M. McKay and V. E. Henrich, Surface electronic structure of NiO: Defect states, O_2 and H_2O interactions, Phys. Rev. B, 1985, 32, 6764-6772

[92] N. Yu, W.-B. Zhang, N. Wang, Y.-F. Wang and B.-Y. Tang, Large-Area Fabrication of ZnO Nanowire Arrays by Chemical Vapor Deposition, J. Phys. Chem. C, 2008, 112, 452-457

[93] M. J. Frisch et al, GAUSSIAN 09 (Revision B.01), Gaussian, Inc., Wallingford CT, 2009

[94] J. Chai, M. Head-Gordon, Long-range corrected hybrid density functionals with damped atom-atom dispersion corrections, Phys. Chem. Chem. Phys. 2008, 10, 6615-6620

[95] A. Bergner, M. Dolg, W. Küchle, H. Stoll and H. Preuß, *Ab initio* energy-adjusted pseudopotentials for elements of groups 13-17, Mol. Phys., 1993, 80, 1431-1441

[96] T. H. Dunning and P. J. Hay, Methods of Electronic Structure Theory, Modern Theoretical Chemistry, Plenum Press, New York, 1976, ch. 1, vol. 2

[97] T. Yanai, D. P. Tew and N. C. Handy, A new hybrid exchange-correlation functional using the Coulomb-attenuating method (CAM-B3LYP)**,** Chem. Phys. Lett., 2004, 393, 51-57

[98] J. Tomasi, B. Mennucci and R. Cammi, Quantum Mechanical Continuum Solvation Models, Chem. Rev., 2005, 105, 2999-3094

[99] R. W. Zoellner, C. D. Latham, J. P. Goss, W. G. Golden, R. Jones, P. R. Briddon, The structures and properties of tetrafluoromethane, hexafluoroethane, and octafluoropropane using the AIMPRO density functional program, J. Fluorine Chem., 2003, 121, 193-199

[100] D. Johnson III, NIST Computational Chemistry Comparison and Benchmark Database, version 21; August 2020, NIST Standard Reference Database N°101

[101] https://cccbdb.nist.gov/vibscalejust.asp

[102] Y. Zhao, D. G. Truhlar, The M06 suite of density functionals for main group thermochemistry, thermochemical kinetics, noncovalent interactions, excited states, and transition elements: Two new functionals and systematic testing of four M06-class functionals and 12 other functionals, Theor. Chem. Acc. 2008, 120, 215-241

[103] J. B. Fenn, M. Mann, C.K. Meng, S. F. Wong, C. M. Whitehouse, Electrospray ionization-principles and practice, Mass Spectrom. Rev. 1990, 9, 37-70

[104] J. B. Fenn, C.K. Meng, S. F. Wong, C. M. Whitehouse, Electrospray ionization for mass spectrometry of large biomolecules, Science 1989, 246, 64-71

[105] A. E. Reed, F. Weinhold, Natural localized molecular orbitals. J. Chem. Phys. 1985, 83, 1736-1740

[106] K. B. Wiberg, Application of the pople-santry-segal CNDO method to the cyclopropylcarbinyl and cyclobutyl cation and to bicyclobutane, Tetrahedron 1968, 24, 1083-1096

[107] R. S. Mulliken, Electronic Population Analysis on LCAO-MO Molecular Wave Functions, J. Chem. Phys. 1955, 23, 1833–1840

[108] P.-O. Löwdin, On the Non-Orthogonality Problem Connected with the Use of Atomic Wave Functions in the Theory of Molecules and Crystals, J. Chem. Phys. 1950, 18, 365-375

[109] E. Espinosa, M. Souhassou, H. Lachekar and C. Lecomte, Topological analysis of the electron density in hydrogen bonds, Acta Cryst., (1999), B55, 563-572

[110] M. A. Blanco, A. Martín Pendás, E. Francisco, Interacting quantum atoms: A correlated energy decomposition scheme based on the quantum theory of atoms in molecules, J. Chem. Theory Comput., 2005, 1, 1096-1109

[111] P. Giannozzi et al, QUANTUM ESPRESSO: a modular and open-source software project for quantum simulations of materials, J. Phys.: Condens. Matter, 2009, 21, 395502

[112] J. P. Perdew, K. Burke and M. Ernzerhof, Generalized Gradient Approximation Made Simple, Phys. Rev. Lett., 1996, 77, 3865-3868

[113] R. Arletti, E. Fois, L. Gigli, G. Vezzalini, S. Quartieri and G. Tabacchi, Irreversible Conversion of a Water–Ethanol Solution into an Organized Two-Dimensional Network of Alternating Supramolecular Units in a Hydrophobic Zeolite under Pressure, Angew. Chem. Int. Ed., 2017, 56, 2105-2109

[114] M. Cococcioni and S. De Gironcoli, Linear response approach to the calculation of the effective interaction parameters in the LDA+U Method, Phys. Rev. B, 2005, 71, 035105

[115] D. Vanderbilt, Soft self-consistent pseudopotentials in a generalized eigenvalue formalism, Phys. Rev. B, 1990, 41, 7892-7895

[116] K. F. Garrity, J. W. Bennett, K. M. Rabe and D. Vanderbilt, Pseudopotentials for high-throughput DFT calculations, Comput. Mater. Sci., 2014, 81, 446-452

[117] L. Bigiani, D. Zappa, D. Barreca, A. Gasparotto, C. Sada, G. Tabacchi, E. Fois, E. Comini and C. Maccato, Sensing nitrogen mustard gas simulant at the ppb scale via selective dual-site activation at Au/Mn_3O_4 interfaces, ACS Appl. Mater. Interfaces, 2019, 11, 23692-23700

[118] L. Bigiani et al, Engineering Au/MnO_2 hierarchical nanoarchitectures for ethanol electrochemical valorization, J. Mater. Chem. A, 2020, 8, 16902-16907

[119] G. Tabacchi, I. Armenia, G. Bernardini, N. Masciocchi, A. Guagliardi and E. Fois, Energy Transfer from Magnetic Iron Oxide Nanoparticles: Implications for Magnetic Hyperthermia, ACS Appl. Nano Mater., 2023, 6, 12914-12921

[120] M. Kawamura, Y. Gohda and S. Tsuneyuki, Improved tetrahedron method for the Brillouin-zone integration applicable to response functions, Phys. Rev. B, 2014, 89, 094515.

[121] P. E. Blöchl, O. Jepsen and O. K. Andersen, Improved tetrahedron method for Brillouin-zone integrations, Phys. Rev. B, 1994, 49, 16223-16233

[122] S. Hüfner, J. Osterwalder, T. Riesterer and F. Hulliger, Photoemission and inverse photoemission spectroscopy of NiO, Solid State Commun., 1984, 52, 793-796

– Chapter 3 –

From Encapsulation to Recognition: Molecular Sensing in Zeolite-Based Nanomaterials

While Chapter 2 focused on the formation of nanomaterials via fragmentation of molecular precursors, the focus here is placed on a fundamentally different design strategy: the encapsulation of functional molecules within confined nanospaces. Rather than decomposing molecular precursors to form extended solids, this approach centers on the stabilization and spatial organization of intact guest species within the inner cavities of porous crystalline frameworks, such as zeolites. The latter are microporous aluminosilicate materials characterized by periodic channel systems and nanoscale voids, which make them ideal candidates for confinement-driven supramolecular chemistry [1]. Their rigid, shape-selective architectures can host a wide variety of organic molecules, enabling the design of hybrid nanomaterials with tunable chemical reactivity, recognition selectivity, and photophysical behavior. [1,2]

In particular, zeolite L has attracted considerable interest for its unique one-dimensional channels (~7.1 Å in diameter), capable of accommodating aromatic and π-conjugated guests along the channel axis with high orientational order. [1,3] Confinement within such well-defined frameworks gives rise to unique physicochemical phenomena usually absent in homogeneous media. The spatial restriction imposed by the host species can affect the geometry, electronic structure, and reactivity of encapsulated molecules, as well as their mutual orientation and dynamics.[4] In this sense, molecular encapsulation offers a platform to engineer nanomaterial properties without the need for covalent modifications, instead relying on host-guest complementarity and non-covalent interactions, such as dispersion forces, hydrogen bonding, and π-π stacking. Moreover, recent theoretical and experimental work has demonstrated that confinement can modulate excited-state dynamics, promote energy or charge transport, and influence reactivity pathways. [2,5] These effects are particularly relevant in the context of molecular recognition, where the restricted environment can enhance selectivity, organize guest molecules, and exclude competing species. Such properties make zeolites attractive for sensing, catalysis, and photoactive hybrid devices. [1,6]

Despite their apparent simplicity, confinement effects are multifaceted and still poorly understood at the molecular level. Computational chemistry, especially periodic DFT methods, offers a powerful lens through which to explore the structural, energetic, and electronic landscape of encapsulated systems, and to unravel the delicate balance of forces that govern host-guest stability. Molecular recognition in aqueous environments is a complex and multifaceted phenomenon governed not only by direct intermolecular interactions but also by the unique role of water as a structure-directing agent. Hydrophobic effects, together with the ability of water molecules to bridge interacting species, play a decisive role in mediating recognition processes. In protein-ligand complexes, for instance, water molecules inside the hydration shell can profoundly influence both the thermodynamics and kinetics of binding events, acting as structural templates that either facilitate or hinder complex formation depending on their arrangement near the binding site. [7] This water-mediated organization,

essential in biological systems, implies that water molecules may either persist as bridging entities or be displaced upon ligand binding, thereby modulating the overall affinity and specificity of the interaction. [8] In contrast, the role of water in molecular recognition within artificial receptors and material-based systems is far less understood. Macrocyclic hosts such as cucurbit[n]urils, calix[n]arenes, and cyclodextrins, though extensively employed in host-guest chemistry, generally present hydrophobic cavities devoid of anchoring sites for structured water. As a result, partial or complete de-wetting of the cavity often occurs, particularly when accommodating larger organic guests. [9] This de-wetting process typically limits binding affinity and selectivity, in marked contrast to protein-ligand complexes, where structured water is a critical enhancer of molecular recognition. Although ordered water molecules are occasionally detected in the solid-state structures of such synthetic receptors, [10] they do not substantially influence their binding properties. Consequently, current artificial hosts lack the ability to reproduce this fundamental water-mediated feature of recognition that characterizes biological systems.

Hybrid organic-inorganic systems based on microporous zeolites incorporating fluorescent dicationic dyes as cofactors have recently been shown to display remarkable affinity and selectivity toward the neurotransmitter serotonin. The sensing process was evidenced by the appearance of new optical bands in the spectra of the receptor upon titration with serotonin. [11] These "nanosensors" obtained through the simple self-assembly of an aqueous zeolite dispersion with a dye solution, outperform other synthetic receptors in key binding parameters. Spectroscopic and calorimetric investigations revealed that both dye-analyte interactions and analyte-zeolite contacts contribute critically to the exceptionally high affinity and selectivity observed, making these systems promising nanomaterials for sensing applications. Computational studies based on static Density Functional Theory (DFT) models initially appeared adequate to rationalize the origin of the new optical spectral bands. [11] However, these calculations neglected two essential components of the experimental system: the aqueous environment and the zeolite framework itself. [11] In addition, the static models failed to account for the spectral differences observed experimentally when compared to host-guest complexes in cucurbit[8]uril (CB8), where the same dye and analyte adopt a well-defined face-to-face stacking arrangement within the macrocyclic cavity. [12] These limitations suggested that an explicit treatment of water molecules, the zeolite framework, and their dynamic interplay was required to gain deeper insight into the binding and sensing mechanism, as well as to rationalize the additional spectral features observed experimentally.

In light of these considerations, this Chapter presents periodic atomistic models of a zeolite-based nanosensor and examines their properties under both static and dynamic conditions in the presence of explicit water molecules. Specifically, the system was composed of negatively charged zeolite L (ZL, Figure 27) as the host matrix, in combination with the dicationic dye 2,7-dimethyldiazapyrenium (MDAP) and the cationic neurotransmitter serotonin (SERO) (Figure 28). This computational study aims to provide a theoretical framework for interpreting the experimental findings, with particular emphasis on elucidating the origin of the optical spectral changes induced by serotonin binding. Moreover, it seeks to clarify how spatial confinement modulates host-guest interactions, thereby offering key insights into the

characterization and functional behavior of the (MDAP)ZL nanomaterial, which constitutes the central subject of this Chapter.

3.1 Computational Methods and Atomistic Models

Before presenting the results of the static and dynamic simulations discussed in the following Sections, it is essential to provide a detailed overview of the computational models and methodologies employed throughout this Chapter. Unlike isolated host-guest complexes in solution, as discussed previously, the systems investigated here involve the encapsulation of charged organic species within the one-dimensional channels of a crystalline zeolite framework, in the presence of water molecules. This level of complexity requires a computational strategy that combines periodic models, geometry optimizations, excited-state calculations, and *ab initio* molecular dynamics (AIMD). This Section, along with its Subsections, describes the construction and characterization of the atomistic models used to simulate the host matrix (ZL), the two molecular guests (SERO and MDAP), and their corresponding host-guest supramolecular assemblies. Particular attention is given to the structural features of the zeolite channels, the charge states of the guest species, and the spatial arrangement of all components within the periodic simulation cell. The theoretical methods adopted, including the choice of functionals, dispersion corrections, and computational parameters, are also detailed. This comprehensive overview provides the methodological basis for the simulations and analyses reported in the remainder of the Chapter.

3.1.1 Periodic Models of Zeolite L and Related Host-Guest Systems

The zeolite host used in this study has LTL framework type, with an ideal unit cell stoichiometry of $K_9Al_9Si_{27}O_{72}\cdot mH_2O$ and belongs to the *P6/mmm* space group. The primary building units are TO_4 tetrahedra (T = Si or Al), which assemble to form a framework composed of cancrinite cages stacked along the *c* axis. [13,14] This arrangement generates parallel 12-membered-ring (12MR) channels with approximately circular cross-sections, as well as smaller 8-membered-ring (8MR) channels with elliptical sections, both aligned along the *c* axis. The channels are interconnected by non-planar 8MR openings characterized by boat-shaped geometry. As illustrated in Figure 27, the parallel 12MR channels impose significant spatial confinement on guest molecules, such as water in the crystallographic structure of hydrated zeolite L. This one-dimensional channel system is characterized by pore openings of approximately 0.71 nm and maximum internal cage diameters of about 1.2 nm, dimensions that are comparable to those of many neutral or positively charged organic chromophores. These structural features have made ZL an effective host matrix for the confinement of photoactive guest species. [15]

The fluorescent nanozeolite receptors described in Ref. [11], which form the basis of the present study, incorporated the chromophore 2,7-dimethyldiazapyrenium (MDAP) as a guest species within the channels of ZL nanocrystals and were employed for the selective detection of the neurotransmitter serotonin (SERO) (Figure 28). The reported sensing ability was attributed to

the high-affinity binding of SERO to the nanosensor, [11] most likely arising from the formation of an MDAP-SERO intermolecular complex inside the ZL channels.

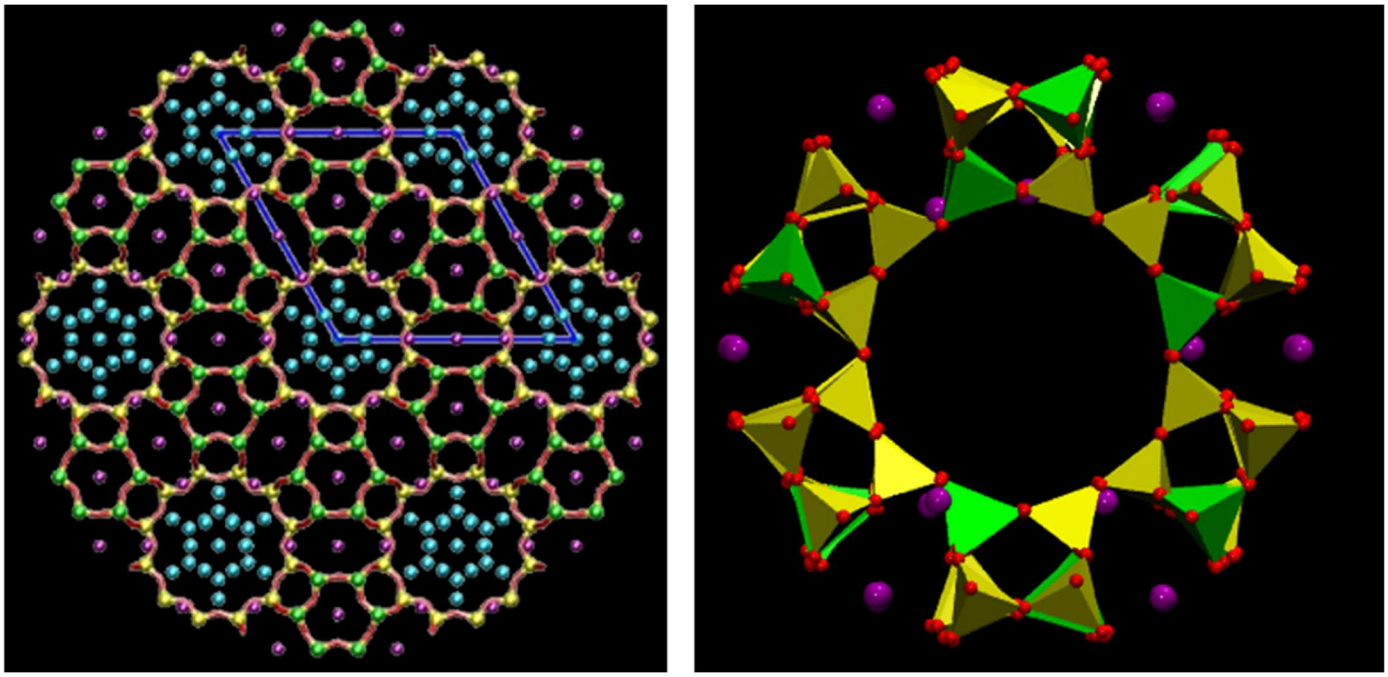

Figure 27: Left panel: Crystal structure of hydrated zeolite L projected onto the *ab* plane, highlighting the main channel, defined by a twelve-membered ring (12MR) and containing water molecules. The channel axis is parallel to *c*. Six-membered-ring (6MR) cancrinite cages and elliptical eight-membered-ring (8MR) channels are also visible. Blue solid lines delineate the unit cell dimensions. Right panel: Graphical representation of a 12MR channel cross-section, showing the 12 TO_4 (T = Al or Si) tetrahedral building units that define the pore opening (diameter: 0.71 nm). Color codes: green/yellow = Al/Si sites; red = framework oxygen atoms; violet = K^+ ions; cyan = water oxygen atoms. Extra-framework sites are displayed with fractional occupancy.

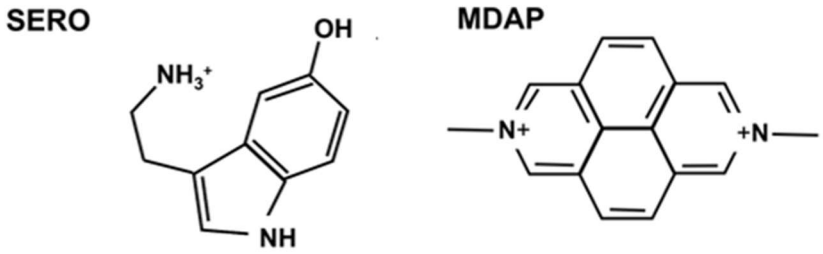

Figure 28: Structural formulas of the neurotransmitter serotonin (SERO, charge: +1) and the chromophore 2,7-dimethyldiazapyrenium (MDAP, charge: +2)

In this study, three periodic models of ZL-based host-guest systems were investigated: (SERO)ZL, containing serotonin as the guest species; (MDAP)ZL, containing the MDAP chromophore as the guest species; and (MDAP+SERO)ZL, containing the MDAP+SERO complex as the encapsulated moiety. In all cases, water molecules were explicitly included within the ZL channels.

3.1.2 Periodic Host-Guest Models: AIMD simulations and Geometry Optimizations

Host-guest inorganic-organic materials based on zeolite systems are crystalline and are typically modeled adopting periodic boundary conditions (PBC). In this approach, the simulation unit cell, containing the coordinates of the zeolite framework, extra-framework cations, guest molecules, and water molecules, is replicated along the three spatial dimensions. The inclusion of water reflects its common presence within zeolite pores under humid conditions. Since crystallographic data were not available in the literature for the three host-guest systems investigated in this work, namely, zeolite L (ZL) hosting SERO, MDAP, or the MDAP+SERO complex, the initial guess structures for the simulations were constructed based on the available crystallographic data of the ZL framework.

The crystallographic unit cell of ZL is hexagonal, with cell parameters $a = b = 18.466$ Å, $c = 7.476$ Å, and $\beta = 120°$. [16] The framework stoichiometry is $Al_9Si_{27}O_{72}$. The crystallographic unit cell also contains 9 extra-framework K^+ cations, which compensate for the negative charge of the 9 AlO_4 tetrahedra. The main channel axis is oriented along the *z*-direction, corresponding to the *c* axis of the crystallographic unit cell. The size of the simulation cell was determined based on the dimensions of the largest guest species considered in this study, namely, the MDAP+SERO supramolecular complex. In particular, a simulation cell composed of three ZL unit cells replicated along the *c* axis was found to be sufficient to accommodate the complex. Special attention was given to ensuring that the periodic images of the guest molecules did not come into close contact. Accordingly, in all calculations performed in this work, the periodic crystal model of ZL consisted of three crystallographic unit cells replicated along the channel axis ($a = b = 18.466$ Å; $c = 3 \times 7.476$ Å; $\beta = 120°$). This model corresponds to a simulation cell with the stoichiometry $K_{27}[Al_{27}Si_{81}O_{216}]$, as 27 monovalent extra-framework cations are required to compensate for the total negative charge introduced by the 27 AlO_4 tetrahedra in the framework.

In the periodic models developed herein, from one to three K^+ cations were removed from the ZL framework to accommodate the incorporation of the charged guest species (SERO and/or MDAP) within the main channel. The eliminated K^+ ions were originally located close to the 12-membered-ring (12MR) channel.

The resulting stoichiometries for the three host-guest systems per simulation cell are as follows:

1) (SERO)ZL: $K_{26}[Al_{27}Si_{81}O_{216}]$, containing SERO (charge +1) and 46 water molecules (total number of atoms in the simulation cell: 514);
2) (MDAP)ZL: $K_{25}[Al_{27}Si_{81}O_{216}]$, containing MDAP (charge +2) and 44 water molecules (total number of atoms in the simulation cell: 513);
3) (MDAP+SERO)ZL: $K_{24}[Al_{27}Si_{81}O_{216}]$, containing the MDAP+SERO complex (charge +3) and 37 water molecules (total number of atoms in the simulation cell: 517).

These stoichiometries were derived by replacing the appropriate number of K^+ cations with the guest species while maintaining overall electroneutrality. In the (SERO)ZL model, only one K^+ was removed to insert the monocationic serotonin; in (MDAP)ZL, two K^+ ions were

replaced by the dicationic MDAP. The corresponding water content amounted to 15.33 and 14.67 H_2O molecules per crystallographic unit cell, respectively, with all water molecules located within the 12MR channels of ZL. Following the same rationale, the guest species in (MDAP+SERO)ZL bear a total positive charge of +3, thus requiring the removal of three K^+ cations to preserve charge balance. The final ZL stoichiometry per simulation cell was $K_{24}[Al_{27}Si_{81}O_{216}]$, with 37 water molecules, corresponding to 12.33 H_2O per unit cell. All water molecules in this model were also confined within the main zeolite channels. The three periodic models described above are graphically represented in Figure 29.

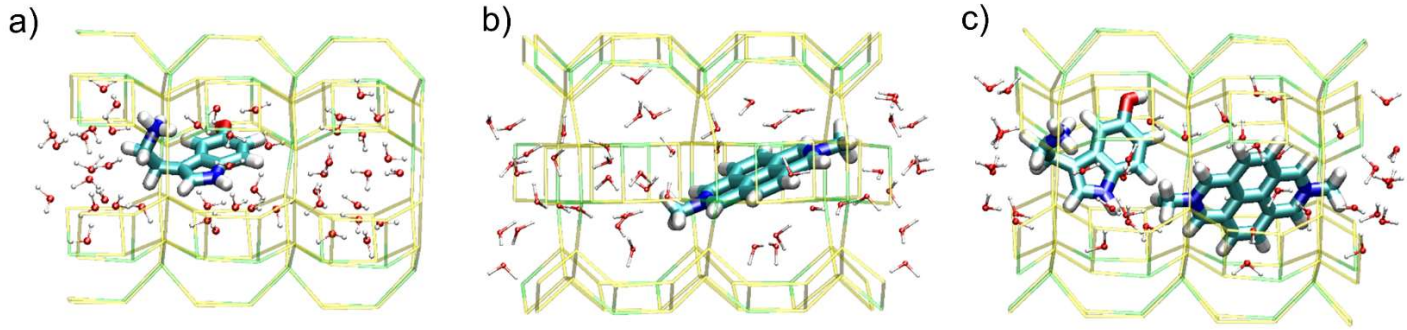

Figure 29: Graphical representation of the simulation cell of the periodic models: a) (SERO)ZL; b) (MDAP)ZL; c) (MDAP+SERO)ZL. In each case, the configuration shown corresponds to the minimum energy structure calculated for each model. Color codes: yellow = Si; green = Al; red = O; cyan = C; blue = N; white=H. Framework oxygen atoms and extra-framework K^+ cations are omitted for clarity.

The number of water molecules included in each model was determined by taking as a reference the water content of hydrated zeolite L. Specifically, the crystallographic unit cell of hydrated ZL contains 18 H_2O molecules, [17] which implies a total of 54 water molecules in the hydrated simulation cell composed of three unit cells. However, the actual number of water molecules in the three host-guest models is lower than 54, as some had to be removed to accommodate the guest species MDAP and SERO. For (SERO)ZL and (MDAP)ZL, the water contents (46 and 44 molecules, respectively) were estimated by subtracting from the total water volume in the simulation cell of hydrated ZL the molecular volume of the corresponding guest species. Similarly, in the (MDAP+SERO)ZL model, the number of water molecules (37) was determined by subtracting the sum of the molecular volumes of MDAP and SERO from the hydrated ZL reference. All molecular volumes were calculated using the Gaussian 09 package. [18] Once the number of water molecules to be removed was established for each model, those found to overlap with the guest species and/or located at less than van der Waals contact distances were eliminated. In the initial guess structures of all models, the main molecular axis of each guest species was aligned with the ZL main channel axis (*z* direction).

For all models, both minimum energy structures at 0 K and structures sampled from the AIMD simulations of the investigated systems at room temperature (298 K) were considered. All calculations were carried out under periodic boundary conditions (PBC) using the PBE [19] approximation to Density Functional Theory (DFT), combined with empirical Grimme's D2 dispersion corrections. [20] Wavefunctions were expanded in plane-waves (PW) basis set and computed at the Γ-point of the Brillouin zone. The PW basis size was defined by cutoff of 25

Ry for the wavefunctions and 200 Ry for the electronic density. The interaction between valence electrons and cores was treated using Vanderbilt-type ultrasoft pseudopotentials for N, O, C, and H atoms, [21,22] while norm conserving pseudopotentials with non-linear core corrections were employed for Si, Al, and K. [23-25] No symmetry constraints were imposed on atomic positions during the calculations; only the simulation cell parameters were kept fixed at the experimental values, while periodic boundary conditions were applied throughout. All AIMD simulations were performed in the framework of the NVT ensemble by using the Nose-Hoover chain thermostats. [26,27] The Car-Parrinello equations of motion [28,29] were integrated with a time step of 5 atomic units (a.u.), corresponding to 0.121 fs, and a fictitious mass of 500 a.u. was assigned to the wavefunction coefficients. The target temperature was set at 298 K. For each of the three models, (SERO)ZL, (MDAP)ZL, and (MDAP+SERO)ZL, an AIMD equilibration of 5 ps was carried out. The total elapsed times for the production AIMD runs were 36.32 ps, 42.35 ps, and 35.09 ps, respectively. Minimum energy structures of the three models were obtained by selecting different configurations sampled along the AIMD trajectories and subjecting them to full geometry optimizations. The lowest-energy structure among these was then retained for further analysis. Geometry optimizations were considered converged when the maximum force on the ions was below 1×10^{-4} Hartree/Bohr. [29] All calculations on the periodic models were performed using the CPMD code. [30]

3.1.3 Calculations on Isolated MDAP and SERO in Gas-Phase

To support the assignment of electronic excitation bands observed in the simulated UV-vis spectra of the MDAP+SERO complex within the ZL framework, additional calculations were carried out on the isolated MDAP and SERO species in vacuum. The geometries of both molecules were optimized at the ωB97XD/6-311G(d,p) level, employing the ωB97XD functional [31], which includes empirical dispersion corrections to account for van der Waals interactions. Subsequently, electronic excitation calculations were performed using the time-dependent density functional theory (TD-DFT) at the CAM-B3LYP/6-311++G(df,pd) level of theory. For both MDAP and SERO, the first 20 excited states were considered. To assess the reliability of the TD-DFT/CAM-B3LYP/6-311++G(df,pd) approach adopted in this study, a benchmark analysis was carried out on the isolated MDAP molecule in the gas phase. First, the MDAP geometry was re-optimized at the MP2/6-311++G(df,pd) level, and the electronic excitations were computed using different levels of theory. Specifically, TD-DFT/CAM-B3LYP/6-311++G(df,pd) results were compared to those obtained using TD-DFT with the PBE0 [32] hybrid functional (TD-DFT/PBE0/6-311++G(df,pd)), and to a higher-level post-Hartree-Fock method, namely Equation-of-Motion - Coupled Cluster with Single and Double excitations (EOM-CCSD). [6,33] For each method, the wavelengths (λ_1, λ_2) and oscillator strengths (f_1, f_2) of the two lowest-energy excitations of isolated MDAP in vacuum were computed. The comparative results are summarized in Table 15.

Table 15: Wavelengths (λ, nm) and oscillator strengths (f) of the two lowest-energy excitations of isolated MDAP in vacuum, calculated at different levels of theory.

Level of Theory	λ_1	λ_2	f_1	f_2
EOM-CCSD/6-311++G(df,pd)	350.07	277.27	0.1294	0.2457
TD-DFT/CAM-B3LYP/6-311++G(df,pd)	355.85	305.43	0.1337	0.2625
TD-DFT/PBE0/6-311++G(df,pd)	374.03	323.57	0.1091	0.2243

From the reported results, it is evident that within the TD-DFT framework the CAM-B3LYP functional reproduces the EOM-CCSD values obtained for the first two excitations of MDAP more accurately than the PBE0 functional. Furthermore, CAM-B3LYP has been shown to provide, on average, the best agreement with EOM-CCSD even for charge-transfer transitions, which could be relevant under the specific confinement conditions investigated in this work. [34] For this reason, the TD-DFT/CAM-B3LYP/6-311++G(df,pd) scheme was adopted for the calculation of the electronic excitations of the target guest species throughout this work. All electronic excitation calculations were performed with the Gaussian 09 code. [18]

3.1.4 TD-DFT Calculations of Electronic Excitation Spectra in Confined Cluster Models

To investigate the electronic excitation of the host-guest systems described above, a complementary computational strategy was adopted. While AIMD simulations based on pure DFT approximations proved effective in predicting the structural properties of ZL-based materials at room temperature, thus enabling meaningful comparison with experimental observations, they do not provide sufficient accuracy for the calculation of electronic excited-state properties, such as UV-vis absorption spectra of embedded photoactive species. To address this limitation, time-dependent density functional theory (TD-DFT) [35] was employed, which, when combined with hybrid functionals and extended basis sets (typically triple-zeta), offers a favorable balance between computational cost and predictive accuracy. In particular, cluster models were adopted to simulate the optical properties of the host-guest complexes. These models were used to calculate the electronic excitation spectra of the guest species incorporated in the zeolite framework, using TD-DFT with the CAM-B3LYP range-separated hybrid functional [36] and the 6-311++G(df,pd) basis set. The cluster models were extracted from the minimum energy structures of the periodic systems, (SERO)ZL, (MDAP)ZL, and (MDAP+SERO)ZL, obtained from the AIMD simulations (see Figure 29). The specific cluster models geometries employed for the TD-DFT calculations are shown in Figure 30.

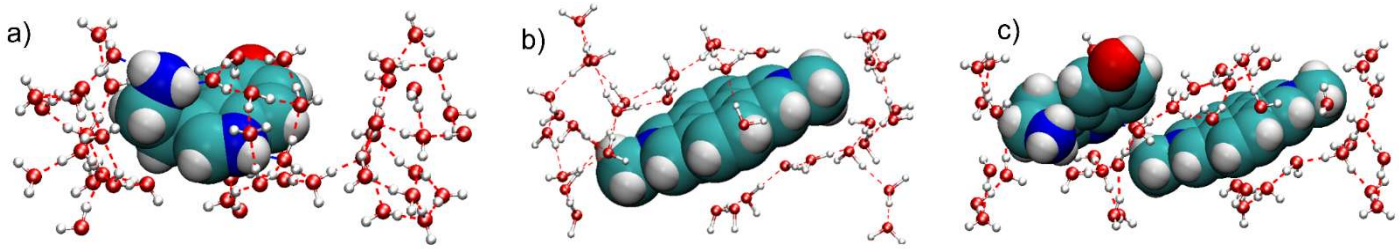

Figure 30: a-c): Graphical representation of the DFT-optimized cluster models employed for the calculation of electronic excitation spectra. Atomic coordinates were extracted from the periodic minimum energy structures of (SERO)ZL, (MDAP)ZL, and (MDAP+SERO)ZL, respectively (see Figure 29). The MDAP and SERO molecules (shown as large spheres) were treated at the CAM-B3LYP/6-311++G(df,pd) level of theory (QM), while surrounding water molecules (ball-and-stick representation) were treated as point charges (MM) using the RESP charges [37] (MM). Atoms color code: red = O; cyan = C; blue = N; white = H. Red dashed lines indicate hydrogen bonds.

To reduce computational costs, MDAP and SERO were treated at the CAM-B3LYP/6-311++G(df,pd) theory level, while the surrounding water molecules were represented as point charges, namely using a "molecular mechanics" (MM) treatment. Specifically, RESP (Restrained Electrostatic Potential) charges [37] were assigned, with values of +0.34195 for hydrogen atoms and -0.6839 for oxygen atoms of water.

The same theoretical protocol was employed to compute the thermally averaged electronic excitation spectra of MDAP and the MDAP+SERO complex. In this case, TD-DFT calculations were performed on similar cluster models, consisting of the organic guest molecules and their surrounding water environments, extracted from 15 and 25 uncorrelated configurations, respectively sampled along the AIMD trajectories of the (MDAP)ZL and (MDAP+SERO)ZL systems. This strategy enabled the generation of thermally-averaged UV-Vis spectra, suitable for direct comparison with the experimental data reported in Ref. 11. Moreover, it provided microscopic insight into the molecular-level factors that may influence both the position and intensity of the absorption bands observed in the experimental UV-Vis spectra [11] of the MDAP+SERO complex confined in ZL. The configurations were randomly selected along the respective AIMD trajectories. For each configuration, the coordinates of the guest organic species, MDAP or MDAP+SERO, were extracted along with those of the nearest surrounding water molecules (43 and 41 for (MDAP)ZL and (MDAP+SERO)ZL, respectively). Periodic images were included where necessary to ensure complete solvation of the guest organic molecules. The thermally-averaged UV-Vis spectra of both the MDAP receptor and the MDAP+SERO complex were then obtained by averaging the electronic excitations calculated for all sampled configurations: 15 for (MDAP)ZL and 25 for (MDAP+SERO)ZL. Representative cluster models employed for the calculation of the thermally averaged UV-Vis spectrum of the MDAP+SERO complex are reported in Sub-section 3.6.2, Figure 88.

To evaluate the influence of the zeolite framework on the electronic spectra, additional calculations were performed including the surrounding ZL atoms treated as point charges. Specifically, a representative slice of the 12-membered-ring (12MR) channel (see Figure 31), encompassing the organic guest molecules, the solvating water molecules, and the pertaining extraframework K^+ cations, was selected from the optimized periodic structures.

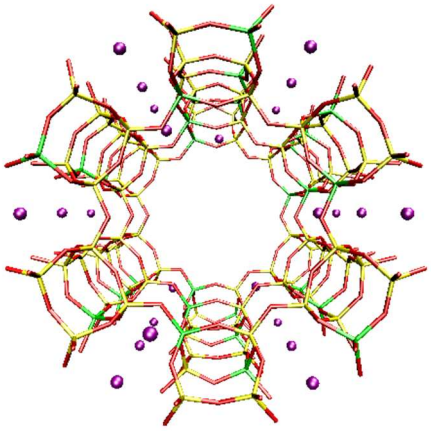

Figure 31: Graphical representation of the zeolite L (ZL) channel used to build the cluster models for the calculation of UV-Vis spectra from the optimized geometries of (MDAP)ZL and (MDAP+SERO)ZL. Atoms color code: yellow = Si; green = Al; red = O; purple = K.

The atomic charges assigned to the zeolite framework were taken from literature data, [38] while the water molecules were described using RESP charges. To preserve electroneutrality, the terminal oxygen atoms of the truncated ZL framework were saturated with hydrogen atoms. A graphical representation of the resulting cluster model for (MDAP+SERO)ZL is shown in Figure 32, clearly illustrating that the framework atoms provide a full embedding environment for the guest species. A similar cluster model was constructed for the (MDAP)ZL system. For both models, the electronic excitation spectra were computed using cluster structures extracted from the respective minimum energy geometries of the periodic systems.

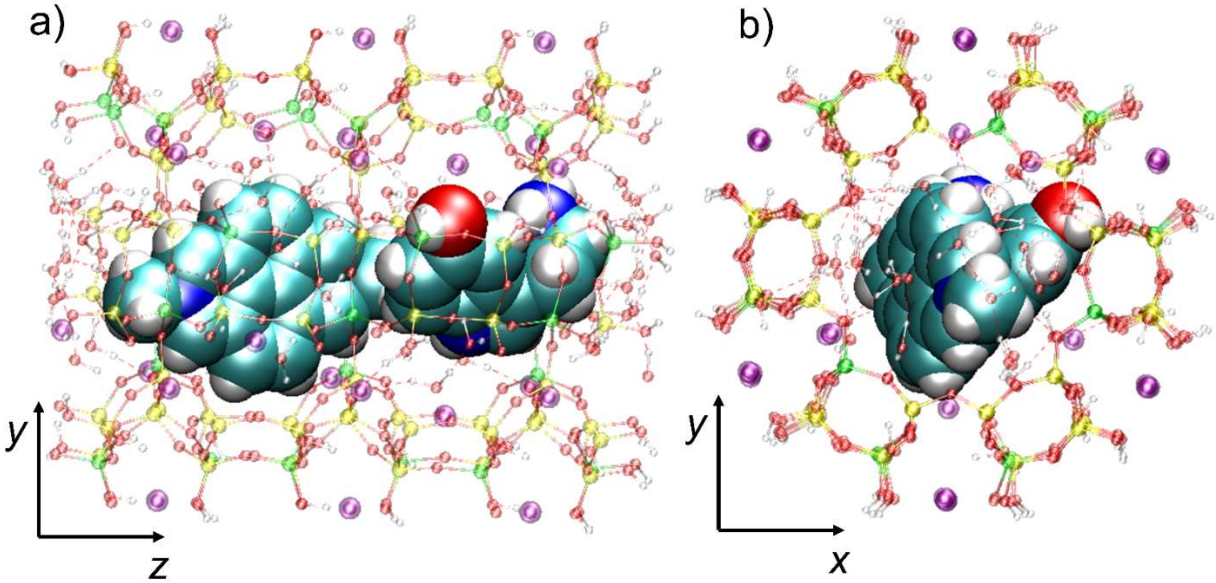

Figure 32: Graphical representation of the cluster model used to compute the UV-Vis spectra of the (MDAP+SERO)ZL minimum energy structure with the ZL environment, shown in two different orientations (a, b). Atomic coordinates were extracted from the optimized periodic geometry reported in Figure 29c. MDAP and SERO (shown as large spheres) were treated at the CAM-B3LYP/6-311++G(df,pd) level (QM), water molecules were included as RESP point charges, and the surrounding zeolite atoms (including capping H atoms) were represented as point charges using values from Ref. [38]. Atoms color code: yellow = Si; green = Al; purple = K; red = O; cyan = C; blue = N; white = H.

With the computational setup and atomistic models established, the following Sections focus on the analysis of the structural and electronic properties of the confined systems. Particular attention is devoted to the interpretation of their spectroscopic response and to the atomistic-level elucidation of the additional absorption band observed upon guest complexation.

3.2 Minimum Energy Structure of the MDAP+SERO Complex Confined within the Zeolite L Channel

The analysis of the confined systems begins with the minimum energy structure of the MDAP+SERO complex within the ZL framework, for which the appearance of a new absorption band was experimentally detected in the UV-Vis spectrum [11]. This system is not only an excellent starting point for understanding the behavior of (MDAP)ZL, namely, the nanomaterial at the core of this study, but also represents the nanomaterial itself in the presence of the target analyte, serotonin. As such, it enables an atomistic interpretation of how two charged species can coexist in proximity despite strong Coulombic repulsion, thereby offering a possible explanation for the experimental spectral signal and shedding light on the factors responsible for its onset. Moreover, this supramolecular system not only provides a structural reference for interpreting the spectroscopic response of the confined species, but also serves as a baseline for comparative analysis across all models investigated in this study.

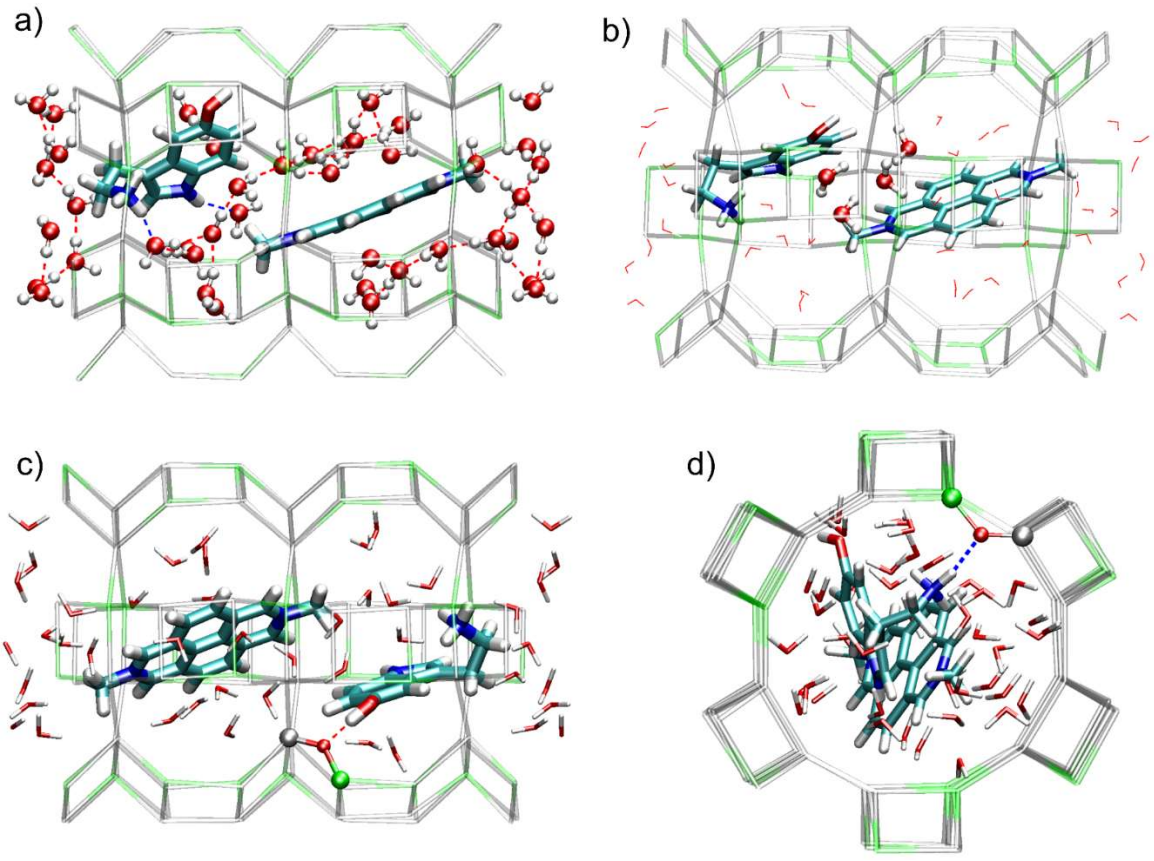

Figure 33: Minimum energy structure of the (MDAP+SERO)ZL system shown in four different orientations, highlighting: a) the MDAP+SERO complex and the surrounding water molecules; b) the four water molecules (ball-and-stick) located between the two positively charged guests, MDAP and SERO; c) the H-bond between SERO -OH group and a framework oxygen atom of ZL (ball-and-stick); d) the H-bonds between the SERO $–NH_3^+$ group and a ZL framework oxygen atom (ball-and-stick). Atoms color codes: grey = Si; green = Al; red = O; blue = N; cyan = C; white = H. Hydrogen bonds are represented as dotted lines. Framework oxygen atoms and extraframework K^+ cations are omitted for clarity.

In the minimum energy structure of (MDAP+SERO)ZL (Figure 33), the aromatic moieties of both MDAP and SERO preserve the characteristic nearly-planar geometry typical of π-

conjugated systems. These units form an intermolecular complex, although they are not directly connected by short-range interactions. The shortest distance between the nitrogen atoms of MDAP and the aromatic carbon atoms of SERO is 5.621 Å, while the closest intermolecular contact is 3.200 Å, indicating a significant spatial separation within the zeolite channel. This observation can be rationalized by considering that both MDAP and SERO are positively charged species (+2 and +1, respectively). Despite the expected Coulomb repulsion, the proximity of the two cationic guests is stabilized by a combination of factors: the negatively charged ZL framework, the geometric confinement imposed by the channel (primarily effective in the *xy* plane, but not along *z*), and most notably, the presence of water molecules. In fact, four water molecules are located between MDAP and SERO (Figure 33b), acting as a dielectric buffer that partially screens the electrostatic repulsion. Zeolitic water molecules are thus found to play a key role in stabilizing this otherwise disfavored supramolecular system. The formation of a triply charged MDAP+SERO complex, highly unfavored in gas phase or in solution, is enabled by the delicate balance between electrostatics, confinement, and solvent-mediated interactions within the zeolite framework. Geometrically, the MDAP molecule is located approximately in the middle of the ZL 12MR channel, with its molecular axis oriented at an about 30° with respect to the ZL channel axis. In contrast, SERO is positioned closer to the pore walls, with its axis forming an angle of 10° relative to the same direction. Notably, the hydroxyl proton of SERO forms a strong hydrogen bond with a framework oxygen atom from an AlO_4 tetrahedron, at a distance of 1.731 Å (Figure 33c). In addition, the $–NH_3^+$ group of SERO establishes two strong hydrogen bonds with the ZL framework (Figure 33d), with N–H···O distances of 1.790 Å and 1.913 Å; the shorter interaction also involves a framework oxygen from an AlO_4 unit. The minimum energy structure of the (MDAP+SERO)ZL system thus serves as the starting point for subsequent investigations, including isolated guest molecules, cluster models, and ab initio molecular dynamics (AIMD) simulations

3.3 Isolated Guest Species: Electronic Excitations for SERO and MDAP

Once the key structural features of the confined (MDAP+SERO)ZL system have been established, attention is turned to the analysis of the individual guest molecules in isolation, with the aim of disentangling their intrinsic electronic properties from those induced by confinement and host-guest interactions.

Serotonin

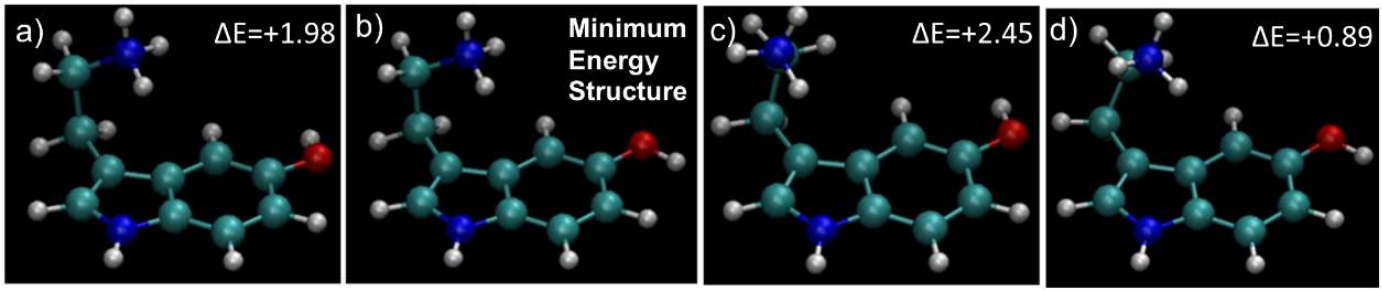

Figure 34: a-d) The four most stable conformers identified for isolated protonated serotonin (SERO). Energy differences (in kcal/mol) are reported with respect to the minimum energy conformer (panel b). Atoms color code: red = O; cyan = C; blue = N; white = H.

As a neutral molecule, serotonin can have many distinct conformational isomers due to conformational flexibility involving both the hydroxyl group and the ethylamine side chain [39]. In this study, serotonin was modeled in its protonated form (Figure 28), consistent with the nanozeolite receptor experiments described in Ref. [11]. A conformational search was thus performed on the protonated species at the ωB97XD/6-311G(d,p) level of theory. The geometries of the four most stable conformers, along with their relative energies (in kcal/mol), are shown in Figure 34. The lowest-energy structure features the hydroxyl group in an outward orientation and the ethylamine chain bent toward the nearly planar aromatic moiety. For the minimum energy structure, electronic excitations were computed using TD-DFT at the CAM-B3LYP/6-311++G(df,pd) level of theory. The molecular orbitals (MOs) involved in the low-energy excitations, as well as the corresponding excitation spectrum, are shown in Figures 35 and 36, respectively.

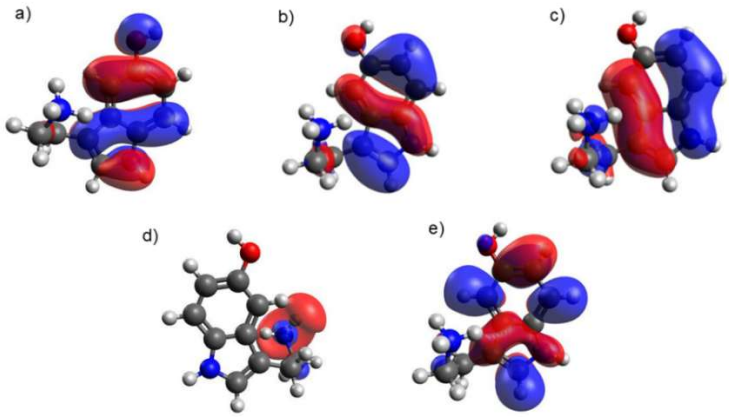

Figure 35: Molecular orbitals of isolated protonated SERO involved in the lower energy electronic excitations: a) HOMO, b) HOMO-1, c) HOMO-2, d) LUMO, e) LUMO+1. Atoms color code: blue = N, gray = C, red = O, white = H.

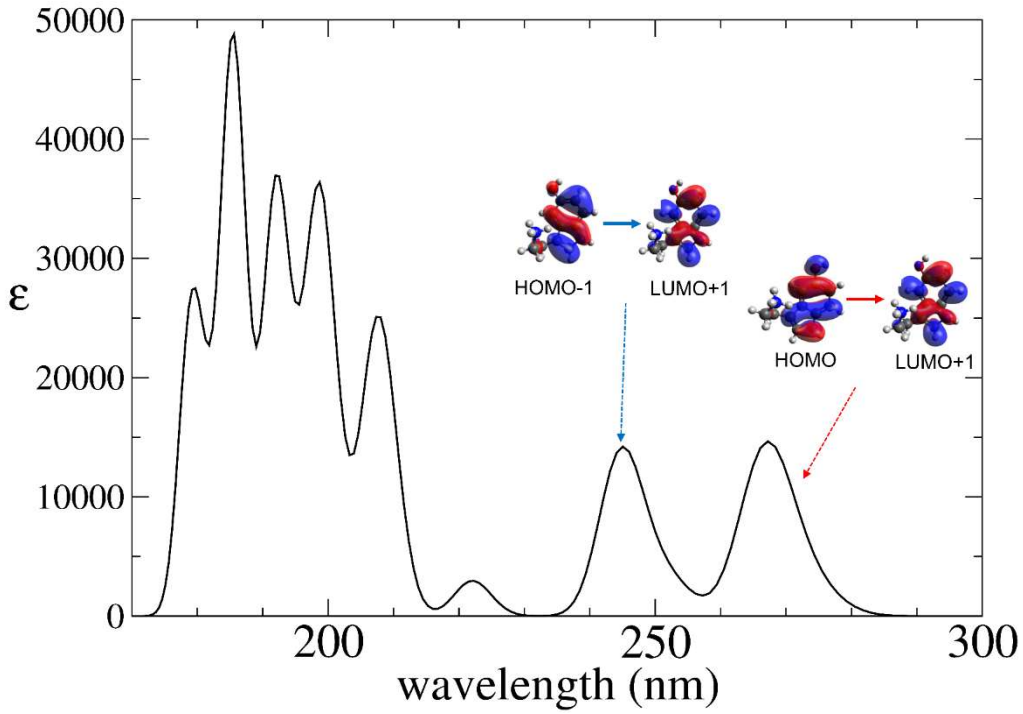

Figure 36: Simulated UV-vis spectrum for isolated protonated SERO in vacuum. The MOs involved in the main components of the two highest-wavelength bands are shown in the insets.

As illustrated in the spectrum, SERO absorbs in the UV region. The two lowest energy absorption bands, peaked at 267 nm and 245 nm, are primarily composed of two electronic transitions (Figure 36). Specifically, the band at 267 nm is mainly assigned to a HOMO → LUMO+1 excitation, while the 245 nm band arises predominantly from a HOMO-1 → LUMO+1 transition. Higher energy peaks, e.g., those at 222 nm, 207 nm, and 198 nm, corresponding to HOMO → LUMO+2, HOMO-2 → LUMO+1, and HOMO → LUMO+5 transitions, respectively, are not expected to significantly contribute to the electronic excitation behavior of the (MDAP+SERO)ZL complex.

MDAP

As previously mentioned, MDAP (Figure 28) was employed as a diacationic reporter dye in the nanozeolite receptors described in Ref. [11]. This molecule is characterized by four condensed aromatic rings and a planar geometry. Electronic excitations were computed using TD-DFT at the CAM-B3LYP/6-311++G(df,pd) level of theory, based on the minimum energy structure of the isolated species. The molecular orbitals (MOs) involved in the low-energy excitations are, as expected, predominantly localized on the aromatic part of the molecule (Figure 37).

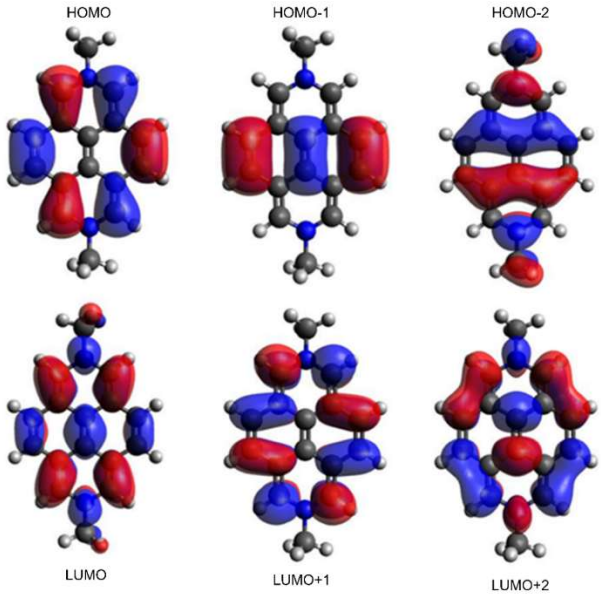

Figure 37: Molecular orbitals of isolated MDAP involved in the electronic excitations spectrum depicted in Figure 67. Atoms color code: blue = N, gray = C, red = O, white = H.

The simulated UV-Vis spectrum is presented in Figure 38, together with the corresponding band assignments. In particular, the highest-wavelength peak at 356 nm is attributed to a HOMO → LUMO excitation, while the peak at 305 nm arises from a HOMO → LUMO+1 transition. At lower wavelengths, the band centered at 223 nm involves HOMO-2 → LUMO and HOMO-2 → LUMO+1 excitations, whereas the band at 188 nm corresponds to a HOMO-1 → LUMO+2 transition. As expected, the computed wavelengths values are lower than those experimentally reported in Ref. [11], primarily because the present calculations refer to an isolated MDAP molecule in vacuum, optimized in its minimum energy structure at 0 K.

Thermal and solvent effects are therefore not accounted for. Nevertheless, these results enable a clear assignment of the MDAP absorption bands in terms of electronic transitions, which will be crucial for interpreting the excitation features of the MDAP+SERO complex.

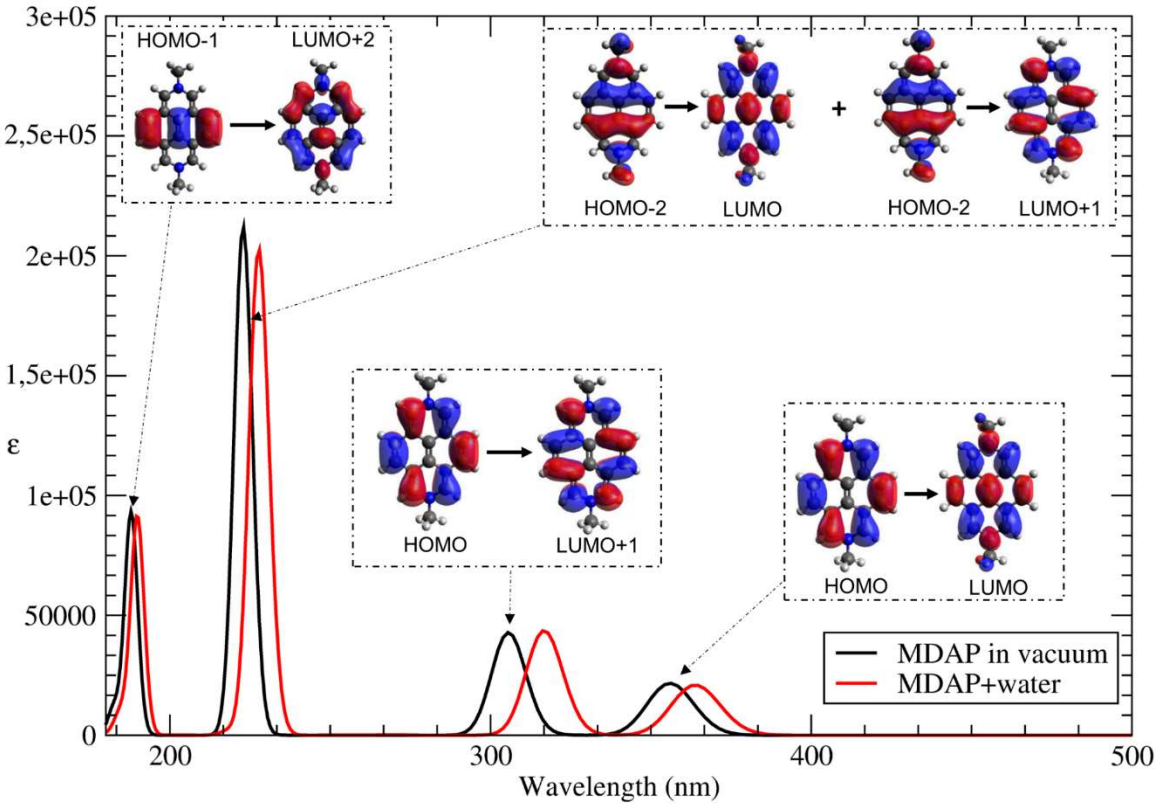

Figure 38: Simulated UV-Vis spectra of isolated MDAP in vacuum (black line) and of a hydrated MDAP cluster model extracted from the minimum energy structure of the (MDAP)ZL system (red line). Band assignments in terms of electronic excitations are shown in the insets, along with the corresponding MDAP molecular orbitals (MOs) involved.

The same computational protocol (TD-DFT/CAM-B3LYP/6-311++G(df,pd)) was employed to calculate the electronic excitations of the MDAP molecule extracted from the minimum energy structure of the (MDAP)ZL system. The molecular orbitals (MOs) involved in the electronic excitations, as well as the band assignments, were found to be analogous to those obtained for MDAP optimized in vacuum. However, the lowest-energy transitions were slightly red-shifted; for instance, the HOMO → LUMO and HOMO → LUMO+1 excitations were found at 367 nm and 317 nm, respectively. This modest red-shift may be attributed to the structural distortion of MDAP in the extracted geometry, which deviates slightly from its optimized structure in vacuum. These findings suggest that, at first approximation, the presence of water within the channel does not alter the nature of the molecular orbitals or the associated electronic transitions. Rather, it induces slight geometric distortions in the MDAP structure, which in turn lead to a modest red-shift in the excitation energies.

3.4 Electronic Spectra of MDAP and SERO: Insights from Cluster Models

As described in Sub-section 3.1.4, the UV-Vis spectra of the investigated host-guest systems were computed using cluster models composed of the organic guest species and the

surrounding water molecules, extracted from the corresponding minimum energy structures. To account for the influence of zeolitic water in the electronic spectra calculations, an explicit description of water molecules was adopted. The simplest approximation for this purpose is to model hydrogen and oxygen atoms as point charges within the Molecular Mechanics (MM) framework. One of the most widely used methods for deriving partial charges in MM approaches with fixed charge force-fields is the Restrained Electrostatic Potential (RESP) [37], which generates charges that reproduce the molecular electrostatic potential in the gas phase, typically computed at the HF/6-31G* level. In this work, partial charges of +0.34195 and -0.6839 were assigned to hydrogen and oxygen atoms of water, respectively. This approach was tested on the minimum energy structure of (MDAP)ZL (see Figure 29b) obtained from periodic DFT calculations. Specifically, to build a cluster model for the excited states calculation of MDAP with a MM treatment of water, the coordinates of both MDAP and the surrounding H_2O molecules were extracted from the optimized (MDAP)ZL structure. A TD-DFT calculation including the first 20 excited states was then carried out. The resulting model, shown in Figure 39, consists of MDAP treated at the QM level and 43 water molecules treated at the MM level. The corresponding electronic spectrum is presented in Figure 38, together with the previously discussed spectrum of isolated MDAP in vacuum (see Section 3.3). As mentioned before, TD-DFT results indicate that both the band assignments and the character of the molecular orbitals involved in the excitations remain unchanged compared to isolated MDAP. However, the comparison between the two spectra in Figure 38 reveals that all absorption bands of hydrated MDAP are red-shifted relative to those of the isolated molecule. Interestingly, the HOMO → LUMO and HOMO → LUMO+1 excitations, found at 364 nm and 316 nm, respectively, are slightly blue-shifted with respect to the values obtained for the same MDAP geometry in the absence of water (367 nm and 317 nm). In addition, the spectrum of hydrated MDAP (Figure 38), the band at 227 nm involves HOMO-2 → LUMO and HOMO-2 → LUMO+1 transitions, while the band at 190 nm corresponds to a HOMO-1 → LUMO+2 excitation. However, these higher-energy transitions are not expected to play a significant role in the sensing mechanism, as suggested by the experimental UV-Vis spectra reported in Ref. [11].

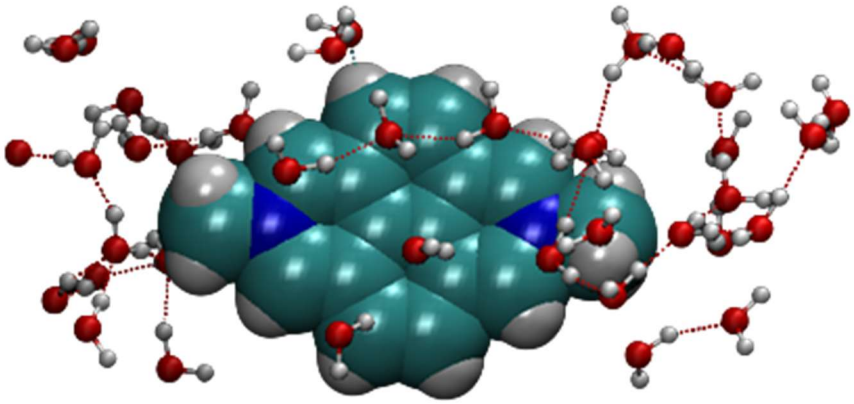

Figure 39: Cluster model extracted from the minimum energy structure of (MDAP)ZL, consisting of MDAP and 43 water molecules. MDAP (represented as large spheres) is treated at the TD-DFT/CAM-B3LYP/6-311++G(df,pd) level (QM), while water molecules (shown in ball-and-stick) are described as point charges within a molecular mechanics (MM) framework.

To validate the point-charge treatment of water molecules, a refined model was considered in which some water molecules were treated at the TD-DFT/CAM-B3LYP/6-311++G(df,pd) level, as in the case of MDAP. To limit the computational cost, this approach was applied only to the eight water molecules closest to MDAP, as these are expected to interact most strongly with the dye. The remaining water molecules were modeled using RESP point charges, as in the previous model. A TD-DFT calculation including the first twenty excited states was performed on this hybrid system. The HOMO → LUMO and HOMO → LUMO+1 excitations were found at 368 nm and 320 nm, respectively, slightly red-shifted relative to the values obtained using point charges for all water molecules. This small difference supports the use of the RESP model for describing the surrounding water molecules in MDAP excitation calculations. Consequently, the RESP point-charge approach was also adopted for the TD-DFT simulations of hydrated SERO. In this context, the first twenty excited states of protonated SERO were calculated using TD-DFT at the CAM-B3LYP/6-311++G(df,pd) level, on a cluster model (Figure 30a) extracted from the periodic minimum energy structure of (SERO)ZL. The model includes the SERO molecule and 46 surrounding water molecules, the latter treated using the RESP point charge approach. The resulting electronic spectrum was compared with that of isolated SERO (Figure 40). The inclusion of explicit solvation leads to a modest red-shift of the highest-wavelength absorption band, from 267 nm to 272 nm.

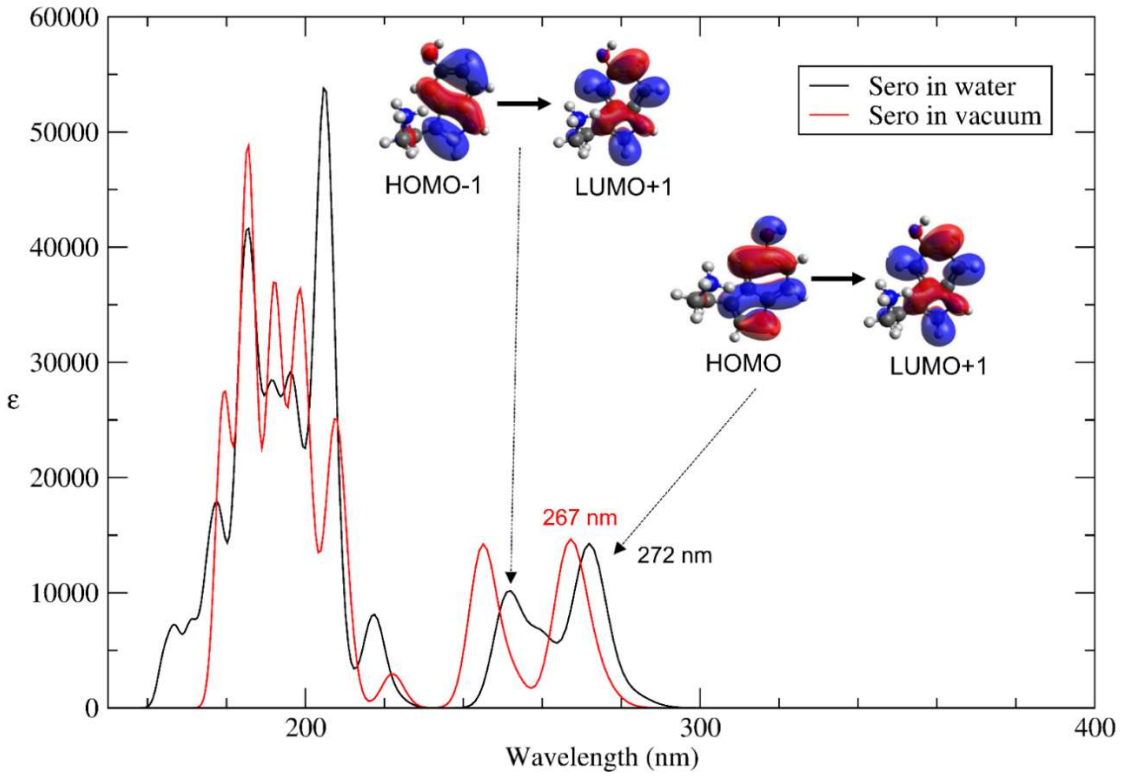

Figure 40: Simulated UV-Vis spectrum of the cluster model extracted from the minimum energy structure of (SERO)ZL, consisting of protonated SERO and 46 surrounding water molecules (Figure 30a). The spectrum of isolated SERO in vacuum is also shown for comparison.

Taken together, these results suggest that the presence of zeolitic water has only a minor effect on the electronic structure and excitation properties of SERO, similarly to what was observed

for MDAP, at least in the first instance. However, this observation does not preclude a more significant role of solvation in modulating intermolecular interactions and electronic behavior in the combined MDAP+SERO system, as will be explored in the following Section.

3.5 Charge-Transfer Interactions in the MDAP+SERO Complex: A Theoretical Insight into the Optical Signature of Supramolecular Recognition

The titration of the (MDAP)ZL nanozeolite receptor with serotonin (SERO) was experimentally shown to induce a strong quenching of MDAP emission, accompanied by the appearance of a broad absorption band in the 430-550 nm range of the UV-Vis spectrum [11]. Structurally, the formation of a supramolecular MDAP+SERO complex within the ZL framework, stabilized by confinement and zeolitic water, offers a plausible microscopic rationale for these experimental observations. To substantiate this hypothesis, the UV-Vis spectrum of the MDAP+SERO complex was simulated using a cluster model extracted from the periodic minimum energy structure of (MDAP+SERO)ZL, previously discussed in Section 3.2. In this Section (and the following Sub-sections), the MDAP+SERO supramolecular system will be investigated in detail through a series of theoretical models. By progressively increasing the complexity of the models and incorporating structural and environmental effects, the goal is to provide an atomistic-level explanation for the emergence of the new spectral feature observed upon serotonin binding. Special attention will be devoted to the role of intermolecular interactions, electronic transitions, and solvation effects in shaping the optical response of this supramolecular sensor complex. This analysis therefore represents a fundamental starting point for understanding the optical response of the (MDAP)ZL nanosensor in the presence of serotonin.

As discussed in the previous Sections, electronic excitation calculations on hydrated MDAP and SERO, based on coordinates extracted from the minimum energy structures of (MDAP)ZL and (SERO)ZL, respectively, have demonstrated that a hybrid QM/MM approach offers a suitable compromise between accuracy and computational cost. In particular, the combination of a quantum mechanical treatment of the organic moieties at the TD-DFT/CAM-B3LYP/6-311++G(df,pd) level with a representation of water via a RESP point-charge model proved to be both reliable and computationally efficient. Accordingly, the same QM/MM methodology was adopted to simulate the electronic excitations of the MDAP+SERO complex. The coordinates of the supramolecular system and the surrounding zeolitic water molecules were extracted from the periodic minimum energy structure of (MDAP+SERO)ZL. The resulting cluster model (Figure 30c) comprises the MDAP+SERO complex, treated at the QM level, and 37 water molecules, treated at the MM level, with the organic guests embedded within the hydrogen-bonding network formed by zeolitic water. A TD-DFT calculation of the first 50 excited states was carried out for this model. The simulated UV-Vis spectrum of the hydrated MDAP+SERO complex is compared with those of the individual hydrated components (MDAP and SERO) in Figure 41.

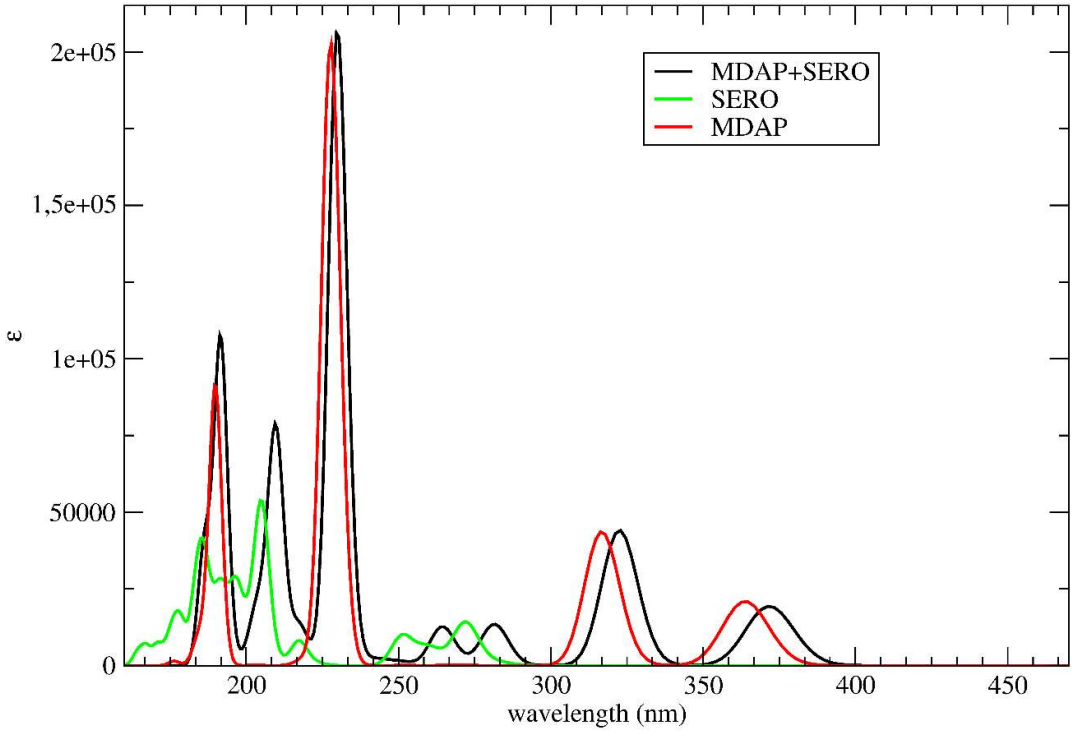

Figure 41: UV-Vis spectra simulated from cluster models extracted from the periodic minimum energy structures of (MDAP+SERO)ZL, (MDAP)ZL, and (SERO)ZL (see Figure 29), highlighting the spectral changes induced by supramolecular interaction.

The simulated spectrum of the MDAP+SERO complex exhibits several similarities with those of the individual components; however, notable differences arise. In particular, the bands associated with the HOMO → LUMO and HOMO → LUMO+1 transitions of isolated MDAP are red-shifted in the supramolecular complex, moving from 364 nm to 372 nm and from 316 nm to 322 nm, respectively. A red-shift is also observed for the higher energy MDAP bands, which shift from 227 to 230 nm and from 190 to 192 nm upon complexation with SERO. Also the absorption features associated with SERO undergo red-shifts in the MDAP+SERO system, particularly in the 240-280 nm region, which corresponds to its two lower energy excitations. These findings are confirmed by the detailed band assignments reported in Table 16 and by the analysis of the molecular orbitals (MOs) involved in the electronic transitions, shown in Figure 42. Although a few MOs are delocalized over both molecular fragments (e.g., MOs 117, 118, and 135 in Figure 42), the majority remain spatially localized either on MDAP or on SERO only. Remarkably, the data reported in Table 16 reveal the presence of two very low-intensity bands in the spectrum of the MDAP+SERO complex, located at 457 nm and 414 nm, i.e., at significantly longer wavelengths than any transition observed in the spectra of the isolated MDAP or SERO components (see also the inset of Figure 43). These new bands correspond to the HOMO → LUMO and HOMO-1 → LUMO excitations in the MDAP+SERO complex, respectively. Crucially, while the HOMO and HOMO-1 molecular orbitals are localized only on SERO, the LUMO is fully localized on MDAP (see Figure 42). Hence, these excitations can be ascribed to charge-transfer (CT) transitions from SERO to MDAP, with SERO acting as the electron donor and MDAP as the acceptor, in line with as proposed in Ref. [11]. Remarkably, such CT bands are completely absent in the spectra of the individual components, and their appearance is attributed to the supramolecular confinement of the two guest molecules within the zeolitic framework. These results thus provide compelling theoretical evidence for the occurrence of a CT process,

offering an atomistic-level explanation for the new absorption feature experimentally observed in the 430-550 nm range upon serotonin addition, as previously hypothesized in Ref. [11].

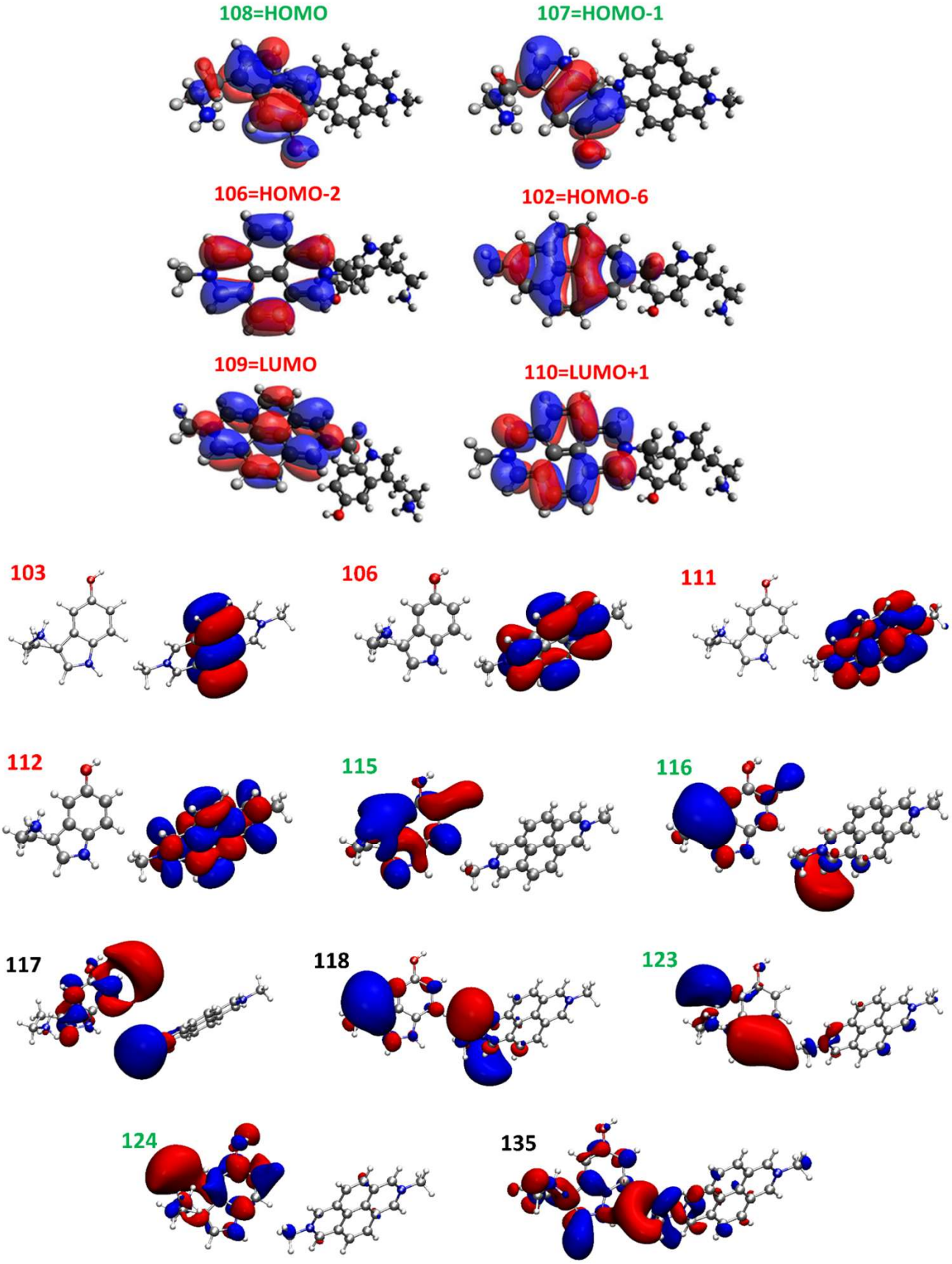

Figure 42: Graphical representation of the MDAP+SERO molecular orbitals (MOs) involved in the electronic excitations reported in Table 16. MOs predominantly localized on MDAP and SERO are highlighted in red and green, respectively, while those delocalized over both moieties are shown in black.

Table 16: Band assignment for the simulated UV-Vis spectrum of the hydrated MDAP+SERO complex (Figures 41 and 43), based on the molecular orbitals depicted in Figure 42. Green and red labels denote MOs predominantly localized on SERO and MDAP, respectively, while black labels indicate orbitals delocalized over both molecular species. Accordingly, excitations colored in green and red can be attributed to transitions localized on the individual SERO and MDAP fragments, whereas black denotes charge-transfer (CT) transitions. For the higher-energy bands, only the main components of the transitions are reported in Table 16.

Excitation	λ	f
108→109 HOMO→LUMO	**456.77**	**0.0001**
107→109 HOMO-1→LUMO	**414.31**	**0.0002**
108→110 HOMO→LUMO+1	403.13	0.0000
106→109 HOMO-2→LUMO	371.74	0.1181
107→110 HOMO-1→LUMO+1	**369.53**	**0.0014**
106→110 HOMO-2→LUMO+1	322.51	0.2724
108→115 HOMO→LUMO+6	281.48	0.0828
107→115 HOMO-1→LUMO+6	264.79	0.0534
108 →116 HOMO→LUMO+7	263.23	0.0248
102→109 HOMO-6→LUMO	229.82	1.1337
106→112 HOMO-2→ LUMO+3	217.01	0.0668
107→116 HOMO-1→ LUMO+7 108→124 HOMO→ LUMO+15	210.39	0.1345
107→117 HOMO-1→ LUMO+8 108→124 HOMO→ LUMO+15	209.59	0.3042
107→118 HOMO-1→ LUMO+9	204.50	0.0513
108→123 HOMO→ LUMO+14	202.74	0.0508
100→110 HOMO-8→LUMO+1	202.50	0.0147
103→111 HOMO-5→LUMO+2	191.57	0.5321
108→135 HOMO→ LUMO+26	186.76	0.1563

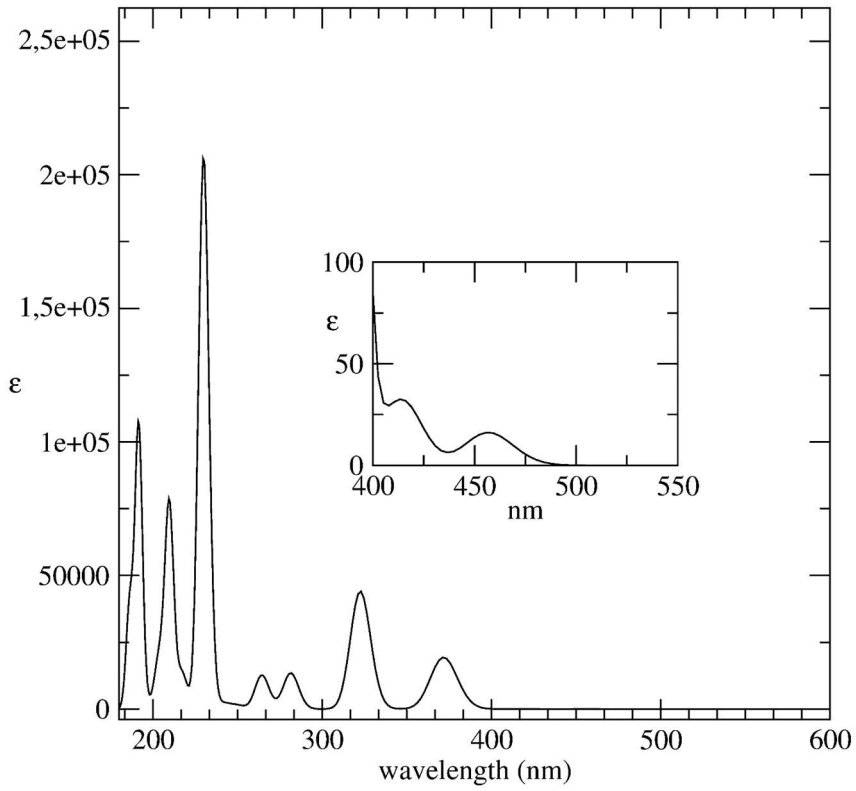

Figure 43: Simulated UV-Vis spectrum of the cluster model extracted from the (MDAP+SERO)ZL minimum energy structure (Figure 29c). The inset highlights the low-intensity charge-transfer (CT) bands observed at 457 nm and 414 nm.

By comparing these findings with those reported in Ref. [11], it appears that, despite the common identification of charge-transfer (CT) bands upon MDAP+SERO complex formation, the present results underestimate both the wavelength and intensity of the experimentally observed CT signal. In particular, experimental UV-Vis spectra revealed the growth of a broad band in the ≈ 430-550 nm range upon titration of the (MDAP)ZL nanozeolite receptors with serotonin. Theoretical calculations reported in Ref. [11] predicted CT transitions in a similar wavelength range. These spectra were obtained using TD-DFT at the PBE0/def2-TZVP level of theory, considering a system composed solely of the MDAP and SERO molecules. The coordinates were extracted from a previously optimized cluster model including two ZL unit cells, MDAP, SERO, and 24 surrounding water molecules [11]. In that study, the influence of water on the electronic properties was accounted for through an implicit solvation approach, namely, the COSMO model [40]. These literature results motivated a complementary analysis in which the MDAP+SERO complex, extracted from the periodic minimum energy structure of (MDAP+SERO)ZL, was subjected to TD-DFT calculations employing an implicit solvent model for water. The aim was to assess the effect of this solvation approach on the computed electronic excitations of the MDAP+SERO complex, particularly on the CT transitions, and to compare the outcomes with those previously obtained using the point-charge model. The results of this investigation are presented in the following Sub-section.

3.5.1 Evaluating the Effect of Implicit Solvent Models on the Electronic Excitations of the MDAP+SERO Complex

In order to investigate the effect of an implicit solvation model, a new cluster was built by extracting the coordinates of the MDAP+SERO complex from the periodic minimum energy structure of (MDAP+SERO)ZL (Figures 29c and 33), excluding the surrounding water molecules. The resulting model therefore includes only MDAP and SERO, preserving their relative geometry and orientation as displayed in Figure 30c. On this cluster, a first TD-DFT calculation was performed in the gas phase (i.e., without any solvation) as a reference. A second calculation was then carried out using the Self-Consistent Reaction Field (SCRF) implicit solvation model for water [41]. Both calculations were conducted at the TD-DFT/CAM-B3LYP/6-311++G(df,pd) level, considering the first 30 excited states. A comparison of the UV-Vis spectra simulated for the MDAP+SERO complex in vacuum, with implicit solvation, and with the RESP point-charge water model is presented in Figure 44. It is worth noting that the molecular orbitals involved in the MDAP+SERO excitations, in both the vacuum and the implicit solvent models, closely resemble those obtained using the explicit point-charge water model (Figure 42). However, the TD-DFT calculation in vacuum, included for reference purposes only, predicts charge-transfer excitations at significantly longer wavelengths compared to the point-charge model. Specifically, the HOMO → LUMO and HOMO-1 → LUMO charge-transfer (CT) transitions, labeled as A and B in Figure 44, are predicted at 612 nm and 466 nm, respectively (Figure 73, top inset). These values, particularly the former, are clearly overestimated with respect to the experimental data, indicating that the MDAP+SERO complex in vacuum does not provide a suitable model for describing the electronic excitation behavior of the complex within the ZL framework. This finding strongly

suggests that a description of the solvent environment, namely water, is essential to accurately reproduce the spectroscopic features of the system. For instance, the RESP point-charge model for water employed throughout this work yields a HOMO → LUMO CT band at 457 nm, i.e., within the 430-550 nm range experimentally observed, although with lower intensity. When considering the TD-DFT calculation using the implicit solvent model, the HOMO → LUMO and HOMO-1 → LUMO CT excitations are found at 351 nm and 333 nm, respectively (Figure 44, bottom inset), i.e., significantly blue-shifted relative to the experimental CT band. These results indicate that the implicit solvation approach fails to capture the essential features of the zeolitic water environment, thereby rendering it unsuitable for modeling this class of confined supramolecular systems. Consequently, the implicit solvent model was not employed in any of the subsequent calculations presented in this work.

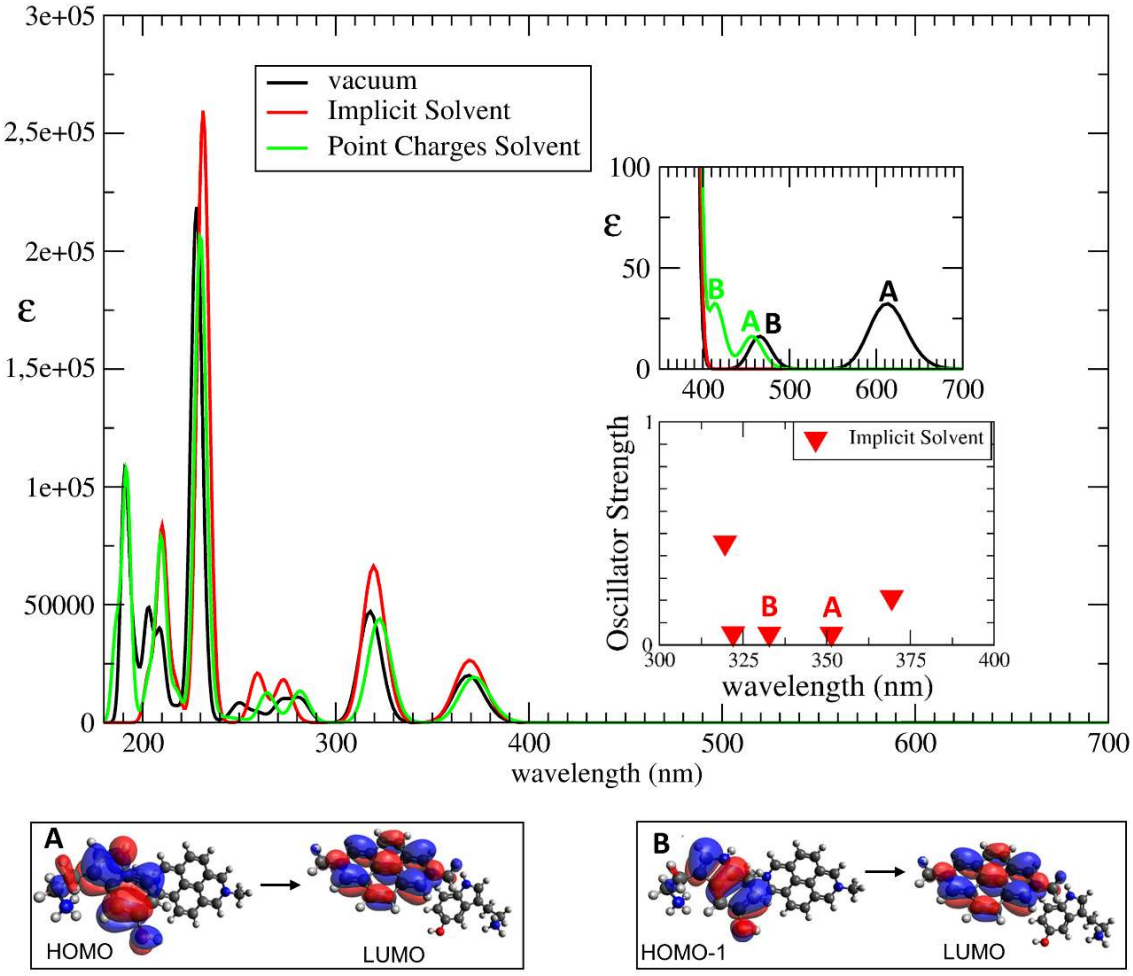

Figure 44: Simulated UV-Vis spectra of the MDAP+SERO cluster model extracted from the minimum energy structure of (MDAP+SERO)ZL, computed in vacuum (black), with an implicit solvent model (red), and with an explicit water environment described via RESP point charges (green). The low-intensity bands corresponding to the HOMO → LUMO and HOMO-1 → LUMO charge-transfer (CT) transitions, labeled A and B, respectively, are highlighted in the insets.

3.5.2 Effect of Periodic Boundary Conditions on Supramolecular Geometry and Charge-Transfer Excitations

To further explore structural factors influencing the occurrence of charge-transfer (CT) excitations in the MDAP+SERO complex, the effect of an alternative molecular arrangement

derived from the periodic (MDAP+SERO)ZL structure has been evaluated. Due to the inherent nature of periodic boundary conditions (PBC), different choices are possible when extracting a finite cluster model from the infinite system. In particular, the relative orientation and positioning of MDAP and SERO units along the crystallographic *c* axis can lead to distinct supramolecular configurations. While the CT analysis presented in the previous Sub-sections was based on a "compact" SERO-MDAP pair, characterized by a short intermolecular separation (3.2 Å), an "inverted" MDAP-SERO arrangement has now been considered, in which the two molecules are geometrically reversed and spatially more distant. This comparative investigation aims to assess whether and how the supramolecular geometry, modulated by the extraction protocol under PBC, may affect the emergence of CT transitions, thus justifying the structural choices adopted throughout this work.

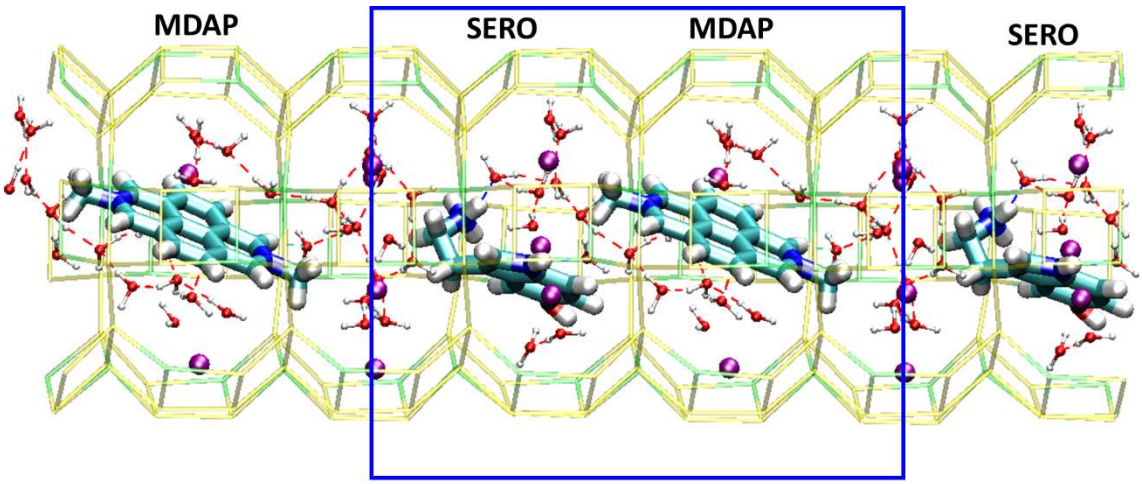

Figure 45: Periodic arrangement of MDAP and SERO units within the ZL channel, illustrating the sequence of neighboring supramolecular pairs along the crystallographic *c* axis. Atoms color code: yellow = Si; green = Al; purple = K; red = O; cyan = C; blue = N; white = H. The blue lines denote the PBC simulation cell along the *c* axis.

In this context, the absence of a unique coordinate origin in systems modeled with PBC can introduce issues when extracting finite clusters from extended periodic structures. In the case of (MDAP+SERO)ZL, the repetition of SERO-MDAP units along the *c* axis generates a continuous supramolecular chain. A representative portion of this sequence is shown in Figure 45, which illustrates the alternating MDAP-SERO-MDAP-SERO arrangement derived from the periodic minimum energy structure. Among the possible geometries, the so-called "inverted" MDAP-SERO cluster, featuring a longer intermolecular separation of 5.6 Å (Figure 46), was selected to assess the impact of this alternative supramolecular orientation on the electronic excitation properties. A TD-DFT calculation was performed on this "inverted" complex at the CAM-B3LYP/6-311++G(df,pd) level of theory, embedding the system in a solvation environment composed of 45 MM water molecules (Figure 46a). For comparison, the structure of the solvated "compact" SERO-MDAP complex is depicted in Figure 46b.

The simulated UV-Vis spectra of both models are compared in Figure 47. In the spectrum of the "inverted" complex, the charge-transfer (CT) signals previously identified at 457 nm and 414 nm for the "compact" MDAP+SERO system are absent (see Table 16 and Figure 43).

Instead, the two highest-wavelength excitations, located at 368 nm and 330 nm, are entirely localized on the MDAP unit and correspond to the HOMO → LUMO and HOMO → LUMO+1 transitions of isolated MDAP, respectively (see also Figure 38). The disappearance of CT bands in the "inverted" geometry can be rationalized by the increased spatial separation between the π-systems of SERO and MDAP. Notably, these findings validate the structural choice adopted in this work: among the two closest SERO periodic images, only one contributes significantly to the optical response of a given MDAP unit. Accordingly, all subsequent calculations will be based on the "compact" MDAP+SERO complex, characterized by the shortest intermolecular distance (3.20 Å).

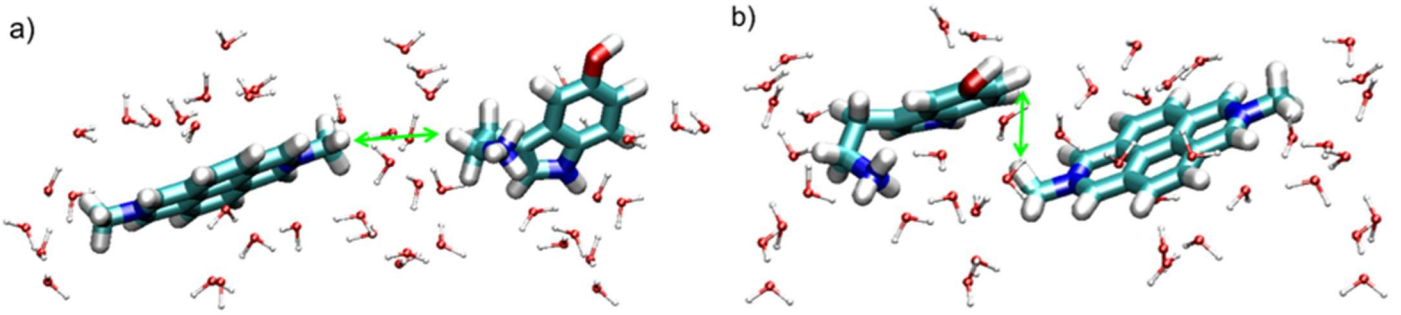

Figure 46: Graphical representation of: (a) the "inverted" MDAP-SERO complex and (b) the "compact" SERO-MDAP complex. Green arrows indicate the shortest intermolecular separations: 5.6 Å in (a) and 3.2 Å in (b). Both geometries are extracted from the minimum energy structure of the periodic (MDAP+SERO)ZL system. Atoms color code: red = O; cyan = C; blue = N; white = H.

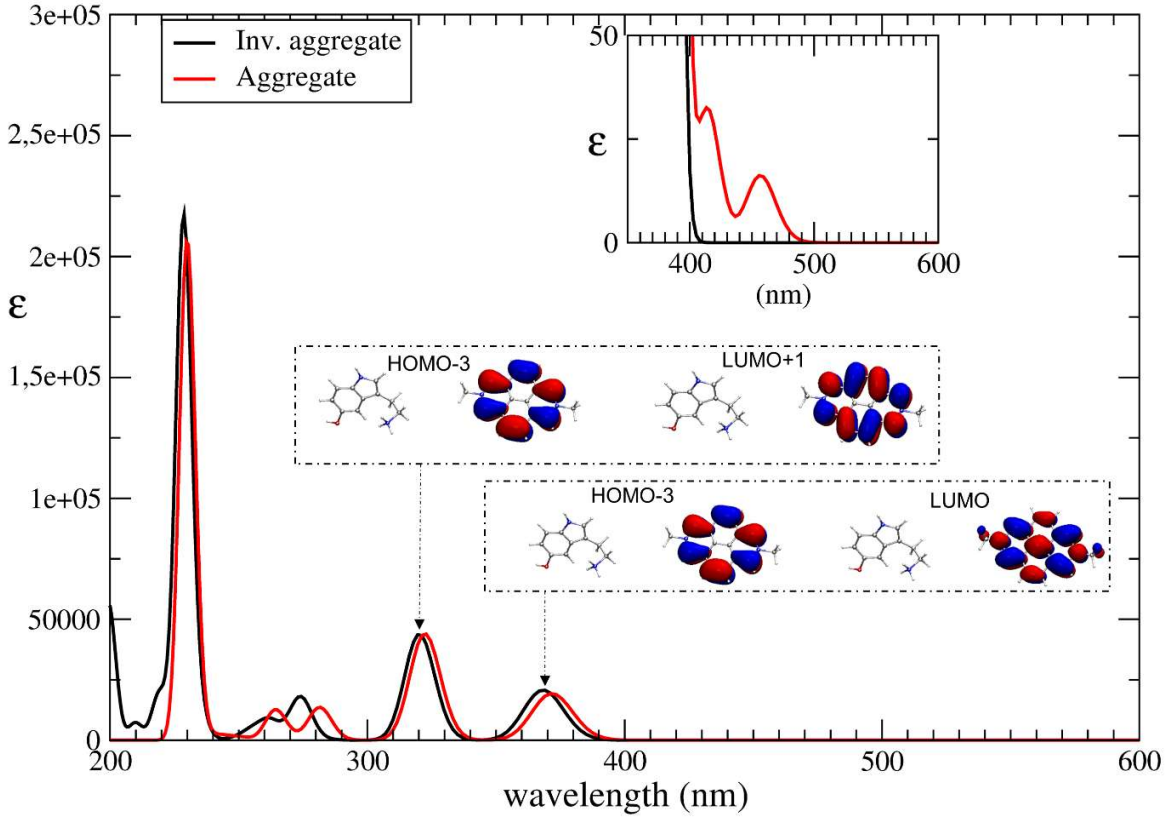

Figure 47: Comparison of the UV-Vis spectra computed for the "compact" MDAP+SERO complex and the "inverted" complex. The top inset provides a magnified view of the 350-600 nm region, highlighting the presence of charge-transfer (CT) bands at 457 nm and 414 nm exclusively in the "compact" model. The bottom insets display the MOs involved in the lowest-energy excitations of the "inverted" complex, which are fully localized on the MDAP unit.

3.6 Thermal Motion and Charge-Transfer Response: AIMD Insights into the Nanosensing Behavior of (MDAP)ZL

The previous Sections were limited to 0 K optimized geometries, neglecting the impact of thermal fluctuations on the structural and electronic properties of the confined systems. However, at room temperature, molecular assemblies undergo continuous nuclear motion, including bond vibrations, rotations, and translations, which may significantly affect both their equilibrium configurations and their spectroscopic response [29]. In order to account for thermal effects, ab initio molecular dynamics (AIMD) simulations were employed. This approach enables the inclusion of finite-temperature nuclear dynamics by propagating classical trajectories under interatomic forces computed at each time from quantum mechanical principles, typically within the framework of density functional theory (DFT) [42]. Originally developed by Car and Parrinello [28], AIMD has become a widely used methodology to explore structure-property relationships in molecular and extended systems beyond the static approximation [28,29]. AIMD simulations at ~300 K were thus carried out for (SERO)ZL, (MDAP)ZL and (MDAP+SERO)ZL systems. Two distinct analyses were performed on the resulting trajectories. First, radial distribution functions (g(r)s) were computed to obtain an average structural picture of the three host-guest materials. Second, thermally averaged UV-Vis spectra were calculated from configurations extracted along the AIMD trajectories of (MDAP)ZL and (MDAP+SERO)ZL, allowing for an evaluation of how dynamic fluctuations influence the spectral signature of the charge-transfer (CT) excitation observed in the static models.

All three host-guest systems considered in this study remain structurally stable along their room-temperature AIMD trajectories. The MDAP molecule consistently occupies a position near the center of the 12MR channel, in agreement with the minimum energy structure of (MDAP)ZL (see Section 3.2). Due to thermal motion, the angle between its molecular axis and the ZL channel axis slightly oscillates around 30°. Nevertheless, within the simulated elapsed time (~42 ps), no translational motion along the channel, which also contains zeolitic water molecules, is observed. Similarly, the SERO molecule maintains its position near the channel walls throughout the trajectory. Both the -NH_3 and -OH groups remain, on average, involved in hydrogen bonding interactions with framework oxygen atoms. In addition, the -NH_3 moiety establishes hydrogen bonds with nearby water molecules. Compared to their respective minimum energy structures, both MDAP and SERO exhibit deviations from planarity in their π-conjugated systems. These distortions are also observed throughout the thermal evolution of the confined MDAP+SERO complex, as illustrated in the trajectory snapshot sequence shown in the "MDAP_SERO_ZL.mpeg" movie available in Ref. [43]. Overall, the complex remains stable under room-temperature conditions. The two guest molecules remain, on average, in close proximity, although a range of intermolecular separations is sampled along the AIMD trajectory. Notably, the individual behavior of the MDAP and SERO units within the complex does not significantly differ from that observed when each species is encapsulated alone within the ZL channel. Specifically, MDAP remains near the center of the channel, while SERO is positioned closer to the pore walls and engages in hydrogen bonding with both framework oxygen atoms and zeolitic water molecules. As previously noted for the optimized (MDAP+SERO)ZL structure, a few water molecules are

located between MDAP and SERO, effectively screening the positive charges of the two moieties. A more detailed structural characterization of the three host-guest systems under room-temperature conditions is provided by the radial distribution functions computed from the AIMD trajectories, as discussed in the following Sub-section. These data not only offer a time-averaged description of key intermolecular interactions, but also provide valuable insights into the role of confinement and solvation effects, which will be further explored in the following Sections and Sub-sections.

3.6.1 Radial Distribution Functions from AIMD: Host–Guest Interactions Supporting Nanosensing Behavior

The H_2O-H_2O radial distribution functions (g(r)) for the three systems, (MDAP+SERO)ZL, (MDAP)ZL, and (SERO)ZL, are reported in Figure 48. In all O-H g(r) profiles, intense and narrow peaks centered at approximately 1.0 Å correspond to intramolecular O-H bonds. The presence of strong intermolecular hydrogen bonding between water molecules is indicated by the prominent peaks at ~1.8 Å, which are consistently observed across all three systems. This is further corroborated by the O-O g(r) functions, which display the main peak near 2.8 Å, characteristic of hydrogen-bonded water networks [44-46]. Additional O-O peaks located around 4.5 Å suggest a close-to-liquid-phase structural organization of water within the ZL channels. This quasi-liquid character appears more pronounced in the (SERO)ZL system and somewhat reduced in the (MDAP+SERO)ZL complex. A third O-O peak at approximately 7.0 Å further supports this interpretation.

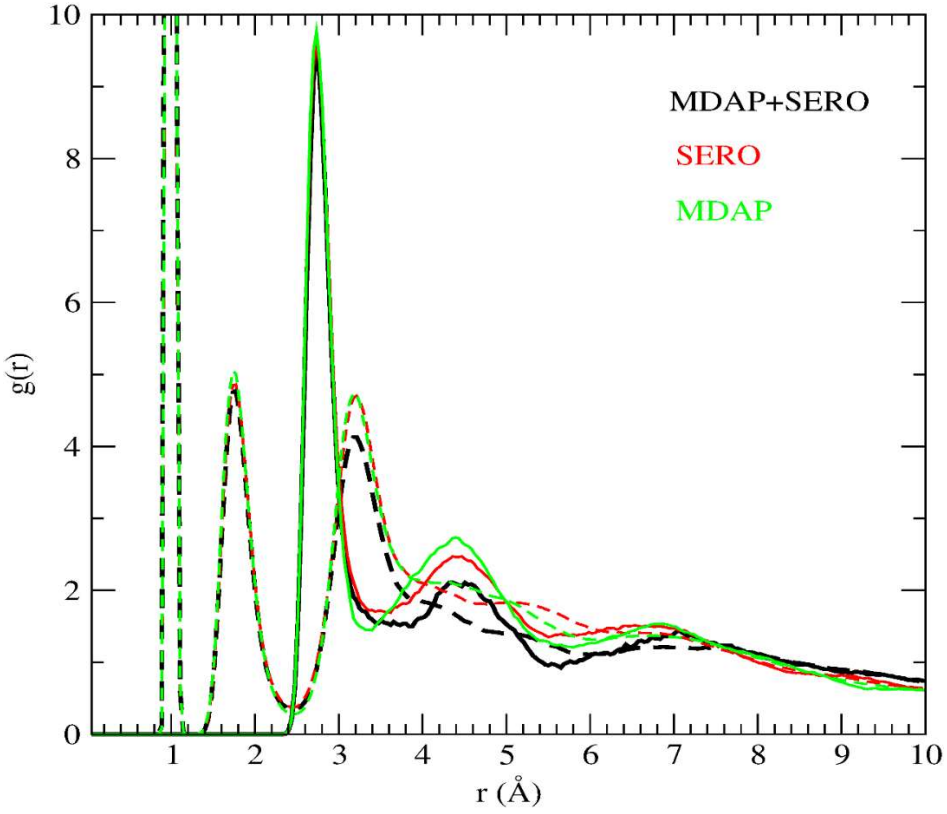

Figure 48: Radial distribution functions g(r) for H_2O molecules computed from the three room-temperature AIMD simulations. Dashed lines correspond to O-H g(r) functions, while solid lines represent O-O g(r) functions. Black, red, and green lines refer to the (MDAP+SERO)ZL, (SERO)ZL, and (MDAP)ZL systems, respectively.

Figure 49 shows the g(r) functions for H_{water}-$O_{framework}$ contacts, highlighting additional interactions between water molecules and the framework oxygen atoms. Peaks located near 1.9 Å indicate the presence of hydrogen bonding between zeolitic water and the ZL framework, in line with typical behavior observed for confined water species [47]. However, this interaction appears weaker than the intermolecular H_2O-H_2O hydrogen bonding discussed above, as evidenced by the comparatively less intense peaks.

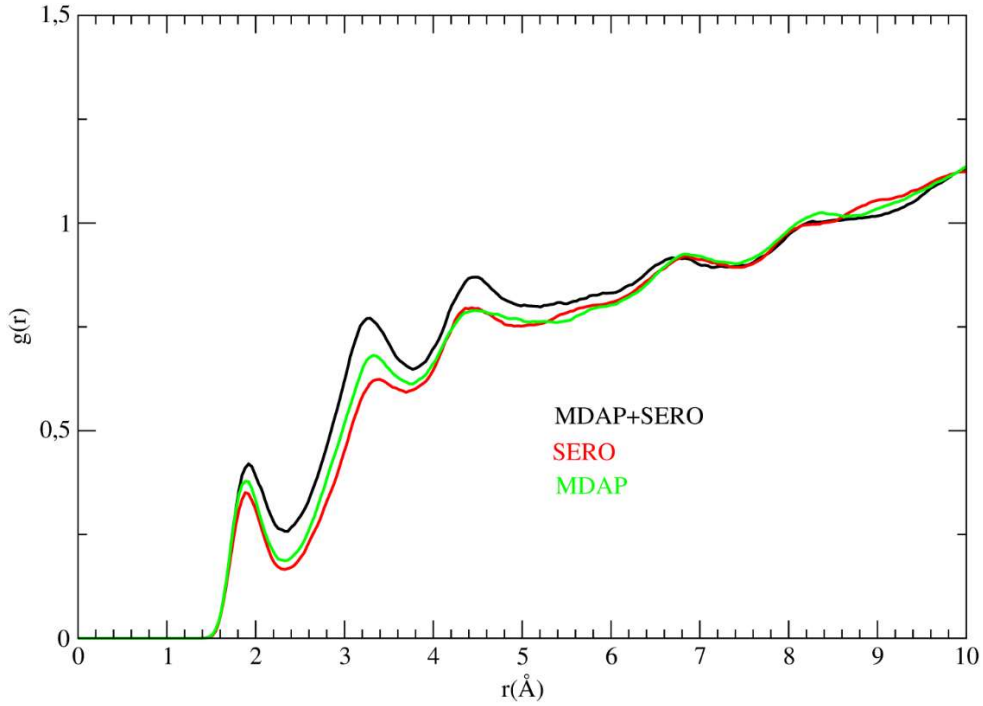

Figure 49: Radial distribution functions g(r) for H_{water}-$O_{framework}$ contacts calculated from the room-temperature AIMD trajectories. The black, red, and green lines correspond to the (MDAP+SERO)ZL, (SERO)ZL, and (MDAP)ZL systems, respectively.

The interactions of SERO with either water molecules or framework oxygen atoms can be quantitatively assessed by examining Figures 50 and 51. The ammonium protons of SERO form strong hydrogen bonds with water oxygen atoms, as indicated by the g(r) peaks at 1.9-2.0 Å. This interaction is particularly pronounced in the (SERO)ZL system. In the presence of MDAP, as in the (MDAP+SERO)ZL system, the strength of this hydrogen bonding is reduced. Conversely, the hydrogen bonding interactions between the SERO ammonium protons and the framework oxygen atoms, generally weaker than those with water, are enhanced upon inclusion of the MDAP dication. This observation is consistent with the experimental results reported in Ref. [11], which indicate an increased affinity of SERO for the nanozeolite receptor (i.e., the (MDAP)ZL system) compared to the parent ZL material. The hydroxyl group of SERO also engages in strong hydrogen bonding with framework oxygen atoms, as evidenced by the sharp peak at 1.9 Å in the top panel of Figure 51. In the presence of MDAP, this interaction is only partially weakened, with the peak position shifting to approximately 2.0 Å. In contrast, the -OH group of SERO exhibits negligible interaction with water molecules, as shown in the bottom panel of Figure 51.

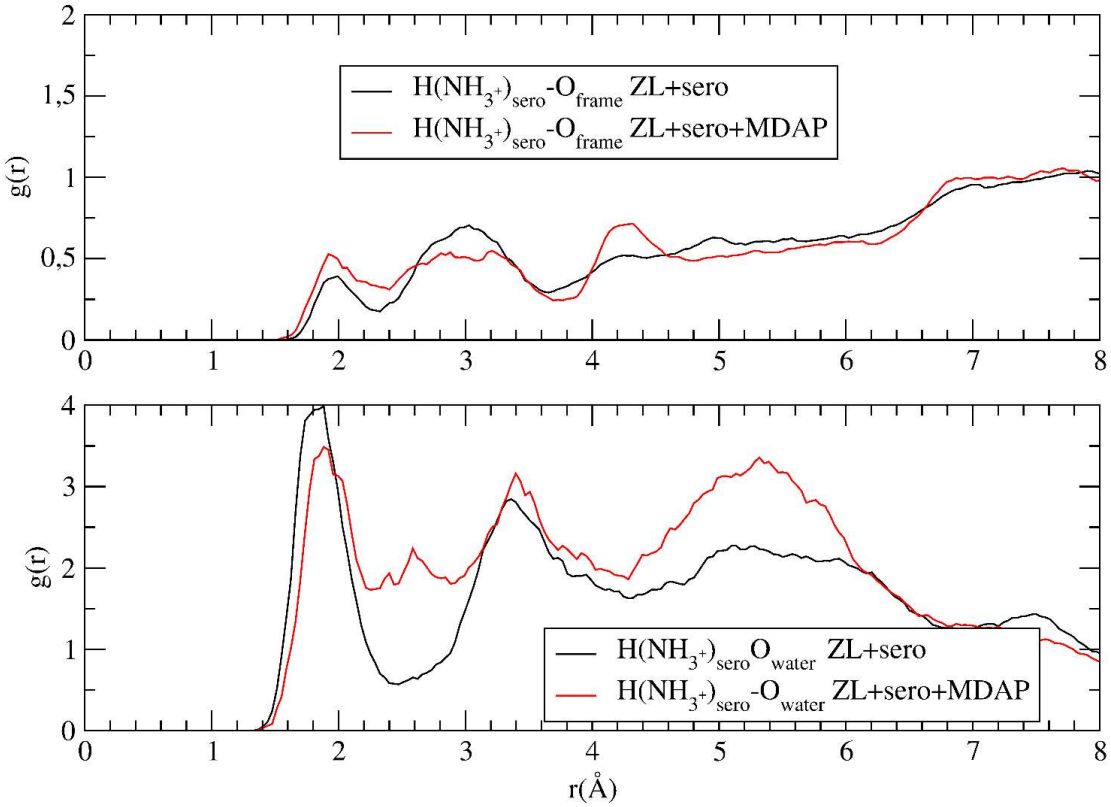

Figure 50: Top panel: Radial distribution functions g(r) between the SERO -NH_3^+ protons and framework oxygen atoms. Bottom panel: Radial distribution functions g(r) between the SERO -NH_3^+ protons and water oxygen atoms. Black and red lines correspond to the (SERO)ZL and (MDAP+SERO)ZL systems, respectively.

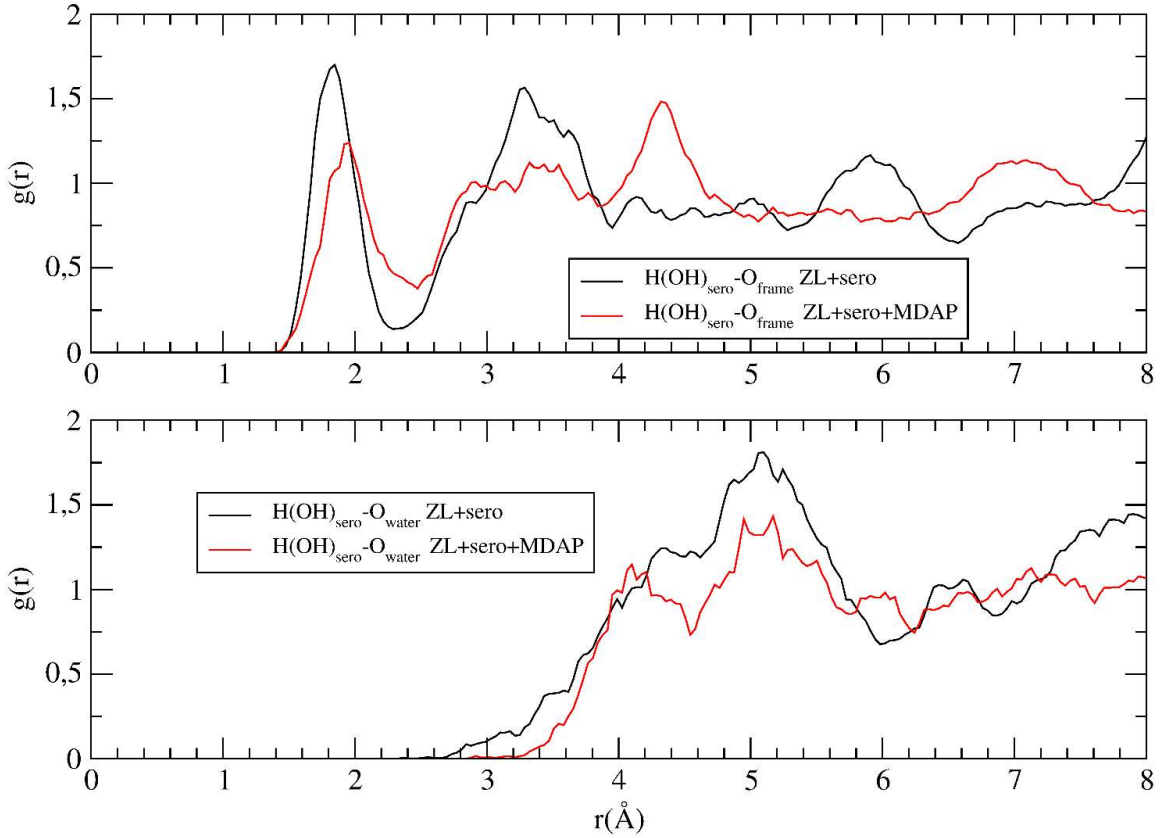

Figure 51: Top panel: Radial distribution functions g(r) between the SERO -OH proton and framework oxygen atoms. Bottom panel: Radial distribution functions g(r) between the SERO -OH proton and water oxygen atoms. Black and red lines correspond to the (SERO)ZL and (MDAP+SERO)ZL systems, respectively.

Analysis of the interactions between the aromatic moiety of SERO and the framework oxygen atoms (Figure 52) indicates that the π-conjugated system of SERO approaches the ZL channel walls more closely in the presence of MDAP. Overall, the g(r) functions describing contacts between SERO atoms and both framework and water oxygen atoms suggest that the binding affinity of SERO toward the host is enhanced upon inclusion of MDAP, in agreement with the experimental findings reported in Ref. [11]. All these observations further support the selective recognition ability of the (MDAP)ZL nanomaterial towards serotonin.

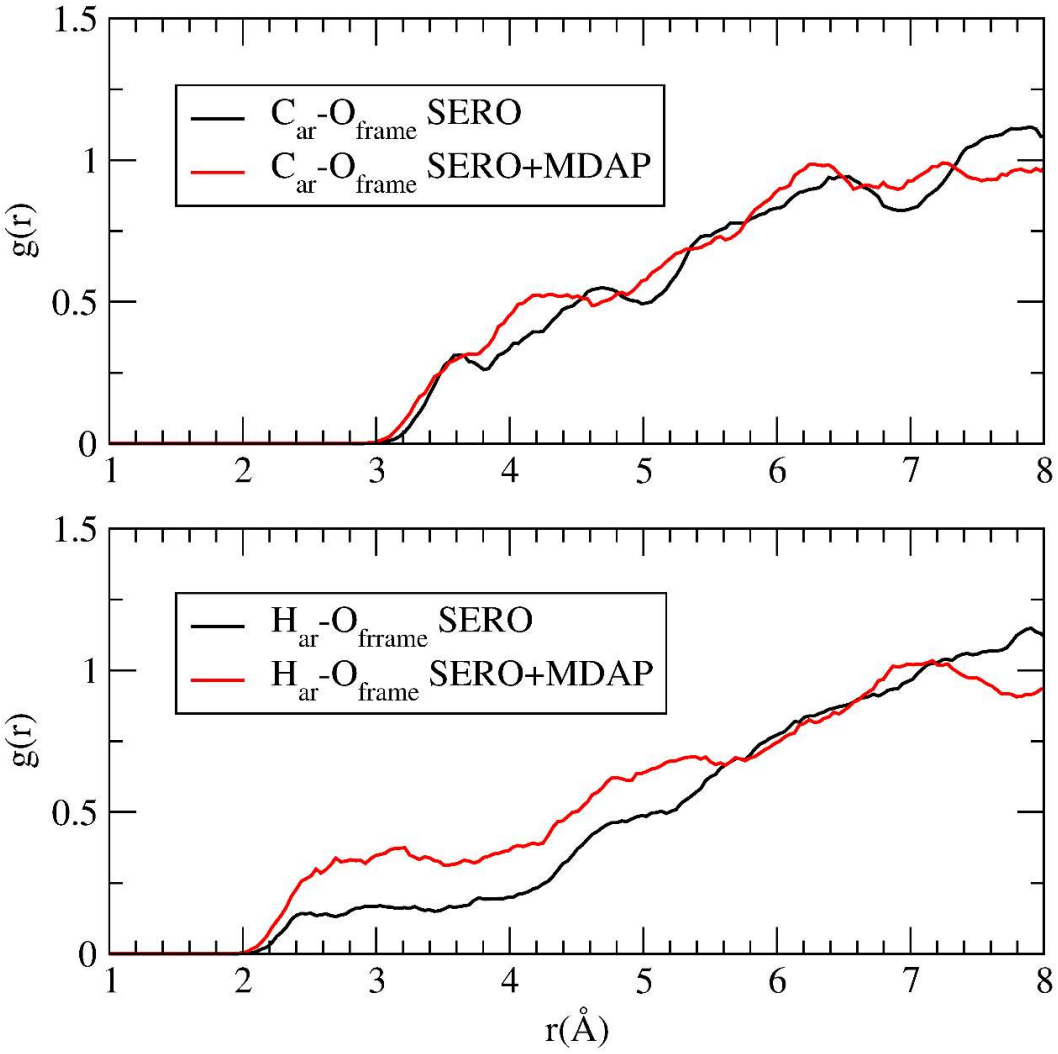

Figure 52: Top panel: Radial distribution functions g(r) between the carbon atoms of the SERO aromatic moiety and the framework oxygen atoms in the (SERO)ZL and (MDAP+SERO)ZL systems. Bottom panel: Radial distribution functions g(r) between the hydrogen atoms of the SERO aromatic moiety and the framework oxygen atoms in the same systems.

The interaction of MDAP with its surrounding environment can be assessed by examining Figure 53, which reports the g(r) functions describing the contacts between the -CH_3 protons and both framework and water oxygen atoms. These g(r) functions are structured, although the broad peaks observed in the 2-3 Å range for the contacts with framework oxygens suggest weak interactions. Moreover, these interactions appear further weakened in the presence of the SERO molecule. Regarding the interaction of the MDAP -CH_3 protons with water oxygens (Figure 53, bottom), the g(r) profiles exhibit relatively high peaks; however, the corresponding distances are more consistent with non-specific van der Waals interactions.

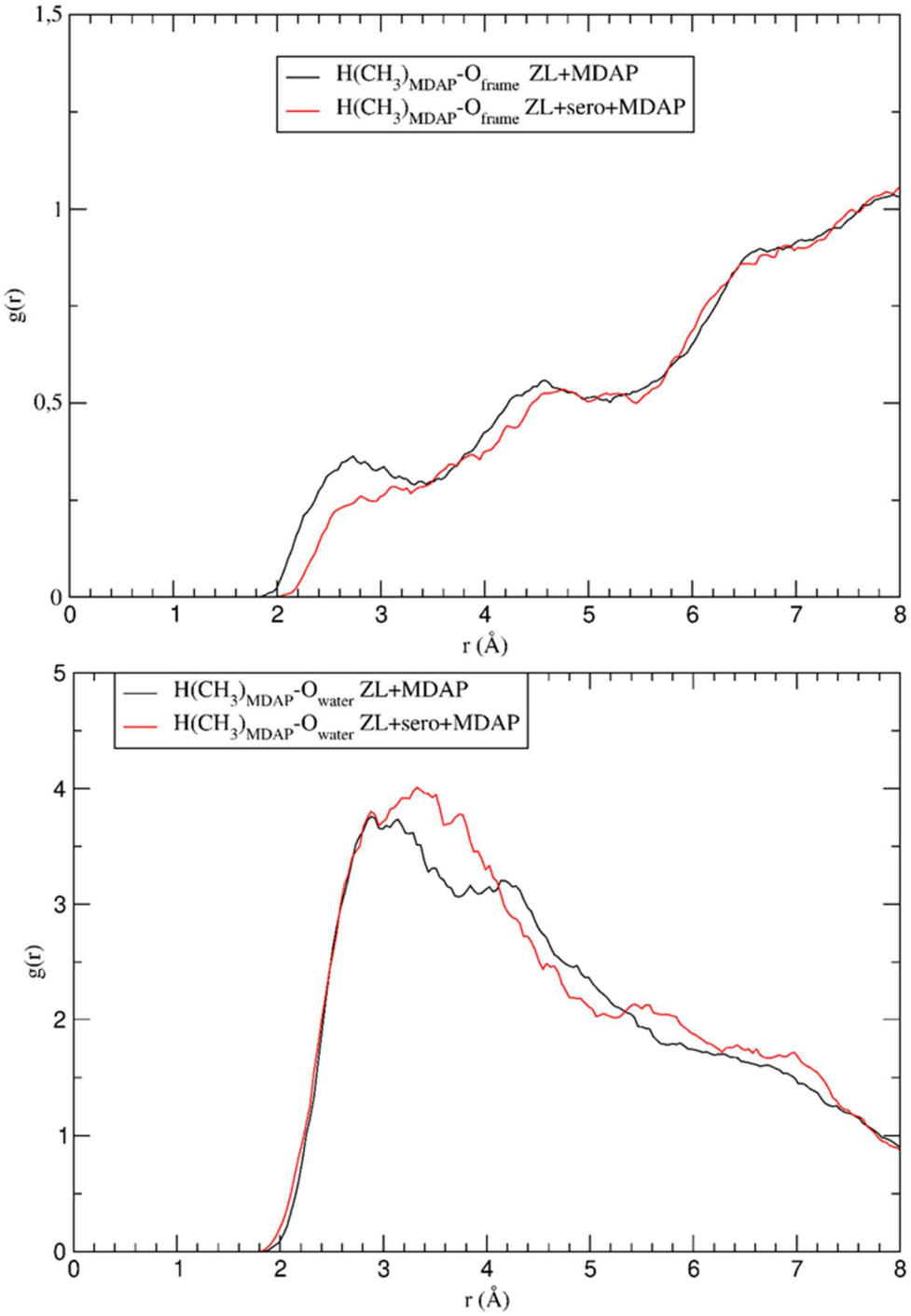

Figure 53: Top panel: Radial distribution functions g(r) describing the interaction between the -CH_3 protons of MDAP and the framework oxygen atoms in the (MDAP+SERO)ZL and (MDAP)ZL systems. Bottom panel: Radial distribution functions g(r) describing the interaction between the -CH_3 protons of MDAP and the water oxygen atoms in the same systems.

Figure 54 provides relevant insight into the behavior of MDAP when encapsulated within the ZL framework. The aromatic core of MDAP, represented by its carbon atoms, remains relatively distant from the channel walls, as evidenced by the absence of distinct features in the g(r) function describing contacts with framework oxygen atoms. In contrast, short-range interactions with water oxygen atoms are observed, with a peak appearing in the 3.2-3.4 Å range. Notably, the interaction between the aromatic carbon atoms of MDAP and water molecules becomes more pronounced in the presence of SERO. This observation suggests that water molecules contribute to screening the Coulomb repulsion between the two positively charged species, SERO and MDAP. A similar effect is seen in the g(r) function describing

contacts between the methyl carbon atoms of MDAP and water oxygen atoms (Figure 54, bottom panel), where the intensity of the peak increases upon inclusion of SERO.

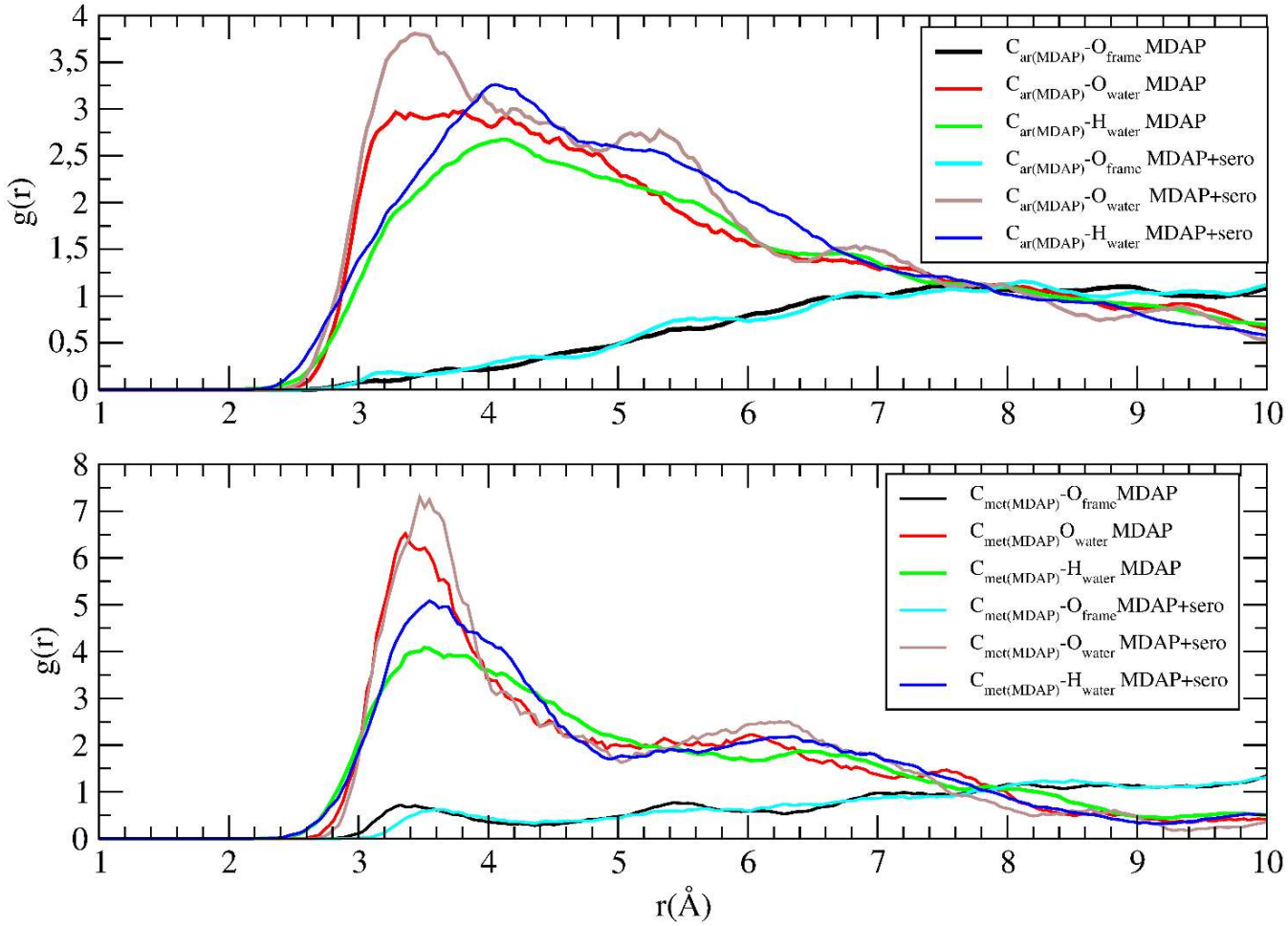

Figure 54: Top panel: Radial distribution functions g(r) describing the contacts between the aromatic carbon atoms of MDAP and both water and framework oxygen atoms in the (MDAP)ZL and (MDAP+SERO)ZL systems. Bottom panel: Radial distribution functions g(r) describing the contacts between the CH_3 carbon atoms of MDAP and both water and framework oxygen atoms in the same systems.

Particularly relevant to the discussion of the sensing behavior of the ZL system upon co-encapsulation of SERO and MDAP is the g(r) function describing the distance between the aromatic moieties of the two guest species. The observed charge-transfer (CT) transition originates from an electron transfer between a singly charged donor (SERO, +1) and a doubly charged acceptor (MDAP, +2), giving rise to a new band. This electronic feature indicates the sensitivity of the (MDAP)ZL system toward serotonin upon guest incorporation. The CT process specifically involves electron transfer from the π system of SERO to a π* orbital of MDAP. As shown in Figure 55, the g(r) function describing the separation between the two π systems highlights the range of intermolecular distances at which such a CT event is likely to occur.

In summary, the radial distribution functions provide essential structural insight into the complex interplay between the confined guest species and the ZL framework under thermal conditions. The enhanced interaction of SERO with the channel walls upon inclusion of

MDAP, the role of water molecules in mitigating Coulomb repulsion between the two cationic guests, and the range of intermolecular distances between their aromatic moieties, all emerge as critical parameters that shape the host-guest architecture and its dynamic evolution. These factors are expected to have a direct impact on the electronic excitation properties of the system, particularly on the charge-transfer (CT) transition, as will be further explored in the following Sub-section through the analysis of thermally-averaged UV-Vis spectra and models including the ZL host explicitly (see Section 3.7).

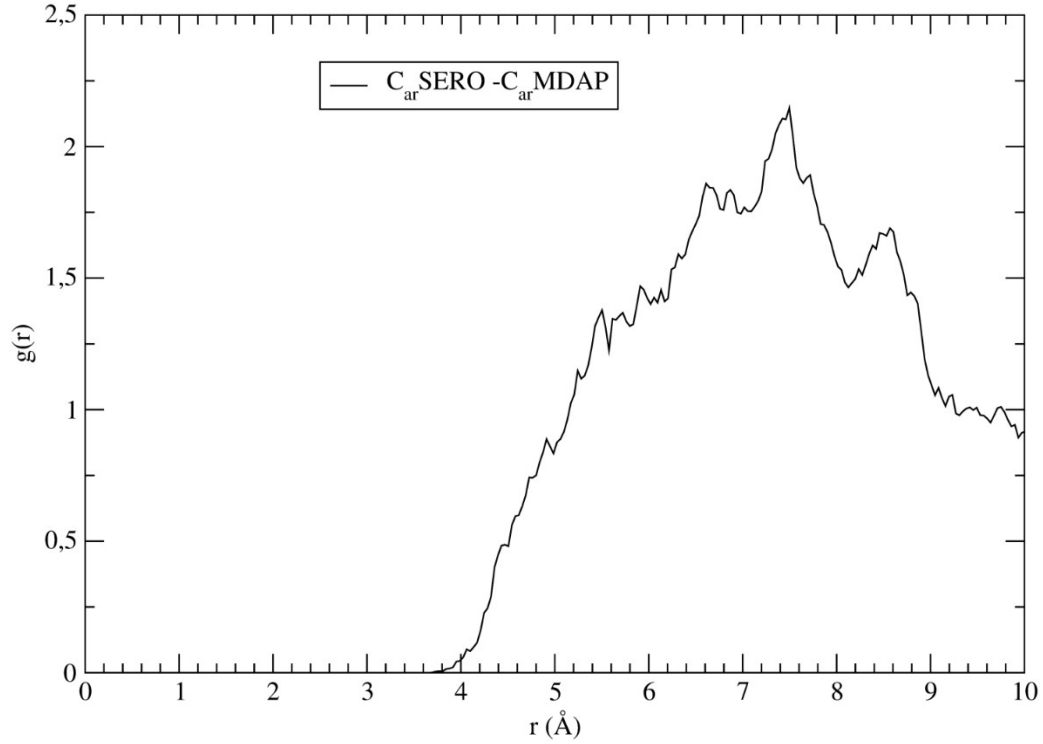

Figure 55: Radial distribution function g(r) describing the intermolecular distances between the aromatic carbon atoms of SERO and those of MDAP in the (MDAP+SERO)ZL system.

3.6.2 Thermally Averaged UV-Vis Spectra and Structural Origins of the Charge-Transfer Response in (MDAP+SERO)ZL

While the UV-Vis spectra calculated for the optimized geometries in Section 3.5 (see Figures 41, 43, 44 and 47) provided useful insight into the nature of the interaction between serotonin and the (MDAP)ZL nanosensor within the zeolite channel, the computed charge-transfer (CT) bands were found to be significantly blue-shifted and less intense than those observed experimentally [11]. This discrepancy suggests that the static approach may underestimate the extent of charge transfer between the two species and neglect important configurational contributions arising from thermal motion. To obtain a more realistic picture of the CT excitation at room temperature, thermally averaged UV-Vis spectra were computed by sampling cluster models of the MDAP system and of the MDAP-SERO complex extracted from randomly selected configurations along the AIMD trajectory.

MDAP

The thermally-averaged electronic spectrum of the (MDAP)ZL system was obtained by averaging the electronic excitations computed for cluster models extracted from 15 representative configurations sampled along the AIMD trajectory. This spectrum was then compared with that calculated for the minimum energy structure of MDAP within the ZL channel using the same computational protocol (see Figure 56).

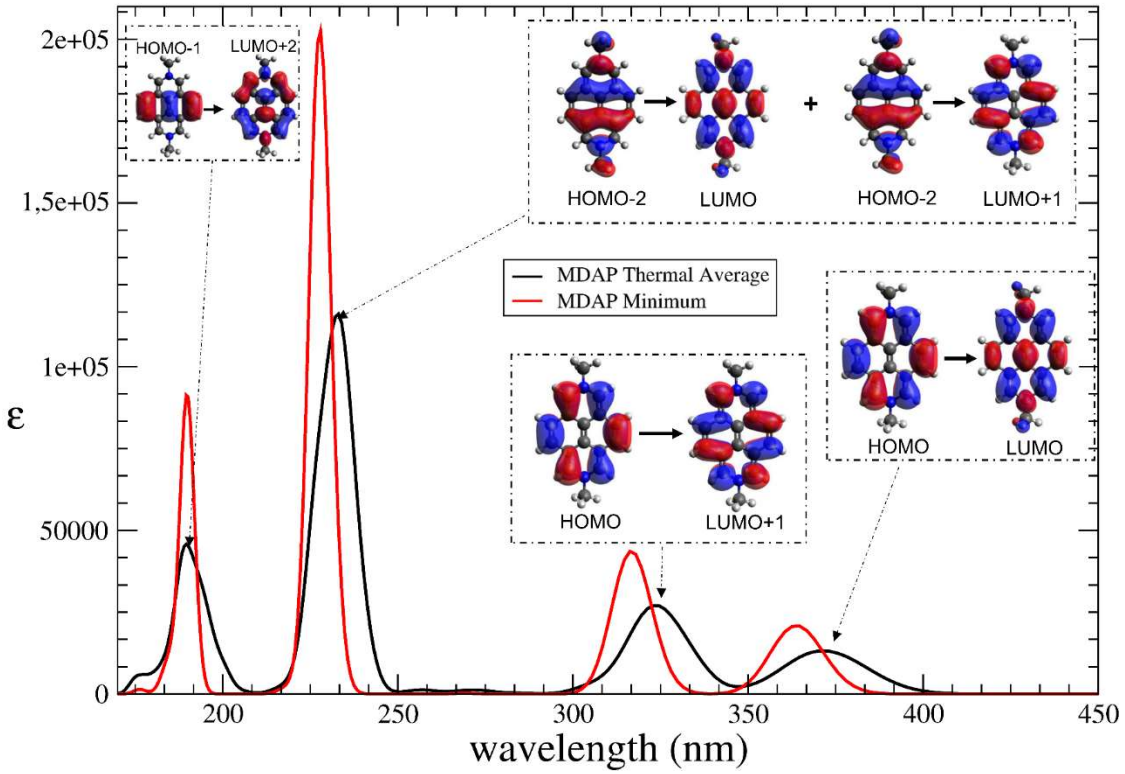

Figure 56: Comparison of UV-Vis spectra calculated for the (MDAP)ZL system: thermally-averaged spectrum obtained from cluster models extracted along the AIMD trajectory (black line) versus the spectrum computed for the minimum energy structure (red line).

As shown in Figure 56, the thermally-averaged spectrum exhibits a closer agreement with the experimental UV-Vis spectrum reported in Ref. [11], both in terms of the relative intensity of the absorption bands and the position of the corresponding wavelengths. Notably, all MDAP-related bands appear broadened and red-shifted with respect to those obtained from the static structure, particularly the transitions involving the HOMO → LUMO and HOMO → LUMO+1 excitations. This red-shift was attributed to slight geometric distortions of the MDAP molecule induced by thermal fluctuations within the zeolite channel, as well as to intermolecular interactions with nearby water molecules. In particular, deviations from planarity of the MDAP π-conjugated system were identified as the primary factor responsible for the observed spectral red-shift and for the emergence of additional low-intensity bands in the 250-280 nm region.

MDAP+SERO

The thermally-averaged UV-Vis spectrum of the MDAP+SERO complex was obtained by averaging the electronic excitations computed for cluster models extracted from 25

configurations sampled along the AIMD trajectory of the (MDAP+SERO)ZL system. As shown in Figure 57, this spectrum is compared with that calculated for the hydrated cluster model derived from the (MDAP+SERO)ZL minimum energy structure (see Figure 30c). As observed for the MDAP-only system, the thermally-averaged spectrum of the MDAP+SERO complex displays broader bands that are red-shifted relative to those obtained from the minimum energy structure. This red-shift is particularly pronounced for the charge-transfer (CT) transitions, which appear as a broad tail in the 450-550 nm region (see inset in Figure 57), in good agreement with experimental observations [11]. Within this CT tail, two distinct features can be identified at 520 nm and 460 nm, corresponding to the HOMO → LUMO and HOMO-1 → LUMO transitions, respectively. These excitations were previously located at 457 nm and 414 nm in the corresponding minimum energy structure (see Figure 43 and Table 16, Section 3.5), highlighting the key role of thermal fluctuations in stabilizing CT transitions towards longer wavelengths, i.e. in lowering the energy cost of electron transfer from SERO to MDAP. Despite this red-shift, the intensity of the CT band remains weak due to the low oscillator strengths associated with these excitations.

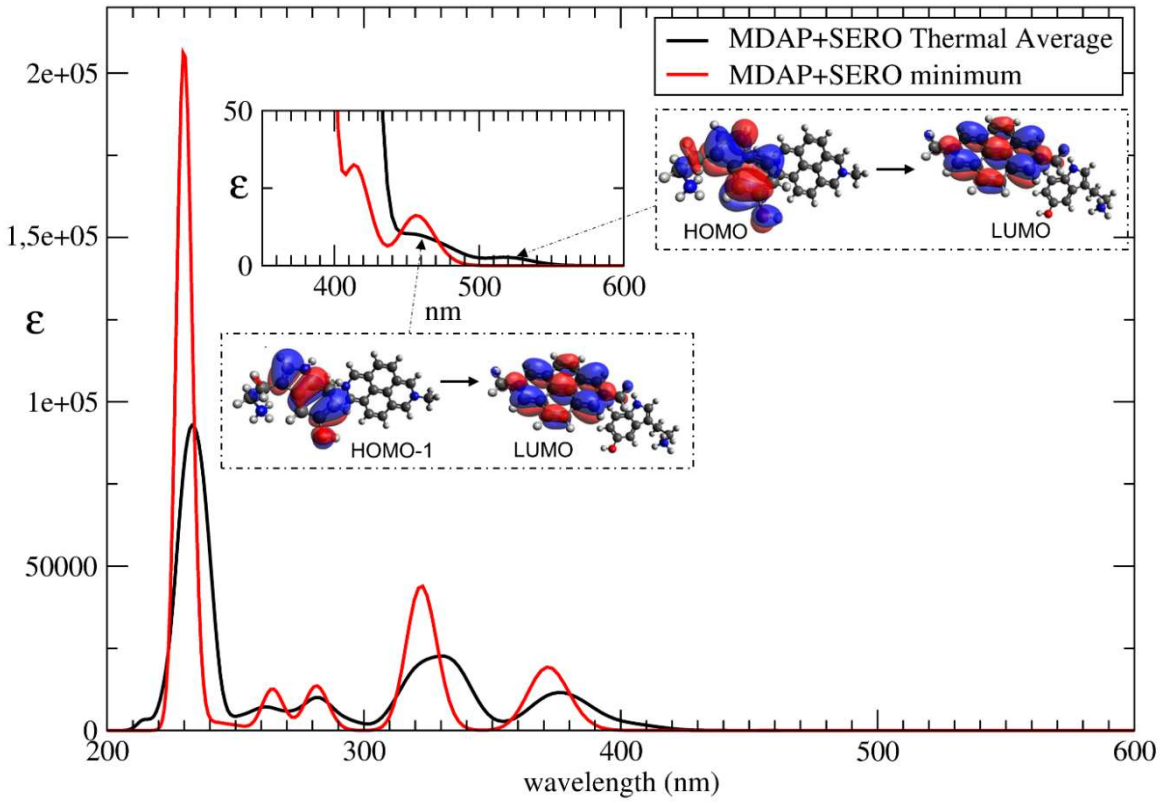

Figure 57: Comparison between the thermally-averaged UV-Vis spectrum obtained from cluster models extracted along the AIMD trajectory of (MDAP+SERO)ZL (black line), and the spectrum computed from a cluster model derived from the corresponding minimum energy structure (red line). Insets highlight the CT bands located at 520 nm and 460 nm, along with the molecular orbitals involved in the electronic transitions.

Figure 58 presents the comparison between the thermally-averaged UV-Vis spectra of MDAP (red line) and the MDAP+SERO complex (black line), both derived from configurations sampled along their respective AIMD trajectories. In addition to the appearance of the previously discussed charge-transfer (CT) bands, absent in the MDAP-only spectrum, the

association of the neurotransmitter (SERO) leads to a noticeable attenuation in the intensity of the MDAP bands, in agreement with experimental trends [11].

To further elucidate the factors governing the CT excitations, particularly those affecting the wavelength and oscillator strength of the HOMO → LUMO transition, a detailed analysis of structural parameters was undertaken. Specifically, appropriately defined geometrical descriptors were monitored along the AIMD trajectory (see Sub-section 3.6.1), with the aim of correlating them with the CT spectral features. In fact, these parameters were expected to have a direct impact on the charge-transfer (CT) transitions. In particular, the following structural descriptors were considered: (i) the conformation of the SERO molecule; (ii) the deviation from planarity of the aromatic structure of both MDAP and SERO; (iii) the relative orientation of MDAP and SERO within the complex; (iv) the intermolecular separation between MDAP and SERO, measured as the distance between the center of the SERO phenyl ring and the closest -CH_3 group of MDAP; and (v) the number and positioning of water molecules located between the two species. Figure 59 shows a representative selection of cluster models randomly sampled from the AIMD trajectory of the MDAP+SERO system, used for the analysis of structural parameters influencing the charge-transfer excitations.

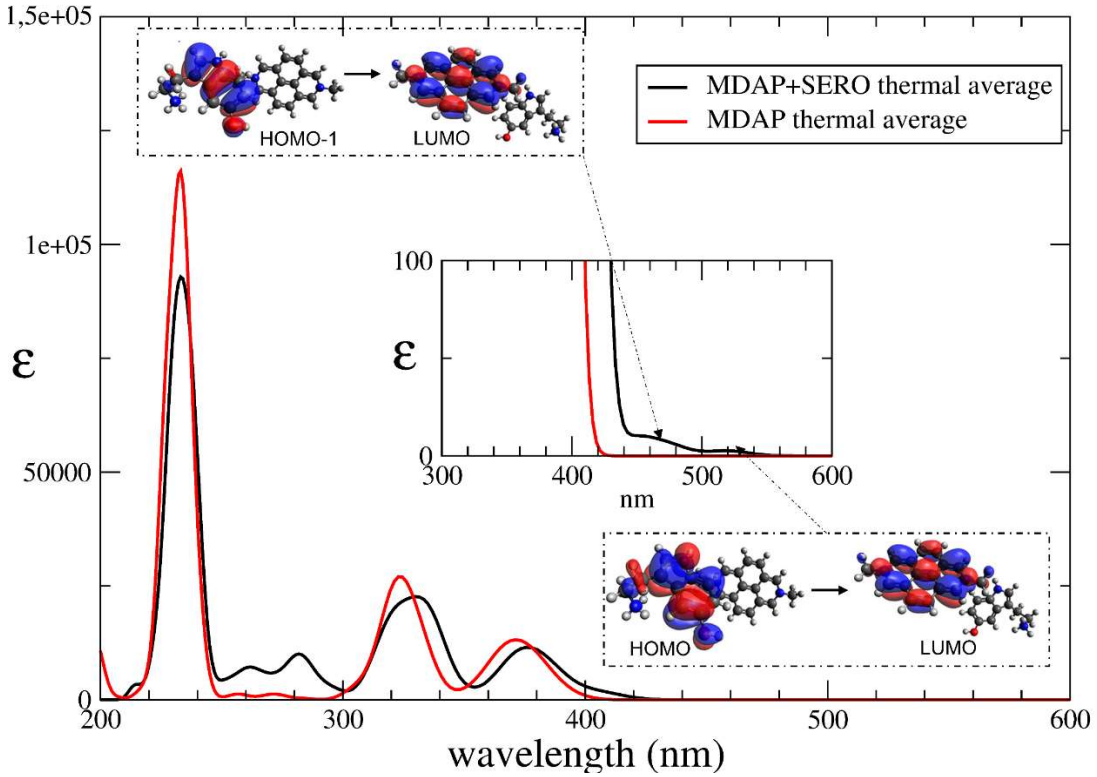

Figure 58: Comparison of the thermally-averaged UV-Vis spectra obtained from cluster models extracted from configurations sampled along the AIMD simulations of (MDAP+SERO)ZL (black line) and (MDAP)ZL (red line). The insets highlight the charge-transfer (CT) bands at 520 nm and 460 nm, along with the corresponding electronic excitations.

With regard to the wavelength of the HOMO → LUMO charge-transfer (CT) transition, configurations featuring an "edge-to-face" arrangement between the π-systems of MDAP and SERO (see Figure 59c and 59d), combined with an almost planar geometry of both aromatic

frameworks (Figure 59a), exhibit a marked red-shift of the CT band, which appears at wavelengths above 500 nm, significantly longer than that computed for the minimum energy structure (457 nm); this behavior is observed regardless of the specific conformation adopted by the SERO molecule. In contrast, configurations in which either MDAP or SERO deviate significantly from planarity (e.g., Figure 59b) display the HOMO → LUMO CT transition at shorter wavelengths relative to the optimized structure. This blue-shift can be rationalized in terms of either stabilization of the HOMO (localized on SERO) or destabilization of the LUMO (localized on MDAP), both induced by distortion of the π-conjugated system. These observations indicate that parameters (ii) (deviations from planarity of the π-structure of MDAP and SERO) and (iii) (relative orientation of the two guest molecules) are the principal structural factors modulating the position of the CT transition. Their effect on the transition intensity appears to be more limited; nonetheless, configurations with a near-planar geometry and edge-to-face orientation tend to display slightly enhanced oscillator strengths, suggesting a modest correlation between these structural motifs and CT band intensity.

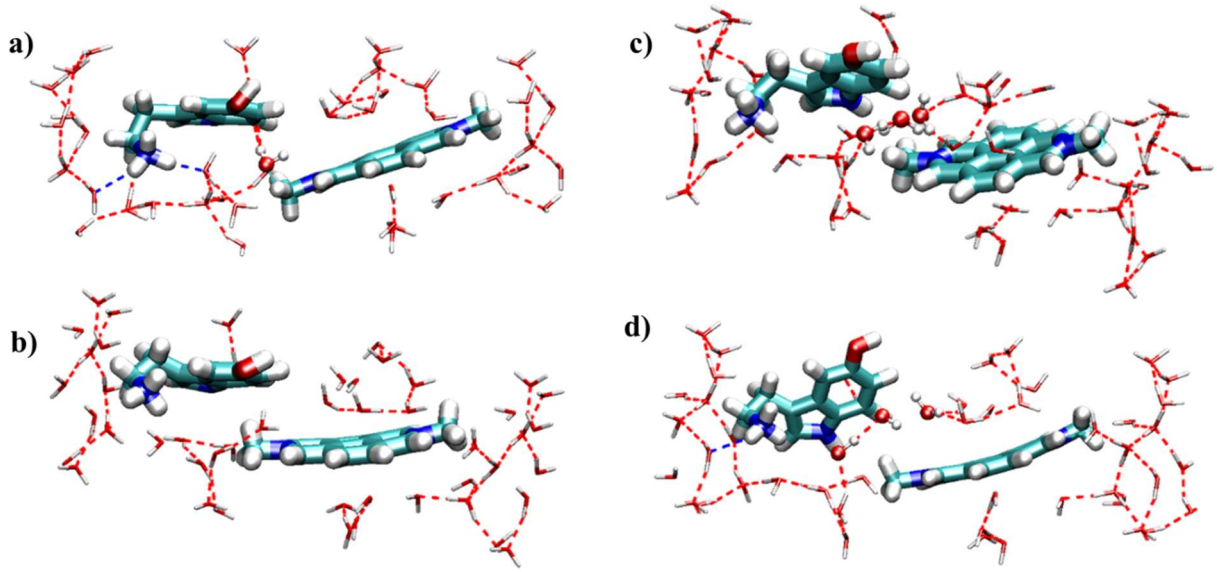

Figure 59: Cluster models extracted from four configurations sampled along the AIMD simulation of (MDAP+SERO)ZL, illustrating representative distortions of MDAP and SERO, their relative orientations, and the arrangement of H_2O molecules. Water molecules located between MDAP and SERO in panels (a), (c) and (d) are highlighted in ball-and-stick representation. Atoms color code: gray = Si, green = Al, red = O, cyan = C, blue = N, white = H. Hydrogen bonds are shown as dashed lines.

Regarding the intensity of the CT transition, attention is now turned to parameters (iv) and (v). These two structural descriptors appear to be closely interconnected: in configurations where no water molecule or only a single H_2O is located between the two positively charged species (see Figures 59a and 59b), the MDAP-SERO separation is reduced compared to the minimum energy structure. Conversely, the presence of multiple water molecules interposed between MDAP and SERO (Figures 59c and 59d) leads to an increased intermolecular distance. This trend indicates that water molecules act as spatial modulators, effectively tuning the proximity between the donor and acceptor units. Importantly, configurations characterized by a shorter MDAP-SERO separation, typically in the absence or presence of only one interposed H_2O,

display a higher oscillator strength for the CT transitions than the minimum structure. This observation suggests that a reduced separation between the π systems may enhance the CT intensity. However, despite this trend, the intensity of the CT band in the thermally-averaged spectrum of the MDAP+SERO complex remains lower than the experimental values. This discrepancy implies that additional contributions, not accounted for in the current cluster models, may play a non-negligible role in modulating the transition intensity.

In summary, ab initio molecular dynamics (AIMD) proved essential in elucidating the complex interplay between finite-temperature structural dynamics, host-guest interactions, and charge-transfer (CT) behavior within the (MDAP)ZL nanosensor. The AIMD trajectories revealed that, under ambient conditions (~300 K), the confined MDAP and SERO molecules present structural motifs, such as hydrogen bonding, relative orientation, and solvation patterns, that critically influence CT excitations. In particular, radial distribution functions (g(r)) quantified how zeolitic water molecules modulate donor-acceptor distances and screen electrostatic repulsion, ultimately shaping the spectral response. Furthermore, thermally-averaged UV-Vis spectra derived from AIMD snapshots enabled a more realistic prediction of CT band positions, aligning theoretical outcomes more closely with experimental observations. The analysis underscored the key role of specific geometric descriptors, such as π-system planarity, edge-to-face stacking, and the location of water molecules, in governing both the wavelength and oscillator strength of the HOMO → LUMO transition. Altogether, these results demonstrate that the nanosensing ability of (MDAP)ZL towards serotonin arises not merely from static host-guest affinity, but from a dynamic ensemble of configurations. The inclusion of thermal motion via AIMD is therefore not only advantageous but indispensable to fully capture the structure-property relationships that govern molecular recognition in confined nanospaces.

3.7 Role of the Zeolite Host: Enhancing Charge-Transfer Excitations through Specific Host-Guest Interactions

Until now, the host system (ZL framework) has not been explicitly included in the cluster models used to investigate the charge-transfer (CT) transitions. In order to assess the influence of the host environment on the position and intensity of the CT bands, new cluster models were built incorporating the zeolite matrix. In this Section, such an analysis was carried out for the minimum energy structures of both (MDAP)ZL and (MDAP+SERO)ZL, with the aim of disentangling the effect of the ZL host from the thermal contributions previously discussed. The rationale for including the ZL framework lies in the strong host–guest interactions observed between the -NH_3^+ and -OH groups of SERO and the framework oxygen atoms, as evidenced by both the optimized geometries (see Figures 33c and 33d) and the radial distribution functions (see Figures 50 and 51), which reveal a marked affinity of SERO for the ZL structure. Notably, the presence of the MDAP dication further enhances this interaction. The ZL matrix was modeled using a point-charge embedding approach [38] (see Figures 31 and 32, Section 3.1), allowing for a direct evaluation of the effect of the electrostatic environment on the CT transitions in the minimum energy structures of (MDAP)ZL and

(MDAP+SERO)ZL. This strategy allowed for the isolation of the specific contribution of the host framework, independently of thermal fluctuations.

(MDAP)ZL

In the case of the cluster model including the ZL framework, extracted from the minimum energy structure of (MDAP)ZL (see Figure 29b), 30 excited states were computed using TD-DFT. The results indicate that the presence of the host matrix exerts only a minor influence on the electronic excitations of MDAP. Figure 60 compares the UV-Vis spectra obtained with (black line) and without (red line) the ZL framework.

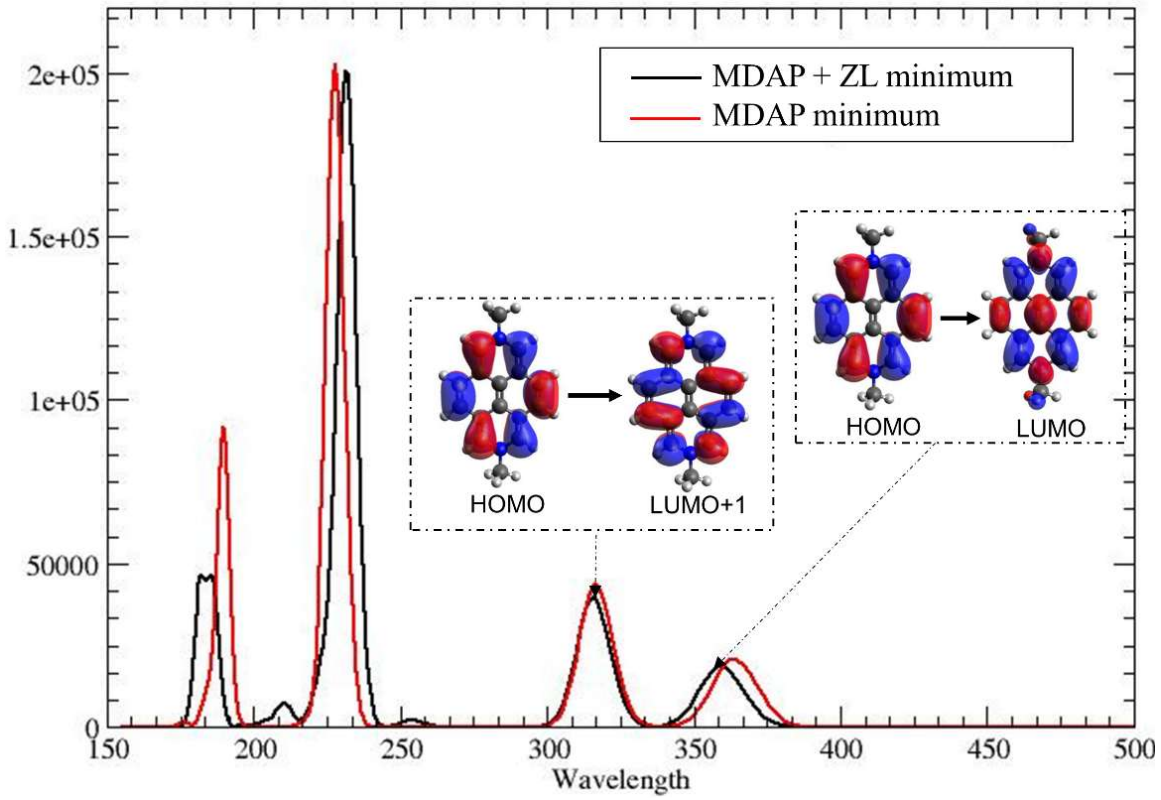

Figure 60: Comparison between the electronic excitation spectra computed for cluster models extracted from the minimum energy structure of (MDAP)ZL, with (black line) and without (red line) inclusion of the ZL framework. Insets show the molecular orbitals involved in the two lowest-energy excitations.

Notably, the inclusion of the host induces only marginal changes in the spectrum. In particular, the two lowest-energy bands, corresponding to the HOMO → LUMO and HOMO → LUMO+1 transitions, undergo a slight blue-shift and a negligible reduction in intensity. The minimal impact of the ZL environment on the electronic excitations of MDAP can be attributed to the screening effect provided by the surrounding zeolitic water molecules, which effectively isolate the dye from direct interactions with the framework (see Figure 39, Section 3.4). This interpretation is further supported by the radial distribution function (g(r)) describing contacts between the aromatic carbon atoms of MDAP and the framework oxygen atoms, which appears completely unstructured (Figure 54, black line, top panel), indicating the absence of specific host-guest interactions involving the π-system of the dye.

(MDAP+SERO)ZL

Regarding the cluster model including the ZL framework extracted from the minimum energy structure of (MDAP+SERO)ZL, representing the nanosensor after serotonin addition, 65 excited states were computed using TD-DFT. The results indicate that the presence of the ZL host exerts a significantly stronger influence on the electronic excitations of the complex compared to (MDAP)ZL. As shown in Figure 61, the comparison between the electronic excitation spectra of (MDAP+SERO)ZL and (MDAP)ZL (both including the ZL framework) reveals a red-shift of the signals associated with excitations localized only on the MDAP unit in the presence of SERO. Most notably, in the spectrum of the (MDAP+SERO)ZL complex, the charge-transfer (CT) transitions become clearly distinguishable, appearing as a broad band in the 457-460 nm region and a shoulder around 395-400 nm. These CT features exhibit substantially higher intensity compared to the corresponding spectrum computed without the ZL host (see also Figure 43), highlighting the role of the framework in enhancing the CT response.

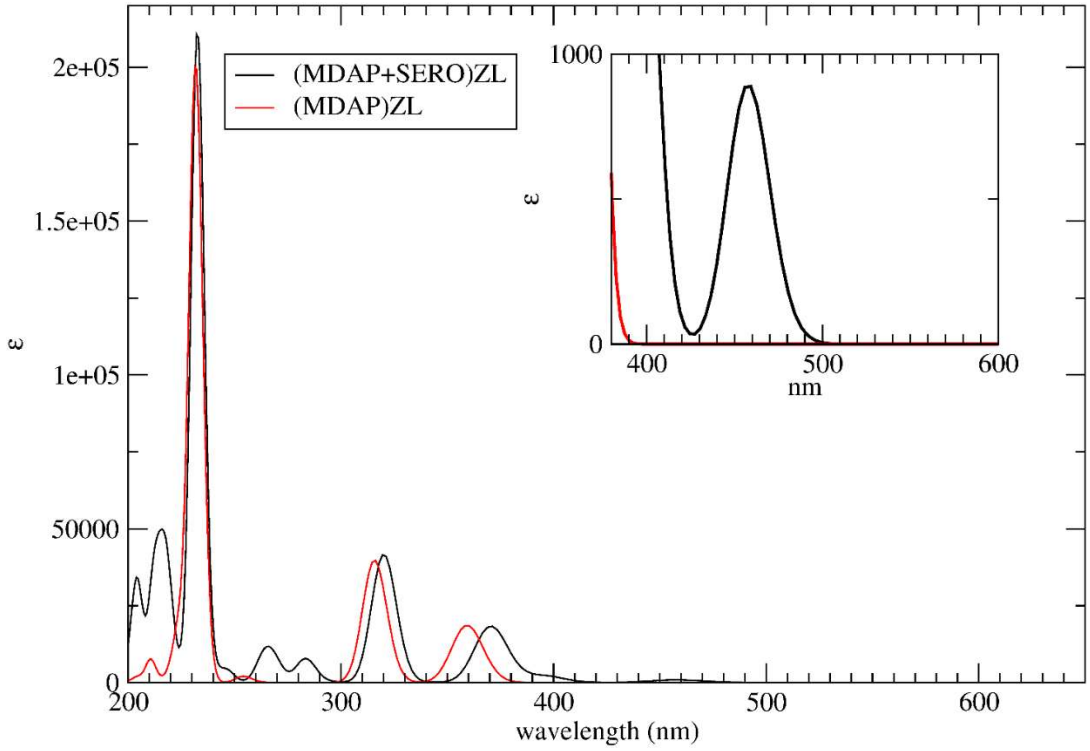

Figure 61: Comparison of the electronic excitation spectra obtained from cluster models extracted from the minimum energy structures of (MDAP+SERO)ZL (black line) and (MDAP)ZL (red line), both including the ZL framework. The inset highlights the HOMO → LUMO charge-transfer (CT) band observed at 457-460 nm (see Table 17).

As shown in Figure 62, the comparison between the electronic excitation spectra of (MDAP+SERO)ZL computed with (black line) and without (red line) inclusion of the ZL framework reveals a marked enhancement in the intensity of the charge-transfer (CT) bands upon explicit consideration of the host environment. In particular, the intensity of the HOMO → LUMO CT transition, barely visible in the spectrum without the framework, increases by approximately one order of magnitude (see also Table 17), while its position in the spectrum remains essentially unchanged. Conversely, the HOMO-1 → LUMO CT band

also undergoes a notable increase in intensity, accompanied by a blue-shift in its position from 414 nm to 395 nm. A plausible explanation for the more pronounced influence of the ZL environment on the MDAP+SERO complex, compared to the MDAP-only system, lies in the incomplete solvation of the complex by water molecules. Unlike MDAP, the MDAP+SERO complex can approach the pore walls of the zeolite, thereby experiencing direct host-guest interactions. As previously discussed, the SERO moiety engages in strong hydrogen bonds with the framework oxygen atoms via its -NH_3 and -OH groups. Consequently, the surrounding water molecules may not provide sufficient electrostatic screening to isolate the complex from the effects of the ZL framework. Nevertheless, the inclusion of the framework does not significantly modify the shape of the molecular orbitals involved in the CT transitions (see Figure 63).

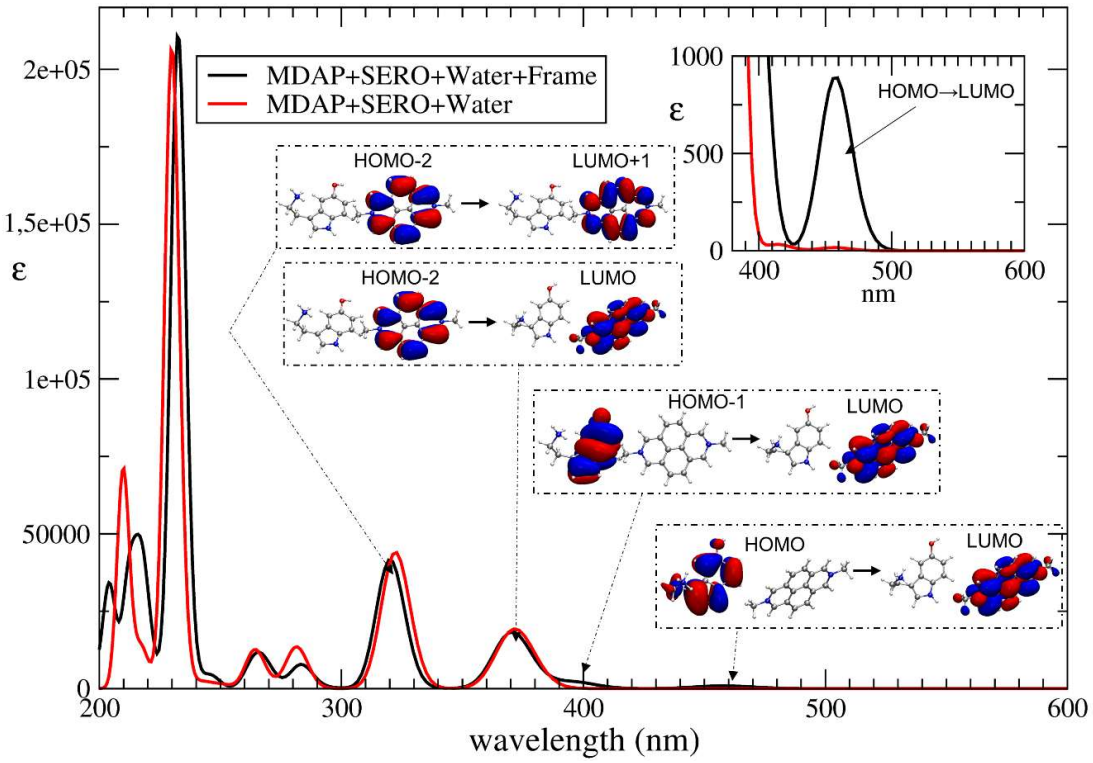

Figure 62: Comparison of the electronic excitation spectra computed for cluster models extracted from the minimum energy structure of (MDAP+SERO)ZL, with (black line) and without (red line) inclusion of the ZL framework. Insets show the molecular orbitals involved in the charge-transfer (CT) transitions and in the two highest-wavelength bands localized on the MDAP moiety.

As already observed for the orbitals computed in the absence of the ZL framework (Figure 42, Section 3.5), most of the molecular orbitals remain localized on either MDAP or SERO individually, as shown in Figure 63. Accordingly, several bands in the simulated UV-Vis spectrum can be attributed to excitations related to a single component. For instance, the bands at 370 nm and 320 nm closely match the HOMO → LUMO and HOMO → LUMO+1 transitions of the MDAP moiety, consistent with the results obtained in the absence of SERO (Figure 61). Additional excitations localized on MDAP are calculated at 232 nm (the most intense band of the spectrum), 203 nm, and 188 nm. Both the excitation energies and the shapes of the involved orbitals (see Table 17 and Figures 61 and 62) are in close agreement with those computed for the MDAP+SERO cluster without the ZL framework (Table 16 and Figures 41 and 42). Similarly, bands associated with SERO-localized excitations appear at 283 nm and 269 nm, as well as in the 211-218 nm region (see Figure 62, Table 17, and Figure 63). Notably,

the reduction in intensity of the 283 nm band (HOMO → LUMO+12), with respect to the spectrum calculated without the ZL host, may be attributed to the concurrent enhancement of the HOMO → LUMO charge-transfer band.

Table 17: Band assignment for the simulated UV-Vis spectrum (Figures 61-62) of the hydrated MDAP+SERO complex with explicit inclusion of the ZL framework (model shown in Figure 32a), based on the molecular orbitals displayed in Figure 63. Green and red indicate MOs predominantly localized on MDAP and SERO, respectively, while black denotes orbitals delocalized over both moieties. Correspondingly, excitations colored in green and red are assigned to MDAP and SERO as individual units, whereas black refers to charge-transfer (CT) transitions. For higher-energy excitations, only the main component(s) contributions are reported in Table 17.

Excitation		λ	f
108→109	HOMO→LUMO	**460.41**	**0.0019**
108→109	HOMO→LUMO	**456.34**	**0.0037**
108→110	HOMO→LUMO+1	**400.52**	**0.0002**
107→109	HOMO-1→LUMO	**397.02**	**0.0056**
107→109	HOMO-1→LUMO	**394.24**	**0.0078**
106→109	HOMO-2→LUMO	370.53	0.1131
107→110	HOMO-1→LUMO+1	351.22	0.0000
106→110	HOMO-2→LUMO+1	320.16	0.2575
108→121	HOMO→LUMO+12	283.34	0.0476
107→121	HOMO-1→LUMO+12	269.68	0.0226
107 →114	HOMO→LUMO+5	**243.17**	**0.0018**
107 →114	HOMO→LUMO+5	**233.03**	**0.1352**
101→109	HOMO-7→LUMO	232.66	1.0076
101→110	HOMO-7→LUMO+1	231.32	0.1699
108→118	HOMO→ LUMO+9	**219.35**	**0.0288**
107→120 108→120 108→121	HOMO-1→ LUMO+11 HOMO→ LUMO+11 HOMO→ LUMO+12	217.68	0.1125
108→121 108→122 107→122 108→120	HOMO→ LUMO+12 HOMO→ LUMO+13 HOMO-1→ LUMO+13 HOMO→ LUMO+11	215.74	0.0303
107→121 108→121 108→129	HOMO-1→ LUMO+12 HOMO→ LUMO+12 HOMO→ LUMO+20	212.60	0.1671
107→122 107→121	HOMO-1→ LUMO+13 HOMO-1→ LUMO+12	210.85	0.0401
107→118 107→129	HOMO-1→ LUMO+9 HOMO-1→ LUMO+20	**204.71**	**0.1301**
107→118 107→120	HOMO-1→ LUMO+9 HOMO-1→ LUMO+11	**203.10**	**0.0493**
99→110	HOMO-9→LUMO	202.82	0.0354
103→114	HOMO-5→LUMO+5	188.39	0.4436

Interestingly, analysis of the data reported in Table 17 reveals the presence of additional charge-transfer (CT) excitations beyond the previously discussed HOMO → LUMO and HOMO-1 → LUMO transitions. These CT bands are absent in the spectrum computed without the ZL framework. While the HOMO → LUMO+1 excitation (at 400 nm) displays a very low oscillator strength, several higher-energy CT transitions, specifically HOMO → LUMO+5, HOMO → LUMO+9, and HOMO-1 → LUMO+9, located at 233-243, 219, and 203 nm,

respectively, exhibit significantly higher oscillator strengths. These transitions provide a substantial contribution to the spectral region between 200 and 250 nm, where the differences between the spectra computed with and without the ZL framework become particularly pronounced (see Figure 62).

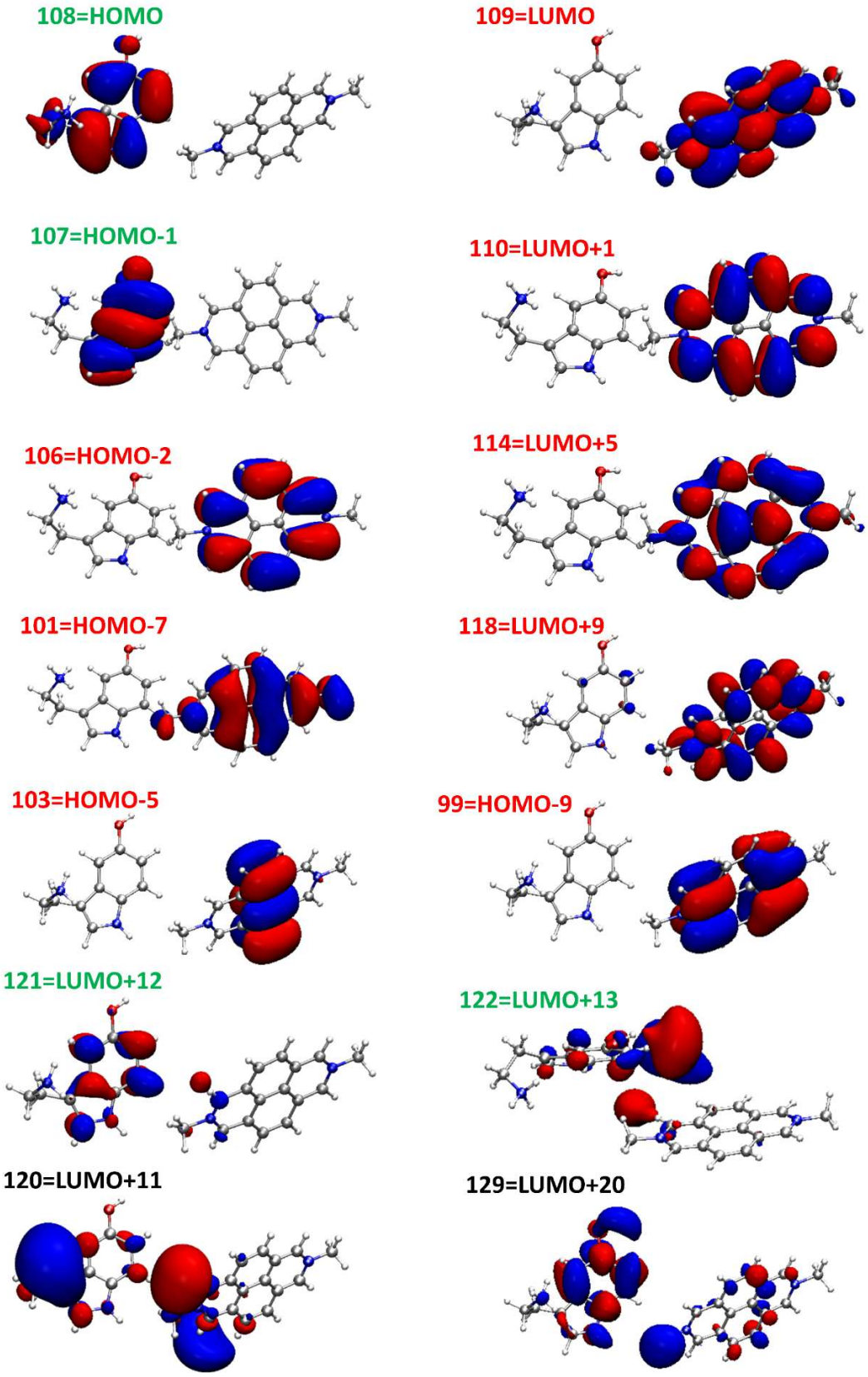

Figure 63: Molecular orbitals of the MDAP+SERO complex involved in the electronic excitations computed with inclusion of the ZL framework (modeled as a point-charge system) in the TD-DFT calculations, as reported in Table 17. Orbitals predominantly localized on MDAP and SERO are highlighted in red and green, respectively, while those delocalized over both moieties, indicative of charge-transfer (CT) character, are shown in black.

Overall, the comparison between the electronic excitation spectra of the MDAP+SERO complex computed with and without the ZL framework clearly demonstrates the pivotal role of the zeolite host in amplifying charge-transfer (CT) excitations across the UV-vis range. In particular, inclusion of the ZL matrix leads to a substantial enhancement, by at least one order of magnitude of the oscillator strengths associated with the HOMO → LUMO and HOMO-1 → LUMO transitions. This increase in CT intensity can be rationalized by considering the specific host-guest interactions established between the SERO unit and the zeolite framework. In the complex, SERO is positioned near the channel walls, where its $-NH_3^+$ and -OH groups engage in strong hydrogen bonds with negatively charged AlO_4 tetrahedral units. Such interactions likely increase the donor capacity of SERO by stabilizing its positive charge and facilitating electron density transfer to the adjacent MDAP dication, thereby reinforcing the CT excitations. These two enhanced CT bands are directly responsible for the high-wavelength tail experimentally observed in the optical spectra of (MDAP)ZL upon serotonin titration [11]. It can thus be concluded that specific host-guest interactions, particularly the direct hydrogen-bonding between SERO and the zeolite framework, play a fundamental role in the sensing mechanism of nanozeolite receptors. They not only underpin the high binding specificity but also critically determine the intensity and detectability of the CT signal, ultimately accounting for the remarkable sensitivity observed experimentally for this nanomaterial [11]. These insights open the way to rational design strategies for optimizing nanozeolite-based sensors. In particular, they suggest that, beyond the formation of confined analyte-dye complexes capable of CT, strong interactions between the analyte and the host framework should be deliberately favored to maximize signal intensity. A careful tuning of the host-dye dyad, optimized as a function of the analyte's chemical nature, could thus provide a powerful route to further enhance the performance of CT-based nanosensors.

3.8 Chapter 3 - Conclusions

Chapter 3 has presented a comprehensive computational investigation on a second strategy for the obtainment of functional nanomaterials: the supramolecular encapsulation of molecular species within confined nanoporous environments. In particular, the present work focused on a nanomaterial composed of the dicationic dye MDAP (charge +2) confined in a zeolite L (ZL) channel, resulting in the (MDAP)ZL nanosensor, whose spectroscopic response is strongly modulated by the addition of serotonin (SERO, charge +1 in solution). Encapsulation in zeolitic cavities thus represents a powerful approach for engineering complex nanomaterials at the molecular scale. This strategy exploits non-covalent host-guest interactions and spatial confinement to control the structural, electronic, and spectroscopic behavior of guest molecules. Importantly, the unique topology and electrostatic environment of ZL enable the stabilization of molecular assemblies that would be otherwise unstable in solution or gas phase, such as the triply charged (MDAP+SERO) complex. The confinement effect thus plays a dual role: it promotes the close spatial arrangement of co-encapsulated species and offers a well-defined environment in which non-covalent interactions are modulated by both geometric constraints and the local environment of the zeolite framework. Therefore, the computational investigation presented in this Chapter has revealed how encapsulation within the ZL channel

promotes a thermally stable supramolecular organization of MDAP and SERO. This feature is in excellent agreement with the spectral changes experimentally observed in the (MDAP)ZL nanosensor upon serotonin titration. The confined MDAP-SERO complex exhibits a spectroscopically detectable charge-transfer transition. The presence of such CT was confirmed by static TD-DFT calculations and refined through ab initio molecular dynamics (AIMD) simulations, which provided a more realistic account of thermal effects, the role of confined water molecules, and conformational dynamics of the system at room temperature. Radial distribution functions obtained from the AIMD trajectories demonstrated how water molecules confined in the ZL cavity play a crucial role in modulating the Coulomb repulsion between MDAP and SERO. By effectively screening their positive charges, these water molecules enable the two species to stay close together, an arrangement that would be unachievable in either solution or the gas phase. Furthermore, thermally-averaged UV-Vis spectra, computed from AIMD-sampled cluster models, were crucial to bridge the gap between theory and experiment. Compared to static calculations, these spectra provided more realistic predictions of CT band positions, confirming the red-shift and band broadening observed experimentally. The analysis highlighted how key geometrical parameters, such as (i) a reduced MDAP-SERO distance mediated by H_2O molecules, (ii) an edge-to-face arrangement of the SERO and MDAP π-systems, and (iii) minimal distortions from planarity in the π-systems, govern the spectroscopic response of the material, revealing higher wavelengths and intensities of the CT bands. Notably, the inclusion of the zeolite host in the TD-DFT models further elucidated its role. While negligible effects were observed for MDAP alone, the presence of the framework significantly enhanced the intensity of the CT transitions in the MDAP+SERO complex, by at least one order of magnitude, without altering orbital features. This effect was related to strong hydrogen bonds formed by the $-NH_3^+$ and -OH groups of SERO with the AlO_4 units of the ZL framework, which enhance SERO's donor character and promote the electron density transfer to the adjacent MDAP dication. These host-guest interactions are therefore key to both molecular selectivity and the enhancing of charge-transfer bands, which underpin the sensing mechanism.

In summary, this Chapter underscores the pivotal role of confinement in enabling molecular recognition processes that are otherwise inaccessible in conventional solution-phase environments. The dynamic interplay between guest geometry, water solvation, and host structural and electrostatic features elucidated here provides valuable design principles not only for next-generation nanozeolite sensors, but also for the broader design of functional nanomaterials in confined aqueous environments.

References

[1] G. Tabacchi, Supramolecular Organization in Confined Nanospaces, ChemPhysChem 2018, 19, 1249-1297

[2] H. Li, A. Devaux, A. Z. Ruix, G. Calzaferri, Electronic excitation energy transfer from dye-loaded zeolite L monolayers to a semiconductor, SPIE Proc. 2006,6195, 61951G

[3] R. Sola-Llano, L. G.-Rivero, A. O.-Sanchez, J. Bañuelos, I. L. Arbeloa, V. M.-Martínez, Dye Encapsulation into One-Dimensional Zeolitic Materials for Optical Applications, In Chemistry of Silica and Zeolite-Based Materials; Elsevier: Amsterdam, 2019, 229-248

[4] F. C. Hendriks, D. Valencia, P. C. A. Bruijnincxa, B. M. Weckhuysen, Zeolite molecular accessibility and host-guest interactions studied by adsorption of organic probes of tunable size, Phys. Chem. Chem. Phys., 2017,19, 1857-1867

[5] G. Calzaferri, S. Huber, H. Maas, and C. Minkowski, Host-Guest Antenna Materials, Angew. Chem. Int. Ed., 2003, 42, 3732-3758

[6] E. Fois, G. Tabacchi, A. Devaux, P. Belser, D. Brühwiler, G. Calzaferri, Host-guest interactions and orientation of dyes in the one-dimensional channels of zeolite L, Langmuir., 2013, 29, 9188-9198

[7] a) Y. Levy and J. N. Onuchic, Water and proteins: a love-hate relationship, P. Natl. Acad. Sci. USA, 2004, 101, 3325; b) E. A. Meyer, R. K. Castellano and F. Diederich, Interactions with Aromatic Rings in Chemical and Biological Recognition, Angew. Chem. Int. Ed., 2003, 42, 1210; c) G. Klebe, Applying thermodynamic profiling in lead finding and optimization, Nat Rev Drug Discov, 2015, 14, 95

[8] J. E. Ladbury, Just add water! The effect of water on the specificity of protein-ligand binding sites and its potential application to drug design, Chem. Biol., 1996, 3, 973

[9] a) W.-B. Hu, W.-J. Hu, Y. A. Liu, J.-S. Li, B. Jiang and K. Wen, Multicavity macrocyclic hosts , Chem. Commun., 2016, 52, 12130; b) L.-P. Yang, X. Wang, H. Yao and W. Jiang, Naphthotubes: Macrocyclic Hosts with a Biomimetic Cavity Feature, Acc. Chem. Res., 2020, 53, 198; c) L.-P. Yang, L. Zhang, M. Quan, J. S. Ward, Y.-L. Ma, H. Zhou, K. Rissanen and W. Jiang, A supramolecular system that strictly follows the binding mechanism of conformational selection, Nat. Commun., 2020, 11, 2740

[10] C. Rando, J. Vázquez, J. Sokolov, Z. Kokan, M. Nečas and V. Šindelář, Highly Efficient and Selective Recognition of Dicyanoaurate(I) by a Bambusuril Macrocycle in Water, Angew. Chem. Int. Ed., 2022, 61, e202210184

[11] L. M. Grimm et al, Fluorescent Nanozeolite Receptors for the Highly Selective and Sensitive Detection of Neurotransmitters in Water and Biofluids, Adv. Mater., 2021, 33, 2104614

[12] a) F. Biedermann and W. M. Nau, Noncovalent Chirality Sensing Ensembles for the Detection and Reaction Monitoring of Amino Acids, Peptides, Proteins, and Aromatic Drugs, Angew. Chem. Int. Ed. 2014, 53, 5694; b) F. Biedermann, G. Ghale, A. Hennig and W. M.

Nau, Fluorescent artificial receptor-based membrane assay (FARMA) for spatiotemporally resolved monitoring of biomembrane permeability, Commun Biol, 2020, 3, 383

[13] Ch. Baerlocher, L. B. McCusker and D. H. Olson, Atlas of Zeolite framework types, Published on behalf of the Structure Commission of the International Zeolite Association by Elsevier, 2007

[14] R. M. Barrer and H. Villiger, The crystal structure of the synthetic zeolite L, Zeitschrift für Kristallographie - Crystalline Materials, 1969, 128, 352-370

[15] G. Calzaferri, R. M.-Renault, D. Brühwiler, R. Pansu, I. Dolamic, T. Dienel, P. Adler, H. Li, A. Kunzmann, Designing Dye-Nanochannel Antenna Hybrid Materials for Light Harvesting, Transport and Trapping, ChemPhysChem, 2011, 12, 580-594

[16] J. M. Newsam, Structures of dehydrated potassium zeolite L at 298 and 78K and at 78K containing sorbed perdeuteriobenzene, The Journal of Physical Chemistry, 1989, 93, 7689-7694

[17] L. Gigli, G. Vezzalini, S. Quartieri and R. Arletti, Compressibility behavior and pressure-induced over-hydration of zeolite K AlSi-L, Microporous and Mesoporous Materials, 2019, 276, 160-166

[18] D. J. Frisch et al, Gaussian 09, Revision E.01, Gaussian, Inc., Wallingford CT 2009

[19] J. P. Perdew, K. Burke and M. Ernzerhof, Generalized Gradient Approximation Made Simple, Phys. Rev. Lett., 1996, 77, 3865-3868

[20] S. Grimme, Semiempirical GGA-type density functional constructed with a long-range dispersion correction, J. Comput. Chem., 2006, 27, 1787-1799

[21] D. Vanderbilt, Soft self-consistent pseudopotentials in a generalized eigenvalue formalism, Phys. Rev. B, 1990, 41, 7892-7895

[22] K. F. Garrity, J. W. Bennett, K. M. Rabe and D. Vanderbilt, Pseudopotentials for high-throughput DFT calculations, Comput. Mater. Sci., 2014, 81, 446-452

[23] L. Kleinman and D. M. Bylander, Efficacious Form for Model Pseudopotentials, Physical Review Letters, 1982, 48, 1425-1428

[24] N. Troullier and J. L. Martins, Efficient pseudopotentials for plane-wave calculations, Physical Review B, 1991, 43, 1993-2006

[25] D. Hamann, M. Schlüter and C. Chiang, Norm-Conserving Pseudopotentials, Physical Review Letters, 1979, 43, 1494-1497

[26] S. Nosé, A unified formulation of the constant temperature molecular dynamics methods, The Journal of Chemical Physics, 1984, 81, 511-519

[27] W. G. Hoover, Canonical dynamics: Equilibrium phase-space distributions, Physical Review A, 1985, 31, 1695-1697

[28] R. Car and M. Parrinello, Unified Approach for Molecular Dynamics and Density-Functional Theory, Physical Review Letters, 1985, 55, 2471-2474

[29] D. Marx and J. Hutter, Ab Initio Molecular Dynamics, Cambridge University Press, Cambridge, 2009

[30] IBM Corp. 1990-2017 and MPI für Festkörperforschung Stuttgart 1997-2001, CPMD: Car Parrinello Molecular Dynamics http://www.cpmd.org 2017

[31] J.-D. Chai and M. Head-Gordon, Long-range corrected hybrid density functionals with damped atom-atom dispersion corrections, Physical Chemistry Chemical Physics, 2008, 10, 6615

[32] C. Adamo and V. Barone, Toward reliable density functional methods without adjustable parameters: The PBE0 model, The Journal of Chemical Physics, 1999, 110, 6158-6170

[33] E. Fois, G. Tabacchi and G. Calzaferri, Orientation and Order of Xanthene Dyes in the One-Dimensional Channels of Zeolite L: Bridging the Gap between Experimental Data and Molecular Behavior, Journal of Physical Chemistry C, 2012, 116, 16784-16799

[34] M. Caricato, G. W. Trucks, M. J. Frisch and K. B. Wiberg, Oscillator Strength: How Does TDDFT Compare to EOM-CCSD?, J. Chem. Theory Comput., 2011, 7, 456-466

[35] M. E. Casida, C. Jamorski, K. C. Casida and D. R. Salahub, Molecular excitation energies to high-lying bound states from time-dependent density-functional response theory: Characterization and correction of the time-dependent local density approximation ionization threshold, J. Chem. Phys., 1998, 108, 4439-4449

[36] T. Yanai, D. P. Tew and N. C. Handy, A new hybrid exchange–correlation functional using the Coulomb-attenuating method (CAM-B3LYP), Chem. Phys. Lett., 2004, 393, 51-57

[37] R. J. Woods and R. Chappelle, Restrained electrostatic potential atomic partial charges for condensed-phase simulations of carbohydrates, J. Mol. Struc. THEOCHEM, 2000, 527, 149-156

[38] J. Kuhn, J. M. C.-Sanchez, J. Gascon, S. Calero, D.Dubbeldam, T. J. H. Vlugt, F. Kapteijn, J. Gross, Adsorption and diffusion of water, methanol, and ethanol in all-silica DD3R: Experiments and simulation, J. Phys. Chem. C, 2009, 113, 14290-14301

[39] C. Cabezas, M. Varela, I. Peña, J. C. López and J. L. Alonso, The microwave spectrum of neurotransmitter serotonin, Phys. Chem. Chem. Phys., 2012, 14, 13618-13623

[40] A. Klamt and G. Schüürmann, COSMO: a new approach to dielectric screening in solvents with explicit expressions for the screening energy and its gradient, J. Chem. Soc., Perkin Trans. 2, 1993, 799-805

[41] J. Tomasi, B. Mennucci and R. Cammi, Quantum Mechanical Continuum Solvation Models, Chem. Rev., 2005, 105, 2999-3094

[42] M. E. Tuckerman, Ab initio molecular dynamics: basic concepts, current trends and novel applications. J. Phys.: Condens. Matter 2002, 14, R1297-R1355

[43] **C. Invernizzi**, L. M. Grimm, F. Biedermann, G. Tabacchi, Mechanistic insights into water-stabilized dye-neurotransmitter intermolecular complexes in zeolite channels, Chem. Commun., 2025, 61, 4160-4163

[44] A. K. Soper, The Radial Distribution Functions of Water and Ice from 220 to 673 K and at Pressures up to 400 MPa., Chem. Phys. 2000, 258 (2-3), 121-137

[45] B. Guillot, A Reappraisal of What We Have Learnt During Three Decades of Computer Simulations on Water., J. Mol. Liq. 2002, 101 (1-3), 219-260

[46] R. T. Cygan, J. A. Greathouse, H. Heinz and A. G. Kalinichev, Molecular models and simulations of layered materials, J. Mater. Chem., 2009, 19, 1-13

[47] S. Calero and P. Gómez-Álvarez, Hydrogen bonding of water confined in zeolites and their Zeolitic Imidazolate Framework counterparts, RSC Adv., 2014,4, 29571-29580

– Chapter 4 –

At the Interface: Molecular Adsorption on Metal Oxide Surfaces for Sensing and Functional Nanomaterials Design

The controlled assembly of nanostructured organic-inorganic materials is a central theme in materials chemistry, particularly in the context of designing next-generation devices for energy conversion, sensing, catalysis, and molecular recognition. Within this broad landscape, surface adsorption represents a powerful and widely applicable strategy for achieving molecular-level functionalization of nanomaterials. Adsorption processes allow the direct modulation of surface reactivity, electronic structure, and interfacial properties by anchoring organic molecules onto well-characterized oxide surfaces with distinct structural and electronic features [1-3]. Among the various classes of inorganic substrates, metal oxide semiconductors occupy a privileged role. Materials such as ZnO, In_2O_3, and indium tin oxide (ITO) are particularly attractive due to their structural robustness, wide band gaps, high surface-to-volume ratios, tunable conductivity through doping or defect engineering, and low cost [4-6]. These oxides are not only chemically and thermally stable, but also exhibit surface properties that can be finely tuned via hydroxylation, or the incorporation of aliovalent dopants (e.g., Sn for In in ITO), enabling specific interactions with adsorbed molecular species. Their widespread use in optoelectronics, transparent electrodes, gas sensors, and photocatalysis underscores the versatility of oxide-based platforms for hybrid nanomaterial engineering [7-9]. In this context, adsorption on oxide surfaces encompasses a wide range of interaction types, including weak physisorption, hydrogen bonding, electrostatic attraction, and in some cases, covalent bond formation. These interactions may affect not only the geometry and orientation of the adsorbed molecules, but also the local electronic density, surface electrostatics, and in some cases, the type and mobility of charge carriers within the oxide substrate [10-12]. In particular, adsorption-induced electronic structure changes, such as from *p*-type to *n*-type, may be relevant for understanding functional responses in chemiresistive sensors [13].

From a molecule-to-material perspective, surface adsorption can be regarded as an effective strategy to engineer hybrid nanomaterials with tailored properties, without requiring high-temperature processing or bulk reorganization. When properly understood and controlled, the formation of molecule-surface complexes can lead to stable, spatially organized, and electronically responsive interfaces, establishing a direct connection between molecular properties and the final material functionality [14].

Building on the previous Chapters, this one introduces a third and complementary molecular strategy for the design of functional nanomaterials: adsorption on metal oxide surfaces. While Chapters 2 and 3 focused respectively on the decomposition of molecular precursors and the encapsulation of guest species in nanoporous frameworks, the present approach relies on the establishment of non-covalent or covalent interactions between organic molecules and the extended surface of inorganic oxides. From a theoretical point of view, modeling adsorption processes on metal oxide surfaces presents both conceptual and technical challenges. Periodic

density functional theory (DFT) calculations represent a standard computational framework for investigating molecule-surface systems, evaluating adsorption or interaction energies, and electronic structure modifications induced by adsorbates [15-17]. Complementary analyses, including Bader charge calculations, density of states (DOS) calculations, and TD-DFT excited-state simulations, provide further insight into charge redistribution, surface-induced electronic transitions, and local modifications in the electronic structure [18-20]. Importantly, the chemical nature of the surface itself, namely its termination, hydroxylation state, or dopant distribution, plays a decisive role in determining adsorption strength, molecular orientation, and electronic effects. For instance, Sn doping in ITO enhances surface reactivity by introducing localized electron-rich sites, whereas oxygen-rich ZnO surfaces may hinder physisorption due to increased competition for adsorption sites [21,22].

Overall, this Chapter presents a case study that explores surface adsorption as a molecular strategy for the design of functional hybrid nanomaterials. Specifically, Paragraph 4.1 investigates the interaction between a macrocycle molecule, Pillar[6]arene (P[6]A), and two indium-based oxide surfaces: pure In_2O_3 and its tin-doped variant, indium tin oxide (ITO). Through DFT simulations, the formation of covalent metal oxide-organic bonds via water elimination is explored, with tin atoms shown to enhance surface reactivity and promote stronger adsorption. The resulting P[6]A-ITO hybrid system exhibits remarkable chemical stability and preserves molecular recognition capabilities, highlighting its potential for electrochemical sensing and catalysis.

In a different way, the second case study addressed in this Chapter highlights the potential of transition metal oxides – namely ZnO – to act as chemiresistive sensors towards Chemical Warfare Agents (CWA), through the adsorption of these organic species on zinc oxide surfaces. In particular, Paragraph 4.2 focuses on the adsorption of nitrogen mustard agents (HN1, HN2, HN3) and their non-toxic simulant Di(propylene glycol) methyl ether (DPGME) on ZnO$(10\bar{1}0)$ surfaces, studied through periodic DFT calculations. Preliminary results show that DPGME and HN2 display similar electronic behavior and surface interactions, inducing a shift from *p*-type to *n*-type character when physisorbed on ZnO. These findings, whether confirmed by further analyses, may provide a molecular-level rationale for using DPGME as a simulant, and useful insight for the development of ZnO-based chemiresistive nanosensors for toxic gas detection.

4.1 Investigating the Covalent Anchoring of Pillar[6]arene on In_2O_3 and ITO Surfaces

This Paragraph presents a theoretical investigation into the adsorption of the macrocyclic host molecule Pillar[6]arene (P[6]A) on indium-based oxide surfaces, specifically pristine In_2O_3 and its tin-doped variant, indium tin oxide (ITO). The nanosystems under study exemplify molecular functionalization via covalent anchoring and hold significant potential for the design of robust and electrochemically active nanomaterials.

In recent years, green chemistry has emerged as a transformative framework for promoting sustainable chemical processes, emphasizing waste minimization, atom economy, and the use of non-hazardous reagents [23]. These principles have promoted innovation in materials science, particularly in the development of catalysts and functional materials [23]. Among such materials, ITO stands out as a widely employed *n*-type degenerate semiconductor with a wide optical band gap of 3.6 eV [24]. Its unique combination of optical transparency and high electrical conductivity has enabled extensive use in applications ranging from optoelectronics to photovoltaics [25], and more recently, as a platform for electrochemical technologies [26]. Within this context, the functionalization of ITO surfaces with organic molecules has attracted growing interest, as it offers opportunities to enhance surface reactivity, tailor interfacial properties, and expand the functional scope of the substrate [26]. In particular, macrocyclic systems have been investigated for their ability to form stable, organized host-guest architectures, while simultaneously facilitating charge-transfer processes at electrode interfaces [27]. Representative examples include calixarenes, cyclodextrins, and pillar[*n*]arenes, all of which have demonstrated the ability to selectively recognize guest molecules and improve the performance of electrochemical devices [28-31]. Among them, pillar[*n*]arenes have gained great relevance in supramolecular chemistry due to their rigid, symmetric, and tunable cylindrical cavities [32]. Composed of p-dialkoxybenzene-based repeating units linked by methylene bridges, these macrocycles offer electron-rich internal cavities that enable the inclusion of guest species through non-covalent interactions, particularly with cationic or electron-deficient molecules [33,34]. Pillar[6]arene (P[6]A), the six-membered variant, is one of the most extensively studied members of this family, owing to its versatility in host-guest chemistry and molecular recognition [35]. Notably, its ability to form robust complexes with a variety of organic and inorganic species makes it an excellent candidate for surface modification of conductive materials such as ITO [36]. Recent studies have proposed the covalent anchoring of P[6]A onto ITO as a promising strategy to construct functionalized electrodes for molecular electrocatalysis [37]. In previous experimental work, it was demonstrated that such covalent immobilization leads to highly stable and pH-resistant host-guest-modified electrodes capable of sustaining electrochemical activity under operational conditions [38]. This hybrid platform thus offers a compelling opportunity to integrate macrocyclic host functionalities with conductive oxide supports, aligning with the principles of green chemistry through the development of efficient nanomaterials, like recyclable electrocatalytic systems. Finally, the present computational study (see Appendix 4, Section A.4.1.1 for further details) aims to provide a molecular-level understanding of this hybrid interface by addressing three main objectives: (i) to assess the structural and electronic factors

underpinning the stability of the P[6]A-metal oxide surface interaction; (ii) to compare the behavior of ITO and In_2O_3 surfaces, highlighting the role of tin doping; and (iii) to elucidate possible reaction pathways for the covalent attachment of the macrocyclic molecule to the oxide surface. To date, no theoretical studies have addressed this hybrid interface. The present investigation therefore provides unprecedented molecular-level insights that could support the rational design of functional hybrid nanomaterials for applications in energy conversion, sensing, electrocatalysis, and environmental remediation.

4.1.1 Hydrogen-Bonded Physisorption of P[6]A on In_2O_3 and ITO

Before modeling the adsorption of Pillar[6]arene (P[6]A) on indium-based oxide surfaces (In_2O_3 and ITO), the central nanomaterial under investigation, the geometry and vibrational properties of the isolated molecule were characterized to provide a reference for subsequent structural modifications upon surface binding. The P[6]A optimized structure is shown in Figure 64, while the simulated infrared (IR) spectrum and the assignment of the main vibrational modes are provided in Appendix 4, Section A.4.1.2.

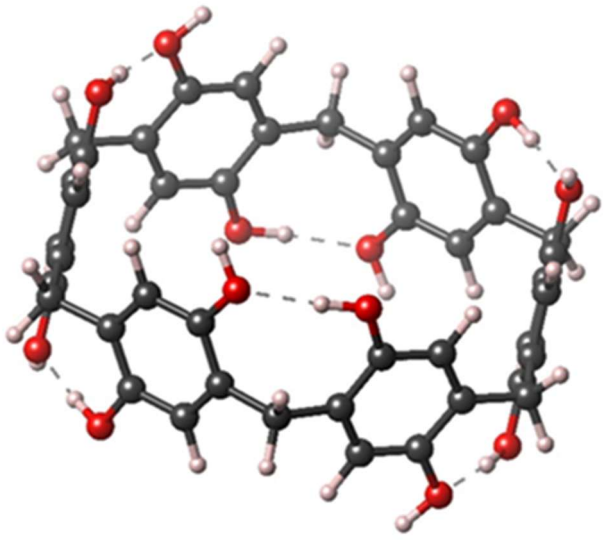

Figure 64: Graphical representation of the DFT-minimum energy structure of Pillar[6]arene. Atoms color code: C = grey, O = red, H = white. Dashed lines represent H-bonds.

A comparison with available experimental IR data [39] shows satisfactory agreement in both peak positions and intensities, thereby validating the theoretical model and supporting the vibrational band assignment. Particularly relevant are the O-H stretching modes located in the 3400-3700 cm^{-1} region (see Table A.21), as the hydroxyl groups represent the primary anchoring sites for interaction with In_2O_3 and ITO (see below). The calculated O-H bond lengths (~0.97 Å), together with the high energy required for their disruption, suggest that, once adsorbed, P[6]A is likely to form a stable hybrid system, with limited tendency toward desorption (see Section 4.1.2 for further details). On this basis, the adsorption of the macrocyclic host was first modeled through hydrogen bonding interactions, considered here as a plausible precursor state preceding the formation of covalent anchoring motifs.

As mentioned above, indium-tin oxide (ITO) is derived from indium oxide (In_2O_3) through tin doping, i.e., by replacing some In atoms with Sn atoms (see Section A.4.1.1). The decision to consider both surfaces arises from the interest in evaluating whether the presence of tin influences the adsorption behavior of the P[6]A molecule, both in energetic and mechanistic terms. In a first instance, according to previous findings [38], the interaction between Pillar[6]arene and the In_2O_3 surface (Figure 65) appears to occur through three hydrogen bonds, labeled A, B, and C. The O-H···O distances differ slightly, measuring 1.40 Å, 1.56 Å, and 1.64 Å, respectively. This variation is attributed to the distinct coordination environments of the surface oxygen atoms acting as H-bond acceptors. In contrast, the three intramolecular hydrogen bonds within the macrocycle (HA, HB, and HC) remain unperturbed. This adsorption complex corresponds to a total adsorption energy of -1.18 eV (calculated using Eqn. A1; see Section A.4.1.1), a relatively high value when compared to hydrogen adsorption on the In_2O_3 (111) surface (~ -2.0 eV [40]).

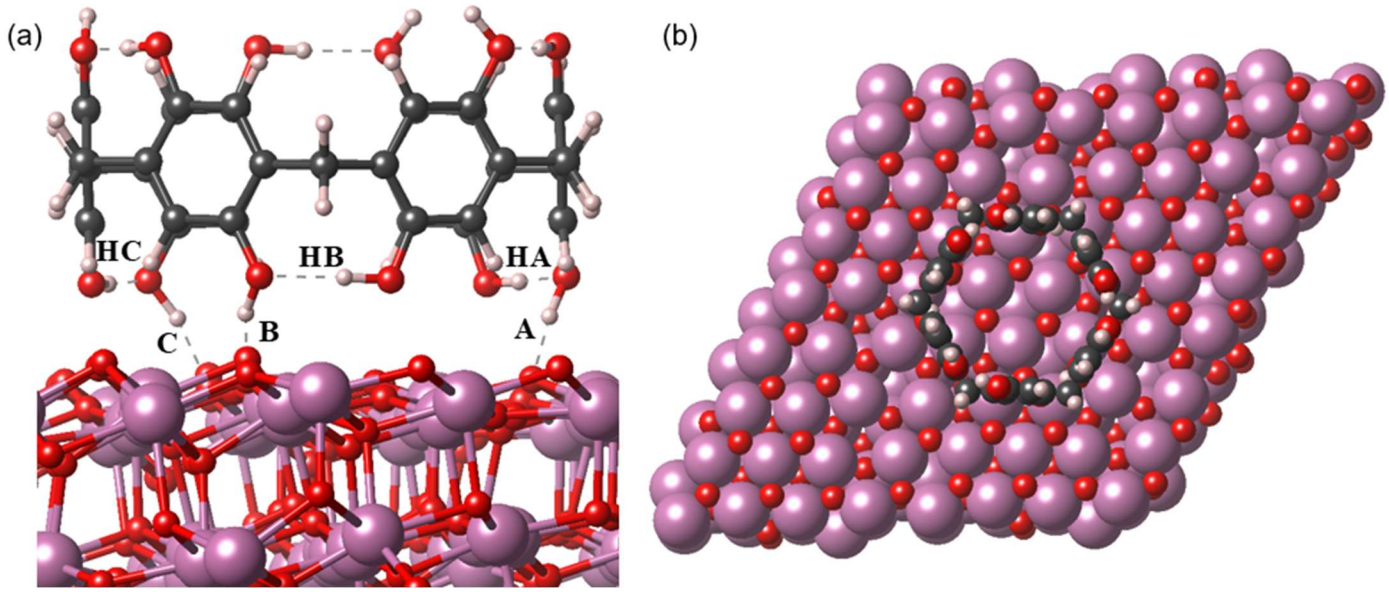

Figure 65: Graphical representation of the DFT-minimum energy structure of Pillar[6]arene on the In_2O_3 (111) surface. (a) Side view; (b) top view. Atoms color code: In = purple, C = grey, O = red, H = white. Dashed lines represent H-bonds.

The P[6]A + ITO system is shown in Figure 66. As in the case of the In_2O_3 surface, the interaction between the macrocyclic molecule and the substrate occurs through three hydrogen bonds (O-H···O), all characterized by slightly different distances from the surface (A = 1.54 Å, B = 1.63 Å, and C = 1.72 Å). The intramolecular hydrogen bonds within the macrocycle (HA, HB, and HC) remain unaltered. The total adsorption energy (E_{ads}) for this system is -3.45 eV, significantly more negative than that obtained for the P[6]A + In_2O_3 complex. This result suggests that the presence of tin atoms in the surface enhances the adsorption of the macrocyclic molecule. Tin, having one valence electron more than indium, acts as an electron-donor [41], thereby increasing the surface reactivity of ITO compared to that of In_2O_3. To further explore the nature of the molecule-surface interaction, a complementary set of calculations was performed using the same structures but without geometry re-optimization. This allowed the evaluation of interaction energies (E_{int}), which exclude the contributions associated with

structural relaxation and thus provide a more direct comparison of the electronic binding strength across different surfaces. In this perspective, both systems, P[6]A + In_2O_3 and P[6]A + ITO, exhibit similar total interaction energies (E_{int}), amounting to -4.07 eV and -5.07 eV, respectively. These values underscore the strong binding of the organic ring to the surface. Interaction energies were computed using Eqn. A.1 (see Section A.4.1.1), as in the case of total adsorption energies. However, in this case, the energy terms ($E_{surf+mol}$, E_{surf}, and E_{mol}) correspond to the single-point energies of the individual P[6]A, In_2O_3, and ITO structures, extracted from the minimum energy structure of the combined systems without performing further geometry optimization. For completeness, a "single-point energy" refers to the total electronic energy of a given molecular system evaluated at a fixed nuclear configuration. In other words, it represents the energy of the electron distribution around the nuclei for a specific geometry, without accounting for any structural rearrangements [18].

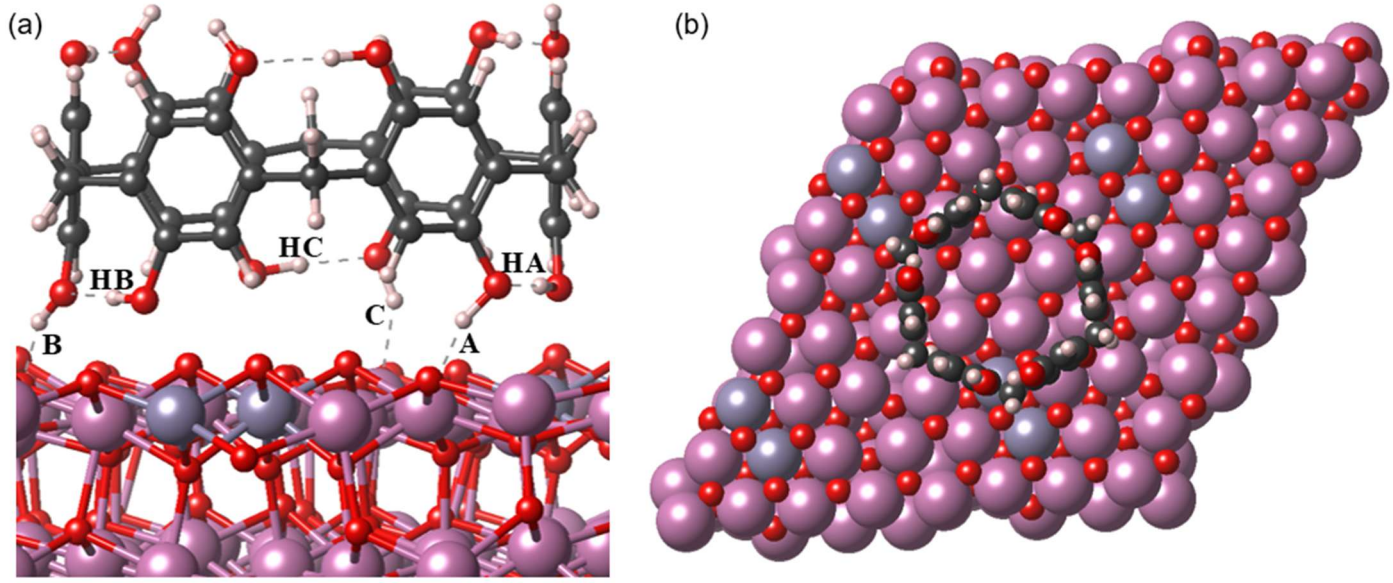

Figure 66: Graphical representation of the DFT-optimized structure of Pillar[6]arene on the BCC ITO (111) surface. (a) Side view; (b) top view. Atoms color code: In = purple, Sn = dark purple, C = grey, O = red, H = white. Dashed lines represent H-bonds.

Furthermore, since hydrogen bonds are inherently weaker than covalent bonds, the H-bonded configuration is considered a plausible physisorption precursor state to a subsequent chemical process that leads to stronger surface binding. This hypothesis is also supported by the experimentally observed high stability of the adsorbed P[6]A molecule [38]. In this context, the hydroxyl groups of Pillar[6]arene are expected to play a key role in this transformation. Indeed, the total adsorption energies calculated for both systems are sufficiently high to activate the O-H bonds stretching modes (~3700 cm^{-1}, see Table A.21), potentially leading to their breaking. However, due to the significant steric hindrance and conformational rigidity of the macrocyclic ring, a fully deprotonated adsorption process is found to be energetically unfavorable. In fact, simulations involving fully deprotonated P[6]A adsorbed on both surfaces yield adsorption energies of approximately +4.0 eV. The positive sign of the calculated E_{ads} indicates that such a configuration is thermodynamically unfavorable, as the system would be energetically more stable with the molecule and the surface remaining non-interacting. Based on these considerations, two possible reaction pathways were hypothesized and

computationally explored in the following Section: (i) proton transfer (PT) from one of the P[6]A hydroxyl groups to a surface oxygen atom; (ii) elimination of water molecules from the system, leading to the formation of covalent bonds.

4.1.2 From Physisorption to Covalent Anchoring: Investigating the Adsorption Process of P[6]A on In_2O_3 and ITO

Following the identification of hydrogen-bonded physisorption complexes as plausible precursor states (see Section 4.1.1), a further step in understanding the reactivity of the P[6]A-metal oxide hybrid systems involves the exploration of possible chemical processes that may lead to the formation of covalent anchoring motifs. In this context, two hypothetical pathways were considered and computationally tested: (i) proton transfer (PT) from one of the hydroxyl groups of Pillar[6]arene to the surface, and (ii) water elimination, leading to the formation of stronger bonds between the organic host and the oxide surface. The goal of this Section is thus to evaluate the energetic and structural viability of these processes, in order to elucidate the molecular-level process behind the formation of a stable P[6]A-surface interface, which constitutes the functional nanomaterial. The analysis begins with the proton transfer scenario, which is ultimately shown to be both energetically and mechanistically less plausible than water elimination, as discussed below.

For both systems under investigation, the proton transfer (PT) process was modeled according to the following reaction:

Surf. + Pillar[6]arene → Pillar[6]arene (-) + Surf.-H (+)

Where Surf. = In_2O_3 or ITO **(Eqn. 1)**

The adsorption energy values computed for the PT process, involving different hydroxyl groups of P[6]A closest to the surfaces, are reported in Table A.22, Section A.4.1.3.

Among these, the most favorable configurations, corresponding to the deprotonation of hydrogen atom C, are shown in Figure 67a (In_2O_3, E_{ads} = -1.71 eV) and Figure 67b (ITO, E_{ads} = -3.47 eV). Overall, the obtained E_{ads} values do not follow a consistent trend and remain comparable to those previously calculated for the hydrogen-bonded precursor states (Figures 65 and 66). This similarity suggests that the reaction pathway described in Eqn. 1 is unlikely to represent the dominant process driving the formation of the final adsorbed state. Nevertheless, the PT process could still be interpreted as a possible intermediate step, bridging the initial physisorption state and a more tightly bound configuration of the macrocyclic ring to the oxide surface. This scenario appears particularly plausible for the configurations illustrated in Figure 67, which exhibit the most favorable adsorption energies among the PT cases considered.

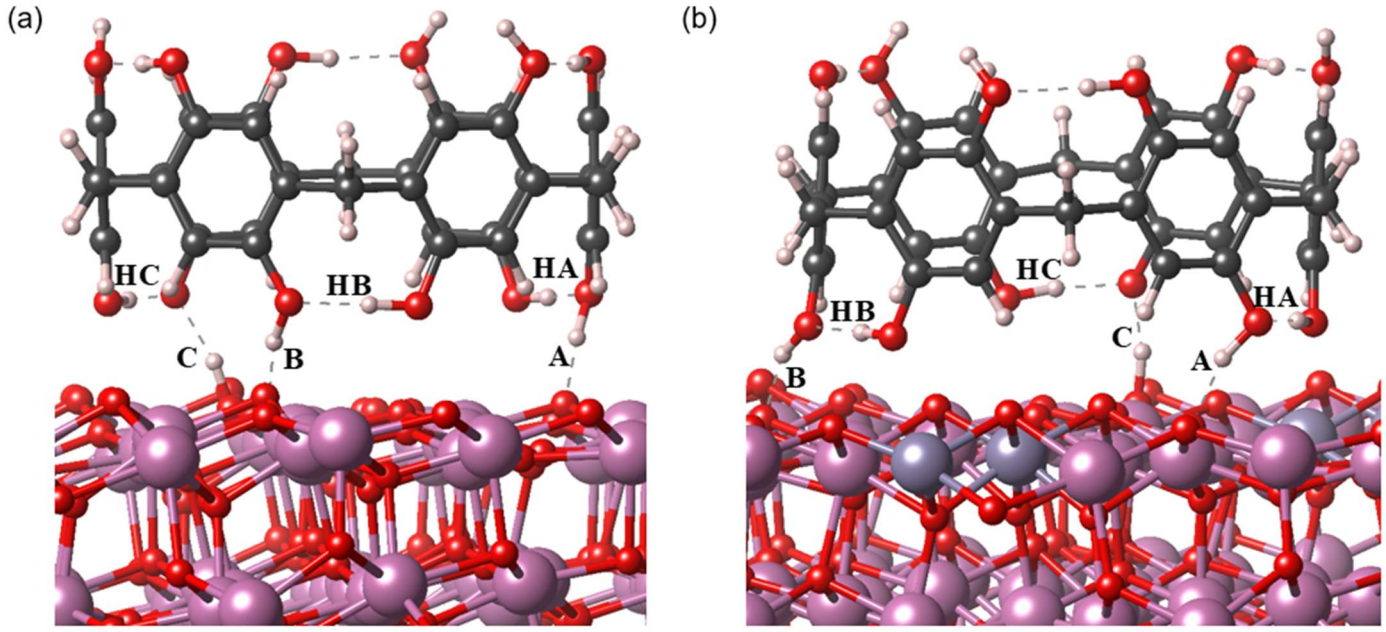

Figure 67: Graphical representation of the DFT optimized structures of the proton transfer (PT) reaction products involving hydrogen C of the P[6]A molecule: a) P[6]A(-) + In_2O_3-H(+); b) P[6]A(-) + ITO-H(+). Atoms color code: In = purple; Sn = dark purple; C = grey; O = red; H = white. Dashed lines represent H-bonds.

However, to account for the experimentally observed robustness and irreversibility of P[6]A adsorption on indium-based oxides [38], a more chemically grounded process must be considered. In this regard, the elimination of water molecules emerges as a more plausible route toward the formation of stable covalent bonds between the macrocyclic host and the oxide surface. The following analysis investigates this reaction pathway, focusing on its energetic profile and structural implications. Within this framework, the optimized structures of the products obtained from the elimination of two water molecules are shown in Figure 68a (P[6]A on In_2O_3) and Figure 68b (P[6]A on ITO). These configurations, found to be the most energetically stable and yielding the most favorable adsorption energies (see Tables A.23 and A.24 in Section A.4.1.3), were constructed by replacing two surface oxygen atoms (assumed to be hydroxylated due to the presence of water under experimental conditions) with two oxygen atoms from the P[6]A molecule. The macrocycle donates two protons (specifically H atoms labeled as C and HC, see Figures 65 and 66) that combine with surface -OH groups to form two H_2O molecules. Notably, in the case of ITO, anchoring occurs preferentially at tin-coordinated surface oxygens, further highlighting the electron-donor character of Sn and the increased reactivity of the corresponding oxygen atoms compared to those bonded to In.

In addition to the two-water elimination pathway, further systems involving the elimination of four and six water molecules were also modeled and optimized (see Figure A.33 in Appendix 4). Adsorption energies for all these systems were calculated using the following reaction scheme:

$$\textbf{Surf. + Pillar[6]arene + n/2 } H_2 \rightarrow \textbf{ Pillar[6]arene on Surf. + n } H_2O$$

Where: Surf. = In_2O_3 or ITO; n = number of formed water molecules **(Eqn. 2)**

The inclusion of H_2 molecules on the reactant side approximates the hydroxylated nature of the oxide surfaces under experimental conditions. Computed adsorption and interaction energies for all investigated configurations are summarized in Table 18.

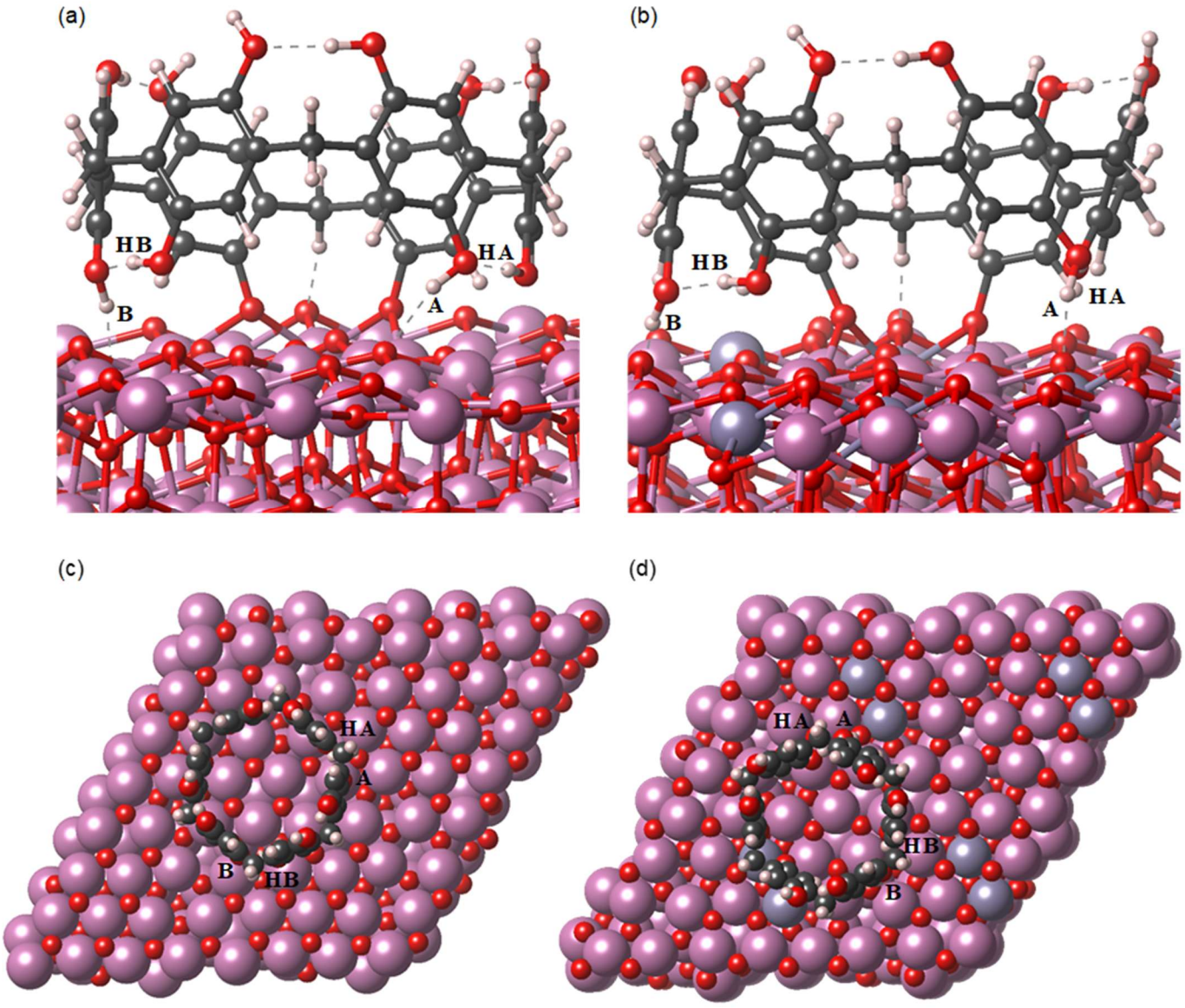

Figure 68: Graphical representation of the DFT-optimized structures of the Pillar[6]arene adsorbed on metal oxide surfaces after the elimination of two water molecules. Panels a) and c) show the side and top views, respectively, of the P[6]A + In_2O_3 system, while panels b) and d) refer to the P[6]A + ITO system. Atoms color code: In = purple; Sn = dark purple; C = dark grey; O = red; H = white.

As shown in Table 18, for the P[6]A + In_2O_3 system, the elimination of two water molecules leads to a structure (Figures 68a and 68c) with a more favorable adsorption energy compared to the hydrogen-bonded precursor state (Figure 65). This outcome cannot be extended to the P[6]A + ITO – $2H_2O$ system (Figures 68b and 68d), nor to the configurations resulting from the elimination of four or six water molecules in either system (Figure A.33). The lower adsorption energies observed in these cases can be primarily ascribed to the pronounced structural deformation undergone by the macrocyclic ring upon anchoring to the surface, which disrupts the remaining intramolecular hydrogen bonds and consequently increases the

total energy. Nonetheless, the computed interaction energy values (Table 18) become progressively more negative as the number of eliminated water molecules increases, indicating that the extent of covalent bonding between the macrocycle and the oxide surface plays a key role in stabilizing the interface. This trend underscores a fundamental point: the enhanced stability of the hybrid system arises directly from the formation of covalent C-O bonds between the aromatic ring of the Pillar[6]arene and the oxide surface, replacing weaker H-bonding interactions with robust anchoring bridges. To gain deeper insight into the electronic nature of the newly formed surface bonds and to validate the proposed anchoring process, additional analyses based on charge density difference (CDD) and Bader charge calculations were performed. These results are presented and discussed in the following Sub-section.

Table 18: Total adsorption energy (E_{ads}) and interaction energy (E_{int}) values (in eV) for the P[6]A - In_2O_3 and P[6]A-ITO systems before and after the elimination of water molecules.

System	E_{ads} (eV)	E_{int} (eV)
P[6]A + In_2O_3	-1.18	-4.07
P[6]A + In_2O_3 -2H_2O	-2.29	-6.92
P[6]A + In_2O_3 -4H_2O	-1.56	-13.13
P[6]A + In_2O_3 -6H_2O	-0.41	-17.18
P[6]A + ITO	-3.45	-5.07
P[6]A + ITO -2H_2O	-2.76	-8.18
P[6]A + ITO -4H_2O	-1.88	-12.53
P[6]A + ITO -6H_2O	-0.47	-15.63

4.1.2.1 Charge Redistribution and Surface Anchoring: Insights from CDD and Bader Charge Analyses

To explore further the interpretation of the adsorption process described in the previous Sections, two complementary electronic analyses were carried out: Charge Density Difference (CDD) [42] and Bader charge analysis [43] (see Appendix 4, Section 4.1.3 for further details). Both techniques are particularly well-suited to elucidate the redistribution of electronic density during surface adsorption, especially in hybrid systems where covalent bonding, hydrogen bonding, and charge transfer phenomena coexist [42-47]. In the following, these two techniques are applied to the P[6]A + In_2O_3 and P[6]A + ITO systems, in order to confirm the structural and energetic trends discussed earlier, and to offer deeper insight into the electronic nature of the anchoring process.

From CDD calculations (Figure A.34), it can be observed that in the physisorbed precursor state (Figures A.34a and A.34b), electrons are mainly located around the O-H bonds of P[6]A, i.e., the hydrogen bonds formed with the surface (OH···O), and the surface oxygen atoms involved in these interactions. This already indicates the existence of a weak but non-

negligible interaction between the macrocyclic host and the oxide support, even before covalent bond formation. As the number of eliminated water molecules increases (Figures A.34c-f), the interaction becomes progressively more pronounced. In these configurations, the electron density is fully localized on the oxygen atoms of P[6]A that have replaced the surface hydroxyl groups, and on the adjacent carbon atoms of the aromatic ring. These data confirm the formation of new covalent linkages and highlight the strong interfacial stability of the resulting nanomaterial.

Complementary insights are obtained from the Bader charge analysis. The data reported in Table A.25 summarize the average atomic charges of the P[6]A, In_2O_3, and ITO components before and after the anchoring process. The overall trend reveals a net electron transfer from the oxygen atoms of P[6]A toward the metal atoms of the surface. This charge displacement leads to a significant decrease in the positive charge of indium and tin atoms, indicating partial electron donation from the organic molecule to the inorganic support. Notably, tin atoms of the ITO surface undergo a larger positive charge depletion than indium atoms, confirming their stronger electron-accepting character. This finding supports the hypothesis that Sn doping enhances the anchoring efficiency of P[6]A by increasing the surface reactivity through localized electronic effects.

In summary, both CDD and Bader analyses consistently indicate that the stability of the P[6]A-metal oxide systems arise from the formation of covalent bonds between the macrocyclic ring and the surface. These interfacial linkages are mediated by electron transfer from the anchoring oxygens of P[6]A to the metal atoms of the surface, with tin atoms playing a particularly active role in the case of ITO. Such insights reinforce the reliability of the proposed adsorption model and provide a deeper understanding of the electronic nature of the hybrid interface.

4.1.3 Evaluation of a Probable Water-Elimination Pathway on In_2O_3 and ITO Surfaces

Following the identification of water elimination as the most plausible process for the covalent anchoring of Pillar[6]arene onto In_2O_3 and ITO surfaces, a simplified reaction pathway was proposed to rationalize the energetic and structural features of the systems under investigation. This approach does not aim to describe a complete reaction mechanism with transition states, but rather to provide a conceptual framework that connects the computed geometries and reaction energies of initial and final states, highlighting the key steps that may be involved in the formation of the hybrid interface. Such a strategy is particularly useful when the identification of transition states is either computationally prohibitive or chemically ambiguous, as in the case of large, flexible organic adsorbates interacting with complex oxide surfaces. Moreover, the adoption of a comparative scheme applicable to both surfaces offers the additional advantage of isolating the effects of surface composition, namely, the presence or absence of tin, on the overall thermodynamic behavior of the system.

The proposed pathway consists of three elementary stages: (1) hydrogenation (protonation) of surface oxygen atoms, (2) physisorption of the macrocyclic molecule, and (3) elimination of water molecules leading to covalent adsorption. This scheme was applied identically to both

In_2O_3 and ITO surfaces, enabling a step-by-step comparison of the energetic contributions and structural rearrangements associated with each process. Particular attention was devoted to the influence of Sn atoms in modulating surface reactivity, especially in the physisorption stage, where strong interactions between the macrocycle and the oxide can be favored by electronic and steric effects induced by dopant atoms. The resulting analysis, supported by computed reaction energies, optimized geometries, and adsorption data, offers a coherent interpretative model for the anchoring process via water elimination. For simplicity, only the elimination of two water molecules was considered in this Section, although pathways involving the removal of four or six water molecules could, in principle, also be possible, especially under higher surface hydroxylation conditions. These alternative pathways were not pursued here, but may be relevant in the context of multi-site adsorption or cooperative surface activation. The reaction steps for the two-water elimination process are as follows:

Surf. + $2H^+$ → Surf-2H **(1)**

Surf-2H + P[6]A → P[6]A_{Surf}-2H **(2)**

P[6]A on Surf-2H → P[6]A_{Surf} + $2H_2O$ **(3)**

Where: Surf = In_2O_3 or ITO **(Eqn. 3)**

The geometries of the species involved in each step are shown in Appendix 4, Figure A.35 (In_2O_3) and Figure A.36 (ITO). These images provide a visual comparison of the structural evolution occurring throughout the reaction sequence, from the initial hydrogenated surfaces to the final covalently bonded hybrid systems. These structural representations serve to illustrate the spatial arrangement of the adsorbate and its evolution along the proposed pathway, thereby clarifying how the nature of the surface, In_2O_3 vs ITO, affects both the interaction mode and the resulting adsorption configuration. Given the key role of the initial hydrogenation step (1) in enabling the overall process (see Table 19 below), several possible adsorption sites for H_2 molecules were considered on both surfaces (see Appendix 4, Section A.4.1.4 for further details).

The computed reaction energies (E_{reac}) for the three steps are summarized in Table 19, and reveal marked differences between the two surfaces. In the case of ITO, the physisorption step (2) is energetically favorable ($E_{reac} < 0$), whereas the water elimination step (3) provides a negative contribution to the total energy ($E_{reac} > 0$). Conversely, for In_2O_3, physisorption is less favorable, but water elimination contributes more significantly to the overall stabilization of the system. These contrasting behaviors are likely attributable to the presence of tin in ITO, which generates more reactive adsorption sites compared to the In_2O_3 surface. The interaction with P[6]A is thus enhanced during the physisorption stage, but destabilized upon elimination of water molecules, explaining the observed energetic penalty. In both cases, however, the initial hydrogenation (protonation) step (1) provides a favorable energetic contribution, underlining the potential role of solvent-derived hydrogen species in the experimental

realization of surface functionalization, suggesting their crucial role in the beginning of the overall reaction.

Table 19: DFT-computed reaction energies (E_{reac}) for the three-step pathway described in Equation 3. The total reaction energy (E_{ads}) corresponds to the sum of the individual contributions from steps (1), (2), and (3).

	E_{reac} (eV)			
Reaction	1	2	3	Total (**Eads**)
Surf				
In_2O_3	-2.14	+0.25	-0.41	-2.29
ITO	-1.53	-1.88	+0.65	-2.76

This result highlights the importance of local surface composition in determining the anchoring behavior of organic species, and suggests that tin doping in ITO not only enhances reactivity at the interface, but may also influence the stability and functional properties of the resulting hybrid nanomaterial.

4.1.4 Concluding Remarks

The DFT computational investigation presented in this Section has provided a detailed assessment of the interaction between Pillar[6]arene and two model oxide surfaces, In_2O_3 and ITO, with particular emphasis on the role of tin atoms in modulating surface reactivity. The analysis demonstrated that Sn dopants in ITO generate more reactive adsorption sites compared to pristine In_2O_3, thereby enhancing the interaction with the macrocyclic molecule already at the physisorption stage. This effect was confirmed by adsorption energy values, charge density difference (CDD) and Bader charge analysis. Among the possible processes leading to covalent immobilization of Pillar[6]arene, water elimination was identified as the most plausible pathway, in contrast to proton transfer, which proved energetically disfavored. The proposed pathway yields a direct oxygen bridge between the macrocyclic ring and the surface, providing a stable covalent configuration. Notably, the energetic analysis revealed opposite trends for the two materials: in ITO, physisorption is stabilized while water elimination is destabilizing, whereas in In_2O_3 the situation is reversed. In both cases, however, the initial hydrogenation of surface oxygen atoms contributes positively to the overall process, emphasizing its relevance as a key initiating step. Taken together, these results establish a first atomistic model of a functional hybrid nanomaterial based on Pillar[6]arene immobilized on ITO. The system can be predicted as a prototype electrode for molecular electrocatalysis, thanks to its higher stability against pH fluctuations and high selectivity, thereby illustrating how surface adsorption processes can be exploited to engineer functional nanomaterials with tailored properties.

Overall, this Paragraph has thus outlined a first example of a hybrid nanomaterial obtained through surface adsorption processes, which represent the central theme of Chapter 4. In the following Paragraph (4.2), the focus will shift to a different class of nanomaterials, namely ZnO-based chemoresistive sensors, where adsorption phenomena will be investigated in the context of toxic gas recognition.

4.2 A First-Principles Investigation of ZnO-Based Chemiresistive Nanosensors for Chemical Warfare Agents and Their Simulant

The rational design of functional nanomaterials for sensing applications requires a precise understanding of molecular adsorption processes at solid interfaces. In the previous Paragraph (4.1), a covalent surface anchoring process was investigated as a strategy to create hybrid nanomaterials with tailored electrocatalytic properties. In this Paragraph, the focus shifts towards semiconducting metal oxide surfaces for gas-phase sensing, particularly in the context of Chemical Warfare Agents (CWAs).

Therefore, the increasing threat posed by CWAs, including their recent use in both military and terrorist contexts, has generated considerable interest in the development of fast and reliable detection technologies. CWAs such as sulfur mustards, nerve agents, and nitrogen mustards (e.g., the azoyprites HN1, HN2, HN3) are among the most toxic compounds synthesized by humans, capable of causing irreversible damage to human health and the environment [48]. Their high volatility, low lethal dose, and delayed effects make them particularly insidious. However, due to international laws and safety regulations, experimental studies involving CWAs are severely restricted, and access to the actual compounds is limited to a handful of authorized military laboratories [49]. As a result, research into detection technologies must often rely on structurally or functionally analogous molecules, commonly referred to as simulants, which mimic the physicochemical behavior of CWAs without posing the same health risks [49-51]. The ideal simulant should reproduce the key chemical features of the target CWA, including vapor pressure, polarity, functional groups, and molecular size. Moreover, it must exhibit similar interactions with the active sensing materials employed in the detection devices. For nitrogen mustards, various ether- or alcohol-based compounds have been proposed as non-toxic simulants, with Di(propylene glycol) methyl ether (DPGME) standing out due to its manageable toxicity, suitable volatility, and demonstrated responsiveness in sensor tests [51,52]. Nevertheless, the selection of simulants has often been empirical, and a molecular-level theoretical validation of their similarity to actual CWAs remains limited in the literature [48]. This has underscored the growing role of first-principles simulations in elucidating the interactions between simulants and sensor surfaces and in supporting experimental strategies aimed at the detection of CWAs [48].

Among the various systems explored for CWA detection, chemiresistive sensors based on semiconducting metal oxides have emerged as particularly promising due to their simplicity, cost-effectiveness, miniaturizability, and high sensitivity in real-time monitoring [53]. These devices operate by monitoring changes in the electrical resistance of a sensitive material upon interaction with gaseous analytes. Typically, the sensing mechanism involves surface adsorption of target molecules, followed by charge transfer or dipole interaction, which modifies the density of charge carriers in the semiconducting layer. In the case of *n*-type semiconducting metal oxides, such as ZnO, it is proposed that adsorbed electron-withdrawing species can lead to a depletion of conduction electrons near the surface, resulting in an increase in resistance, while electron-donating analytes can cause a decrease [53,54]. The performance of chemiresistive sensors depends on multiple factors, including the intrinsic electronic structure

of the oxide, the density and nature of surface defects, crystallographic orientation, and environmental variables such as humidity and temperature [55-57].

In this context, zinc oxide (ZnO) has become a material of choice for gas sensing applications, owing to its wide band gap (~3.37 eV), high electron mobility, good thermal and chemical stability, and its ease of fabrication in various nanostructured morphologies (nanorods, nanowires, thin films) [56,58]. The high surface-to-volume ratio of nanostructured ZnO enhances its responsiveness to adsorbed species, while the presence of native defects, such as oxygen vacancies and interstitial Zn, can modulate the availability of reactive sites and influence sensor selectivity [59]. Moreover, ZnO's compatibility with various functionalization strategies, including doping, decoration with noble metals, and surface modification with organic or inorganic moieties, allows for tuning of its sensing behavior toward specific analytes, including CWA's and their simulants [60,61].

Several studies have demonstrated the feasibility of using ZnO-based chemiresistive sensors for the indirect detection of CWAs through simulants. For instance, ZnO nanostructures have shown measurable responses to dimethyl methylphosphonate (DMMP), a well-established simulant for nerve agents such as sarin [51,58]. Similarly, responses to DPGME as a mustard gas simulant have been reported on ZnO platforms functionalized or doped to enhance specificity and stability [51]. The ability to engineer ZnO surfaces at the nanoscale and modulate their electronic and adsorption properties offers a versatile framework for the rational design of sensors targeting CWAs and related compounds. Furthermore, the relatively simple chemiresistive transduction mechanism facilitates integration into portable devices suitable for field deployment. Despite this progress, a detailed understanding of the fundamental interactions between CWAs or their simulants and ZnO surfaces remains limited. In particular, theoretical studies aimed at disentangling the electronic and adsorption behavior of simulants on ZnO at the atomic level are still scarce [48,51,52]. In this context, density functional theory (DFT) provide powerful tools to probe the geometry, electronic structure, and adsorption energies of relevant systems [48,51,61]. These insights are essential not only to validate the use of specific simulants, such as DPGME, but also to identify structural or electronic features that govern sensor selectivity and sensitivity [48,51,61].

The present Paragraph, therefore, aims to explore this topic through a theoretical DFT investigation (see Appendix 4, Section A.4.2.1 for further details) focused on the adsorption of nitrogen mustard agents (HN1, HN2, HN3) and their simulant DPGME on ZnO surfaces. By comparing structural, electronic, and surface-interaction properties, this study - which is still "work in progress" - aims to provide a computational rationale for the use of DPGME as a non-toxic simulant of the three azoyprites, as well as molecular-level insight on the sensing mechanism. Particular attention is devoted to the ZnO$(10\bar{1}0)$ surface. From a broader perspective, the results described in this Paragraph, whether corroborated by deeper analyses, may contribute to achieve a further understanding of ZnO-based nanomaterials for toxic gas sensing.

4.2.1 Electronic and Structural Insights into DPGME and Nitrogen Mustards (HN1, HN2, HN3) in the Gas Phase

Before thoroughly addressing the interaction of DPGME and nitrogen mustard agents $C_6H_{13}Cl_2N$ (HN1), $C_5H_{11}Cl_2N$ (HN2) and $C_6H_{12}Cl_3N$ (HN3) with the ZnO surface, representing the functional nanomaterial at the heart of this Paragraph 4.2, it is essential to examine the intrinsic features of these molecules in the gas phase. This preliminary step, fully described in Appendix 4, is not only necessary to identify their most stable conformations and key structural properties, but also to assess possible similarities between CWAs and their proposed simulant, DPGME, prior to any surface interaction. Furthermore, this investigation is especially relevant given the restricted access to CWAs for non-military research institutions worldwide.

A conformational analysis was performed for DPGME and the nitrogen mustard agents HN1, HN2, HN3. In the case of DPGME, a folded isomer, previously unreported in the literature, was identified as the energetically favored one. This conformer is stabilized by an intramolecular hydrogen bond. As for the nitrogen mustards, their respective minimum-energy structures were obtained (see Section A.4.2.2 for further details). Among them, HN2 was selected for the adsorption on the ZnO surface as representative of this class of CWAs. The optimized geometries of DPGME and HN2 are shown in Figure 69 and were used as the starting point for subsequent surface interaction modeling.

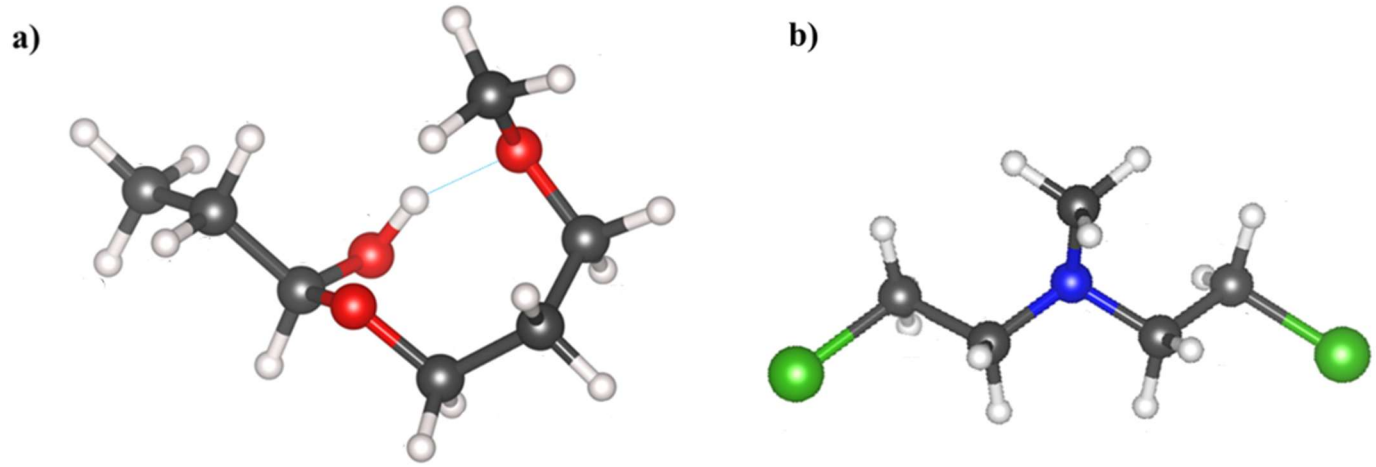

Figure 69: Optimized molecular structure of a) DPGME in its folded conformation and b) $C_5H_{11}Cl_2N$ (HN2). Atoms color code: Cl = green; N = blue; C = grey; O = red; H = white. Dashed cyan line represents the H-bond.

A comparative analysis was conducted to evaluate the rationale behind the use of DPGME as a simulant for nitrogen mustards, despite the apparent lack of structural or functional group resemblance.

As reported in Section A.4.2.2, the three azoyprites share closely related chemical features, reflected in the similarity of their molecular electrostatic potential maps (Figure A.43) and computed infrared spectra (Figure A.44). These observations are consistent with their common molecular scaffold.

In contrast, DPGME exhibits a markedly different chemical architecture, characterized by a polyether backbone with an hydroxyl group, and lacks the alkylamine and halogenated functionalities typical of nitrogen mustards. Nonetheless, a review of the literature [12,48,51,52,62] confirms that DPGME is commonly employed as a simulant for vesicant CWAs in experimental studies, particularly in the context of chemiresistive sensing (see also the introduction of Paragraph 4.2). While this choice is supported by practical considerations, such as safety and accessibility, it remains largely empirical and lacks a rigorous molecular-level justification. To address this gap, a series of time-dependent DFT (TD-DFT) calculations were carried out to explore the electronic excitation properties of the four compounds (see Appendix 4, Section 4.2.1 for further details). More specifically, for HN1, HN2, HN3, and DPGME the frontier molecular orbitals (Figures A.46 and A.47), the main electronic transitions with the highest oscillator strengths (Table A.31), and the corresponding UV-visible spectra (Figure 70) are presented.

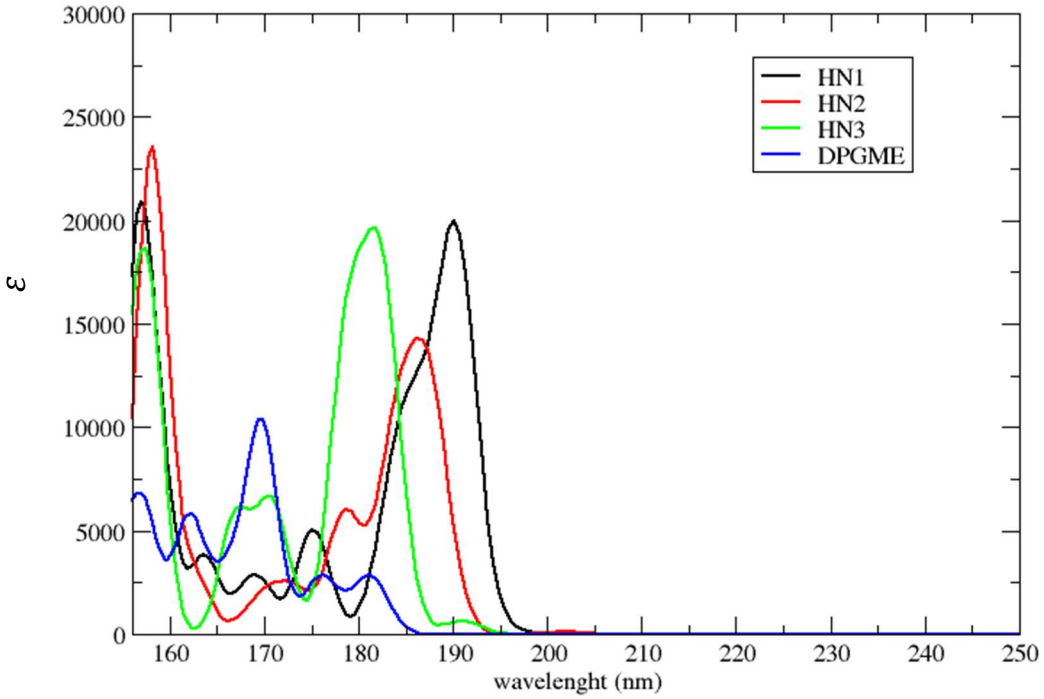

Figure 70: Simulated UV-visible absorption spectra of the nitrogen mustard agents HN1, HN2, and HN3, compared to the DPGME molecule. Spectra were computed at the TD-DFT level (CAM-B3LYP/6-311++G(df,pd)). Despite structural dissimilarities, all species absorb in the UV region and exhibit electronic transitions that fall within the same wavelength range.

Besides the structural diversities DPGME and the nitrogen mustards show also differences in the UV spectra, even among the three CWAs. Nevertheless, the HOMO-LUMO energy gap (ΔE_{H-L}), reported in Table 20 are comparable. This result is of particular relevance, given that the chemical reactivity of molecular systems is largely governed by their frontier orbitals [63]. Indeed, the HOMO-LUMO energy gap is often correlated with the activation barrier of chemical reactions and is frequently used as a predictor of reactivity trends. Accordingly, chemically distinct species, such as those considered here, that display similar ΔE_{H-L} values might be expected to exhibit analogous reactivity profiles [63].

Table 20: HOMO–LUMO energy gap ($\Delta E_{H\text{-}L}$, in eV) and corresponding absorption wavelength (λ, in nm) for the vesicant agents (HN1, HN2, HN3) and the simulant molecule (DPGME), computed in the gas phase.

Species	*$\Delta E_{H\text{-}L}$ [eV]*	*Wavelength, λ [nm]*
DPGME	6.80	181.2
HN1	6.32	196.0
HN2	6.15	201.0
HN3	6.49	190.9

These results suggest that, despite their structural differences, a comparable behavior might emerge across all four species, offering a plausible rationale for the empirical use of DPGME as a simulant in chemiresistive sensing applications. Altogether, the insights gained from this gas-phase study establish a basis for understanding the interaction of these molecules with metal oxide surfaces.

4.2.2 Structural Analysis of HN2 and DPGME Adsorption on Regular and O-Enriched ZnO$(10\bar{1}0)$ Surfaces

The present Section reports the investigation on the molecular-level interaction between the ZnO surface and two analytes: the vesicant nitrogen mustard HN2 and its proposed simulant DPGME. While DPGME has been successfully employed as simulant in several experimental setups [62,64], a theoretical validation of its suitability as a simulant, particularly in terms of adsorption behavior and electronic response, remains lacking.

All calculations were performed using the ZnO$(10\bar{1}0)$ surface, the energetically most favorable termination. This surface has been selected also for its non-polar character, arising from the simultaneous exposure of Zn and O atoms. In addition to the regular stoichiometric slab, two oxygen-enriched surface models were considered, featuring additional oxygen adatoms. This approach enables the investigation of how more realistic defected environments affect adsorption energetics, charge redistribution, and electronic properties at the hybrid interface. Among the nitrogen mustards (HN1-HN3), the smallest HN2 molecule was selected as the target system for computational convenience. Indeed, as discussed in Appendix 4, HN2 shares similar IR and UV-vis spectral features with the other azoyprites, suggesting that its adsorption behavior can be considered representative of this class of CWAs.

4.2.2.1 Adsorption on the Regular ZnO$(10\bar{1}0)$Surface

The adsorption of both HN2 and DPGME molecules was first investigated on a regular stoichiometric ZnO$(10\bar{1}0)$ surface. This non-polar surface model, as previously described, exposes both Zn and O atoms in the outermost atomic layers, thereby providing different potential interaction sites for analyte molecules.

The fully optimized structures of the resulting adsorption complexes are shown in Figure 71, highlighting the preferred adsorption geometries and coordination patterns of each species. In the case of DPGME, the folded isomer was selected due to its higher stability (see Section

4.2.1). Following the same computational protocol adopted in Paragraph 4.1, both total adsorption energies (E_{ads}) and interaction energies (E_{int}) were evaluated. The adsorption energy was computed according to the expression:

$$\mathbf{E_{ads} = E_{surf/mol} - (E_{surf} + E_{mol})} \qquad \textbf{(Eqn.4)}$$

Where $E_{surf/mol}$ = total energy of the surface with the adsorbed molecule; E_{surf} = energy of the clean surface; E_{mol} = energy of the isolated molecule.

The interaction energies were instead computed using the same formal expression, but in this case the energy terms ($E_{surf+mol}$, E_{surf}, and E_{mol}) correspond to the single-point energies of the individual DPGME, HN2 and ZnO($10\bar{1}0$) structures, extracted from the minimum energy structure of the combined systems without performing further geometry optimization (see also Section 4.1.1).

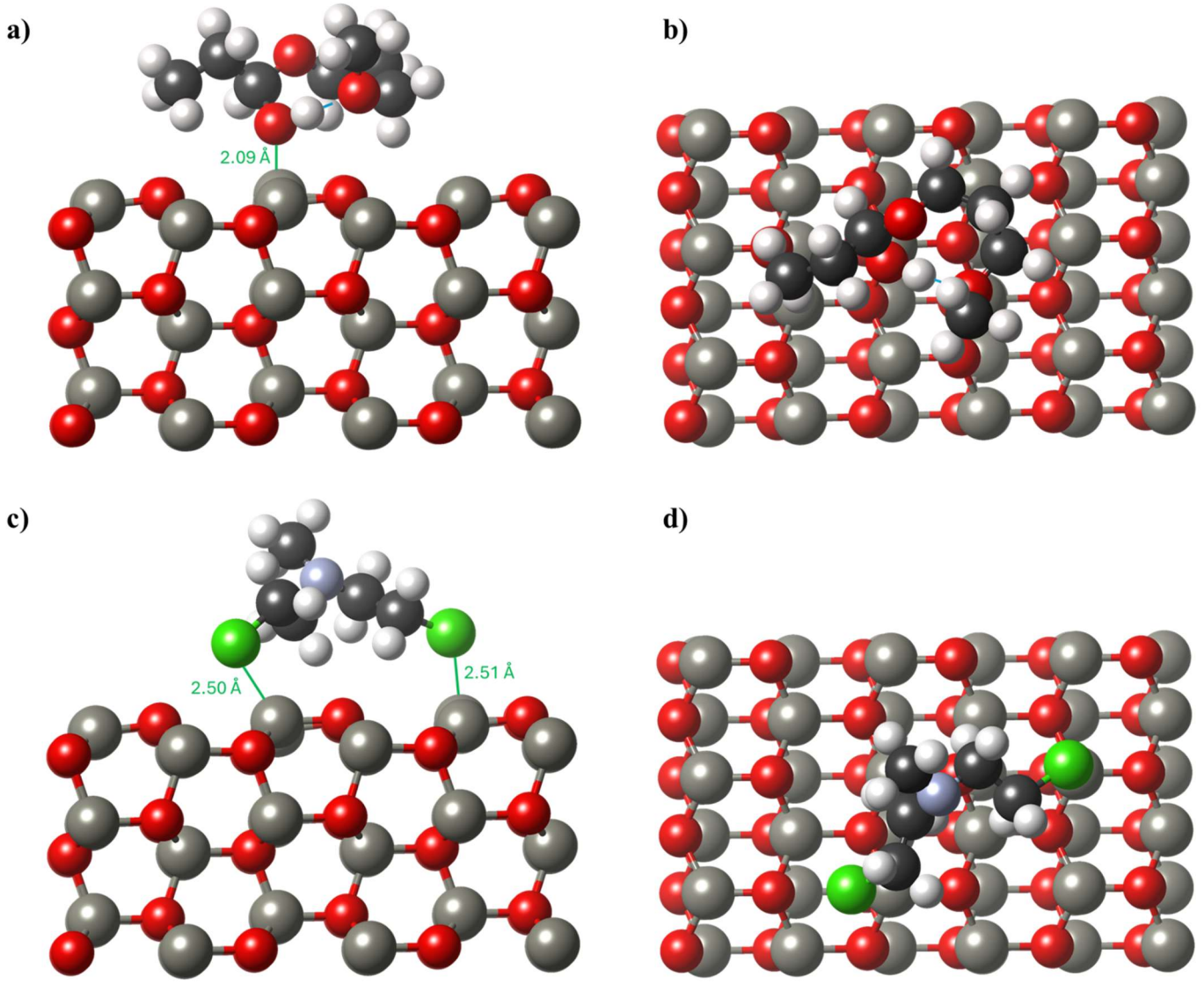

Figure 71: DFT-optimized adsorption geometries of DPGME, shown in side view (a) and top view (b), and of HN2, shown in side view (c) and top view (d), on the regular ZnO($10\bar{1}0$) surface. Green labels indicate the Zn-O and Zn-Cl coordination distances between the hydroxyl oxygen of the simulant or the chlorine atoms of the vesicant and the respective Zn surface atoms, with the corresponding bond lengths reported. The intramolecular hydrogen bond in DPGME is highlighted in blue. Atom color code: Zn = grey; O = red; Cl = light green; C = black; H = white.

As shown in Figure 71, both analytes undergo a physisorption process on the regular ZnO$(10\bar{1}0)$ surface. In the case of DPGME (Figure 71a), the hydroxyl oxygen atom interacts with a surface Zn site, forming a coordination bond characterized by a distance of 2.09 Å and an adsorption energy of -33.31 kcal mol^{-1} (Table 21, Sub-section 4.2.2.2), while the intramolecular hydrogen bond involving the ether oxygen is preserved. E_{int} amounts to -34.38 kcal mol^{-1}. By contrast, the adsorption of the vesicant HN2 involves its two terminal chlorine atoms, which possess non-bonding electron pairs, coordinating to two top layer t Zn atoms. This interaction is associated with an average Zn-Cl bond length of 2.51 Å, an adsorption energy of -31.47 kcal mol^{-1} and E_{int} = -35.63 kcal mol^{-1}. (Table 21). These preferential interaction sites are consistent with the molecular electrostatic potential (MEP) maps of the two organic species (see Section A.4.2.2), which indicated high electron density on the hydroxyl oxygen of DPGME (Figure A.40) and on the chlorine atoms of HN2 (Figure A.43). Accordingly, these electronegative sites interact with the surface Zn cations, which act as Lewis acids capable of accepting electron pairs [65,66]. Based on the current findings, several key similarities can be identified between the vesicant agent HN2 and its proposed simulant DPGME:

i) Both species interact with the ZnO$(10\bar{1}0)$ surface by positioning their electron-rich groups, namely, the hydroxyl oxygen atom in DPGME and the terminal chlorine atoms in HN2, in close proximity to surface Zn sites. This leads to comparable coordination geometries, with Zn-O and Zn-Cl bond lengths of approximately 2.1 Å and 2.5 Å, respectively.

ii) The adsorption energies of the two systems are similar (see Table 21). The difference between the adsorption energies of DPGME + ZnO and HN2 + ZnO is approximately 1.84 kcal mol^{-1}. This result is consistent with previous theoretical studies conducted on the same ZnO surface involving the nerve agent Sarin and its simulant dimethyl methylphosphonate (DMMP), for which adsorption energy differences within a range of approximately 3 kcal mol^{-1} were reported [67], despite the stronger chemical resemblance between Sarin and DMMP.

iii) Finally, the computed interaction energies (Table 21), which provide a more direct estimate of the intrinsic strength of surface-molecule interactions, are even more closely aligned, with a difference of only 1.25 kcal mol^{-1} between the two systems.

Overall, these findings suggest that, from an energetic standpoint, the vesicant and its simulant exhibit comparable affinities towards the ZnO$(10\bar{1}0)$ surface.

4.2.2.2 Adsorption on O-Enriched ZnO$(10\bar{1}0)$ Surfaces

Since the experimental addition of either atomic or molecular oxygen to metal oxide semiconductor (MOX) surfaces has been shown to enhance the detection of CWAs [48], the interaction of DPGME and HN2 with oxygen-enriched ZnO surfaces was also investigated. The presence of excess surface oxygen atoms may alter the conductivity of the oxide by modulating the carrier density near the surface [48,65,66]. Under operating conditions typically ranging from 150 to 400 °C, the ZnO surface can host a variety of oxygen species, including molecular O_2, ionized superoxide (O_2^-), and atomic oxygen (O). While O_2 and O_2^- are predominant at lower temperatures, atomic oxygen becomes the dominant adsorbate at higher

temperatures (above ca. 400 °C), where it is primarily present in dissociated chemisorbed form [65,66]. These adsorbed species act as electron acceptors, creating surface depletion layers that modulate the semiconductor's response upon exposure to reducing gases. The ability of MOX surfaces to incorporate and exchange such oxygen species is therefore considered a key feature for selective analyte recognition [48,65,66]. To simulate these experimentally relevant conditions, two oxygen-enriched ZnO$(10\bar{1}0)$ slab models were constructed: one incorporating a single additional oxygen atom, and one including a pre-adsorbed O_2 molecule in a dissociated form. In the latter case, two atomic oxygen species were directly placed on the surface to mimic dissociative O_2 adsorption. These modified surfaces may allow the evaluation of how increased oxygen coverage influences both the adsorption behavior and the interaction strength of HN2 and DPGME, providing further insight into the role of oxidizing surface conditions in chemoresistive sensing.

To illustrate the structural models employed in this Sub-section, Figure 72 shows the two oxygen-enriched ZnO$(10\bar{1}0)$ surfaces used as substrates for adsorption calculations. The first model (Figure 72a) incorporates a single additional oxygen atom, while the second (Figure 72b) represents the dissociative O_2 adsorption scenario, in which two atomic oxygen species are pre-adsorbed on the surface.

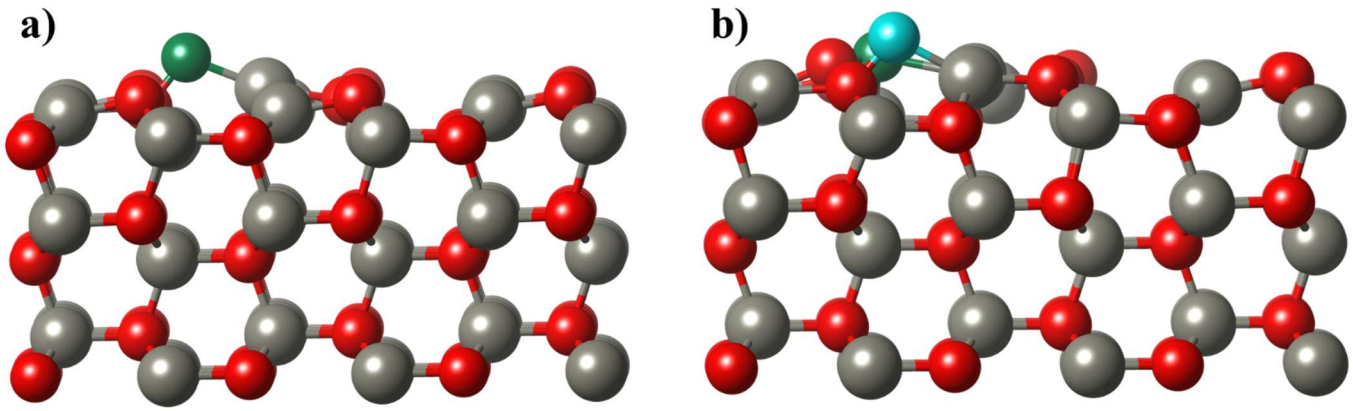

Figure 72: Top-view of the optimized ZnO$(10\bar{1}0)$ surface models used for oxygen-enriched conditions: (a) surface with one additional oxygen atom; (b) surface with two oxygen atoms mimicking dissociative O_2 adsorption. The added oxygen species are depicted in green and cyan, while Zn and lattice O atoms are colored gray and red, respectively.

Following the construction of these oxidized Zn$(10\bar{1}0)$ surface models, the adsorption of both DPGME and HN2 was investigated on each substrate to determine their preferred binding configurations. As in the case of the regular ZnO$(10\bar{1}0)$ surface, both total adsorption energies (E_{ads}) and interaction energies (E_{int}) were computed. The fully optimized structures of the resulting adsorption complexes are displayed in Figure 73, while the corresponding E_{ads} and E_{int} values are reported in Table 21. As can be seen, both the total adsorption energies and interaction energies calculated for DPGME and HN2 on oxygen-enriched ZnO$(10\bar{1}0)$ surfaces are significantly less negative than those obtained for the corresponding regular surface complexes. This trend indicates a notable decrease in the adsorption affinity upon increasing surface oxygen coverage.

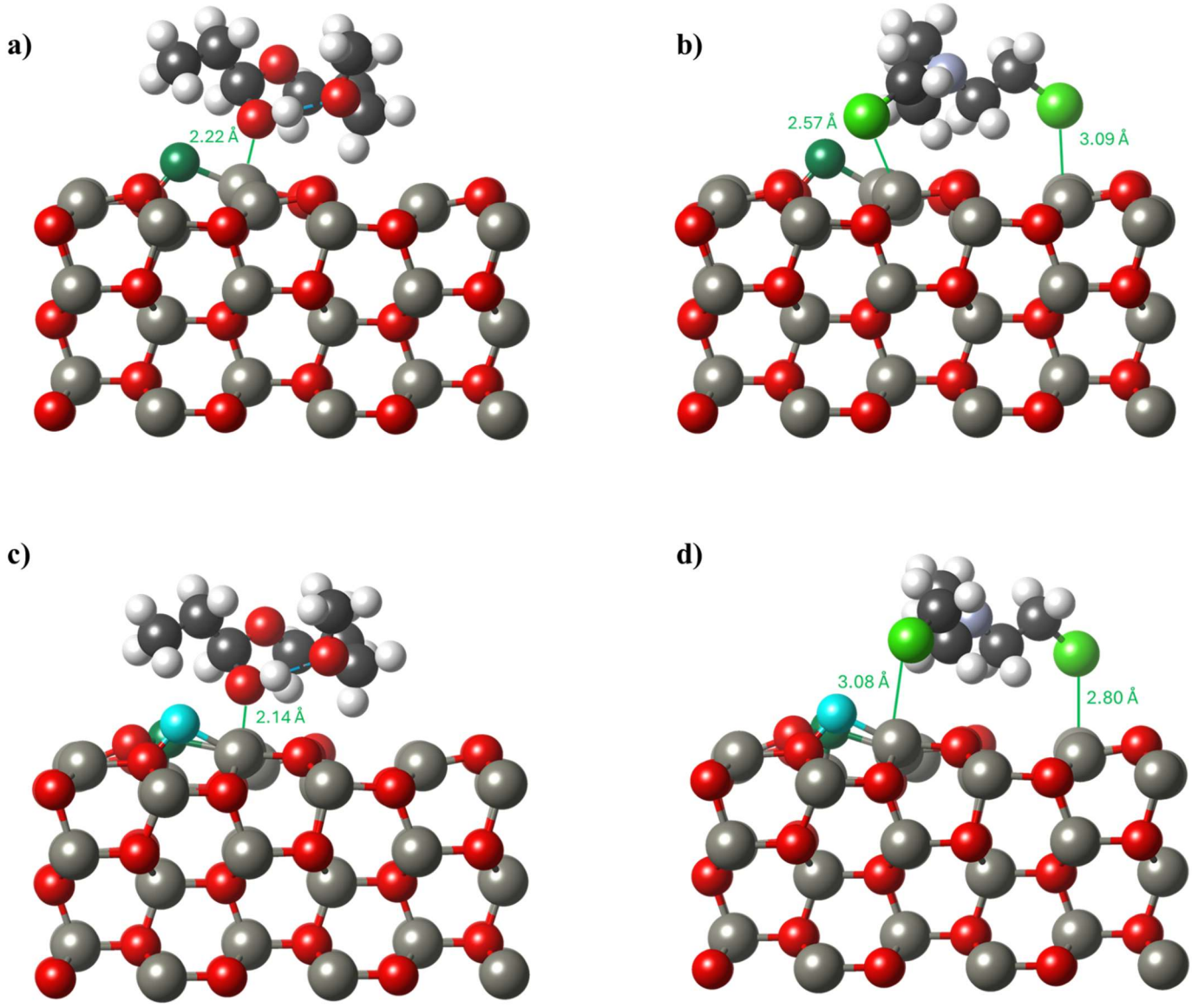

Figure 73: DFT-optimized adsorption geometries of (a) DPGME on ZnO($10\bar{1}0$) + O, (b) HN2 on ZnO($10\bar{1}0$) + O, (c) DPGME on ZnO($10\bar{1}0$) + O_2, (d) HN2 on ZnO($10\bar{1}0$)) + O_2. Green labels indicate the Zn-O and Zn-Cl coordination distances between the hydroxyl oxygen of the simulant or the chlorine atoms of the vesicant and the respective Zn surface atoms, with the corresponding bond lengths reported. The intramolecular hydrogen bond in DPGME is highlighted in blue. Atoms color code: Zn = grey; O_{surf} = red; $O_{adatoms}$ = dark green and cyan; Cl = light green; C = black; H = white.

Table 21: Computed total adsorption energies (E_{ads}) and interaction energies (E_{int}) for DPGME and HN2 adsorbed on regular (Figure 71) and oxygen-enriched (Figure 73) ZnO($10\bar{1}0$)) surfaces. Oxygen-enriched models include either an additional O atom or a dissociated adsorbed O_2 molecule.

System	E_{ads} (kcal/mol)	E_{int} (kcal/mol)
DPGME + ZnO	-33.31	-34.14
DPGME + ZnO + O	-19.93	-24.62
DPGME + ZnO + O_2	-27.22	-30.77
HN2 + ZnO	-31.47	-35.63
HN2 + ZnO + O	-23.77	-27.93
HN2 + ZnO + O_2	-21.86	-22.21

The reduction in adsorption affinity is further supported by the optimized geometries (Figure 73), which reveal larger average distances between the adsorbed molecules and the surface, exceeding those observed on the regular ZnO$(10\bar{1}0)$ substrate (Figure 71; for DPGME: Zn-O = 2.10 Å, for HN2: Zn-Cl = 2.51 Å). In particular, average distances between the key interacting atoms and the surface Zn sites were found to be approximately Zn-O = 2.22 Å for DPGME and Zn-Cl = 2.83 Å for HN2 on the ZnO + O model, and Zn-O = 2.14 Å and Zn-Cl = 2.97 Å respectively on the ZnO + O_2 surface. These structural features are consistent with the computed energies and confirm the weakening of the surface-analyte interactions under oxidizing conditions. This attenuated interaction can be rationalized in light of previous investigations on ZnO-based systems, where pre-adsorbed water molecules were shown to hinder the adsorption of Sarin and its simulant dimethyl methylphosphonate (DMMP) by introducing steric hindrance at the preferred adsorption sites [67]. A similar adsorption-limiting effect may be proposed in the present case, whereby co-adsorbed oxygen species, either atomic or molecular, reduce the accessibility of Lewis acidic Zn sites, thus limiting the ability of the analyte to establish direct physisorption. In this light, co-adsorbed species such as O_2 or H_2O on the ZnO surface may weaken direct physisorption of intact organic molecules.

Despite the observed reduction in adsorption strength, the energetic differences between DPGME and HN2 adsorption remain rather small across all surface models. Specifically, ΔE_{ads} and ΔE_{int} values between the two analytes are limited to 3.84 and 3.31 kcal mol^{-1}, respectively, on the ZnO + O surface, and 5.36 and 8.56 kcal mol^{-1} on the ZnO + O_2 surface. These findings might provide further support to the ability of DPGME to replicate the adsorption behavior of the vesicant HN2, even under oxidizing surface conditions, thereby reinforcing its suitability as a simulant molecule.

In summary, the structural and energetic data presented in this Section 4.2.2 indicate that both DPGME and HN2 are capable of physisorbing on ZnO$(10\bar{1}0)$ surfaces, irrespective of the presence of additional surface oxygen species. This theoretical analysis has enabled the establishment of physicochemical correlations between the two analytes, suggesting that DPGME represents a suitable simulant for HN2 beyond the experimental evidence available to date. These findings might contribute to the rational design of functional nanomaterials for gas sensing applications, where the identification of safe and reliable molecular mimics plays a critical role. The next Section will focus on the electronic structure of the adsorbed systems, through charge density difference (CDD) maps, Bader charge analysis, and density of states (DOS). These results will provide further insight into the analyte-surface interaction.

4.2.3 Electronic Structure Modulation and Electron Transfer upon Adsorption of DPGME and HN2 on ZnO$(10\bar{1}0)$

As anticipated at the end of the previous Section, a more detailed understanding of the electronic interactions between the analytes (DPGME and HN2) and the ZnO$(10\bar{1}0)$ surfaces can be obtained through Charge Density Difference (CDD) analysis, already introduced in Paragraph 4.1.2. Here, the CDD maps enable a direct visualization of how electron density is

redistributed at the interface upon analyte adsorption, offering spatially resolved insight into the nature of surface interactions. Figure A.48 displays the CDD isosurfaces computed for DPGME and HN2 adsorbed on ZnO($10\bar{1}0$) surfaces under different conditions, including both regular and oxygen-enriched models. The comparison among the three surface models, regular, with a single O adatom, and with a co-adsorbed dissociated O_2 molecule, reveals how the presence of additional oxygen species slightly alters the spatial distribution of charge density, particularly in the proximity of the adsorption site.

Notably, the electron accumulation is consistently localized along the Zn-O (for DPGME) and Zn-Cl (for HN2) bonds, indicating that the electron density is redistributed from the adsorbed molecules toward the Zn surface atoms. This spatial pattern suggests the establishment of non-covalent interactions with partial electron transfer character. Although the interactions remain non-covalent in nature, the electron redistribution observed in the CDD maps supports a donor-acceptor interaction mechanism, in which electron density is transferred from the adsorbed molecule toward the oxide surface. This qualitative picture aligns with the Bader charge analysis discussed below, reinforcing the interpretation of both DPGME and HN2 as electron donors toward ZnO. Taken together, the CDD results provide a complementary and intuitive representation of the local electronic effects associated with physisorption, offering molecular-level insight into the interfacial behavior of these systems.

To complement the qualitative insights provided by the CDD maps, a quantitative assessment of electron transfer was carried out through Bader charge analysis for all systems under investigation (see Section A.4.1.3 for theoretical details). The resulting charge values are summarized in Table A.32. In all cases, both analytes, DPGME and HN2, act as electron donors toward the ZnO($10\bar{1}0$) surfaces, in agreement with the donor-acceptor interaction pattern deducted from the CDD analysis.

For DPGME, the computed electron transfer amounts to +0.09*e* on the regular ZnO surface, slightly decreasing upon surface enrichment with an oxygen adatom (+0.06*e*) or an adsorbed O_2 molecule (+0.07e). A similar trend is observed for HN2, which donates a larger amount of electronic charge overall: +0.16*e* on regular ZnO, +0.14*e* on ZnO + O, and +0.08*e* on ZnO + O_2. These values confirm that HN2 establishes a stronger electronic interaction with the substrate compared to DPGME for all the considered surface conditions. The observed reduction in transferred electrons on oxygen-enriched surfaces suggests that the presence of pre-adsorbed oxygen species either screens the active Zn sites or competes directly for interaction with the incoming analyte. This effect weakens the interaction between the molecules and the surface, thereby reducing the extent of electron transfer. Notably, on the O_2-adsorbed surface, DPGME and HN2 donate nearly identical amounts of charge, indicating a convergence of their adsorption behavior under oxidizing conditions. Overall, these results reinforce the interpretation of both analytes as electron donors and highlight the sensitivity of electron transfer processes to the local surface composition. Moreover, Bader charge analysis supports the conclusion that DPGME closely mimics the electronic behavior of HN2, providing further theoretical validation of its use as a simulant for this type of CWAs.

To gain further insight into how the ZnO electronic structure responds to molecular adsorption, a detailed analysis of the Density of States (DOS) was carried out for all systems under

investigation. In this context, the electronic structure type (*p* or *n*) of each model was determined from the computed DOS by comparing the energies of the VB and CB band edges with the Fermi level, conventionally set to 0 [68-70]. This approach provides complementary evidence to the CDD and Bader charge analyses, offering a possible link between electronic properties and the potential sensing capabilities of ZnO nanostructures in the context of the development of chemiresistive nanosensor.

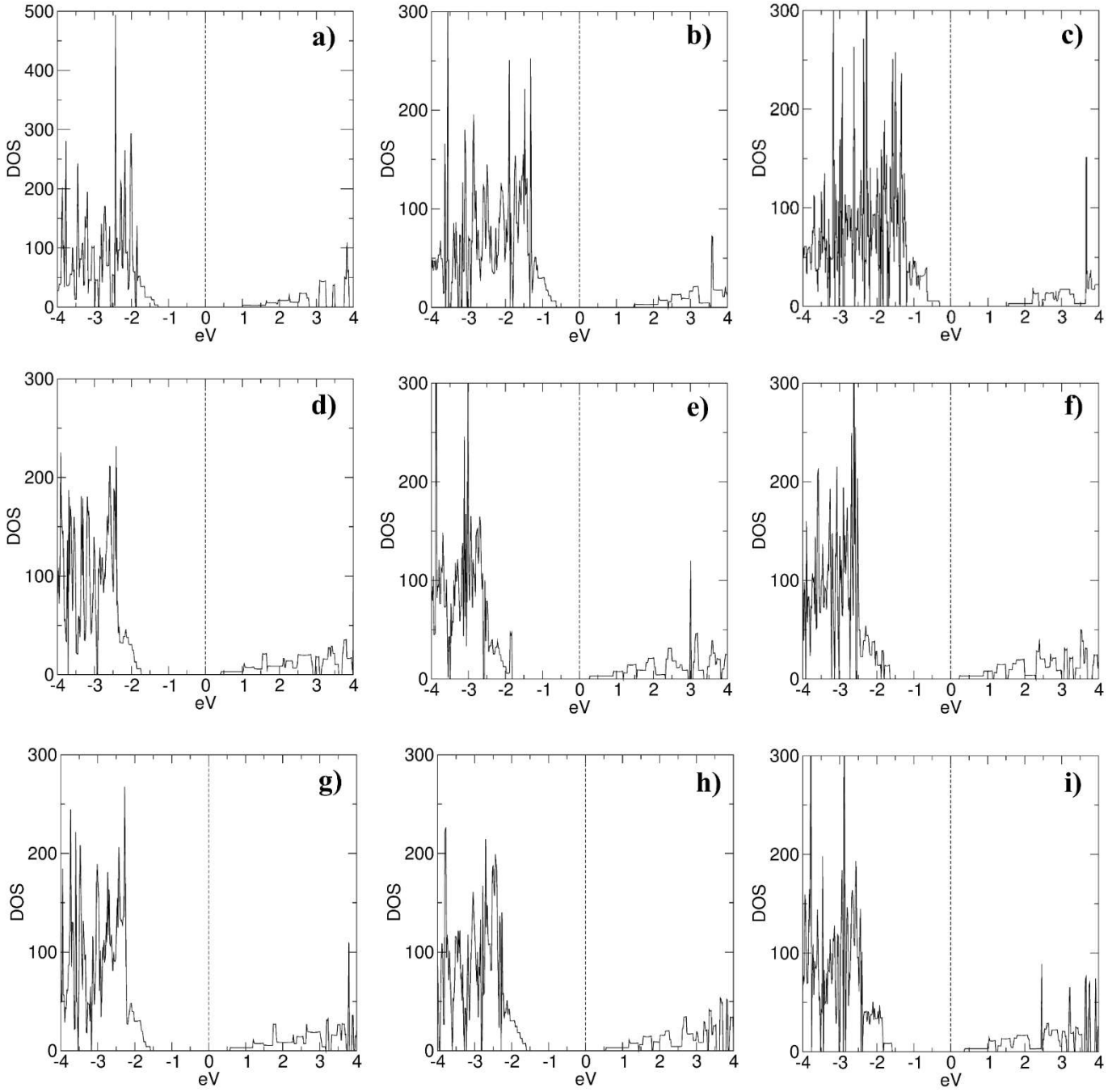

Figure 74: Density of states (DOS) computed for: a) regular ZnO($10\bar{1}0$) slab (ZnO); b) mono-oxygenated ZnO($10\bar{1}0$) slab (ZnO + O); c) di-oxygenated ZnO($10\bar{1}0$) slab (ZnO + O_2); d) DPGME on ZnO; e) DPGME on ZnO + O; f) DPGME on ZnO + O_2; g) HN2 on ZnO; h) HN2 on ZnO + O; i) HN2 on ZnO + O_2. The dashed vertical line indicates the Fermi Level, conventionally set to 0.

Table 22: Band gap energy values (E_G, in eV) computed for regular and O-enriched ZnO($10\bar{1}0$) slab models, as well as after adsorption of DPGME and HN2.

System	E_G (eV)	Type
ZnO	2.28	n
ZnO + O	2.12	p
ZnO + O_2	1.92	p
DPGME + ZnO	2.14	n
DPGME + ZnO + O	2.10	n
DPGME + ZnO + O_2	1.90	n
HN2 + ZnO	2.16	n
HN2 + ZnO + O	2.16	n
HN2 + ZnO + O_2	1.98	n

The DOS plots are presented in Figure 74, and the corresponding band gap energies are collected in Table 22. As expected, these data confirm the *n*-type character of the stoichiometric ZnO($10\bar{1}0$) surface (Figure 74a, Table 22). Notably, the introduction of an oxygen adatom induces a conversion to *p*-type behavior (Figure 74b, Table 22), which becomes more evident with increasing surface oxygen concentration (Figure 74c, Table 22). This finding is in line with experimental observations reporting that *p*-type ZnO samples exhibit higher oxygen to zinc ratios compared to their *n*-type counterparts [71-73]. Interestingly, the electronic band gap, calculated as 2.28 eV for the regular ZnO($10\bar{1}0$) surface, undergoes a progressive reduction upon surface oxygenation, decreasing to 2.12 eV for the mono-oxygenated model and further to 1.92 eV for the di-oxygenated system. This result suggests that the oxygen adatoms might have a detectable effect on the electronic structure of the sensing material.

The impact of HN2 and its simulant DPGME on the electronic structure of regular and oxygen-enriched ZnO ($10\bar{1}0$) surfaces is now considered. For the regular slab model, adsorption of DPGME (Figure 74d) and HN2 (Figure 74g) does not result in substantial modifications of the DOS, but leads to a moderate reduction of the band gap (E_G), with comparable values observed for both molecules (Table 22). The effect of analyte adsorption on the electronic structure of oxygen-enriched ZnO ($10\bar{1}0$) surfaces is shown in Figure 74e,f,h,i, which report the DOS after interaction with DPGME or HN2 molecules. In all cases, a marked shift of the Fermi level towards the bottom of the CB is observed, indicating a transition from *p*-type to *n*-type character. This *p*-*n* inversion could be of particular interest in the context of chemiresistive gas sensing [71,72,74], where variations in carrier concentration directly influence the sensor response [75,76]. These results may thus support the hypothesis of a potential "on-off" recognition mechanism, in which exposure to DPGME or HN2 induces a switch in the electronic response of the sensor, leading to a measurable change in resistance [71].

Moreover, the DOS analysis provides additional support for the role of DPGME as a reliable simulant for HN2. Despite their different chemical structures, the two analytes induce similar electronic responses upon adsorption, both in terms of electron transfer (as previously shown) and in terms of DOS modulation. This strengthens the physicochemical foundation for using DPGME in the design and testing of sensor materials aimed at detecting nitrogen mustard-

type chemical warfare agents. From a broader perspective, these findings highlight the importance of gathering atomistic-level insight into the organic-inorganic interfaces. By suggesting that molecular adsorption could modulate the electronic character of ZnO surface, these results might contribute to the rational design of gas-sensing nanomaterials, as the one shown in Ref. [56-58,60].

4.2.4 Concluding Remarks

Paragraph 4.2 has presented a theoretical investigation aimed at elucidating the molecular-level interactions between nitrogen mustard agents and ZnO-based chemiresistive sensors. In particular, the study focused on HN2 as representative vesicant compound and on DPGME as their widely used, but empirically selected, simulant. The initial gas-phase analysis established the most stable conformers for all species. Molecular electrostatic potential (MEP) maps offered insights into the spatial distribution of electron density, highlighting key nucleophilic regions that correlate with preferred adsorption sites on ZnO surfaces. Despite their marked structural differences, DPGME and the nitrogen mustards displayed similar HOMO-LUMO energy gaps, thus supporting a molecular-level rationale for the simulant's use in sensing applications. Subsequent adsorption studies demonstrated that both HN2 and DPGME undergo physisorption on regular and oxygen-enriched ZnO$(10\bar{1}0)$surfaces. In all cases, the adsorbates interact through their electron-rich functional groups (Cl atoms for HN2, hydroxyl oxygen for DPGME), coordinating with surface Zn cations. Adsorption and interaction energies, as well as structural parameters, were found to be comparable between the two molecules across all surface models, reinforcing the role of DPGME as a faithful simulant under both stoichiometric and oxidized conditions. Electronic structure analyses further supported these findings. Charge Density Difference (CDD) maps revealed consistent donor-acceptor interactions at the interface, with partial electron transfer from the analytes toward the ZnO surface. Bader charge analysis quantified this electron donation, confirming a slightly higher electron transfer for HN2 but a nearly convergent behavior under oxygen-rich conditions. Finally, Density of States (DOS) profiles show in the oxygen-enriched surfaces a transition from *p*-type to *n*-type character upon adsorption, which might play a role in the sensing mechanism. Taken together, the results of this Paragraph may represent a starting point for improving our atomistic-level understanding of the interaction of nitrogen mustards and their simulants with ZnO-based chemiresitive sensors. The demonstrated electronic and energetic similarities between DPGME and HN2 validate the former as a reliable model molecule for experimental and computational studies.

4.3 Chapter 4 - Conclusions

This Chapter presented a theoretical investigation into molecular adsorption at oxide surfaces. Two complementary case studies were considered to address different aspects of this phenomenon: the first focused on the covalent binding of a macrocyclic organic host (Pillar[6]arene) onto ITO and In_2O_3 surfaces, while the second examined the physisorption of a nitrogen mustard vesicant (the azoyprite HN2) and its simulant (DPGME) on ZnO$(10\bar{1}0)$.

In the case of Pillar[6]arene (P[6]A), a prototypical macrocyclic host with multiple hydroxyl groups in its structure, periodic DFT calculations revealed that the most probable process for surface adsorption involves the elimination of water molecules, leading to the formation of robust covalent bonds between some carbon atoms of the molecule and surface oxygen atoms. The resulting hybrid structures were shown to preserve both geometrical integrity and the molecular recognition properties typical of the host species, namely P[6]A. These findings highlight the potential of surface-anchored systems for applications in molecular sensing and (photo)electrocatalysis, where both stability and functionality are required under operative conditions.

Conversely, the ZnO-based case study focused on weaker, non-covalent adsorption phenomena. A computational approach, including periodic DFT geometry optimizations, and electronic properties analysis (CDD, Bader Charge and DOS), was employed to understand the interaction of nitrogen mustard CWAs with the ZnO$(10\bar{1}0)$ surface. In this context, HN2, chosen as representative of the three azoyprites, and DPGME were shown to interact with ZnO$(10\bar{1}0)$ via coordination to exposed Zn atoms, without significant structural perturbation of the surface. Charge density difference (CDD) and Bader charge analyses revealed electron transfer from the adsorbates to the oxide, modulating the surface electronic structure in a way that might enable detection of volatile analytes. In this regard, DOS calculations indicated a transition in surface electronic character (from *p*-type to *n*-type) suggesting a potential sensing mechanism based on modulation of the metal oxide's electronic structure. The similarity both in energetic and electronic properties between DPGME and HN2 upon adsorption on ZnO$(10\bar{1}0)$ may support from a first-principles standpoint the use of DPGME as a simulant for nitrogen mustard CWAs.

– Appendix Chapter 4 –

Supplementary Information Paragraph 4.1

A.4.1.1 Computational details

All density functional theory (DFT) calculations were performed the CP2K code [77], within the Gaussian and plane-wave (GPW) formalism. In particular, the Perdew-Burke-Ernzerhof (PBE) approximation [78] was adopted for exchange and correlation functionals, combined with the non-local rVV10 correction [79] to account for dispersion interaction. Based on the partial density of states of the In_2O_3 bulk structure, for all the atoms the TZV2P-MOLOPT-SR-GTH basis set [80] (In: 13, O: 6, C: 4, H: 1 valence electrons) was selected and the Goedecker-Teter-Hutter (GTH) pseudopotentials [81] were employed for the description of the core electrons. The plane-wave basis set was truncated using an energy cutoff of 600 Ry. All calculations found convergence at an accuracy of 10^{-6} Hartree. The In_2O_3 slab was derived from an optimized bulk structure (space group: Ia-3 [206], computed lattice parameter: 10.41 Å; Literature: 10.18 Å [82]) using the Atomic Simulation Environment (ASE) [83]. Since the (111) facet is the thermodynamically most stable for indium oxide [84], an 8 × 8 × 4 supercell of In_2O_3 (111) was modeled, with the bottom two atomic layers kept fixed during structural optimization. The corresponding ITO surface was instead constructed by partial substitution of indium atoms with tin ones to achieve a ~9 wt% Sn doping level, consistent with previous computational studies [85,86]. Despite the possible emergence of a metastable rhombohedral (rh) phase at this doping level, all calculations were performed on the ITO (111) slab model with a body-centred cubic (BCC) crystal structure, which is more thermodynamically stable [87]. To minimize inter-slab interactions due to periodic boundary conditions, a vacuum layer exceeding 15 Å was introduced perpendicular to the surface. In adsorption models (molecule + slab), the vacuum was adjusted to fully accommodate the height of the adsorbate. Adsorption energies (E_{ads}) were computed from the fully optimized geometries of the considered systems, according to the formula (Eqn. A1):

$$\mathbf{E_{ads} = E_{surf/mol} - (E_{surf} + E_{mol})} \qquad \textbf{(Eqn. A1)}$$

Where $E_{surf/mol}$ = total energy of the surface with the adsorbed molecule; E_{surf} = energy of the clean surface; E_{mol} = energy of the isolated molecule.

Atomic charges reported in Table A.25 were calculated through the Bader approach [88] using the same level of theory adopted in the geometry optimizations. The infrared (IR) spectrum of the optimized P[6]A structure (Figure A.32) was simulated by performing vibrational frequency analysis at the same theoretical level. All computed frequencies were positive. The IR spectrum was broadened with a Gaussian function of 2 cm^{-1}. To ensure accuracy of low-frequency modes, a stringent wavefunction convergence criterion of 10^{-8} was adopted for the vibrational analysis.

A.4.1.2 Isolated Pillar[6]arene: Structural and Spectroscopic Features

Before investigating the adsorption of Pillar[6]arene (P[6]A) on metal oxide surfaces (namely, In_2O_3 and ITO), a detailed characterization of the isolated molecule, focusing on its geometry, intramolecular interactions, and vibrational properties, was essential to provide a reference for the structural and spectroscopic changes expected upon surface binding.

The optimized molecular structure of P[6]A is shown in Figure A.32. The molecule consists of six p-substituted benzene rings connected by methylene bridges, forming a well-defined cylindrical macrocycle with twelve hydroxyl (-OH) groups located at the periphery. These -OH moieties participate in multiple intramolecular hydrogen bonds, alternating above and below the plane of the macrocycle, which contribute to the structural rigidity of the system. The calculated internal cavity diameter of P[6]A is approximately 8.0 Å, which is significantly larger than the value reported in the literature (6.7 Å) [89]. This discrepancy may be attributed to the known limitations of generalized gradient approximation (GGA) functionals, such as PBE, in accurately describing hydrogen bonding interactions [90]. In particular, the incorrect estimation of hydrogen bond distances could lead to an expanded macrocyclic ring geometry, and thus to an overestimation of the cavity size. Figure A.32 also reports the simulated infrared (IR) spectrum of the isolated P[6]A molecule, and Table A.21 provides the assignment of the main vibrational modes to the corresponding absorption bands. A comparison with available experimental IR data [39] shows satisfactory agreement in terms of both peak positions and intensities, thereby validating the theoretical model and supporting the vibrational band assignment.

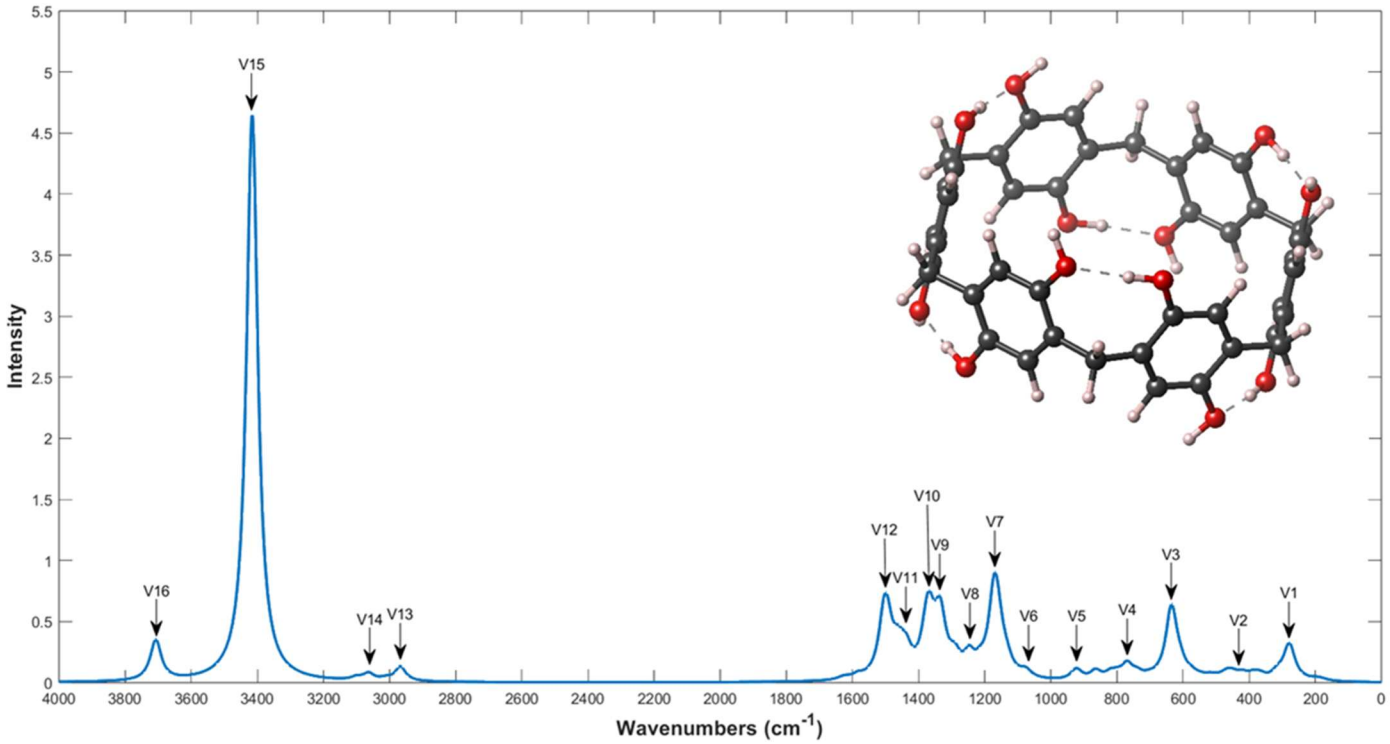

Figure A.32: Computed IR vibrational spectrum of Pillar[6]arene (top right). Atoms color code: C = grey, O = red, H = white. Dashed lines represent H-bonds.

Table A.21: Computed wavenumbers ($\tilde{\nu}$, cm^{-1}) and corresponding band assignments for the IR spectrum of isolated Pillar[6]arene shown in Figure A.32.

	$\tilde{\nu}$ (cm^{-1})	Intensity	Assignment
V1	270-280	0.330	O-H In-Plane-Bending (Oxygen of H-bond)
V2	417-421	0.105	Benzene ring Out-of-Plane-Bending
V3	632-644	0.620	O-H In-Plane-Bending (Hydrogen of H-bond)
V4	768-776	0.170	Benzene ring's C-H Asymmetrical Out-of-Plane Bending
V5	927	0.114	CH_2 Rocking
V6	1071-1079	0.130	Stretching of C_6H_4-OH and C_6H_4-CH_2 bonds
V7	1160-1214	0.900	C-H and O-H (no H of H-bond) In-Plane-Bending
V8	1247	0.310	C-H and O-H (no H of H-bond) In-Plane-Bending
V9	1331-1332	0.700	All O-H In-Plane-Bending
V10	1370	0.750	O-H (H bond) In-Plane-Bending and benzene C=C stretching
V11	1460	0.470	O-H (H bond) In-Plane-Bending and CH_2 Scissoring
V12	1500	0.730	Benzene C-H In-Plane-Bending
V13	2967	0.130	CH_2 Symmetrical and Asymmetrical Stretching
V14	3064-3100	0.060	C-H Symmetrical Stretching
V15	3407-3422	4.200	Stretching O-H (H-bond)
V16	3706-3708	0.350	Stretching O-H (no H-bond)

A.4.1.3 Additional Information on the Adsorption Process of P[6]A on In_2O_3 and ITO Surfaces

This Section collects additional computational data and structural models supporting the discussion on the adsorption of Pillar[6]arene (P[6]A) on In_2O_3 and ITO surfaces presented in Section 4.1.2 of the main text. It includes a comparative analysis of adsorption energies associated with proton transfer and water elimination processes, alongside detailed structural representations of the resulting systems. Charge Density Difference (CDD) maps and Bader charge analyses are also provided to elucidate the electronic changes occurring at the interface between P[6]A and the oxide surfaces.

Table A.22: Total adsorption energy values (in eV) computed for the proton transfer (PT) process in the systems P[6]A + In_2O_3 and P[6]A + ITO, involving different hydroxyl groups of the macrocyclic ring (the ones closest to the surfaces).

	P[6]A + In_2O_3	***P[6]A + ITO***
Hydrogens under PT	**Eads (eV)**	
None	-1.18	-3.45
A	-1.27	-3.08
B	-1.62	-3.30
C	-1.71	-3.47
A + B + C	-1.41	-2.51
HA	-0.94	-2.41
HB	-1.10	-2.56
HC	-1.07	-1.80

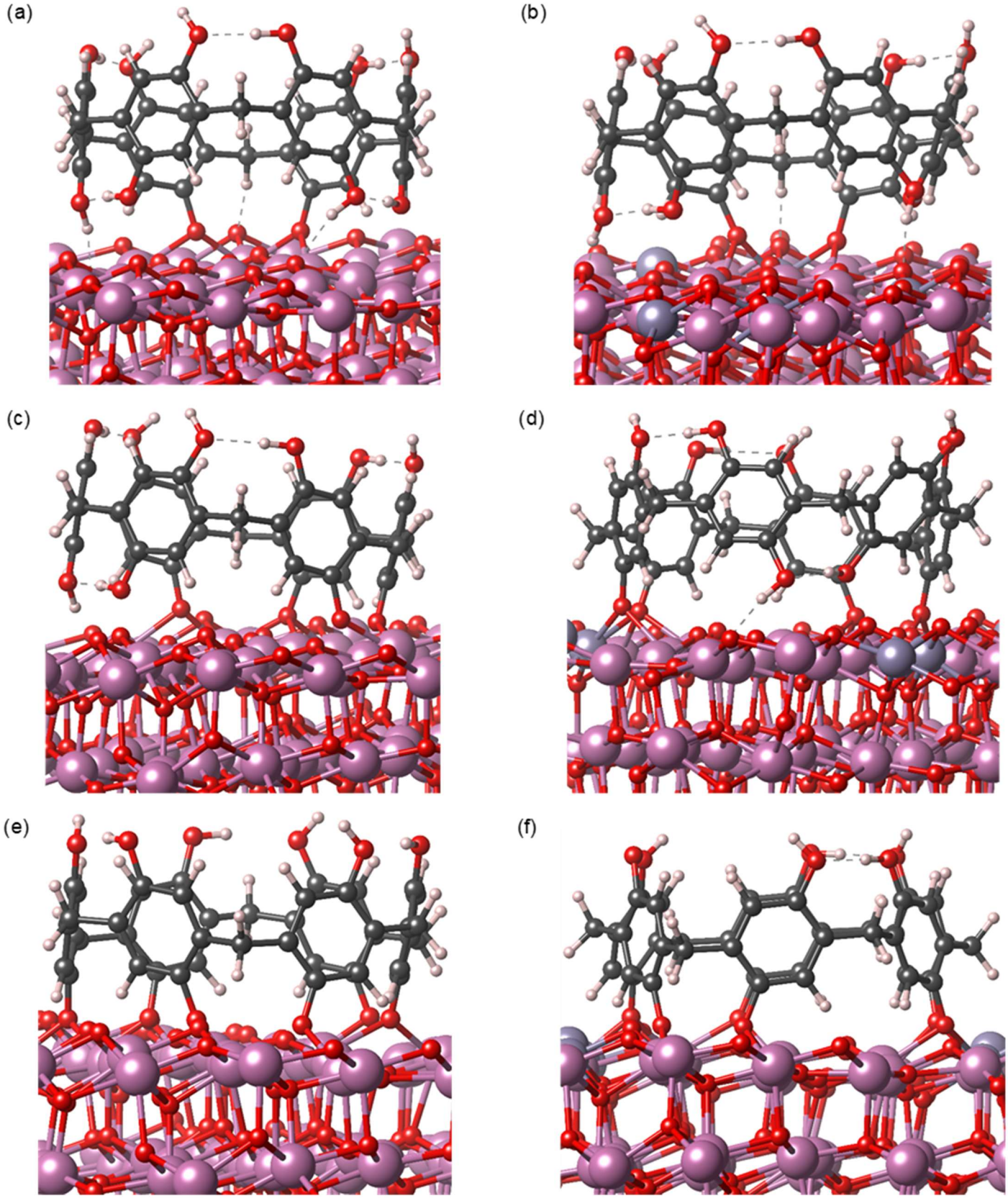

Figure A.33: Graphical representation of the DFT-optimized structures of the P[6]A + In_2O_3 and P[6]A + ITO systems after the elimination of 2 (a, b), 4 (c, d), and 6 (e, f) water molecules. Panels a, c, e refer to In_2O_3-based systems; panels b, d, f to ITO-based systems. Atoms color code: In = purple; Sn = dark purple; C = dark grey; O = red; H = white.

Table A.23: Total adsorption energy (E_{ads}) values and relative energy differences (ΔE) for the isomers of the P[6]A - In_2O_3 - $2H_2O$ system. The ΔE values were computed with respect to the most stable configuration, in which the P[6]A molecule gives its C and HC hydrogen atoms to form two water molecules. H atoms labeled as in Figure 65.

Hydrogens	***A + HA***	***B + HB***	***C + HC***	***A + B***	***B + C***	***A + C***
E_{ads} ***(eV)***	-1.48	-2.06	-2.29	-1.60	-2.03	-1.90
ΔE (eV)	0.81	0.23	0	0.68	0.26	0.39

Table A.24: Total adsorption energy (E_{ads}) values and relative energy differences (ΔE) for the isomers of the P[6]A - ITO - $2H_2O$ system. The ΔE values were computed with respect to the most stable configuration, in which the P[6]A molecule donates its C and HC hydrogen atoms (labels as in Figure 66) to form two water molecules. Isomers in which the macrocyclic ring anchors to the ITO surface via tin-coordinated oxygen atoms are generally more stable than those involving In-O sites.

Hydrogens	***In:*** ***A + HA***	***Sn:*** ***A + HA***	***In:*** ***B + HB***	***Sn:*** ***B + HB***	***In:*** ***C + HC***	***Sn:*** ***C + HC***
E_{ads} ***(eV)***	-0.36	-1.07	-0.66	-2.68	-0.56	-2.76
ΔE (eV)	2.40	1.69	2.10	0.07	2.20	0

CDD and Bader Charge Analyses

Charge Density Difference (CDD) analysis allows for the visualization of electron redistribution upon the adsorption of a molecular system onto a surface. By computing the difference between the total electron density of the combined system and the sum of the electron densities of the isolated components (each evaluated at the same geometry), CDD highlights regions of electron accumulation and depletion. This enables a direct spatial representation of chemical bonding and non-covalent interactions such as hydrogen bonds and donor-acceptor effects, underlying its use in the study of organic-inorganic interfaces, making it a powerful tool for this kind of systems [44,46,47]. Bader charge analysis, on the other hand, quantitatively estimates the electron population associated with each atom, based on the topological partitioning of the total electron density ρ(r) into atomic basins defined by zero-flux surfaces in the gradient of ρ(r) [42,45]. The charge of each atom is then computed by subtracting the integrated electron density within its basin from the nuclear charge, thus providing a physically grounded measure of charge transfer. This method (already employed in Chapter 2 to investigate gas-phase fragmentation processes) has become a standard approach for the analysis of donor-acceptor interactions, covalency, and electronic polarization in surface adsorption phenomena [42,45]. In this work, these two techniques were applied to the P[6]A + In_2O_3 and P[6]A + ITO systems, in order to confirm the structural and energetic trends discussed in the main text, and to offer deeper insight into the electronic nature of the anchoring process.

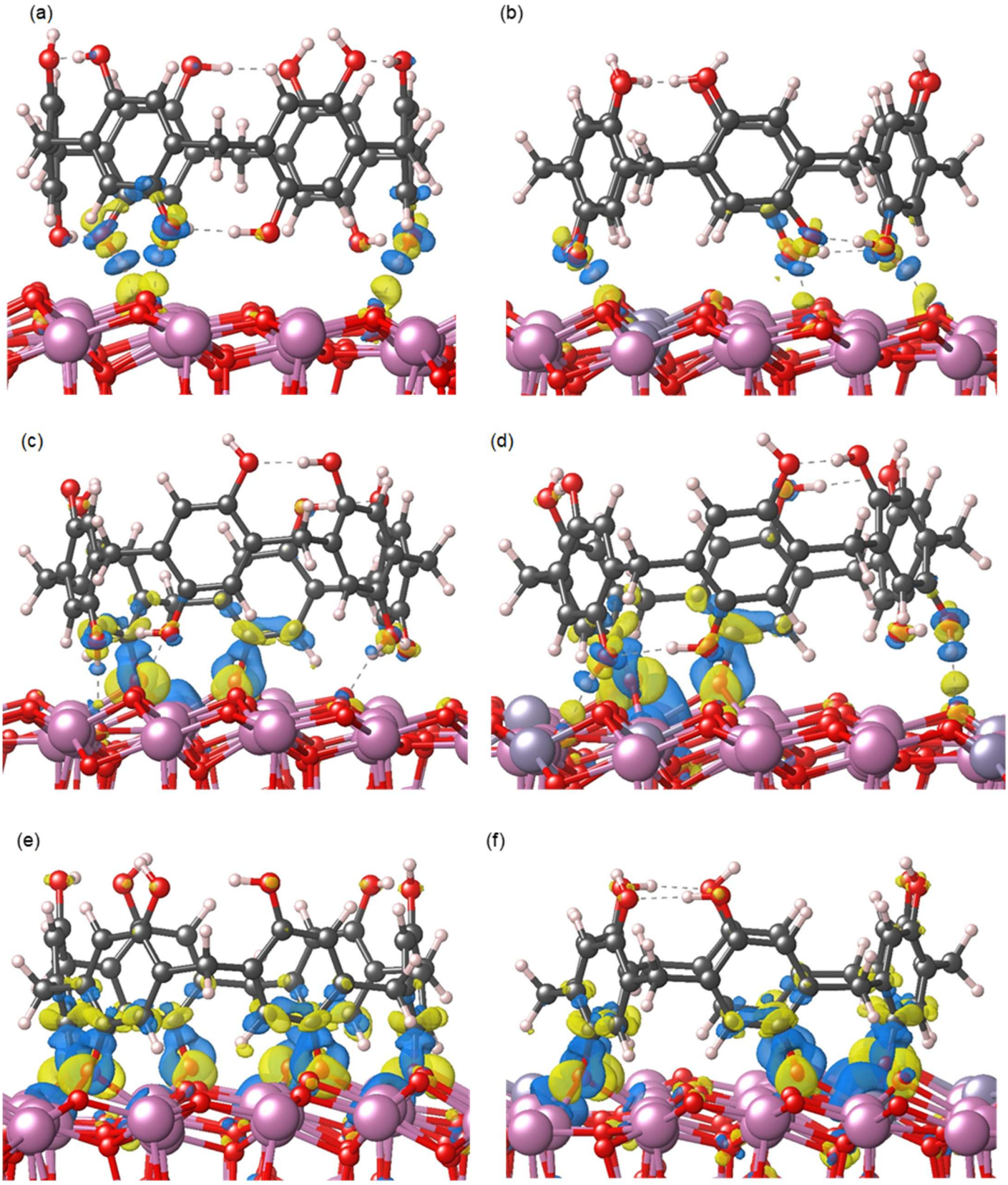

Figure A.34: Graphical representation of the charge density difference (CDD) for the systems: a) P[6]A + In_2O_3; b) P[6]A + ITO; c) P[6]A + In_2O_3 -2H_2O; d) P[6]A + ITO -2H_2O; e) P[6]A + In_2O_3 -6H_2O; f) P[6]A + ITO -6H_2O systems. All CDD were computed using an isosurface level of 0.0056 a.u.^{3}. Regions of electron depletion are shown in blue, whereas regions of electron accumulation are shown in yellow. Atoms color code: In = purple; Sn = dark purple; C = grey; O = red; H = white.

Table A.25: Average Bader charges computed for the In_2O_3 and ITO surfaces and for the P[6]A molecule before and after adsorption and subsequent water elimination. The labels O_{surf} and O_{ring} refer to the surface oxygen atoms and the Pillar[6]arene oxygen atoms, respectively. When water molecules are eliminated, O_{ring} atoms replace O_{surf} sites at the interface. The table reports the evolution of atomic charges following the addition of P[6]A to the oxide surfaces (and vice versa) and as a function of increasing water elimination.

	In_2O_3 Surf.	***+ P[6]A***	***+ P[6]A – $2H_2O$***	***+ P[6]A – $4H_2O$***	***+ P[6]A – $6H_2O$***
ATOM					
O_{surf}	-1.165	-1.177	-1.173	-1.177	-1.171
In	+1.770	+1.767	+1.760	+1.749	+1.635
	P[6]A	**+ In_2O_3**	**+ In_2O_3 – $2H_2O$**	**+ In_2O_3 – $4H_2O$**	**+ In_2O_3 – $6H_2O$**
ATOM					
O_{ring}	-1.576	-1.592	-1.555	-1.478	-1.466
H	+0.776	+0.689	+0.749	+0.649	/
C	+0.758	+0.871	+0.750	+0.773	+0.800
	ITO Surf.	**+ P[6]A**	**+ P[6]A – $2H_2O$**	**+ P[6]A – $4H_2O$**	**+ P[6]A – $6H_2O$**
ATOM					
O_{surf}	-1.162	-1.171	-1.174	-1.177	-1.171
In	+1.746	+1.760	+1.753	+1.749	+1.653
Sn	+2.096	+2.097	+1.981	+1.859	+1.849
	P[6]A	**+ ITO**	**+ ITO – $2H_2O$**	**+ ITO – $4H_2O$**	**+ ITO – $6H_2O$**
ATOM					
O_{ring}	-1.576	-1.612	-1.602	-1.456	-1.459
H	+0.776	+0.665	+0.649	+0.684	/
C	+0.758	+0.669	+0.773	+0.708	+0.766

The surface oxygen atoms are labeled as O_{surf}, while the oxygen atoms of the Pillar[6]arene ring are labeled as O_{ring}, even when the latter replace O_{surf} during water elimination. The table should be read from left to right and shows how the atomic charges evolve upon P[6]A adsorption and with increasing number of eliminated water molecules (n = 2, 4, 6).

A.4.1.4 Hypothesized H_2O-Elimination Pathway on In_2O_3 / ITO Surfaces

This Section complements the discussion in the main text (Section 4.1.3) by reporting the optimized geometries of the key intermediates and final products involved in the proposed covalent anchoring pathway of Pillar[6]arene (P[6]A) on In_2O_3 and ITO surfaces via water elimination. The simplified reaction scheme consists of three elementary steps:

(i) Hydrogenation (protonation) of surface O atoms;

(ii) Physisorption of the P[6]A on the surface;

(iii) Adsorption of P[6]A by elimination of two H_2O molecules.

This strategy provides a conceptual representation to understand the energetic trends of the adsorption process, without explicitly addressing transition states. Furthermore, the geometries provided herein (Figures A.35 and A.36) offer a comparative visualization of the structural evolution on both oxide surfaces.

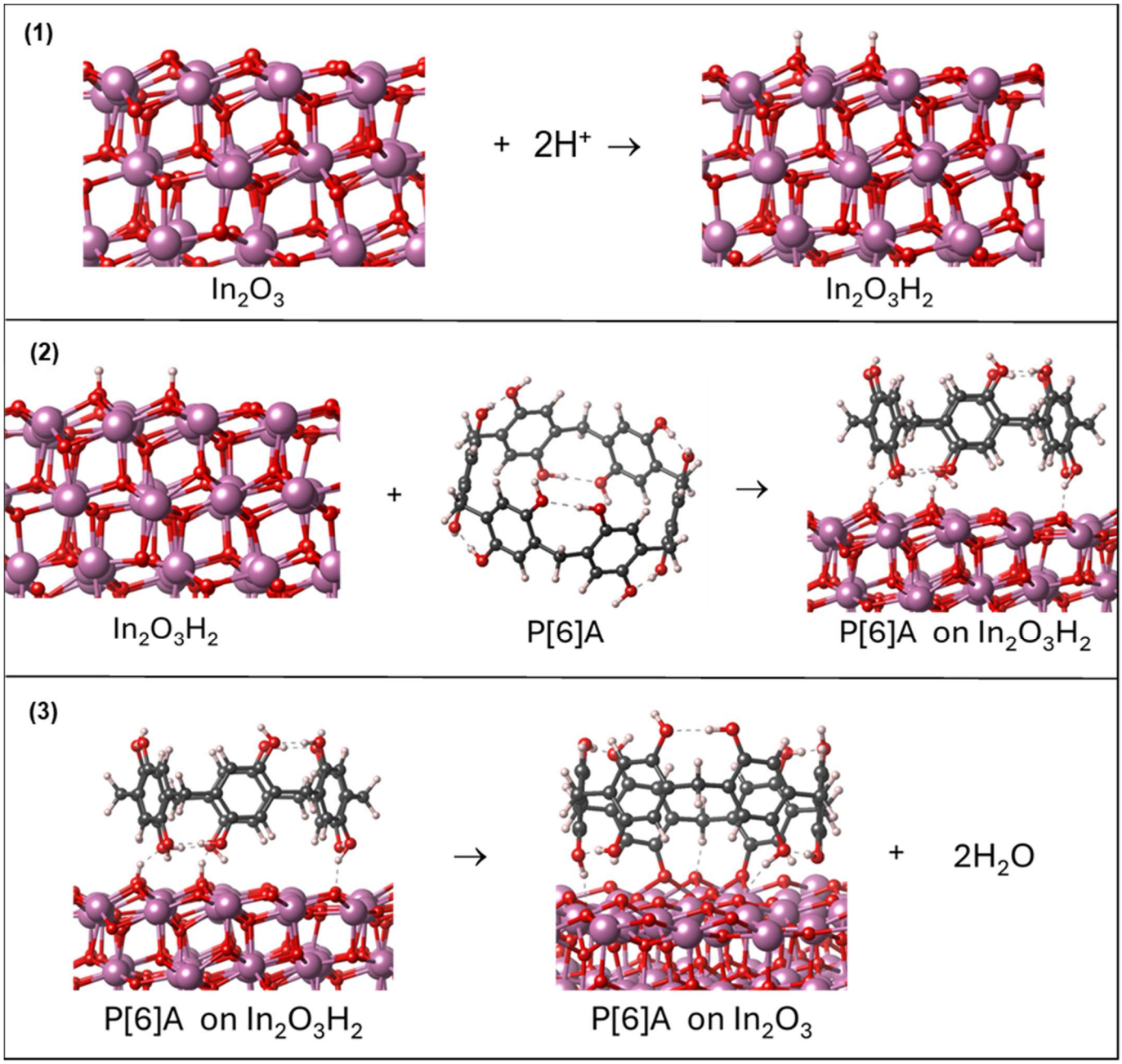

Figure A.35: Graphical representation of the proposed reaction pathway for the adsorption of Pillar[6]arene onto the In_2O_3 surface via elimination of water molecules. The three steps include: (1) hydrogenation (protonation) of surface oxygen atoms; (2) physisorption of the macrocycle; (3) covalent anchoring through water elimination. Atoms color code: In = purple; Sn = dark purple; C = grey; O = red; H = white.

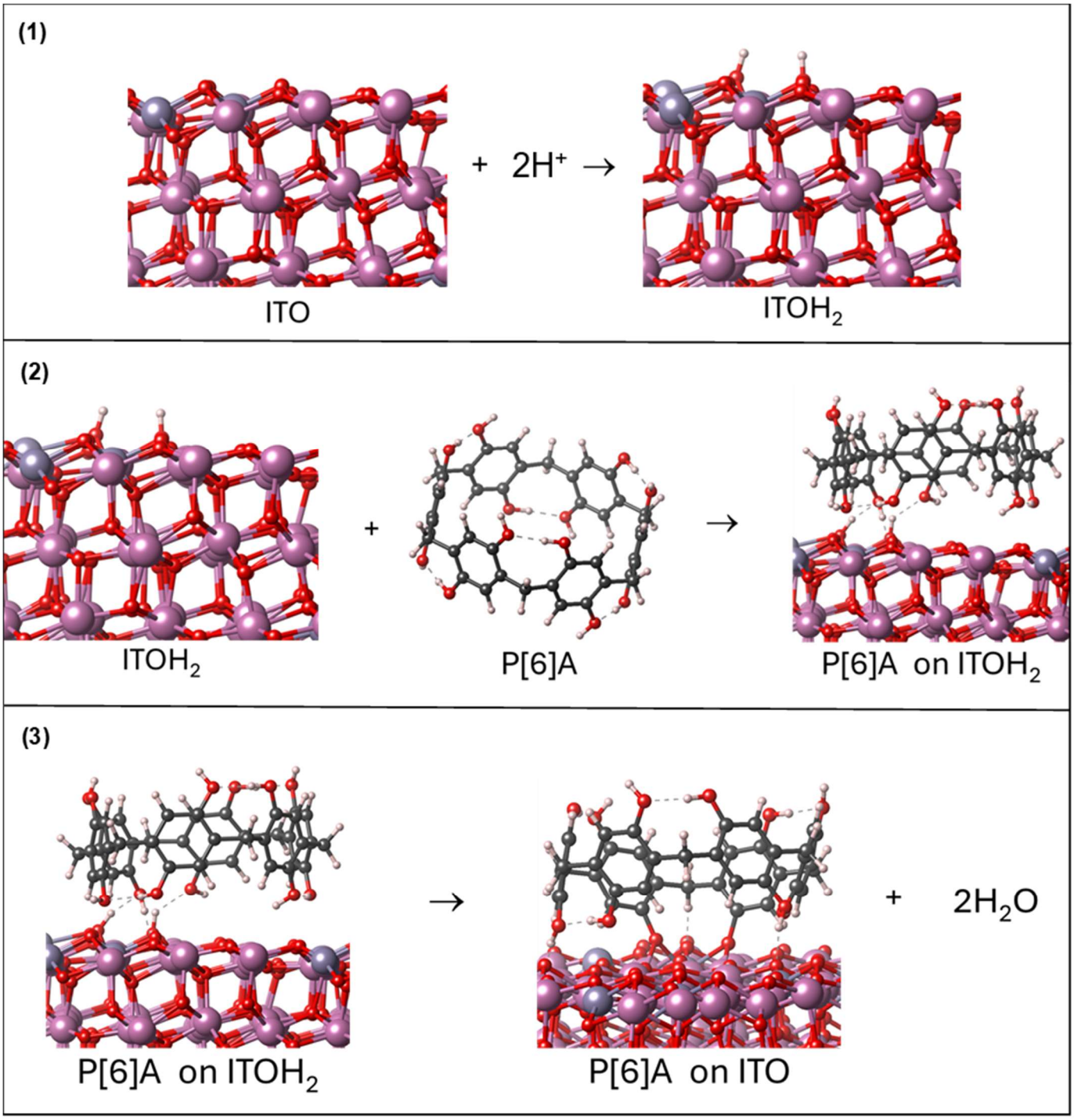

Figure A.36: Graphical representation of the proposed reaction pathway for the adsorption of Pillar[6]arene onto the ITO surface via elimination of water molecules. The three stages include: (1) hydrogenation (protonation) of surface oxygen atoms; (2) physisorption of the macrocyclic molecule; (3) covalent anchoring through water elimination. Atoms color code: In = purple; Sn = dark purple; C = grey; O = red; H = white.

Since process (1) is crucial for the beginning of the overall reaction in both cases (see main text), several hydrogenation (protonation) positions at the surface were evaluated, choosing the energetically most favorable one (providing the best E_{ads} value). In each case, three distinct configurations, labelled A, B, and C, were tested, corresponding to different surface oxygen positions (see Figure A.37a for In_2O_3 and Figure A.37b for ITO). These configurations were selected based on surface symmetry, local coordination environment, and accessibility for hydrogen adsorption. The corresponding total adsorption energies (E_{ads}) and relative energy differences (ΔE) are summarized in Table A.26. In both cases, configuration A emerged as the most stable, with E_{ads} values of -2.14 eV for In_2O_3 and -1.53 eV for ITO. The other configurations (B and C) exhibited higher adsorption energies, confirming that adsorption in position A is thermodynamically preferred. These most stable geometries were thus selected as the reference states for the subsequent steps in the reaction pathway.

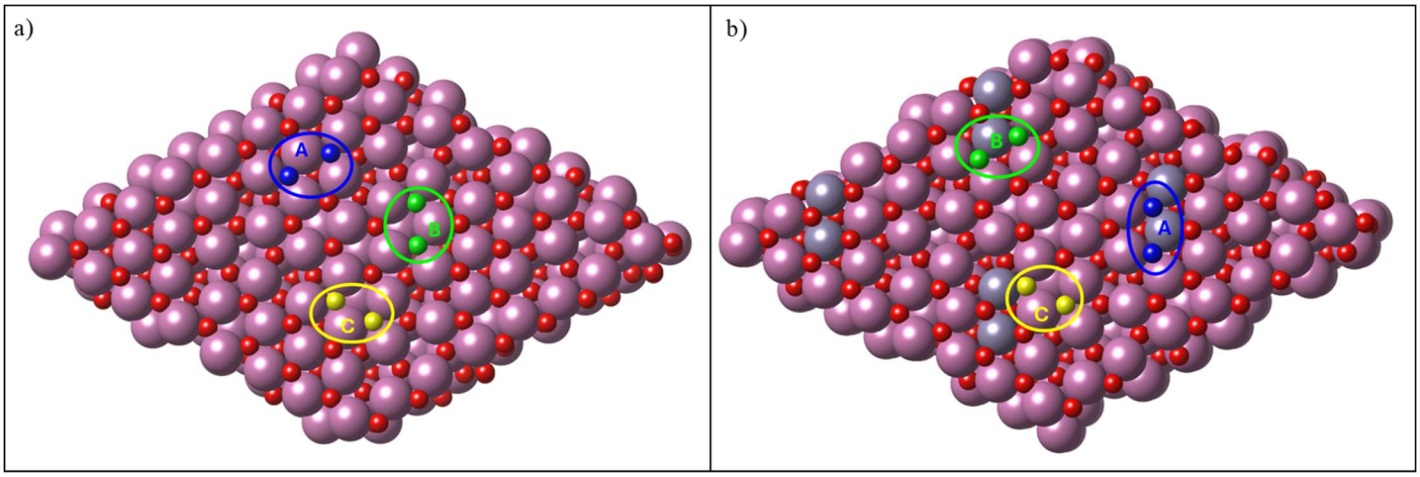

Figure A.37: Selected positions for the hydrogenation reaction on (a) In_2O_3 and (b) ITO surfaces. The three considered configurations (A, B, and C) correspond to different surface oxygen sites and were evaluated to determine the most favorable adsorption geometry for H_2. Colored circles indicate the specific positions tested, as reported in Table A.26. Atoms color code: In = purple; Sn = dark purple; C = grey; O = red; H = white.

Table A.26: Total adsorption energy (E_{ads}) values and relative energy differences (ΔE) for the isomeric configurations resulting from the hydrogenation of In_2O_3 and ITO surfaces at positions A, B, and C. ΔE were computed with respect to the most stable configuration (A), that was used as reference for subsequent reaction steps.

In_2O_3	***Position A***	***Position B***	***Position C***
E_{ads} (eV)	-2.14	-1.45	-1.35
ΔE (eV)	0	0.68	0.78
ITO	**Position A**	**Position B**	**Position C**
E_{ads} (eV)	-1.53	-1.30	-0.69
ΔE (eV)	0	0.23	0.84

Supplementary Information Paragraph 4.2

A.4.2.1 Computational details

The molecular structures of DPGME and HN1, HN2, HN3 were modeled by taking their atomic coordinates from the PubChem [91] and Reaxis [92] databases. A conformer search was then performed using the Avogadro software [93] to identify the most stable geometries. All subsequent calculations on the isolated molecules were carried out in the gas phase. Geometry optimizations were first performed at the density functional theory (DFT) level using the ωb97XD approximation [94] for exchange and correlation functionals in combination with the 6-311++G(2df,pd) basis set, and the Gaussian 09 code [95]. To improve the accuracy of structural parameters and to simulate the IR spectra, geometry optimization and frequency analyses were further conducted at the MP2 level of theory [96] with the 6-311G(d) basis set applied to all atoms. All optimized structures showed no imaginary harmonic frequencies, and all reported relative energies include zero-point energy (ZPE) corrections. The electronic excited states (120 in all cases) and optical absorption spectra of the isolated molecules were calculated by time dependent (TD)-DFT at the CAM-B3LYP[97]/6-311++G(df,pd) theory level.

The interaction between DPGME and HN2 with the ZnO surface was instead investigated by periodic DFT calculations using the *Quantum Espresso* code [98]. Particularly, the Perdew-Burke-Ernzerhof (PBE) functional [99] was adopted with dispersion effects accounted for via the Grimme-D3BJ [100] correction for dispersion. Vanderbilt ultrasoft pseudopotentials were employed for all atoms [101]. The plane-wave basis set was truncated at 30 Ry (240 Ry for electron density), and a 4 × 6 × 1 mesh was adopted for the Brillouin zone sampling. The unit cell of ZnO adopts a wurtzite-type crystal structure with hexagonal symmetry, characterized by lattice parameters $a = b = 3.1590$ Å and $c = 5.0796$ Å, taken from the literature [102]. The resulting surface model consisted of 54 Zn and 54 O atoms ($Zn_{54}O_{54}$), with an exposed surface area of 151.3 Å^2 and a crystallographic orientation corresponding to the $(10\bar{1}0)$ facet. This surface is non-polar, as it exposes both Zn and O atoms on the top and bottom layers. To minimize inter-slab interactions, a 15 Å vacuum layer was initially introduced above the surface. This spacing was later increased to 16.9 Å along the z-axis to minimize periodic image interactions, also during the HN2 and DPGME adsorption simulations. The slab model employed consists of three Zn-O bilayers. The final optimized simulation cell parameters were a = 15.5945 Å, b = 9.7011 Å, and c = 23.4740 Å. During geometry optimizations, the two bottommost layers of the slab were kept fixed, whereas all remaining atoms were allowed to relax freely, until the forces on the nuclei reached a convergence threshold of 1.0×10^{-4} Rydberg·Bohr^{-1} (1.0×10^{-7} Rydberg for the wavefunction convergence). To accurately describe the electronic structure and reproduce the electrical and optical properties of the investigated systems, the Density of States (DOS) calculations were performed using the DFT+U approach, which introduces an effective Hubbard correction (U_{eff}) to account for the on-site Coulomb repulsion in localized states [104-105]. The Hubbard U parameters adopted in this study were U_{Zn} =12.0 eV and U_O = 6.5 eV, for Zn and O atoms respectively, as reported in the literature [106]. In this case, Projector augmented-wave (PAW) pseudopotentials [107] were employed. For each system, the electronic band gap (E_G) was computed as the difference between the conduction band (CB) and the valence band (VB) edges.

A.4.2.2 Structural and Vibrational Characterization of DPGME and Nitrogen Mustards (HN1, HN2, HN3) in Vacuum

This Section presents a detailed computational investigation of DPGME and nitrogen mustard agents (HN1, HN2, HN3) in the gas phase, aimed at characterizing their intrinsic structural, vibrational, and electronic properties prior to surface interaction. Both DFT and post-Hartree-Fock methods were employed with the aim of increasing the robustness of the results. Particular attention was devoted to comparing the three nitrogen mustards with the simulant DPGME, in order to evaluate their chemical affinity and potential interchangeability under conditions relevant to surface-based sensing applications, despite their markedly different chemical structure. Specifically, this Section addresses the following aspects for all species considered: (i) geometry optimization and IR spectra simulation; and (ii) analysis of the Molecular Electrostatic Potential (MEP) maps to visualize the global electronic distribution of each system.

A.4.2.2.1 DPGME: Structural and Spectroscopic Analysis

The molecular structure of DPGME was initially taken from online available chemical databases [91,92], and subsequently optimized in the gas phase using the DFT approach described in the previous Section. The resulting minimum energy structure corresponds to a linear geometry, as shown in Figure A.38.

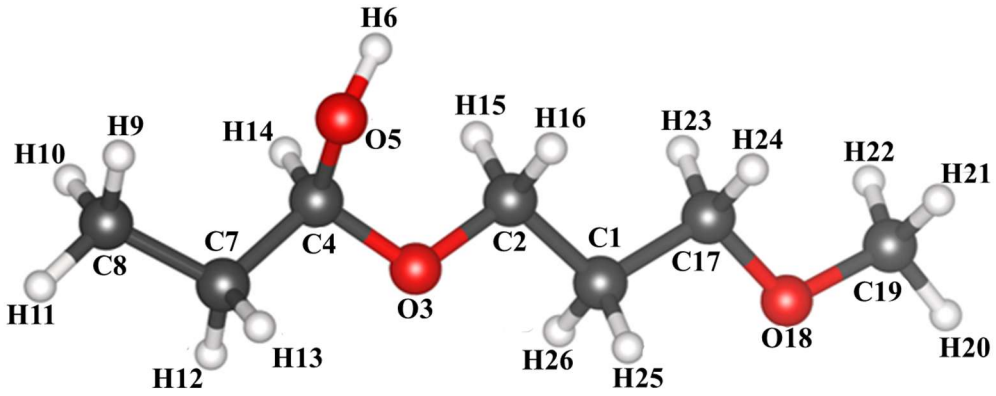

Figure A.38: Optimized molecular structure of DPGME in its linear conformation, as obtained at the MP2/6-311G(d) level of theory. The geometry is visually indistinguishable from that obtained using the ωB97XD/6-311++G(2df,pd) approach and is therefore shown here as representative of both methods. Atoms color code: C = grey; O = red; H = white.

Particular attention was then devoted to the potential formation of an intramolecular hydrogen bond between the hydroxyl group (O5-H6) and the ether oxygen atom (O18), given their favorable spatial arrangement. To explore this hypothesis, a conformational search was carried out to identify alternative low-energy structures potentially stabilized by such an interaction. Among the conformers generated, a folded isomer, previously unreported in the literature, was found to exhibit a distinct intramolecular H-bond, as illustrated in Figure A.39. Notably, this folded conformer was calculated to be 3.04 kcal/mol more stable than the linear structure (including zero-point energy correction) and is therefore expected to be the preferred isomer under isolated conditions.

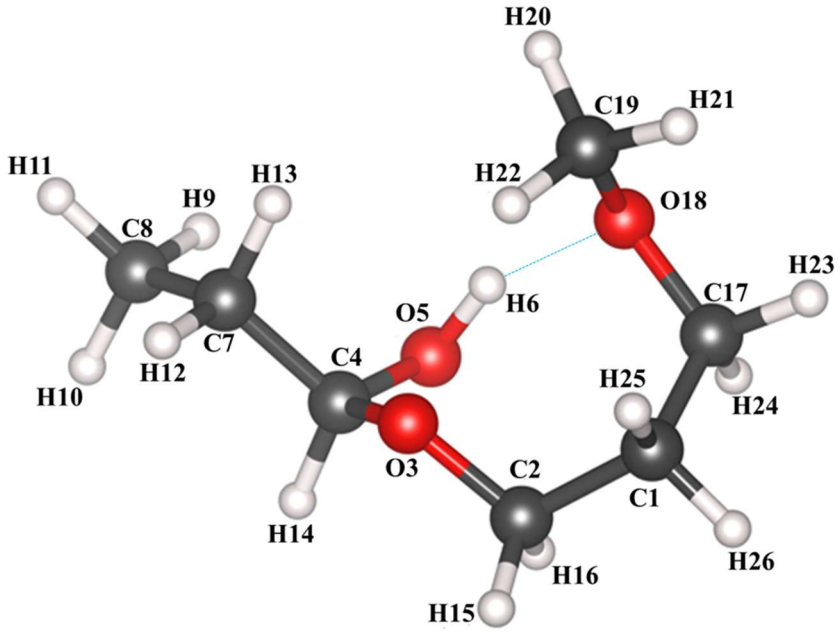

Figure A.39: Optimized molecular structure of DPGME in its folded conformation, as obtained at the MP2/6-311G(d) level of theory. The structure is stabilized by an intramolecular hydrogen bond (O5-H6···O18) and was found to be energetically favored over the linear conformer. The geometry is visually indistinguishable from that obtained using the ωB97XD/6-311++G(2df,pd) approach and is therefore shown here as representative of both methods. Atoms color code: C = grey; O = red; H = white. Dashed cyan line represents the H-bond.

To improve the accuracy of the structural description, both conformers were further optimized using a post-Hartree-Fock method, namely second-order Møller-Plesset perturbation theory (MP2). In agreement with the DFT findings, the MP2 results also identified the folded conformer as the most stable structure, with an energy difference of 5.38 kcal/mol relative to the linear geometry. The most relevant bond lengths and angles are reported in Table A.27, as obtained from both DFT and MP2 calculations. A comparison of the geometrical parameters achieved at the ωB97XD and MP2 levels of theory reveals only minor variations in both bond lengths and angles. For instance, in the case of the linear DPGME conformer, the O5-H6 bond length increases slightly from 0.958 Å (ωB97XD) to 0.961 Å (MP2), while the C7-C4 and O3-C4 distances change from 1.513 to 1.512 Å and from 1.397 to 1.408 Å, respectively. Similarly, small deviations are observed in the bond angles: the C8-C7-C4 angle varies from 112.9° to 112.6°, O3-C4-O5 from 112.4° to 112.6°, and C17-O18-C19 from 112.9° to 111.2° when moving from ωB97XD to MP2. Comparable differences are also observed for the folded conformer, confirming the consistency of the structural predictions across both computational methods. Overall, the limited magnitude of these variations indicates that the ωB97XD functional provides molecular geometries close to those obtained from the more accurate, though computationally expensive, MP2 method. This point becomes particularly relevant in the context of periodic simulations on ZnO surfaces (see Section 4.2.4), where the use of generalized-gradient DFT functionals such as PBE represents a practical compromise between accuracy and computational efficiency.

Table A.27: Selected bond lengths (in Å) and bond angles (in °) for the linear and folded conformers of DPGME, as obtained from geometry optimizations at the ωB97XD/6-311++G(2df,pd) and MP2/6-311G(d) levels of theory. Atoms labels are consistent with those shown in Figures A.38 and A.39.

	ωB97XD		***MP2***	
	DPGME-linear	**DPGME-folded**	**DPGME-linear**	**DPGME-folded**
Bond Distances [Å]	***6-311++G(2df,pd)***		***6-311G(d)***	
C8-C7	1.521	1.521	1.525	1.525
C7-C4	1.513	1.519	1.512	1.518
C4-O5	1.406	1.396	1.410	1.403
O5-H6	0.958	0.972	0.961	0.977
C4-O3	1.397	1.405	1.408	1.417
O3-C2	1.406	1.415	1.417	1.430
C2-C1	1.514	1.520	1.517	1.521
C1-C17	1.514	1.520	1.517	1.528
C17-O18	1.403	1.415	1.412	1.426
O18-C19	1.400	1.408	1.411	1.423
Bond Angles [º]				
C8-C7-C4	112.9	112.5	112.6	112.2
O5-C4-O3	112.4	111.8	112.6	111.6
C4-O3-C2	114.9	110.3	112.9	113.9
C2-C1-C17	111.7	116.2	112.0	115.4
C17-O18-C19	112.9	114.8	111.2	114.6

Considering the good agreement observed between the geometries optimized at the DFT and MP2 levels, the ωB97XD functional was selected to compute the molecular electrostatic potential (MEP). While MP2 offers superior accuracy for total energies and vibrational analyses, the DFT-derived electron density is well suited for generating reliable MEP maps, especially when combined with an extended basis set [108,109]. This approach enables a qualitative assessment of the electronic distribution across the molecular surface, which is particularly relevant for identifying potential interaction sites in view of surface adsorption studies [110]. Using the same functional and basis set adopted for the geometry optimizations (ωB97XD/6-311++G(2df,pd)), the molecular electrostatic potential was calculated on an electron density isosurface for the most stable DPGME conformer, namely the folded isomer (see Figure A.39). Electrostatic potential maps provide an intuitive means of visualizing the spatial distribution of electron density, allowing the identification of electron-rich and electron-poor regions that may serve as potential sites for non-covalent interactions. As shown in Figure A.40, the red-colored regions surrounding the oxygen atoms (both hydroxyl and ether) correspond to areas of negative electrostatic potential, indicating high electron density and thus nucleophilic character. Conversely, the green and blue regions, located around carbon and hydrogen atoms, respectively, highlight electron-poor sites that may be prone to nucleophilic attack.

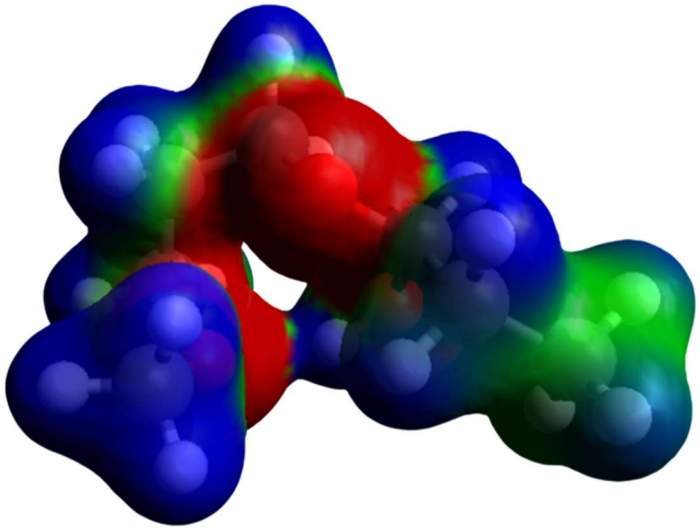

Figure A.40: Molecular electrostatic potential (MEP) map of the most stable DPGME conformer (folded structure, Figure A.39), calculated at the ωB97XD/6-311++G(2df,pd) level. The MEP is projected onto an electron density isosurface: red regions correspond to areas of high electron density (negative potential), while green and blue regions indicate electron-poor zones (positive potential).

Notably, the MEP also covers the spatial region between the hydroxyl hydrogen and the ether oxygen, reflecting a localized electron density accumulation that is consistent with the formation of a strong intramolecular hydrogen bond, in agreement with the structural analysis presented in Table A.27. This interaction likely contributes to the enhanced stability of the folded conformer relative to the linear one. Furthermore, the MEP analysis anticipates a key interaction that will be discussed in Sections 4.2.4: the physisorption of DPGME on the ZnO surface is predicted to occur via the hydroxyl group, with the nucleophilic oxygen atom directly interacting with a surface zinc atom. The observed negative electrostatic potential surrounding the hydroxyl oxygen in the gas-phase conformation supports this hypothesis and provides a rationale for the preferred adsorption geometry.

The infrared (IR) spectrum of DPGME was calculated at the MP2/6-311G(d) level of theory and compared with an experimental spectrum taken from the literature [91]. While the calculated spectrum refers to the molecule in the gas phase, the experimental one was recorded in ethanol solution. Despite this difference, a fair agreement was observed between the two spectra, allowing the possibility to perform a detailed band assignment based on the normal modes, which is typically unfeasible at the experimental level. The calculated frequencies were scaled by a factor of 0.9503, following the standard correction for harmonic approximations used in computational methods (see Chapter 2, Section 2.1.3 for further details) [111]. Both the experimental and calculated IR spectra are shown in Figure A.41, and the main spectral features can be summarized as follows:

- In the region between 2851 and 3015 cm^{-1} (highlighted in red), a series of bands corresponding to C-H stretching modes are visible in both spectra.
- Between 1463 and 1280 cm^{-1} (green), multiple twisting and wagging modes involving C-H bonds are observed, delocalized over the entire molecular structure.

- The intense band at approximately 1102 cm^{-1} (brown) is attributed to C-O stretching normal modes of the molecule ether moieties.
- The high-frequency signal at 3659 cm^{-1} (violet, Figure A.41b) corresponds to the O-H stretching mode of the hydroxyl group. This band is not detected experimentally due to the overlap with ethanol solvent.

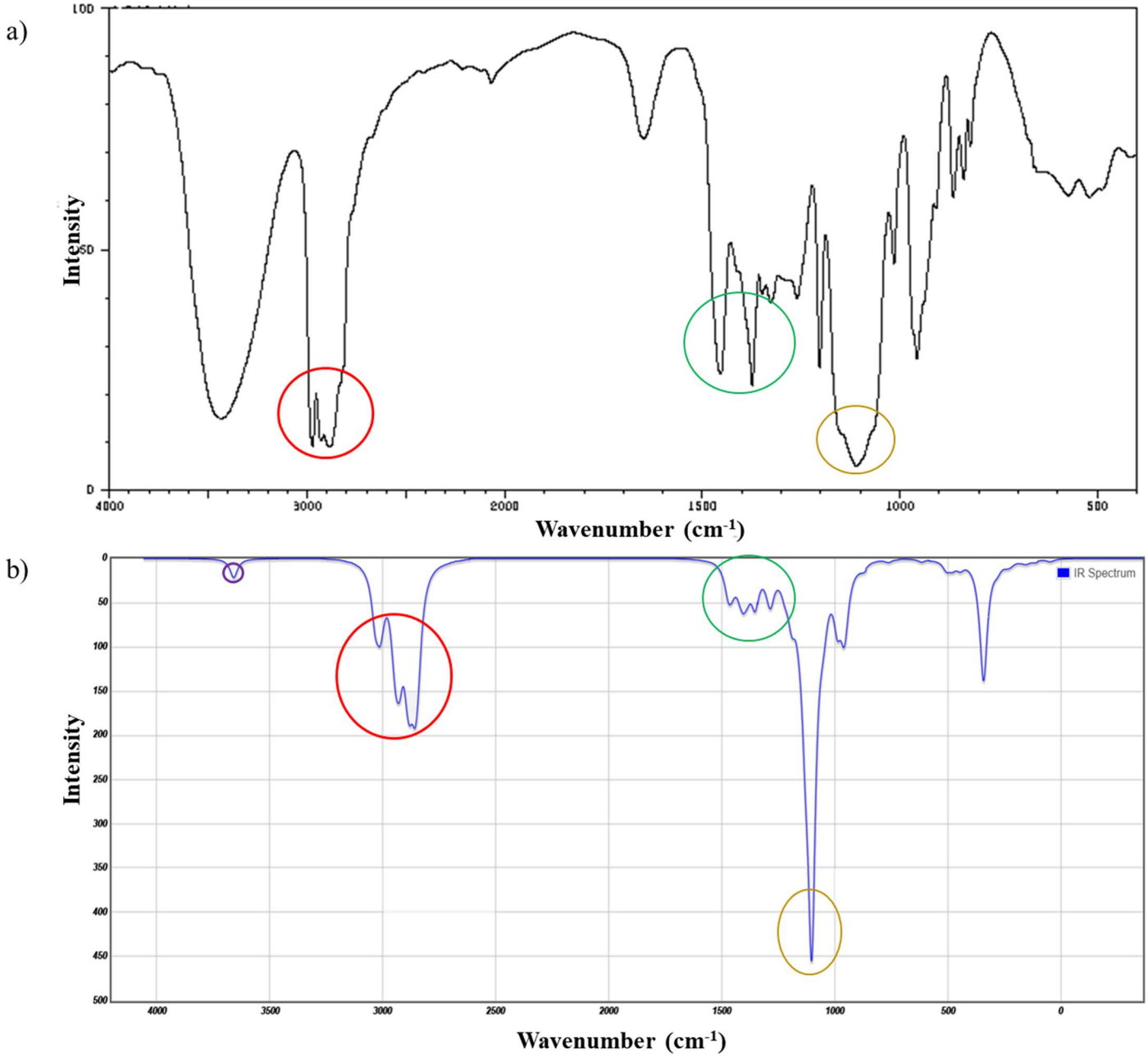

Figure A.41: (a) Experimental IR spectrum of DPGME in ethanol solution, adapted from reference [91]; (b) Simulated IR spectrum of the folded conformer of DPGME, calculated at the MP2/6-311G(d) level of theory in the gas phase. The vibrational frequencies in (b) were scaled by a factor of 0.9503. Colored circles highlight the main spectral regions discussed in the text: red for C-H stretching modes, green for C-H twisting and wagging, brown for C-O stretching, and violet for the O-H stretching vibration.

Overall, the comparison between the simulated and experimental IR spectra supports the suitability of the adopted computational approach to describe this type of molecules.

A.4.2.2.2 Nitrogen Mustards (HN1, HN2, HN3): Structural and Spectroscopic Analysis

Similarly to the approach adopted for DPGME, the molecules $C_6H_{13}Cl_2N$ (HN1), $C_5H_{11}Cl_2N$ (HN2) and $C_6H_{12}Cl_3N$ (HN3), collectively referred to as the azoyprites, were optimized in the gas phase, starting from atomic coordinates reported in the literature [91,92]. Geometry optimizations were first performed using a DFT approach and subsequently refined at the MP2 level of theory. The resulting minimum energy structures of HN1, HN2, and HN3 are depicted in Figure A.42, while the key bond lengths and angles are summarized in Tables A.28, A.29, and A.30, respectively. A conformational search was also performed for each compound in order to identify possible alternative low-energy structures. Nonetheless, for all three nitrogen mustards, the most energetically favorable conformers were found to coincide with those shown in Figure A.42.

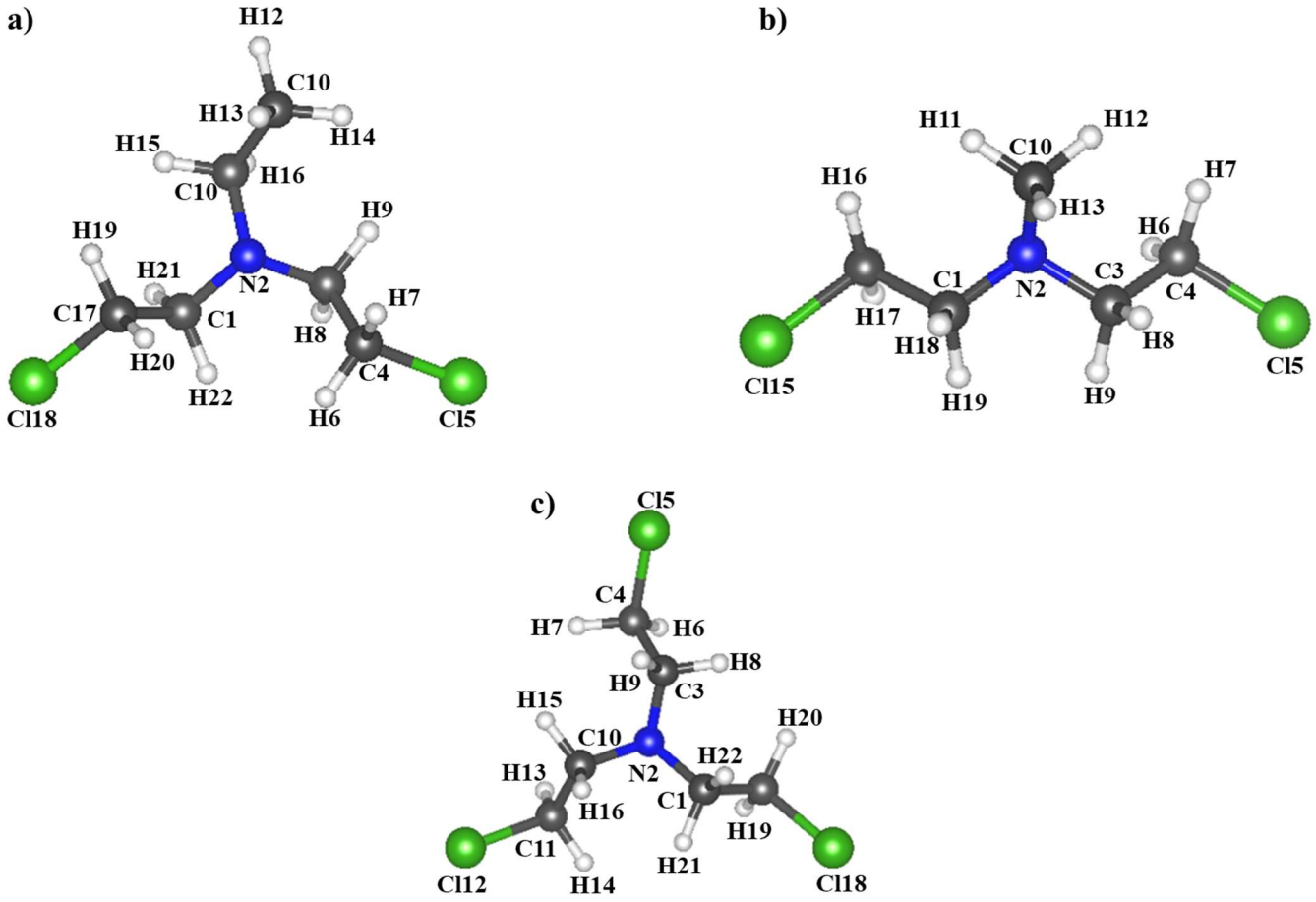

Figure A.42: Optimized molecular structures of (a) $C_6H_{13}Cl_2N$ (HN1), (b) $C_5H_{11}Cl_2N$ (HN2) and (c) $C_6H_{12}Cl_3N$ (HN3), obtained at the MP2/6-311G(d) level of theory. Since the geometries are visually indistinguishable from those obtained using the ωB97XD/6-311++G(2df,pd) method, the MP2 structures are shown as representative of both computational approaches. Atoms color code: Cl = green; N = blue; C = grey; O = red; H = white.

Table A.28: Selected bond lengths (in Å) and bond angles (in °) for the HN1 azoyprite, obtained from geometry optimizations performed at the ωB97XD/6-311++G(2df,pd) and MP2/6-311G(d) levels of theory. Atom labels correspond to those shown in Figure A.42.

	ωB97XD	**MP2**
	HN1	**HN1**
Bond Distances [Å]	***6-311++G(2df,pd)***	***6-311G(d)***
Cl18-C17	1.792	1.840
C17-H20	1.089	1.088
C17-C1	1.518	1.515
C1-N2	1.453	1.463
N2-C10	1.459	1.468
Cl5-C4	1.792	1.840
C4-C3	1.519	1.516
C4-H7	1.088	1.088
C10-C11	1.519	1.523
C10-H16	1.092	1.094
Bond Angles [º]		
C10-N2-C3	112.9	111.3
Cl5-C4-H7	107.5	106.3
C3-N2-C10	112.9	111.3
Cl18-C17-C1	110.9	110.4
C17-C1-N2	110.1	110.8

Table A.29: Selected bond lengths (in Å) and bond angles (in °) for the HN2 azoyprite, obtained from geometry optimizations performed at the ωB97XD/6-311++G(2df,pd) and MP2/6-311G(d) levels of theory. Atom labels correspond to those shown in Figure A.42.

	ωB97XD	**MP2**
	HN2	**HN2**
Bond Distances [Å]	***6-311++G(2df,pd)***	***6-311G(d)***
Cl5-C14	1.792	1.840
C14-C1	1.520	1.518
C1-N2	1.453	1.463
N2-C10	1.452	1.462
N2-C3	1.453	1.463
C3-C4	1.520	1.518
C4-Cl5	1.792	1.840
C14-H16	1.087	1.087
C3-H9	1.102	1.103
C10-H13	1.090	1.091
Bond Angles [º]		
C10-N2-C1	110.2	110.6
Cl5-C4-H7	107.5	105.9
C3-N2-C10	109.0	110.6
Cl15-C14-C1	110.9	110.3
C14-C1-N2	110.1	110.4

Table A.30: Selected bond lengths (in Å) and bond angles (in °) for the HN3 azoyprite, obtained from geometry optimizations performed at the ωB97XD/6-311++G(2df,pd) and MP2/6-311G(d) levels of theory. Atom labels correspond to those shown in Figure A.42.

	ωB97XD	**MP2**
	HN3	**HN3**
Bond Distances [Å]	***6-311++G(2df,pd)***	***6-311G(d)***
Cl12-C11	1.790	1.838
C11-C10	1.519	1.516
C10-N2	1.453	1.464
N2-C3	1.453	1.464
C3-C4	1.519	1.516
C4-Cl5	1.790	1.838
N2-C1	1.453	1.464
C1-C17	1.519	1.516
C17-Cl18	1.790	1.838
C10-H16	1.099	1.101
Bond Angles [º]		
C10-N2-C3	113.9	111.8
Cl5-C4-H7	107.5	106.2
C3-N2-C10	110.3	111.8
Cl12-C11-C10	110.8	110.2
C11-C10-N2	110.3	111.8

As evidenced by the data reported in Tables A.28-A.30, the comparison between the geometrical parameters obtained using the ωB97XD and MP2 methods reveals only minor differences, in line with the trends previously observed for the DPGME molecule. For example, in the case of HN2, the N2-C3 bond length increases slightly from 1.453 Å (ωB97XD) to 1.463 Å (MP2), the N2-C10 bond distance from 1.452 to 1.462 Å, and the C14-C1 distance decreases marginally from 1.520 to 1.518 Å (Table A.29). A comparable level of agreement is also observed for the bond angles: C3-N2-C10 changes from 109.0° to 110.6°, Cl5-H7-C4 from 107.5° to 105.9°, and C1-N2-C10 from 110.2° to 110.6°. Analogous conclusions can be drawn for HN1 and HN3, as detailed in Tables 48 and 50, *i.e.*, ωB97XD-calculated geometrical parameters show a good agreement with those obtained at the MP2 level. As previously highlighted for DPGME, this result is particularly relevant for the subsequent periodic simulations on ZnO surfaces (see Section 4.2.4), where the adoption of generalized-gradient corrected DFT approximations, such as PBE, offers a practical and widely accepted balance between computational efficiency and accuracy.

To complement the geometrical analysis and gain further insight into the electronic properties of the azoyprites, molecular electrostatic potential (MEP) maps were computed at the DFT level for the most stable conformers of HN1, HN2, and HN3 (Figure A.43). As previously discussed for DPGME, these maps offer a visual representation of the electron density distribution across the molecular surface and help to identify regions of potential reactivity. For all three nitrogen mustards, a significant accumulation of negative electrostatic potential is observed around the central nitrogen atom and the chlorine atoms, highlighting electron-rich regions that may act as favorable sites for electrophilic interactions. Conversely, the

carbon and hydrogen atoms are surrounded by areas of positive or mildly positive potential, suggesting electron-deficient regions that may interact preferentially with nucleophiles. Notably, the pronounced electron density localized on the chlorine atoms is particularly relevant in view of the subsequent surface adsorption analysis (see Section 4.2.4), where HN2 is shown to physisorb onto the ZnO surface via Cl···Zn interactions.

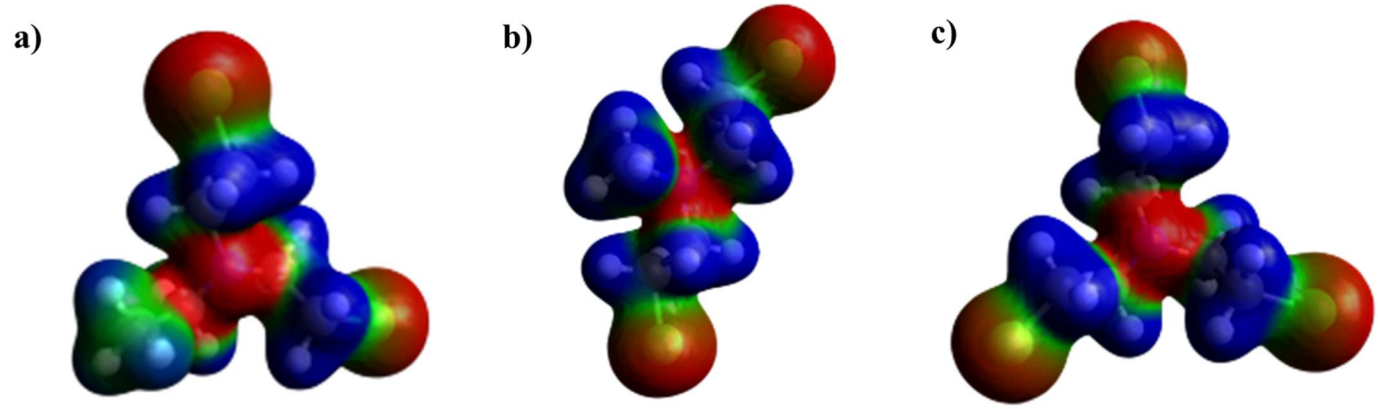

Figure A.43: Molecular electrostatic potential (MEP) map of (a) HN1, (b) HN2 and (c) HN3 (Figure A.42), calculated at the ωB97XD/6-311++G(2df,pd) level of theory. The MEP is projected onto an electron density isosurface: red regions correspond to areas of high electron density (negative potential), while green and blue regions indicate electron-poor zones (positive potential).

Following the same strategy employed for the DPGME molecule, theoretical infrared (IR) spectra were computed at the MP2/6-311G(d) level for the three nitrogen mustards HN1, HN2, and HN3. These spectra were compared with available experimental data. Among the three compounds, only HN3 has an experimental IR spectrum reported in the literature [91]. As previously done for DPGME, a scaling factor of 0.9503 was applied to the computed harmonic frequencies, in accordance with standard corrections adopted in quantum chemical calculations [111]. The computed spectra of HN1, HN2, and HN3 are shown in FigureA.44, while the experimental IR spectrum of HN3 is presented in Figure A.45. Despite being recorded in deuterated water (D_2O), and therefore not directly comparable to gas-phase calculations, the experimental spectrum exhibits an overall fair agreement with the theoretical predictions. This correspondence enabled a detailed vibrational band assignment based on normal modes. The comparison between the computed (Figure A.44c) and experimental (Figure A.45) IR spectra of HN3 highlights the following key features:

- In the 3069-2885 cm^{-1} region (red), both spectra display distinct bands corresponding to asymmetric C-H stretching modes.
- The 1463-1395 cm^{-1} range (green) is characterized by asymmetric C-H stretching combined with global wagging motions.
- Between 1264 and 1220 cm^{-1} (blue), C-H wagging modes are detected, along with global twisting contributions.

- A prominent signal at 1103 cm^{-1} (brown) is attributed to a general twisting vibration, with significant involvement of the central nitrogen atom.
- Finally, an intense peak around 763 cm^{-1} (purple) is observed in both spectra and assigned to a global rocking mode. Moreover, the experimental spectrum exhibits a broad absorption band in the 800-700 cm^{-1} region, consistent with the C-Cl stretching vibration calculated at 712 cm^{-1}.

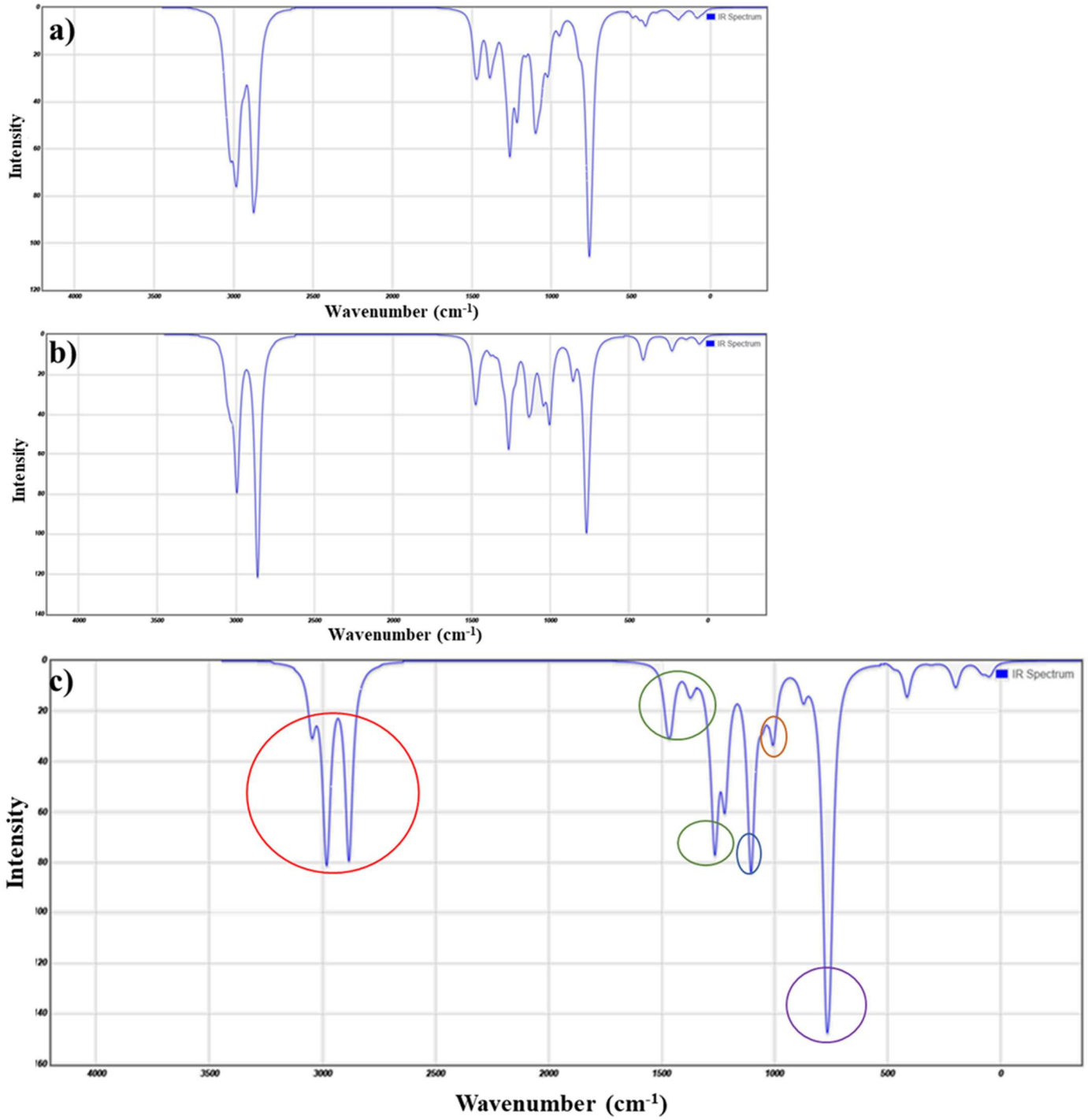

Figure A.44: Theoretical infrared (IR) spectra of (a) HN1, (b) HN2, and (c) HN3 computed at the MP2/6-311G(d) level of theory, with vibrational frequencies scaled by a factor of 0.9503. In panel (c), the main vibrational regions of the HN3 spectrum are highlighted: red = asymmetric C-H stretching, green = asymmetric C-H stretching and wagging, blue = wagging and twisting modes, brown = general twisting mode involving the central nitrogen, purple = global rocking mode and C-Cl stretching.

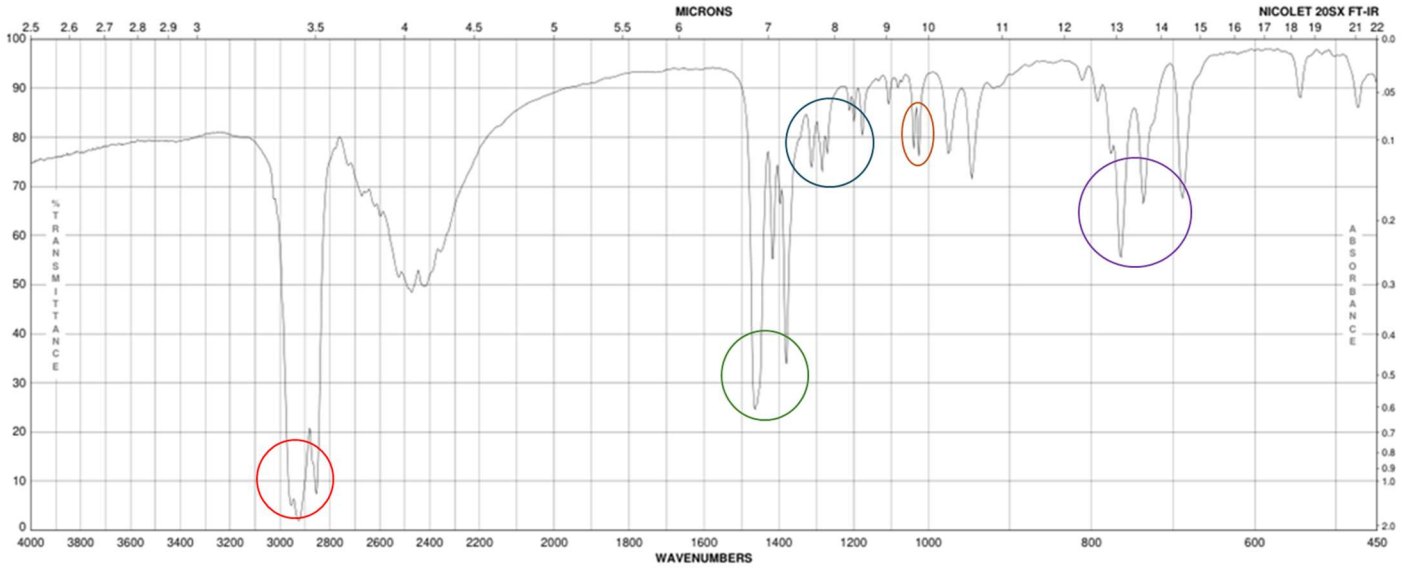

Figure A.45: Experimental infrared (IR) spectrum of HN3, recorded in deuterated water (D_2O), as reported in reference [91]. The main vibrational bands have been highlighted using colored circles for ease of comparison with the computed spectrum shown in Figure A.44c.

Although only the theoretical IR spectrum of HN3 could be directly compared against experimental data, the strong resemblance among the computed IR spectra of HN1, HN2, and HN3 justifies the extension of the vibrational assignments to all three compounds. These results suggest that the MP2 method, when combined with a triple-Z basis set, provides a satisfactory framework for modeling the vibrational behavior of nitrogen mustard species. The favorable comparison between calculated and experimental IR spectra of HN3 is especially significant given the lack of structural experimental data for these compounds.

In summary, this Section has provided an analysis of gas-phase DPGME and nitrogen mustard agents (HN1, HN2, HN3), focusing on their structural, electronic, and vibrational properties. The combined use of DFT and MP2 methodologies was aimed to provide reliable predictions for key molecular descriptors, namely geometrical parameters, electrostatic potential maps, and infrared spectra. These molecular-level insights lay the groundwork for the investigation of excited electronic states and UV-visible absorption spectra, which will offer further criteria to evaluate the relevance of DPGME as a simulant for the three azoyprites examined in this Section, in the context of sensing applications.

A.4.2.3 Additional TD-DFT Data for DPGME and Nitrogen Mustards

This Section complements the TD-DFT analysis presented in the main text by reporting the graphical representations of the frontier molecular orbitals (HOMO and LUMO) for DPGME (Figure A.46) and nitrogen mustard agents (HN1, HN2, HN3, Figure A.47), along with the electronic transitions with the main electronic transitions and the highest oscillator strengths (Table A.31). These data provide further insight into the excited-state behavior of the investigated molecules and support the discussion on the spectroscopic similarities between the simulant and the CWAs.

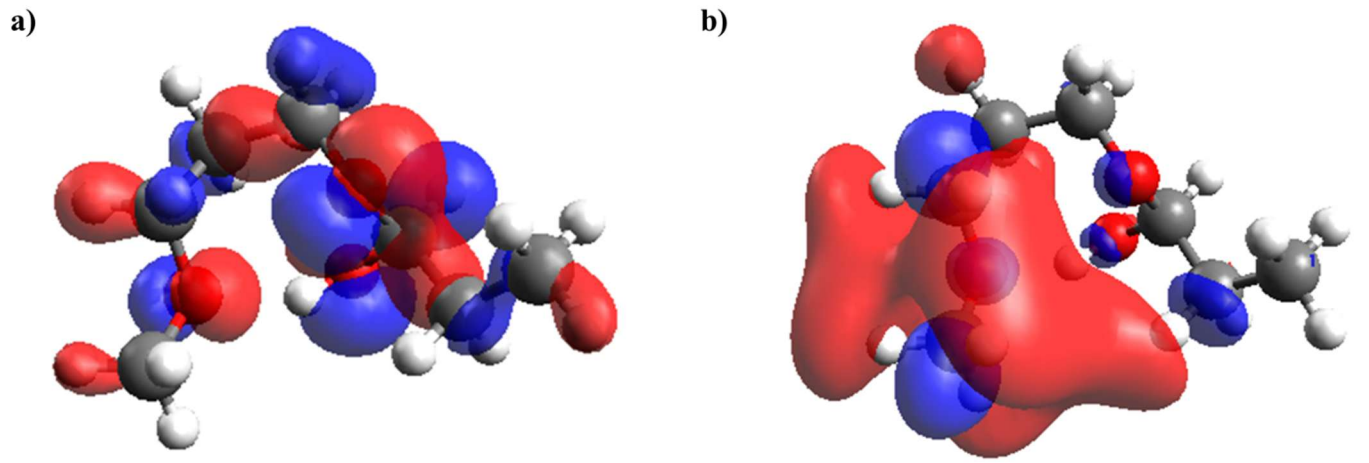

Figure A.46: Graphical representation of the (a) HOMO and (b) LUMO orbitals for the DPGME molecule, computed at the ωB97XD/6-311++G(2df,pd) level of theory. Red and blue regions indicate the positive and negative orbital lobes, respectively.

As shown in Figure A.46, the HOMO of DPGME is primarily localized over the ether and hydroxyl oxygen atoms. In contrast, the LUMO is mainly distributed within the spatial region between the hydrogen atom of the hydroxyl group and the more distant ether oxygen, namely, the region associated with the intramolecular hydrogen bond. For all the three nitrogen mustards, the highest occupied molecular orbital (HOMO) is consistently localized on the central nitrogen atom, which carries a non-bonding lone pair. Conversely, the lowest unoccupied molecular orbital (LUMO) is delocalized on the entire molecule, with significant contributions from the terminal chlorine atoms (Figure A.47).

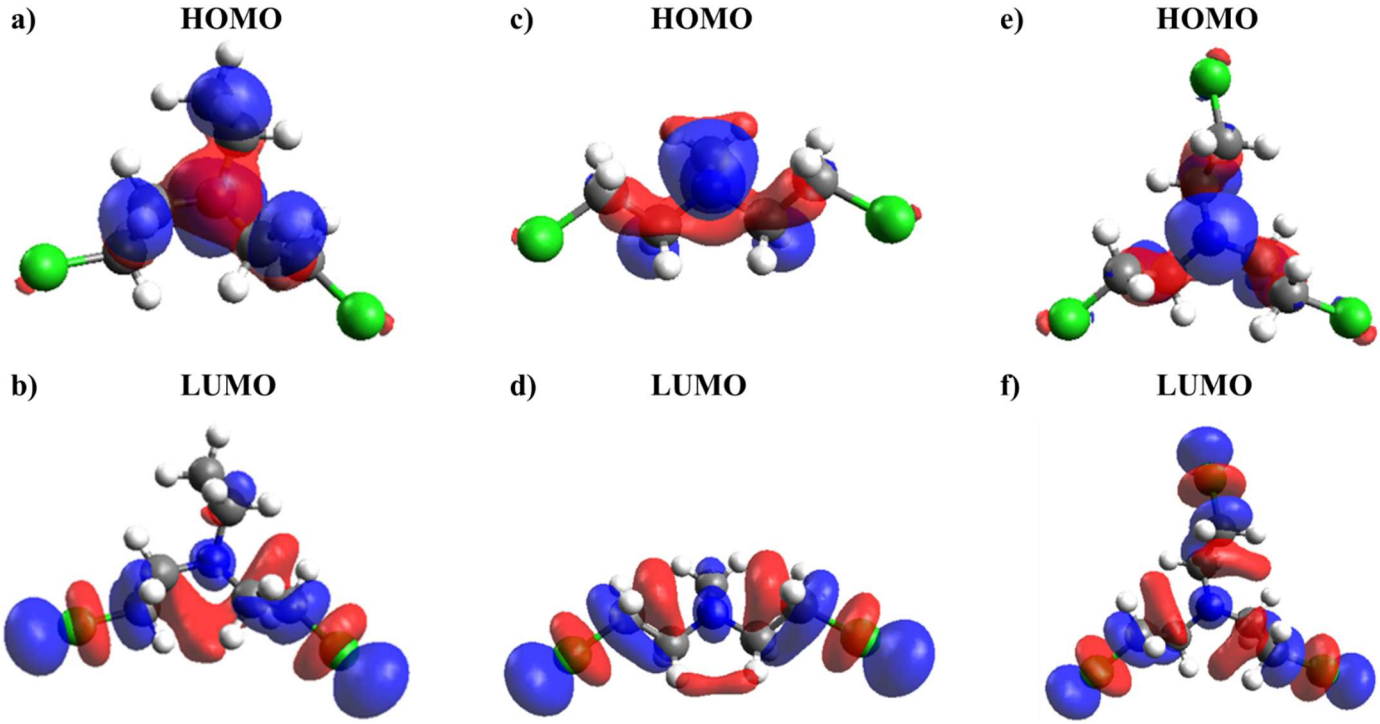

Figure A.47: Graphical representation of the HOMO (a, c, e) and LUMO (b, d, f) molecular orbitals for the nitrogen mustard agents HN1, HN2, and HN3, respectively. All orbitals were calculated at the ωB97XD/6-311++G(2df,pd) level of theory. Red and blue regions represent the positive and negative lobes of the molecular orbitals, respectively.

Table A.31: Summary of the main electronic excitations contributing to the UV-visible spectra of DPGME, HN1, HN2, and HN3 (Figure 70). For each species, the corresponding excitation wavelengths (in nm) and oscillator strengths are reported.

Transition	*Wavelength, λ [nm]*	*Oscillator Strenght*
	DPGME	
HOMO→LUMO	181.2	0.0173
HOMO→LUMO+1	176.1	0.0174
HOMO→LUMO+3	169.5	0.0447
HOMO-1→LUMO+3	161.6	0.0224
HOMO→LUMO+5	157.5	0.0259
	HN1	
HOMO→LUMO	196.0	0.0011
HOMO→LUMO+1	190.4	0.1153
HOMO→LUMO+5	175.2	0.0311
HOMO→LUMO+8	163.8	0.0141
HOMO-1→LUMO	158.0	0.0069
	HN2	
HOMO→LUMO	201.7	0.0008
HOMO→LUMO+1	187.6	0.0693
HOMO→LUMO+3	178.5	0.0344
HOMO-3→LUMO+4	171.7	0.0050
HOMO-4→LUMO	156.2	0.0154
	HN3	
HOMO→LUMO	190.9	0.0039
HOMO→LUMO+1	182.5	0.1037
HOMO→LUMO+3	171.4	0.0125
HOMO→LUMO+7	166.8	0.0149
HOMO-5→LUMO	157.9	0.0138

In contrast to the infrared analysis discussed in Section A.4.2.2, no comparison between the computed and experimental UV-visible spectra could be performed for any of the species studied, due to the absence of relevant data in the literature.

A.4.2.4 CDD Maps and Bader Charges for DPGME / HN2 + ZnO$(10\bar{1}0)$

This Section reports the charge density difference (CDD) isosurfaces and Bader charge values associated with the adsorption of DPGME and HN2 on ZnO$(10\bar{1}0)$ surfaces under different conditions: regular surface, surface with an adsorbed oxygen atom (ZnO + O), and surface with a co-adsorbed dissociated O_2 molecule (ZnO + O_2).

The CDD maps provide a spatial representation of the electronic redistribution upon analyte adsorption, highlighting regions of electron accumulation and depletion at the molecule-surface interface.

Complementarily, the Bader charge analysis offers a quantitative evaluation of electron transfer from the adsorbates to the substrate. These results support the qualitative discussion presented in the main text, Section 4.2.3 and reinforce the interpretation of both analytes as electron donors toward the ZnO$(10\bar{1}0)$ surface.

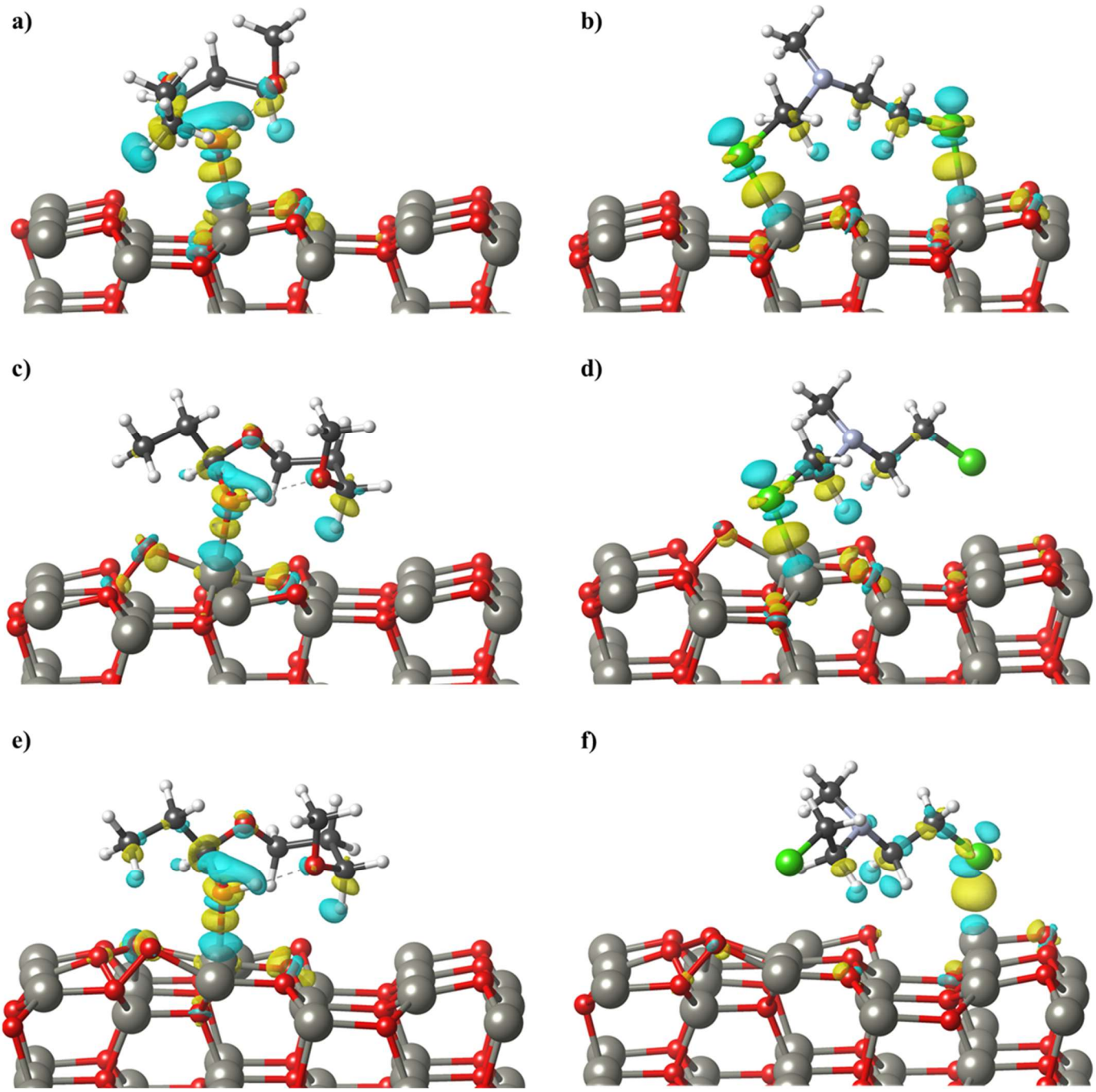

Figure A.48: Graphical representation of the charge density difference (CDD) for the systems: a) DPGME + ZnO($10\bar{1}0$); b) HN2 + ZnO($10\bar{1}0$); c) DPGME + ZnO($10\bar{1}0$) + O; d) HN2 + ZnO($10\bar{1}0$) + O; e) DPGME + ZnO($10\bar{1}0$) + O_2; f) HN2 + ZnO($10\bar{1}0$) + O_2. All CDD were computed using an isosurface level of 0.0080 a.u.^{3}. Regions of electron depletion are shown in blue, whereas regions of electron accumulation are shown in yellow. Atoms color code: Zn = grey; O = red; Cl = light green; C = black; H = white.

In all cases, both electron-rich (yellow) and electron-poor (cyan) regions are observed at the analyte-surface interface.

Table A.32: Bader charge values (in units of elementary charge (*e*) computed for DPGME and HN2 physisorbed on regular and O-enriched ZnO($10\bar{1}0$) surfaces. The analysis quantifies the net electron transfer from the adsorbed molecule to the surface, highlighting the impact of pre-adsorbed oxygen species on the donor-acceptor behavior.

BADER CHARGES			
DPGME	**+ ZnO**	**+ ZnO + O**	**+ ZnO + O_2**
0	0.09	0.06	0.07
HN_2	**+ ZnO**	**+ ZnO + O**	**+ ZnO + O_2**
0	0.16	0.14	0.08

Bader charge analysis supports the fact that DPGME closely mimics the electronic behavior of HN2, providing further theoretical validation of its use as a simulant for this type of CWAs.

References

[1] H. J. Freund, G. Pacchioni, Oxide ultra-thin films on metals: new materials for the design of supported metal catalysts, Chem. Soc. Rev. 2008, 37, 2224-2242

[2] C. T. Campbell, J. Sauer, Surface chemistry in real life: Introduction to special issue on oxide surfaces and interfaces, Chem. Rev. 2013, 113, 3859-3862

[3] E. Salvadori, P. C. Bruzzese, E. Giamello, M. Chiesa, Single Metal Atoms on Oxide Surfaces: Assessing the Chemical Bond through 17O Electron Paramagnetic Resonance, Acc. Chem. Res. 2022, 55, 24, 3706-3715

[4] C. G. Granqvist, Transparent conductors as solar energy materials: A panoramic review, Sol. Energy Mater. Sol. Cells 2007, 91, 1529-1598

[5] K. Ellmer, Past achievements and future challenges in the development of optically transparent electrodes. Nat. Photonics 2012, 6, 809-817

[6] J. Zhang, X. Liu, G. Neri, N. Pinna, Nanostructured materials for room-temperature gas sensors. Adv. Mater. 2016, 28, 795-831

[7] E. Comini, Metal oxide nanowire chemical sensors: innovation and quality of life, Mater. Today 2016, 19, 559-567

[8] D. Barreca et al, Surface Functionalization of Nanostructured Fe_2O_3 Polymorphs: From Design to Light-Activated Applications, ACS Appl. Mater. Interfaces 2013, 5, 15, 7130-7138

[9] E. Fortunato, D. Ginley, H. Hosono, D. C. Paine, Transparent conducting oxides for photovoltaics., MRS Bull. 2007, 32, 242-247

[10] G.D. Parfitt, Surface chemistry of oxides, Colloid and Surface Science 1977, 415-418

[11] S. Muthukrishnan, R. Vidya, A. O. Sjåstad, Illustrating the surface chemistry of nitrogen oxides (NO_x) adsorbed on rutile TiO_2(110) with the aid of STM and AIMD simulation, Catal. Sci. Technol., 2025,15, 1850-1864

[12] G. Tasić, M. Ćurčić, I. Perović, Comparative analysis of physicochemical characteristics of chemical warfare agents and their simulants, Vinča Institute, Univ. of Belgrade (2020)

[13] Z. Liu, X. R. Cheng, Y. M. Yang, H. Z. Jia, B. Q. Bai, L. Zhao, DFT Study of N_2O Adsorption onto the Surface of M-Decorated Graphene Oxide (M = Mg, Cu or Ag). Materials (Basel) 2019, 12(16), 2611

[14] C.-L. Yu et al, Y.-C. Lin, S.-Y. Jhang, J.-D. Fu, Y.-C. Chen, P.-L. Liu, Novel Insights into Surface Energies and Enhanced Gas-Sensing Capabilities of $ZnGa_2O_4$(111) via Ab Initio Studies, Sensors 2025, 25(2), 548

[15] G. Kresse, J. Furthmüller, Efficiency of ab-initio total energy calculations for metals and semiconductors using a plane-wave basis set, Comput. Mater. Sci., 1996, 6, 15-50

[16] G. Henkelman, A. Arnaldsson, H. Jónsson, A fast and robust algorithm for Bader decomposition of charge density, Comput. Mater. Sci., 2006, 36, 354-360

[17] M. E. Tuckerman, Ab Initio Molecular Dynamics: Basic Concepts, Current Trends and Novel Applications, J. Phys. Condens. Matter, 2002, 14, R1297-R1355

[18] A. R. Leach, Molecular Modelling: Principles and Applications, 2nd ed.; Pearson Education: Harlow, 2001

[19] Y. Jiang, C.-H. Xu, G.-Q. Lan, First-principles thermodynamics of metal-oxide surfaces and interfaces: A case study review, Transactions of Nonferrous Metals Society of China, 2013, 23(1), 180-192

[20] C. Noguera, F. Finocchi, J. Goniakowski, First principles studies of complex oxide surfaces and interfaces, J. Phys.: Condens. Matter, 2004, 16, S2509

[21] W. S. Silva, C. Stiehler, E. A. Soares, E. M. Bittar, J. C. Cezar, H. Kuhlenbeck, H.-J. Freund, E. Cisternas, F. Stavale, Hydrogen-induced metallization on the ZnO(0001) surface, Phys. Rev. B 2018, 98, 155416

[22] Y. Paukku, A. Michalkova, J. Leszczynski, Quantum-Chemical Comprehensive Study of the Organophosphorus Compounds Adsorption on Zinc Oxide Surfaces, J. Phys. Chem. C 2009, 113, 4, 1474-1485

[23] P. T. Anastas, J. C. Warner, Green Chemistry: Theory and Practice, Oxford University Press: Oxford, 1998

[24] S. H. Brewer, S. Franzen, Calculation of the electronic and optical properties of indium tin oxide by density functional theory, Chemical Physics, 2004, 300, 285-293

[25] C. G. Granqvist, Transparent conductors as solar energy materials: A panoramic review, Solar Energy Materials & Solar Cells, 2007, 91, 1529-1598

[26] K. Ellmer, Past achievements and future challenges in the development of optically transparent electrodes, Nature Photonics, 2012, 6, 809-817

[27] J. L. Sessler, P. A. Gale, W.-S Cho, Anion Receptor Chemistry, Royal Society of Chemistry: Cambridge, 2006

[28] D. Astruc, Electron-transfer processes in dendrimers and their implication in biology, catalysis, sensing, and nanotechnology, Chem. Rev. 2010, 110, 1857-1959

[29] M. T. Rojas, R. Koeniger, J. F. Stoddart, A. E. Kaifer, Supported Monolayers Containing Preformed Binding Sites. Synthesis and Interfacial Binding Properties of a Thiolated β-Cyclodextrin Derivative, J. Am. Chem. Soc., 1995, 117, 336-343

[30] A. Méndez-Ardoy, T. Steentjes, T. Kudernac, J. Huskens, Self-Assembled Monolayers on Gold of β-Cyclodextrin Adsorbates with Different Anchoring Groups, Langmuir, 2014, 30, 3467-3476

[31] A. H. Abdelhay, A. D. Bani-Yaseen, Recent advances and perspectives of supramolecular host-guest systems for electrochemical energy storage, Materials Today Chemistry, 2024, 40, 102259

[32] T. Ogoshi, T.-A. Yamagishi, Y. Nakamoto, Pillar-shaped macrocyclic hosts pillar[n]arenes: New key players for supramolecular chemistry, Chem. Rev., 2016, 116, 7937-8002

[33] M. Xue, Y. Yang, X. Chi, Z. Zhang, F. Huang, Pillararenes, a new class of macrocycles for supramolecular chemistry, Acc. Chem. Res., 2012, 45, 1294-1308

[34] S. Fa, T. Kakuta, T.-A. Yamagishi, T. Ogoshi, One-, Two-, and Three-Dimensional Supramolecular Assemblies Based on Tubular and Regular Polygonal Structures of Pillar[n]arenes, CCS Chem., 2019, 1, 50-63

[35] N. L. Strutt, H. Zhang, S. T. Schneebeli, J. F. Stoddart, Functionalizing pillararenes, Acc. Chem. Res., 2014, 47, 2631-2642.

[36] Y. Yao, Y. Wang, F. Huang, Synthesis of various supramolecular hybrid nanostructures based on pillar[6]arene modified gold nanoparticles/nanorods and their application in pH- and NIR-triggered controlled release, Chem. Sci. 2014, 5, 4312-4316

[37] C. Tsuneishi, Y. Koizumi, R. Sueto, H. Nishiyama, K. Yasuhara, T.-a. Yamagishi, T. Ogoshi, I. Tomita, S. Inagi, The controlled synthesis of pillar[6]arene-based hexagonal cylindrical structures on an electrode surface via electrochemical oxidation, Chem. Commun., 2017, 53, 7454-7456

[38] H. Roithmeyer, J. Bühler, O. Blacque, I. Tuncay, T. Moehl, **C. Invernizzi**, F. Keller, M. Iannuzzi, S. D. Tilley, The Swiss Army Knife of Electrodes: Pillar[6]arene-Modified Electrodes for Molecular Electrocatalysis Over a Wide pH Range, Angew. Chem. Int. Ed., 2024, e202413144

[39] T. Ogoshi et al, K. Yoshikoshi, R. Sueto, H. Nishihara, T.-A. Yamagishi, Porous Carbon Fibers Containing Pores with Sizes Controlled at the Angstrom Level by the Cavity Size of Pillar[6]arene, Angew.Chem. Int. Ed. 2015, 54, 6466-6469

[40] A. P.-Borbòn, H. Groenbeck, Hydrogen adsorption on In_2O_3(111) and In_2O_3(110)"; Phys. Chem. Chem. Phys., 2020, 22, 16193-16202

[41] L. N. Bai, Y. Wei, J. Lian, Q. Jiang, Stability of indium-tin-oxide and its optical properties: A first-principles study, Journal of Physics and Chemistry of Solids, 74 (2013), 446-451

[42] J. Zhang et al, G. Bai, Y. Xu, W. Wu, Y. Liu, B. Teng, Teaching Practice of Charge Density Difference in Electronic Structure Analysis, University Chemistry, 2022, 37(6), 2107125

[43] R. F. W. Bader, Atoms in Molecules: A Quantum Theory; Oxford University Press: Oxford, 1990

[44] G. Henkelman, A. Arnaldsson, H. Jónsson, A fast and robust algorithm for Bader decomposition of charge density, Comput. Mater. Sci. 2006, 36 (3), 354-360

[45] W. Tang, E. Sanville, G. Henkelman, A grid-based Bader analysis algorithm without lattice bias, J. Phys. Condens. Matter 2009, 21 (8), 084204

[46] T. Lu, F. Chen, Multiwfn: A multifunctional wavefunction analyzer, J. Comput. Chem. 2012, 33, 580-592

[47] G. Kresse, J. Furthmüller, Efficiency of ab-initio total energy calculations for metals and semiconductors using a plane-wave basis set, Comput. Mater. Sci. 1996, 6, 15-50

[48] D. Barreca et al, Functional Nanosystems for the Detection of Chemical Warfare Agents and Their Simulants: From Materials Design to Sensing Mechanisms, Advanced Materials Interfaces 2022, 9 (7), 2102525.

[49] S. Chauhan, S. Chauhan, R. D. Cruz, S. Faruqi, K. K. Singh, S. Varma, M. Singh, V. Karthik, Chemical warfare agents, Environ. Toxicol. Pharmacol. 2008, 26, 113

[50] K. Ganesan, S. K. Raza, R. Vijayaraghavan, Chemical warfare agents, J. Pharm. Bioallied Sci. 2010, 2 (3), 166-178

[51] S. Mukhopadhyay, M. Schoenitz, E. L. Dreizin, Vapor-phase decomposition of dimethyl methylphosphonate (DMMP), a sarin surrogate, in presence of metal oxides, Defence Technology 2021, 17(4) 1095-1114

[52] M. Grabka, Z. Witkiewicz, K. Jasek, K. Piwowarski, Acoustic Wave Sensors for Detection of Blister Chemical Warfare Agents and Their Simulants, Sensors 2022, 22, 5607

[53] N. Yamazoe, New approaches for improving semiconductor gas sensors, Sens. Actuators B Chem. 1991, 5, 7-19

[54] R. Leturcq, R. Bhusari, E. Barborini, Physical mechanisms underpinning conductometric gas sensing properties of metal oxide nanostructures, Advances in Physics: X, 2022, 7(1)

[55] E. Comini, G. Faglia, G. Sberveglieri, Z. Pan, Z. L. Wang, Stable and Highly Sensitive Gas Sensors Based On Semiconducting Oxide Nanobelts, Applied Physics Letters, 81, 2002, 869-1871

[56] S. Diodati, J. Hennemann, F. Fresno, S. Gialanella, P. Dolcet, U. Lavrenčič Štangar, B.M. Smarsly, and S. Gross, “Easy and Green Route towards Nanostructured ZnO as an Active Sensing Material with Unexpected H2S Dosimeter-Type Behaviour,” European Journal of Inorganic Chemistry 2019, 6, 837-846

[57] D. Degler, U. Weimar, N. Barsan, Current Understanding of the Fundamental Mechanisms of Doped and Loaded Semiconducting Metal-Oxide-Based Gas Sensing Materials, ACS Sens. 2019, 4, 9, 2228-2249

[58] J. Zhang, Z. Qin, D. Zeng, C. Xie, Metal-oxide-semiconductor based gas sensors: screening, preparation, and integration, Phys. Chem. Chem. Phys., 2017,19, 6313-6329

[59] A. Gurlo, Interplay between O_2 and SnO_2: Oxygen Ionosorption and Spectroscopic Evidence for Adsorbed Oxygen, ChemPhysChem 2006, 7, 2041-2052

[60] D. Zappa et al, "Metal oxide-based heterostructures for gas sensors"- A review, Anal Chim Acta. 2018, 1039, 1-23

[61] M. Liangruksa et al, P. Sukpoonprom, A. Junkaew, W. Photaram, C. Siriwong, Gas sensing properties of palladium-modified zinc oxide nanofilms: A DFT study, Applied Surface Science, 2021, 544, 148868

[62] L. Bigiani et al, D. Zappa, D. Barreca, A. Gasparotto, C. Sada, G. Tabacchi, E. Fois, E. Comini, C. Maccato, Sensing Nitrogen Mustard Gas Simulant at the ppb Scale via Selective Dual-Site Activation at Au/Mn_3O_4 Interfaces, ACS Appl. Mater. Interfaces 11, 23692, (2019)

[63] R. G. Pearson, Electronic Spectra and Chemical Reactivity, J. Am. Chem. Soc. 1988, 110, 2092

[64] K.-H. Yun, K.-Y. Yun, G.-Y. Cha, B. H. Lee, J. C. Kim, D.-S. Lee, J.-S. Huh, Gas Sensing Characteristics of ZnO-doped SnO_2 Sensors for Simulants of the Chemical, Agents. Mater. Sci. Forum 2005, 486, 9

[65] G. Eranna, B. C. Joshi, D. P. Runthala, R. P. Gupta, Oxide Materials for Development of Integrated Gas Sensors - A Comprehensive Review, Crit. Rev. Solid State Mater. Sci. 2004, 29, 111-188

[66] N. Barsan, U. Weimar, Conduction model of metal oxide gas sensors, J. Electroceram. 2001, 7, 143-167

[67] R. Tsyshevsky, S. Holdren, B. W. Eichhorn, M. R. Zachariah, M. M. Kuklja, Sarin Decomposition on Pristine and Hydroxylated ZnO: Quantum Chemical Modeling, J. Phys, Chem. C 2019, 123, 26432

[68] P.E. Blöchl, O. Jepsen, and O.K. Andersen, Improved tetrahedron method for Brillouin-zone integrations, Phys. Rev. B 49(23), 16223-16233 (1994)

[69] M. Kawamura, Y. Gohda, and S. Tsuneyuki, Improved tetrahedron method for the Brillouin-zone integration applicable to response functions, Phys. Rev. B 89(9), 094515 (2014)

[70] E. Fois, C. Maccato, D. Barreca, **C. Invernizzi**, and G. Tabacchi, Impact of -OH surface defects on the electronic and structural properties of nickel oxide thin films, Dalton Transactions 54(7), 2765-2775 (2025)

[71] X. Yang, X. Liu, N. Zhao, X. Chang, W. Zheng, and J. Zhang, Beyond conventional sensing paradigms: Multiscale analysis of conductivity-type switching in semiconductor gas sensors, Coordination Chemistry Reviews 549, 217286 (2026)

[72] Y. Liu, H. Zhang, Z. Zhang, Y. Xie, and E. Xie, Conversion of p-type to n-type conductivity in undoped ZnO films by increasing operating temperature, Applied Surface Science 257(4), 1236-1238 (2010)

[73] R.-C. Wang, Y.-X. Lin, and J.-J. Wu, Intrinsic n- and p-Type MgZnO Nanorods for Deep-UV Detection and Room-Temperature Gas Sensing, J. Phys. Chem. C 119(52), 29186-29192 (2015)

[74] C.-J. Chang, S.-T. Hung, C.-K. Lin, C.-Y. Chen, and E.-H. Kuo, Selective growth of ZnO nanorods for gas sensors using ink-jet printing and hydrothermal processes, Thin Solid Films 519(5), 1693-1698 (2010)

[75] D. Barreca, C. Maccato, and A. Gasparotto, Metal Oxide Nanosystems As Chemoresistive Gas Sensors for Chemical Warfare Agents: A Focused Review, Advanced Materials Interfaces 9(14), 2102525 (2022)

[76] M. Yadav, M. Kumar, S. Chaudhary, K. Yadav, and A. Sharma, "A Review on Chemiresistive Hybrid Zinc Oxide and Nanocomposites for Gas Sensing," Ind. Eng. Chem. Res. 62(29), 11259-11278 (2023)

[77] T. D. Kühne, M. Iannuzzi et al, CP2K: an electronic structure and molecular dynamics software package - quickstep: efficient and accurate electronic structure calculations, J. Chem. Phys., 2020, 152, 194103

[78] J. P. Perdew, K. Burke, M. Ernzerhof, Generalized Gradient Approximation Made Simple, Phys. Rev. Lett., 1996, 77, 3865-3868

[79] R. Sabatini, T. Gorni, S. De Gironcoli, Nonlocal van der Waals density functional made simple and efficient, Phys. Rev. B, 2013, 87, 041108

[80] J. VandeVondele, J. Hutter, Gaussian basis sets for accurate calculations on molecular systems in gas and condensed phases, J. Chem. Phys., 2007, 127, 114105

[81] S. Goedecker, M. Teter, J. Hutter, Separable dual-space Gaussian pseudopotentials, Phys. Rev. B, 1996, 54, 1703-1710

[82] Materials Project, In_2O_3; database version v2023.11.1, can be found under https://nextgen.materialsproject.org/materials/mp-22598, 2023 (accessed 22.05.24)

[83] A. H. Larsen et al, The atomic simulation environment-a Python library for working with atoms, J. Phys. Condens. Matter, 2017, 29, 273002

[84] S. M. Gericke et al, Effect of Different In2O3 (111) Surface Terminations on CO_2 Adsorption, ACS Appl. Mater. Interfaces, 2023, 15, 45367-45377

[85] S. Kumari, P. Sautet, Highly dispersed Pt atoms and clusters on hydroxylated indium tin oxide: a view from first principles calculations, J. Mater. Chem. A, 2021, 9, 15724-15733

[86] J. Harrel, M. Acikgoz, H. L. Sasson, I. V.-Fisher, A. Genova, M. Pavanello, Models of Surface Morphology and Electronic Structure of Indium Oxide and Indium Tin Oxide for Several Surface Hydroxylation Levels, J. Phys. Chem. C, 2018, 122, 584-595

[87] A. Fattahi et al, P. Koohsari, M. S. Lakmehsari, K. Ghandi, The Impact of the Surface Modification on Tin-Doped Indium Oxide Nanocomposite Properties, Nanomaterials 2022, 12, 155

[88] R. F. W. Bader, A quantum theory of molecular structure and its applications, Chem. Rev. 1991, 91, 893-928

[89] T. Ogoshi, R. Sueto, K. Yoshikoshi, T.-a. Yamagishi, One-dimensional channels constructed from per-hydroxylated pillar[6]arene molecules for gas and vapour adsorption, Chem. Commun., 2014, 50, 15209-15211

[90] J. G. Brandenburg, M. Alessio, B. Civalleri, M. F. Peintinger, T. Bredow, S. Grimme, Geometrical Correction for the Inter- and Intramolecular Basis Set Superposition Error in Periodic Density Functional Theory Calculations, J. Phys. Chem. A 2013, 117, 9282-9292

[91] S. Kim et al, PubChem in 2023: new data content and improved web interfaces, Nucleic Acids Res. 2023, 51(D1), D1373-D1380

[92] Reaxys®, Elsevier, www.reaxys.com

[93] M. D. Hanwell et al, D. E. Curtis, D. C. Lonie, T. Vandermeersch, E. Zurek, G. R. Hutchison, Avogadro: An Advanced Semantic Chemical Editor, Visualization, and Analysis Platform. J. Cheminform. 2012, 4, 17

[94] J.-D. Chai and M. Head-Gordon, Long-range corrected hybrid density functionals with damped atom–atom dispersion corrections, Phys. Chem. Chem. Phys., 2008, 10, 6615-6620

[95] M. J. Frisch, et al, GAUSSIAN 09 (Revision B.01), Gaussian, Inc., Wallingford CT, 2009

[96] C. Møller and M. S. Plesset, Note on an approximation treatment for many-electron systems, Phys. Rev. 1934, 46, 618-622

[97] T. Yanai, D. P. Tew and N. C. Handy, A new hybrid exchange-correlation functional using the Coulomb-attenuating method (CAM-B3LYP), Chem. Phys. Lett., 2004, 393, 51-57

[98] P. Giannozzi et al, QUANTUM ESPRESSO: A Modular and Open-Source Software Project for Quantum Simulations of Materials, J. Phys.: Condens. Matter, 21, 395502, (2009)

[99] J. P. Perdew, K. Burke, M. Ernzerhof, Generalized Gradient Approximation Made Simple, Phys. Rev. Lett. 77, 3865, (1996)

[100] S. Grimme, S. Ehrlich, L. Goerigk, Effect of the damping function in dispersion corrected density functional theory, Journal of Computational Chemistry, 32, 1456, (2011)

[101] Kevin F. Garrity, Joseph W. Bennett, Karin M. Rabe, and David Vanderbilt, GBRV high-throughput pseudopotentials site, https://www.physics.rutgers.edu/gbrv/

[102] Q.-L. Tang, and Q.-H. Luo, Adsorption of CO_2 at ZnO: A Surface Structure Effect from DFT+U Calculations, J. Phys. Chem. C, 117(44), 22954-22966 (2013)

[103] J. Hubbard, Electron correlations in narrow energy bands, Proc. R. Soc. Lond. A 1963, 276, 238-257

[104] V. I. Anisimov, F. Aryasetiawan, A. I. Lichtenstein, First-principles calculations of the electronic structure and spectra of strongly correlated systems: the LDA+U method, J. Phys.: Condens. Matter 1997, 9, 767-808

[105] S. L. Dudarev, G. A. Botton, S. Y. Savrasov, C. J. Humphreys, A. P. Sutton, Electron-energy-loss spectra and the structural stability of nickel oxide: An LSDA+U study, Phys. Rev. B 1998, 57, 1505-1509

[106] D. G. Gonzalez, R. Palai, J. P. Velev, First principle calculation of the electronic structure and optical properties of ZnO and Al:ZnO, MRS Communications, 14, 1388, (2024)

[107] P.E. Blöchl, Projector augmented-wave method, Phys. Rev. B 50(24), 17953-17979 (1994)

[108] L. González, O. Mó, M. Yáñez, High level ab initio and density functional theory studies on methanol-water dimers and cyclic methanol(water)$_2$ trimer, J. Chem. Phys. 109, 139-150 (1998)

[109] A. Erba et al, C. Pisani, S. Casassa, L. Maschio, M. Schütz, D. Usvyat, MP2 versus density-functional theory study of the Compton profiles of crystalline urea, Phys. Rev. B 2010, 81, 165108

[110] C. H. Suresh, G. S. Remya, P. K. Anjalikrishna, Molecular Electrostatic Potential Analysis: A Powerful Tool to Interpret and Predict Chemical Reactivity, WIREs Comput. Mol. Sci. 2022, 12, e1601

[111] Computational Chemistry Comparison and Benchmark DataBase, Standard Reference Database,101 National Institute of Standards and Technology

– Conclusions –

This Thesis has explored a series of distinct aspects all related to functional nanomaterials: molecular fragmentation, encapsulation in confined nanospaces, and surface adsorption. Despite the differences in the explored chemical systems, theoretical models, and target applications, the presented case studies are unified by a common rationale: control at the molecular scale determines the structure and function of the investigated nanomaterial. Using first-principles methods, primarily Density Functional Theory (DFT), its time-dependent extension (TD-DFT), and its periodic implementations, the work demonstrates how molecular structure, electronic behavior, and chemical surrounding (*e.g.*, the solvent) can be quantitatively analyzed to understand diverse aspects of materials science. The goal of this concluding part is to consolidate the scientific outcome of the Thesis, establishing connections between the individual cases and evaluating the broader implications of the computational results.

Each Chapter has addressed a chemically different system.

In Chapter 2, nickel(II) β-diketonate-TMEDA precursors for chemical vapor deposition (CVD) processes adopted for the fabrication of nickel oxide nanostructures were investigated by modeling their gas-phase structure. This work was integrated by investigating the precursors' interaction with water vapor, in order to understand some favorable water-induced features observed in the NiO nanofilm growth in the CVD processes. While it is experimentally very difficult to study at the atomistic level the fate of the precursors in the CVD reactors, it is a widespread practice to gather information on precursor fragmentation via MS-based experiments. In these cases, however, only the fragment masses are available. In this scenario, the fragments' structure was investigated by testing plausible molecular geometries compatible with the experimentally obtained fragment masses. DFT calculations suggest that the fragmentation process could be driven by a sequential redistribution of electron density from the β-diketonate ligands toward the Ni(II) center. This tendency is further enhanced in subsequent fragmentation steps, resulting in the formation of a cation-π interaction involving the Ni center and a C=C double bond in the investigated final fragments. Comparison with ESI-HRMS and MS/MS experimental data validated the computational predictions and supported the identification of key dissociation pathways. The study highlights how molecular-level descriptors, such as bond strengths, charge distribution, and coordination geometry, may suggest the decomposition behavior of the precursors. In the final Section, periodic slab models of NiO(100) were used to simulate the structural features of the resulting oxide nanomaterial and the effect of surface hydroxylation. It has been found that type and concentration of -OH defects play a key role in determining the surface electronic properties and behaviour. The surface reconstructions evidenced at high surface density of defects, exposing under-coordinated Ni sites, might contribute to the reactivity of NiO-based nanomaterials in processes relevant for *e.g.* heterogeneous catalysis.

Chapter 3 shifted the focus to supramolecular organization within confined nanospaces. In this part, a fluorescent dicationic dye (MDAP) encapsulated in a zeolite L channel was studied as a nanosensor for neurotransmitter recognition. In particular, the serotonin neurotransmitter has

been investigated in detail. Periodic DFT and TD-DFT calculations were adopted for the study of the nanosensor structural organization and of the electronic properties of the confined complex respectively. Ab initio molecular dynamics (AIMD) simulations provided finite temperature structures that allowed for the study of the electronic excitation spectra averaged over a room-temperature trajectory. Such an approach enabled to understand at the microscopic level the origin of the UV-vis signature of the serotonin presence, *i.e.* the appearance of a visible-range charge-transfer (CT) band. This spectroscopic signal is due to a HOMO-LUMO transition from serotonin to MDAP, corresponding to a charge-transfer transition from a monocationic to a dicationic species. The CT signal presents higher intensity values exclusively in configurations sampled from the AIMD trajectory where serotonin and MDAP are in close proximity and separated by no more than one water molecule. In other words, upon serotonin encapsulation, the host-guest complex undergoes a supramolecular reorganization that enables this charge-transfer interaction, resulting in a new, guest-guest interaction-induced absorption band. Finally, this work demonstrates how confinement can modulate both geometry and charge distribution, enabling selective optical response and enhancing molecular recognition at the nanoscale. The combination of static and dynamic models provides a powerful strategy to assess the optical functionalities of hybrid nanosystems under realistic room-temperature conditions.

In Chapter 4, molecular adsorption on semiconductor surfaces was investigated. First, attention has been focused on a case where molecular adsorption can transform a bare oxide surface in a sensing device. Indeed, in Section 4.1, the covalent anchoring of a Pillar[6]arene macrocycle onto indium oxide (In_2O_3) and indium-tin oxide (ITO) surfaces was investigated via two distinct models: one based on proton transfer and the other one on water elimination. Between them, the latter emerged as the most energetically and structurally favorable mechanism, enabling the formation of stable covalent bonds between the organic host and the metal oxide surface. Charge density difference (CDD) maps and Bader charge analysis confirmed the formation of covalent bonds between the surface oxygen atoms and the carbon atoms of Pillar[6]arene, accompanied by a localized accumulation of electron density at the anchoring sites. Notably, in the ITO surface, the presence of Sn dopants contributes to the stabilization of the hybrid interface compared to pure In_2O_3. The second case study, presented in section 4.2, consisted in a computational investigation on a Chemical Warfare Agent (CWA) and its simulant. First, both the CWA and the simulant were studied in vacuum. Subsequently, the adsorption of these species on ZnO$(10\bar{1}0)$ surfaces was investigated via periodic DFT studies adopting slab models. Despite their different functional groups and geometries, both CWA and its simulant exhibit similar HOMO-LUMO energy gaps. Upon adsorption on both regular and O-enriched ZnO surfaces, charge density difference (CDD) analysis showed that both species act as electron donors, transferring electron density to the surface. This electron transfer is accompanied by modifications in the density of states (DOS), from which a prototype model for the sensing mechanism can be proposed. These findings suggest that surface-induced electronic perturbations, driven by molecular adsorption and modulated by surface composition, play a central role in the chemiresistive response of ZnO-based nanosensors towards CWAs and related compounds.

A comparative analysis of the studied systems highlights key similarities and differences in the mechanisms through which molecular-level control is exerted, the observables used to characterize structure and function, and the specific chemical surrounding factors, such as gas-phase conditions, spatial confinement, or surface composition, that most critically influence the system's behavior.

In this context, regarding the molecular fragmentation described in Chapter 2, control is achieved through the electronic and structural features of the β-diketonate ligands, which dictate the strength of the metal-ligand bonds that lead to specific fragment structures. The structure of the pristine precursors was modeled under dry conditions and in the presence of water vapor, simulated by introducing water molecules, in order to evaluate their promoting effect on the film growth experimentally detected. Concerning the fragments' stability, DFT calculations indicate how charge redistribution, electronic stabilization, and ligand rearrangements may help to rationalize the structure of fragments obtained experimentally, thus providing a molecular-level rationale for precursor reactivity and efficiency in CVD processes.

In the supramolecular confinement problem discussed in Chapter 3, molecular control originates from the combined effect of the zeolite L channel, its framework charge, and the water molecules inside it. Indeed, the nanoporous framework imposes spatial and electrostatic constraints that stabilize the organization of the encapsulated species, while water plays a pivotal role in mediating their mutual interactions. Within this confined environment, the presence and arrangement of a few water molecules help two positively charged species, serotonin and MDAP, to stay close together, a condition unattainable in the gas phase or in bulk solution. This unique confinement-induced stabilization allows the charge-transfer (CT) transition, whose intensity and wavelength depend on both the number and the position of water molecules as well as on the geometric features of the zeolite channel. To capture both structural and dynamical effects, the system was investigated through a combination of TD-DFT and AIMD simulations, which together elucidate how confinement and hydration cooperate in controlling the optical response and selectivity of the resulting nanosensor.

In the molecular adsorption cases examined in Chapter 4, molecular-level control operates at the interface between the adsorbate and the metal oxide surface. The nature and strength of the interaction, ranging from weak physisorption to covalent bonding, are governed by the local surface composition, including the presence of hydroxyl groups, oxygen adatoms, or dopant atoms such as Sn. These interfacial features modulate both the thermodynamic stability of the adsorbed complex and the electronic properties of the resulting hybrid system. The environment is modeled as a heterogeneous solid surface, with explicitly introduced defects and compositional variations to mimick realistic adsorption sites. DFT simulations provide detailed insight into the anchoring geometry, interfacial charge redistribution, and spectroscopic signals, allowing for the identification of structure-property relationships that underpin sensing activity and electronic modulation in the final nanomaterial.

The computational results obtained have not only supported the interpretation of experimental observations, but have also offered access to atomistic-level details that would be challenging to obtain through experimental methods only. It is important to acknowledge, however, that

all quantum chemistry methods rely on specific approximations. The accuracy of the computed results may be influenced by the choice of the level of theory, or the structural model adopted. Nevertheless, within the scope of the present study, these methods have proven adequate to provide chemically consistent and physically meaningful insight into systems of increasing complexity.

– Ringraziamenti –

Desidero esprimere la mia più sincera e profonda gratitudine alla Prof.ssa Gloria Tabacchi ed al Prof. Ettore Fois, punti di riferimento costanti lungo tutto il mio percorso accademico, dalla laurea triennale fino al dottorato. Al di là dei ruoli puramente formali, ho sempre considerato entrambi come guide fondamentali del mio cammino. Da loro non ho soltanto appreso ciò che so nell'ambito della chimica computazionale, ma ho ricevuto anche insegnamenti che vanno ben oltre la dimensione scientifica, lasciando un segno duraturo nel mio modo di pensare ed affrontare la vita. A loro va un ringraziamento speciale.

Un ringraziamento colmo di affetto va ai miei genitori, Giampiero e Luisella, che mi hanno sostenuto in ogni fase di questo percorso, senza mai farmi mancare il loro supporto, la loro fiducia e la loro presenza.

Desidero ringraziare anche Mauro, Paola e Salvatore, da lungo tempo parte integrante della mia famiglia, per il costante sostegno e la sincera vicinanza.

Un pensiero particolarmente sentito è rivolto a mia nonna Gianna. Sebbene non sia più qui, il suo sostegno ha accompagnato ogni fase del mio percorso di studi: dai pomeriggi trascorsi ad ascoltarmi con pazienza fino ai traguardi raggiunti. A lei è dedicata una parte di questo lavoro, così come, idealmente, tutti i risultati che ho conseguito.

Ringrazio tutti gli amici che mi sono stati accanto durante questi anni. In particolare, Luca, per me molto più di un amico, ed i ragazzi di Vivicivico, che mi hanno aiutato a comprendere il valore autentico delle cose importanti, regalandomi leggerezza, sorrisi ed una prospettiva più ampia.

Un sincero grazie va anche ai colleghi incontrati lungo il percorso universitario - Emanuele, Luca, Simone, Matteo, Eddy, Nello, Jessica, Isabella, Martina, Hamed e Stefano - ed a molti altri che, pur non citati esplicitamente, porto con me nel ricordo. Con loro ho condiviso non solo momenti di lavoro, ma anche risate, difficoltà e frammenti di vita che hanno reso questo cammino più umano e meno solitario.

Infine, ma non per importanza, Giulia, la mia compagna di vita. A te, che mi sei stata accanto nei momenti più difficili, che mi hai visto cadere e rialzarmi più volte senza mai smettere di crederci, che mi hai sostenuto con una dedizione totale e silenziosa, dedico questo lavoro e questo traguardo così importante. Semplicemente, grazie.